ISBN : 978-625-00-1057-0

ISC '22

2'nd International Symposium on Characterization

www.jcharacterization.com

2'nd INTERNATIONAL SYMPOSIUM ON CHARACTERIZATION ISC'22

PROCEEDINGS BOOK

22 - 25 September 2022

JOURNAL OF CHARACTERIZATION

Afyonkarahisar Türkiye

ISC'22
2'nd International Symposium on Characterization
Designed by Soner Savaş

==========

2nd INTERNATIONAL SYMPOSIUM on CHARACTERIZATION

PROCEEDINGS Book

ISBN: 978-625-00-1057-0

EDITORS

Prof. Dr. Atilla Evcin

Prof. Dr. Ibrahim Gunes

Dr. Ferit Artkın

Publication Date: 15.12.2022

CONTENTS

CONTENTS 3
INVITED SPEAKERS 8
SCIENTIFIC COMMITTEE 18
ORGANIZING COMMITTEE 20
Mikro-sulama Sistemi Lateral Boru Unitelerinin Hidrolik Tasarımında Analitik ve Nümerik Hesap Metotlarının Karşılaştırmalı Analizi 22
Farklı Cam Elyaf Oranlarına Sahip POM Malzemesinin Digimat ile Karakterizasyonu ve Yataklama Elemanı Üzerindeki Etkisinin İncelenmesi 35
Back-Step Computation Procedure for Evaluating Minor Pressure Loss Components along Laterals Equipped with Integrated In-Line and On-Line Emitters 44
Çok Cidarlı Karbon Nanotüp Takviyeli Poliüretan Kompozitlerin Eğilme Dayanımı 63
Determination of Steel Strand Effect on Dynamic Parameters of Composite Structure 70
Doğaltaş Üretim Tesisleri Atık Granit Tozunun Beton Katkı Maddesi Olarak Kullanılabilirliğinin İncelenmesi 81
Elektrokimyasal Empedans Spektroskopisi Yöntemi ile Çeşitli Malzemelerin Karakterizasyonu 88
Atık Cam ve Deniz Kabuklarından Cao-Al2o3-Sio2 (Cas) Esaslı Seramiklerin Üretim İmkânlarının Araştırılması Ve Özelliklerinin İncelenmesi 93
Viskoelastik Polimerik Köpük (Rtv-2) Çekirdekli Alüminyum Sandviç Panellerin Basma Davranışlarının İncelenmesi 101
The Use Of Solar Energy In The Profile Of Prefabrication And Its Effect On The Behavior And Durability Of Concrete 111
Tek Bir Banyodan Elektro Depolama Yöntemi İle Elde Edilen Ni-W Ve Ni-W/Hbn Kaplamalarının Karşılaştırılması 115
Variation of Design Parameters for Micro-irrigation System Subunit Laterals by Using *LATCAD* .. 137
İnşaat Sektöründe Yeni Bir Yalıtım Malzemesinin Geliştirilmesi 152
Investigation of Shear Wall Effect on Dynamic Parameters of Reinforced Concrete Building 156
Mineral Katkılı Betonların Fiziksel Özellikleri 166
Power Law Friction Factor Equation for Commercial Pipeline 170
Hydraulic Design Accounting Local Pressure Losses Using *MathCAD* 170
Enantiyoselektif Michael Reaksiyonu İçin Diazadioksokaliks[2]Aren[2]Triazin Bazlı Kiral Organokatalizörler 187
Comparative study on TiAlN and TiCN Coatings Tribological Performance for Dental Implant Drills 196

2343 Kodlu Çelik Dökümü Sonrası Atık Haline Gelen Hassas Döküm Kumunun Şamot Refrakter Üretiminde Kullanımı 204

An Internet of things for Data security using Artificial Intelligence 224

Axial Dynamics of Elastic Deformable Supported Nonlocal Rods Using A Higher-Order Nonlocal FEM 233

Cape Town, Güney Afrika'dan toplanan atık kehribar renkli şişe camları üzerinde karakterizasyon çalışmaları 242

Nonlocal Natural Frequencies of Shear Deformable Functionally Graded Nanobeams Via Nonlocal FEM 249

Portland Çimentolu Alternatif Polipropilen Elyaf Katkılı Beton 261

Requirements for specialists in the Industry 4.0 environment: problems and solutions 265

Effect of Silane Treatment on the Mechanical Properties of Cellulose Nanocrystal (CNC) Based Polymer Composites 269

About intelligent software system and development method for the intelligent interface 275

Susuz Boraks Katkısının Alüminyum Malzemelerin Vickers Sertlik ve İz Modülü Değerlerine Etkisinin İncelenmesi ve Eniyilenmesi 278

The Effect of Steel Strip on Dynamic Parameters of Steel Structure 289

The effect of an aluminum alloy on its fluidity when alloyed with a lithium-fluorine-containing compound 299

Çimento Fabrikası Emisyon Ölçümlerinde Ölçüm Belirsizlikleri İçin Yeni Yaklaşımlar 304

The Effect of Stud Walls on Dynamic Characteristics of Steel Building 313

Borlu Çimento Harçlarının Fizikomekanik Özellikleri 324

Production of Antibacterial Powders 328

Fabrication of Durable Hydrophobic coating on Glass Substrate 334

Microstructural Investigations In Increasing The Durability Of Cold Forging Dies (U8 Steel) By The Method Of Double Heat Treatment 337

Investigation of Deformation Induced Martensitic Transformation and Powder Morphology of 304 Stainless Steel as a Function of Milling Time 343

Antibacterial and Hydrophobic TiO2 coating on wall tiles by the sol-jel method 351

Controlled Drug Release with Diatomite 357

Influence of zinc borate and borax decahydrate on the flame retardancy of polymer composite 362

Improvements in Characterization of Pozzolanic Cement Mortars After Different Grinding Methods 366

Preliminary Investigation of the Use of Magnesium Slag as a New Cement Replacement Pozzolan 383

Coating of Glass Substrate with Luminescent Powder Added Silicone Polymer 394

Sol-jel Yöntemiyle Kumaşların Antibakteriyel Kaplanması 399

Symposium Pictures 403

SPONSORS 412

Dear 2nd International Symposium on Characterization attendees,

We successfully completed the 2nd International Symposium on Characterization in the last week of September. We had a great time in Afyonkarahisar with our participants and sponsors. We wanted to send a thank you for the wonderful connections made, the good memories and the moments shared.

Thank you for all your excellent work!

It was a great pleasure to meet you face to face in the second symposium. Despite minor mistakes, we achieved a great success with 52% foreign participation. Nearly 200 researchers contributed to this event with very interesting presentations, posters and discussions.

I would like to thank the international scientific and organizing committees for giving structure to the program and organizing the second symposium.

I would like to thank all the sponsors for their generosity and interest in the conference.

Now let me talk about the people who made great contributions to the symposium. Soner Savaş was very helpful with his original ideas, logo design and knowledge. He designed the graphic style of the symposium. İsmail Yıldız helped with the social media contacts and announcements. Special thanks to the Engineering Faculty students at the symposium table for their support. They coordinated the zoom meetings during the symposium. Ferit Artkın took part in the preparation of the program book and summary book.

As the organizing committee, we thank you for all your great scientific contributions and scientific interaction. We look forward to your participation and support at the symposium we will organize next year in Antalya/Türkiye.

Thank you to our friends who expressed their satisfaction during and after the symposium for being so positive!

Prof. Dr. Atilla Evcin Prof. Dr. Ibrahim Güneş Dr. Yasemin Tabak

Değerli 2nd International Symposium on Characterization katılımcıları

Eylül ayının son haftasında 2. International Symposium on Characterization başarıyla tamamladık. Katılımcılarımız, sponsorlarımızla birlikte Afyonkarahisarda harika zaman geçirdik. Kurulan harika bağlantılar, yaşanan güzel anılar ve paylaşılan dakikalar için bir teşekkür göndermek istedik.

Tüm mükemmel çalışmalarınız için teşekkür ederiz!

Sempozyumun ikincisinde sizlerle yüzyüze karşılaşmaktan büyük bir mutluluk duyduk. Ufak tefek hatalara rağmen % 52 yabancı katılımıyla büyük bir başarı elde ettik. 200 e yakın araştırmacı, bu etkinliğe çok ilginç sunumlar, posterler ve tartışmalarla katkıda bulundu.

Programa yapı kazandırdıkları ve sempozyumumuzun ikincisini organize ettikleri için uluslararası bilimsel ve organizasyon komitelerine çok teşekkür ederim.

Tüm sponsorlara konferansa gösterdikleri cömertlik ve ilgiden dolayı teşekkür ederim.

Şimdi sempozyuma büyük katkıları olan kişilerden bahsedeyim. Soner Savaş özgün fikirleri, logo tasarımı ve bilgisi ile çok yardımcı oldu. Sempozyumun grafik stilini tasarladı. Sosyal medya ile temas ve duyurularda İsmail Yıldız yardımcı oldu. Sempozyum masasında görevli Mühendislik Fakültesi öğrencilerine, destekleri için özellikle teşekkür ederiz. Sempozyum sırasında zoom toplantılarını koordine ettiler. Program kitabı ve özet kitabının hazırlanmasında Ferit Artkın görev aldı.

Organizasyon komitesi olarak sizlere, tüm büyük bilimsel katkılarınız ve bilimsel etkileşim için teşekkür ediyoruz. Seneye Antalya'da düzenleyeceğimiz sempozyumda sizlerin katılımını ve desteklerini bekliyoruz.

Sempozyum sırasında ve sonrasında memnuniyetini bildiren dostlarımıza bu kadar pozitif olduğunuz için teşekkürler!

Prof. Dr. Atilla Evcin Prof. Dr. Ibrahim Güneş Dr. Yasemin Tabak

INVITED SPEAKERS



Fayaz Hussain joined the department of Materials Engineering in 2007, first as a Lecturer, then after Assistant Professor in 2010 and promoted as an Associate Professor in 2020. Prior to this, he worked three years in metal industry. He is also editorial board member of journals of "Frontiers in Materials" and "Electroactive Materials". He has completed his PhD from the University of Sheffield, England, UK, in 2016-2017, worked on "KNN based lead-oxide free piezoelectric ceramics". This ABO3 system has been studied from the perspective of optimizing its performance for multilayer actuators; potentially for energy harvesting applications under the supervision of Professor Ian Reaney at the University of Sheffield. To fabricate the multilayers, a novel Wet-Multilayer-Method (WMM) was also developed to overcome the issues of delamination during firing of multilayers actuators. He has authored/co-authored publications in well reputed journals, around 30 papers including key articles on piezoelectric, capacitor and microwave dielectric ceramics in bulk and multilayers with 238-citations, h-index 8 and i10-index 6 of last five years. Current research interests: ynthesis of Piezoelectric Ceramics and their multilayers, Multiferroics, Thermoelectric Ceramics and Microwave dielectrics. Characterisation Methods: LCR, impedance spectroscopy, d33 meter for piezoelectric coefficient, Vibrating Sample Magnetometer for magnetic properties, XRD Analysis, SEM/ EDX, ferroelectric testing, etc.



Prof. Cenk Aktas earned his BSc and MSc in Materials Science and Engineering from Middle East Technical University-Turkey and Christian-Albrechts University-Germany, respectively. He joined Leibniz Institute for New Materials (Leibniz-INM) in 2004. After completing his PhD with distinction (summa cum laude) he was appointed as the Deputy Head of CVD Research Division. Between 2010-2015, Aktas acted as the Director of CVD/Biosurfaces Division at Leibniz-INM, which is situated in Saarbrücken/Germany. In addition to his academic duties (acting as senior instructor at Saarland University and Applied University of Kaiserslautern), he gained invaluable experiences at Leibniz-INM since it is a well-known scientific partner to national and international institutes and a provider of research and development for companies throughout the world. Aktas also acted as advisor and instructor in several professional training programs of various institutions including German Chemistry Society, Korean University of Technology, European Postgraduate School and etc. Currently he is carrying out research activities on synthesis of functional nanomaterials and their potential applications in diverse fields including energy, medicine, textile, surface, and composite technologies at the Institute of Materials Science, CAU-Kiel. In addition, he acts as the PI at Cardiovascular Materials Laboratory at UdS-Homburg and is giving lectures in the Medical Faculty, UdS-Homburg. Aktas has been involved in various projects funded by EU, DFG, BMBF and similar public institutions. Aktas published more than 70 research papers and 10 patents in different fields (on nanomaterials and nanotechnology). He has several prestigious awards including Prof. Werner Petersen Award, Prof. Horst Hardt Award, Prof. Baki Komsuoglu Award, International Nanomedicine Foundation Award and etc.

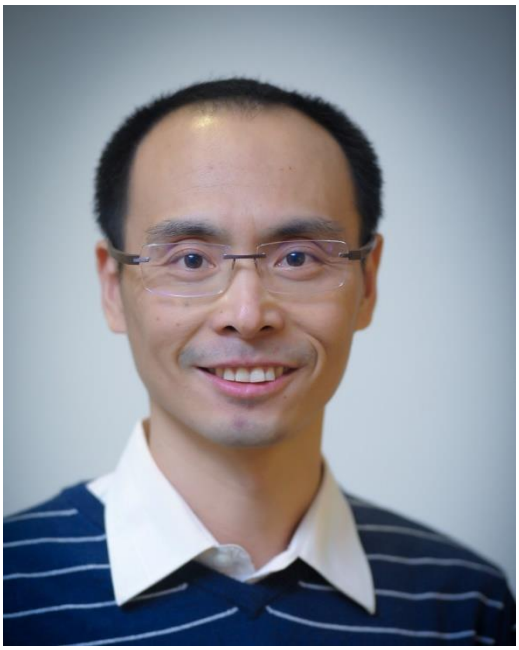


Dr. Dawei Wang is a Professor at Shenzhen Institute of Advanced Technology, Chinese Academy of Sciences, who was a Research Associate at the Department of Materials Science and Engineering of The University of Sheffield (2014-2020) and a joint PhD student/visiting scholar at the Materials Research Institute of Pennsylvania State University (2010.9-2011.9/2016.4-6). He received his PhD degree in Materials Processing Engineering from Beijing Institute of Technology in 2012. He is an Associate editor for *Journal of American Ceramic Society* / *Frontiers in Materials* and an Editorial board member for *Materials Today Communications* / *Journal of Advanced Ceramics* / *Journal of Advanced Dielectrics* / *Crystals*. His research focuses on the advanced electronic ceramics for energy storage/conversion/harvesting, and translation of new materials to porotype devices/components for electronic systems. He has published 150+ refereed papers, with a total citation of 5700+ and a google scholar h-index of 45. Also, he holds 20 issued patents and has given 30+ invited talks on international conferences.



Zhi Hong Chen is an associate professor from Wuhan University of Technology. He received his B. S. in 2009 from Central South University, China and Ph. D degree in 2014 from the University of Sheffield, United Kingdom, with “Ceramic Award” for his high quality Ph.D thesis. His research interest focuses on the design, fabrication and characterization of novel electromagnetic functional materials, including electromagnetic absorption materials and metamaterials. He has been a PI and achieved several funding support from national grants of China. He has published more than about 30 papers in peer-reviewed journals, including Adv. Mater., Adv. Optical. Mater., Nanoscale, Phys. Chem. Chem. Phys. and J. Appl. Crystallogr. etc. He is also the author of 3 chapters in two academic books published by Royal Society of Chemistry and World Scientific.

Email: z_chen@whut.edu.cn

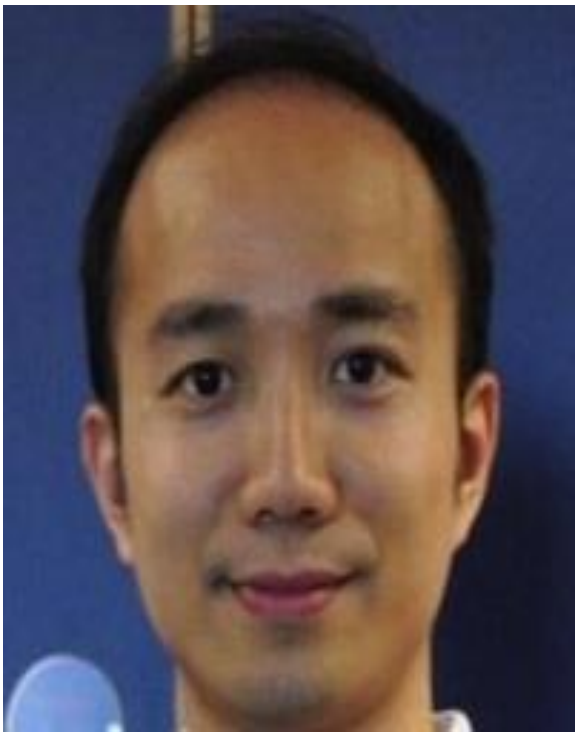


Dr David Fengwei Xie is currently an EPSRC Fellow and Lecturer at Newcastle University, UK. He was a Marie Curie Fellow at the University of Warwick. Before moving to the UK, he worked as a postdoctoral research fellow/research fellow at the University of Guelph (Canada) and The University of Queensland (Australia). Besides, he had visiting research experiences at Université de Strasbourg (France) and California Institute of Technology (USA). Dr Xie specialises in polymer engineering and science. His research particularly focuses on biopolymers (polysaccharides and proteins) for both materials and food applications. His interest lies in the modification, processing, and characterisation of biopolymers and the design of biopolymer-based materials and composites with desired application performance. He has led and involved in multiple research projects with a total research funding of about £5.9M. His research has led to over 130 refereed journal articles with an h-index of 43 and >6900 citations (Google Scholar), 1 monograph, and 5 book chapters. He is an editorial board member for several journals such as Carbohydrate Polymers, Polymers, Coatings, and PLOS ONE.



Dr. Fan Yang obtained her PhD of Materials from University of Manchester, UK. She remained in Manchester as a Postdoctoral Research Associate (PDRA) before joining the group of Functional Materials and Devices (FMD) at Department of Materials Science & Engineering at the University of Sheffield, UK. She was appointed as an associate professor at the Institute of Fuel Cells, School of Mechanical Engineering, Shanghai Jiao Tong University in late 2018.

Fan's research covers a wide range of oxide-based functional ceramics, including solid-state electrolytes, mixed conductors, dielectrics and electrocatalysts. She specializes in probing the defect chemistry and the composition-structure-electrical property relationships of perovskite, fluorite, pyrochlore-type oxides, particularly using impedance spectroscopy (couple with finite element modelling) to study the electrical properties of ceramics, composites, coatings and interfaces. Fan has published more than 80 peer-reviewed journal papers and was selected by the Royal Society of Chemistry in the themed collection "Celebrating excellence in research: 100 women of materials science" in recognition of her work on defect chemistry and electrical properties of sodium bismuth titanate-based perovskites in 2018.



Dr Zhilun Lu is a Lecturer (Assistant Professor) at Edinburgh Napier University's School of Engineering and the Built Environment. He obtained his PhD from the University of Sheffield with the High-Quality PhD Thesis Prize. He then held postdoctoral positions at the Helmholtz-Zentrum Berlin for Materials and Energy (member of the largest scientific organisation in Germany-The Helmholtz Association of German Research Centres) and the Henry Royce Institute (The UK's National Institute for advanced materials research and Innovation).

Dr Lu is a Professional Member (MIMMM) of the IOM3, a Member (MRSC) of the Royal Society of Chemistry and a Member of the American Chemical Society. He is on the editorial boards 5 prestigious materials journals. He serves as a peer reviewer for high impact journals, including Nature Communications, Advanced Functional Materials, Physical Review Letters, Chemistry of Materials, and Acta Materialia. He has also delivered 10+ keynote speeches at international conferences. Dr Lu has published 60+ journal papers (H-index=24). One of his papers was selected as a Hot Article (as one of the top 10% of papers) in Energy & Environmental Science in 2020. And another paper was selected as a Highly Cited Article by Web of Science in 2021.

Dr Lu's research group focuses on the structure-composition-property relations of a broad spectrum of advanced functional materials and the translation of novel materials into prototype devices. Dr Lu is an expert in utilising Impedance Spectroscopy to examine "electrical microstructure", as well as Neutron Scattering to analyse atomic and magnetic structures, the dynamic interplay of quasi-particle and charge transport, including phonon excitations in solids and spin waves in magnetic materials.



Salih Veziroğlu received his Ph.D. from the Institute of Material Science at Kiel University- Germany in 2020. He got the prestigious Thesis Award by Kiel Nano Surface & Interface Science (KiNSIS) due to his outstanding achievements (co-authorship in more than 19 articles) during his doctoral studies. Currently, he is working as a young group leader (Nano, Energy, and Surface Engineering Group) at the same institute. He involves many national (e.g, DFG, etc.) and international (e.g, EU, etc.) projects and focuses on the fabrication of metal-metal oxide thin films and particles for photocatalysis, energy, self-cleaning, and sensing applications.

Doktora derecesini 2020 yılında Kiel Üniversitesi-Almanya Malzeme Bilimi Enstitüsü'nden aldı. Doktora çalışmaları sırasında gösterdiği üstün başarıları nedeniyle (19'dan fazla makalede ortak yazarlık) Kiel Nano Yüzey & Arayüzey Bilimi (KiNSIS) tarafından verilen prestijli Doktora Tez Ödülü'nü kazandı. Halen aynı enstitüde genç grup lideri (Nano, Enerji ve Yüzey Mühendisliği Grubu) olarak çalışmaktadır. Birçok ulusal (ör. DFG, vb.) ve uluslararası (ör. AB, vb.) projeye dahil olmakta ve fotokataliz, enerji, kendi kendini temizleme ve algılama uygulamaları için metal-metal oksit ince film ve parçacıkların üretimine odaklanmaktadır.



Attila Alkan worked as a specialist for 2 years in the electron microscope laboratory, where he completed his master's degree in Physics Engineering, Faculty of Science, Ankara University. Then, in order; He worked as a research assistant in the Physics Engineering department for 3 years, as an electron microscope specialist for 4 years in the Cement Manufacturers' R&D micro-examination laboratory and for 26 years in the Brisa R&D micro-examination laboratory. He completed his doctorate in Kocaeli University Metallurgical and Materials Engineering Department in 2019. He took part in EUROSTARS projects completed in 2017 and EUREKA projects completed in 2019. He retired from Brisa in 2012. Since 2014, he has been working as an electron microscope specialist in the application department of Atomika Technical Devices. Atomika Teknik firm is the Turkey representative of TESCAN electron microscope and micro CT firm.



Associate Professor Havva Kazdal Zeytin was born in Rize Muradiye Village in 1962 and completed primary school in Muradiye Village Primary School. She completed her secondary and high school education at Istanbul Nişantaşı Girls' High School, and her university education at Istanbul Technical University, Faculty of Chemistry and Metallurgy, Department of Metallurgy and Materials (1984). I did my master's and doctorate in the field of materials at the same university. She worked as an engineer at PARSAT PİSTON A.Ş and NASAŞ Aluminum factories between 1987-1991. He is still working as a chief researcher as the Manager of the Critical Metallic Materials Group at the TÜBİTAK MARMARA RESEARCH CENTER Materials Institute, which he entered in 1991. Associate Professor. Havva Kazdal Zeytin has worked with metal materials as a researcher and engineer in a heavy industry branch such as metallurgy throughout her career. She carried out studies in areas such as bringing advanced technologies of materials such as steel industry, aluminum industry, superalloy materials to our country, and developing materials with high added value that we cannot produce. It has made technology acquisition and development studies by establishing the infrastructure for the production of Steam Turbine materials, Gas Turbine materials and Aircraft Engine Turbine materials, which our country is completely dependent on abroad. He supported the R&D projects of many companies and acted as a project referee in TÜBİTAK TEYDEB R&D projects. Since 2012, TÜBİTAK MARMARA RESEARCH CENTER-Materials Institute has been continuing its efforts to train human resources and establish infrastructure in the country for research, development and production on advanced materials used in aviation, nuclear materials, advanced materials used in automotive. In this context, Assoc. Dr. Havva Kazdal Zeytin continues to work to develop and expand this infrastructure to serve the country. In addition, he has nearly 50 papers and articles presented in national and international journals and conferences.

==========

SCIENTIFIC COMMITTEE

- Prof. Dr. İlker Bekir TOPÇU, Osmangazi University, Türkiye
- Prof. Dr. Ahmet ÜNAL, Yıldız Tecnical University, Metallurgical and Materials Eng. Department, Türkiye
- Prof Dr. Şenol YILMAZ, Sakarya University, Metallurgical and Materials Eng. Department, Türkiye
- Prof. Dr. İskender AKKURT, Süleyman Demirel University, Türkiye
- Prof. Dr. Cenk AKTAŞ, URTEMM (Additive Manufacturing Excellence Centre), Türkiye
- Prof. Dr. Yogendra Kumar MISHRA, University of Southern Denmark, The Mads Clausen Institute, Denmark
- Prof. Dr. Erol KAM, Yıldız Teknik University, Türkiye
- Prof. Dr. Ender SARIFAKIOĞLU, Çankırı KaratekinUniversity, Türkiye
- Prof. Dr. Bahri ERSOY, Afyon Kocatepe University, Türkiye
- Prof. Dr. Mahmut ÖZACAR, Sakarya University, Türkiye
- Prof. Dr. Atila Gürhan ÇELİK, Giresun Universityi, Türkiye
- Prof. Dr. Rabia ALMAMLOOK, Western Michigan University, USA
- Prof. Dr. Michal KULKA, Poznan University of Technology, Poland
- Prof. Dr. Nodar LEKISHVILI, Ivane Javakhishvili Tbilisi State University, Georgia
- Prof. Dr. Alma Gabriela Palestino Escobedo, Universidad Autonoma de San Luis Potosi, Mexico
- Prof. Dr. Şerafettin EROĞLU, Istanbul University- Cerrahpaşa, Metallurgical and Materials Eng. Department,, Türkiye
- Prof. Dr. Karima Akool AL-SALİHİ, Al Muthanna University, Iraq
- Prof. Dr. Kaveh Ostad-Ali-ASKARI, Isfahan University of Technology (IUT), Iran
- Assoc. Prof. Ayşe KALEMTAŞ, Bursa Teknik University, Türkiye
- Assoc. Prof. Mustafa YAMAN, Istanbul Sabahattin Zaim Univeristy, mustafa.yaman@izu.edu.tr
- Assoc. Prof. Hasan KOTAN, Necmettin Erbakan University, Türkiye
- Assoc. Prof. Ali GÜNEN, Iskenderun Technical University, Türkiye
- Assoc. Prof. Mustafa ULUTAN, Eskişehir Osmangazi University, Türkiye
- Assoc. Prof.Zahide Bayer ÖZTÜRK, Nevşehir Hacı Bektaş Veli University, Türkiye
- Assoc. Prof.Mürsel EKREM, Necmettin Erbakan University, Türkiye
- Assoc. Prof. Fuat KARA, Düzce University, Türkiye
- Assoc. Prof.Jale ÇATAK, İstanbul Sabahattin Zaim University, Türkiye
- Assoc. Prof. Soner SAVAŞ, Erciyes University, Türkiye
- Assoc. Prof. Nevin ÇANKAYA, Uşak University, Türkiye
- Assoc. Prof. Alicja Krystyna KRELLA, Institute of Fluid Flow Machinery, Poland
- Assoc. Prof. Şeyda POLAT –KOÜ Metallurgical and Materials Eng. Department, Türkiye
- Assoc. Prof. Hakan ATAPEK-KOÜ Metallurgical and Materials Eng. department, Türkiye
- Assoc. Prof. Meltem YILDIZ, Kocaeli University, Chemical Engineering Department, Kocaeli, Türkiye
- Assoc. Prof.Tuba Erdoğan Bedri, TÜBİTAK MRC, Materials Institute, Türkiye
- Assoc. Prof. Dolunay Şakar, Yıldız Tecnical University, Chemistry Department, Türkiye

==========

- Assist. Prof. Dr. Murat Efkan KİBAR, Kocaeli University, Chemical Engineering Department, Kocaeli, Türkiye
- Dr. Massimo ROGANTE, Studio D'ingegneria Rogante, Contrada San Michele, Civitanova Marche (MC), Italy
- Dr. Angeliki Christogerou, University of Patras, Department of Chemical Engineering, Greece
- Dr. Maria Canillas Perez, Laser Center from Universidad Politeecnica of Madrid, Spain
- Dr. Peter Tatarko, Institute of Inorganic Chemistry, Slovak Academy of Sciences, Slovakia
- Dr. Engin Açıkalın, TUBITAK MRC, Materials Institute, Türkiye
- Kerim Çoban, TUBITAK MRC, Materials Institute, Türkiye
- Dr. Cansu KURTULUŞ, Afyon Kocatepe University, Türkiye
- Assist. Prof. Dr. Ömer Saltuk BÖLÜKBAŞI, İskenderun Technical University, Türkiye
- Assist. Prof. Dr. Mustafa KOCABAŞ, Konya Teknik University, Türkiye
- Dr. Manjunath Patel G C, PES Institute of Technology and Management, India
- Assist. Prof. Dr. Ali ERÇETİN, Bingöl University, Türkiye
- Dr. Avinash Lakshmikanthan, Nitte Meenakshi Institute of Technology, India
- Dr. Ying-Sui SUN, National Yang Ming University, Taiwan

==========

ORGANIZING COMMITTEE

- Prof. Dr. Atilla EVCİN, Afyon Kocatepe University, Afyonkarahisar, Türkiye
- Prof. Dr. İbrahim GÜNEŞ, Giresun University, Giresun, Türkiye
- Prof. Fayaz HUSSAIN, NED University of Engineering and Technology, Pakistan
- Dr. Yasemin TABAK, TUBITAK MRC, Gebze, Türkiye
-
- Prof. Dr. Baki AKKUŞ, Istanbul University, President of Turkish Physical Society, Türkiye
- Prof. Dr. Ender SARIFAKIOĞLU, Çankırı Karatekin University, Civil Engineering Department, Çankırı, Türkiye
- Prof. Dr. Beata Podkościelna PODKOSCIELNA, Maria Curie-Skłodowska University, Poland
- Prof. Dr. Mourad KEDDAM, University of Science and Technology Houari Boumediene, Algeria
- Prof. Dr. Danute Vaičiukynienė-Palubinskaitė, Kaunas University of Technology, Lithuania
- Prof. Dr. Svetlana Velkova Lilkova-Markova, University of Architecture, Civil Engineering and Geodesy, Bulgaria
- Prof. Dr. German Anibal Rodriguez CASTRO, Instituto Politecnico Nacional, Mexica
- Prof. Dr. Greg Haidemenopoulos, Physical Metallurgy, Department of Mechanical Engineering, University of Thessaly, Greece
- Dr. Jürgen M. LACKNER, JOANNEUM RESEARCH Forschungsgesellschaft mbH MATERIALS - Institute of Surface Technologies and Photonics Laser and Plasma Processing, Austria
- Assist. Professor Anna D. Zervak, National Technical University of Athens, School of Naval Architecture and Marine Engineering, Athens, Greece
- Assoc. Prof Tuba ERDOĞAN BEDRİ, TUBİTAK Marmara Research Center (MRC), Türkiye
- Assoc. Dr. Soner SAVAŞ, Erciyes University, Materials Science and Engineering Department, Kayseri, Türkiye
- Assoc. Dr. Aytekin HİTİT, Afyon Kocatepe University, Afyonkarahisar, Türkiye
- Assist. Prof. Dr. Metin ÖZGÜL, Afyon Kocatepe University, Afyonkarahisar, Türkiye
- Dr. Fikriye KURTOĞLU, National Defence University, Türkiye
- Dr. Şahin ATEŞ, TUBITAK Marmara Research Center (MRC), Türkiye
- Dr. Massimo ROGANTE, Studio D'ingegneria Rogante, Contrada San Michele, Civitanova Marche (MC) Italy
- Dr. David Fengwei Xie, Newcastle University, England
- Dr. Angeliki Christogerou, University of Patras, Greece
- Dr. Jelana Vukmirović, University of Novi Sad, Sirbia
- Assist. Prof. Dr. Büşra Tuğba ÇAMİÇ, Sabancı University, Nanotechnology Research and Application Center (SUNUM), Türkiye
- Assist. Prof. Dr. S. Bahar BAŞTÜRK, Manisa Celal Bayar University, Department of Metalurgy and Materials Engineering, Manisa, Türkiye
- Assist. Prof. Dr. Abdul Vahap KORKMAZ, Afyon Kocatepe Üniversity, Türkiye
- Assoc. Prof. Zeynep TAŞLIÇUKUR ÖZTÜRK, National Defence University, Türkiye
- Dr. Ahmet Burçin BATIBAY, Necmettin Erbakan University, Türkiye
- Assist. Prof. Dr. Cansu KURTULUŞ, Afyon Kocatepe University, Türkiye
- Arş. Grv. Recep KURTULUŞ, Afyon Kocatepe University, Türkiye

- Abdullah Noman Alawadhi, Afyon Kocatepe University, Türkiye
- Oğuzhan Evcin, Afyon Kocatepe University, Türkiye
- Zeynep Özkan, Afyon Kocatepe University, Türkiye
- Ikbal Yaren Polat, Afyon Kocatepe University, Türkiye
- Zeynep Çetinkaya, Afyon Kocatepe University, Türkiye

Mikro-sulama Sistemi Lateral Boru Unitelerinin Hidrolik Tasarımında Analitik ve Nümerik Hesap Metotlarının Karşılaştırmalı Analizi

Gürol Yıldırım

Giresun University, Civil Engineering Department, Hydraulics Division, Giresun, Turkey.

Abstract

Mikro-sulama sisteminin temel unsuru olan lateral borular, sistemin tamamında öngörülen üniformluk seviyesi, basınç yükü değişimi ve toplam sürtünme kaybı kriterlerine bağlı olarak tasarlanabilen hidrolik yapılardır. Hidrolik bakımdan lateraldeki akım, mansap yönünde damlatıcı debisindeki azalmayla birlikte, yere bağlı değişken debi fonksiyonunun geçerli olduğu düzenli boru akımıdır. Mikro-sulama sistemi lateral borularının projelendirilmesinde genellikle takip edilen metot, öngörülen damlatıcı özelliği, lateral boru uzunluğu ve boru çapı için, damlatıcı debileri arasındaki değişimin belirli bir sınır değerini aşmamasını sağlamaktır. Bir başka anlatımla, damlatıcı debileri arasındaki değişimin kabul edilebilir bir üniformluk katsayısını sağlayacak biçimde düzenlenmesidir. Diğer taraftan, lateral boyunca menba ve mansap noktalarındaki başlangıç ve sınır şartları ile belirlenen bir projelendirme aralığı içerisinden, sistemde öngörülen toplam yük kaybı ve üniformluk seviyesi kriterlerini sağlayacak optimum giriş basınç yükü değerinin belirlenmesi lateral hidroliğinin temel problemidir. Zira lateral boyunca enerji çizgisinin değişimi ve çıkış akımı dağılımı, lateral girişindeki basınç yükü değerine bağlı olarak farklı profillerde oluşmaktadır. Çalışmanın ilk kısmında, üniform eğimli ve sabit çaplı bir lateral boru için lateral hidroliğinin temel prensipleri sunulmaktadır. Çalışmanın ikinci kısmında, sabit veya yere bağlı değişken debi yaklaşımlarından hareketle ortaya konan 7 adet hidrolik hesap metodunda, tasarım parametreleri için elde edilen başlıca denklemlere yer verilerek, optimum giriş basınç yükünün belirlenmesinde, sağlanması gereken hidrolik kriterler değerlendirilmektedir. Söz konusu metotların karşılaştırmalı analizi için, farklı eğim koşulları ve damlatıcı karakteristikleri için örnek bir uygulama seçilerek, her bir metottan elde edilen sonuçlar, boyutsuz eğriler halinde karşılaştırılmaktadır.

Keywords: Sulama sistemleri, mikro-sulama, lateral hidroliği, pürüzsüz boru akımı, hidrolik tasarım, analiz, analitik ve nümerik yöntemler.

*Author e-mail: gurol.yildirim@giresun.edu.tr

1. Giriş

Mikro-sulama sisteminin başarısı, sistemin önemli bir parçası olan lateral boruların hidrolik prensiplere uygun biçimde tasarlanmasına ve lateral boru üzerindeki damlatıcı özelliklerinin iyi bilinmesine bağlıdır (Ağıralioğlu vd., 2000; Ağıralioğlu ve Yıldırım, 2002).

Mikro-sulama sisteminin temel unsuru olan lateral borular, sistemin tamamında öngörülen üniformluk seviyesi, basınç yükü değişimi ve toplam sürtünme kaybı kriterlerine bağlı olarak tasarlanabilen hidrolik yapılardır. Hidrolik bakımdan lateraldeki akım, mansap yönünde damlatıcı debisindeki azalmayla birlikte, yere bağlı değişken debi fonksiyonunun geçerli olduğu düzenli boru akımıdır (Yıldırım, 2001; Yıldırım ve Ağıralioğlu, 2001). Lateral borunun hidrolik tasarımı için araştırıcılar iki temel kabulden yola çıkarak analitik ve nümerik çözüm yöntemleri geliştirmişlerdir.

Bu kabullerden birincisi, lateral boyunca üniform bir ortalama birim boy debisinin geçerli olduğu kabulüdür. Ancak, bu basitleştirmeden yola çıkılarak elde edilen analitik metotların çözümlerinden elde edilen sonuçların doğru nümerik metotların çözümlerinden elde edilen sonuçlardan önemli mertebede sapma gösterdiği ortaya konmuştur.

Araştırıcıların lateral boyunca enerji çizgisinin (basınç profilinin) doğru biçimde belirlenebilmesi için esas aldıkları ikinci temel kabul, lateral boyunca boru girişinden itibaren mansap yönünde damlatıcı çıkış akımındaki azalma ile birlikte, yere göre değişen bir debi fonksiyonunun geçerli olduğu kabulüdür.

Son yıllarda yapılan çalışmalarda, lateraldeki değişken debi profilinin belirlenebilmesi için farklı yaklaşımlardan ve kabullerden yola çıkılarak analitik ve nümerik çözüm metotları ortaya konmuştur. Lateral boruların hidrolik hesaplamalarına ilişkin literatürdeki mevcut çalışmalar şu ana başlıklar altında gruplandırılabilir:

1. Lateral borulardaki sürtünme kayıplarının belirlenmesi (Anwar, 1999a,b, 2000; Scaloppi ve Allen, 1993; Vallesquino ve Luque-Escamilla, 2002; Yitayew, 1989; von Bernuth, 1990; von Bernuth ve Wilson, 1989; Watters ve Keller, 1978).

2. Damlatıcı bağlantılarından kaynaklanan yersel kayıpların belirlenmesi (Howell ve Barinas, 1980; Al-Amoud, 1995; Bagarello vd., 1995, 1997; Juana vd., 2002a,b; Sinobas vd., 1999; Provenzano ve Pumo, 2004; Provenzano vd., 2005; Yıldırım ve Ağıralioğlu, 2006; Yıldırım ve Ağıralioğlu, 2004c,e; Yıldırım, 2006).

3. Lateral boyunca debi ve basınç profillerinin belirlenmesi (Anyoji ve Wu, 1987; Wu ve Gitlin, 1973, 1974, 1975; Wu, 1992, 1997; Wu ve Yue, 1993; Keller ve Bliesner, 1990; Warrick ve Yitayew, 1987, 1988; Yitayew ve Warrick, 1987, 1988; Vallesquino ve Luque-Escamilla, 2001; Yıldırım ve Ağıralioğlu, 2002a; 2003a,b; 2004d; 2005a,b).

4. Lateral boruların hidrolik tasarımı (Howell ve Hiler, 1974; Bralts vd. 1993; Kang ve Nishiyama, 1996a,b; Hathoot vd., 1993, 2000; Jain vd., 2002; Saad ve Marino, 2002; Valiantzas, 1998, 2002; Yıldırım ve Ağıralioğlu, 2002b; 2004a,b,f; 2005c).

Ancak, üzerinde çok detaylı çalışmaların yapıldığı ve halen yapılmakta olan mikro-sulama sistemi lateral borularının tasarımında, literatürde ortaya konan belli başlı hidrolik hesap metotlarında ortaya konan yaklaşımların detaylı bir analizine ve çözümlerinden elde edilen sonuçların kapsamlı biçimde karşılaştırılmasına yönelik bir çalışma bulunmamaktadır.

Çalışmanın ilk kısmında, üniform eğimli ve sabit çaplı bir lateral boru için lateral hidroliğinin temel prensipleri detaylı olarak sunulmaktadır. Çalışmanın ikinci kısmında, sabit ve yere bağlı değişken debi yaklaşımlarından hareketle ortaya konan analitik ve nümerik hidrolik hesap metotlarında kullanılan denklemler, ilk kısımda verilen yönetici denklemlerle ilişkilendirilerek sunulacaktır. Söz konusu metotların uygulamaları için farklı tipte lateral tasarım problemleri seçilerek; farklı eğim koşulları ve damlatıcı karakteristikleri için elde edilen sonuçlar, boyutsuz eğriler halinde karşılaştırılmaktadır. Göz önüne alınan hidrolik hesap metotları şunlardır:

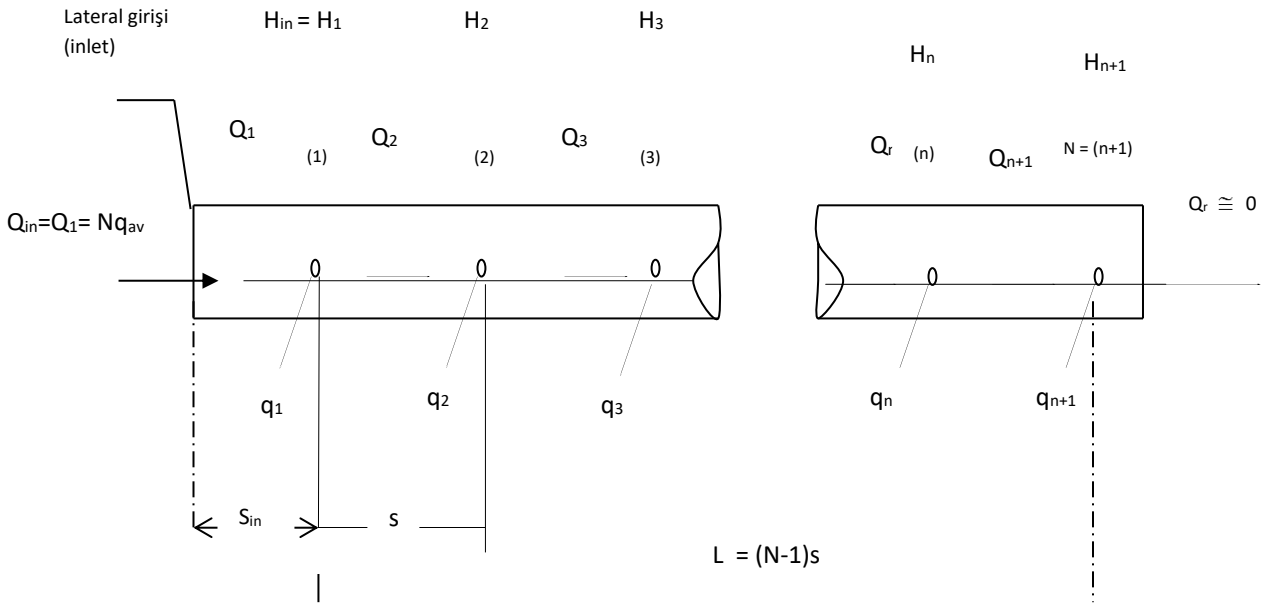
1) İleri-adım metodu (Forward-Step Method, **FSM**) (Hathoot vd., 1993),
2) Diferansiyel Metot (Differential Method, **DM**) (Warrick ve Yitayew, 1988),
3) Runge-Kutta Nümerik Metodu (Runge-Kutta Numerical Method, **RKM**)
(Yitayew ve Warrick, 1988),
4) Basitleştirilmiş Analitik Yaklaşım (Simplified Analytical Approach, **SAA**) (Yitayew, 1989),

5) Sabit Debi Metodu (Constant Discharge Method, **CDM**) (Valiantzas, 1998),
6) Değişken Debi Metodu (Variable Discharge Method, **VDM**) (Valiantzas, 1998) ve
7) Ardışık Yaklaşımlar Metodu (Successive Approximations Method, **SAM**) (Vallesquino ve Luque-Escamilla, 2001).

2. Lateral Boru Akımı Hidroliğinin Temel Prensipleri

Üzerinde nokta kaynaklı damlatıcılar bulunan yatay bir lateral borunun boy kesiti ve akım boyunca değişken akım parametreleri Şekil 1'de gösterilmektedir. Şekilde görüldüğü gibi, lateral boru üzerindeki özdeş tekil damlatıcılar lateral üzerine eşit mesafelerle yerleştirilirler. Uniform eğimli bir lateral boruda damlatıcı ara mesafesi, s (m), damlatıcı katsayısı, c ($m^{3-y}s^{-1}$) ve lateral borunun kesit alanı, A (m^2) sabittir.

Şekilde, N, lateral üzerindeki toplam damlatıcı sayısı; Q_{in}, lateral girişindeki menba debisi; Q_2, Q_3,...,Q_N, damlatıcıların ayırdığı boru dilimlerindeki lateral debileri; Q_r, lateral mansabında son damlatıcıdan itibaren artık lateral debisi; q_{av}, lateral boyunca ortalama damlatıcı debisi; q_1, lateral girişinden itibaren ilk damlatıcı debisi; q_2, q_3,..., q_N, mansap istikametinde diğer damlatıcı debileri; $H_{in} = H_1$, ilk damlatıcıya ait giriş basınç yükü; H_2, H_3,..., H_N, mansap istikametinde diğer damlatıcılara ait basınç yükleri; s_{in}, ilk damlatıcının lateral girişine olan mesafesi; s, lateral üzerindeki ardışık tekil damlatıcılar arasındaki mesafe ve L, ilk ve son damlatıcılar arasındaki lateral uzunluğudur.



Şekil 1. Lateral boru boykesiti, yere bağlı değişken (spatially-variable) akım parametreleri

Damlatıcıların akım karakteristikleri aşağıdaki bağıntı ile tanımlanmaktadır (Howell ve Hiler, 1974; Keller ve Karmeli, 1974):

$$q_n = cH_n^{\,y} \qquad (1)$$

Bağıntıda; n, damlatıcının konumunu gösteren indis; q_n, özdeş tekil damlatıcıdan hasıl olan çıkış akımı; H_n: damlatıcı basınç yükü; c, ampirik damlatıcı katsayısı ve y, akım rejimine ve damlatıcı tipine bağlı akış üssüdür.Lateral boyunca çok sayıda damlatıcı bulunduğu ve çıkış akımının yere göre sürekli olarak değiştiği göz önüne alınarak, birim boru uzunluğundaki çıkış akımı q, aşağıdaki bağıntı ile belirlenebilir (Warrick ve Yitayew, 1988)

$$q = \left(\frac{c}{s}\right) H_n^{\ y} \tag{2}$$

Lateral boyunca kütlenin korunumu denklemi şu genel formda yazılabilir:

$$\frac{dQ}{dx} + \frac{dA}{dt} = -q \tag{3}$$

Denklemde; *A*: Lateral borunun kesit alanı; *x* ve *t*, yer ve zaman koordinatlarıdır.

Mikro-sulama lateralleri için düzenli boru akımı şartı (dA/dt = 0) düşünülerek (3) denklemi aşağıda formda yazılabilir:

$$A\frac{dv}{dx} = -q \tag{4}$$

Denklemde; v, lateral borudaki ortalama akım hızıdır.

Şekilde gösterildiği gibi, (n) ve (n+1) inci damlatıcılar arasındaki lateral debisi, Qn+1, (4) denklemi ile verilen süreklilik prensibinden hareketle elde edilebilir:

$$Qn+1 = Qn - qn \tag{5}$$

Mansap yönünde lateral debisindeki azalmanın sonucu olarak momentumdaki değişim, momentumun korunumu denkleminin aşağıdaki formu ile belirlenebilir (Streeter ve Wylie, 1983):

$$\Delta F = \rho(Q_{n+1}V_{n+1} - Q_nV_n) \tag{6}$$

Denklemde; ΔF , basınç kuvvetindeki değişim; ρ , sulama suyunun yoğunluğu; Vn, Vn+1, (n-1)~(n) ve (n)~(n+1) damlatıcıları arasında kalan boru dilimlerindeki ortalama akım hızlarıdır.

Ardışık (n) ve (n+1) damlatıcıları arasındaki boru diliminde momentum değişiminden dolayı meydana gelen basınç yükü değişimi, ΔHn+1, (6) denklemi yardımıyla aşağıdaki şekilde elde edilebilir.

$$\Delta H_{n+1} = \frac{\Delta p}{\gamma} = \frac{\Delta F}{A\gamma} = \frac{\rho(Q_{n+1}V_{n+1} - Q_nV_n)}{A\gamma} \tag{7a}$$

$$V_{n+1} = \frac{Q_{n+1}}{A} \qquad V_n = \frac{Q_n}{A} \qquad \gamma = \rho g \tag{7b}$$

eşitlikleri (7a) denkleminde yerlerine yazılıp düzenlenerek,

$$\Delta H_{n+1} = \frac{(Q^2{}_{n+1} - Q^2{}_n)}{gA^2} \tag{7c}$$

elde edilir (Streeter ve Wylie, 1983; Featherstone ve Nalluri, 1982). Denklemde; g, yerçekimi ivmesidir.

Darcy-Weisbach formülü, ardışık (n) ve (n+1)'inci damlatıcılar arasındaki boru kısmı için aşağıdaki şekilde yazılabilir.

$$H_{fn+1} = f_{n+1}\frac{s}{D}\frac{Q_{n+1}^{\ 2}}{2gA^2} \tag{8}$$

Formülde; fn+1, ardışık (n) ve (n+1)'inci damlatıcılar arasındaki boru kısmı için Darcy-Weisbach sürtünme katsayısı ve D, lateral borunun iç çapıdır.

Bagarello ve diğ. (1997); Juana vd. (2002a), damlatıcının menbasında büzülme ve mansabında genişleme (Chadwick ve Morfett, 1993) nedeniyle ortaya çıkacak yerel kayıpların Belanger veya Borda-Carnot denklemleri ile hesaplanabileceğini belirterek, toplam yerel yük kaybı için her iki durumun birlikte göz önüne alınması gerektiğine işaret etmişlerdir. Buna göre toplam yerel yük kaybı, aşağıdaki eşitlikle belirlenebilir:

$$h_c + h_e = \frac{(V_c - V_r)^2}{2g} + \frac{(V_r - V_{n+1})^2}{2g} = \left(\frac{1}{C_c r} - 1\right)^2 \frac{V_{n+1}^2}{2g}$$

$$hk' = K \frac{V_{n+1}^2}{2g} \quad (9)$$

Denklemde; K, yersel yük kaybı katsayısıdır.

Enerji denklemi, (n) ve (n+1)'inci damlatıcılar arasında (7), (8) ve (9) denklemleri ile birlikte hız yükü de dikkate alınarak, aşağıdaki formda yazılabilir:

$$H_n + \frac{V_n^2}{2g} + z_n + h_{kn}' = H_{n+1} + \frac{V_{n+1}^2}{2g} + z_{n+1} + H_{fn+1} + \Delta H_{n+1} + h_{kn+1}' \quad (10)$$

Denklemde; $V_n^2/2g$, $V_{n+1}^2/2g$, (n) ve (n+1)'inci boru bölümlerindeki hız yükleri; zn ve zn+1: ardışık (n) ve (n+1)'inci damlatıcıların kıyas düzlemine göre geometrik kotlarıdır.

Yukarıdaki açıklamalardan görüleceği üzere, lateral hidrolik problemleri 4 temel denklemle çözülebilir: 1) Damlatıcının debi-basınç yükü ilişkisi, 2) Süreklilik denklemi, 3) Darcy-Weisbach sürtünme kaybı formülü ve yerel yük kayıpları için Borda-Carnot veya Belanger formülleri, 4) Momentumun korunumu ve enerjinin korunumu denklemleri.

Neticede, yukarıdaki temel denklemlere dayanılarak, lateralin herhangi bir (n+1)' inci bölümüne ait 4 adet bilinmeyen hidrolik değişkene (Qn+1, qn+1, Hn, Hfn+1), bir önceki (n)'inci bölüme ait bilinen değişkenlerine (Qn, qn ve Hn) ve diğer tasarım parametrelerine (zn, zn+1, fn+1, D, s, c, y, N) bağlı olarak, herhangi bir metot yardımıyla hesaplanabilir.

3. Hidrolik Hesap Metotları

Aşağıdaki bölümde, çalışmada göz önüne alınan hidrolik hesap metotlarından kısaca bahsedilecektir. Söz konusu metotların algoritmaları hakkında detaylı bir çalışma literatürde mevcuttur (Yıldırım ve Ağıralioğlu, 2004b).

İleri Adım Metodu (FSM: Forward Step Method)

Hathoot vd. (1993), lateral boyunca hidrolik parametrelerin değişken lateral debisine bağlı olarak menbadan mansaba doğru adım adım belirlendiği nümerik bir hesap metodu geliştirmişlerdir (Forward-Step Method, FSM). Bilgisayar destekli bu metoda göre lateral girişindeki basınç yükü (Hin), ortalama basınç yüküne (Hav) makul bir yük artışı (Δ_0) eklenmek suretiyle hesaplanır (Başlangıç şartı).

$$H_{in} = H_{\max} = H_1 = H_{av} + \Delta_0 \quad (11)$$

(5) ile verilen süreklilik denklemi ve (9) ile verilen enerji denkleminden hareketle, basınç yükü için aşağıdaki genel form denklemi elde edilir.

$$H_{n+1} = H_n + B\left[Q_n^2 - (Q_n - q_n)^2\right] - Ef_{n+1}(Q_n - q_n)^2 \pm ss_0 \quad (12)$$

Denklemde; s0, üniform lateral eğimi olup aşağı eğim halinde pozitif yukarı eğim halinde ise negatif alınır. Denklemdeki B ve E sabitleri ilgili eşitlikler yardımıyla hesaplanır.

Araştırıcılar, lateral üzerindeki tüm damlatıcı debilerinin ortalama damlatıcı debisinden sapmalarının değerlendirildiği UC üniformluk katsayısının aşağıdaki eşitlik yardımıyla hesaplanabileceğini göstermişlerdir.

$$U_C = 1 - \left[\frac{1}{Nq_{av}}\right] \sum_{n=1}^{n=N} |q_n - q_{av}| \quad (13)$$

Diğer taraftan lateralin son çeyreğindeki ortalama debinin, lateralin tamamındaki ortalama debiye oranı olarak tanımlanan DULQ üniformluk katsayısı şu eşitlikle verilmektedir.

$$DU_{LQ} = \frac{4\left[\sum_{n=3N/4}^{n=N} q_n\right]}{Nq_{av}} \quad (14)$$

Diferansiyel Metot (DM: Differential Method)

Warrick ve Yitayew (1988) lateral boyunca sürekli ve üniform olmayan debi yaklaşımından hareketle, lateral boruda cereyan eden akımın ikinci mertebeden lineer olmayan basit diferansiyel denklem formunda incelendiği analitik bir çözüm metodu geliştirmişlerdir (Differential Method, DM).

(2), (4) ve (8) bağıntıları (10) ile verilen enerji denkleminde yazılıp, boyutsuz hız (V = v/v0) ve boyutsuz mesafe (X = x/x0) için düzenlenerek,

$$\frac{d}{dx}\left(-\frac{dV}{dX}\right)^{1/y} x_0 + aV\left(\frac{dV}{dX}\right) + V^m + S_0 = 0 \tag{15}$$

diferansiyel denklemi elde edilir.

Denklemde; m, akım rejimine bağlı debi üssüdür. Karakteristik uzunluk (x0) ile kinetik enerji sabiti (a) ve türetilmiş eğim sabiti (S0), ilgili formuller yardımıyla hesaplanır.

(15) diferansiyel denklemi için şu sınır şartları geçerlidir. Lateralin menba uç noktasında; $X = x/x_0 = 0$ $(x = 0)$; $V = v/v_0 = 1$ $(v = v_0)$; ve mansap uç noktasında; $X = L/x_0 = X_0$ $(x = L)$; $V = v/v_0 = 0$ $(v = 0)$.

Boyutsuz hız (V) ve mesafe (X) için verilen bağıntılar (2) denkleminde yazılarak ve a = 0 için yeniden düzenlenerek, lateral boyunca rölatif debi dağılımı için aşağıdaki denklem elde edilir.

$$\frac{q}{q_{av}} = -\frac{X_0}{F(V)} \tag{16}$$

$$F(V) = \left[(y+1)\left(\frac{V^{m+1}}{m+1} + S_0 V\right) + C\right]^{-y/(y+1)} \tag{17}$$

Denklemde; F(V), boyutsuz hız fonksiyonu ve C, sınır şartlarına bağlı olarak belirlenen integrasyon sabitidir (Yıldırım ve Ağıralioğlu, 2004b).

UC ve DULQ üniformluk katsayıları aşağıdaki denklemler yardımıyla hesaplanmaktadır.

$$U_C = 1 - \left(\frac{2}{X_0}\right)\left[X_0(1 - V_{div}) - X_{div}\right] \tag{18}$$

Burada; Xdiv, Vdiv, $q/q_{av} = 1.0$ noktasına ait boyutsuz koordinat ve hız değerleridir.

$$DU_{LQ} = 4V_{LQ} \tag{19}$$

Burada; VLQ, lateralin son çeyreğinde, $X = 0.75X_0 = 0.75(L/x_0)$ noktasındaki boyutsuz koordinata tekabül eden boyutsuz hız değeridir.

Runge-Kutta Nümerik Metodu (RKM: Runge-Kutta Numerical Method)

Yitayew ve Warrick (1988), analitik çözüm metodundan elde edilen sonuçların doğruluğunu kontrol etmek üzere, Runge-Kutta nümerik çözüm metodunu (Runge-Kutta Numerical Method, RKM) kullanmışlardır. Runge-Kutta nümerik çözüm metodunda, (18) ve (19) denklemleri ile verilen UC ve DULQ üniformluk katsayıları $q/q_{avg} = 1.0$; $X = 0.75X_0$; $V_{LQ} = v/v_0$ boyutsuz parametrelerine ait değerlerin, söz konusu X, V ve q/qavg parametrelerinin tablolaştırılmış değerleri arasında uygun enterpolasyonlar yapılmak suretiyle belirlenmektedir.

Basitleştirilmiş Analitik Yaklaşım (SAA: Simplified Analytical Approach)

Yitayew (1989), bir önceki çalışmada (Warrick and Yitayew, 1988) geliştirilen analitik çözüm metoduna dayanarak, eğimsiz mikro-sulama lateral boruları veya yan ana borularda sürtünmeden doğan toplam enerji kayıplarının belirlenmesi için basitleştirilmiş bir analitik yaklaşım (Simplified Analytical Approach, SAA) sunmuştur.

Yatay lateral borudaki toplam enerji kaybı ΔH, menba ve mansap uç noktalardaki toplam enerjilerin farkı alınarak elde edilir.

$$\Delta H = H'(0) - H'(1)$$

$$\Delta H = \frac{v_0^2}{2g}\left[\frac{\beta}{L^2}\left[\left(\frac{q(0)}{q_{avg}}\right)^2 - \left(\frac{q(1)}{q_{avg}}\right)^2\right] + 1\right] \tag{20}$$

Eşitlikte görülen menba ve mansap uç noktalarındaki rölatif debiler $q(0)/q_{avg}$, $q(1)/q_{avg}$; (16) denklemi yardımıyla hesaplanır.

Sabit Debi Metodu (CDM: Constant Discharge Method)

Valiantzas (1998), enerji çizgisi eğimi metoduna (Wu ve Gitlin, 1974), dayanarak, boru boyunca sürekli ve sabit çıkış akımı dağılımı kabulünden hareketle analitik bir yaklaşım geliştirmiştir (Constant Discharge Method, CDM).

Sabit debi metodunda, lateralin mansap uç noktasından itibaren herhangi bir x mesafedeki bölümünden geçen toplam debi, $Q(x)$, lateral girişindeki toplam debiye (Qin) bağlı olarak rölatif mesafenin lineer azalan bir fonksiyonudur.

$$Q(x) = Q_{in}\left(x/L\right) \tag{21}$$

Enerjinin korunumu prensibinden hareketle, lateral mansap uç noktasından itibaren herhangi bir x mesafesindeki basınç yükü, H(x) için aşağıdaki denklem elde edilmektedir.

$$H(x) = H_{av} + \frac{H_{f0}}{(m+1)}\left[\left(\frac{x}{L}\right)^{m+1} - \frac{1}{(m+2)}\right] + s_0\left(\frac{L}{2} - x\right) \tag{22}$$

Denklemde; Hav, ortalama basınç yükü; Hf0, aynı çap ve uzunluk değerlerine sahip damlatıcısız düz bir borudaki toplam sürtünme kaybıdır.

UC üniformluk katsayısı için aşağıdaki denklem verilmektedir.

$$\mathrm{UC} = 1 - 0.798\frac{y}{H_{av}}\left[\frac{{H_{f0}}^2}{(2m+3)(m+2)^2} - \frac{H_{f0}s_0L}{(m+2)(m+3)} + \frac{(s_0L)^2}{12}\right]^{1/2} \tag{23}$$

Değişken debi metodu (VDM: Variable Discharge Method)

Valiantzas (1998) çalışmasının ikinci safhasında, lateral boyunca yere bağlı değişken debi temel yaklaşımından hareketle, sabit debi yaklaşımından hareketle elde edilen analitik denklemlerin geliştirildiği alternatif analitik bir metot ortaya koymuştur (Variable Discharge Method, VDM).

Değişken debi metoduna göre, lateral debisinin rölatif mesafe ile değişimi aşağıdaki güç formu denklemi ile verilmektedir.

$$Q(x) = Q_{in}\left(x/L\right)^{\alpha} \tag{24}$$

Denklemde; α, değişken debi dağılımını karakterize eden üstel bir değerdir. Değişken debi metodu için, sabit debi metodu ile verilen tüm analitik denklemlerde m yerine, düzeltilmiş $m_\alpha = \alpha m$ değeri geçerlidir.

Ardışık Yaklaşımlar Metodu (SAM: Successive Approximation Method)

Vallesquino ve Luque-Escamilla (2001), lateral hidrolik hesaplamaları için, ardışık yaklaşımlar yöntemine dayanan alternatif bir metot (Successive-Approximations Method, SAM) ortaya koymuşlardır.

Bu metoda göre, mansaptan menba istikametine doğru her bir damlatıcıdan hasıl olan değişken çıkış akımı ayrık formda göz önüne alınarak, Taylor polinom serisi formunda ifade edilmektedir.

Buna göre, lateral boyunca damlatıcı debisi dağılımı, qn için, aşağıdaki bağıntı geçerlidir.

$$q_n = q_0 + n\Delta_1 + \frac{n(n+1)}{2}\Delta_2 + \frac{n(n+1)(2n+1)}{6}\Delta_3 + \ldots \tag{25}$$

Bağıntıda; q0, mansap uç noktasından itibaren ilk damlatıcının debisi, n, damlatıcının konumunu gösteren indis; Δ1, Δ2, Δ3, ardışık damlatıcılara ait debilerin farkını gösteren karakteristik düzeltme parametreleridir.

Lateral boyunca debi dağılımı, Qn için, (25) denkleminden hareketle aşağıdaki denklem elde edilir.

$$Q_n = (n+1)q_0 + \left[\frac{n(n+1)}{2}\right]\Delta_1 + \left[\frac{n(n+1)(n+2)}{6}\right]\Delta_2 + \left[\frac{n(n+1)^2(n+2)}{12}\right]\Delta_3 + Q_r \tag{26}$$

Laminer rejim halinde, toplam sürtünme kaybı için, (27) denkleminden hareketle,

$$\Delta H_{fN} = \left(\frac{128\upsilon l}{g\pi D^4}\right)(N+1)\left\{Q_r + (N+2)\left[\frac{q_0}{2} + N\left[\frac{\Delta_1}{6} + (N+3)\left(\frac{\Delta_2}{24} + \frac{(2N+3)\Delta_3}{120}\right)\right]\right]\right\} \tag{27}$$

ve türbülanslı rejim halinde,

$$\Delta H_{fN} = \chi\left[f_0(q_0 + Q_r)^2 + \alpha_N + \beta_N + \gamma_N + \delta_N + \zeta_N \right] \quad (28)$$

denklemleri elde edilmektedir.

(28) denkleminde; $\chi = 8l/\pi^2 gD^5$ ile hesaplanan sabit; $\alpha_N, \beta_N, \gamma_N, \delta_N, \zeta_N$ türbülanslı rejim hali için toplam düzeltme faktörleri olup, ilgili formüller yardımıyla hesaplanmaktadır.

4. Örnek Uygulama

Problemin verileri: Ortalama damlatıcı debisi, $q_{av} = 2lh^{-1} \cong 5.555\times10^{-7} m^3 s^{-1}$; ortalama basınç yükü, $H_{av} = 7.2m$; damlatıcı ara mesafesi, $s = 1.0m$; lateral boru iç çapı ve uzunluğu, $D = 14mm$, $L = 150m$; suyun kinematik viskozitesi $\upsilon = 1.01\times10^{-6} m^2 s^{-1}$; damlatıcı debi üssü, y = 0.2, 0.5, 0.54 ve 1.0; üniform lateral eğimi, s0 = 0.0, -0.02, -0.05 (yukarı eğim).

Bilinmeyen parametreler: 7 adet hidrolik hesap metoduna göre, projelendirme aralığı içerisinde rölatif giriş basınç yükü [H_{in}/H_{av}] değerlerine bağlı olarak rölatif enerji kaybı [H_f/H_{in}], Christiansen üniformluk katsayısı [U_C] ve rölatif artık debi [Q_r/Q_{in}] değerlerindeki değişimin grafiksel olarak elde edilmesi.

5. Sonuçlar ve Karşılaştırmalı Analiz

Bilinmeyen tasarım parametreleri, damlatıcı debi üssü, y = 1.0 ve verilen eğim değerleri için 5 metot (FSM, DM, CDM, VDM, SAM) esas alınarak hesaplanmış, elde edilen sonuçlar Şekil 2'de boyutsuz grafiklerle gösterilmiştir (RKM ve SAA metotlarının çözümü y = 0.5 ile sınırlı olduğundan, y = 1.0 için yapılan bu karşılaştırmada söz konusu metotlar yer almamaktadır). Şekil 2'de rölatif giriş basınç yükü (H_{in}/H_{av}) değerleri yatay eksende, buna tekabül eden rölatif enerji kaybı (H_f/H_{in}), Christiansen üniformluk katsayısı (U_C) ve rölatif artık lateral debisi (Q_r/Q_{in}) değerleri düşey eksende gösterilmektedir.

Şekil 2'den görüleceği üzere y = 1.0 için yapılan çözümlemede, 5 metot arasında FSM metodundan elde edilen sonuçlar diğer 4 metodun (DM, CDM, VDM, SAM) sonuçlarından şu yönüyle farklıdır. FSM metodunda, rölatif enerji kaybı, Christiansen üniformluk katsayısı ve rölatif artık lateral debisi değerleri, rölatif giriş basınç yükünün projelendirme aralığı içerisinde verilen değerleri ile değişirken, diğer 4 metot (DM, CDM, VDM, SAM) söz konusu tasarım parametreleri [(H_{in}/H_{av}), (H_f/H_{in}), (U_C)] için sabit değerler vermektedir. Diğer taraftan Şekil 2.a'dan görüleceği üzere, artık lateral debisinin rölatif giriş basınç yükü ile değişimi de ancak FSM metodu ile elde edilebilmektedir.

FSM metodunda, verilen eğim şartları için rölatif giriş basınç yükünün projelendirme aralığı $[A \le (H_{in}/H_{av}) \le B]$, başlangıç ve sınır şartlarına uygun olarak belirlenmiştir. Şekil 2.c'de gösterildiği gibi, en uygun giriş basınç yükü değerinin tayininde, $s_0 = 0.0$ eğim durumu için $[A = 1.0 \le (H_{in}/H_{av}) \le B = 1.19]$, $s_0 = -0.02$ için $[A = 1.0 \le (H_{in}/H_{av}) \le B = 1.39]$ ve $s_0 = -0.05$ için $(A = 1.36 \le H_{in}/H_{av} \le B = 1.68)$ projelendirme aralıkları belirlenmiştir.

Genel tasarım halinde, farklı eğim şartları ve damlatıcı debi üssü değerleri için gerekli projelendirme aralığı değerlerinin, y = 1.0 için hesaplanan değerlere oldukça yakın olduğu görülmüştür. Karşılaştırma testi sonucunda, tüm tasarım kombinasyonları ve eğim şartlarında FSM metodu için şu genel sonuç elde edilmektedir. Giriş basınç yükü oranının değeri A'dan B'ye doğru arttıkça $[A \le (H_{in}/H_{av}) \le B]$, toplam sürtünme kaybı ve artık lateral debisi değerleri gittikçe azalmakta buna mukabil üniformluk katsayısının değeri gittikçe artmaktadır.

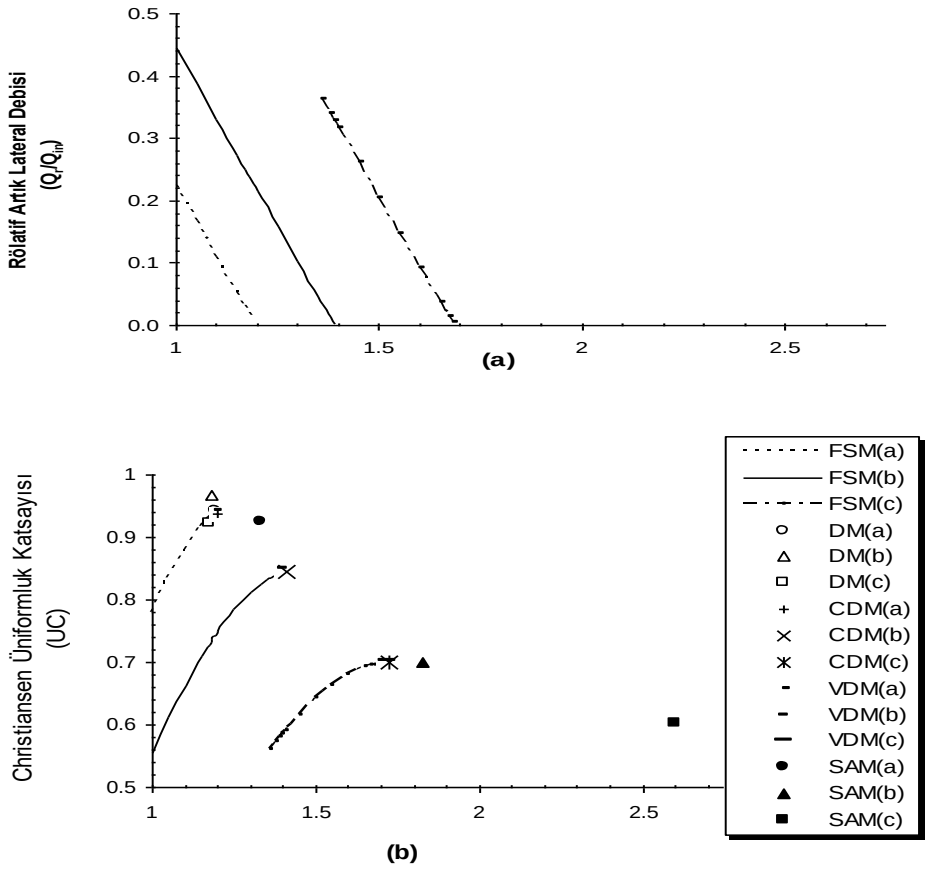
Şekil 2.a'dan; rölatif artık lateral debisi (Q_r/Q_{in}); $s_0 = 0.0$ eğim şartı için $[A = 1.0 \le (H_{in}/H_{av}) \le B = 1.19]$ projelendirme aralığında 0.2'den başlayıp 0'a doğru azalan; $s_0 = -0.02$ eğim şartı için $[A = 1.0 \le (H_{in}/H_{av}) \le B = 1.39]$ projelendirme aralığında 0.44'den 0'a doğru azalan ve $s_0 = -0.05$ eğim şartı için $(A = 1.36 \le H_{in}/H_{av} \le B = 1.68)$ projelendirme aralığında 0.36'dan 0'a doğru azalan değerler almaktadır.

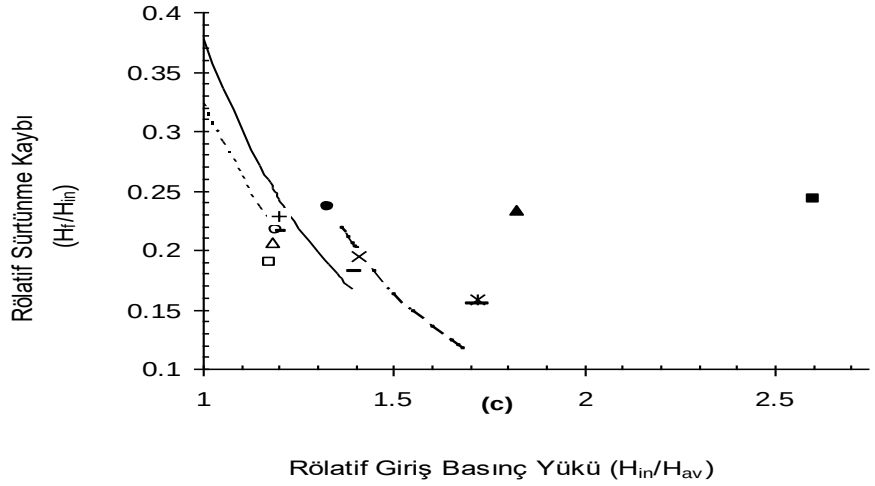
Şekil 2.b'den; Christiansen üniformluk katsayısı $[A = 1.0 \le (H_{in}/H_{av}) \le B = 1.19]$ projelendirme aralığında 0.80'den 0.94'e doğru artan; $s_0 = -0.02$ eğim şartı için $[A = 1.0 \le (H_{in}/H_{av}) \le B = 1.39]$

projelendirme aralığında 0.56'dan 0.84'e doğru artan ve $s_0 = -0.05$ eğim şartı için $(A = 1.36 \le H_{in}/H_{av} \le B = 1.68)$ projelendirme aralığında 0.56'dan 0.69'a doğru artan değerler almaktadır.

Benzer halde Şekil 2.c'den; rölatif enerji kaybı (H_f/H_{in}), $s_0 = 0.0$ eğim şartı için $[A = 1.0 \le (H_{in}/H_{av}) \le B = 1.19]$ projelendirme aralığında 0.34'den 0.22'ye doğru azalan; $s_0 = -0.02$ eğim şartı için $(A = 1.36 \le H_{in}/H_{av} \le B = 1.68)$ projelendirme aralığında 0.24'den 0.12'ye doğru azalan değerler almaktadır. Buna göre tüm tasarım kombinasyonları için projelendirme aralığı içerisinde en uygun giriş basınç yükünün değeri, artık lateral debisi ve toplam sürtünme kayıplarının minimum; buna mukabil üniformluk katsayısının maksimum olduğu $(H_{in}/H_{av} = B)$ sınır değerlerinde elde edilebilmektedir.

Şekil 2.b ve 2.c'den görüleceği üzere $s_0 = 0.0$ eğim durumu için, (H_{in}/H_{av}), (H_f/H_{in}), (U_C) tasarım parametrelerinin belirlenmesinde, FSM, DM, CDM ve VDM metotları birbirine yakın sonuçlar verirken, SAM metodu bunlardan çok farklı sonuçlar vermektedir.





Şekil 2. FSM, DM, CDM, VDM ve SAM metotlarına göre: s0 = 0.0, -0.02, -0.05; y = 1.0 için tasarım parametrelerinin rölatif giriş basınç yükü ile değişimi

6. Sonuç ve Değerlendirmeler

Çalışmada elde edilen sonuçlar aşağıdaki gibi özetlenebilir:

1. Karşılaştırma testi sonucunda, tasarım parametrelerinin belirlenmesinde damlatıcı debi üssünün $y=1.0$ değeri için; ileri adım metodu, diferansiyel metot ve değişken debi metodu birbiri ile uyumlu sonuçlar verirken; sabit debi metodu ve ardışık yaklaşımlar metodundan elde edilen sonuçlar diğer metotların sonuçlarından önemli mertebede sapmaktadır. Ardışık yaklaşımlar metodu diğer metotlara kıyasla, giriş basınç yükü ve toplam sürtünme kaybı için daha yüksek değerler verirken, üniformluk katsayısı için daha düşük değer vermektedir.

2. Tüm tasarım kombinasyonları ve eğim şartları göz önüne alındığında, üniformluk katsayısı için diferansiyel metot diğer metotlara göre en yüksek değerleri vermektedir. Damlatıcı debi üssünün $y=1.0$ değeri için Runge-Kutta nümerik metodundan elde edilen sonuçlar üniformluk katsayısının başlangıçtaki sınırlı bir aralığında diferansiyel metodun sonuçları ile uyum sağlarken; basitleştirilmiş analitik yaklaşım üniformluk katsayısının tüm değerleri için diferansiyel metotla uyumlu sonuçlar vermektedir.

3. İleri-adım metodunda, rölatif sürtünme kaybı, Christiansen üniformluk katsayısı ve rölatif artık lateral debisi değerleri, rölatif giriş basınç yükünün projelendirme aralığı içerisinde verilen değerleri ile değişirken; diğer metotlarda söz konusu tasarım parametreleri rölatif giriş basınç yükünün sabit bir değerine bağlı olarak değişmektedir.

4. Projelendirme aralığı içerisinde en uygun giriş basınç yükünün, artık lateral debisi ve toplam sürtünme kayıplarının minimum düzeyde; buna mukabil üniformluk katsayısının maksimum düzeyde olduğu, maksimum giriş basınç yükü sınır değerinde elde edilmektedir. Şayet, giriş basınç yükü için maksimum giriş basınç yükü sınır değerinden büyük olacak şekilde bir değer seçilirse, lateral boyunca tüm damlatıcı debileri toplamının lateral giriş debisinden büyük bir değerde çıkacağı anlaşılır ki bu durum, lateralin mansap uç noktasından menba istikametine doğru bir geri akımın oluştuğunu göstermektedir.

5. Çap ve uzunluk değerlerinin sabit olması halinde lateral eğiminin tasarım parametreleri üzerindeki etkisini araştırmak üzere yapılan analiz sonucunda şu sonuca varılmaktadır. Eğimsiz bir lateral boruya nazaran, yukarı eğim değeri arttıkça giriş basınç yükü değeri artarken, üniformluk katsayısının değeri azalmakta; buna mukabil aşağı eğim değeri arttıkça giriş basınç yükü değeri azalırken, üniformluk katsayısının değeri artmaktadır.

6. Lateral çapı, uzunluğu ve eğimi değerlerinden bağımsız olarak, damlatıcı debi üssünün üniformluk katsayısı üzerindeki etkisini belirlemek üzere yapılan analiz sonucunda, damlatıcı debi üssünün küçük değerlerinde üniformluk katsayısı yüksek değerler alırken, büyük değerlerinde üniformluk katsayısının daha küçük değerler aldığı belirlenmiştir. Buradan hareketle, damlatıcı debi üssü ile üniformluk katsayısı arasında ters bir ilişki olduğu sonucuna varılmaktadır.

Kaynaklar

Ağıralioğlu, N., Eren, R. H. ve Yıldırım, G., (2000). İstanbul'da peyzaj sulaması için su kaynakları, teknik bülteni, *İstanbul Teknik Üniversitesi, İnşaat Fak*., İstanbul.

Ağıralioğlu, N., ve Yıldırım, G., (2002). Determining water requirements for landscape irrigation in Istanbul region. *Proc., International Conference on Water Resources Management in Arid Regions*, Kuwait Institute for Scientific Research, Kuwait.

Al-Amoud, A.I., (1995). Significance of energy losses due to emitter connections in trickle irrigation lines. *J. Agricultural Engineering Researches*, **60,** 1, 1-5.

Anyoji, H., ve Wu, I.P., (1987). Statistical approach for drip lateral design. *Transaction ASAE,* **30,** 1, 187-192.

Anwar, A. A., (1999a). Factor G for pipelines with equally spaced multiple outlets and outflow. *J. Irrigation and Drainage Eng., ASCE*, **125,** 1, 34-39.

Anwar, A. A., (1999b). Adjusted factor G_a for pipelines with multiple outlets and outflow. *J. Irrigation and Drainage Eng., ASCE*, **125,** 6, 355-359.

Anwar, A. A., (2000). Inlet pressure for horizontal tapered laterals. *J. Irrigation and Drainage Eng., ASCE*, **126,** 1, 57-63.

Bagarello, V., Ferro, V., Provenzano, G., ve Pumo, D., (1995). Experimental study on flow resistance law for small diameter plastic pipes. *J. Irrigation and Drainage Eng., ASCE*, **121,** 5, 313-316.

Bagarello, V., Ferro, V., Provenzano, G., ve Pumo, D., (1997). Evaluating pressure losses in drip irrigation lines. *J. Irrigation and Drainage Eng., ASCE*, **123,** 1, 1-7.

Bralts, V. F., Kelly, S.F., Shayya, W. H., ve Segerlind, L. J., (1993). Finite element analysis of microirrigation hydraulics using a virtual emitter system. *Transaction ASAE*, **36,** 3, 717-725.

Chadwick, A., ve Morfett, J., (1993). *Hydraulics in civil and environmental engineering*, E&FN SPON, London, U.K.

Featherstone, R.E., ve Nalluri, C., (1982). *Civil engineering hydraulics, essential theory, worked examples.* Granada Publishing, New York, N.Y.

Hathoot, H. M., Al-Amoud, A. I., and Mohammad, F. S., (1993). Analysis and design of trickle-irrigation laterals. *J. Irrigation and Drainage Eng., ASCE*, **119,** 5, 756-767.

Hathoot, H.M., Al-Amoud, A.I., Al-Mesned, A.S., (2000). Design of trickle irrigation laterals considering emitter losses. *Irrigation and Drainage*, **49,** 2, *1-14.*

Howell, T. A. ve Hiler, E. A., (1974). Trickle irrigation lateral design. *Transaction ASAE*, **17,** 5, 902-908.

Howell, T. A. ve Barinas, F. A., (1980). Pressure losses across trickle irrigation fittings and emitters. *Transaction ASAE*, **23,** 4, 928-933.

Jain, S. K., Singh, K. K., ve Singh, R. P., (2002). Micro-irrigation lateral design using lateral discharge equation. *J. Irrigation and Drainage Eng., ASCE,* **128,** 2, 125-128.

Juana, L., Sinobas, L. R., Losada, A., (2002a). Determining minor head losses in drip irrigation laterals.I: methodolgy. *J. Irrigation and Drainage Eng., ASCE*, **128,** 6, 376-384.

Juana, L., Sinobas, L. R., Losada, A., (2002b). Determining minor head losses in drip irrigation laterals.II: experimental study and validation. *J. Irrigation and Drainage Eng., ASCE*, **128,** 6, 385-396.

Kang, Y., ve Nishiyama, S., (1996a). Analysis and design of microirrigation laterals. *J. Irrigation and Drainage Eng., ASCE*, **122,** 2, 75-81.

Kang, Y., ve Nishiyama, S., (1996b). Design of microirrigation submain units. *J. Irrigation and Drainage Eng., ASCE*, **122,** 2, 83-89.

Keller, J., ve Karmeli, D., (1974). Trickle irrigation design parameters. *Transaction ASAE*, **17,** 4, 678-683.

Keller, J., ve Bliesner, R. D., (1990). *Sprinkle and trickle irrigation*, Van Nostrand Reinhold, New York.

Provenzano, G., Pumo, D., (2004). Experimental analysis of local pressure losses for microirrigation laterals. *J. Irrigation and Drainage Eng., ASCE,* **130,** 4, 318-324.

Provenzano G., Pumo, D., ve Di Dio, P., (2005). Simplified procedure to evaluate head losses in drip irrigation laterals. *J. Irrigation and Drainage Eng., ASCE,* **131,** 6, *525-532.*

Saad, J. C. C., ve Marino, M. A., (2002). Optimum design of micro-irrigation systems in sloping lands. *J. Irrigation and Drainage Eng., ASCE*, **128,** 2, 116-124.

Scaloppi, E. J., ve Allen, R.G., (1993). Hydraulics of irrigation laterals: Comparative analysis. *J. Irrigation and Drainage Eng., ASCE*, **119,** 1, 91-115.

Sinobas, L. R., Juana, L., Losada, A., (1999). Effects of temperature changes on emitter discharge. *J. Irrigation and Drainage Eng., ASCE*, **125,** 2, 64-73.

Streeter, V. I., ve Wylie, B. E., (1983). *Fluid Mechanics*, McGraw-Hill Co., New York, N.Y.

Valiantzas, J. D., (1998). Analytical approach for direct drip lateral hydraulic calculation. *J. Irrigation and Drainage Eng., ASCE*, **124,** 6, 300-305.

Valiantzas, J. D., (2002). Continuous outflow variation along irrigation laterals: Effect of the number of outlets. *J. Irrigation and Drainage Eng., ASCE*, **128,** 1, 34-42.

Vallesquino, P., ve Luque-Escamilla, P. L., (2001). New algorithm for hydraulic calculation in irrigation laterals. *J. Irrigation and Drainage Eng., ASCE*, **127,** 4, 254-260.

Vallesquino, P., ve Luque-Escamilla, P. L., (2002). Equivalent friction factor method for hydraulic calculation in irrigation laterals. *J. Irrigation and Drainage Eng., ASCE*, **128,** 5, 278-286.

von Bernuth, R. D., (1990). Simple and accurate friction loss equation for plastic pipe. *J. Irrigation and Drainage Eng., ASCE*, **116,** 2, 294-298.

von Bernuth, R. D., ve Wilson, T., (1989). Friction factors for small diameter plastic pipes. *J. Hydraulic Eng., ASCE*, **115,** 2, 183-192.

Warrick, A.W., ve Yitayew, M., (1987). An analytical solution for flow in a manifold. *Advances in Water Resources*, 10, 58-63.

Warrick, A. W., ve Yitayew, M., (1988). Trickle lateral hydraulics.I: Analytical solution. *J. Irrigation and Drainage Eng., ASCE*, **114,** 2, 281- 288.

Watters, G. Z., ve Keller, J., (1978). Trickle irrigation tubing hydraulics. *Summer Meeting of ASAE*, Utah State University, Logan, Utah.

Wu, I. P., ve Gitlin, H. M., (1973). Hydraulics and uniformity for drip irrigation. *J. Irrigation and Drainage Div., ASCE*, 99, IR2, Proc. Paper 9786, June, pp. 157-168.

Wu, I.P., ve Gitlin, H. M., (1974). Drip irrigation design based on uniformity. *Transaction. ASAE*, **17,** 429-432.

Wu, I.P., ve Gitlin, H. M., (1975). Energy gradient line for drip irrigation laterals. *J. Irrigation and Drainage Eng., ASCE*, **101,** 4, 323-326.

Wu, I. P., (1992). Energy gradient line approach for direct hydraulic calculation in drip irrigation design. *Irrigation Science*, **13,** 21-29.

Wu, I.P., ve Yue, R., (1993). Drip lateral design using energy gradient line approach. *Transaction ASAE*, **36,** 2, 389-394.

Wu, I. P., (1997). An assessment of hydraulic design of microirrigation systems. *Agricultural Water Management*, **32**, 275-284.

Yıldırım, G., (2001). Damla sulamasında lateral boruların bilgisayar destekli projelendirilmesi. Yüksek lisans tezi, *Istanbul Teknik Üniversitesi, Fen Bilimleri Enstitüsü*, Istanbul.

Yıldırım, G., ve Ağıralioğlu, N., (2001). Computer aided design of lateral pipes in drip irrigation. *Proc., International Symposium on Water Resources and Environmental Impact Assessment*, Technical University of Istanbul, Istanbul.

Yıldırım, G., ve Ağıralioğlu, N., (2002a). Variation of total friction head losses and uniformity coefficients based on inlet pressure head in trickle laterals. *Proc., International Conference on Water Resources Management in Arid Regions*, Kuwait Institute for Scientific Research, Kuwait.

Yıldırım, G., ve Ağıralioğlu, N., (2002b). Variation of design parameters in micro-irrigation laterals. *Proc., International Conference on Advances of Civil Engineering*, Technical University of Istanbul, Istanbul.

Yıldırım, G., ve Ağıralioğlu, N., (2003a). Discussion of "New algorithm for hydraulic calculation in irrigation laterals" *J. Irrigation and Drainage Eng., ASCE*, **129,** 2, 142-143.

Yıldırım, G., ve Ağıralioğlu, N., (2003b). Discussion of "Continuous outflow variation along irrigation laterals: effect of the number of outlets" *J. Irrigation and Drainage Eng., ASCE*, **129,** 5, 382-386.

Yıldırım, G., ve Ağıralioğlu, N., (2004a). Linear solution for hydraulic analysis of tapered microirrigation laterals. *J. Irrigation and Drainage Eng., ASCE*, **130,** 1, 78-87.

Yıldırım, G., ve Ağıralioğlu, N., (2004b). Comparative analysis of hydraulic calculation methods in design of microirrigation laterals. *J. Irrigation and Drainage Eng., ASCE*, **130,** 3, 201-217.

Yıldırım, G., ve Ağıralioğlu, N., (2004c). Discussion of "Determining minor losses in drip irrigation laterals.I: methodology" *J. Irrigation and Drainage Eng., ASCE*, **130,** 3, 248-252.

Yıldırım, G., ve Ağıralioğlu, N., (2004d). Discussion of "Equivalent friction factor method for hydraulic calculation in irrigation laterals" *J. Irrigation and Drainage Eng., ASCE*, **130,** 4, 335-339.

Yıldırım, G., ve Ağıralioğlu, N., (2004e). Discussion of "Determining minor losses in drip irrigation laterals.II: experimental study and validation" *J. Irrigation and Drainage Eng., ASCE*, **130,** 4, 344-346.

Yıldırım, G., ve Ağıralioğlu, N., (2004f). Variation of design parameters in micro-irrigation laterals. *ARI Interdisciplinary Journal of Physical and Engineering Sciences*, **54,** 1, 42-53.

Yıldırım, G., ve Ağıralioğlu, N., (2005a). Discussion of "Inlet pressure, energy cost, and economic design of tapered irrigation submains" *J. Irrigation and Drainage Eng., ASCE*, **131,** 2, 220-224.

Yıldırım, G., ve Ağıralioğlu, N., (2005b). Discussion of "Explicit hydraulic design of microirrigation submain units with tapered manifold and laterals" *J. Irrigation and Drainage Eng., ASCE*, **131,** 3, 299-300.

Yıldırım, G., ve Ağıralioğlu, N., (2005c). Closure to "Linear solution for hydraulic analysis of tapered microirrigation laterals" *J. Irrigation and Drainage Eng., ASCE*, **131,** 5, 490-491.

Yıldırım, G., ve Ağıralioğlu, N., (2006). Closure to "Comparative analysis of hydraulic calculation methods in design of microirrigation laterals" *J. Irrigation and Drainage Eng., ASCE,* **132,** 1, 85-88.

Yıldırım, G., (2006). Discussion of "Experimental analysis of local pressure losses for microirrigation laterals." *J. Irrigation and Drainage Eng.,* **132,** 2, 189-192.

Yitayew, M., (1989). Head loss in manifolds or trickle lateral: Simplified approach. *J. Irrigation and Drainage Eng., ASCE,* **115,** 4, 739-743.

Yitayew, M., ve Warrick, A. W., (1988). Trickle lateral hydraulics.II: Design and examples. *J. Irrigation and Drainage Eng., ASCE,* **114,** 2, 289-300.

Yitayew, M., ve Warrick, A. W., (1987). Velocity head considerations for trickle laterals. *J. Irrigation and Drainage Eng., ASCE,* **113,** 4, 611-615.

==========

Farklı Cam Elyaf Oranlarına Sahip POM Malzemesinin Digimat ile Karakterizasyonu ve Yataklama Elemanı Üzerindeki Etkisinin İncelenmesi

Yoncagül ÇELİK EREZ[1*], Cem TANYERİ[2], Ozan DEVLEN[3]

[1*] Kastaş Sızdırmazlık Teknolojileri, İzmir, Türkiye, (ORCID: 0000-0002-0163-5097), ycelik@kastas.com
[2] Kastaş Sızdırmazlık Teknolojileri, İzmir, Türkiye, (ORCID: 0000-0002-1290-2875), ctanyeri@kastas.com
[3] Kastaş Sızdırmazlık Teknolojileri, İzmir, Türkiye, (ORCID: 0000-0002-8079-0553), odevlen@kastas.com

Öz

Gelişen teknolojinin beraberinde getirdiği yeni talepler malzemelerin daha sağlam, daha ucuz ve daha hafif gibi özelliklere sahip olması ihtiyacını doğurmuştur. Bu ihtiyaç doğrultusunda yapılan çalışmalar sonucunda ortaya çıkan kompozit malzemeler sürekli bir gelişim halindedir. Malzemelerin ve ürünlerin optimizasyonu için gerekli olan zaman ve maliyet tasarrufunun kritik olduğu bu dönemde en sık kullanılan metotlardan biri sonlu elemanlar analizidir. Bu çalışmada Digimat programı kullanılarak POM (Polioksimetilen) malzemesinin %20, %25 ve %30 cam elyaf katkı oranlarına göre karakterizasyonun ve bu malzemeden üretilen sızdırmazlık elemanlarının davranışının incelenmesi amaçlanmaktadır. Bu amaç doğrultusunda ilk olarak yataklama elemanlarının MSC Marc ile nonlineer analizleri gerçekleştirilmekte, Moldex3D ile plastik enjeksiyon sırasındaki fiber yönelimlerinin tespit edilerek analizlerin çıktıları Digimat ortamında map edilmektedir. Ardından farklı fiber oranlarına sahip malzemeler modellenerek analiz sonucu iç gerilim ve temas kuvvetleri açısından değerlendirilip karşılaştırılmaktadır. Çalışma boyunca sonlu elemanlar metodunun kullanılması gereksiz prototip ve malzeme imalatının önüne geçerek zaman ve maliyet açısından tasarruf sağlamaktadır. Bu çalışma ışığında elde edilen veriler kompozit malzemelerin modellenmesi ve karakterize edilmesi için farklı takviye unsur ve oranları kullanılarak çalışma koşullarına uygun ürün üretimi için ciddi avantaj sağlayacaktır.

Anahtar Kelimeler: POM, Cam Elyaf, Kompozit Malzeme, Digimat, Sonlu Elemanlar Analizi

Characterization of POM Material with Different Glass Fiber Ratios with Digimat and Investigation of its Effect on the Guide Element

Abstract

The new demands brought by the developing technology have led to the need for more robust, cheaper, and lighter materials. Composite materials, which emerged as a result of the studies carried out in line with this need, are in continuous development. Finite element analysis is one of the most frequently used methods in this period when time and cost savings are critical for the optimization of materials and products. This study aims to examine the characterization of POM (Polyoxymethylene) material according to 20%, 25%, and 30% glass fiber additive ratios and the behavior of sealing elements produced from this material by using the Digimat program. For this purpose, firstly, nonlinear analyzes of the bearing elements are performed with MSC Marc, the fiber orientations during plastic injection are determined with Moldex3D and the outputs of the analyzes are mapped in the Digimat environment. Then, materials with different fiber ratios are modeled and the analysis result is evaluated and compared in terms of internal tension and contact forces. The use of the finite element method throughout the study prevents unnecessary prototype and material production and saves time and cost. The data obtained in light of this study will provide a serious advantage for the production of products suitable for working conditions by using different reinforcement elements and ratios for modeling and characterizing composite materials.

Keywords: POM, Glass Fiber, Composite Material, Digimat, Finite Element Analysis.

1. Giriş

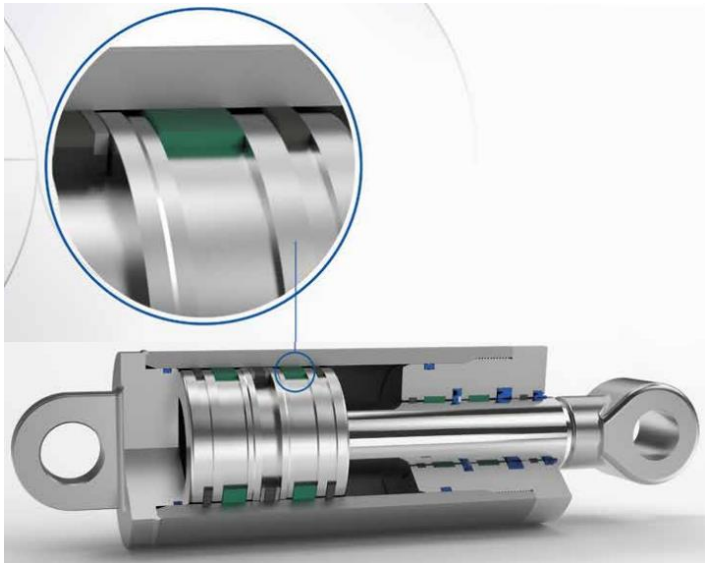
Günümüzde hidrolik ve pnömatik sistemlerin çoğunda kullanılan sızdırmazlık elemanı olan yataklama elemanlarının üretimi için sıklıkla POM malzemeler kullanılmaktadır. Cam elyaf takviyeli POM kompozit malzemeler, iyi mekanik özellikler, kolay işlenebilirlik, hafiflik ve daha düşük maliyetli olma gibi özelliklere sahiptir (Kastaş, 2022).

Parçanın şekli, enjeksiyon parametreleri ve işleme koşulu, malzemenin nihai mekanik özellikleri ve dolayısıyla parça üzerinde büyük bir etkiye sahiptir. Bu nedenle çalışmanın nihai ürün üzerinde malzemenin davranışının modellenmesi kritiktir.

Özellikle POM malzemelerin mekanik özelliklerini en çok etkileyen faktörlerden biri içerisindeki takviye oranı ve fiber oryantasyonudur. Bu etkiyi incelemek için MSC Marc, Moldex3D ve Digimat çözücüleri kullanmaktır. MSC Marc ürünün çalışma koşullarındaki davranışını simüle etmek için kullanılır. Fiber oryantasyonu, enjeksiyon sürecini simüle eden özel Moldex3D yazılımı kullanılarak elde edilir. Fiberler daha sonra dışa aktarılır ve Digimat ile yapısal modele eşlenir. Haritalamanın yanı sıra Digimat yazılımı ile SFRC için malzeme modeli oluşturabilirsiniz. MSC Marc ve Moldex3D arasında, bir arayüz yazılımı olarak Digimat kullanılarak birleştirilmiş analizler geçmişte gerçekleştirilmiştir (Kurkin et al., 2017; Adam & Assaker, 2014; Pedro, 2017; Lindhult & Ljungberg, 2015.; G. Soni et al.,2014). Sayısal incelemede fiber oryantasyonunu dikkate almanın önemini ve dikkate alınmadığı takdirde hatanın ne kadar olduğunu gösterirler. Doğru tasarım simülasyonları için anizotropik çok ölçekli malzeme modelleri, tasarım süresini doğrulamak ve azaltmak için endüstri için bir zorunluluktur. Bu nedenle, bu üç yazılım paketi arasında net bir iş akışı gereklidir. Ayrıca gerçekçi olmayan tahminlere yol açabilecek parametrelerin de incelenmesi gerekmektedir. Bu parametrelerden biri hem MSC Marc hem de Moldex3D'deki ağın boyutudur.

2. Materyal ve Metod

Silindirin eş merkezli çalışmasını sağlayarak sızdırmazlık görevi yapan elemanların ezilmesini önleyen ve güvenli bir çalışma ortamı oluşturan yataklama elemanları, yük altında düşük deformasyon ve ölçü kaybına sahip yüksek mukavemetli kompozit malzemeden imal edilmektedirler. SFRC malzemeden yapılan yataklama elemanlarının davranışının modellenmesi ve öngörülmesi, maksimum verim elde etmek için sonlu elemanlar analizi kullanılmaktadır. Sonlu elemanlar analizi bir mühendislik yaklaşımı olup sonuçlarının deneysel çalışmalarla doğrulanması gerekmektedir. Bu çalışmada ilk etapta sonlu elemanlar analizi ile %20, %25 ve %30 cam elyaf katkı oranlarına sahip malzemeli ürünlerin sonlu elemanlar analizi yapılmıştır. Ardından optimum sonucu veren malzeme için prototip ürün yapıp üzerinde saha testleri gerçekleştirilmiştir.



Şekil 1. Yataklama Elemanları Silindirdeki Görünümü

2.1. Sonlu Elemanlar Analizi

Sızdırmazlık elemanları çeşitli uygulama alanlarında farklı ve zorlayıcı çalışma koşulları altında çalışmaktadır. Ağır hizmet sektörüne hizmet eden yataklama elemanlarının üzerine gelen yükleri taşıyabilmesi ve metal metal temasını engellemesi gerekmektedir. Bu nedenle sonlu elemanlar analizi yapmak sistemin sağlıklı çalışması için gerekli olan yataklama elemanlarının doğru tasarımı ve optimizasyonu için kritiktir. Bu çalışmada ilk etapta ürünün MSC Marc programı kullanarak nonlineer analizi ve Moldex3D programı ile plastik enjeksiyon prosesinin simülasyonu yapılmıştır. İki ayrı programdan elde edilen çıktılar malzeme modellemesi için DİGİMAT programına aktarılmış ve MSC Marc-Digimat arayüzü ile tekrar analiz koşturulmuştur.

2.1.1. Nonlineer Analiz

Cam elyaf katkılı POM (Polioksimetilen) malzeme nonlineer davranış sergilemektedir. İçerisindeki farklı elyaf oranlarına göre değişkenlik gösteren mekanik özellikleri gözlemleyebilmek ve karşılaştırmak adına MSC Marc program ile tasarımı yapılan ürün, çalışma koşullarına göre simule edilmektedir. Bu çalışmada, iş makineleri, vinçler, enjeksiyon tezgâhları, tarım makineleri, hafif ve orta hizmet silindirleri kullanıma uygun olan ve cam elyaf katkılı POM malzemeden üretilen K68 yataklama elemanı referans ürün olarak alınmıştır. Müşteri talepleri ve test merkezinde gerçekleşen testler sonucunda belirlenen pozisyon ve yükleme durumlarındaki nonlineer analizlerin sonuçları Eşdeğer Cauchy Stress ve Contact Stress'lerin dağılımı olarak incelenmektedir.

Tablo 1. Sınır şartları

Sınır Şartları	**Özellikleri**
Malzeme	*%20 Cam Elyaf Katkılı POM* *%25 Cam Elyaf Katkılı POM* *%30 Cam Elyaf Katkılı POM*
Sıcaklık	*25 °C*
Deplasman	0.2 mm

Bu çalışmada ürünün nominal çalışma parametrelerden elde edilen veriler yükleme ve sınır şartları olarak kullanılmıştır. Analiz kurgusu ilk adım yataklama elemanın kanala oturtulması, ikinci adım milin ürünün içine geçmesi ile montaj işleminin tamamlanması ve son adım olarak da mile dik yönlü kuvvet verilmesi şeklindedir.

2.1.2. Plastik Enjeksiyon Üretim Analizi

Enjeksiyon kalıplama işlemini simule etmek için kullanılan Moldex3D programı, ürün tasarımının ve üretilebilirliğinin optimize edilmesi ve ürün kalitesini en üst düzeye çıkarılması amacıyla kullanılmaktadır. Bu çalışmada, üstün performanslı yataklama elemanlarının üretimi için cam elyaf katkılı POM malzeme yapısından kaynaklı kritik olan üretim prosesinin ürün üzerindeki etkisini görmek ve optimize etmek amaçlanmıştır. Plastik enjeksiyon makinasından alınan proses parametrelerine göre yapılan çalışmanın sonucunda ürünün dolum durumu, çekinti değeri ve yarattığı basınç değeri gösterilecektir. Ayrıca proses sonucunda meydana gelen fiber yönelimleri ve mesh yapısı Digimat Programında girdi olarak kullanılmak üzere MSC Marc programına uygun olacak şekilde dışarı aktarılacaktır.

2.1.3. Malzeme Modelleme

Gerek içerisindeki malzeme kütüphanesini kullanarak gerekse deneysel sonuçların aktarılması ile oluşturulan malzeme modellerinin kesintisiz olarak ve herhangi ek bir ara yüze ihtiyaç kullanılmadan MSC Software sonlu eleman çözücülerine ve diğer yazılımlara aktarılması için Digimat kullanılmaktadır. Çalışmada Digimat MSC Software ve Moldex 3D programından gelen datalar kullanılarak kompozit malzeme elde edilmiştir. Modelleme çalışmaları yapılırken Marc implict çözücüsü ile birlikte kullanılmak için Digimat yeteneklerini ve gerekli kütüphaneleri içeren Digimat-CAE modülü kullanılmıştır.

2.2. Saha Testleri

Statik & Dinamik Yataklama Elemanı Test Cihazı ile test ürünlerinin silindirler içerisindeki çalışma koşulları yaratılıp ürünlerin yük taşıma kabiliyetleri ve yüke bağlı oluşan deplasman miktarı arasındaki ilişki incelenmektedir.

2.2.1 Statik test

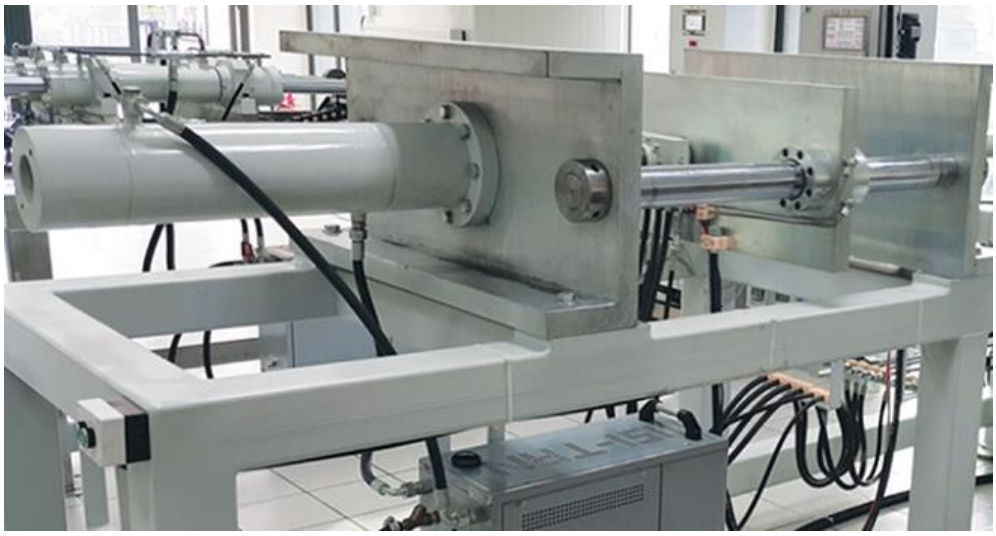
Bir yataklama elemanının uygun ölçülerde işlenmiş düz veya dairesel kanal aparatları içine yerleştirilip hedeflenen test sıcaklığına ulaşıldıktan sonra sabit bir atış hızına sahip olan kuvvet uygulanması ve bu kuvvet sonucunda oluşan deplasman (ezilme miktarı) arasında bir ilişki kurulması ile yapılır.



Şekil 2. Statik Test Aparatı

2.2.1 Dinamik Test

Dinamik test yöntemi, test edilecek yataklama elemanının bir test silindirinin piston ve boğaz yataklama kanallarına takılmasının ardından test silindirinin radyal bir yük altında ileri ve geri sürekli hareket etmesiyle gerçekleştirilir. Bu yöntem sıcaklık, yağlama ve aşınma gibi etkilerin de test koşullarına eklenmesi ile ürünün saha şartlarına daha yakın bir performansta test edilmesini sağlar.



Şekil 3. Dinamik Test Cihazı

3. Sonuçlar

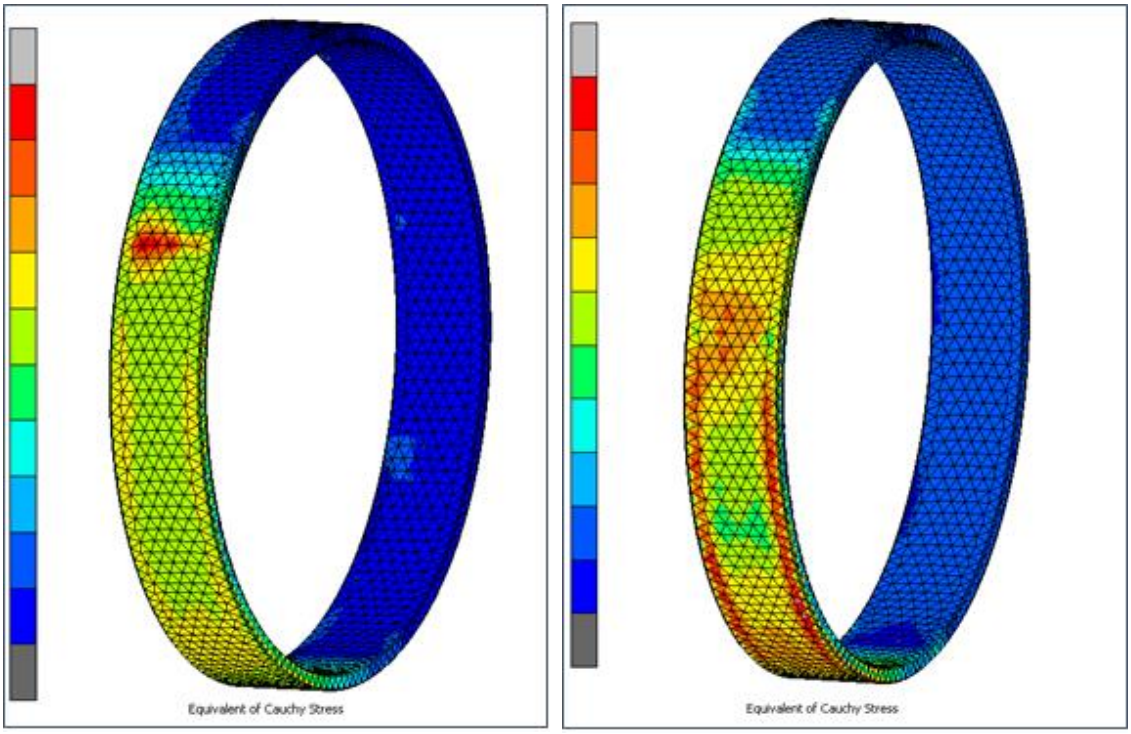
3.1. Sonlu Elemanlar Analiz Sonuçları

Yataklama elemanının maksimum Eşdeğer Cauchy Gerilme ve Kontak Gerilme değerleri tabloda verilmiştir.

Tablo 2. Analiz sonuçları

Program	**Değişkenler**	**Durum-1**	**Durum-2**	**Durum-3**
Moldex3D	*Yolluk*			
Digimat	*Malzeme*	*%20 Cam Elyaf*	*%25 Cam Elyaf*	*%30 Cam Elyaf*
	Sonuçlar			
Deplasman	Eşdeğer Cauchy Gerilme	Ref.	10%	12%
	Kontak Gerilme	Ref.	2%	-2%
	Kuvvet	Ref.	5%	1%

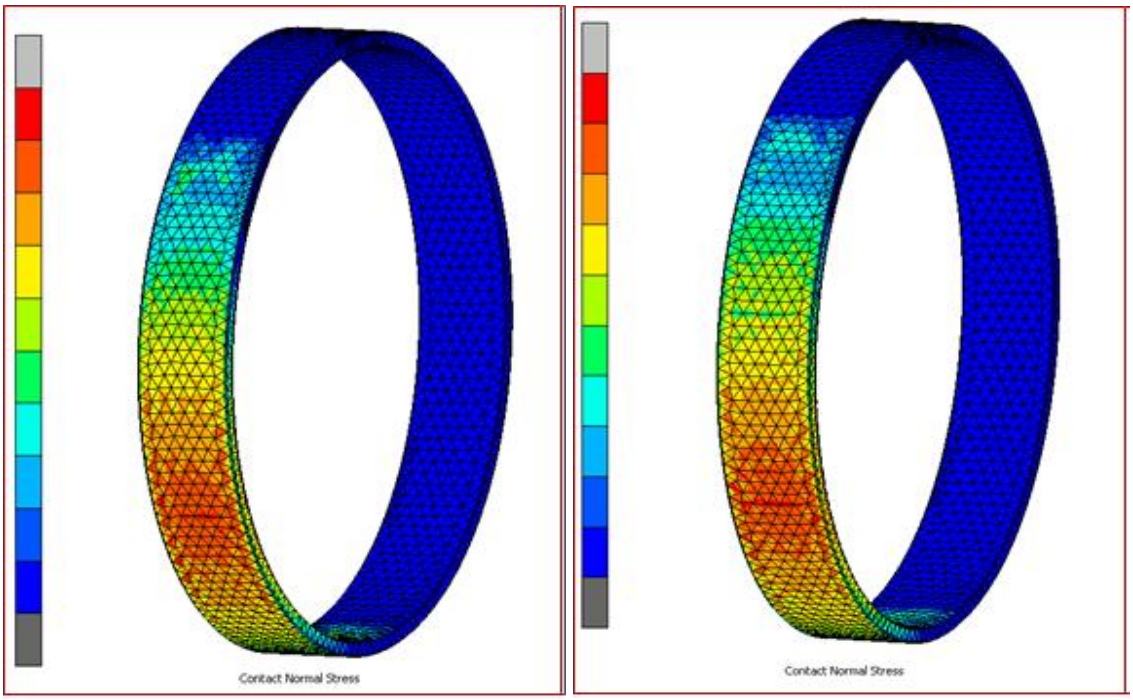
Eşdeğer Cauchy Gerilme, yataklama elemanının iç gerilmesinin incelenmesi ve karşılaştırılmasında kullanılmaktadır.



Mevcut Model *Optimum Model*

Şekil 4. Eşdeğer Cauchy Gerilmesi

Kontak Gerilme yataklama elemanının aşınma durumunun incelenmesinde kullanılmaktadır.

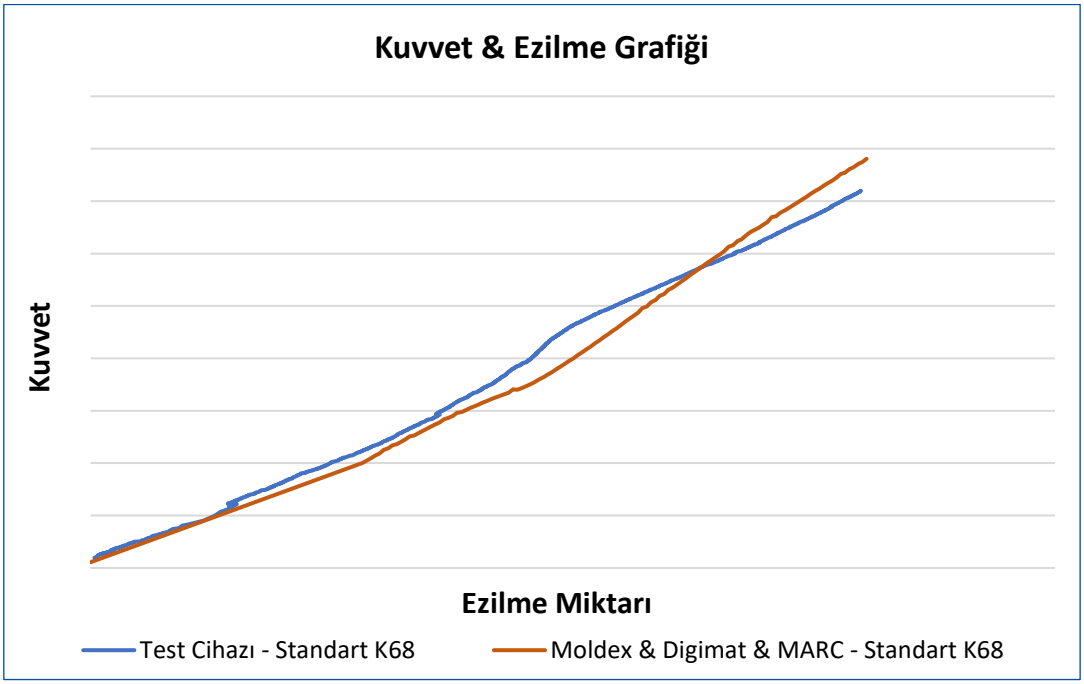


Mevcut Model *Optimum Model*

Şekil 4. Kontak Gerilmesi

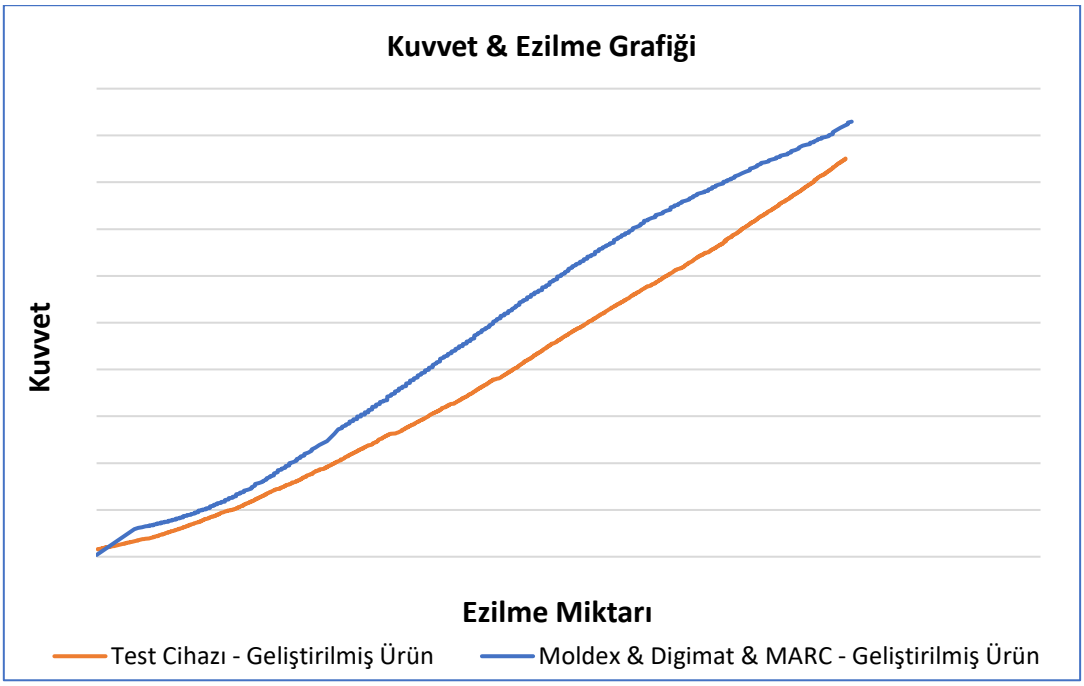
3.2. Test Sonuçları

Yataklama elemanının 0,2 mm ezilmesi sonucunda ürün üzerinde oluşan yükler aşağıdaki grafikte belirtilmiştir.



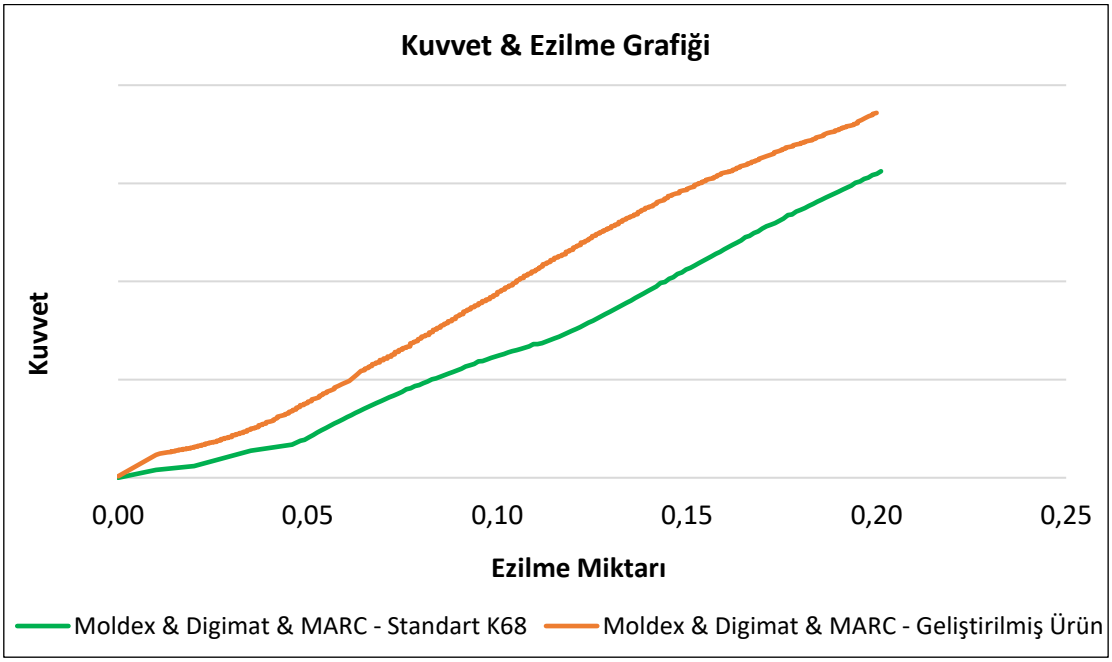
Şekil 5. Kuvvet-Ezilme Grafiği (Ref. Ürün Karşılaştırma)

Sonlu elemanlar analiz sonucu ile test cihazından elde edilen sonucun %92 oranında tutarlılık göstermektedir.

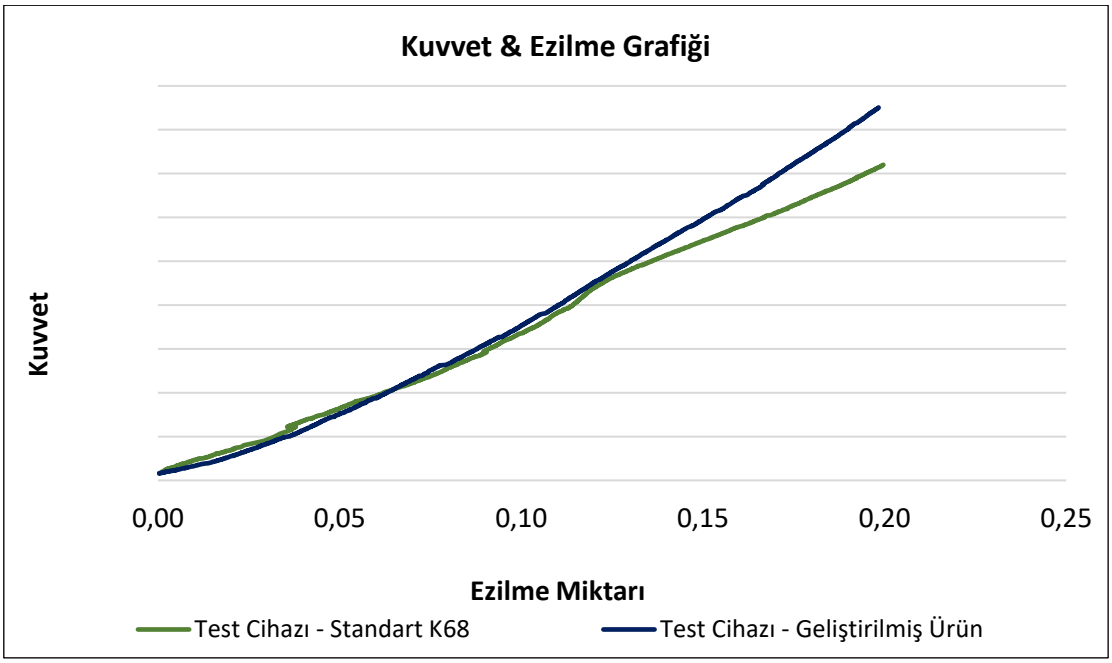


Şekil 6. Kuvvet-Ezilme Grafiği (Geliştirilmiş Ürün Karşılaştırma)

Sonlu elemanlar analiz sonucu ile test cihazından elde edilen sonucun %90 oranında tutarlılık göstermektedir.



Şekil 7. Kuvvet-Ezilme Grafiği (Ref. Ve Geliştirilmiş Ürün SEA Sonuçları Karşılaştırma)



Şekil 8. Kuvvet-Ezilme Grafiği (Ref. ve Geliştirilmiş Ürün Test Sonuçları Karşılaştırma)

Standart ürün ile iyileştirilmiş ürünün bilgisayar destekli analiz programlarına göre sonuçları ve test cihazı ile gerçekleştirilen testlerden elde edilen sonuçların karşılaştırmalı değer ve grafikleri Şekil 7 ve Şekil 8'de sunulmuştur

4. Bulgular ve Tartışma

Sonlu elemanlar analizinde 3 programın ve birbirini destekleyen kurguların kullanılması bilimsel açıdan oldukça önemlidir. Ürünlerin malzemeden imalata yaşam döngüsünün simüle edilmesi gelişim ve optimizasyonun sürekliliğini sağlamaktadır. Digimat programı kullanılarak malzeme modellenmesi deneysel çalışmanın zaman ve mali yükünü azaltmıştır.

Yapılan çalışma sonucunda kompozit malzeme içerisindeki fiber oranının mekanik özelliklerini doğrudan etkilediği gözlemlenmiştir. Kompozit malzemelerin mekanik özelliklerini incelemede malzeme içeriğinin yanı sıra artan fiber oranının işlenebilirliği ve üretebilirliği olumsuz etkileyebileceği gözlemlenen sonuçlardan biridir. Öte yandan yapılan malzeme karakterizasyon çalışması kompozit malzemenin ve plastik enjeksiyon prosesinin optimizasyonu için ışık tutmuştur.

5. Acknowledge

Test cihazının tasarlanması, test cihazında kullanılacak numunenin temin edilmesi ve testlerin doğrulanmasında maddi manevi destek ve kaynaklarını esirgemeyen Kastaş Sızdırmazlık Teknolojileri firmasına ve emeği geçen AR-GE Test Merkezi Teknisyeni Recai Bıçakçı'ya teşekkür ederiz.

Referans

[1] J. Kastaş, "Materials", Oct. 14, 2022. [Online]. Available: https://www.kastas.com.tr/en/materials. [Accessed Oct. 14, 2022].

[2] E.I. Kurkin, V.O. Sadykova, Application of short fiber reinforced composite materials multilevel model for design of ultra-light aerospace structures, Procedia Eng. 185 (2017) 182–189.

[3] L. Adam, R. Assaker, ''Integrated nonlinear multi-scale material modelling of fiber reinforced plastics with digimat: Application to short and continuous fiber composites," 11th World Congr. Comput. Mech. WCCM 2014, 5th Eur. Conf. Comput. Mech. ECCM 2014 6th Eur. Conf. Comput. Fluid Dyn. ECFD 2014, no. Wccm Xi, pp. 2322–2333, 2014.

[4] E. Pedro, ‘‘Structural Analysis of Injection Molded Components Using Digimat As an Interface Software,” pp. 1–10, 2017.

[5] J.-A. Lindhult, M. Ljungberg, ‘‘Fatigue Analysis of Anisotropic Short Fibre Reinforced Polymers-by Use of Digimat and nCode DesignLife,” Master’s thesis in Applied Mechanics, CHALMERS UNIVERSITY OF TECHNOLOGY, 2015.

[6] G. Soni, R. Singh, M. Mitra, B.G. Falzon, Modelling matrix damage and fibrematrix interfacial decohesion in composite laminates via a multi-fibre multilayer representative volume element (M2RVE), Int. J. Solids Struct. 51 (2) (2014) 449–461.

Back-Step Computation Procedure for Evaluating Minor Pressure Loss Components along Laterals Equipped with Integrated In-Line and On-Line Emitters

Gürol Yıldırım

Giresun University, Civil Engineering Department, Hydraulics Division, Giresun, Turkey.

Abstract

Accurate estimation of trickle (drip) irrigation lateral head losses requires calculation of the combined friction losses due to pipe and emitters. Minor losses are caused by the protrusion of emitters barbs into the flow. In routine design applications, assessment of total energy losses is usually carried out by assuming the hypothesis that minor losses can be neglected. However, experimental studies have shown that these minor losses can become a significant percentage of total energy losses, especially in the case of closely spaced emitters along the lateral line. In this study first, simple mathematical expressions for computing three energy loss components -minor friction losses through the path of an integrated in-line emitter, the local pressure losses due to emitter connections, and the major friction losses along the pipe- are deduced based on the backward stepwise procedure. These expressions are quickly implemented in a simple Excel spreadsheet, to rapidly evaluate the relative contribution of each energy loss component to the amount of total energy losses. Hence, an approximate combination formulation is finally proposed to evaluate total energy drop at the end of the lateral line. For practical purpose, two design figures were also prepared to demonstrate the variation of total friction losses (due to pipe and emitters) with emitter local losses, and the variation of pipe friction losses with emitter minor friction losses, regarding two kinds of the integrated in-line emitters with varying spacing. Comparison test covering two design applications for different kinds of integrated in-line and on-line emitters revealed that, the present mathematical model is simple, practical, but sufficiently accurate in all design cases examined, in comparison with the alternative procedures available in the literature.

Keywords: Water pipelines, in-line and on-line emitters, friction, analysis, minor loss, emitter barb connection, steady-state pipe flow, hydraulic networks, turbulent flow, friction coefficient, Reynolds number, flow regime, design criteria, pressure profiles, hydraulic-grade line (HGL), energy-grade line (EGL).

* Corresponding author e-mail: gurol.yildirim@giresun.edu.tr

1. Introduction

In a trickle irrigation system, water is distributed through small dissipating devices called emitters installed on polyethylene pipes called laterals [1-4, 6, 7, 9, 10, 12-15]. Lateral pipeline is a hydraulic structure whose design is limited by the inlet pressure head and water application uniformity that is affected by the total energy losses, the field topography as well as the emitter hydraulic characteristics [5, 8, 16-25].

The insertion of emitters along a trickle lateral modifies the flow streamlines, inducing local turbulence that results in additional local pressure losses, sometimes called minor losses, rather than the pipe friction losses [26, 27].

To accurately evaluate total energy losses in the laterals, these minor losses due to the protrusion of emitter connections in the pipe wall that must be added to the friction losses occurring in the pipe [8]. On-line emitters cause the contraction and subsequent enlargement of flow streamlines due to the protrusion of emitter bars into the flow [17, 24, 26]. The introduction of integrated in-line emitters determines the contraction of the flow paths at the upstream connection between the emitters and the lateral pipe, and the expansion of the flow paths immediately downstream from the emitters; because the emitters usually have a smaller diameter than the pipe, an additional minor friction losses must be considered [12-14]. Fig. **1** presents the lateral-emitter configuration for (a): integrated in-line and (b): on-line emitters.

In the past, numerous researches have been done on the hydraulic analysis of trickle irrigation pipeline networks [27-41]. As a matter of fact, a significant amount of these researches [5, 28-30, 31-35] do not taken into account the effect of local losses in the design procedure, although the importance of minor losses has been recently

presented in the experimental analysis [3, 4, 6, 7, 9, 10, 12-14, 19, 21], and the alternative analytical and numerical approaches [6, 8, 11, 24, 26, 31].

Recently, the author [17, 24, 26] presented simple analytical procedures for hydraulic design of trickle laterals which takes into consideration the effect of minor head losses, expressing the amount of minor head losses as a fraction of the kinetic head, as well as the effect of the emitter outflow non-uniformity, the kinetic head change, the number of emitters, and different uniform line slopes, on the lateral hydraulic computations.

For any desired uniformity level, the analytical procedure gives one an opportunity to evaluate the influence of local energy loss on the pipe geometric characteristics (pipe size and length) and on the corresponding hydraulic variables (operating inlet and downstream end pressure heads and total energy losses) [18, 22, 23]. This study showed that in some design cases, neglecting minor losses may lead to erroneous designs of the lateral diameter and length [42-49].

This paper offers a simple mathematical model based on the stepwise procedure to accurately determine the pressure head profile along the lateral line. Essentially, the present work extends the earlier discussion [19] on the experimental analysis of local pressure losses along micro-irrigation laterals [12] to a systematic comparison of different kinds of in-line/on-line emitters and various design configurations. In this chapter, relative contributions of each of the energy loss components are calculated with the appropriate mathematical equation. This procedure is used to evaluate two examples with different types of in-line and on-line emitters; thus the results are compared with those of obtained from the recent analytical and experimental procedures, for all performed simulations

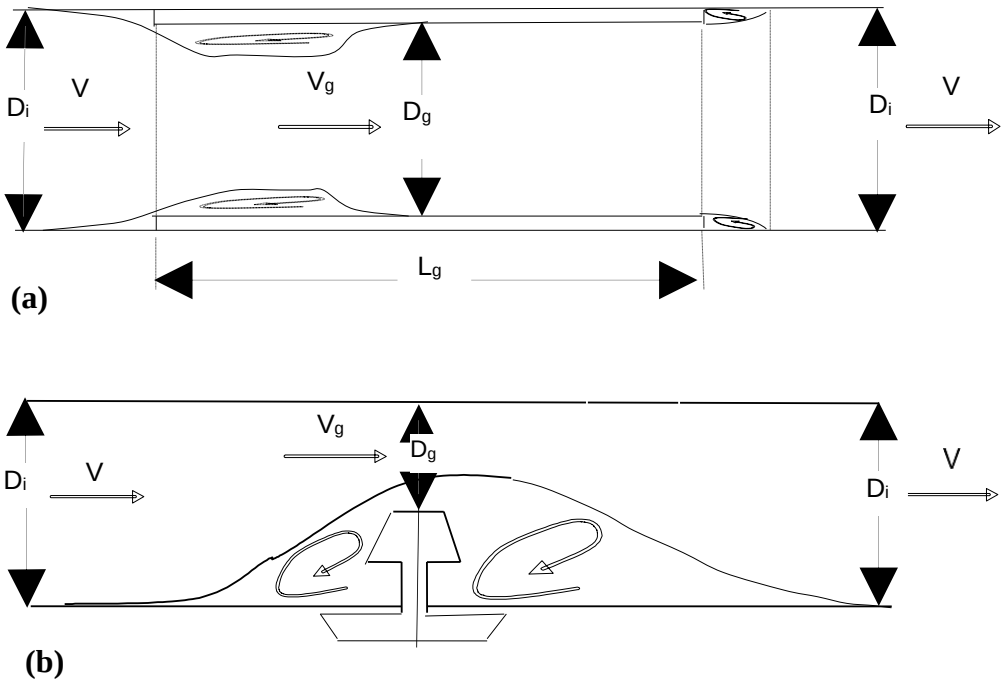


Figure 1: Flow variation (sudden contraction and subsequent enlargement) and hydraulic variables along lateral with (a): Integrated in-line emitter, (b): on-line emitter

2.1. Minor Frictional Pressure Losses through Integrated In-line Emitters

Integrated in-line emitters cause contraction of the flow path at the upstream connection between the emitter and the lateral pipe, and the expansion of the flow path immediately downstream from the emitter; thus,

an additional minor friction loss must be considered [12]. Integrated in-line emitters have an inner diameter, D_g (m), smaller than the pipe inner diameter, D_i (m), and therefore the emitters determine higher frictional head losses due to the lower cross-section area. Emitter friction loss per unit emitter length, J_e (m/m), can also be evaluated by the Darcy-Weisbach friction formula:

$$J_e = \frac{f_e}{D_g}\frac{V_g^2}{2g} \tag{1}$$

where f_e = friction coefficient for the emitter flow; D_g = internal diameter of an integrated in-line emitter (m); V_g = flow velocity inside the emitter (ms^{-1}); and g = acceleration due to gravity (ms^{-2}).

The emitter friction loss for an individual in-line emitter, $h_{f(e)}$, can be evaluated from

$$h_{f(e)} = J_e L_g \tag{2}$$

where L_g = longitudinal length of integrated in-line emitter (m).

Using the continuity equation, the following relationships between the pipe and the emitter flow velocity, V and V_g, can then be written:

$$V_g = V\left(\frac{D_i}{D_g}\right)^2 = \frac{4}{\pi}\frac{Q}{D_g^2} \tag{3}$$

where V = flow velocity in the pipe section (ms^{-1}); D_i = lateral pipe inner diameter (m); and Q = total lateral inflow rate (m^3s^{-1}).

For the interval of the Reynolds number, R, 2,000<R<36,000 for the friction coefficient, *f*, the Blasius equation is practically used to determine friction losses. For a large range of the Reynolds number, for the flow into the integrated in-line emitter the following expression can be used:

$$f_e = cR_g^{-0.25} \tag{4}$$

where c = coefficient which can be assumed to equal 0.316 and 0.302 [3].

R_g = Reynolds number for the flow occurred in the integrated in-line emitter which can be expressed as:

$$R_g = \frac{V_g D_g}{\nu} = \frac{4}{\pi\nu}\frac{Q}{D_g} \tag{5}$$

where ν = kinematic viscosity of water at standard temperature, $\nu = 1.01\times10^{-6}$ m^2s^{-1}.

Substituting eq. (5) into eq. (4), then yields

$$f_e = c\left(\frac{\pi\nu}{4}\right)^{0.25}\left(\frac{D_g}{Q}\right)^{0.25} \tag{6}$$

Substituting eqs. (3) and (6) into eq. (1) then, into eq. (2), the friction loss in the integrated in-line emitter along its length, L_g, can then be written:

$$h_{f(e)} = K \frac{Q^{1.75}}{D_g^{4.75}} L_g \tag{7}$$

where

$$K = c \frac{\upsilon^{0.25}}{2g} \left(\frac{4}{\pi} \right)^{1.75} \tag{8}$$

The value of the constant K is equal to $7.792\ 10^{-4}$ if the friction coefficient is determined by using the classical Blasius formula (c = 0.316) and $7.447\ 10^{-4}$ if the value of c is taken into account 0.302 [3].

Assuming N emitters are located from the lateral inlet (1st emitter) toward to the downstream closed end (Nth emitter), using eq. (7), then the sum of friction losses along the integrated in-line emitters, $\Delta H_{f(e)}$, can be practically evaluated from the following mathematical expression

$$\Delta H_{f(e)} = \sum_{i=1}^{i=N} \Delta H_{f(e)i} = K L_g \frac{Q_n^{1.75}}{D_g^{4.75}} \sum_{i=1}^{i=N} i^{1.75} \tag{9}$$

where Q_n = nominal flow rate which assumed equal to the average value of the emitter outflow (Q_{av}) (Lh^{-1}); and i = an integer represents consecutive order of emitters. It can be assumed, the nominal flow rate is approximately equal to the average emitter outflow when the maximum allowable difference in the extreme pressure heads along the lateral is approximated by 10% of the average pressure head [14].

2.2. Local Pressure Losses for Integrated In-Line and On-Line Emitter Barb Coonections

The introduction of an integrated in-line or on-line emitter in a lateral causes a local pressure loss, λ, due to the obstruction of emitter connection into the pipe flow, that can be expressed as an "α" fraction of the kinetic head [8]:

$$\lambda = \alpha \frac{V^2}{2g} = \alpha \frac{8}{\pi^2 g} \frac{Q^2}{D_i^4} \tag{10}$$

where α = local loss coefficient due to both the contraction and the subsequent enlargement, can then be expressed as a function of the diameter ratio D_i/D_g, which is experimentally verified by the following expression [12, 13]:

$$\alpha = 0.056 \left[\left(\frac{D_i}{D_g} \right)^{17.83} - 1 \right] \tag{11}$$

The amount of local pressure losses due to the presence of integrated in-line and/or on-line emitters, ΔH_l, can be easily determined by the following mathematical expression (Provenzano et al. 2005):

$$\Delta H_l = \sum_{i=1}^{i=N-1} \Delta H_{li} = \alpha \left(\frac{8}{\pi^2 g} \right) \frac{Q_n^{\,2}}{D_i^{\,4}} \sum_{i=1}^{i=N-1} i^2 \qquad (12)$$

2.3. Major Frictional Pressure Losses along Lateral with Integrated In-Line and On-Line Emitters

Assuming integrated in-line emitters are located at an equal spacing, S then, sum of the friction losses along the length of the straight pipe sections between the consecutive in-line emitters, $(S - L_g)$, can be computed from the following expression:

$$\Delta H_{f(p)} = \sum_{i=1}^{i=N-1} \Delta H_{f(p)i} = K \frac{Q_n^{\,1.75}}{D_i^{\,4.75}} (S - L_g) \sum_{i=1}^{i=N-1} i^{1.75} \qquad (13)$$

For the lateral with on-line emitters, eq. (13) simply transforms to the following:

$$\Delta H_{f(p)} = \sum_{i=1}^{i=N-1} \Delta H_{f(p)i} = KS \frac{Q_n^{\,1.75}}{D_i^{\,4.75}} \sum_{i=1}^{i=N-1} i^{1.75} \qquad (14)$$

2.4. Total Energy (Pressure) Losses along Lateral with Integrated In-Line and On-Line Emitters

Finally, the amount of total energy losses, ΔH_T, is a function of three energy loss components given by eqs. (9), (12) and (13) or (14), finally, it can be approximated by the following expression:

$$\Delta H_T = \sum_{i=1}^{i=N} \Delta H_{Ti} = \Delta H_{fi} + \Delta H_{li} = \Delta H_{f(p)i} + \Delta H_{f(e)i} + \Delta H_{li} \qquad (15)$$

3. Computational Applications

3.1. For Integrated In-Line Emitter Model

In order to check the practicability of the present procedure, we will try to compute total energy loss components using the simple formulations deduced in here. An *Excel* spreadsheet was set up to carry out the hydraulic calculations.

The analysis was realized by considering two types of integrated in-line emitters B and C which are characterized by the following experimental relationships given by [12] (please, see Table **1**):

B model (*Siplast Tandom*): $Q_{(Lh^{-1})} = 0.612\ H_{(m)}^{\ 0.537}$ (16)

C model (*Rainbird Goccialin*): $Q_{(Lh^{-1})} = 0.667\ H_{(m)}^{\ 0.514}$ (17)

Table 1. Values of hydraulic characteristics for two kinds of the integrated in-line emitter models (B: Siplast Tandem and C: Rainbird Goccialin) for different emitter spacing (S) ranging from 0.2 to 1.5 m, and various number of emitters (N) for the desired (fixed) level of the Christiansen's uniformity coefficient, UC = 97%, for the present mathematical model.

B model (*Siplast Tandem*) *(α = 0.671)*							**C model (*Rainbird Goccialin*) *(α = 0.297)***					
S	**N**	**L_e**	**$Q_{in} = \sum_{i=1}^{i=N} q_i$**	**$H_{in} = H_{(1)}$**	**$H_{(N)}$**	**ΔH_T**	**N**	**L_e**	**$Q_{in} = \sum_{i=1}^{i=N} q_i$**	**$H_{in} = H_{(1)}$**	**$H_{(N)}$**	**ΔH_T**
(m)	(-)	(m)	(Lh^{-1})	(m)	(m)	(m)	(-)	(m)	(Lh^{-1})	(m)	(m)	(m)
0.2	172	34.2	356.2	10.231	8.165	2.066	188	37.4	402.3	10.154	8.305	1.849
0.4	153	60.8	316.4	10.203	8.165	2.038	159	63.2	339.3	10.094	8.305	1.789
0.6	140	83.4	289.3	10.190	8.165	2.025	143	85.2	305.4	10.111	8.305	1.806
0.8	130	103.2	268.4	10.169	8.165	2.004	132	104.8	282.1	10.134	8.305	1.829
1.0	123	122.0	254.1	10.191	8.165	2.026	123	122.0	262.7	10.125	8.305	1.820
1.5	109	162.0	224.9	10.166	8.165	2.001	109	162.0	233.3	10.174	8.305	1.869

N = total number of emitters along the lateral line; L_e = (N-1) S = length of lateral between the first and last emitters; Q_{in} = total inflow rate which is accumulated by all emitter outflows; $H_{in} = H_{(1)}$ = pressure head at the first emitter in lateral inlet; $H_{(N)}$ = downstream closed end pressure head at the last emitter and; ΔH_T = the amount of total energy (head) losses which consist of total friction and local losses.

The analysis was conducted with the zero slope case and with standard commercial emitter spacing of 0.2, 0.4, 0.6, 0.8, 1.0, and 1.5 m. The specifications of both the emitter models are as follows:

For the **B** model:

Nominal flow rate of the emitter outflow (as indicated by the manufacturer), Q_n = 2.1 Lh^{-1} = 5.833 10^{-7} m^3s^{-1}; nominal diameter and inner diameter of the lateral pipe, ND = 16 mm and D_i = 13.29 mm, respectively; inner diameter and longitudinal length of the integrated in-line emitter, D_g = 11.51 mm and L_g = 67.89 mm, respectively. The ratio of the pipe diameter to the emitter diameter, D_i/D_g = 1.155 and therefore the local loss coefficient from eq. (11):

$$\alpha = 0.056\left[\left(\frac{13.29}{11.51}\right)^{17.83} - 1\right] = 0.671$$

For the **C** model:

Q_n = 2.2 Lh^{-1} = 6.111 10^{-7} m^3s^{-1}; ND = 16 mm, D_i = 13.46 mm; D_g = 12.14 mm; and L_g = 68.22 mm. D_i/D_g = 1.108 and finally the local loss coefficient from Eq. (11), α = 0.297, is computed. Further discussion on results for this application will be presented in the following section "*Results and Discussion*".

3.2. For On-Line Emitter Model

Determine the percentages of total energy losses for two on-line emitter models (labyrinth and orifice-vortex) by considering the horizontal trickle lateral, for the following input parameters. Inner diameter of the lateral pipe is 13.4 mm (D_i = 13.4 mm), the emitter spacing, S, values are 0.3, 0.6, 0.9 and 1.2 m, respectively, and the overall Christiansen uniformity coefficient of the system is U_C = 98.8%.

The following relationships with local loss coefficients, α, for both emitter models are experimentally verified as follows [10]:

Labyrinth on-line emitter model [Q_{av} = 4.1 Lh^{-1} ; H_{av} = 9.65 m; α = 0.34]:

$$Q_{(Lh^{-1})} = 1.32\ H_{(m)}^{\ 0.5} \qquad (18)$$

Orifice-vortex on-line emitter model [Q_{av} = 4.2 Lh^{-1}; H_{av} = 10.34 m; α = 0.67]:

$$Q_{(Lh^{-1})} = 1.65\ H_{(m)}^{\ 0.4} \qquad (19)$$

Detailed analysis of results and discussion on this application will be presented in the following section "*Results and Discussion*".

4. Implementation of Backward Stepwise Procedure

The numerical stepwise procedure in the backward form based on the present mathematical model can be implemented for the data given in the present applications, starting from the downstream closed end (N^{th} emitter), toward to the lateral inlet (1^{st} emitter).

First, in accordance with the first application (for integrated in-line emitter model), the following calculation steps are applied, respectively:

1. The outflow of the N^{th} emitter as a function of the corresponding pressure head, was assumed to equal 90% of that corresponding to the nominal discharge.

The outflows at the downstream end for the B model: $q_N = 0.90 \times 2.1 = 1.89$ Lh^{-1} and, for the C model: $q_N = 0.90 \times 2.2 = 1.98$ Lh^{-1} and the corresponding pressure heads were computed from their outflow-pressure head relationships;

2. The friction loss along both the Nth emitter, $\Delta H_{f(e)\,(N)}$, by eq. (9) and, the friction loss along the pipe segment between the consecutive Nth and (N-1)th emitters, $\Delta H_{f(p)\,(N-1)}$, by eq. (13) then, the local loss due to insertion of the (N-1)th emitter, $\Delta H_{l\,(N-1)}$, by eq. (12), were individually evaluated;

3. The pressure head for the (N-1)th emitter, as the pressure head for the Nth emitter plus the sum of total head losses between the two consecutive emitters then, the corresponding outflow for the (N-1)th emitter, $q_{(N-1)}$ were determined, respectively.

4. Using the continuity equation, the lateral discharge along the pipe segment between the consecutive Nth and (N-1)th emitters was computed by assuming the residual lateral flow rate at the downstream closed end from the last emitter is equal to zero, $Q_{(N)} = q_{(N)}$ and; $Q_{(N-1)} = Q_{(N)} + q_{(N-1)}$. Finally, total lateral inflow rate, Q_{in}, must be equal to the sum of whole emitter outflows, $Q_{in} = \sum_{i=1}^{i=N} q_i$ [46-54].

5. The uniformity level of the system was evaluated with the well-known Christiansen's uniformity coefficient, $UC = 1 - (1/\ NQ_n) \sum_{i=1}^{i=N} |q_i - Q_n|$. Noting that in the UC formula, the nominal discharge is taken into consideration as the average emitter outflow [25, 36, 41-45]. Finally, the computation steps were improved to keep to the right the fixed value of UC = 97%. For each computation step, the uniformity coefficient UC was evaluated and then, the steps 1, 2, 3 and 4, were repeated until the desired value of UC = 97% was finally reached.

5. Results and Discussion

5.1. On Application-I (for Integrated In-Line Emitter Model)

In accordance with the first application (Application-I), Table **1** and Table **2** synthesize the complete results for the main hydraulic variables regarding two kinds of integrated in-line emitter models **B** ($\alpha = 0.671$) and C ($\alpha = 0.297$) for the desired level of uniformity, UC = 97%. From Table **1** for both the emitter models, the values of total inflow rate, Q_{in} (4th and 10th columns), the inlet pressure head at the upstream end, $H_{in} = H_{(1)}$ (5th and 11th columns) and the pressure head at the downstream closed end, $H_{(N)}$ (6th and 12th columns), the amount of the total energy losses, ΔH_T (7th and 13th columns) are calculated, respectively, regarding with different emitter spacing, S ranging from 0.2 to 1.5 m (1st column), various total number of emitters, N (2nd and 8th columns) and total length of the lateral line, L_e (3rd and 9th columns).

As indicated in Table **1**, as the emitter spacing (S) increases and the total number of emitters (N) decreases, the total length of the lateral line (L_e) increases, in relation to the expression $L_e = (N-1)\,S$, for both the emitter models. The total inflow rate (Q_{in}) decreases with decreasing in the total amount of emitter outflows ($Q_{in} = q_1 + q_2 + \ldots + q_N$)]. For both the emitter models, the inlet pressure head ($H_{in} = H_1$) yields similar values around 10 m, except for a little deviation.

It is clearly observed from this table [regarding the data sets for S = 1.0 m, N = 123 L_e = 122.0 m and for S = 1.5 m, N = 109, L_e =162.0 m], the values of ΔH_T for the **B** model ($\alpha = 0.671$) with respect to the **C** model ($\alpha = 0.297$) increases with increasing the amount of local losses caused by the higher local loss coefficient, as also evaluated in eq. (10). Regarding with different emitter spacing the ΔH_T yields fixed values; for instance, for the **B** model the ΔH_T yields values varying from 2.0 to 2.07 m, and for the **C** model varying from 1.79 to 1.87 m. Regarding both the emitter models **B** and **C**, and different emitter spacing, S, various total number of emitters and total length of the lateral line, L_e, three components of total energy losses (ΔH_l, $\Delta H_{f(p)}$ and $\Delta H_{f(e)}$) are computed then the results synthesized, in Table **2**.

In Table **2** first, the total energy losses (ΔH_T) are divided by the total friction losses (ΔH_f) and total emitter local losses (ΔH_l), and then, the total friction losses (ΔH_f) are subdivided by the major pipe friction losses ($\Delta H_{f(p)}$) and minor emitter friction losses ($\Delta H_{f(e)}$). Accordingly, the ratio of emitter local losses to the emitter friction losses

[$\Phi_{e(l,f)} = \Delta H_l / \Delta H_{f(e)}$], and the emitter local losses as percentage of total energy losses [$\Phi_l(\%) = \Delta H_l / \Delta H_T$] are computed from the present mathematical model, and the results are compared with the recent experimental analysis [12].

From this table, the analysis for three energy loss components reveals that, the emitter local losses (ΔH_l) and the emitter minor friction losses ($\Delta H_{f(e)}$) decrease due to decreasing in the total number of emitters (N) [ie., with increasing in the emitter spacing (S)], whereas the pipe friction losses ($\Delta H_{f(p)}$) [ie., the total friction losses (ΔH_f)] increase due to increasing in the total length of the lateral line (L_e). Thus, the amount of total energy losses (ΔH_T) does not change more (please see, 7th and 13th columns, in Table **1**), since the total increasing in the amount of ΔH_f is just balanced with the total decreasing in the amount of ΔH_l.

Table 2: Relative contribution of three energy loss components [$\Delta H_l, \Delta H_{f(p)}, \Delta H_{f(e)}$] to the amount of total energy losses (ΔH_T) with the amount of local losses as percentage of total energy losses [Φ_l] and the range of emitter local losses to the emitter friction losses [$\Phi_{e(l,f)}$], regarding two kinds of the integrated in-line emitter models (B: Siplast Tandem and C: Rainbird Goccialin), for different emitter spacing (S) ranging from 0.2 to 1.5 m and various number of emitters (N) from to 109 to 188, for the desired level of the Christiansen's uniformity coefficient, UC = 97%, according to the present mathematical model and the recent experimental procedure (Provenzano and Pumo 2004).

		Present Mathematical Model						Recent Experimental Analysis (Provenzano and Pumo 2004)					
		ΔH_T (m)		ΔH_f (m)				ΔH_T		ΔH_f (m)			
J	L_e	ΔH_f	ΔH_l	$\Delta H_{f(p)}$	$\Delta H_{f(e)}$	$\Phi_{e(l,f)} = \Delta H_l / \Delta H_{f(e)}$	$\Phi_l = \Delta H_l / \Delta H_T$	ΔH_f	ΔH_l	$\Delta H_{f(p)}$	$\Delta H_{f(e)}$	$\Phi_{e(l,f)} = \Delta H_l / \Delta H_{f(e)}$	$\Phi_l = \Delta H_l / \Delta H_T$
)	(m)	(m)	(m)	(m)	(m)	(-)	(%)	(m)	(m)	(m)	(m)	(-)	(%)
B model (*Siplast Tandem*) ($\alpha = 0.671$)													
72	34.2	1.031	1.035	0.511	0.520	1.99	50.1	0.969	0.95	0.482	0.487	1.95	49.5
53	60.8	1.309	0.729	0.932	0.377	1.93	35.8	1.231	0.67	0.878	0.353	1.90	35.2
40	83.4	1.467	0.559	1.171	0.296	1.89	27.6	1.38	0.514	1.103	0.277	1.85	27.1
30	103	1.556	0.448	1.315	0.241	1.86	22.4	1.465	0.411	1.239	0.226	1.82	21.9
23	122	1.645	0.379	1.438	0.207	1.83	18.7	1.550	0.349	1.356	0.194	1.80	18.4
09	162	1.737	0.265	1.588	0.149	1.78	13.2	1.636	0.243	1.496	0.140	1.74	12.9
C model (*Rainbird Goccialin*) ($\alpha = 0.297$)													
3	37.4	1.226	0.623	0.664	0.562	1.11	33.7	1.156	0.573	0.626	0.530	1.08	33.1
)	63.2	1.412	0.377	1.057	0.355	1.06	21.1	1.33	0.347	0.996	0.334	1.04	20.7
3	85.2	1.531	0.275	1.266	0.265	1.04	15.2	1.444	0.253	1.194	0.250	1.01	14.9
2	105	1.612	0.216	1.399	0.213	1.01	11.8	1.521	0.199	1.320	0.201	0.99	11.6
3	122	1.644	0.175	1.469	0.175	1.0	9.6	1.551	0.161	1.385	0.166	0.97	9.4
)	162	1.747	0.122	1.621	0.126	0.97	6.5	1.649	0.112	1.530	0.119	0.94	6.4

Thus, the amount of total energy losses (ΔH_T) does not change more (please see, 7th and 13th columns, in Table **1**), since the total increasing in the amount of ΔH_f is just balanced with the total decreasing in the amount of ΔH_l.

In Table **2**, from the comparison of the energy loss parameters [4th, 5th, 6th and 7th columns], the following finding can be observed. For both the emitter models **B** and **C**, as the total number of emitters (N) decreases and the total length of the lateral line (L_e) increases, the discrepancy between the amount of the ΔH_f and the ΔH_l, and between the amount of the $\Delta H_{f(p)}$ and the $\Delta H_{f(e)}$ more increases. However, as an exceptional case for the B emitter model, if the smallest value of the emitter spacing (S = 0.2 m) is regarded (N = 172 and L_e = 34.2 m), the amount of emitter local losses (ΔH_l = 1.035 m) is nearly identical to the amount of total friction losses (ΔH_f = 1.031 m); similarly, the amount of emitter friction losses ($\Delta H_{f(e)}$ = 0.52 m) closely follows the amount of pipe friction losses ($\Delta H_{f(p)}$ = 0.511 m). For S = 0.2 m, these findings are also confirmed by the recent experimental work (Provenzano and Pumo 2004) as follows: ΔH_f = 0.969 m with ΔH_l = 0.95 m, and $\Delta H_{f(p)}$ = 0.482 m with $\Delta H_{f(e)}$ = 0.487 m, respectively.

For the **B** emitter model, the ratio of emitter local losses to the emitter friction losses [8th column] generally yields around 2.0 (for S = 0.2 m, $\Phi_{e(l,f)} = 1.99$], and little decreases to 1.78 for S = 1.5 m. The emitter local losses as the percentage of total energy losses [9th column] reach to the highest range of 50% [for S = 0.2 m, $\Phi_l = 50.1\%$], and rapidly decreases to 13.2% (for S = 1.5 m). The recent experimental work (Provenzano and Pumo 2004) gives similar results as follows: $\Phi_{e(l,f)}$ values are 1.95 for S = 0.2 m and 1.74 for S = 1.5 m; and Φ_l values are 49.5(%) for S = 0.2 m and 12.9% for S = 1.5 m.

For the **C** emitter model with respect to the **B** model (regarding with 4th – 7th columns) for the smallest value of emitter spacing, S = 0.2 m, the amount of total friction losses [ΔH_f = 1.226 m] is approximately equal to two times of the amount of emitter local losses [ΔH_l = 0.623 m], since the amount of emitter local losses decrease in proportion to the value of the local loss coefficient for the **C** model ($\alpha = 0.297$) which is approximately half of the value for the **B** model ($\alpha = 0.671$). As also previously pointed out for the **B** emitter model (for S = 0.2 m), the amount of emitter friction losses [$\Delta H_{f(e)}$ = 0.562 m] nearly approaches to the amount of pipe friction losses [$\Delta H_{f(p)}$ = 0.664 m], for the **C** emitter model, as well. For S = 0.2 m, these findings are also justified with those of obtained in the recent experimental work (Provenzano and Pumo 2004) as follows: ΔH_f = 1.156 m with ΔH_l = 0.573 m and $\Delta H_{f(p)}$ = 0.626 m with $\Delta H_{f(e)}$ = 0.53 m, respectively.

For the **C** emitter model, the ratio of emitter local losses to the emitter friction losses [8th column] generally yields around 1.0 [for S = 0.2 m, $\Phi_{e(l,f)} = 1.11$] and little decreases to 0.97 for S = 1.5 m. The emitter local losses as the percentage of total energy losses [9th column] approach to the range of 34% [for S = 0.2 m, $\Phi_l = 33.7\%$], and rapidly decreases to 6.5% for S = 1.5 m. Hence, there is a good agreement with those of the experimental analysis as: $\Phi_{e(l,f)}$ values are 1.08 for S = 0.2 m and 0.94 for S = 1.5 m; and Φ_l values are 33.1(%) for S = 0.2 m and 6.4% for S = 1.5 m.

As a remarkable result from this table [regarding the data set given for S = 1.0 m (N = 123, L_e = 122.0 m) and for S = 1.5 m (N = 109, L_e =162.0 m)] for both the emitter models (**B** and **C**), the amount of pipe friction losses for the **C** model [$\Delta H_{f(p)}$ = 1.47 m and 1.62 m] is higher than those of the **B** model [$\Delta H_{f(p)}$ = 1.44 m and 1.59 m]. Because, the **C** model has a higher nominal flow rate (Q_n = 2.2 Lh^{-1}) with respect to the **B** model (Q_n = 2.1 Lh^{-1}) even if the **C** model has higher values of the emitter length (L_g) and inner lateral diameter (D_i) than those of the B model, as concluded in eq. (13).

For both the emitter models (**B** and **C**) [regarding the data set for S = 1.0 m (N = 123, L_e = 122.0 m) and for S = 1.5 m (N = 109, L_e =162.0 m)], the amount of emitter friction losses for the **B** model [$\Delta H_{f(e)}$ = 0.207 m and 0.149 m] is higher than those of the **C** model [$\Delta H_{f(e)}$ = 0.175 m and 0.126 m]. Because, since the **B** model has a smaller inner emitter diameter (D_g = 11.51 mm) with respect to the **C** model (D_g = 12.14 mm) even if the **B** model has smaller values of the emitter length (L_g) and nominal flow rate (Q_n) than those of the **B** model, as concluded in eq. (9).

For both the emitter models (**B** and **C**), to illustrate the variation of three energy loss components to each other, two figures were also prepared and represented by Fig. **2** and Fig. **3**, respectively. For the **B** model of integrated- in-line emitter, Fig. **2** illustrates variation of total friction (ΔH_f) [premier axis of y] and emitter local (ΔH_l) losses [secondary axis of y] regarding with different values of emitter spacing (S) [premier axis of x] , and various number of emitters (N) [secondary axis of x], according to both the mathematical (straight bold line) and

experimental (dotted line) procedures. For the **C** model of integrated- in-line emitter, Fig. **3** illustrates variation of total friction loss components due to pipe ($\Delta H_{f(p)}$) and due to emitter ($\Delta H_{f(e)}$) with regarding different values of emitter spacing (S) and various number of emitters (N), according to both the mathematical (straight line) and experimental (dotted line) procedures. Fig. **2** and Fig. **3** also reveal that, a good justification between the results of both the mathematical and experimental procedures is observed, for all performed simulations.

5.2. On Application-II (for On-Line Emitter Model):

The same calculation steps for the backward stepwise procedure clarified-above are repeated (from 1st to 5th) using the related formulations given only for on-line emitters [eqs. (12), (14), (15), (18) and (19)] for the overall desired uniformity level, UC = 98.8%.

Table **3** synthesizes the complete results for the main hydraulic variables for two kinds of on-line emitter models [labyrinth ($\alpha = 0.34$) and orifice-vortex ($\alpha = 0.67$)] in comparison with those of obtained from the previous analytical procedure [30]. In this table, for both the emitter models, two energy loss components (ΔH_f and ΔH_l) [4th-8th and 5th-9th columns], the ratio of total pipe friction losses to the emitter local losses, $\Phi_f = \Delta H_f / \Delta H_l$ [6th and 10th columns], and the emitter local losses as percentage of total energy losses, $\Phi_l = \Delta H_l / \Delta H_T$ [7th and 11th columns] regarding with different emitter spacing, S, total number of emitters, N, and total length of the lateral line, L_e, are presented, respectively.

Regarding the values presented in Table **3**, the following remarks can be observed. First, the values of emitter local losses for the labyrinth on-line emitter model [ΔH_l =0.598, 0.335, 0.241 and 0.192 m] are approximately half of the values for the orifice-vortex on-line emitter model [ΔH_l =1.179, 0.657, 0.459 and 0.374 m] since the emitter local losses proportionally increase with increasing the value of local loss coefficient, α (from 0.34 to 0.67).

Practically, as the length of the lateral increases and the number of emitters decreases with increasing in emitter spacing, the amount of emitter local losses decrease whereas the pipe friction losses increase; so the discrepancy between the pipe friction losses and the emitter local losses increases with increasing in the emitter spacing [1st, 2nd, 3rd, 4th-8th and 5th-9th columns].

For the labyrinth on-line emitter model ($\alpha = 0.34$), if the smallest value of the emitter spacing, S = 0.3 m, is selected, the amount of pipe friction losses is approximately equal to two times of the amount of emitter local losses whereas for the orifice-vortex on-line emitter model ($\alpha = 0.67$), the amount of pipe friction losses is approximately equal to the amount of emitter local losses.

Accordingly, for the labyrinth on-line emitter, the ratio of the friction losses to the emitter local losses (Φ_f) yields around 2, 4, 6 and 8 whereas it yields around 1, 2, 3 and 4, for the orifice-vortex on-line emitter, for the emitter spacing, S = 0.3, 0.6, 0.9 and 1.2 m, respectively. Moreover, the amount of emitter local losses, Φ_l (%) expressed as a percentage of the total energy losses, decreases with increasing emitter spacing, then its values can reach 32.9 and 50.1% (33.5 and 50% according to the previous analytical procedure) with respect to the labyrinth and orifice-vortex on-line emitters, respectively. It can be concluded from this comparison, a good justification is observed between the results obtained from the present mathematical and the previous analytical procedures.

6. Concluding Remarks

In this chapter a simplified mathematical model based on the backward stepwise for three energy loss components (local and friction losses due to emitters and pipe friction losses) to finally evaluate total energy losses along a trickle lateral line with integrated in-line and/or on-line emitters, is presented. The proposed eq. (9), eq. (13) or eq. (14) allow one to evaluate the minor friction losses through the path of an integrated in-line emitter, and the major friction losses along the pipe, and eq. (12) allows one to evaluate the local losses attributable to the emitters' connection. Hence, an approximate combination formulation [eq. 15)] which incorporates three energy loss components allows one to accurately evaluate total energy losses at the end of the lateral line.

The present technique is applied on two numerical applications covering different types of integrated in-line and on-line emitters to demonstrate its practicability and validity with respect to the recent literature.

Examination of results for applications confirmed that, the proposed technique is efficient in all design cases examined, and justifies with the results reported in the recent analytical and experimental procedures.

Based on the present assessment regarding different kinds of integrated in-line and on-line emitters, the following remarks can be underlined:

1. First, the amount of emitter local losses (ΔH_l) increases with increasing in the local loss coefficient, α .

2. Reducing the length of the lateral (L_e) and increasing the number of emitters (N) with decreasing the emitter spacing (S), the amount of local (ΔH_l) [and friction, $\Delta H_{f(e)}$] losses due to presence of emitters increase whereas the pipe friction losses ($\Delta H_{f(p)}$) (ie., total friction losses, ΔH_f) decrease. For both the integrated in-line emitter models **B** and **C** (Table **2**), the discrepancy between the amount of the ΔH_f and the ΔH_l; and between the amount of the $\Delta H_{f(p)}$ and the $\Delta H_{f(e)}$ more increases as the total number of emitters (N) decreases and the total length of the lateral line (L_e) increases. Therefore, the amount of total energy losses (ΔH_T) (which is combination of total friction and emitter local losses) does not change more, except for a little deviation (Table 1), since the total increasing in the amount of total friction losses (ΔH_f) is just balanced with the total decreasing in the amount of emitter local losses (ΔH_l).

3. For both the **B** and **C** integrated in-line emitter models (Table **1**), and regarding different values of the emitter spacing and total number of emitters the inlet pressure head ($H_{in} = H_1$) yields similar values around 10 m, since the amount of total energy losses (ΔH_T) yields fixed values, in all design cases examined.

4. The amount of emitter local losses, Φ_l , expressed as the percentage of total energy losses (ΔH_T) increases with decreasing in the emitter spacing. As an exceptional case for the smallest value, S = 0.2 m, the summation of emitter local losses nearly approach to half of the amount of the total energy losses [$\Phi_l = \Delta H_l / \Delta H_T \cong 50\%$].

5. For both the integrated in-line [B-siplast tandem: $\alpha = 0.671$] and on-line [orifice vortex: $\alpha = 0.67$] emitters (Table **2** and Table **3**), and regarding the data set for the smallest value of the emitter spacing (S = 0.2 or 0.3 m), the summation of emitter local losses nearly identical to the amount of total friction losses (due to pipe and emitters) [$\Delta H_f \cong \Delta H_l$].

6. For both the **B** and **C** integrated in-line emitter models (Table **2**), and regarding the data set for the smallest value of the emitter spacing (S = 0.2 m), the summation of minor friction losses due to in-line emitters nearly identical to the amount of major friction losses along the pipe sections between successive in-line emitters [$\Delta H_{f(e)} \cong \Delta H_{f(p)}$].

7. Regarding the data set given for different emitter spacing (from 0.2 to 1.5 m) (Table **2**), if the **B** model (α = 0.671) is selected the summation of emitter local losses is approximately equal to two times of the amount of emitter minor friction losses [$\Delta H_l \cong 2 \times \Delta H_{f(e)}$], whereas for the **C** model (α = 0.297) the summation of emitter local losses is nearly identical to the summation of minor friction losses due to in-line emitters [$\Delta H_l \cong \Delta H_{f(e)}$].

Table 3: Relative contribution of two energy loss components [ΔH_f and ΔH_l] to the amount of total energy losses [ΔH_T] with the range of total friction losses to the total emitter local losses [Φ_f], and the amount of local losses as percentage of total energy losses [Φ_l], regarding two kinds of the on-line emitter models (*Labyrinth and orifice-vortex*), for different emitter spacing (S) ranging from 0.3 to 1.2 m and various number of emitters (N) from to 75 to 110, for the desired level of the Christiansen's uniformity coefficient, UC = 98.8%, according to the present mathematical model and the previous analytical procedure.

			Present Mathematical Model				**Previous** Analytical Method [30]			
			ΔH_T (m)		Φ_f =	Φ_l =	ΔH_T (m)		Φ_f =	Φ_l =
S	N	L_e	ΔH_f	ΔH_l	$\Delta H_f / \Delta H_l$	$\Delta H_l / \Delta H_T$	ΔH_f	ΔH_l	$\Delta H_f / \Delta H_l$	$\Delta H_l / \Delta H_T$
(m)	(-)	(m)	(m)	(m)	(-)	(%)	(m)	(m)	(-)	(%)
Labyrinth On-Line Emitter ($\alpha = 0.34$)										
0.3	110	32.70	1.215	0.598	2.03 ≅ 2.0	32.9	1.108	0.559	1.98 ≅ 2.0	33.5
0.6	90	53.40	1.322	0.335	3.95 ≅ 4.0	20.2	1.277	0.307	4.16 ≅ 4.0	19.4
0.9	80	71.10	1.421	0.241	5.89 ≅ 6.0	14.5	1.386	0.216	6.42 ≅ 6.0	13.5
1.2	75	88.80	1.578	0.192	8.22 ≅ 8.0	10.9	1.548	0.178	8.70 ≅ 9.0	10.3
Orifice-Vortex On-Line Emiter ($\alpha = 0.67$)										
0.3	110	32.70	1.172	1.179	0.99 ≅ 1.0	50.1	1.155	1.156	0.99 ≅ 1.0	50.0
0.6	90	53.40	1.343	0.657	2.04 ≅ 2.0	32.9	1.332	0.635	2.10 ≅ 2.0	32.3
0.9	80	71.10	1.462	0.459	3.18 ≅ 3.0	23.9	1.446	0.447	3.23 ≅ 3.0	23.6
1.2	75	88.80	1.625	0.374	4.34 ≅ 4.0	18.9	1.614	0.368	4.38 ≅ 4.0	18.6

$\Phi_f = \Delta H_f / \Delta H_l$: the ratio of total friction losses to the total emitter local losses; $\Phi_l = \Delta H_l / \Delta H_T$: the amount of total emitter local losses as percentage of total energy losses.

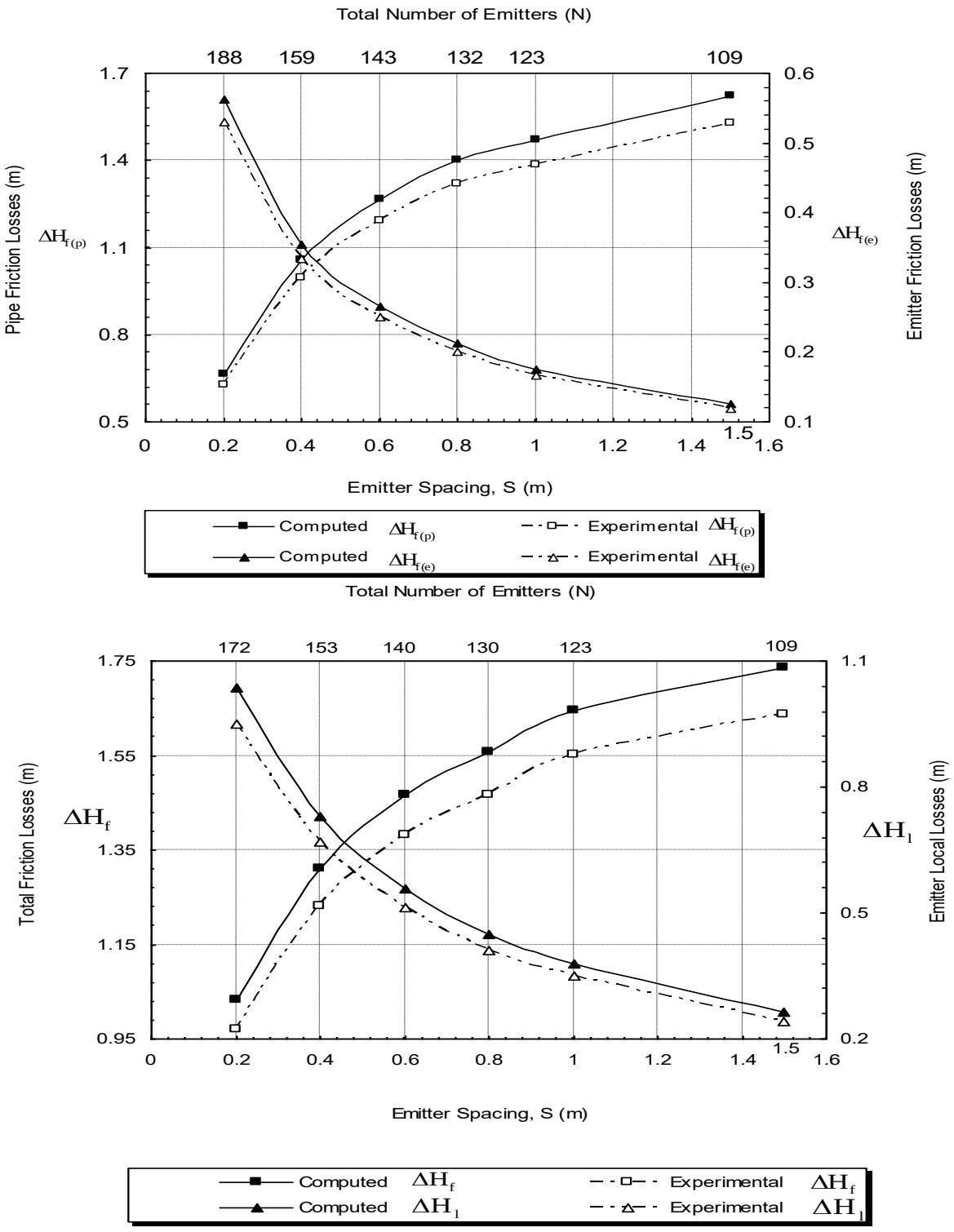


Figure 2: For the B model (*Siplast Tandem*) of integrated- in-line emitter, variation of total friction [ΔH_f] and local [ΔH_l] losses versus different values of emitter spacing (S) varying from 0.2 to 1.5 m, and various number of emitters (N), according to both the mathematical and experimental procedures.

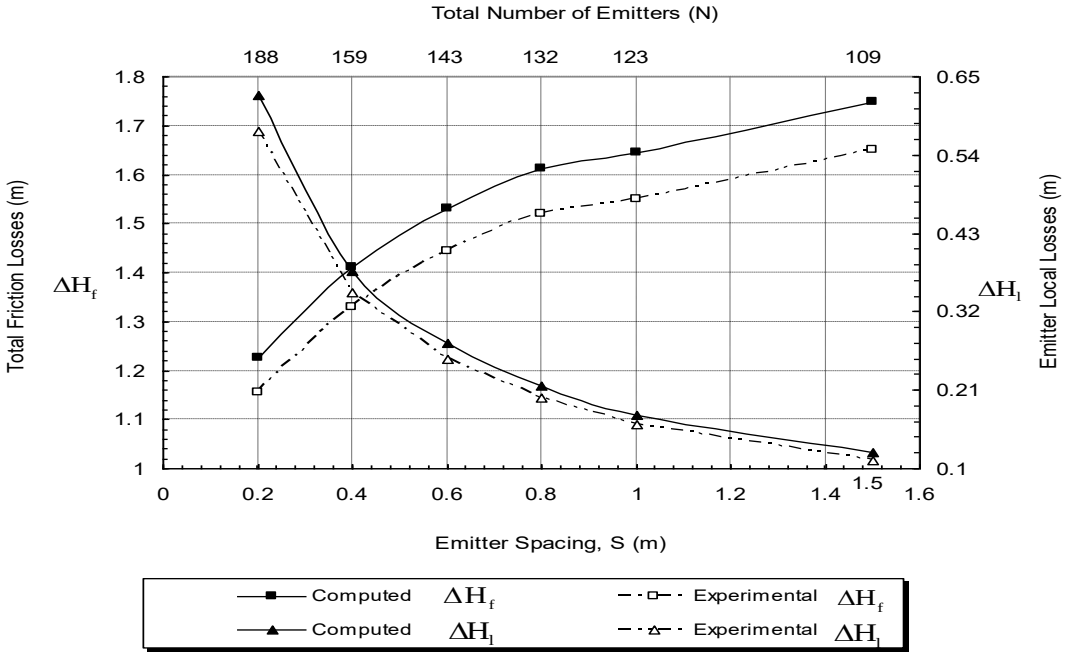


Figure 2: For the B model (Siplast Tandem) of integrated- in-line emitter, variation of total friction [ΔH_f] and local [ΔH_l] losses versus different values of emitter spacing (S) varying from 0.2 to 1.5 m, and various number of emitters (N), according to both the mathematical and experimental procedures.

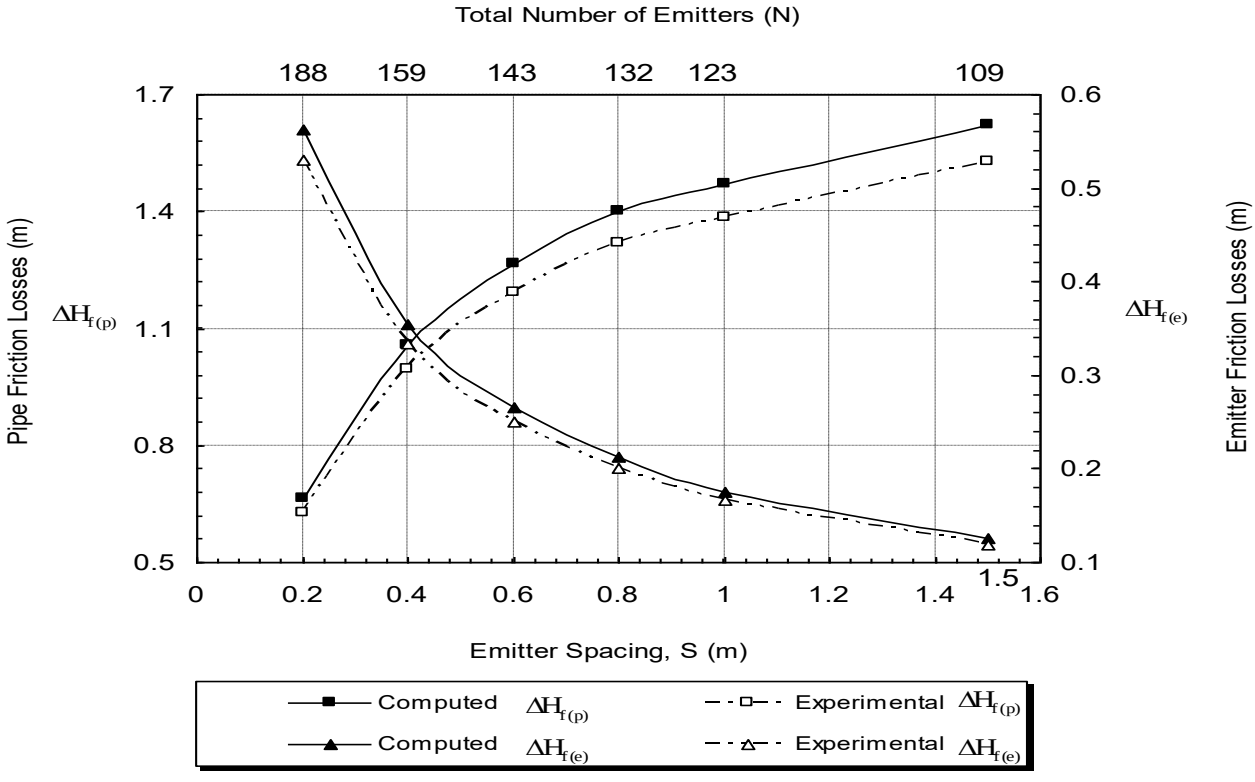


Figure 3: For the C model (*Rainbird Goccialin*) of integrated- in-line emitter, variation of total friction loss components due to pipe [$\Delta H_{f(p)}$] and due to emitter [$\Delta H_{f(e)}$] versus different values of emitter spacing (S) varying from 0.2 to 1.5 m, and various number of emitters (N), according to both the mathematical and experimental procedures.

References

[1] A.I. Al-Amoud, "Significance of energy losses due to emitter connections in trickle irrigation lines." *J. Agric. Eng. Res*60(1): 1-5, 1995.
[2] H. Anyoji, I.P. Wu, "Statistical approach for drip lateral design." Trans. ASAE, 30(1), 187-192, 1987.
[3] V. Bagarello, V. Ferro, G. Provenzano, D. Pumo, "Experimental study on flow resistance law for small diameter plastic pipes." J. Irrig. and Drain. Eng., ASCE, 121(5), 313-316, 1995.
[4] V. Bagarello, V. Ferro, G. Provenzano, D. Pumo, "Evaluating pressure losses in drip irrigation lines." J. Irrig. and Drain. Eng., ASCE 123(1): 1-7, 1997.
[5] H.M. Hathoot, A.I. Al-Amoud, F.S. Mohammad, "Analysis and design of trickle irrigation laterals." J. Irrig. and Drain. Eng. ASCE 119(5): 756-767, 1993.
[6] H.M. Hathoot, A.I. Al-Amoud, A.S. Al-Mesned, "Design of trickle irrigation laterals considering emitter losses."*International Commission on Irrigation and Drainage (ICID) Journal*, 49(2): 1-14, 2000.
[7] T.A. Howell, F.A. Barinas, "Pressure losses across trickle irrigation fittings and emitters." *Trans. ASAE,* 23(4): 928-933, 1980.
[8] R.W. Jeppson, "Analysis of flow in pipe networks." 5th Ed., *Ann Arbor Science*, Ann Arbor, Mich, 1982.
[9] L. Juana, L. Rodriguez-Sinobas, A. Losada, A. "Determining minor head losses in drip irrigation laterals. I: methodology." *J. Irrig. and Drain. Eng. ASCE*, 128(6): 376-384, 2002.a.
[10] L. Juana, L. Rodriguez-Sinobas, A. Losada, "Determining minor head losses in drip irrigation laterals. II: experimental study and validation." *J. Irrig. and Drain. Eng. ASCE*, 128(6): 385-396, 2002.b.
[11] Y. Kang, S. Nishiyama, "Analysis and design of microirrigation laterals." J. Irrig. and Drain. Eng. ASCE 122(2): 75-82, 1996.
[12] G. Provenzano, D. Pumo, D. "Experimental analysis of local pressure losses for microirrigation laterals." J. Irrig. and Drain. Eng., ASCE 130(4): 318-324, 2004.
[13] G. Provenzano, and D. Pumo, and P. Di Dio, "Simplified procedure to evaluate head losses in drip irrigation laterals." J. Irrig. and Drain. Eng., ASCE 131(6): 525-532, 2005.

[14] G. Provenzano, D. Pumo, Closure to "Experimental analysis of local pressure losses for microirrigation laterals." by Giuseppe Provenzano and Domenico Pumo" *J. Irrig. and Drain. Engrg., ASCE,* 132(2), 193-194, 2006.

[15] E.J. Scaloppi, R.G. Allen, "Hydraulics of irrigation laterals: comparative analysis." J. Irrig. and Drain. Eng., ASCE 119(1): 91-115, 1993.
[16] G. Yıldırım, "Analytical relationships for designing multiple outlets pipelines. " J. Irrig. and Drain. Eng. ASCE, 133(2), 140-154, 2007.a.
[17] G. Yıldırım, "An Assessment of Hydraulic Design of Trickle Laterals Considering Effect of Minor Losses." *Irrig. and Drain. (ICID Journal)* 56(4), 399-421, 2007.b.
[18] G. Yıldırım, "Hydraulic analysis and direct design of multiple outlets pipelines laid on flat and sloping lands." J. Irrig. and Drain. Eng. ASCE, 132(6), 537-552, 2006.a.

[19] G. Yıldırım, Discussion of "Experimental analysis of local pressure losses for microirrigation laterals' by Provenzano and Pumo" *J. Irrig. and Drain. Engrg., ASCE,* 132(2), 189-192, 2006.b.

[20] G. Yıldırım, and N. Ağıralioğlu, Discussion of "Determining minor losses in drip irrigation laterals.I: methodology." *J. Irrig. and Drain. Engrg., ASCE,* 130(3), 248-252, 2004.c.

[21] G. Yıldırım, and N. Ağıralioğlu, Discussion of "Determining minor losses in drip irrigation laterals.II: experimental study and validation" *J. Irrig. and Drain. Engrg., ASCE,* 130(4), 344-346, 2004.d.

[22] G. Yıldırım, "Comparative analysis of hydraulic calculation methods in design oh micro-irrigation laterals and linear solution of hydraulic analysis of tapered laterals" PhD. Thesis, Istanbul Technical University, Hydraulics Division, Istanbul, Turkey, 2007.

[23] G. Yıldırım, "Computer-aided design of micro-irrigation laterals by using LatCAD", MSc. Thesis, Istanbul Technical University, Hydraulics Division, Istanbul, Turkey, 2001.

[24] G. Yıldırım, "Total energy loss assessment for trickle lateral lines equipped with in-line and on-line emitters" Irrig. Sci., 28(4), 341-352, 2010.

[25] G. Yıldırım, "Discussion of "Statistical Analysis of Non-Pressure-Compensating and Pressure-Compensating Drip Emitters" by H. Perea, J. Enciso-Medina, V. P. Singh, D. P. Dutta, and B. J. Lesikar (DOI: 10.1061/(ASCE)IR.1943-4774.0000644). *J. Irrig. and Drain. Eng., ASCE*, 2016.

[26] G. Yıldırım, "Simplified Procedure for Hydraulic Design of Small-Diameter Plastic Pipes." *Irrig. and Drain. (ICID Journal)* 58(2), 209-233, 2009.a.

[27] G. Yıldırım, "An Assessment for Hydraulically Efficient Design of Uniformly Sloping Submain, Lines" Irrigation and Drainage, 64(2),157-168, 2015.

[28] J.D. Valiantzas, "Analytical approach for direct drip lateral hydraulic calculation." J. Irrig. and Drain. Eng. ASCE 124(6): 300-305, 1998.
[29] J.D. Valiantzas, "Continuous outflow variation along irrigation laterals: effect of the number of outlets." J. Irrig. and Drain. Eng., ASCE, 128(1), 34-42, 2002.
[30] P. Vallesquino, P.L. Luque-Escamilla, "New algorithm for hydraulic calculation in irrigation laterals." J. Irrig. and Drain. Eng. ASCE 127(4): 254-260, 2001.
[31] P. Vallesquino, P.L. Luque-Escamilla, "Equivalent friction factor method for hydraulic calculation in irrigation laterals." *J. Irrig. and Drain. Eng. ASCE*, 128(5): 278-286, 2002.
[32] I.P. Wu, H.M. Gitlin, "Energy gradient line for drip irrigation laterals." J. Irrig. and Drain. Eng. ASCE 101(4): 323-326, 1975.
[33] I.P. Wu, "Energy gradient line approach for direct hydraulic calculation in drip irrigation design." Irrig. Sci. 13: 21-29, 1992.
[34] I.P. Wu, "An assessment of hydraulic design of microirrigation systems." Agric. Water Manag. 32: 275-284, 1997.
[35] I.P. Wu, R. Yue, "Drip lateral design using energy gradient line approach." Trans. ASAE 36(2): 389-394, 10, 1993.

[36] G. Yıldırım, and O. Kose, "New Software (Multi-flowCAD) Development for Sub-main Line Hydraulic Design Computational Algorithm, Computer Visualization and Implementation" Arabian Journal for Science and Engineering, 41, 1551-1560, 2016.

[37] G.Yıldırım, "Computer-Based Analysis of Hydraulic Design Variables for Uniformly Sloping Microirrigation System Laterals" J. Irrig. and Drain. Eng., ASCE, 141(7): 04014079, 2015.

[38] G. Yıldırım, and V.P. Singh, "A *MathCAD* Procedure for Commercial Pipeline Hydraulic Design Considering Local Energy Losses" *Advances in Engineering Software*, 41(2), 489-496, 2010.

[39] G. Yıldırım, "Computer-Based Analysis of Explicit Approximations to the Implicit Colebrook-White Equation in Turbulent Flow Friction Factor Calculation." *Advances in Engineering Software*, 40(11), 1183-1190, 2009.

[40] G. Yıldırım, and M. Özger, "Neuro-Fuzzy Approach in Estimating Hazen-Williams Friction Coefficient for Small-Diameter Polyethylene Pipes." *Advances in Engineering Software*, 40(8): 593-599, 2009.

[41] M. Özger, M. and G. Yıldırım, "Determining Turbulent Flow Friction Coefficient Using Adaptive Neuro-Fuzzy Computing Technique." *Advances in Engineering Software*, 40(4): 281-287, 2009.

[42] G. Yıldırım, Discussion of "Field-Scale Assessment of Uncertainties in Drip Irrigation Lateral Parameters" by Yeboah Gyasi-Agyei" *J. Irrig. and Drain. Eng., ASCE,* 135(2), 261-263, 2009.b.

[43] G. Yıldırım, Discussion of "Simplified Method for Sizing Laterals with Two or More Diameters" by Muluneh Yitayew" *J. Irrig. and Drain. Eng., ASCE (accepted for publication), 2009.c.*

[44] G. Yıldırım, "Determining Operating Inlet Pressure Head Incorporating Uniformity Parameters for Multioutlet Plastic Pipelines." *J. Irrig. and Drain. Eng., ASCE,* 134(3), 341-348, 2008.a.

[45] G. Yıldırım, Discussion of "Turbulent Flow Friction Factor Calculation Using a Mathematically Exact Alternative to the Colebrook-White Equation' by Sonnad and Goudar" *J. Hydraulic Eng., ASCE*, 134(8):1185-1186, 2008.b.

[46] G. Yıldırım, N. Ağıralioğlu, Closure to "Comparative analysis of hydraulic calculation methods in design of microirrigation laterals" by G. Yıldırım and N. Ağıralioğlu. J. Irrig. and Drain. Eng., ASCE 132(1): 85-90, 2006.c.

[47] G. Yıldırım, and N. Ağıralioğlu, Discussion of "Inlet pressure, energy cost, and economic design of tapered irrigation submains' by Valiantzas" *J. Irrig. and Drain. Engrg., ASCE,* 131(2), 220-224, 2005.a.

[48] G. Yıldırım, and N. Ağıralioğlu, Discussion of "Explicit hydraulic design of microirrigation submain units with tapered manifold and laterals' by Valiantzas" *J. Irrig. and Drain. Engrg., ASCE,* 131(3), 299-300, 2005.b.

[49] G. Yıldırım, and N. Ağıralioğlu, Closure to "Linear solution for hydraulic analysis of tapered microirrigation laterals' by Yıldırım and Ağıralioğlu" *J. Irrig. and Drain. Eng., ASCE,* 131(5), 490-491, 2005.c.

[50] G. Yıldırım, N. Ağıralioğlu, "Comparative analysis of hydraulic calculation methods in design of microirrigation laterals." J. Irrig. and Drain. Eng. ASCE 130(3): 201-217, 2004.a.

[51] G. Yıldırım, and N. Ağıralioğlu, "Linear solution for hydraulic analysis of tapered microirrigation laterals." *J. Irrig. and Drain. Eng., ASCE,* 130(1), 78-87, 2004.b.

[52] G. Yıldırım, and N. Ağıralioğlu, Discussion of "Equivalent friction factor method for hydraulic calculation in irrigation laterals." *J. Irrig. and Drain. Engrg., ASCE*, 130(4), 335-339, 2004.e.

[53] G. Yıldırım, and N. Ağıralioğlu, Discussion of "New algorithm for hydraulic calculation in irrigation laterals" *J. Irrig. and Drain. Engrg., ASCE*, 129(2), 142-143, 2003.a.

[54] G. Yıldırım, and N. Ağıralioğlu, Discussion of "Continuous outflow variation along irrigation laterals: effect of the number of outlets." *J. Irrig. and Drain. Engrg., ASCE,* 129(5), 382-386, 2003.b.

Çok Cidarlı Karbon Nanotüp Takviyeli Poliüretan Kompozitlerin Eğilme Dayanımı

Müşerref Rana Kavuncu[1*], Mürsel Ekrem[2],

[1*] Necmettin Erbakan Üniversitesi, Mühendislik Fakültesi, Makine Mühendisliği Bölümü, Konya, Türkiye , (ORCID: 0000-0002-3505-969X), muserrefranakavuncu974205@gmail.com

[2] Necmettin Erbakan Üniversitesi, Mühendislik Fakültesi, Makine Mühendisliği Bölümü, Konya, Türkiye , (ORCID: 0000-0001-5324-7929),mekrem@erbakan.edu.tr

Öz

Yazılar Geleneksel monolitik malzemelerin (örneğin metal, seramik, polimer vb.) farklı uygulamalarda kullanımı, insan uygarlığının başlangıcından bugüne kadar yaygın olarak uygulanmaktadır. Günümüzde ise kompozit malzemeler, birkaç farklı bileşen malzemenin avantajlarını birleştirerek malzeme performansının optimizasyonunda büyük bir potansiyel sunan ve en hızlı büyüyen malzeme sınıfları arasındadır. Poliüretan kompozitler (PUC'ler) düşük yoğunluk, mükemmel esneklik, şekil hafızası, yüksek aşınma direnci, korozyon direnci, kopmada yüksek uzama, sönümleme yeteneği, hava koşullarına dayanıklılık, yüksek elastikiyet, yaşlanma önleyici, iyi işlenebilirlik, yüksek darbe dayanımı, mükemmel parlaklık gibi takdire şayan özelliklere sahiptir. CNT ile güçlendirilmiş polimer nanokompozitler hem akademik hem de endüstriyel alanlarda malzeme biliminde dikkate değer bir dönüm noktası haline gelmiştir. Takviye için CNT'nin eklenmesi PU kompozitin sertliğini, çekme dayanımını, modülünü, eğilme dayanımını, ısıl iletkenliğini ve ısıl kararlılığını arttırdığı yapılan araştırmalarda gözlemlenmiştir. Yapılan bu çalışmada PU / MWCNT kompozitlerin üç noktalı eğilme testleri, ağırlıkça % 0.25 MWCNT içeren PU kompozitin eğilme dayanımı, saf PU ile karşılaştırıldığında iyileştirildiğini ortaya koymuştur. MWCNT takviyeli poliüretan nanokompozit malzemeler ASTM D790-02 standardına göre hazırlanarak eğilme dayanımı ve birim şekil değişimi değerleri incelenmiştir. Saf poliüretanın eğilme dayanımı 25 MPa iken %0.25 MWCNT takviyeli poliüretanın eğilme dayanımı 41.05 MPa olarak ölçülmüş ve %64.2'lik bir artış gözlemlenmiştir. Birim şekil değişiminde ise saf poliüretan 7.76 mm\mm iken %0.25 MWCNT takviyeli nanokompozit malzemenin birim şekil değişimi 1.31 mm\mm olarak hesaplanmış ve %83.11'lik bir azalma sergilemiştir. Ayrıca kırık yüzeylerin hasar davranışları taramalı elektron mikroskobu (SEM) ile incelenmiştir.

Anahtar Kelimeler: MWCNT, Poliüretan, Nanokompozit, Eğilme dayanımı, Hasar mekanizmaları.

Flexıble Strength Of Multı-Wall Carbon Nanotubı Reınforced Polyurethane Composıtes

Abstract

The use of traditional monolithic materials (eg metal, ceramic, polymer, etc.) in different applications has been widely practiced since the beginning of human civilization. Today, composite materials are among the fastest growing material classes, offering great potential in optimizing material performance by combining the advantages of several different component materials. Polyurethane composites (PUC) such as low density, excellent flexibility, shape memory, high wear resistance, corrosion resistance, high elongation at break, damping ability, weather resistance, high elasticity, anti-aging, good workability, high impact resistance, excellent gloss It has admirable features. CNT-reinforced polymer nanocomposites have become a remarkable landmark in materials science in both academic and industrial fields. It has been observed in research that the addition of CNT for reinforcement increases the hardness, tensile strength, modulus, flexural strength, thermal conductivity and thermal stability of the PU composite. In this study, three-point bending tests of PU / MWCNT composites revealed that the flexural strength of the PU composite containing 0.25 wt% MWCNT was improved compared to

pure PU. MWCNT reinforced polyurethane nanocomposite materials were prepared according to ASTM D790-02 standard, and their flexural strength and strain values were investigated. While the flexural strength of pure polyurethane was 25 MPa, the flexural strength of 0.25% MWCNT reinforced polyurethane was measured as 41.05 MPa and an increase of 64.2% was observed. While pure polyurethane was 7.76 mm\mm in unit deformation, the unit deformation of 0.25% MWCNT reinforced nanocomposite material was calculated as 1.31 mm\mm and showed a decrease of 83.11%.

In addition, the damage behavior of the fractured surfaces was investigated by scanning electron microscopy (SEM).

Keywords: MWCNT, Polyurethane, Nanocomposite, Flexural strength, Damage mechanisms.

1. Giriş

Geleneksel metal malzemelere alternatif olarak poliüretan matriksli kompozit malzemelerin kullanımı yaygınlaşmaktadır. Bu malzemelerin temel teknolojik avantajları, düşük ağırlık, yüksek özgül mukavemet ve sertlik, çevresel direnç ve uzun ömürdür. Metallerle karşılaştırıldığında, kompozit parçalar nispeten düşük bir takım maliyeti ile kolayca yapılabilir(Ekrem, 2019b). Bilim ve endüstri, avantajlı fiziksel ve kimyasal özellikleri ve amaçlanan kullanıma bağlı olarak yapılarını değiştirme olasılığı nedeniyle poliüretanlarla (PU) ilgilenmektedir. Poliüretanların bugün dünyadaki çok yönlü malzemelerden biri olması nedeniyle duvar yalıtımı, termoplastik poliüretan çatılar ve zemin kaplamalar, otomotivde kullanılan iç kaplamalar, yapıştırıcılar, dolgu maddeleri, tıbbi cihazlar gibi birçok kullanım alanı bulunmaktadır (Zia et al., 2007). PU'nun CNT'lerle modifiye edilmesiyle, mekanik özelliklerde, termal stabilitede ve termal iletkenlikte önemli gelişme, iyi dağılımlarının ve güçlü bir arayüzey bağlarının bir sonucu olarak elde edilebilir (Szatkowski et al., 2017). MWCNT'ler, mükemmel mekanik mukavemetleri, nano ölçekli çapları ve çok yüksek en boy oranları nedeniyle en umut verici dolgu malzemesi olarak kabul edilir. Araştırmacılar, MWCNT'lerin Young modülünün (1000 GPa) geleneksel karbon fiberlerinkinden (200-800 GPa) çok daha yüksek olan mükemmel bir değere sahip olduğunu kanıtladılar (Wong et al., 2003). Bu nedenle, mükemmel özellikleri nedeniyle MWCNT'ler, saf polimere göre gelişmiş mekanik özelliklerle sonuçlandıklarından fiber takviyeli polimer kompozitlerin üretiminde kullanılabilir (Chen et al., 2006).

Polimer kompozitlerde MWCNT'leri etkin kullanımını için, MWCNT'lerin polimer matris içerisinde uygun şekilde dağıtılması çok önemlidir. MWCNT'lerin polimer matriksi içerisinde homojen dağılım ve dağıtım elde etmek, nanotüpler arasındaki moleküller arası van der Walls etkileşimi nedeniyle zordur, bu da nanotüplerin topaklanmasına neden olur (Ekrem, 2019a). Bu nedenle, nanotüplerin polimer matris içinde homojen bir şekilde dağılmasını sağlamak için son on yılda birkaç teknik geliştirilmiştir. Tüm üretim teknikleri arasında, çözelti karıştırmanın, karbon nanotüplerin polimer matriks içinde homojen olarak dağılması için daha uygun olduğu bulunmuştur (Kumar et al., 2017, Vaithylingam et al., 2017, Mohamad et al., 2020, Yıldırım et al., 2020).

Bu çalışmamızda ağırlıkça % 0.25 oranında MWCNT takviyeli poliüretan nanokompozit malzemenin eğilme dayanımı, elastiklik modülü, tokluk ve şekil değişimi saf poliüretan malzemeyle karşılaştırılmıştır. Numuneler ASTM D790 standardına uygun olarak üretilmiştir. Ayrıca SEM görüntülerine bakılarak hasar mekanizmaları incelenmiştir.

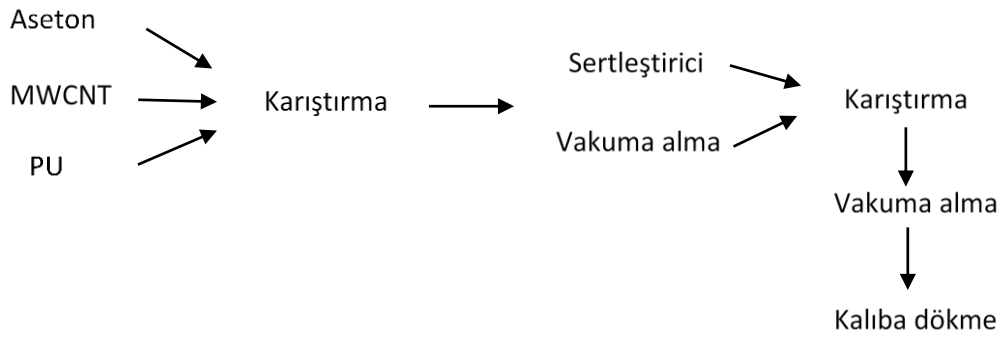
2. Materyal ve Metod

2.1. Materyal

Bu çalışmamızda poliüretanı sertleştirmek için KLB 75 kodlu Duratek firmasına ait solvent içermeyen, 2 100 mPa viskoziteye sahip iki bileşenli poliüretan esaslı yapıştırıcı kullanılmıştır. Poliol üretan ile izosiyanat sertleştiricinin ağırlıkça karışım oranı 80/20'dir. MWCNTler buhar biriktirme yöntemiyle NANOCYL firması tarafından üretilmiştir. Çapı 5-50 nm ve uzunluğu 10 ila 30 µm'dir.

2.2. Metot

Şekil 1'de görüldüğü gibi farklı ağırlıklarda MWCNT takviyeli poliüretan esaslı nanokompozitlerin hazırlanışı şematik olarak verilmiştir. Öncelikle poliüretan malzeme hassas terazide bir beher içerisinde 40 g olarak tartılmıştır. Sonra poliüretan polimerin ağırlıkça % 0.25 oranında MWCNT alüminyum folyo üzerine konularak hassas terazide tartılmış sonrasında da poliüretan beherinin içine dikkatli bir şekilde konulmuştur. Hazırlanan bu karışımı homojen olarak dağıtmak ve viskozitesini düşürmek amacıyla çözelti karıştırma metodunu kullanarak bir beher içine konulan MWCNT'nin ağırlığının 1/100 g/mL oranında aseton ilavesi eklenmiştir. Problu homojenizatörle 10 dk. süreyle 3 defa olmak üzere toplam 30 dk karıştırılmıştır. Bu işlem nanoparçacıkların ve polimerin maruz kaldığı ısıdan zarar görmemesi için belli aralıklarla yapılmıştır. Daha sonra karışımın içerisinde oluşan hava kabarcıklarından kurtulmak ve asetonu tamamen uçurmak için vakum fırını içerisinde 60 °C 10 incHg basınçta 12 saat bekletilmiştir. Buharlaşan aseton ile basınç düşmelerinde vakum tekrar aynı basınca çıkarılmıştır. Poliüretan/sertleştirici 80/20 oranında ilavesi gerçekleşmiş ve mekanik olarak hava kabarcığı olmayacak şekilde en az 15 dk karıştırılmıştır. Son olarak elde edilen bu karışım, mekanik karıştırma işlemi sırasında oluşan hava kabarcıklarının giderilmesi için tekrar 10 incHg basınçta 15 dk vakumlanarak kullanıma hazır hale gelmiştir.



Şekil 1. Nanokompozit malzemelerin üretim aşamaları

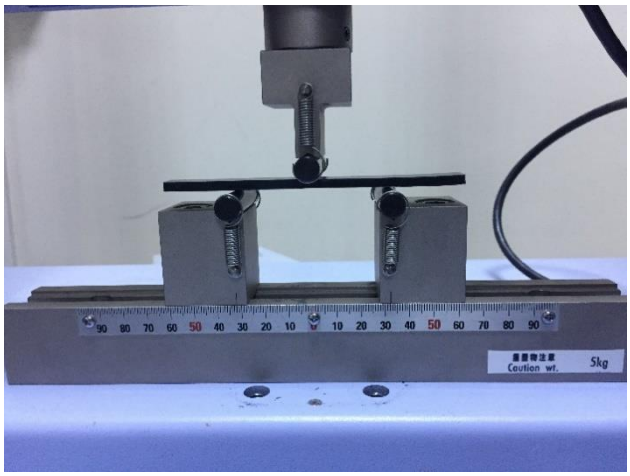
Eğilme testleri için ASTM D790 standardına uygun olarak önceden hazırlanan çelik kalıplara, poliüretan polimerin yapışmaması için vaks yardımıyla ince bir film oluşturacak şekilde sürülmüştür. Montajı yapılan bu kalıplara hazırlanan poliüretan nanokompozit katkılı/katkısız karışımının yavaş olarak dökümü gerçekleştirilmiştir (Şekil 2.). Eğilme numunesi kalıbı kürleştirme işlemi için üretici firmanın tavsiyesi doğrultusunda 168 saat oda sıcaklığında bekletilmiştir. Test sonuçlarının güvenilirliğini sağlamak için aynı özellikteki numuneden 5 adet üretilmiştir.



Şekil 2. Nanokompozit malzeme üretim kalıbı

2.2.1. Nanokompozit Malzemelerin Eğilme Deneyleri

ASTM D790'a göre 125x13x6 mm ölçülerinde dikdörtgen kesitli bir parça halinde olan numuneler üretilmiştir. Testler 2 mm/dk hızında uzama kontrollü yapılmıştır. Shimadzu AGS-X Üniversal Çekme Test Cihazı kullanılarak 1kN yük hücresinde deneyler gerçekleştirilmiştir. Test numuneleri ASTM D790 standardı gereğince beşer adet üretilmiştir. Bütün testler oda sıcaklığında yapılmıştır.



Şekil 3. Nanokompozit malzemenin eğme testi

Numuneye uygulanan yük değerleri (P) ve sehim değerleri (δ) çekme test cihazında anlık olarak kaydedilmiştir. Bu değerleri kullanarak eğilme gerilmesini Denklem 2.1'e göre hesaplanmıştır.

$$\sigma_{ei} = \frac{L \times 3P_i}{2bh^2} \quad (2.1)$$

Burada *P*i numuneye uygulanan anlık kuvvet (N), L mesnetler arası mesafe (mm), b numunenin eni (mm), h ise numunenin kalınlığı ve □i ise anlık gerilme değeridir.

$$\varepsilon_{bmax} = \frac{6h\delta_e}{L^2} \quad (2.2)$$

Numunenin şekil değişimi Denklem 2.2'ye göre hesaplanmıştır. Şekil değiştirme miktarını (mm/mm), δ orta noktadaki sehimi (mm), L mesnetler arası açıklığı (mm) ve h ise numune kalınlığını (mm) temsil etmektedir.

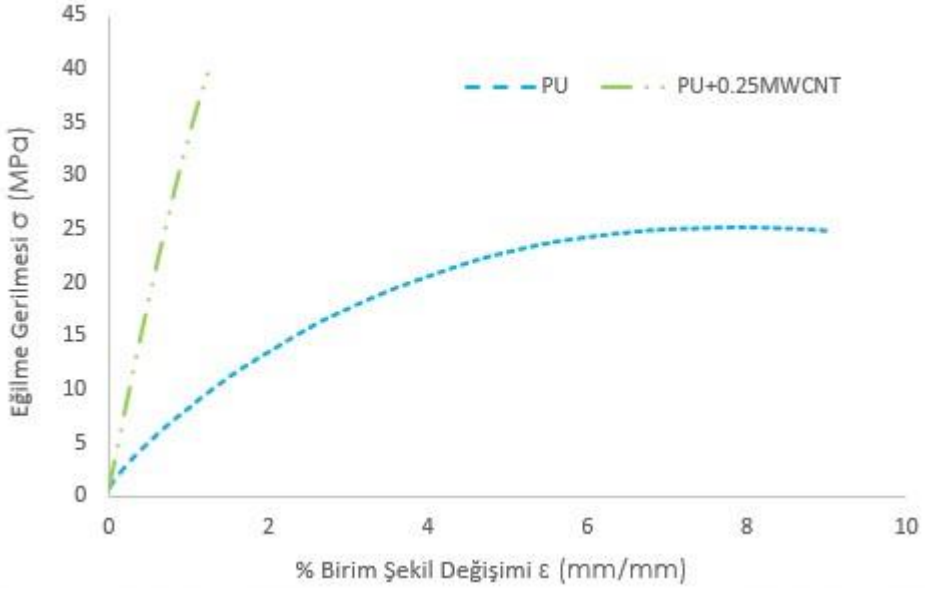
$$E_e = \frac{\Delta\sigma}{\Delta\varepsilon} \quad (2.3)$$

Ayrıca eğilme elastiklik modülü ise Denklem 2.3'e göre hesaplanmaktadır. Elastisite modülü (E), Young modülü olarak da bilinir ve gerilme-birim şekil değişimi eğrisinin başlangıçtaki elastik deformasyon bölgesinin eğimi olarak tanımlanır.

3. Bulgular

3.1. Nanokompozit Malzemelerin Eğilme Deneyleri

Şekil 4'te, PU / MWCNT kompozitinin, PU'nun ve %0.25 MWCNT takviyeli poliüretanın üç noktalı yükleme sırasında tipik gerilme-birim şekil değiştirme grafikleri temsil edilmiştir. Tüm numuneler, yükleme sırasında indüklenen daha düşük stresle doğrusal olmayan davranış gösterir. Bu kompozitlerin eğilme modülü, artan MWCNT bileşimlerinin etkisiyle iyileştirilmiştir.



Şekil 4. Nanokompozitlerin eğilme gerilme-birim şekil değişim grafiği

Saf poliüretanın eğilme dayanımı 25 MPa iken %0.25 MWCNT takviyeli poliüretanın eğilme dayanımı 41.09 MPa olarak ölçülmüş ve %64.2 lik bir artış gözlemlenmiştir. % Birim şekil değişiminde ise saf poliüretan 9.60 mm\mm iken %0.25 MWCNT takviyeli nanokompozit malzemenin % birim şekil değişimi 1.31 mm\mm olarak hesaplanmış ve %86.11 lik bir azalış sergilemiştir.

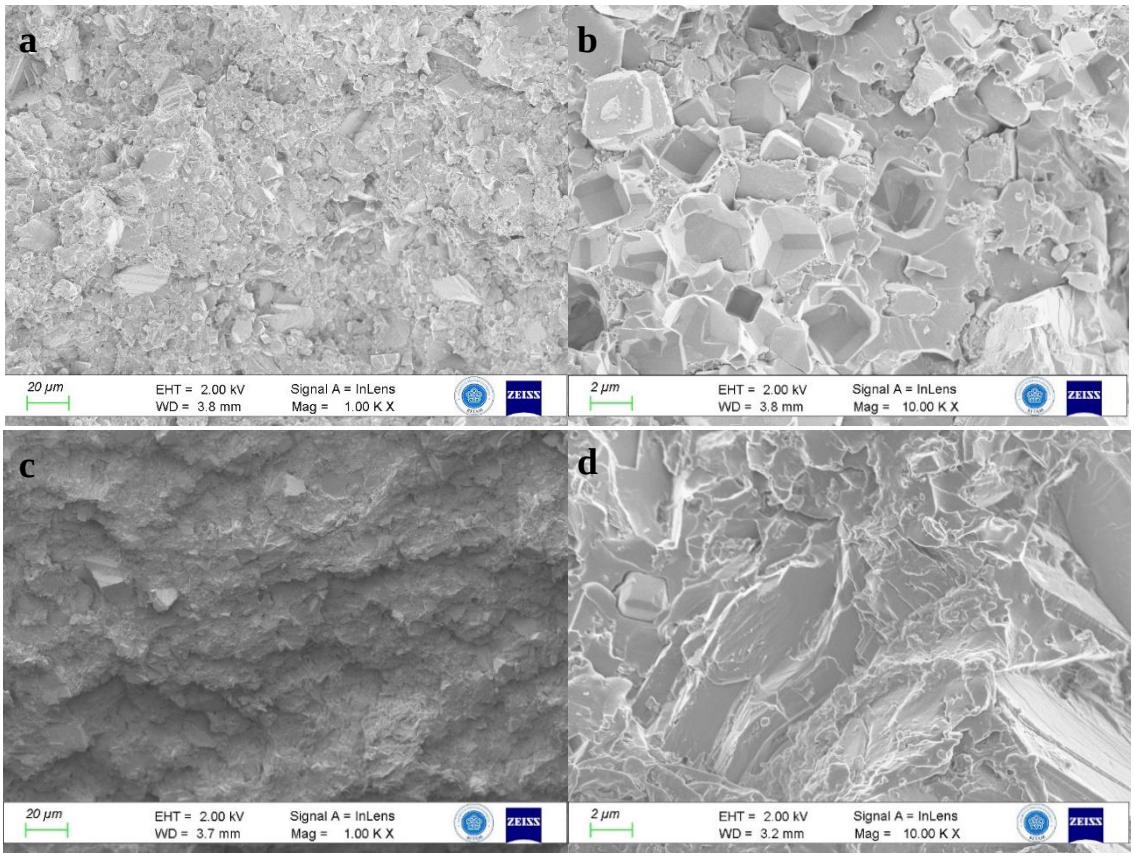
Tablo 1. Mekanik Dayanım Değerleri

	Maks yük (N)	**Maks ε (mm/mm)**	**Eğilme gerilmesi (MPa)**	**Elastiklik modülü (GPa)**	**Tokluk (kJ/m^3)**
PU	63.17	0.096	25.23±0.21	0.541	689.7
PU+0.25 MWCNT	107.72	0.013	41.09±0.16	0.880	302.6

Poliüretan polimerin maksimum yükleme, maksimum birim şekil değişimi ve elastiklik modülü sırasıyla 63.13 N, 0.096 mm/mm ve 0.541 GPa elde edilmiştir. Ağırlıkça %0.25 MWCNT takviyeli poliüretan nanokompozit malzemenin maksimum yükleme ve elastiklik modülü sırasıyla % 70.5 ve % 62.7 artış ile 107,72 N ve 0.880 GPa değerlerine artmıştır. Kırılma hasarı incelendiği zaman PU polimeri sünek kırılma görülürken PU+0.25 MWCNT nanokompozit malzemede gevrek kırılmayla elastik olarak kırılmıştır. Böylece tokluğunda % 56.5 oranında bir azalma gözlemlenmiştir.

3.2. Poliüretan nanokompozitlerin hasar mekanizmaları

Literatürde bildirildiği gibi, nanokompozitlerin mekanik mukavemeti, MWCNT'lerin polimer matris içinde homojen dağılımına bağlıdır. Bu nedenle, MWCNT'lerin matris boyunca dağılımını incelemek oldukça önemli hale gelir. Bu bağlamda farklı büyütme oranlarında (1.0 KX ve 10.0 KX) PU ve PU+0.25 MWCNT malzemelerin SEM görüntüleri incelenmiştir (Şekil 5). Yapılan gözlemler sonucunda ise matris boyunca düzgün dağılımın başarıyla sağlandığı gözlenmiştir. Her iki uzunluk ölçeğinde de ayrı ayrı tüpler görülebilir ve bu, matris boyunca takviye elde edildiğini ve ağırlıkça %0.25 kompozit için MWCNT'lerin toplanmasının görülmediği gözlemlenmiştir.



Şekil 5. Kırık yüzeylerin SEM görüntüleri; PU malzemesinin a) 1.0 KX ve b) 10.0 KX büyütmeleri ile PU+0.25 MWCNT nanokompozitinin c) 1.0 KX ve d) 10.0 KX büyütmeleri

4. Sonuçlar

Bu çalışmamızda, MWCNT nanoparçacıkları poliüretan polimerin içerisine ilave ederek eğilme dayanımını geliştirmek için bir metodoloji önerdik. Nanokompozitlerin üretiminde, nano boyuttaki mükemmel özellikli MWCNTs takviye maddelerinin kullanılması, daha iyi mekanik özelliklere sahip poliüretan esaslı nanokompozit malzemeler elde etmemize olanak sağlamıştır.

References

[1] Ekrem, M. Hexagonal Boron Nitride Nanoplates-Nano Ag / Epoxy Composites: Production, Mechanical and Thermal Properties. El-Cezeri Journal of Science and Engineering 6(3):585-593,2019.

[2] Ekrem, M. (2019b) Shear strength of boron nitride nanoplatelets and nano Ag reinforced structural adhesives. Journal of Bor 4(3):128-1342019.

[3] Kumar, D., Kumar, N. & Jindal, P. Elastic modulus behavior of multi-walled carbon nano-tubes/polyurethane composites using nano-indentation techniques. Indian J Sci Technol 10(17):974-6846,2017.

[4] Chen, G.-X., Kim, H.-S., Park, B. H. & Yoon, J.-S. Multi-walled carbon nanotubes reinforced nylon 6 composites. Polymer 47(13):4760-4767, 2006.

[5] Mohamad, M., Abd Razak, J., Mohamad, N., Ahmad, S. H., Junid, R. & Puspitasari, P. A short review on polyurethane-based nanocomposites for various applications. In IOP Conference Series: Materials Science and Engineering.) IOP Publishing, vol. 957, pp. 012029, 2020.

[6] Szatkowski, P., Pielichowska, K. & Blazewicz, S. Mechanical and thermal properties of carbon-nanotube-reinforced self-healing polyurethanes. Journal of Materials Science 52(20):12221-12234, 2017.

[7] Vaithylingam, R., Ansari, M. N. M. & Shanks, R. A. Recent Advances in Polyurethane-Based Nanocomposites: A Review. Polymer-Plastics Technology and Engineering 56(14):1528-1541, 2017.

[8] Wong, M., Paramsothy, M., Xu, X., Ren, Y., Li, S. & Liao, K. Physical interactions at carbon nanotube-polymer interface. Polymer 44(25):7757-7764, 2003.

[9] Yıldırım, F., Ataberk, N. & Ekrem, M. Mechanical and thermal properties of a nanocomposite material which epoxy based and reinforced with polyvinyl alcohol nano fibers contained multiwalled carbon nanotube. Journal of Composite Materials, 2020.

[10] Zia, K. M., Bhatti, H. N. & Bhatti, I. A. Methods for polyurethane and polyurethane composites, recycling and recovery: A review. Reactive and functional polymers 67(8):675-692, 2007.

==========

Determination of Steel Strand Effect on Dynamic Parameters of Composite Structure

Furkan Günday[1*]

[1*] Giresun Üniversitesi, Mühendislik Fakültesi, İnşaat Mühendisliği Bölümü, Giresun, Türkiye, (ORCID: 0000-0003-2979-9373), furkan.gunday@giresun.edu.tr

Öz

Depremlerin yapılar üzerindeki yıkıcı etkileri bilinmektedir. Ayrıca çevresel titreşimin zararlı etkileri ve etkileri de göz ardı edilmemelidir. Bu gereksinimin yapı tasarımlarında değişiklik ve gelişmelere neden olduğu bilinmektedir. Yapıyı etkileyecek etkileri en aza indirmek için çeşitli çalışmalar ve uygulamalar mevcuttur. Tasarımlarda yapı kütlesini düşük tutmak öncelikler arasındadır. Kompozit yapılar bu ihtiyaçtan doğmuştur. Kompozit yapılarda amaç, daha az kütle ile daha fazla yük taşıma prensibine dayanmaktadır. Ancak kompozit yapılarda etkilere bağlı olarak güçlendirme ihtiyacı ortaya çıkabilir veya tasarım zorlukları olabilir. Bu durumda daha az kütle ile daha fazla yük taşıma prensibine bağlı kalabilmek için çelik halatlarla güçlendirme yönteminin kullanılması daha mantıklı düşünülebilir. Çelik halat ile güçlendirme yönteminin yapı üzerine nispeten küçük bir kütle yerleştirerek yapının rijitliğini arttırdığı birçok çalışmada kanıtlanmıştır. Bu çalışmada, sonlu elemanlar yöntemi kullanılarak modal analiz yapılarak örnek bir kompozit yapıda çelik halat takviyesinin etkileri ortaya konmuştur. Özellikle ilk 5 modun yapı titreşim periyotları ve serbest titreşim modu şekilleri detaylı olarak ele alınmıştır. Böylece çelik halat kullanımının kompozit yapının rijitliğine olumlu etkisi daha net bir şekilde ortaya konmuştur. Tüm bu çalışmalar sonucunda kompozit yapılarda çelik halat ile güçlendirme yönteminin kullanılabilirliği öngörülmektedir.

Anahtar Kelimeler: Kompozit yapılar, Çelik halat, Sonlu elemanlar metodu, Dinamik parametreler, Güçlendirme

Determination of Steel Strand Effect on Dynamic Parameters of Composite Structure

Abstract

The destructive effects of earthquakes on structures are known. In addition, the harmful effects of environmental vibration and effects should not be ignored. This requirement is known to cause changes and developments in building designs. There are various studies and applications to minimize the effects that will affect the structure. Keeping the building mass low in designs is among the priorities. Composite structures were born out of this need. The aim in composite structures is based on the principle of carrying more load with lower mass. However, in composite structures, depending on the effects, the need for reinforcement may arise or there may be design difficulties. In this case, it may be considered more logical to use the reinforcement method with steel strands in order to adhere to the principle of carrying more load with a lower mass. It has been proven in many studies that the reinforcement method with steel strand increases the rigidity of the structure by placing a relatively small mass on the structure. In this study, the effects of steel strand reinforcement in a sample composite structure are revealed by making modal analysis using the finite element method. In particular, the structure vibration periods and free vibration mode shapes of the first 5 modes are discussed in detail. Thus, the positive effect of the use of steel strand the rigidity of the composite structure has been more clearly demonstrated. As a result of all these studies, the reinforcement method with steel strand can be used in composite structures.

Keywords: Composite structures, Steel strand, Finite element method, Dynamic parameters, Reinforcement

1. Introduction

The strands produced by the steel strand in a wide range of diameters from 6 mm to 83 mm have been used in various sectors such as construction, marine, fishing, oil, mining and in elevators, chairlifts, cranes for many years. Strands produced in accordance with international standards such as BS, DIN and JIS according to federal specifications and API specifications are increasingly preferred by the world's most developed countries. Steel strands are often used in oil drilling wells, mines, bridges, constructions, stadiums and similar areas. Some steel strand knitting techniques are used in order to increase the durability of steel strand products, which are resistant to high weights and are often used with high weights. The steel strand is named for the structure in which it is processed. Specially processed strands can have their own unique names. Extensions such as Filler, Standard, Warrington Seale, Seale express the thickness, thinness and arrangement of the wires in the veins. Steel strands are manufactured by helically wrapping at least 4 cores around a core (p.p.c, sızal or steel) formed by braiding the wires according to various compositions. Strands are generally named in two different ways as cross and straight winding according to their winding directions. They also have four different configurations: right cross winding (s/Z), left cross winding (z/S), right straight winding (z/Z), left straight winding (s/S). We mentioned in our article that steel strands have a very strong structure. However, the area where the strand is used and the production technique are completely different. If steel strand; if it will be used in marine, cranes and as a tow strand; The most suitable type of strand is nuflex strand. The knitting technique of this wire strand is quite different from the others. Therefore, it is among the ideal strands for high use. If you are looking for a steel strand that you will use in drilling works or mining; It would be appropriate to choose Filler steel cored wire strand with thick outer wires. It is very flexible with its thick outer wires. Therefore, it is a suitable type of strand for pulling operations. If you are looking for a type of strand that can be used for sand quarries, mining, load pulling, cranes drilling and drilling; Again, filler fiber core steel strand is suitable for your use. These steel strands; It is brought together with the use of different knitting techniques in wires of different fineness. It is known as a very durable strand type. Steel strand cross section is given in figure 1.

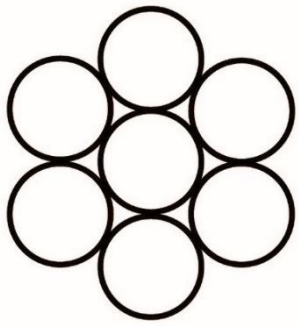


Figure 1. Steel strand cross section

Researchers have carried out many studies using both the finite element method and the reinforcing methods. There are many other studies by the authors using the finite element method before. In this study, studies [1], [2], [3], [4], [5], [6], [7] on the use of the finite element method were used. With all this knowledge, this new study has been carried out.

Researchers have conducted studies [8], [9], [10], [11], [12], [13], [14], [15] about steel strands which also contributing to this study.

The aim of this study is to examine the effects of reinforcement with steel strands on dynamic parameters in composite structures. There may be a need for a retrofit method without architectural disadvantages or excessive dead load increments. In such cases, the reinforcement method with steel strands is also known to be an option. For this reason, it is very important to reveal the effect of steel strands on dynamic parameters.

2. Material and Method

In this study, A composite structure model was created and modal analysis was carried out with the finite element method. The composite structure model was reinforced with steel strands and a reinforced model structure model was created for comparison. In the application of the finite element method, the SAP2000 package program, which is used in the field of academic and engineering applications all over the world, was used.

2.1. Description of Model Composite Structure

It is a 5-storey composite building with two spans (5 m) in x and y directions, with a floor height of 3 meters. Columns and beams are 20x20x1 cm steel box profile, slab thickness is 20 cm reinforced concrete.

By designing the building as symmetrical and simple, it is aimed to reveal the result of the reinforcement to be applied more clearly. The profile and dimensions of the columns and beams are therefore chosen the same. Also, the spans are therefore taken equal.

The 3D finite element model in SAP2000 package software of the model composite structure is given in Figure 2.

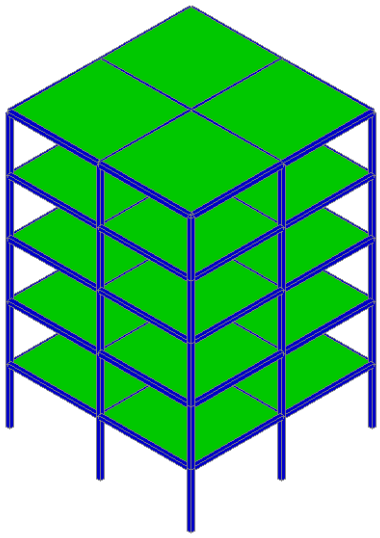


Figure 2. The model composite structure's 3D view

2.2. Description of Reinforced Model Composite Structure

Strand element was applied to one opening of the structure in the x and y directions. Strand element has a diameter of 2 cm and is made of steel. The 3D finite element model in SAP2000 package software of the reinforced model composite structure is given in Figure 3.

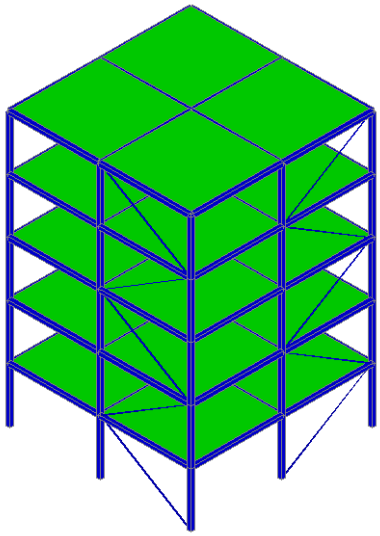


Figure 3. The reinforced model steel structure's 3D view

3. Result and Discussion

Model composite structure and reinforced model composite structure were analysed separately. The modal analysis results of each model are shared under separate headings. The results include the analysis results of the first five modes. Mode shape and period values are taken into consideration for each mode. The parameters obtained for both models were compared for each mode separately. During the analysis, the SAP2000 package software, which is a finite element method software, was used. The steel material used was taken according to ANSI/AISC 360-10 standards.

3.1. Analysis Results of Model Composite Structure

The model composite structure was analysed without reinforcing. When the first five modes are examined, the results obtained are presented in figure 4,5,6,7,8 as period values and mode shapes for each mode.

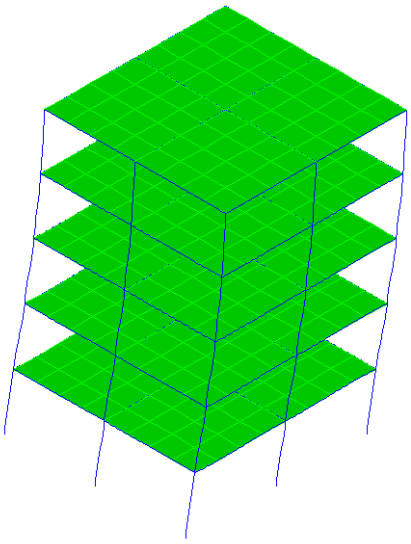


Figure 4. 1. Mode shape (T = 0.95 s)

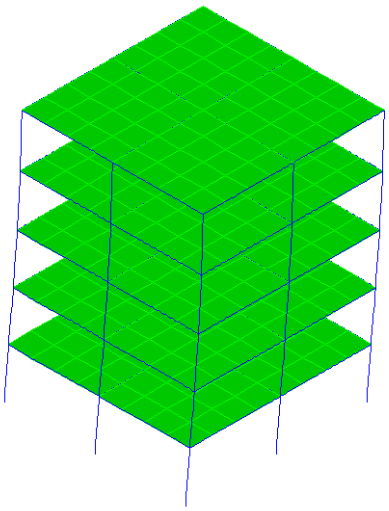


Figure 5. 2. Mode shape (T = 0.71 s)

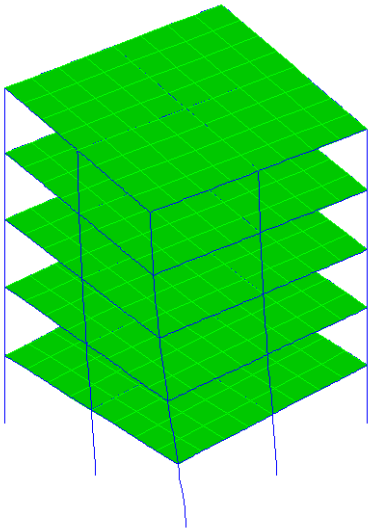


Figure 6. 3. Mode shape (T = 0.32 s)

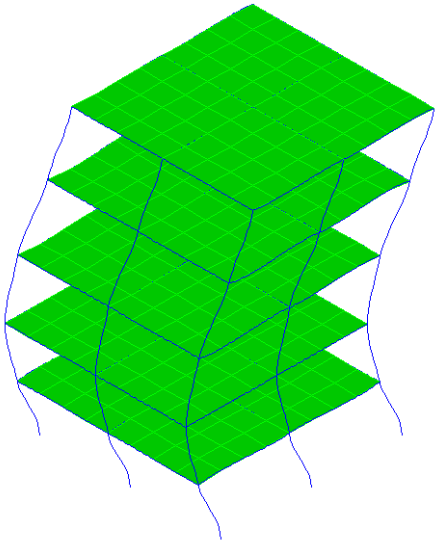


Figure 7. 4. Mode shape (T = 0.25 s)

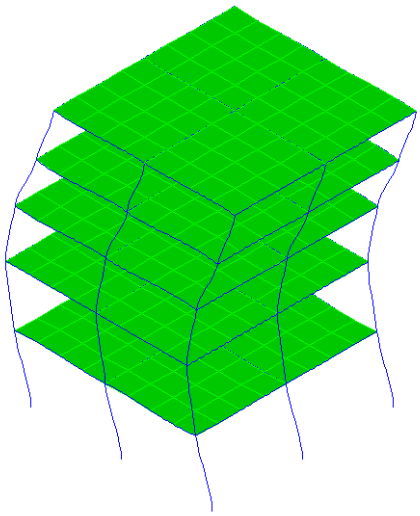


Figure 8. 5. Mode shape (T = 0.20 s)

3.2. Analysis Results of Reinforced Model Composite Structure

The model composite structure was analysed with reinforcing by steel strands. When the first five modes are examined, the results obtained are presented in figure 9,10,11,12,13 as period values and mode shapes for each mode.

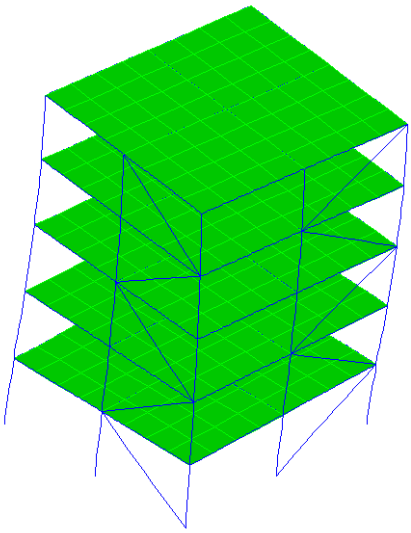


Figure 9. 1. Mode shape (T = 0.58 s)

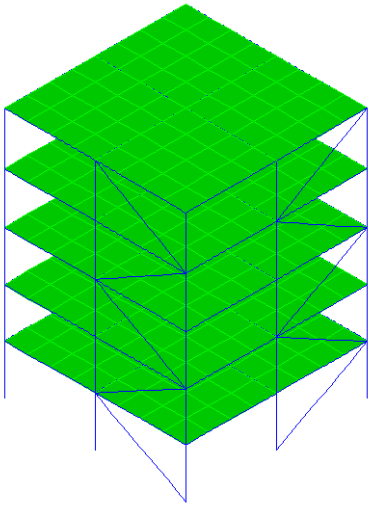


Figure 10. 2. Mode shape (T = 0.32 s)

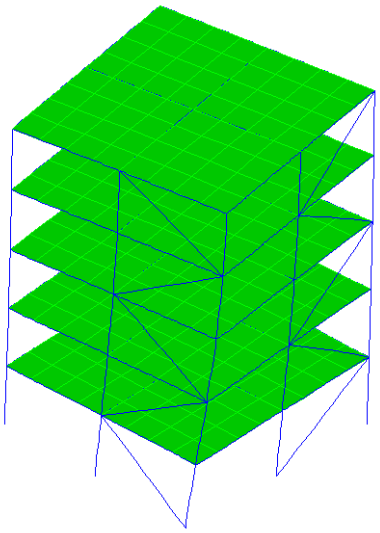


Figure 11. 3. Mode shape (T = 0.26 s)

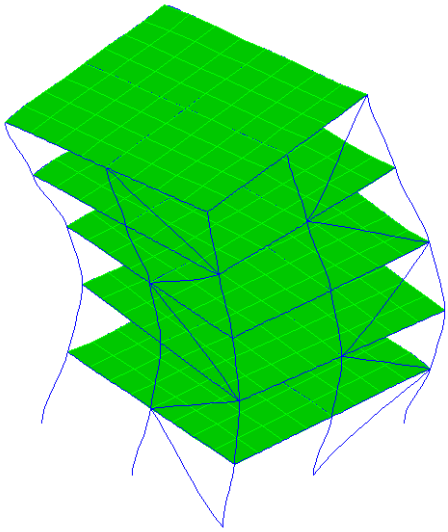


Figure 12. 4. Mode shape (T = 0.22 s)

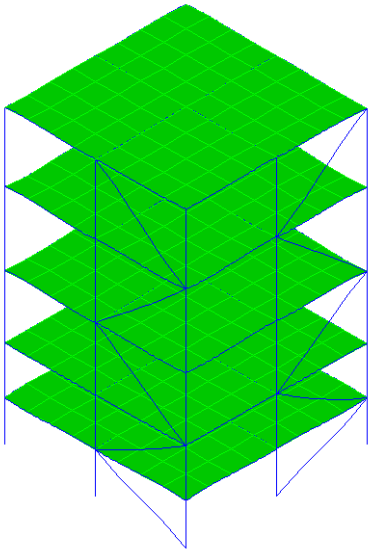


Figure 13. 5. Mode shape (T = 0.13 s)

3.3. Comparison of Analysis Results

The comparison of period values of the model composite structure and reinforced model composite structure is given in Table 1.

***Table 1**. Comparison of period values*

Mode	**1**	**2**	**3**	**4**	**5**
Non-Reinforced	0.95	0.71	0.32	0.25	0.20
Reinforced	0.58	0.39	0.26	0.22	0.13
Difference (s)	0.37	0.32	0.06	0.03	0.07
Difference (%)	38.95	45.07	18.75	12.00	35.00

The comparison of mode shapes of the model composite structure and reinforced model composite structure is given in Table 2.

Table 2. Comparison of mode shapes type

Mode	**1**	**2**	**3**	**4**	**5**
Non-reinforced	Translational	Translational	Torsional	Translational	Translational
Reinforced	Torsional	Translational	Torsional	Translational	Translational

4. Conclusions

In the mode 1, the period difference between non-reinforced model and reinforced model status was obtained as 0.37 s. The effect of period retrofitting with steel strands as a percentage was determined as 38.95.

In the mode 2, the period difference between non-reinforced model and reinforced model status was obtained as 0.32 s. The effect of period retrofitting with steel strands as a percentage was determined as 45.07.

In the mode 3, the period difference between non-reinforced model and reinforced model status was obtained as 0.06 s. The effect of period retrofitting with steel strands as a percentage was determined as 18.75.

In the mode 4, the period difference between non-reinforced model and reinforced model status was obtained as 0.03 s. The effect of period retrofitting with steel strands as a percentage was determined as 12.00.

In the mode 5, the period difference between non-reinforced model and reinforced model status was obtained as 0.07 s. The effect of period retrofitting with steel strands as a percentage was determined as 35.00.

When the mod shapes were examined, in the 1st mode, the mode shape has changed from the translational mode to the torsional mode. Although it is dangerous to see the torsional mode in the 1st mode, this problem can be solved by changing the places of the strands.

In the light of all these results, it is clearly seen that the rigidity of the structure increases by strengthening the model composite structure with steel strands. In the 1st mode, in other words, there is a decrease of 38.95 percent in the dominant period value. In addition, there is a large decrease of 45.07 percent in the period value in the 2nd mode. A significant increase in stiffness was observed. Of course, it should be taken into account that the design of the structure and reinforcement is very important in obtaining the data in this way. Incorrect model selection and faulty retrofit designs can make data more unreliable. In the light of all this obtaining information, the reinforcement method with steel strand may be used in composite structures.

References

[1] Ziada, M., Tuhta, S., Gençbay, E. H., Günday, F., & Tammam, Y. (2019). Analysis of Tunnel Form Building Retrofitted with CFRP using Finite Element Method. International Journal of Trend in Scientific Research and Development, 3(2), 822–826.

[2] Tuhta, S., Günday, F., & Pehlivan, N. C. (2019). Investigation of Cfrp Retrofitting Effect on Masonry Dome on Bending Moment Using Finite Element Method. International Journal of Innovatıons in Engineering Research and Technology, 6(6), 18–22.

[3] Tuhta, S., Günday, F., & Alihassan, A. (2020). The Effect of CFRP Reinforced Concrete Chimney on Modal Parameters Using Finite Element Method. International Journal of Innovations in Engineering Research and Technology, 7(2), 1–6.

[4] Tuhta, S., Günday, F., & Köroğlu, E. (2021). The Effect of TMD on The Periods and Mode Shapes of The Reinforced Concrete Building by Finite Element Analysis. JournalNx, 7(12), 5–13.

[5] Bakkour, F., Tuhta, S., & Günday, F. (2022). Determination of Modal Parameters of Reinforced Concrete Box Culvert Retrofitted with GFRP Using Finite Element Method. International Journal of Innovations in Engineering Research and Technology, 9(4), 1–9.

[6] Kasimzade, A.A., Tuhta, S., Günday, F. & Aydın, H. (2021). Obtaining Dynamic Parameters by Using Ambient Vibration Recordings on Model of The Steel Arch Bridge. Periodica Polytechnica Civil Engineering, 65(2), 608-618.

[7] Hammoud, M. A., Tuhta, S., & Günday, F. (2022). Determination of Modal Parameters of Reinforced Concrete Tunnel Retrofitted with CFRP using Finite Element Method. International Journal of Innovations in Engineering Research and Technology, 9(4), 10–18.

[8] Xia, R., Zhou, J., Zhang, H., Liao, L., Zhao, R., & Zhang, Z. (2018). Quantitative Study on Corrosion of Steel Strands Based on Self-Magnetic Flux Leakage. Sensors, 18(5), 1396.

[9] Kim, J-M., Kim, C-M., Choi, S-Y., & Lee, BY. (2017). Enhanced Strain Measurement Range of an FBG Sensor Embedded in Seven-Wire Steel Strands. Sensors, 17(7), 1654.

[10] Farhidzadeh, A., & Salamone, S. (2015). Reference-free corrosion damage diagnosis in steel strands using guided ultrasonic waves. Ultrasonics, 57(2015), 198-208.

[11] Treyssède, F. (2016). Dispersion curve veering of longitudinal guided waves propagating inside prestressed seven-wire strands. Journal of Sound and Vibration, 367(2016), 56-68.

[12] Foti, F., & Martinelli, L. (2019). Modeling the axial-torsional response of metallic strands accounting for the deformability of the internal contact surfaces: Derivation of the symmetric stiffness matrix. International Journal of Solids and Structures, 171(2019), 30-46,

[13] Judge, R., Yang, Z., Jones, S.W., & Beattie, G. (2012). Full 3D finite element modelling of spiral strand cables. Construction and Building Materials, 35(2012), 452-459.

[14] Liu, L., Liu, D., Wu, X., & He, Y. (2021). Optimal structural patterns of multi-strand wire ropes. International Journal of Solids and Structures, 225, 111070.

[15] Wang, H., Nie, X., & Pan, P. (2017). Development of a self-centering buckling restrained brace using cross-anchored pre-stressed steel strands. Journal of Constructional Steel Research,138, 621-632.

Doğaltaş Üretim Tesisleri Atık Granit Tozunun Beton Katkı Maddesi Olarak Kullanılabilirliğinin İncelenmesi

Resul Kazanbaş[1*], Andaç Akdemir[2]

[1*] Samsun Büyükşehir Belediyesi Özel Kalem Müdürlüğü. Samsun, Türkiye , (ORCID: 0000-0002-0223-472X), resulkazanbas@gmail.com

[2] Ondokuz Mayıs Üniversitesi, Mühendislik Fakültesi, Çevre Mühendisliği Bölümü, Samsun, Türkiye, (ORCID: 0000-0002-7592-4449), aakdemir@omu.edu.tr

*: Sorumlu Yazar

Öz

Doğaltaş Elemanları Üretim Tesisine gelen granit bloklarından yapılan elmas soket kesiminde oluşan atık granit tozunun su ile karışımı sonucu ortaya çıkan çamur, atık çamur olarak bertaraf edilmektedir. Çevreye ciddi sorunlar oluşturan atık granit tozunun etkilerini en aza indirmek ve ekonomiye yeniden kazandırılması için beton karışımında kullanılması planlanmıştır. Yapılan çalışmada, atık granit tozu ile üretilen çevre dostu betonların karışım hesabında kullanılan atık granit tozu miktarı, hacimce toplam karışımın, %0, %2, %4'ü şeklinde aynı zamanda iri ve ince agrega yerinde yer değiştirerek kullanılmıştır. Üretilen betonun dayanım ve dayanıklılık özelliklerini, taze ve sertleşmiş beton üzerine olan etkilerini belirlemektir Üretilen betonların çimento oranı iki farklı (350 kg/m3 ve 425 kg/m3) şeklinde ve agrega granülometrisi ise üç farklı (%65 İnce-%35 İri), (%55 İnce-%45 İri), (%45 İnce-%55 İri) şeklinde kullanılmıştır. Atık granit tozunun beton karışımında kullanarak çevre dostu betonun üretilmesinin mümkün olduğunu ve ekonomiye katkıda bulunacağını söylenebilir.

Anahtar Kelimeler: Doğaltaş, Atık, Granit Tozu, Beton, Katkı Maddesi

Investigation of Usability of Natural Stone Production Facilities Waste Granite Powder as Concrete Additive

Abstract

The sludge that comes out as a result of mixing the waste granite dust formed in the diamond socket cut made from granite blocks coming to the Natural Stone Elements Production Facility with water is disposed of as waste sludge. It is planned to be used in the concrete mix in order to minimize the effects of waste granite dust, which creates serious problems for the environment, and to reintroduce it to the economy. In the study, the amount of waste granite dust used in the mixing calculation of environmentally friendly concretes produced with waste granite dust was used as 0%, 2%, 4% of the total mixture by volume, as well as by replacing the coarse and fine aggregates in place. It is to determine the strength and durability properties of the produced concrete and its effects on the fresh and hardened concrete. 55% Thin-45% Coarse), (45% Thin-55% Coarse). It can be said that it is possible to produce environmentally friendly concrete by using waste granite dust in the concrete mixture and it will contribute to the economy.

Keywords: Natural Stone, Waste, Granite Powder, Concrete,Additive Matter

1. Giriş

Granit, sert, kristal yapılı minerallerden meydana gelen tane görünüşlü magmatik bir kayaç türüdür. Bünyesinde fazla oranda kalsiyum karbonat, az oranda ise magnezyum karbonat ve farklı metal oksitler bulunduran magmatik kayaçlardır (1). Taş ocaklarında ve doğaltaşların işlem gördüğü alanlar olan fabrikalarda ebat ve şekil verilmesi için uygulanan kesme, biçme uygulamalarına göre ortalama % 30-60'ı oranında doğaltaş atığı meydana çıkmaktadır. Doğaltaş fabrikalarında oluşan atıklar, doğaltaşın formuna, biçimine, ebatına göre sınıflandırılabilir. Büyük ölçekli, taş ocağındaki uygulama sonrası üretimin yaklaşık %30'unu oluşturur ve boyutları santimetre ile metre arasında değişkenlik gösterebilir. Doğaltaşın işleme tabi tutularak istenilen şeklin verildiği alanlar olan fabrikalarda doğaltaş miktarlarının yaklaşık 1/3'ü toz boyutunda olan toz atıklardır. Bu atıklar su ile birlikte bekleme havuzuna alındıktan sonra kamyon ya da traktör yardımı ile ve bertaraf sahalarına transfer edilmektedir (2, 3, 4, 5).

Blok haline gelen taş fabrika içine alınarak istenilen ürünün elde edilmesi için işleme alınıyor. Doğaltaş kesme işlemlerinde kesici elmas soket ile doğaltaşın teması esnasında fazlasıyla doğaltaş tozu ortaya çıktığı ve bu tozun etrafa uçuşmasını



(a) *(b)*

Şekil 1. Doğaltaş Sulu Kesim İşlemi (a) ve Oluşan Atık Çamur (b)

Atık Doğaltaş atıkları (moloz, toz), asfalt zeminlerde agrega (sürtünme tabakası ile temel ve sathi tabaka arasında bulunan binder tabakalarında), ince malzeme veya bağlayıcı malzeme niyeti ile kullanılabilir. Doğaltaş atıklarının sürtünmeye karşı dayanmalarının tespit edilmesi, asfalt yol kaplamalarında kullanılabilmeleri açısından çok önemli olmaktadır. Olağanüstü sürtünmeyle etkilenen bu alanlarda değerlendirilecek agregaların cilalanma dayanımlarının standardın üstünde olması gerekmektedir (6). Bilindiği üzere, agregaların üzerindeki pürüzlü katmanları kaplama üzerindeki tozlarla da aşındırılabilir. Agreganın yapısındaki minerallerin sertliklerinin yüksek olmaması bu işlemler için uygulama vaktini azaltmaktadır. Bu durumdan başka, agreganın yapısının yumuşak ve sert mineraller tarafından meydana gelmesi de agrega yüzeyinin pürüzlü olması bakımından olumlu sonuç vermektedir. Aşınım esnasında, sert olan mineraller çıkıntı olarak, düşük sertlikteki mineraller ise silinip çukur şeklinde kalmaktadır. Bu şekilde meydana gelen pürüzlülük kayma dayanımının iyileştirilmesine olanak verilmektedir. Uygun bir agreganın yapısında hemen hemen yarı yarıya oranında sert ve düşük sertlik yapısında mineraller olmalıdır. Cilalı yüzey elde edilmesi için dayanım açısından agrega olarak değerleme için ideal olan atık granit, bazalt, diyorit, gibi magmatik ve metamorfik kökeni olan Doğaltaş ocak atıklarıdır (7, 8, 9).

Çevre dostu beton, yukarıda bahsedilen aşamalarda da ifade edildiği gibi doğal kaynaklarımızın ticari ya da mimari estetiğe sahip olan ürünler olarak elde edilmesi için işlenmesi esnasında ortaya çıkan sanayi atıklarının çevremize olan olumsuz etkisini azaltmak için beton karışımında kullanılarak elde edilen beton, çevreci beton

olarak isimlendirilmektedir. Bu tür betonlar yeşil beton olarak da tanımlanmaktadır. Çevre dostu betonun bileşiminde değerlendirilen atıkların sadece çevreye olan etkileri önem arz etmemektedir. Bunun yanında dayanımı, direnci, dayanıklılığı ve ticari olarak da değerli bir ürün elde edilmesi bakımından önem arz etmektedir. Beton karışımı içeriğinde bulunan ana ürünler olan çimento ve agrega ile bu Doğaltaş atıkları belirli oranda yer değiştirilerek değerlendirilmektedir.

2. Materyal ve Metot

2.1. Beton Üretiminde Kullanılan Materyaller

Beton içeriğinde tam olarak agrega, çimento, mineral katkı, kimyasal katkı, hava ve su bulunmaktadır.

Agrega, doğada hâlihazırda bulunan ya da taş ocaklarından farklı geometrik şekillerde elde edilen parçalanmış yapı malzemesidir. Agrega, beton üretiminde en çok kullanılan ve Doğaltaş atıklarına nazaran maliyeti çok daha fazla olan bir malzemedir. Çalışmada, Samsun Canik ilçesi Kaleboğazı mahallesinde bulunan ocaktan elde edilen ve dane çap aralıkları 0-5 mm, 5-15 mm, 15-25 mm olan agregalar kullanılmıştır.

Çimento, doğada doğal olarak bulunan kalker taşları ile kilin karıştırılmasından sonra yüksek sıcaklık ve basınçta ısıtıldıktan sonra öğütülmesi sonucu elde edilen hidrolik bir bağlayıcı olan inorganik bir toz maddedir. çalışmasında da Portland çimentonun CEM I 42.5 R tipi kullanılmıştı. Fabrika tarafından bu çimentonun özellikleri TS EN 197-1 'e göre üretilmiştir.

Kimyasal Katkı, Betonun birtakım özelliklerini değiştirmek için, karma uygulamasından sonra, çimentonun ağırlığı ölçüsünde daha az miktarda ilave edilen malzemelere kimyasal katkı denir. Çalışmasında da TS EN 934-2 'ye göre elde edilen kimyasal katkı maddesi olan CHRYSO® Fluid GT – X su azaltıcı / akışkanlaştırıcı kimyasal katkı maddesi kullanılmıştır.

Mineral Katkılar, Doğal ya da yapay halde bulunan puzolanik maddelerdir. Çimentonun elde edilmesinde kullanılmalarından dolayı doğal olarak betonun üretiminde de kullanılmış olmaktadırlar. Tek başlarına herhangi bir bağlayıcılıkları bulunmamaktadır. Ancak betonun içindeki Kalsiyum Hidroksit Ca(OH)2 ile tepkimeye girerek bağlayıcılık özelliği kazanan puzolanik maddelerdir. Çalışma da mineral katkı olarak Doğaltaş atık tozu kullanılmıştır. Tesis de oluşan toz atık sulu formda olduğu için önce etüvde 110 ºC' de 24 saat kurutulmuş ve sonrasında belirli miktarlarda beton karışımına eklenmiştir.

Karışım Suyu, Bunlar çimento ile agrega arasında birleştirerek işlenebilir akışkan bir forma getirmek ve kimyasal katkı ile birlikte çimento ile tepkimeye girerek plastik haldeki malzemenin sertleşmesini sağlamaktır. Beton karışımında kullanılan suyun özelliği asidik olması gerekmektedir. Bu yüzden pH 7'nin altında olması gerekmektedir. Çalışma da kullanılan su Samsun ilinin şebeke suyudur ve TS EN 1008 standartlarına uygun bir şekilde kullanılmıştır.

Hava, betonun dayanımı ve dayanıklılık özelliğini negatif yönde etkilediği için beton hesabı yapılırken %2 oranında hava varlığı kabul edilerek hesaplama yapılmıştır.

2.2. Beton Reçetesi

Beton reçetesi ya da bir başka deyişle karışım hesabı beton içerisinde çimento, agrega, karışım suyu ve kimyasal madde ilavesinin hangi oranda ne kadar olacağının belirlendiği hesaptır. Hazırlanan numuneler için beton reçetesi özeti Tablo 1' de verilmiştir. Görüldüğü üzere kum, su ve katkı madde miktarı her bir numune için sabit tutulmuştur. Çimento miktarı granit tozuyla ters orantılı olarak değiştirilmiştir.

Tablo 1. Hazırlanan Numuneler İçin Beton Reçete Özeti

Eklenen Madde (kg/m³)	***ÖN-1 Numune Beton***	***ÖN-2 Numune Beton***	***ÖN-3 Numune Beton***	***ÖN-4 Numune Beton***	***ÖN-5 Numune Beton***
0-5 Kum Ağırlık	980	980	980	980	980
5-15 Kum Ağırlık	350	350	350	350	350
15-25 Kum Ağırlık	700	700	700	700	700
Çimento Ağırlık	320	310	300	290	280
Katkı Ağırlık	4	4	4	4	4
Su Ağırlık	175	175	175	175	175
Max Su/Çimento Oranı	0,547	0,564	0,583	0,603	0,625
Atık Granit Tozu Ağırlık	0	10	20	30	40
Toplam Ağırlık	***2529***	***2529***	***2529***	***2529***	***2529***

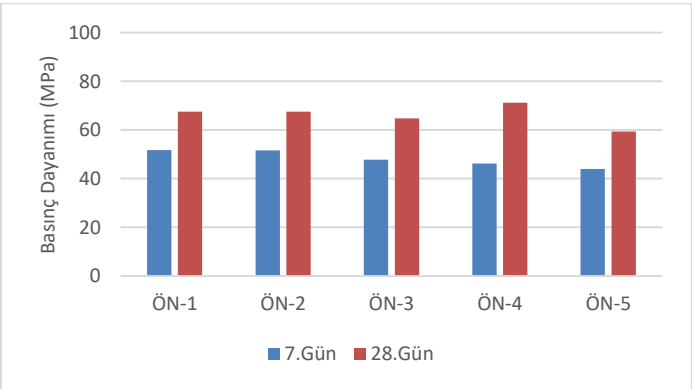
3. Bulgular ve Tartışma

Çalışma sonucunda; 7 ve 28 günlük kürlenme süreleri sonunda Çökme Testi TS EN 206-1' e göre, Kuru ve Yaş Birim Hacim Ağırlık TS EN 206-1' e göre, Kürleme TS EN 12390-2' e göre ve Basınç Dayanım Testi TS EN 12390-2'e göre Belediyenin Türkak tarafından akredite laboratuvarında gerçekleştirilmiştir (10, 11, 12). İlk numune ÖN-1, C30/37 standartına uygun olarak tesiste rutin hazırlanan karışım oranıdır. Diğer Ön-2, ÖN-3, ÖN-4 e ÖN-5 çimento ve atık granit tozu oranları değiştirilen numunelerdir. Beton testlerine ait özet bilgi Tablo-2' de gösterilmiştir.

Tablo 2. Beton Test Sonuçları

Numune	Deney Süresi (gün)	Çökme (Slump) Miktarı (cm)	Kıvam Sınıfları	Yaş Birim Hacim Ağırlık (g/m3)*	Kuru Birim Hacim Ağırlık (g/m3)*	Su İçeriği (%)	Basınç Dayanımı (MPa)*
ÖN-1	7	7	*S2*	8620,33±26,18	8595±34,64	0,29	51,73±0,78
	28			8632,17±36,21	8625±21,79	0,08	67,53±1,14
ÖN-2	7	5	*S2*	8654,5±40,29	8633,33±18,93	0,25	51,6±1,33
	28			8653,17±17,92	8670,33±39,50	-0,20	67,5±0,95
ÖN-3	7	8	*S2*	8587,33±12,55	8563,33±15,27	0,28	47,87±0,83
	28			8625±19,58	8643,33±17,60	-0,21	64,73±0,21
ÖN-4	7	6	*S2*	8593,67±21,73	8570±20,00	0,28	46,17±0,80
	28			8608,33±25,79	8635±26,46	-0,31	61,27±0,72
ÖN-5	7	8	S2	8602±16,80	8561,67±20,21	0,47	44,03±1,17
	28			8601,17±34,71	8615±31,23	-0,16	59,4±0,78

C30 tavsiye edilen köy yollarında slump değerinin 8-11 arasında olması beklenir. Tablo.2' de slump değeri ilave granit tozu artışı ile arttığı ve uygun aralığa geldiği gözlenmektedir. Yaş birim hacim ağırlığı artıkça boşluk oranı az olur ki, bu durum basınç dayanımını arttırır. Bu durumda standart beton numunesine ilave atık granit tozu ilave edildiğinde basınç dayanımları % 30 granit tozu ilavesine kadar düşmekte % 30 dan sonra basınç dayanımları tekrar artmaktadır. Özellikle 28 günlük kürleme neticesinde basınç dayanımları daha fazla artmaktadır. Yani beton yaşı arttıkça basınç dayanımı artmaktadır. Granit tozunun ilavesi durumunda olumsuz bir durum söz konusu değildir. Ancak bu etki miktarının belirlenmesi için daha düşük ağırlık yüzdeleri ile granit tozu ilave edilmeli ve % 40 üzerinde granit ilavesinin de incelenmesi gerekmektedir. Granit tozunun basınç dayanımına pozitif etki gösterdiği özellikle daha uzun beton yaşlarında daha belirgin olduğu ancak granit tozunun doğrusal olarak artışı durumunda dayanımın negatif etki göstermeye başladığı bu nedenle optimum toz ilave miktarının belirlenmesinin oldukça önemli olduğu görülmüştür.



Şekil 2. Farklı Denemeler Neticesindeki Betonun Basınç Dayanım Değerleri

Su çimento oranları artan şekilde en büyük su/çimento oranları Tablo.1' de 0,547 ile 0,625 arasında değişmektedir. TS EN 206 standardının Çizelge F.1'e göre 0,50-0,55 arasında değiştiği için seçilen su/çimento oranları uygundur (10, 11, 12). Aynı standarta göre beton katkısının ağırlık olarak 280 den fazla olması istenmez. Bu nedenle Beton köy yolları için basınç dayanım miktarı C30/37 için 7 gün için 30 MPa ve 28 gün için 37 MPa' ın üstünde olması pratikte uygulanır. Tablo.2' de verildiği gibi gerek standart numunenin (ÖN-1) gerekse granit tozu ilaveli numunelerin basınç dayanım miktarları 7 ve 28 günlük test sonuçlarında istenen kriterlerin arasındadır. Ancak Şekil.2' de görüldüğü gibi ilave granit tozunun orantılı artması durumunda basınç dayanımları önce artış gösterip daha sonra azalma eğilimi göstermektedir.

4. Sonuçlar

Çimentonun yoğunluğu ile Doğaltaş atığının yoğunluğu birbirine yakın olduğu için çimento maliyetini azaltma noktasında atık Doğaltaş tozunu kullanmak uygun olacaktır. Üretilen çevre dostu beton içeriğinde kullanılan atık Doğaltaş tozu çimento yerine değerlendirilmesinde herhangi bir sakınca tespit edilmemiştir. Doğaltaş Elemanları Üretim Fabrikası ve bertaraf edildiği doğa için ciddi sorun olan Doğaltaş atıklarının geri kazanımı noktasında uygun bir çalışma sahası olduğu ortaya çıkmaktadır.

Doğaltaş Elemanları Üretim Tesisinde sulu kesme işleminde kullanılan suyun içeriğinde bulunan kimyasal atık Doğaltaş tozuna karıştığı için bu kimyasalın betona nasıl bir etki edeceği konusu hakkında farklı bir çalışma yapılması gerekmektedir.

Donatısız, kalıp kullanılmadan asfalt ekipmanları ile hazırlanan köy yolları bütçe sıkıntısı çeken yerle yönetimler için özellikle köy yollarında beton yollar önemli bir seçenek olmuştur. Fayda/maliyet analizlerinin detaylı yapılması durumunda granit tozu gibi alternatif atıkların betonda kullanılması döngüsel ekonomi ve atık yönetiminde önemli bir örnek teşkil etmektedir.

5. Teşekkürler

Çalışmaya destek veren Samsun Büyükşehir Belediye Başkanı, Samsun Büyükşehir Belediyesi Doğaltaş Elemanları Üretim Tesisi Şube Müdürü ve teknik personelline teşekkür ederiz. Bu çalışma Ondokuz Mayıs Üniversitesi tarafından PYO.MUH.1904.22.002 proje numaralı Bilimsel Araştırma Projesi ile desteklenmiştir.

Referanslar

[1] Z.A. Kisman, Ö.D. Kan, "Elazığ Mermeri Sektörel Araştırması Raporu" Fırat Kalkınma Ajansı, 2011.

[2] G.Aydın, I.Karakurt, K. Aydıner, "Investigation of the surface roughness of rocks sawn by diamond sawblades" Intenational Journal of Rock Mechanics ad Mining Sciences, vol. 61, pp.171-172, 2013a,

[3] G.Aydın, I.Karakurt, K. Aydıner, "Development of predictive models for specific energy of circular diamond sawblades in sawing of granitic rocks" Rock Mechanics ad Rock Engineering, vol. 46(4), pp.767-783, 2013a, 2013b.

[4] G.Aydın, I.Karakurt, C., Havzaçebi, "Performance prediction of diamond sawblades using artificial neural network and regression analysis" The Arabian Journal for Science Egineering, vol. 40, pp.2003-2012, 2015.

[5] N.Ural, G.Yakşe, "Atık mermer parçalarının yol temel malzemesi olarak değerlendirilmesi " Bilecik Şeyh Edebali Üniversitesi Fen Bilimleri Dergisi, vol. 2(2), pp.53-62, 2015.

[6] H.Akbulut, C.Gürer: "Mermer atıklarının çevresel etkileri ve yol katmanlarında kullanarak faydalanma ve atık azaltma imkanları" Türkiye IV.Mermer Sempozyumu Bildiriler Kitabı, , 18-19 Aralık 2003, pp. 371-378.

[7] H.Akbulut, C.Gürer: "Atık mermerlerin asfalt yol kaplamalarda agrega olarak değerlendirilmesi " İMO Teknik Dergisi, vol. 261, pp.3943-3960, 2006.

[8] A. Karakurt, "Investigating on possible use of Diyarbakır basalt waste in Stone Mastic Asphalt" Construction and Building Materials, vol. 25, pp.3502-3507, 2011.

[9] A.M.M. Soltan, F.A.El-Raoof, B.Abdel-Hanid, "Lightweight aggregates from mixtures of granite wastes wtih clay" *Journal of Cleaner Production*, vol. 117, pp.139-149, 2016.

[10] TS 13515, Complementary Turkish Standard for the implementation of TS-EN-206, Türk Standartları Enstitüsü, 2021

[11] TS-EN-206, Beton Standardı, Türk Standartları Enstitüsü, 2002

[12] TS EN 12390-3, Beton- Sertleşmiş Beton Deneyleri – Bölüm 3 : Deney Numunelerinde Basınç Dayanım Tayini, Türk Standartları Enstitüsü, 2003

==========

Elektrokimyasal Empedans Spektroskopisi Yöntemi ile Çeşitli Malzemelerin Karakterizasyonu

Sedef Arslan[1*], Salim Erol[2]

[1*] Eskişehir Osmangazi Üniversitesi, Mühendislik-Mimarlık Fakültesi, Kimya Mühendisliği Bölümü, Eskişehir, Türkiye, sdf_arsln@hotmail.com

[2] Eskişehir Osmangazi Üniversitesi, Mühendislik-Mimarlık Fakültesi, Kimya Mühendisliği Bölümü, Eskişehir, Türkiye, (ORCID: 0000-0002-07219-6642), esalim@ogu.edu.tr

Öz

Elektrokimyasal empedans spektroskopisi (EIS) korozyon, biyomedikal cihazlar, yarı iletkenler, sensörler, piller, yakıt hücreleri, elektrokimyasal kapasitörler, dielektrik ölçümler, kaplamalar, elektrokromik malzemeler, analitik kimya, elektrokataliz gibi alanlarda kullanılan geniş uygulamaları olan bir analitik tekniktir. Kolay ve hızlı bir teknik olup, ölçüm sisteminde kalıcı kusurlu etkiler bırakmayan güçlü bir yöntemdir. Bu çalışmada, çalışma elektrodu olarak farklı alanlarda kullanılan karbon nanotüp kompozit malzemeler, çelik, titanyum alaşımları, farklı aktif karbon malzemeler kullanarak elektrokimyasal hücreler oluşturulmuş ve EIS ile bu malzemelerin karakterizasyonu yapılmıştır. Platin karşıt elektrot ve Ag/AgCl referans elektrot kullanılan hücrede empedans, 10 mV salınmım potansiyeli ve 100 kHz-10 mHz frekans aralığı kullanılarak ölçülmüştür. Oluşan empedans cevapları eşdeğer elektrik devresi ile modellenmiş ve ohmik direnç, yük aktarım direnci ve kapasitans değerleri regresyon ile elde edilmiştir. EIS, elektrot yüzeylerini de incelemek için güçlü bir elektrokimyasal karakterizasyon tekniğidir. Bu çalışma elektrotlarının EIS sayesinde yüzey pürüzlülüğü ve yüzeyde akım dağılımı hakkında da bilgi elde edilmiştir.

Anahtar Kelimeler: Elektrokimyasal Empedans Spektroskopisi, Elektroaktif Malzemeler, Çalışma Elektrodu, Eşdeğer Elektrik Devresi

Characterization of Various Materials by Electrochemical Impedance Spectroscopy Method

Abstract

Electrochemical impedance spectroscopy (EIS) is an analytical technique with wide applications used in areas such as corrosion, biomedical devices, semiconductors, sensors, batteries, fuel cells, electrochemical capacitors, dielectric measurements, coatings, electrochromic materials, analytical chemistry, electrocatalysis. It is an easy and fast technique, and it is a powerful method that does not leave permanent imperfect effects on the measurement system. In this study, electrochemical cells were created by using carbon nanotube composite materials, steel, titanium alloys, different activated carbon materials used in different fields as working electrodes and the characterization of these materials was made with EIS. In the cell using platinum counter electrode and Ag/AgCl reference electrode, impedance was measured using 10 mV oscillation potential and frequency range of 100 kHz-10 mHz. The resulting impedance responses were modeled with an equivalent electrical circuit and the ohmic resistance, load transfer resistance and capacitance values were obtained by regression. EIS is a powerful electrochemical characterization technique to study electrode surfaces as well. Thanks to the EIS of these working electrodes, information was obtained about the surface roughness and current distribution on the surface.

Keywords: Electrochemical Impedance Spectroscopy, Electroactive Materials, Working Electrode, Equivalent Electric Circuit

1. Giriş

Elektrokimyasal empedans spektroskopisi (EIS), malzeme biliminde analitik bir araçtır ve katılarda kütle taşınımı, kimyasal reaksiyon hızları, korozyon, dielektrik özellikler, kusurlar, mikro yapılar ve iletkenliği incelemek için kullanılabilir. EIS ayrıca elektrokimyasal sensörlerin ve yakıt hücrelerinin performansının değerlendirilmesinde, elektrokimyasal süreçlerin ve canlı hücrelerin zar davranışının incelenmesinde uygulama alanı bulmaktadır [1-3].

Farklı malzemeler üzerinde empedans çalışması yakın zamanda çokça yapılmıştır. Örneğin, potasyum seçici silikon kauçuk membranlar [4], Cr konsantrasyonunun SnO_2 bazlı seramiklerin elektriksel özellikleri üzerindeki etkisi [5], CdS nanoparçacıkları [6], kurşunsuz $(Na_{0.5}Bi_{0.5})TiO_3$ (NBT) ferroelektrik seramikler [7], manganez cıva tiyosiyanat (MMTC) [8], polikristalin $Pr_{0.8}Ca_{0.2}MnO_3$ [9], ZnO tek kristaller [10] ve granüler tip bariyer manyetik tünel bağlantıları $Co/Co_x(Al_2O_3)_{1-x}/Co$ üç katmanlı yapılar [11]. Biyomedikal uygulamalarda, yerleştirilen sinir implantlari [12] doku tepkilerinin izlenmesi ve vücut sıvısı hacim ölçümleri [13] için empedans spektroskopisi kullanılmıştır.

Bu çalışmada aynı akım yoğunluğunda kaplanan iki farklı kaplama korozyon eğilimleri EIS ölçümleri ile incelenmiştir. Bu yöntemle metal uygulanan küçük genlikli alternatif akım yüzey yapısını fazla değiştirmez, bu nedenle metalin direnci ve yüzey yapısı ile ilgili daha doğru sonuçlar elde edilebilir. Sistemde belirlenen direnç polarizasyon direnci olup, ek olarak yüzeydeki kaplama veya film direnci, yük aktararım direnci, ve iyon difüzyonuna karşı gösterilen dirençler ile ilgili bilgiler elde edilebilmektedir. Alternatif akım empedans yöntemi ile Nyquist grafikleri elde edildi.

2. Materyal ve Metod

Deneylerde kadmiyum (Cd) ve titanyum-kadmiyum (Ti-Cd) kaplı paslanmaz çelik (SS) numuneler çalışma elektrotları olarak kullanılmıştır. Cd ve Ti-Cd kaplamalarının 6 M potasyum hidroksit (KOH) çözeltisi içerisinde, farklı frekans değerlerinde empedans cevapları incelenmiştir. Şekil 1'de deney düzeneği verilmiştir.

2.1. Elektrokimyasal empedans spektroskopisi

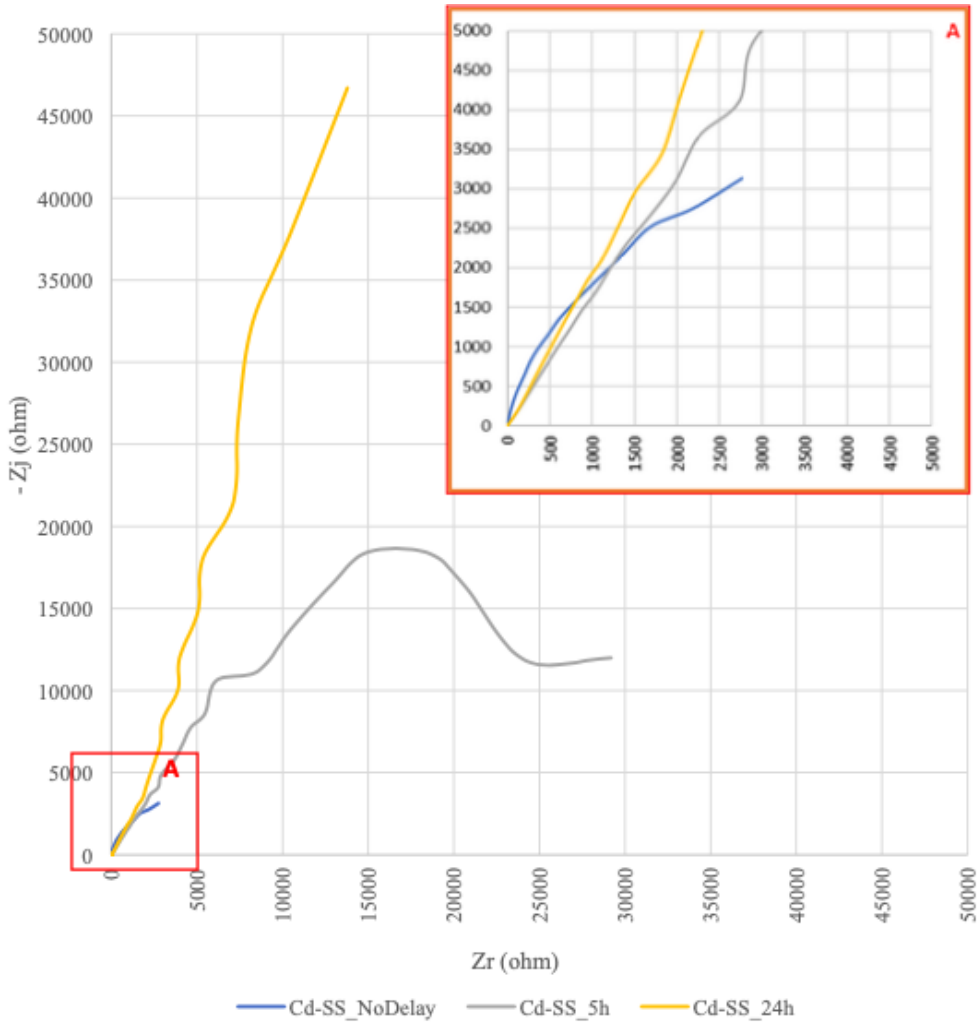
Potensiyostatik EIS tekniği sabit potansiyelde tutulan elektrokimyasal bir arayüzü karakterize etmede kullanılır. Bu teknik özellikle kaplanmış metallerde korozyonun araştırılmasında kullanılan güçlü bir tekniktir. Analiz sonucu elde edilen Bode ve Nyquist grafiklerinden polarizasyon direnci, çift tabaka kapasitansı, solüsyon direnci gibi veriler elde edilebilmektedir. Sistem üzerinde eşdeğer devre similasyon yazılımı yardımıyla elde edilen empedans grafikleri kullanılarak çalışma hücresinin karşılığı oluşturulabilir. Daha sonra eşdeğer elektrik devre ile alınan ölçüm sonuçları çakıştırılarak (fitting) kesin sonuca ulaşılabilir.



Şekil 1. Potansiyostat ve deney düzeneği

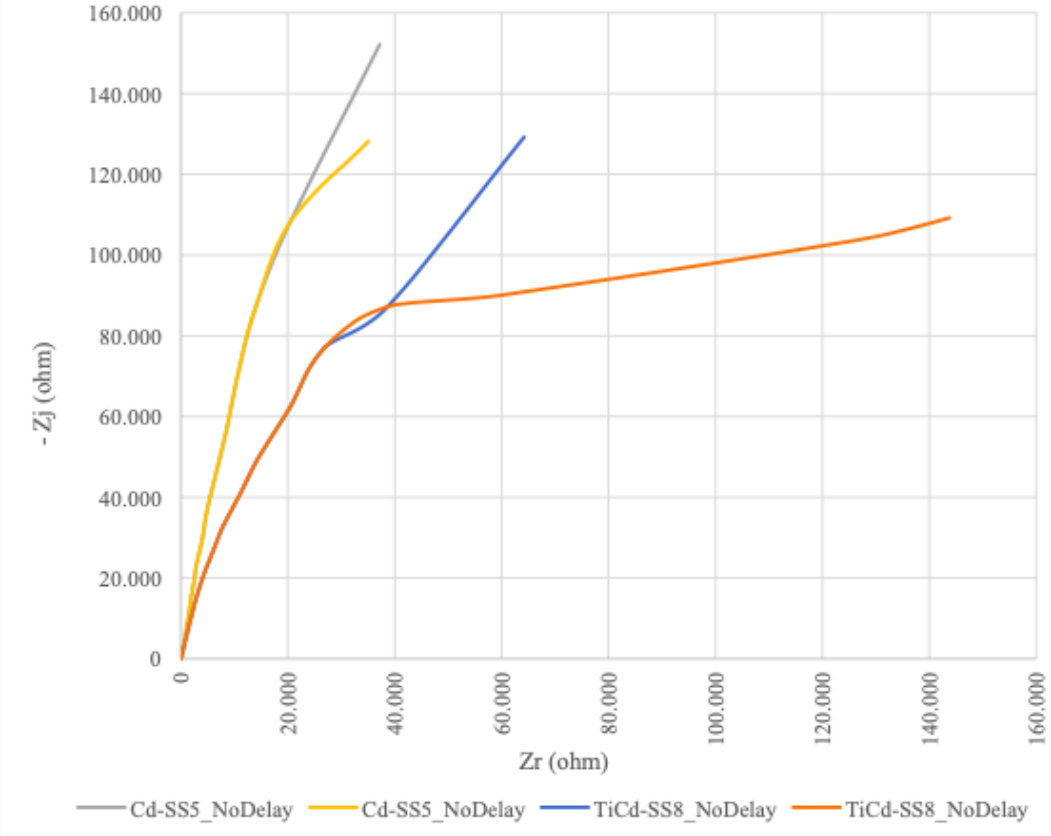
3. Bulgular ve Tartışma

Gecikmesiz (no-delay), çözelti içerisinde 5 saat gecikmeli ve çözelti içinde 24 saat gecikmeli olarak analizleri yapılan Cd kaplı numuneye ait Nyquist formatında empedans cevabı Şekil 2'de verilmiştir. Elde edilen veriler incelendiğinde daldırma süresindeki artışla, muhtemelen yüzeylerde daha fazla korozyon ürününün gelişmesinden dolayı, direnç değerlerinde hafif artışlar olmuştur.



Şekil 2. Cd kaplı SS numuneye ait Nyquist diyagramı

Aynı kaplama kalınlıklarına sahip Cd ve Ti-Cd numuneleri korozyon dayanımları açısından kıyaslanarak eldi edilen empedans değerleri Şekil 3'de verilmiştir. Elde edilen diyagram incelendiğinde kadmiyum kaplı numune için 20.000 ohm, titanyum-kadmiyum kaplı numune için 30.000 ohm değerleri üzerinde farklı bir lup oluştuğu gözlenmiştir. Diyagramda oluşan bu ayrılma yeni bir direnç bölgesi oluştuğunu göstermektedir. Oluşan yeni direnç bölgesinin düşük frekansta uzun süre beklenmesine bağlı olarak yeni bir oksit tabakasının oluşumuna bağlı olduğu düşünülmektedir. Karşılaştırmalı sonuçlar her iki kaplamanın korozyon dayanımının oldukça yüksek olmasına rağmen kapasitansın oksit tabakasıyla ters orantılı olmasına bağlı olarak Cd kaplı numunenin kaplama kalınlığının Ti-Cd kaplı numuneye ait kaplama kalınlığından yüksek olduğunu düşündürmektedir. Bu veriler deney öncesi yapılan kalınlık ölçüm sonuçları ile de uyuşmaktadır. Eşit hücre potansiyellerinde Cd kaplamanın empedansı Ti-Cd kaplamadan daha yüksektir ancak kalınlık farkının yakın olması nedeniyle bu farkın aynı zamanda yüzey pürüzlülüğünden de kaynaklandığı düşünülebilir. Kaplama korozyon direncinin Cd kaplı numune için küçük bir farkla daha yüksek olduğunu görülmektedir. Ti-Cd kaplamanın gözenekli yapısı gevreklik konusunda avantaj sağlarken yüksek konsantrasyonlu elektrolit ortamında korozyon dayanımı açısından olumsuz etkileyebileceği de düşünülmektedir.



Şekil 3. Cd kaplı ve Ti-Cd kaplı SS numunelere ait Nyquist diyagramı

4. Sonuçlar

EIS ölçüm sonuçları her iki kaplamanın da korozyon açsından oldukça dirençli olduğunu ortaya koymuştur. Cd ve Ti-Cd numaralı empedans numuneleri kıyaslandığında kaplama kalınlığı arttıkça korozyon direncin arttığı saptanmış ve ölçüm sonuçları kaplama kalınlığıyla korozyon direnci arasında ters orantılı bir ilişki olduğunu doğrulamıştır.

References

[1] J.R.MacDonald and W.B. Johnson, “Fundamentals of Impedance Spectroscopy”, Impedance Spectroscopy: Theory, Experiment and Applications, 2nd Edn., Eds. E.Barsoukov, Wiley InterScience, 2005.

[2] J.R. Macdonald and W.R. Kenan, “Impedance Spectroscopy: Emphasizing Solid Materials and Systems”, Wiley, 1987.

[3] B. Pejcic and R. de Marco, Impedance Spectroscopy: Over 35 years of Electrochemical Sensor Optimization, Electrochimica acta, 51 (2006) 6217.

[4] P. D. Van der Wal, E. J. R. Sudholter, B. A. Boukamp, H. J. M. Bouwmeester and D. N. Reinhoudt; J. Electroanal. Chem., 317 (1991) 153.

[5] D. R. Leite, W. C. Las, G. Brankovic, M. A. Zaghete, M. Cilense and J. A. Varela; Materials Science Forum, 498-499 (2005) 337.

[6] J. S. Kim, B. C. Choi and J. H. Jeong; J. of Korean Phys. Soc., 55(2) (2009) 879.

[7] R. Tripathi, A. Kumar and T. P. Sinha; Pramana J. Phys., 72(6) (2009) 969.

[8] R. Josephine Usha, J. Arul Martin and V. Joseph; Arch. Appl. Sci. Res., 4(1) (2012) 638.

[9] M. Shah, M. Nadeem and M. Atif; J. Appl. Phys., 112 (2012) 103718 1-8.

[10] M. Younas, L. L. Zou, M. Nadeem, Naeem-ur-Rehman, S. C. Su, Z. L. Wang, W. Anwand, A. Wagner, J. H. Hao, C. W. Leung, R. Lortz , F. C. C. Ling; Phys. Chem. Chem. Phys., 16 (2014) 16030.

[11] A.T. Nguyen, T.A. Nguyen, T.N. Nguyen,A.T. Nguyen,V.C. Giap, J. Electronic. Mater. 45 (2016) 3200.

[12] J.C. Williams, J.A. Hippensteel, J. Dilgen, W. Shain and D.R. Kipke, J. Neural. Eng. 4 (2007) 410.

[13] M.Y. Jaffrin and H. Morel, Med. Eng. Phys. 30 (2008) 1257.

==========

Atık Cam ve Deniz Kabuklarından Cao-Al2o3-Sio2 (Cas) Esaslı Seramiklerin Üretim İmkânlarının Araştırılması Ve Özelliklerinin İncelenmesi

Esra Tavukçuoğlu[1*], Ediz Ercenk[2], Şenol Yılmaz[3]

[1*] Sakarya Üniversitesi, Mühendislik Fakültesi, Metalurji ve Malzeme Mühendisliği Bölümü, Sakarya,Türkiye, (ORCID: 0000-0002-7942-0520), esratavukuoglu@gmail.com

[2] Sakarya Üniversitesi, Mühendislik Fakültesi, Metalurji ve Malzeme Mühendisliği Bölümü, Sakarya,Türkiye, (ORCID: 0000-0002-6792-1248), ercenk@sakarya.edu.tr

[3] Sakarya Üniversitesi, Mühendislik Fakültesi, Metalurji ve Malzeme Mühendisliği Bölümü, Sakarya,Türkiye, (ORCID: 0000-0003-2082-5109), symaz@sakarya.edu.tr

Özet

Bu çalışmada deniz kabuğu ve pencere camlarından $CaO-Al_2O_3-SiO_2$ (CAS) esaslı seramiklerin üretim imkânları araştırılmıştır. Deniz kabuğu ve atık pencere camının yanı sıra Al_2O_3, SiO_2 ve CaF_2'de ilave edilerek hazırlanan 3 farklı bileşimden ergitme yöntemi ile cam fritler elde edilmiştir. Cam fritler bilyeli değirmende öğütülüp elenmiş (<45µm) ve hidrolik pres ile şekillendirilerek silindirik ve dikdörtgen numuneler üretilmiştir. Bu numuneler 850°C, 900°C, 950°C ve 1000°C'de 2 saat sinterlenerek CAS esaslı seramikler elde edilmiştir. Sinterlenen numunelerin X-ışını difraksiyonu (XRD) ile faz analizleri, taramalı elektron mikroskobu (SEM) ile de mikroyapı incelemeleri yapılmıştır. Ayrıca bazı fiziksel ve mekanik testlerle de mekanik ve yapısal özellikleri incelenmiştir. Elde edilen sonuçlar deniz kabuğu ve atık pencere camlarından CAS esaslı seramiklerin üretimlerinin mümkün olduğunu göstermiştir.

Anahtar Kelimeler: Atık malzemeler, cam-seramik, CAS, deniz kabuğu, sinterleme

The Investıgatıon Of Cao-Al2o3-Sio2 (Cas) Based Ceramıcs Productıon Condıtıons And Its Propertıes By Usıng Sea Shell And Waste Glass

Esra Tavukçuoğlu[1*], Ediz Ercenk[2], Şenol Yılmaz[3]

[1*]Sakarya University, Engineering Faculty, Department of Metallurgical and Materials Engineering, Sakarya, Turkey, (ORCID: 0000-0002-7942-0520), esratavukuoglu@gmail.com

[2]Sakarya University, Engineering Faculty, Department of Metallurgical and Materials Engineering, Sakarya, Turkey, (ORCID: 0000-0002-6792-1248), ercenk@sakarya.edu.tr

[3]Sakarya University, Engineering Faculty, Department of Metallurgical and Materials Engineering, Sakarya, Turkey, (ORCID: 0000-0003-2082-5109), symaz@sakarya.edu.tr

Abstract

In this study, the production conditions of $CaO-Al_2O_3-SiO_2$ (CAS) based ceramics by using sea shell and waste glass were investigated. Glass frits were obtained by melting method from 3 different compositions prepared by adding Al_2O_3, SiO_2 and CaF_2 as well as sea shell and waste window glass. Glass frits were ground and sieved (<45µm) in a ball mill and shaped by a hydraulic press to produce cylindrical and rectangular samples. CAS-based ceramics were obtained by sintering these samples for 2 hours at 850°C, 900°C, 950°C and 1000°C. Phase analyzes of the sintered samples by X-ray diffraction (XRD) and microstructure examinations were performed by scanning electron microscope (SEM). In addition, its mechanical and structural properties were examined by some physical and mechanical tests. The results obtained showed that it is possible to produce CAS based ceramics from sea shells and waste window glasses.

Keywords: CAS, glass-ceramic, sea shell, sintering, waste materials

1. Giriş

Cam seramikler, uygun bileşime sahip camın belirli ısıl işlemler ile kontrollü kristalizasyonu (devitrifikasyonu) ile üretilen ince taneli polikristal bir malzemelerdir [1-2]. Cam-seramik malzemeler, çoğu camdan çok daha yüksek mukavemete sahiptir. Yüksek sıcaklık mukavemeti iyidir, düşük genleşme katsayına sahiptir ve termal şoka karşı direnci mükemmeldir [3]. Cam-seramikler, önceden şekillendirilmiş bir camın ısıl işlemiyle veya sinterleme yolu ile de elde edilebilir [4].

Günümüzde araştırmacılar yeni bir ürün üretmek için genellikle ya atıkları kullanarak geri dönüşümünü sağlamakta ya da doğal hammaddeleri kullanmaktadırlar [5]. Cam seramik hazırlamada yumurta kabuğu, uçucu kül, soda kireç silikat camı ve deniz kabuğu gibi atık maddelerin kullanımı araştırmacıların ilgisini çekmektedir [6]. İstiridye kabuğu gibi gıda atığı büyük miktarda $CaCO_3$ içerirken, soda kireç silikat camı cam atığı SiO_2 içerir. Saf CaO ve silikanın, belirli ürünler için gerekli olan miktarları çok olduğu için endüstride kullanımı pahalıdır. Bu nedenle ihtiyaç duyulan saf madde miktarını elde etmek ve üretim maliyetini azaltmak için atık istiridye kabuğu, soda kireç silikat camı gibi atıklar kullanılmaya başlanmıştır [5].

Bu çalışmada deniz kabuğu ve atık camlardan $CaO-Al_2O_3-SiO_2$ (CAS) esaslı cam-seramiklerin üretim imkânları araştırılmıştır.

2. Materyal ve Metod

Çalışmada atık pencere camları ve Sakarya/ Kocaali sahilinden toplanan doğal deniz kabukları ana malzeme olarak kullanmıştır. Ayrıca bileşimlere camlaşma özelliklerini iyileştirmek için CaF_2, Al_2O_3 ve SiO_2'de ilave edilmiştir. İlk aşamada deniz kabukları ve atık pencere camı kabaca kırılmış daha sonra 250 devir/dk. ile dönen alümina bilyeli değirmende 1 saat öğütülerek 125 µm elek altına elenmiştir. Elenen deniz kabukları 3°C/dk. ısıtma hızı ile ısıtılan elektrikli fırında 900°C'de 2 saat bekletilerek kalsine edilmiştir. Bileşimleri ağırlıkça x DK- (69-x) C- 15 CaF_2- 5 Al_2O_3- 5 SiO_2 (x:13,19,25) olacak şekilde üç farklı cam bileşimi hazırlanmıştır (Tablo 1). Deniz kabuğu, atık pencere camı, CaF_2, Al_2O_3 ve SiO_2 içeren cam bileşimleri homojen bir karışım elde etmek için bilyalı değirmende öğütme ve karıştırma işlemine tabi tutulmuştur. Klasik ergitme yöntemi ile alümina pota içerisine konulan cam bileşimleri 7 °C/dk ısıtma hızında ısıtılan elektrikli cam ergitme fırınında 1500°'de 2 saat bekletilerek ergitilmiş ve suya dökülerek cam fritler elde edilmiştir. Üretilen cam firitler tekrar bilyeli değirmende öğütülüp-elenmiş (- 45 µm) daha sonra 198 MPa basınç altında hidrolik pres ile şekillendirerek silindirik ve dikdörtgen cam numuneler elde edilmiştir. Camlar 3°C/dk. ısıtma hızı ile ısıtılan fırında 850°C, 900°C, 950°C ve 1000°C sıcaklıkta 2 saat bekletilerek ısıl ileme tabi tutularak cam-seramik dönüşümü gerçekleştirilmiştir.

Tablo 1. hazırlanan bileşimlerin ağırlıkça yüzdeleri ve numune kodları

Numune Kodu	% Ağırlıkça				
	Deniz Kabuğu	Atık pencere camı	CaF_2	SiO_2	Al_2O_3
CS 1	13	56	19	6	6
CS 2	19	50	19	6	6
CS 3	25	44	19	6	6

Ergitme sonrası cam numunelerde X-Işınları Floresans Analizi (XRF) analizi yapılarak kimyasal bileşimleri belirlenmiştir. Cam numunelerde camsı amorf yapının tespiti, cam-seramiklerde ise kristallenen fazları analiz etmek için tarama açısı (2θ) 0-90° arasında, tarama hızı 2°/dk ve dalga boyu λ=1,54056 nm olan CuK_α ışın demeti kullanarak X-ışınları difraksiyon (XRD-Rigaku D-Max) analizi gerçekleştirilmiştir. Cam-seramik numunelerin kırık yüzeyleri kullanılarak taramalı elektron mikroskobunda (SEM Jeol JSM-5410) mikro yapıları incelenmiştir. Ayrıca yoğunluk, molar hacim, üç nokta eğme ve mikrosertlik analizleri ile mekanik ve yapısal özellikleri incelenmiştir.

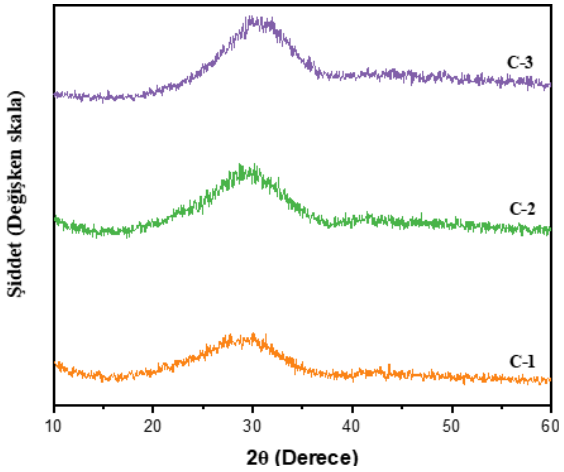
3. Sonuçlar

Üç farklı bileşimde hazırlanarak ergitilen camların XRF analizi sonucunda elde edilen kimyasal analizleri Tablo 2'de verilmiştir. Artan deniz kabuğu ilavesi ile bileşimlerdeki CaO miktarı da artış göstermektedir.

Tablo 2. Ergitilen camların XRF ile yapılan kimyasal analizi (% ağ.)

Bileşenler	SiO_2	CaO	Al_2O_3	Na_2O	F	MgO	K_2O	TiO_2	Fe_2O_3
CS 1	44,34	22,91	17,15	7,010	6,04	2,175	0,179	0,110	0,086
CS 2	42,15	26,23	17,98	6,469	4,39	2,402	0,174	0,103	0,102
CS 3	39,28	31,07	18,97	5,264	2,76	2,232	0,194	0,111	0,130

Üç camın da XRD sonuçlarından amorf yapıda oldukları tespit edilmiştir (Şekil 1). Farklı sıcaklıklarda ısıl işleme tabi tutulan tüm numunelerin XRD analizleri incelendiğinde hepsinde kristallenmenin gerçekleştiği gözlenmiştir (Şekil 2)

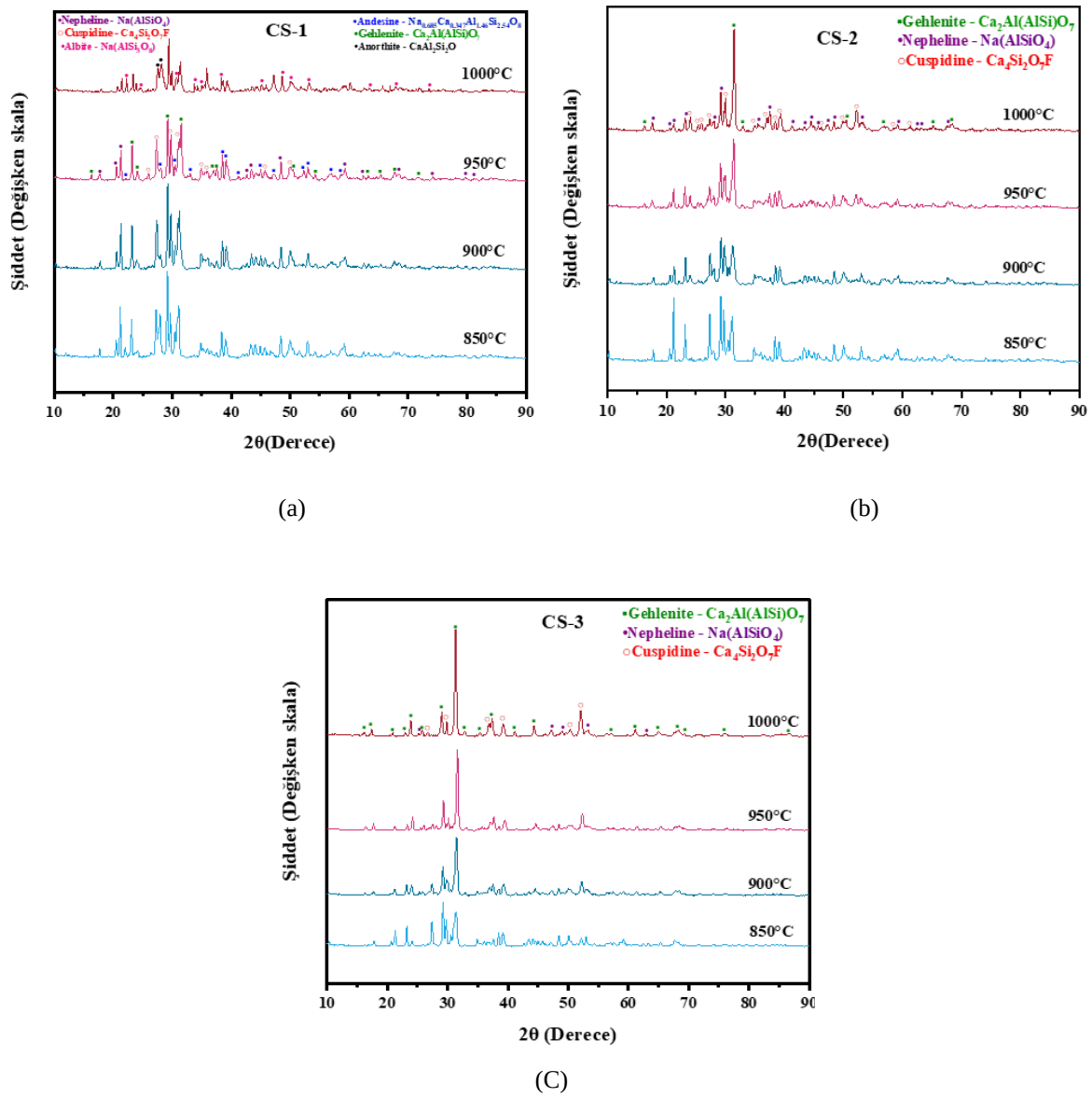


Şekil 1. Camların XRD analizi

CS-1 bileşiminde 850°C ve 900°C'lerde ısıl işlem görenlerde Nephelin, Cuspidin ve Andesin fazları mevcuttur, bu fazlarda iki sıcaklık içinde aynı 2Θ açılarında gözlenmiştir. 950°C'de ise Nephelin, Cuspidin, Andesin fazları ile birlikte Gehlenit fazı da görülmektedir. 1000°C'de Nephelin, Cuspidin, Gehlenit, Albit ve Anortit fazları oluşmuştur ve diğer sıcaklıklarda oluşan Andesin fazı oluşmamıştır. Sıcaklık artıkça Cuspidin ve Andesin fazlarının pik şiddetinde düşüş gözlemlenirken Nephelin fazının pik şiddetinde artış görülmektir. 1000°C'de Anortit fazına 2Θ= 27,54°, 28,16° açılarında rastlanmıştır.

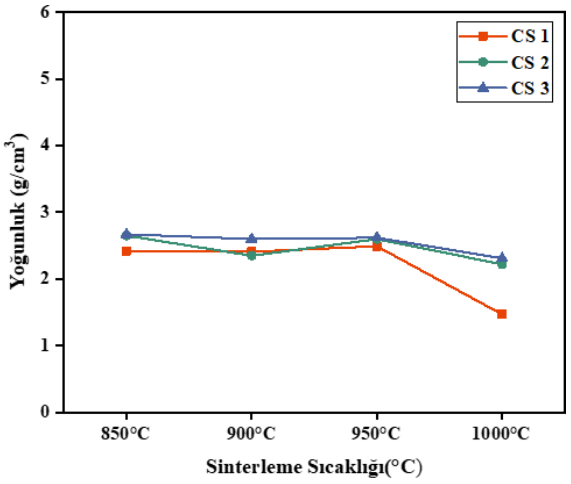
CS-2 cam-seramik malzemede 850°C'de sadece Nephelin, Cuspidin fazları oluşmuştur. 900°C, 950°C ve 1000°C sıcaklıklarda yapılan ısıl işlemlerde ise aynı Nephelin, Cuspidin fazlarının yanı sıra Gehlenit fazının da oluştuğu tespit edilmiştir. Bu bileşimde ısıl işlem sıcaklıklarına göre fazların pik şiddetleri incelendiğinde Gehlenit fazının pik şiddetinin arttığı görülmektedir.

CS-3 cam seramiklerin XRD faz analizlerinde Nephelin, Gehlenit ve Cuspidin fazları belirlenmiştir. Bu fazların pik şiddetleri incelendiğinde Nephelin ve Cuspidin fazlarının pik şiddetlerinin artan ısıl işlem sıcaklığı ile azaldığı bununla birlikte Gehlenit fazının pik şiddetinin ise önemli ölçüde arttığı gözlenmiştir.



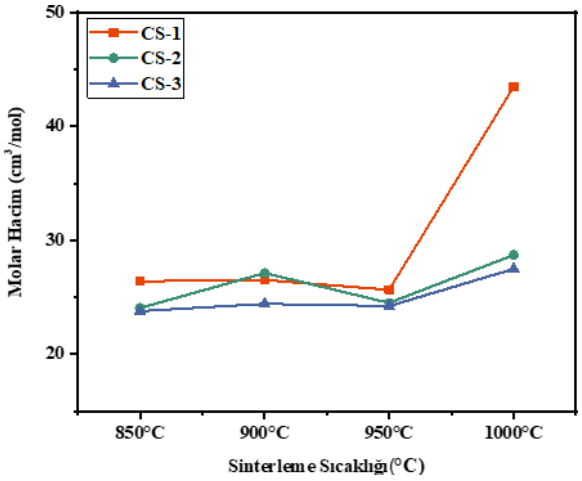
Şekil 2. Cam-seramik malzemelerin XRD analizi. a) CS-1, b) CS-2, c) CS-3.

Cam-seramiklerin yoğunlukları Arşimet yöntemi ile hesaplanmıştır (Şekil 3). CS-1 cam-seramik için en yüksek yoğunluk değeri 950°C'de ısıl işlem sonrasında 2,49 g/cm^3 olarak ölçülmüştür. CS-2 de ve CS-3 de en yüksek yoğunluk değerleri 850°C 'de ısıl işlem sonrasında sırasıyla 2,65 g/cm^3 ve 2,67 g/cm^3' olarak tespit edilmiştir. Deniz kabuğu miktarının artmasıyla yoğunluk değerlerinin artığı görülmektedir. Isıl işlem sıcaklığı 1000°C'ye ulaştığında yoğunluk azalmıştır. Bu durum daha önce kalsine edilmesine rağmen deniz kabuğundaki kalsine olmamış CaCO3 'ün parçalanması sonucunda oluşan kapalı gözeneklerden kaynaklanabilir [5]. Aynı zamanda ısıl işlem sıcaklığı artıkça yüzey çatlakları ve porozite artar, bu da yoğunluğun azalmasına sebep olabilir [7]. SEM mikroyapı incelemeleri de bu durumu desteklemektedir.



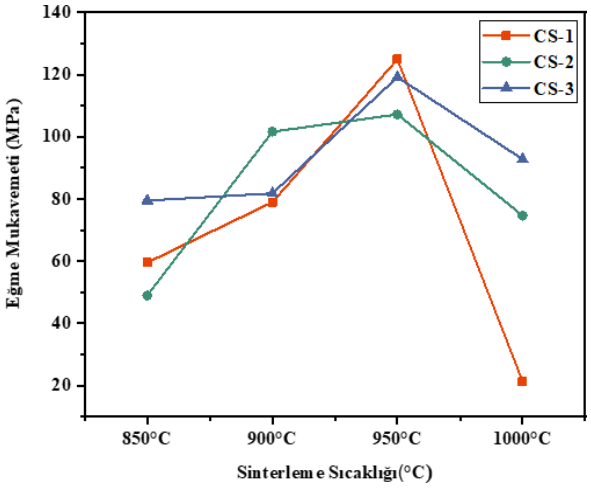
Şekil 3. Cam-seramik malzemelerin ısıl işlem sıcaklığına göre yoğunlukları

Molar hacim, yoğunluk ile ters orantılıdır. Yoğunluk artıkça molar hacim azalır [6]. Molar hacim değerleri incelendiğinde (Şekil 4) en yüksek molar hacim ve en düşük yoğunluk 1000°C'de kristallendirilen CS-1 cam-seramikte gözlenmiştir. Molar hacim değerleri incelendiğinde yoğunluk artıkça molar hacim değerinin düştüğü görülmektedir.



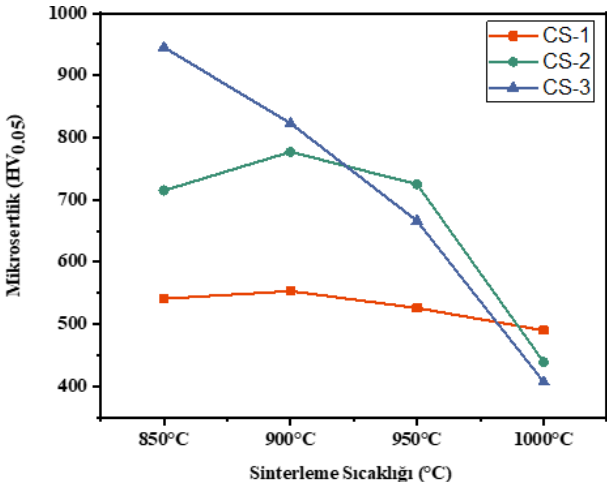
Şekil 4. *Cam-seramik malzemelerin ısıl işlem sıcaklığına göre molar hacim değerleri*

Cam-seramiklerin ısıl işlem sıcaklığına bağlı olarak üç nokta eğme mukavemeti incelendiğinde (Şekil 5) artan deniz kabuğu miktarı ve ısıl işlem sıcaklığına göre artış gösterdiği görülmektedir. 1000 °C'de ise yoğunluk düşüşüne bağlı olarak azalma meydana gelmektedir.



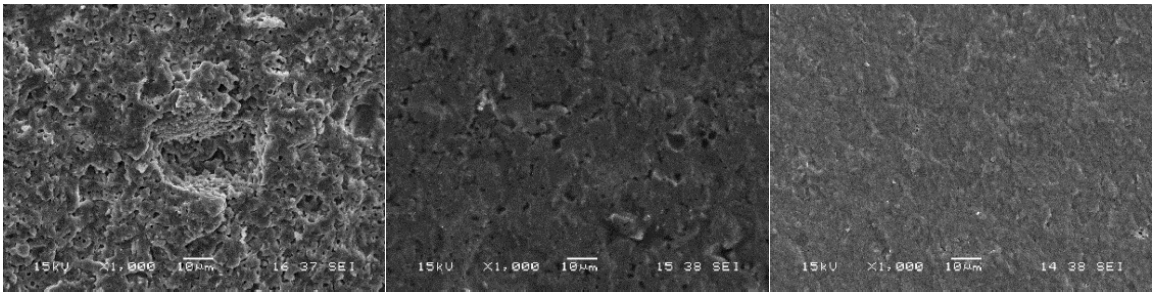
Şekil 5. Cam-seramik malzemelerin ısıl işlem sıcaklığına göre 3 nokta eğme mukavemetleri

Cam-seramik malzemelerin mikrosertlik sonuçları incelendiğinde verilerini incelendiğinde (Şekil 6) deniz kabuğu miktarının atmasıyla mikrosertlik değerlerinin arttığı, 1000 °C de ısıl işlem sonrasında ise üç bileşim içinde de düşüş eğiliminde olduğu görülmektedir. Cheng ve ark. CAS cam-seramikleri ile ilgili yaptıkları çalışmada kristalizasyon işlemi ile gerçekleşen kristal büyümenin sonucu olarak malzemenin fiziksel ve mekanik özelliklerinin düştüğünü rapor etmişlerdir [7].



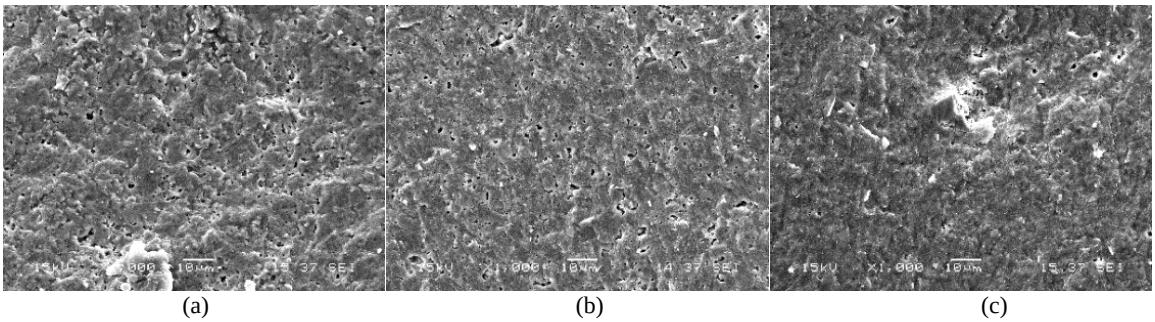
Şekil 6. Cam-seramik malzemelerin ısıl işlem sıcaklığına göre mikrosertlik değerleri

Cam-seramik malzemelerin üç nokta eğme testinde kırılan kırık yüzeylerinde ısıl işlem sıcaklığına göre SEM mikroyapı incelemesi yapılmıştır (Şekil 7-10). Numunelerde gözenekler ve kristal oluşumlar göze çarpmaktadır. Yoğunluk artışıyla daha yoğun yapılar gözlenirken yoğunluk düşüşüyle artan gözenekli mikro yapılar görülmektedir.



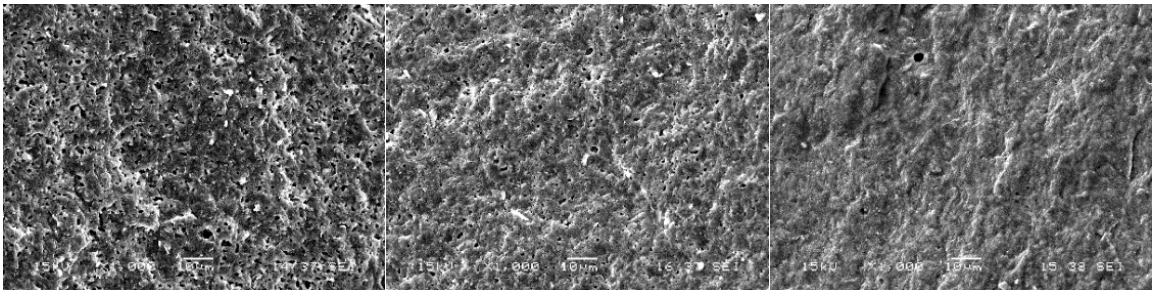
(a) (b) (c)

Şekil 7. 850 °C de ısıl işlem yapılan (a) CS-1, (b) CS-2 ve (c) CS-3 cam-seramiklerin SEM mikroyapıları



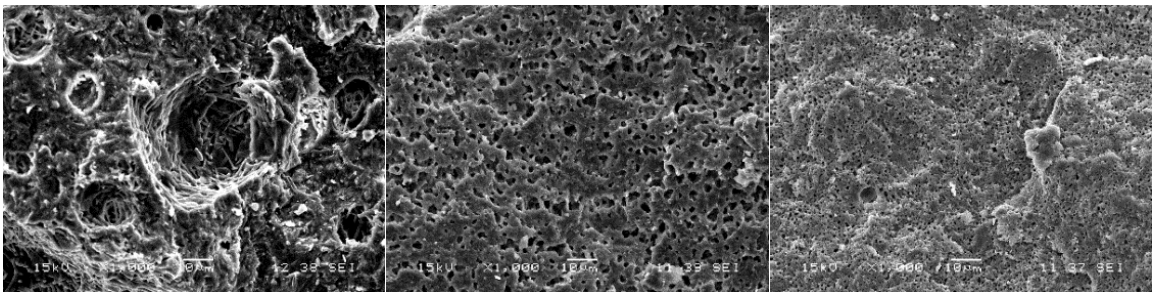
(a) (b) (c)

Şekil 8. *900 °C de ısıl işlem yapılan (a) CS-1, (b) CS-2 ve (c) CS-3 cam-seramiklerin SEM mikroyapıları*



(a) (b) (c)

Şekil 9. 950 °C de ısıl işlem yapılan (a) CS-1, (b) CS-2 ve (c) CS-3 cam-seramiklerin SEM mikroyapıları



(a) (b) (c)

Şekil 10. 1000 °C de ısıl işlem yapılan (a) CS-1, (b) CS-2 ve (c) CS-3 cam-seramiklerin SEM mikroyapıları

4. Genel Sonuçlar

Bu çalışmanın amacı, deniz kabuğu ve atık camlardan $CaO-Al_2O_3-SiO_2$ (CAS) esaslı seramiklerin üretim imkânları araştırılmasıdır ve elde edilen sonuçlar deniz kabuğu ve atık pencere camlarından CAS esaslı seramiklerin üretimlerinin mümkün olduğu görülmüştür. Elde edilen sonuçlar aşapıda özetlenmiştir.

a) Deniz kabuğu içeriğine göre üç farklı bileşimde hazırlanan ve 1500°C'de ergitilerek dökülen cam numunelerin amorf yapıya sahip oldukları tespit edilmiştir.

b) Isıl işlem ile yapılan kristalizasyon sonrasında CAS cam-seramiklerde ana faz olarak Cuspidin, Gehlenit ve Nephelin fazları tespit edilmiştir. Ayrıca CS-1 cam-seramiğinde 900°C ve 950°C'de Andesin fazına rastlanırken 1000°C'de üç ana faz ile Anortit ve Albit fazları da tespit edilmiştir. Fazların pik şiddetleri incelendiğinde Nephelin ve Cuspidin fazlarının pik şiddetlerinin azaldığı bununla birlikte Gehlenit fazının pik şiddetinin ise önemli ölçüde arttığı gözlemlenmiştir.

c) Deniz kabuğu miktarı artıkça mikrosertlik değerleri de artmıştır.

d) Cam-seramik mikroyapılarında gözenekler ve kristal oluşumlar görülmüştür.

Kaynaklar

[1] Mukherjee, D. P., Datta, T., Das, S. K., "Effects of CaF_2 vis-a-vis TiO_2 as nucleating agent in SiO_2–Al_2O_3–CaO glass-ceramics", American Institute of Physics, In AIP Conference Proceedings, Vol. 1536, No. 1,625-626, 2013.

[2] Rawlings, R. D., Wu, J. P., Boccaccini, A. R., "Glass-ceramics: their production from wastes—a review", Journal of materials science, 41(3), 733-761, 2006.

[3] Higgins, R. A., "Materials for engineers and technicians", Fourth Edition, Routledge, Elsevier, 306-312, 2006.

[4] Banijamali, S., Yekta, B. E., Rezaie, H. R., Marghussian, V. K., "Crystallization and sintering characteristics of CaO–Al_2O_3–SiO_2 glasses in the presence of TiO_2, CaF_2 and ZrO_2", Thermochimica Acta, 488(1-2), 60-65, 2009.

[5] Rahman, N. A. A., Matori, K. A., Zaid, M. H. M., Zainuddin, N.,Aziz, S. A., Khiri, M. Z. A., Jalil, R. A., Jusoh, W. N.W., "Fabrication of Alumino-Silicate-Fluoride based bioglass derived from waste clam shell and soda lime silica glasses", Results in Physics, 12, 743–747,2019.

[6] Jusoh, W. N. W., Matori, K. A., Zaid, M. H. M., Zainuddin, N., Khiri, M. Z. A., Rahman, N. A. A., Khiri, M. Z. A., Kul, E.,"Effect of sintering temperature on physical and structural properties of Alumino-Silicate-Fluoride glass ceramics fabricated from clam shell and soda lime silicate glass", Results in Physics, 12, 1909-1914,2019.

[7] Merkit, Z.Y., "Doğal Hammaddelerden ve Atıklardan Korozyona Dayanıklı $CaO-Al_2O_3-SiO_2$ (CAS) Cam Seramiklerin Üretimi", Sakarya Üniversitesi, Fen Bilimleri Enstitüsü, Metalurji ve Malzeme Mühendisliği Anabilim Dalı, Yüksek Lisans Tezi, 2016.

Viskoelastik Polimerik Köpük (Rtv-2) Çekirdekli Alüminyum Sandviç Panellerin Basma Davranışlarının İncelenmesi

[1]Muhammed İhsan Özgün, [2]Hakan Burak Karadağ, [3]Yasin Ramazan Eker

[1] Necmettin Erbakan University, Department of Metallurgy and Material Engineering, Konya, Türkiye, (ORCID: 0000-0003-0048-3439), miozgun@erbakan.edu.tr

[2] Necmettin Erbakan University, Department of Metallurgy and Material Engineering, Konya, Türkiye, (ORCID: 0000-0003-1045-7277), hbkaradag@erbakan.edu.tr

[3] Necmettin Erbakan University Department of Metallurgy and Material Engineering, Konya, Türkiye, (ORCID: 0000-0001-7395-4364), yeker@erbakan.edu.tr [1*]

Öz

Polimer köpük dolgulu sandviç panel yapısı, hafif taşıma sistemlerinin tasarımı ve yapımı için yüksek mukavemet/ağırlık oranı ile yapısal açıdan verimlilik sağlar. Bu sistemlerin panel bileşenleri, yarı statik koşullar altında sıkıştırma kuvvetlerine maruz kalmaktadır. Viskoelastik malzemenin deformasyon hızına göre daha yüksek rijitliği sayesinde, polimer köpük çekirdekli sandviç panel kompozit yapı, statik yükleme koşullarından gelen enerjiyi yüksek oranda absorbe etmektedir. Bu çalışmada, poli dimetil siloksan bazlı RTV polimer köpük, ara dolgu olarak iki alüminyum panel arasına sıkıştırılmıştır. Farklı kalınlıklarda imal edilen bu sandviç panellerin farklı deformasyon oranlarındaki sıkıştırma kuvveti altındaki davranışları incelenmiştir. Sıkıştırma testleri, köpük dolgulu sandviç panel numunelerin deformasyon direncinin, deformasyon hızındaki ve polimer çekirdek kalınlığındaki artışla önemli ölçüde arttığını göstermiştir. Bu çalışmada elde edilen sandviç panel, yarı statik koşullarda çalışan yapı elemanlarında yüksek deformasyon hızına neden olacak yüklerin enerjisini absorbe edebilecektir.

Anahtar Kelimeler: Alüminyum Sandviç Panel, Polimer Köpük, Statik Basma Testi, Viskoelastisite

Investigation of the Compression Behavior of Aluminum Sandwich Panels with Viscoelastic Polymeric Foam (Rtv-2) Core

Abstract

Polymeric foam cored sandwich panel structure provides excellent structural efficiency with a high ratio of strength to weight for the design and the construction of lightweight transportation systems. The panel components of these systems are exposed to compression forces under quasi-static conditions. Due to the higher stiffness relative to the deformation rate of viscoelastic material, the polymeric foam cored sandwich panel composite structure highly absorbs the energy from the static loading conditions. In this study, poly dimethyl siloxane-based polymeric RTV foam core was sandwiched between two aluminum panels. The behavior of these sandwich panels produced in different thicknesses under compression force at different deformation rates was investigated. Compression tests showed that the deformation resistance of the foam-filled sandwich panel specimens increased significantly with the increase in deformation rate and polymer core thickness. The sandwich panel obtained in this study will be able to absorb the energy of loads that will cause a high deformation rate in structural elements operating in quasi-static and quasi-dynamic conditions.

Keywords: Aluminum Sandwich Panel, Compression Test, Polymeric Foam, Viscoelasticity.

1. Introduction

Polymeric foams are preferred in energy absorption applications with compression and high strain rates [1]. Foam material made of Silicone rubber (SR), one of the elastomers, is preferred in vehicles and equipment for aviation, light transport, and military use due to its high-excellent flexibility, low compression ratio, high thermal

insulation, and increased shock absorption [2]. As shown Figure 1 strong chain bonds, a flexible backbone, ease of side group rotation, and low intermolecular and intermolecular forces are provided by alternating silicon and oxygen atoms in the main chain of the inorganic compound, as well as two pendant organic groups, typically

methyl. [3]. Since the Si-O bond energy is higher than the C-C bond energy, the Si-O bond in the main chain structure of the molecule makes the network a molecule with a more flexible and robust bond structure [4]. As a result, compounds in the C-C chain structure are lighter than those in the Si-O chain structure. However, foaming the silicon polymer can compensate for the weight problem in the Si-O chain structure.

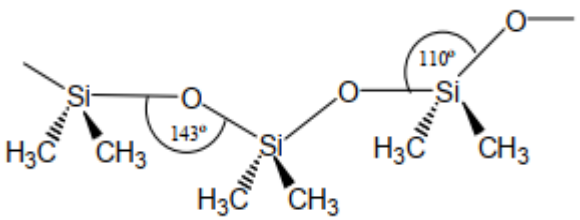


Figure 1. Poly di methyl siloxane (PDMS) chains showing bond angles in the siloxane skeleton [5]

Typically polymeric foams display high strain rate sensitivity, as seen by the higher elastic modulus, elevated plateau stress, and reduced densification strain (Figure 2) [1]. Increasing strain rate causes the material to behave more rigidly until failure occurs. In the linear elastic region, elastic materials have the same elastic modulus, while in the linear elastic area, the elastic modulus increases further, as seen in Figure 2.

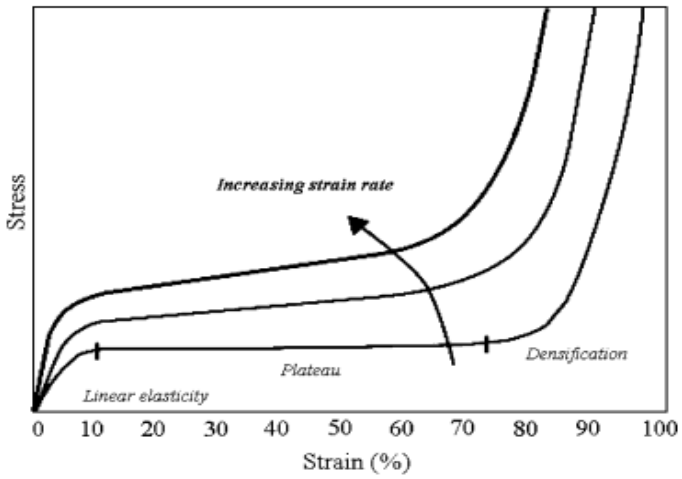


Figure 2. General compressive stress–strain behavior for polymeric foam [1]

Sandwich panels are designs with a high specific strength. Sandwich panel structures consist of low-density core material between two high-strength plates [6]. The low-density material is the polymer foam material in this study. Silicone foams can be used as structural material by confining it between the aluminum panels. The mechanical properties of panel structures are related to the amount of energy absorption for polymeric foam-cored sandwich panels [7]. Three main features that determine the mechanical properties of sandwich panels with foam core structure can be mentioned: foam structure, polymer material, and strain loading conditions [8]. Increasing the compression speed, scanning the strain rate from semi-static to semi-dynamic conditions, and evaluating energy absorption performance. The scale of increasing strain ratio evolves from quasi-static to quasi-dynamic conditions.

In this study, sandwich panel structures made of poly dimethyl siloxane-based Room temperature Vulcanization (RTV) polymer foam material with different heights produced in the same process parameters were subjected to compression tests at different speeds. As a result of the compression tests, the amount of material and the amount of energy absorption were evaluated. In addition, its physical properties were correlated with the results obtained from this study.

2. Materials and Methods

Sandwich panel samples were prepared with PDMS-based RTV polymer (Aydın Kompozit, Turkey) and 1002 series, 0.5 mm thick aluminum sheets. The polymeric material monomer solution is provided with 2% by a mass activator supplied by the company. Pore formation during polymerization is done by adding 0.03% by mass with the Azodicarbonamide chemical. Since the completion time of the polymerization reaction takes 24 hours at room temperature, homogenization of the mixture at 100 rpm for 3 minutes is possible. The mixture was poured into a steel profile mold (91 x 90 mm) with a wall thickness of 4 mm, between the upper and lower aluminum panels, was ensured. The curing process at atmospheric condition, was carried out in an oven preheated to 175 °C for 2 hours. The core material thickness specified for the sandwich panel was adjusted by calculating the amount of mixture poured into the mold and the amount of swelling (Table 1). No external adhesive was used, which directly adhered to the aluminum panels during the firing of the core material. An example of an aluminum sandwich panel produced is shown in Figure 3.

Table 1. Amount of core material for related thickness

Core Thickness (millimeter)	Weight (gram)
4±0.5	*22*
8±0.5	*47*
12±0.5	*75*

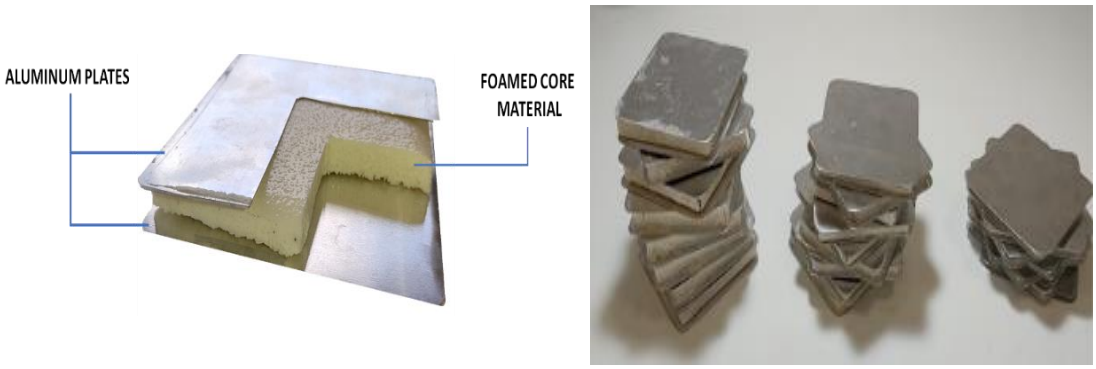


Figure 3. RTV polymeric foam cored aluminum sandwich panels

PDMS-based polymeric foam materials were characterized with Shore F (Loyka, Turkey) for the hardness, with helium pycnometer (Micromeritics, USA) for the density and dynamic-mechanical analyzes (DMA) in compression mode (PerkinElmer, USA) for defined elastic modulus. The pore distributions and morphology of the samples was determined by using pictures of the samples cross-section and image processed software (KameramGEN, Turkey).

The DMA method, allow to determine the materials' storage elastic modulus and loss elastic modulus under stress or strain according to a fixed frequency value. Prismatic samples (2 x 3.5 x 5 mm) were used for each foam core. The mechanical properties were observed for the perpendicular and parallel directions described according

to the polymer foaming (Figure 5). The measurement was made at a frequency of 1Hz and an amplitude of 0.05 mm.

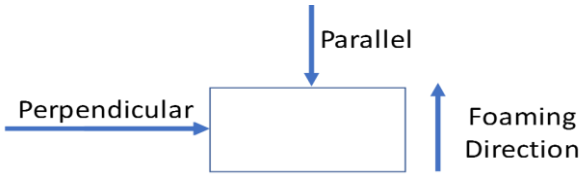


Figure 5. Sample cutting direction for preparing to DMA Analysis

The highest energy absorption degree of the compressed polymeric materials can be determined via the *tan δ* value which can be defined as the ratio of the loss modulus (E″) and the storage modulus (E′) given by the instrument (Eq. 1). Furthermore, the *tan δ* value can also be used for determining the glass transition of the polymer.

$$tan\ \delta = \mathrm{E''/E'} \qquad \text{(Eq. 1)}$$

The compression test performance of the sandwich panel groups was carried out on a Shimadzu AG-X model Universal test instrument. In order to investigate the viscoelastic behavior of the foam structure, the characterization was done in quasi-static and quasi-dynamic conditions. Therefore, the strain rates parameter were 1 mm/min, 10 mm/min, and 50 mm/min. For each measurement, freshly prepared sample were used to avoid any effect of previous analysis.

3. Results

3.1. Polymer Foam Characterization

The polymer hardness was measured with Shore F method specified for foam materials via 25.30 mm diameter cylindrical penetrating tip. Figure 6 shows Shore F results from measuring 4, 8, and 12 mm thick polymer foams five times from different points. These measurements were compared with the poured non-foam bulk material as a reference. The stiffness of the foam material is lower than that of the bulk material. Furthermore, it was observed that as the thickness of the foam materials produced under the same recipe and process conditions increased, the hardness values decreased.

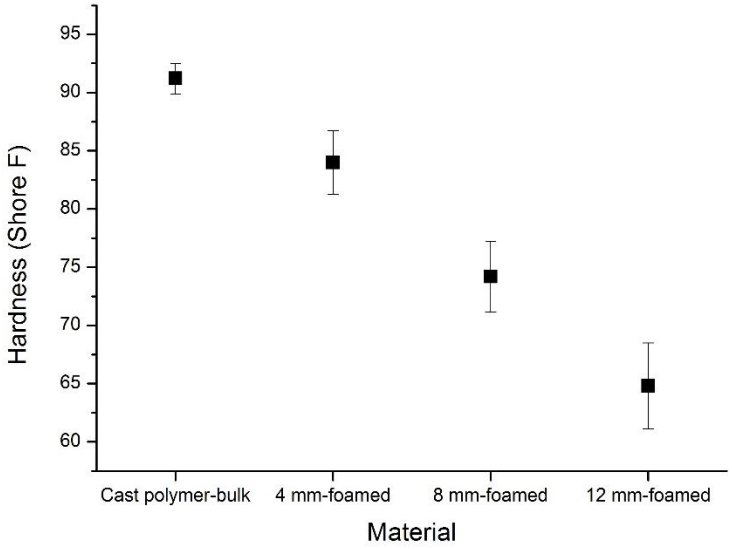


Figure 6. Aluminum sandwich panel core Thicknesses and Shore F Foam hardness

The density measurement of foam materials was made according to ASTM 3575 standard. The measurements were repeated five times for each sample. Compared to bulk material, the densities of polymer foams are lower than expected. However, while the densities of the 4 and 8 mm thickness foams are close to each other, the density of the foam with 12 mm thickness is lower (Figure 7). This is because the curing of the polymer over 8 mm thick is delayed, and the pore development continues for a longer time.

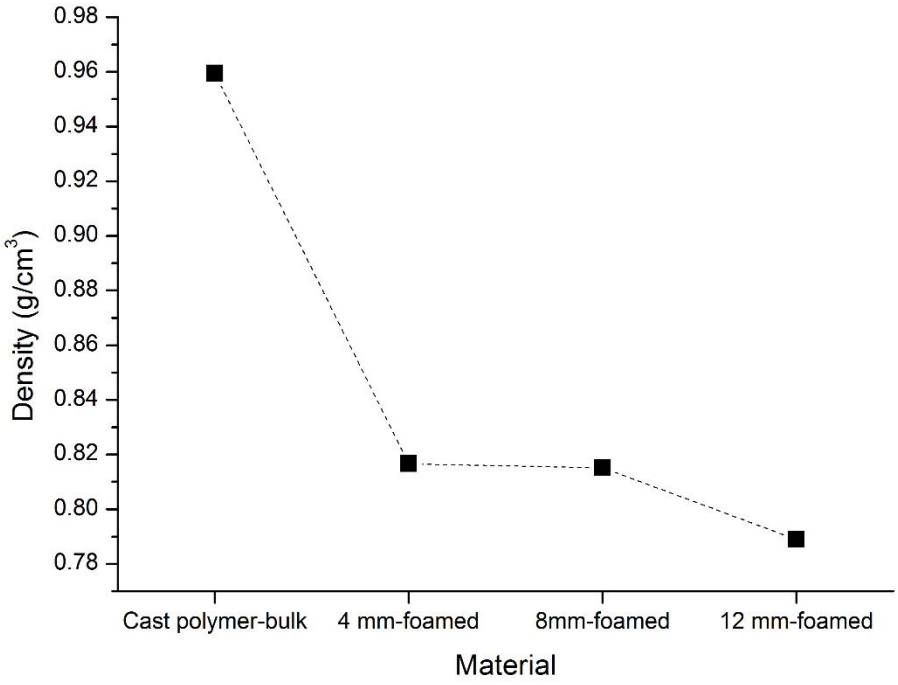


Figure 7. Aluminum sandwich panel core thicknesses and Shore F foam hardness

Prismatic samples were cut for using DMA analysis from RTV polymer foam materials of 4, 8, and 12 mm thickness to perpendicular (v) and parallel (h) to the foaming direction. The storage and loss modules corresponding to the samples defined based on thickness and direction are given in Figure 8, and *tan δ values* are shown in Figure 9. When the DMA analysis results are examined, the polymer samples cut in the direction parallel to the foaming direction taken from the 8 mm thick core stand out as the sample that absorbs the most energy. In

the samples with 4 and 12-mm thickness, parallel or perpendicular to the foaming direction did not make a practical difference. However, the polymer samples produced as 8mm showed a more effective energy absorption performance.

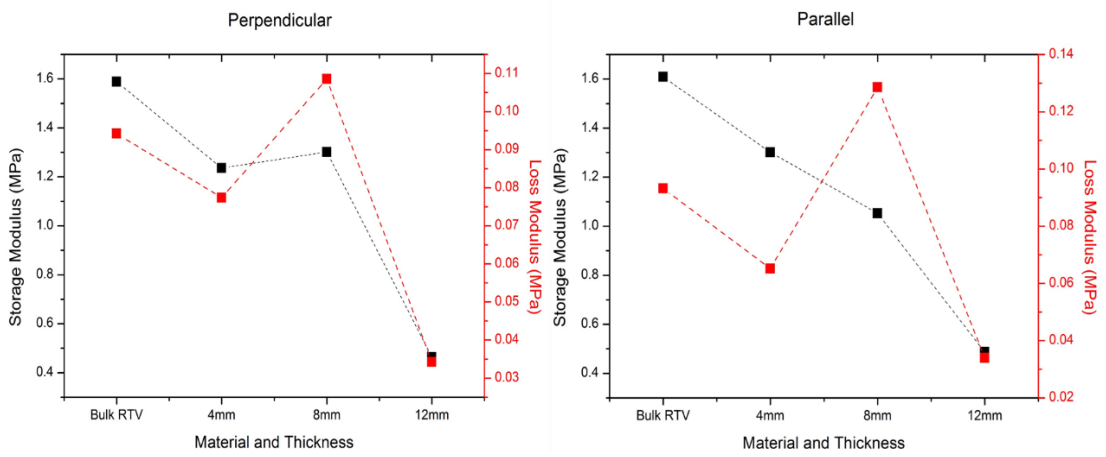


Figure 8. Storage modulus (E') and loss modulus (E") of the samples defined based on thickness and direction

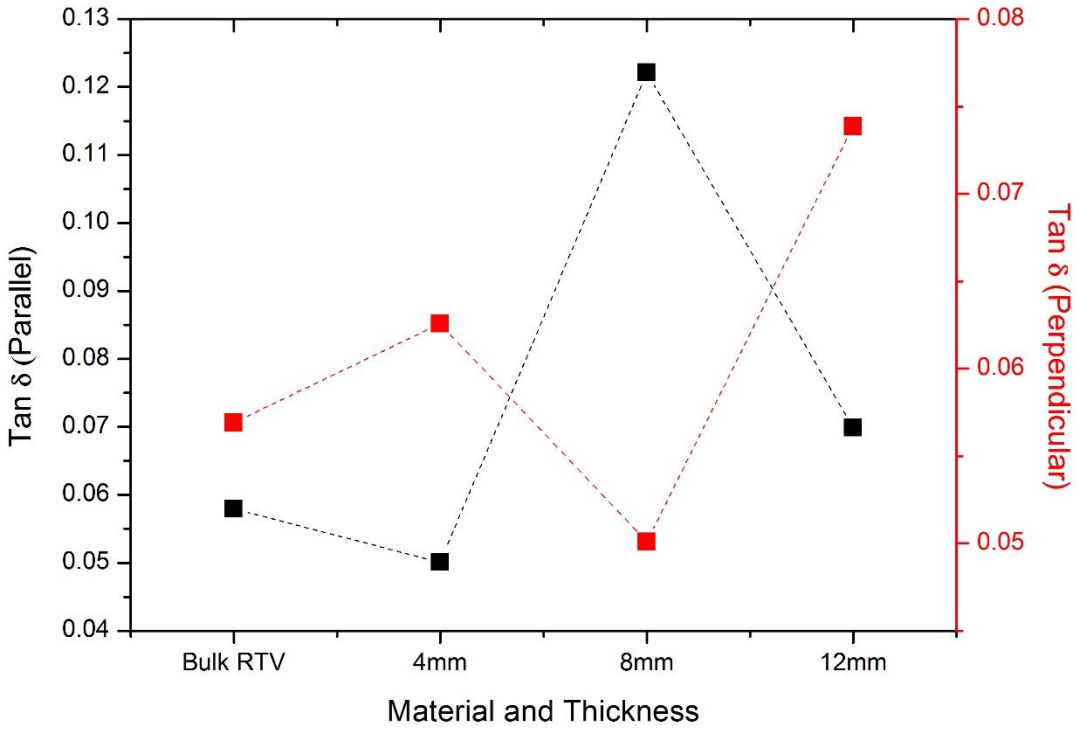


Figure 9. Tan δ values of the samples defined based on thickness and direction

Macro structures were photographed from the sample cross-sections cut from 4, 8, and 12 mm thickness groups, and the distribution and morphology of the cavity structures were examined with the image processing program.

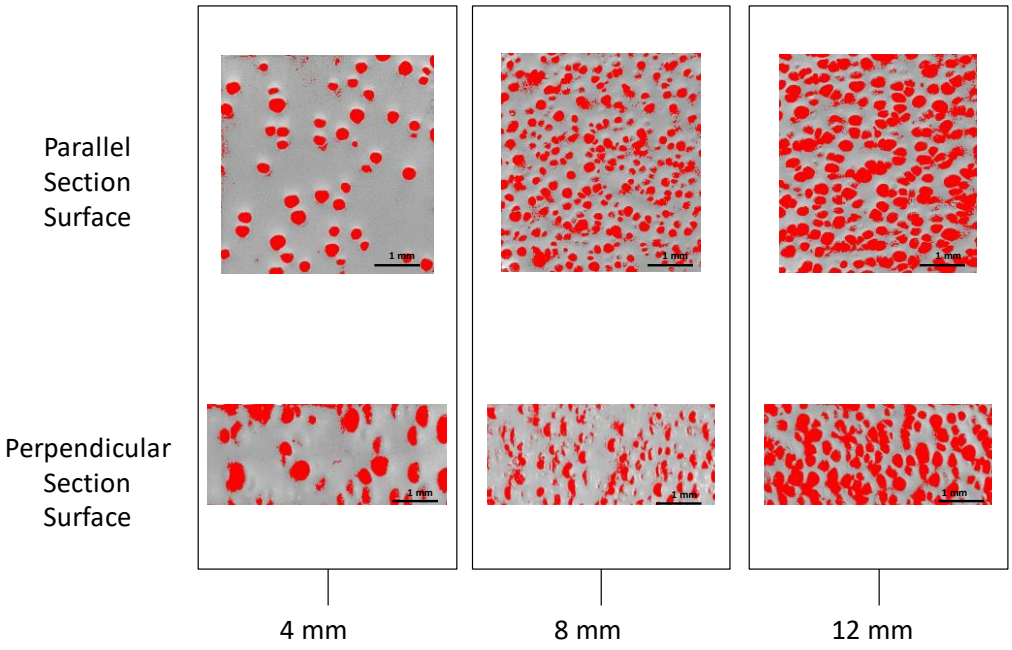


Figure 10. Image-processed macrographs of polymeric foam core with described thickness values

When the macro photographs given in Figure 10 are examined, the number of pores increases as the thickness increases. When the pore morphologies are examined, the pore orientation is different in the direction perpendicular and parallel to the foaming direction of the polymer. The pores had a spherical appearance in the foaming direction of the polymer. In contrast, the pore morphology shifted from spherical to elliptical in the cross-section perpendicular to the foaming direction. Figure 11 shows the variation in pore sphericity depending on the direction and thickness.

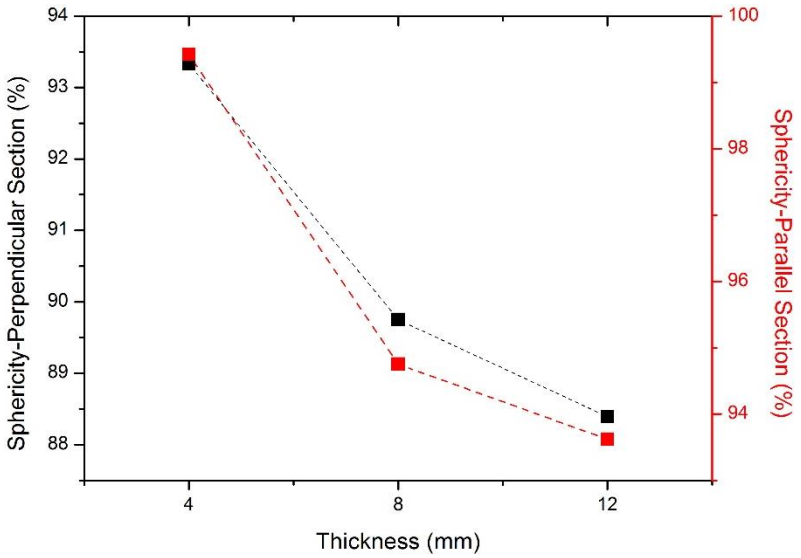


Figure 11. Sphericity of polymeric foam core with described thickness values

3.2. Compression Test Results

The samples prepared as aluminum sandwich panels, grouped as 4, 8, and 12 mm according to their core thickness, and were deformed with compression speeds of 1, 10, and 50 mm/min. In compression tests, the core of the sandwich panel was deformed up to 95% of its thickness. Force-displacement graphs are given in according to thickness values at Figure 11.

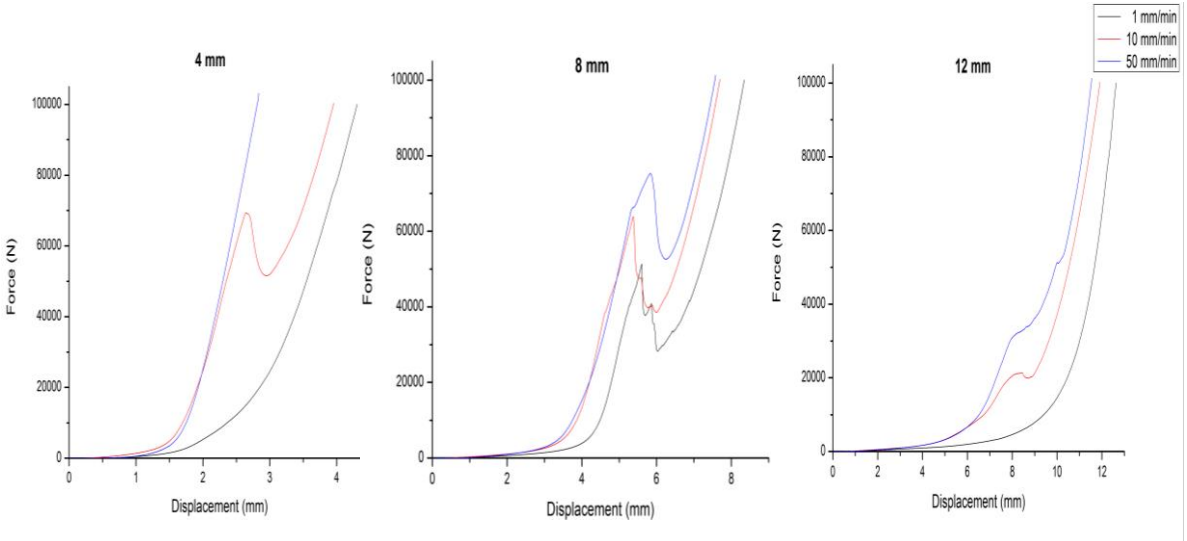


Figure 12. Compression test charts of polymeric foam-cored aluminum sandwich panels grouped according to thickness values

When the compression test results are evaluated according to the test speed, the sample shows higher strength at increasing test speeds with the same thickness. However, the material behaved more rigidly at decreasing thickness values.

The integration of the force-displacement curves gives the amount of energy absorbed during the compression test. The energy absorbed on these graphs was calculated numerically and is shown in Figure 12.

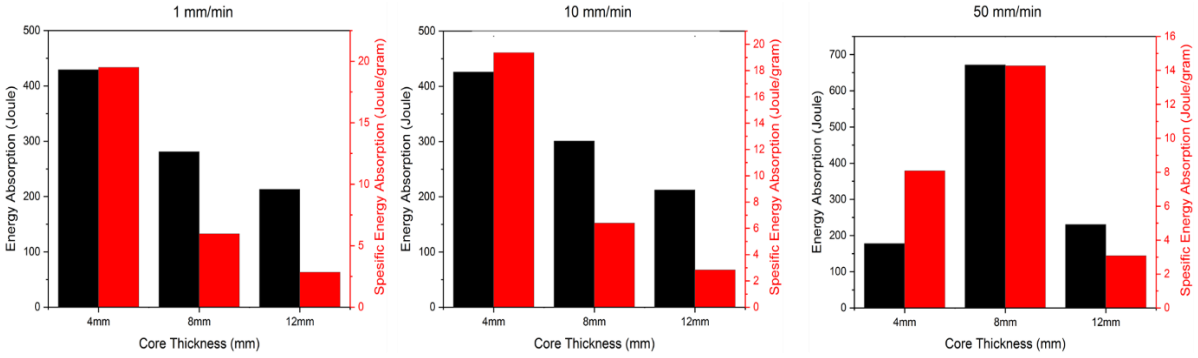


Figure 13. Energy absorption values of polymeric foam-cored aluminum sandwich panels grouped according to thickness and compression speed values

It has been observed that the deflection and breakage in the force-displacement curves given in Figure 11 cause damage in the samples. When the damage is analyzed, breaks on the curve show delamination damage and deviations show tearing in the polymer. The damage type and its appearance in the force-displacement graph are given in Figure 13.

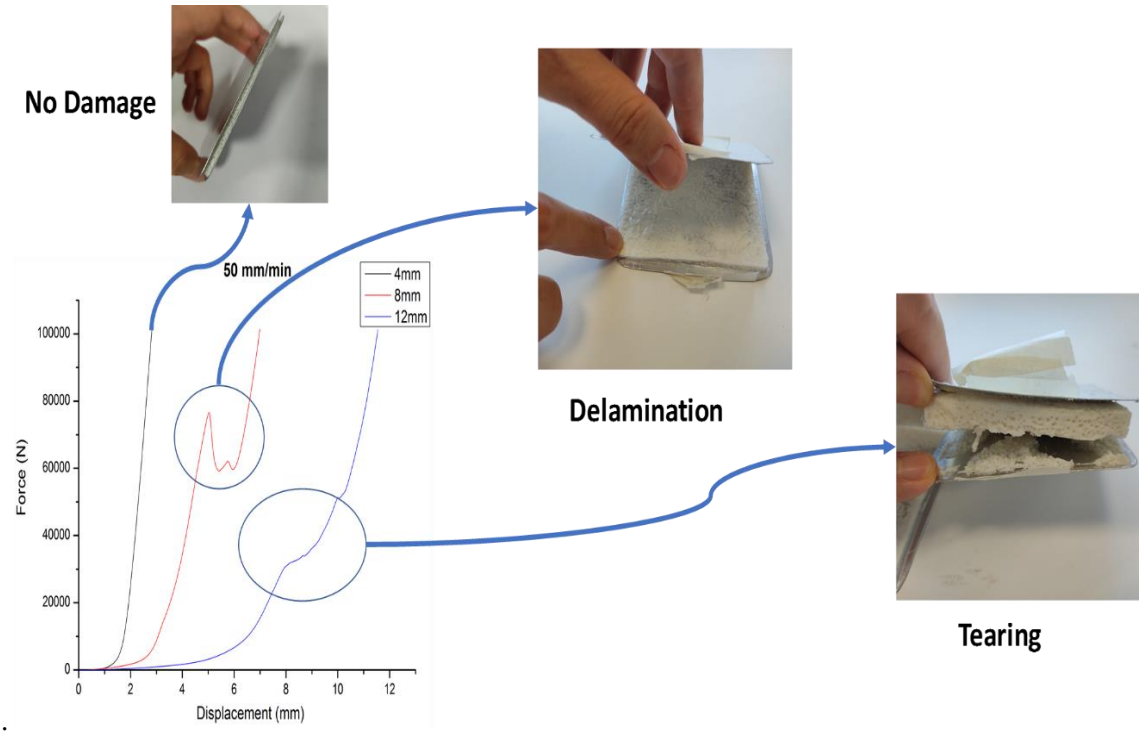


Figure 14. Failure analysis for compression test results of RTV foam cored aluminum sandwich panel

4. Discussion and Conclusion

Within the scope of this study, RTV polymer foam material produced in 4, 8, and 12 mm thicknesses were made into a sandwich panel between 0.5 mm thick aluminum sheets. The behavior of aluminum sandwich panels with viscoelastic RTV polymer foam core in three different thicknesses at compression speeds of 1, 10, and 50 mm/min was investigated. During the thermal foaming of the polymer, the polymer foam material adhered to the aluminum sheets.

Since the polymerization and foaming processes co-occurred, it was concluded that the amount of substance that changes with the thickness directly affects the product properties. When the macro photographs are evaluated together with the density measurements of the RTV foam material, the increase in pore formation explains the decrease in Shore F hardness measurements.

The change in material hardness is also reflected in other mechanical properties. Therefore, the samples were analyzed with DMA, and the results were evaluated. When the dynamic-mechanical analysis results are examined, the polymer foam with a thickness of 4 mm polymerized faster than the samples with a thickness of 8 and 12 mm. The thickness related to amount of material increasing with the delayed the polymerization, which caused the pores to form an elliptical geometry in the foaming direction. The decrease in strength can be explained by the pore number, size, and pore morphology change. While the number of pores increases in direct proportion to the thickness, the pore size is smaller and more homogeneous in 8 mm core materials than in 4 and 12 mm core materials. As the pores were directed from the spherical geometric structure to the elliptic geometry in the foaming direction, the strength decreased, as seen in Figure 8. In silicon-based polymeric structures, intermolecular interaction causes polymer viscous behavior [9]. Viscosity is a parameter to be considered in process design.

The panel core material exhibits high strength under low thickness and high compression speed conditions in the compression test results. Furthermore, the amount of energy absorbed by the polymer during the compression test parallels the DMA results. In light of these results, it is possible to say that there is an optimum thickness value for the RTV polymer foam production process with the thermal processes under the conditions determined in this

study. In addition, in the force-displacement graphs in Figure 11, increasing speed with increasing thickness increased the tendency to damage the polymer foam structure.

As a suggestion, instead of using 12 mm sandwich panels, making 8+4 mm will give more effective results and will be able to meet both high and low deformation amounts. As another usage area, an adequate amount of material can be used by designing an 8 mm sandwich panel structure where there is a high-speed impact and a 4 mm sandwich panel structure where there will be a low-speed impact.

5. Acknowledge

This study was supported by the Necmettin Erbakan Research Foundation of Necmettin Erbakan University with the project number NEU-BAP 211451003.

References

[1] S. Ouellet, D. Cronin, and M. Worswick, "Compressive response of polymeric foams under quasi-static, medium and high strain rate conditions," *Polymer Testing*, vol. 25, no. 6, pp. 731–743, 2006.

[2] P. Cassagnau, "New trends in cellular silicone: Innovations and applications," *Journal of Cellular Plastics*, vol. 55, no. 2, Oct., pp. 151-200, 2019.

[3] K. E. Polmanteer, "Silicone Rubber, Its Development and Technology Progress," Rubber Chemistry and Technology, vol. 61, no. 3, pp. 470–502, 1988.

[4] M. A. Brook, *Silicon in Organic, Organometallic, and Polymer Chemistry*, USA, New York, Wiley, 2000.

[5] M. J. Zeigler and F. W. G. Fearon, Eds., *Silicon-Based Polymer Science*, Washington, American Chemical Society, 1990.

[6] Q. Ma, M. R. M. Rejab, J. P. Siregar, and Z. Guan, "A review of the recent trends on core structures and impact response of sandwich panels," *Journal of Composite Materials*, vol 55, no. 18, pp. 2513-2555, 2021.

[7] F Tarlochan, "Sandwich Structures for Energy Absorption Applications: A. Review," *Materials*, vol. 14, pp. 4731-4751, 2021.

[8] A. Yonezu, K. Hirayama, H. Kishida, and X. Chen, "Characterization of the compressive deformation behavior with strain rate effect of low-density polymeric foams," *Polym. Test.*, vol. 50, pp. 1–8, 2016.

[9] K. F. Johannes, Ed., *Liquid Silicone Rubber*, USA, New Jersey, Wiley, 2019.

The Use Of Solar Energy In The Profile Of Prefabrication And Its Effect On The Behavior And Durability Of Concrete

Ben Ammar Ben Khadda[1*]

[1*]Biskra University, Faculty of Science and Technology, Departmant of Civil and Hydraulique Engineering, Biskra, Algeria, (ORCID: 0000-0000-0000)
b.benammar@univ-biskra.dz

Abstract

This research shows the advantage of using solar energy for the hardening of fresh concrete for the prefabricated elements of constructions. An experimental program was carried out to study the effect of the initial hardening time and the environmental conditions, humidity and ambient temperature and inside the stoving chamber on the compressive strength; the water/cement ratio (E/C) is 0.40 for the whole year heated by 2 cycles for both hot and cold periods. The results show the beneficial effect of this type of accelerated hardening and high quality and durability and beneficial for the environment.

Keywords: Solar energy, Prefabricated elements, Hardening, Compressive strength.

1. Introduction

Public and political awareness of environmental and energy security issues have led to the promotion of solar energy sources [1]. The needs of the modern world require producing more, faster and cheaper, it's the prefabricated concrete (precast elements). The setting time and hardening of hydraulic concrete, building materials most used today, is incompatible with the requirements of industrial production. In order to accelerate the setting and hardening concrete heat treatments prominently among the different possible methods. The atmospheric steam curing is the way to thermo maturation most used. Steaming of the concrete in the enclosures continues until the minimum resistance is reached, considered essential for the good resistance of the element after stripping [2]. This minimum compressive strength should be around 50 to 60% of the required strength (28 days under natural conditions) [3]. Steam curing is an important technique for obtaining high strength values at the start of precast concrete [4]. The required objective is to evaluate through experiments the influence of atmospheric steam curing on the mechanical strength of concrete.

2. Experimental Program

In this section we present the materials used, formulation of concrete and the preparation of specimens.

2.1 Materials

02 cements (CEM I42.5 and (CEM II/B) 42.5 Mpa, the water used is drinking water (NFP 18-404 standard), the sand (0/5 mm) and crushed stones (3/8, 8/15 and 15/25 mm).

2.1.1 Study of the temperature in the steam curing chamber and at ambient air

Our study is first to raise the temperatures in the open air using a thermometer and within the confines of conservation (Figure 1) by other thermometers hourly and daily same time of 07 h to 21 h for 12 months of the year, the average of these monthly records are illustrated in figure 2.

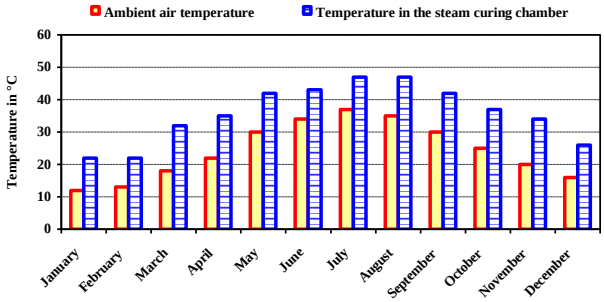


Figure 1. Monthly Exchange In Outdoor Temperatures And The Steam Curing Chamber



Figure 2. Steam Curing Chamber

2.1.2 Concrete test methods and compositions

From the graphs of the temperature variation with time of 12 months, we can say that for six months from April to September, the average temperature coefficient (K_1 = 1.70), and October to March, the average temperature coefficient is: (K_2 = 1.40). With: T° is the temperature in °c and K: the average temperature coefficient (K = 1.55). Based on the findings deduced from the variation curves of temperature versus time inside the chamber, we select the six months which corresponds to the seasons: spring and summer as shown in table 1.

Table 1. Steaming cycles and maximum temperatures in the room (spring-summer)

Month	Apr	May	Jun	Jul	Aug	Sept
Cycles	3×8×3	3×8×3	3×8×3	3×9×3	3×9×3	3×8×3
Max. T°	38	43	44	46	48	43

We opt for steam curing cycle1: (3×8×3) with a maximum temperature bearing 45 °c. We do the same for the other six (06) months representing the fall and winter and the pattern of the cycle (table 2)

Table 2. Steaming cycles and maximum temperatures In the room (autumn - winter)

Month	Oct	Nov	Dec	Jan	Feb	Mar
Cycles	3×8×3	3×7×3	3×7×3	3×7×3	3×7×3	3×8×3
Max. T°	34	32	30	28	23	34

We opt for steam curing cycle$_2$: (3×7×3) with a maximum temperature bearing 29°c.

Table 3. Composition of Concrete (kg/m^3)

Concrete type	Cement	Sand	Gravel (3/8)	Gravel (8/15)	Gravel (15/25)	*w/c* ratio
B1	475	533	143	126	909	0.4
	380	613				0.5
	317	666				0.6
B2	500	490				0.4
	400	575				0.5
	333	640				0.6

3. Results and discussions

Maneuverability: The NF P 18-451 slump test, The consistency class of concrete is plastic.

Compressive strength: Are estimated at 1, 2, 3, 7 and 28 days for the 04 curing methods.

After mixing, molding and demoulding, the samples were introduced into the open air steaming chamber (Figure 3)

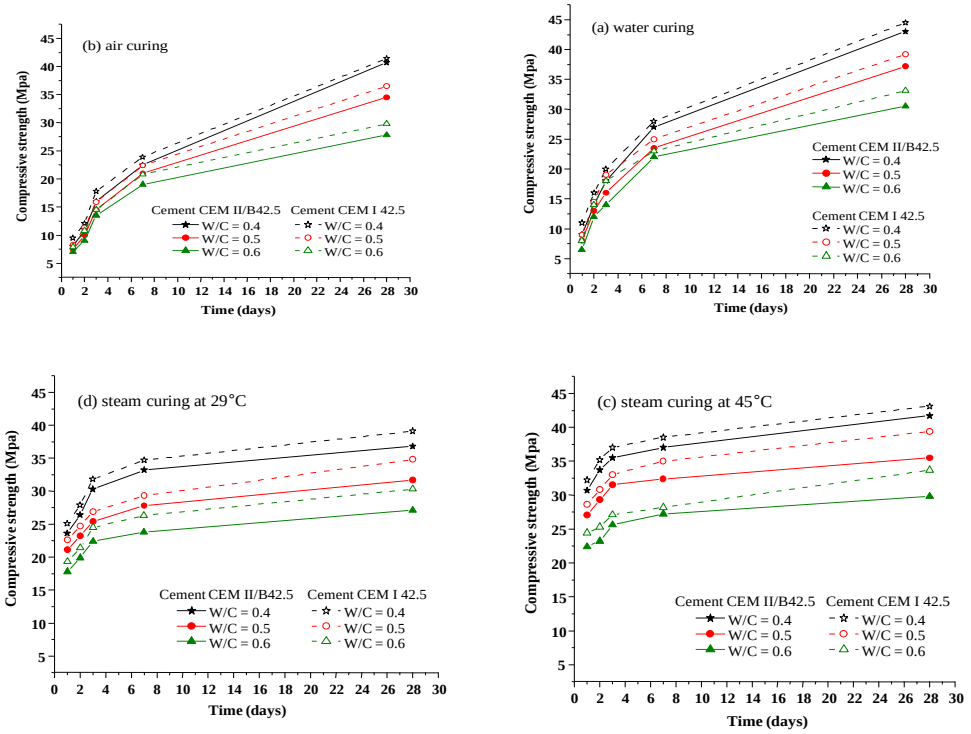


Figure 3. Effects of curing methods, cement type and w/c ratio on the compressive strength development

4.

1. The solar-powered steaming technique in Algeria is an effective technique for hardening concrete for CEM cement.

2. Water hardening promotes hydration regardless of the w/c ratio and the type of cement. Air hardening has a negative effect on the mechanical properties of concrete.

3. This heat treatment by solar energy provides us with time savings and shorter manufacturing times to achieve compressive strength at 28 days in air after 1 day of baking and 03 days of curing in air.

References

[1] Michel Vénuat (1989). *La pratique des ciments mortier et bétons* tome 1, caractéristiques des liants et des bétons, mise en œuvre des coulis et mortiers 2° édition p 215-217.

[2] Bhutto Abdul Waheed, Bazmi Aqeel Ahmed, Zahedi Gholamreza. Greener energy: issues and challenges for Pakistan-solar energy prospective. Renew Sustain Energy Rev 2012; 16(5):2762–80

[3] ACI Committee 517. Accelerated curing of concrete at atmospheric pressure, ACI 517. 2R 87, revised 1992, American Concrete Institute, Farmington Hills Michigan, 17 p, 1992.

[4] Turkel S, Alabas V. The effect of excessive steam curing on Portland composite cement concrete. Cem Concr Res 2005; 35(2):405–11

Tek Bir Banyodan Elektro Depolama Yöntemi İle Elde Edilen Ni-W Ve Ni-W/Hbn Kaplamalarının Karşılaştırılması

Gözde ZÜBARİOĞLU[1*], Erdoğan KANCA[1], Mehmet DEMİR[1], İsmail Hakki KARAHAN[2]

[1] İskenderun Teknik Üniversitesi Makine Mühendisliği Bölümü, Hatay, Türkiye

[2] Hatay Mustafa Kemal Üniversitesi Fizik Bölüm, Hatay, Türkiye

Öz

Nikelin (Ni) korozyona karşı dayanıklılığı, sertliği, manyetik alanda boyut değiştirme kabiliyeti ve adezyon kuvveti olduğu bilinmektedir. Tungstenin (W) sert sağlam, yüksek erime sıcaklığı ve çatlak giderme yönteminde kullanıldığı yapılan incelemelerde görülmüştür. Buna ek olarak Hekzegonal Bor Nitrürün (hBN) yağlayıcılığı, sertliği ve korozyon direncini arttırması kullanılarak elektrodepolama yöntemiyle Ni-W/hBN alaşımlı yeni bir kompozit kaplama malzemesi oluşturulmuştur. Bu çalışmada elektrodepolama yöntemi kullanılarak elde edilen Ni-W ve Ni-W/hBN kaplamalarının tek bir banyo içerisinden dört ayrı numune elde edilmesi ve bu numuneler arasındaki mikrosertlik, yüzey pürüzlülüğü, korozyon direnci, optik mikroskop ve XRD görüntüleri karşılaştırılmıştır. Yapılan bu karşılaştırmalar sonucunda yapışma testinde aynı banyo içerisinde elde edilen dört ayrı Ni-W numunesinden ilk iki numunenin yapışmasının üçüncü ve dördüncü numuneye göre daha iyi olduğu Ni-W/hBN banyosunda ise ilk üç numunenin dördüncü numuneye göre yapışma kabiliyetinin daha iyi olduğu görülmüştür. Aynı zamanda Ni-W banyosu içerisine eklenen hBN parçacıklarının sertliği arttırmada da büyük rol oynadığı gözlemlenmiştir.

Anahtar Kelimeler: Elektro depozisyon, Ni-W, Ni-W/hBN, kaplama

Comparison Of Ni-W And Ni-W/Hbn Coatings Obtained By Electro Deposition Method From A Single Bath

Abstract:

It is known that nickel (Ni) has resistance to corrosion, hardness, ability to change size in magnetic field and adhesion strength. It has been seen in the examinations that tungsten (W) is used in hard, high melting temperature and crack removal method. In addition, a new Ni-W/hBN alloy composite coating material was formed by electrodeposition method, using Hexegonal Boron Nitride (hBN) to increase its lubricity, hardness and corrosion resistance. In this study, four different samples of Ni-W and Ni-W/hBN coatings obtained by using the electro-deposition method were obtained from a single bath and the microhardness, surface roughness, corrosion resistance, optical microscope and XRD images between these samples were compared. As a result of these comparisons, in the adhesion test, it was seen that the first two samples of four different Ni-W samples obtained in the same bath had better adhesion than the third and fourth samples, and the adhesion ability of the first three samples was better than the fourth sample in the Ni-W/hBN bath. It has also been observed that hBN particles added to the Ni-W bath play a major role in increasing the hardness.

Keywords: electro deposition, Ni-W, Ni-W/hBN, coating

1. Giriş

Gelişen teknoloji ile birlikte yeni malzeme üretme ihtiyacı, ekonomik ve kolay olması, katma değeri daha düşük olan malzemenin daha iyi hale getirilmesi ve malzemelerin istenilen özellikleri verebilmesi adına kaplama yöntemine sıkça başvurulmaktadır.

Hızla gelişen teknoloji ile beraber malzemelerin çevreye karşı korunması ve geliştirilmesine ihtiyaç duyulmuştur. Bu amaçla malzemelere alaşımlama yapılmış fakat zamanla alaşımlamanın oldukça maliyetli olduğu ve malzemelerin yalnızca dış yüzeylerinin korunmasının daha doğru olacağı düşünülmüştür. Kaplama

malzemelerin korunması ve gerekli özelliklerin kazandırılması amacıyla ülkemizde çok sık kullanılmaktadır. Kaplama çeşitlerinden birisi de elektro-depolama yöntemiyle kaplamadır. Elektrodepolama yöntemi ile koruma, dekoratif, korozyon direnci, manyetik özellik, ısı direnci, aşınma direnci, yağlayıcılık, elektrik geçirgenliği ve mücevher kaplamalar gibi çok çeşitli amaçlar için kullanılabilir.[1], [2]

Elektrodepolama, bir altlık üzerine elektrolit içerisindeki metal iyonlarının elektrokimyasal indirgenmesi ile oluşturulan film biriktirme işlemidir. İndirgeme bir çözelti (elektrolit) içerisinde gerçekleşir. Elektrokimyasal depolama işlemi, kaplanacak nesne, elektrolit ve bir karşı elektrodu içeren bir sistemdir. Akımı mümkün kılmak için iki elektrodun harici bir güç kaynağına bağlanması gerekir. Kaplanacak nesne, güç kaynağının negatif ucuna bağlanır ve metal iyonları metal atomlara indirgenir ve bu da sonunda yüzeyde birikinti oluşturur[2]

Günümüzde elektrodepolama yöntemi kullanılarak kaplama yapılmış birçok çalışma bulunmaktadır. Bunlardan bazıları şöyledir:

Farzeneh, Co ve W alaşım elementlerinin elektrodepozisyon özellikleri üzerine etkileri ve nanokristal Ni alaşımlı kaplamaların özelliklerini incelemiştir. Yapmış olduğu bu çalışmada elektrodepozisyon banyosu içerisinde Ni-Co-W elementlerini kullanan Farzeneh 36°C sıcaklık ve 13-14 dakikalık bir kaplama süresi ile Ni,Co,W,Ni-Co,Nİ-W ve Ni-Co-W metallerini biriktirmiş 13µm kalınlığında bir kaplama elde etmiştir. Elde edilen bu kaplama Ni-Co birikiminde rastgele piramidal, Ni-W birikiminde rastgele yönelimli yarım küre piramidal, Ni-Co-W birikiminde ise koloni benzeri morfoloji gösterdiğini görmüştür.[3]

Portela, Antikorozif Ni-W-Co sentezi için devre dışı bırakılmış bir Ni banyosundan elektrodepozisyon ile kaplamayı incelemiştir. Elektrodepozisyon banyosu içerisinde Ni-Co-W elementlerini kullanan Portela, 100°C sıcaklık ve 3.8 pH değerleri altında yüzey morfolojisini korozyon direncini ve biriktirme verimliliğini araştırmıştır. Yapılan bu çalışmada altlık olarak kare bakır levha kullanan Portela Ni-Co-W alaşımını endüstri atık suyundan üretmiş olup biriktirme verimliliğini %86.89 olarak bulmuştur. Alaşımda %30'a yakın W elementi olduğu saptanmış ve W'nin çatlak azaltmaya katkı sağladığı gözlenmiştir. Homojen yuvarlak taneler korunmuş, tane boyutları küçültülmüş ve en iyi antikorozif özelliği elde etmiştir.[4]

Olivera, elektrodepozisyon ile elde edilen Ni-Co-W alaşımlarının sıcaklığın ve pH'ın akım yoğunluğuna ve banyo özelliklerine etkisini incelemiştir. Elektrodepozisyon banyosu içerisinde Ni-Co-W elementlerini kullanan Olivera 55°C sıcaklık için 5 pH ve 8 pH ile korozyon direncini, yüzey morfolojisini ve akım yoğunluğunu incelemiştir. Yapılan bu çalışmada pH 8 ile 9.02 için Ni üst seviyelerde, pH 3.98 ile 5 için Co düşük seviyelerde tercih edilmiş olup en yüksek akım verimliliği %71.02 olarak bulunmuştur. Pürüzlü bir yapı olduğu ve mikro modüllerin varlığının olduğu gözlemlenmiştir. Kaplamaların çoğunda mikro çatlaklar olduğu gözlemlenmiştir.[5]

Li, Ni-B'nin mikroyapısal yüzey ve elektrokimyasal özellikleri ile birlikte elektrodepozisyon yöntemiyle yeni bir Ni-W/BN dubleks kompozit kaplamasını incelemiştir. Elektrodepozisyon banyosu içerisinde Ni-W elementleri ile BN parçacıklarını kullanan Li 65°C de 8.0-8.5 pH değerleri arasında 10-30 dakika biriktirme yaparak tek tip kompakt ve çatlaksız yoğun yapılara sahip kaplamalar elde etmiştir. Ni-W/BN dubleks nanokompozitinin kaplaması Ni-W kaplamasından daha yüksek korozyon direnci sergilemiştir. BN parçacıklarının Ni-W matrisine dahil edilmesi Ni ve W'nin sertliğini arttırdığı ve dubleks kompozit kaplamanın aşınma kaybını da azalttığı görülmüşür.[6]

Yapılan incelemelerin ardından Ni'in korozyona karşı dayanıklılığı, sertliği, manyetik alanda boyut değiştirme kabiliyeti ve adezyon kuvveti W'nin sertliği, sağlamlığı, yüksek erime sıcaklığı ve çatlak giderme özellikleri ile hBN parçacıklarının güçlü termal dayanıklılığı, elektriksel yalıtkanlığı, düşük termal genleşmesi ve yüksek iletkenliği kullanılarak elektrodepolama yöntemiyle yeni bir kaplama malzemesi oluşturmak için Ni-W/hBN kompozit kaplaması yapılmıştır.

Bu çalışmada tek bir banyodan elde edilen Ni-W kaplamaları ile tek bir banyodan elde edilen Ni-W/HBN kompozit kaplamaları arasındaki farklar karşılaştırılmış olup aynı zaman da tek bir banyodan elde edilen kaplamaların özellikleri de karşılaştırılmıştır. Bu çalışma da tek bir banyo içerisinden elde edilen tüm kaplamaların özelliklerinin karşılaştırılmasının yanı sıra aynı zaman da daha az malzeme ile daha çok kaplama yapılarak çevre kirliliğinin önlenmesi amaçlanmıştır.

Materyal ve Metod

Ni-W ince film kaplamalı numuneler 2,5-2 cm olacak şekilde kesilmiş olan 2024 Alüminyum altlıkta depolanmıştır. Kesilen 2024 Al altlıklar kaplama yüzeyinde kesimden kalan pürüzlü yüzey ve ince parçacıkların

Tablo 1: Ni-W ve Ni-W/hBN banyo bileşenleri

Bileşen adı	Kullanılan Miktar
$NiSO_4 . 6H_2O$	9,28 g/l
$C_6H_5Na_3O_7 . 2H_2O$	45 g/l
$Na_2WO_4 . 2H_2O$	41,13 g/l
NH_4Cl	26,74 g/l
$NaBr$	15,45 g/l
$NaOH$	40 g/mol
hBN	10 g/l
SDS	0,5 g/l
PEG	40 g/l

giderilmesi adına P 400 ile P1200 aralığındaki zımpara kâğıtları ile birer dakika olacak şekilde zımparalanmış olup Alüminyum altlıkların yüzeyi parlatılmıştır. Yüzey üzerindeki metal tozları önce alkol ile daha sonra da saf su ile temizlenmiştir. Daha sonra metal yüzeyi aseton ile yıkanmış tekrar saf su ile temizlenmiştir. Son olarak temizlenmiş olan 2024 Al malzeme HCl asit içerisine 10 s daldırılarak dağlanmış ve saf su ile temizlenmiştir. Böylelikle kaplama yapılacak yüzey kaplama işlemine hazır hale getirilmiştir. Kaplama yapılacak yüzeyin üst kısmı 0,5 cm olacak şekilde oje ile kapatılmış olup daha sonra Ni-W banyosu içerisine daldırılarak elektrodepolama yöntemi ile kaplanmıştır. Deneyler oda sıcaklığında ve 3 elektrotlu klasik sistemde yapılmıştır. Elektrokimyasal korozyon hücresinin tamamlayıcısı referans elektrot (RE) olarak Ag/AgCl karşıt elektrot olarak ve çalışma elektrotu (WE) olacak şekilde deney numunelerine tanımlanmıştır. Tablo I'de tek bir banyodan elde edilen Ni-W alaşım ve Ni-W/hBN kompozit kaplamaların bileşen özellikleri verilmiştir. Tek banyodan 4 numune çekilmiş olup numuneler kendi aralarında karşılaştırılmıştır.

Numunelerin akım yoğunluğu,pH , sıcaklık, karıştırma hızı değerleri Tablo II'de gösterilmiştir.

Tablo 2: Ni-W ve Ni-W/hBN banyolarının akım yoğunluğu, pH, sıcaklık ve karıştırma hızı değerleri

	I.	II.	III.	IV.
Akım Yoğunluğu (A/dm2)	0,035	0,035	0,0355	0,035
pH	8	8	8	8
Sıcaklık (◦C)	70	70	70	70
Karıştırma hızı (rpm)	600	600	600	600

Bu çalışmada tek bir banyodan elde edilen Ni-W kaplamaları GM olarak adlandırılmış olup yine tek bir banyodan elde edilen Ni-W/hBN kaplamaları da GMH olarak adlandırılmıştır. GMH serisinin banyo bileşenleri arasında ek olarak Hekzogonal bor nitrür (hBN), Sodyum Dedosil Sülfat (SDS) ve Polietilen Glikol (PEG) bulunmaktadır.

Çalışmada elektrodepolama yöntemi ile elde edilen Ni-W alaşım kaplamalar ve Ni-W/hBN kompozit kaplamalarının altlık üzerine yapışma özelliğini belirlemek için VDI 3198 standartlarına göre kaplamaların yapışma kalitesi ölçülmüştür. İyi bilinen Rocwell-C girinti testi ile VDI 3198 normuna göre kaplanmış bileşiklerin yapışma kalitesi ölçülebilir.

Kaplamaların mikrosertlik ölçümlerinde Vickers sertlik ölçme yöntemi kullanılmış olup, Vickers sertlik ölçme yönteminde 136°'lik tepe açısına sahip elmas piramit uç kullanılmıştır. Vickers testinde elde edilen sertlik HV olarak gösterilmektedir ve iz köşeleri ölçülerek bulunur. HV değerini aşağıdaki formülü kullanarak bulabiliriz:

$$HV = 0{,}1897\ P.d^2 \quad (1)$$

Buradaki P, malzeme üzerine uygulanan yük olup d ise iz köşeleri arasındaki uzaklıkların ortalamasını göstermektedir. Bu çalışmada elde edilen numunelere 0.2 HV yük her nokta için 5 sn boyunca uygulanmıştır. Deneylerde NOKSEL Çelik Boru A.Ş de bulunan Qness sertlik ölçme cihazı kullanılmıştır.

2024 Alüminyum yüzeyinde oluşan Nikel-Tungsten fazlarının varlığı Hatay Mustafa Kemal Üniversitesi'nde bulunan bilgisayar kontrollü bir RIGAKU Smart LabTM cihazı kullanılarak X-ışını kırınımı (XRD) analizleri ile tespit edilmiştir.

Kaplamaların içerisine eklenen katkı maddeleri ve seramik partikülleri malzeme yüzeyinde değişiklikler yapmaktadır. 2024 Alüminyum altlık üzerindeki Ni-W ve Ni-W/hBN ince film kaplamalarının yüzey pürüzlülükleri MMK Metalurji A.Ş'de bulunan Wave system Hommelweke T8000 marka Yüzey Pürüzlülük ölçüm cihazı kullanılarak tespit edilmiştir. Deney parametreleri olarak 0.10 mm/s hız 2 mm tarama uzunluğu ve 400µm ölçüm aralığı seçilmiştir.

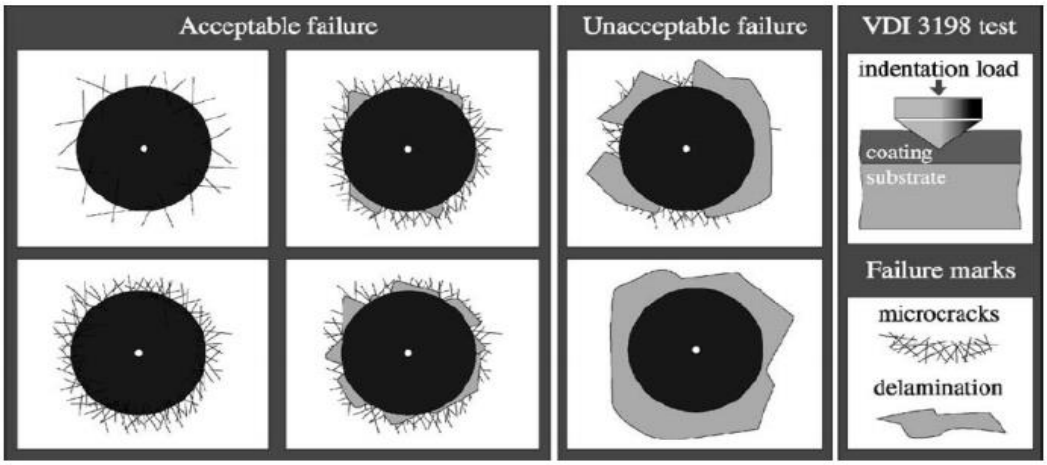
Ni-W ve Ni-W/hBN ince film kaplamalı numunelerin korozyon testleri açık devre potansiyeli (OCP) ve Tafel Ekstrapolasyon yöntemi kullanılarak yapılmıştır. Bu çalışmada OCP deneyleri ağırlıkça %3,5 NaCl çözeltisi içerisinde 3600 s olarak yapılmış ve zamanın bir fonksiyonu olarak grafiğe alınmıştır. Tafel ekstrapolasyon deneyi, numunelerden ölçülen serbest korozyon negatifinden ve pozitifinden 250 mV daha büyük seçilerek 0.001 mV/s hızla polarizasyon çalışmaları yapılmıştır.

3. Araştırma Bulgular

3.1. Yapışma Testi

Nikel – Tungsten ve Ni-W/hBN kaplama sonrası oluşan ince film tabakası VDI 3198 normu ile Daimler Benz Rockwell-C testi kullanılarak değerlendirilmiştir. Rocwell-C girinti testi 62,5 kg yük altında her numunenin üç farklı yerinden girinti testi uygulaması yapılmış olup, test sonuçları MMK Metalürji AŞ'nin mekanik test laboratuvarında Nikon-MA200 mikroskop altında görüntülenmiştir.

VDI 3198 normu Daimler Benz Rockwell-C yapışma testi prensibi Şekil-1'de gösterilmiştir. Şekilde görüldüğü üzere konik bir elmas uç kaplanmış yüzeye girinti uygulayarak kaplanmış yüzey ve alt tabakada plastik deformasyona neden olmaktadır. Tüm girinti testlerinde olduğu gibi 1/10 kuralı bu testte de geçerli olup genel numune kalınlığı girinti derinliğinden 10 kat daha büyük olmalıdır. [7] Kaplanmış numune yüzeyi geleneksel optik mikroskop ile 600 büyütme ile görüntülenmiştir.

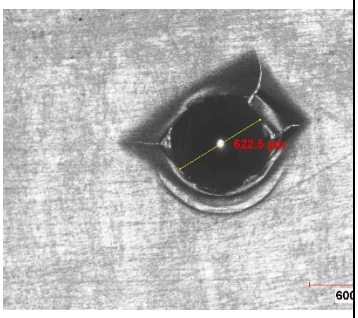
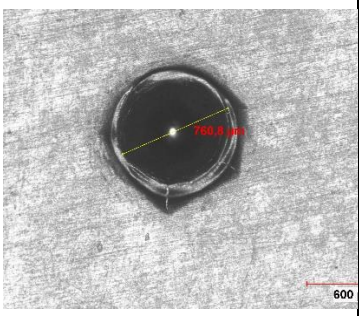
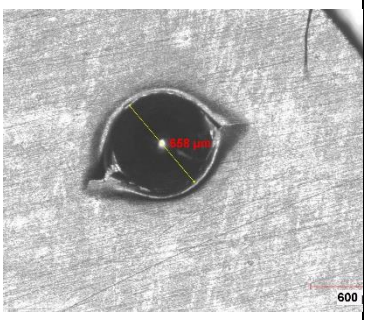
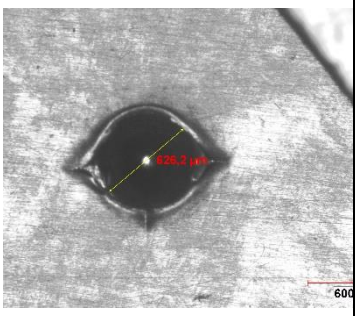
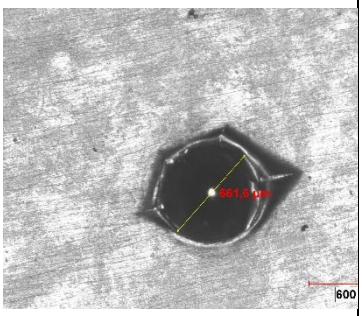
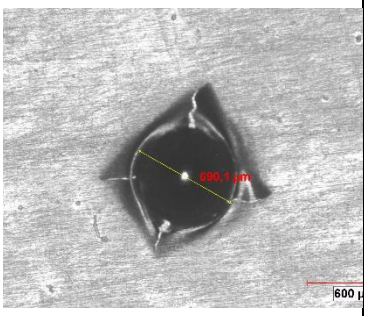
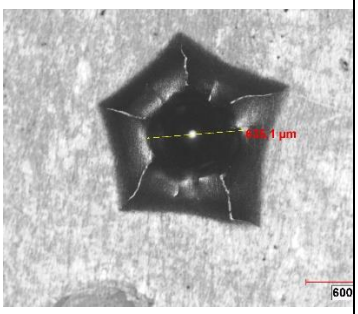
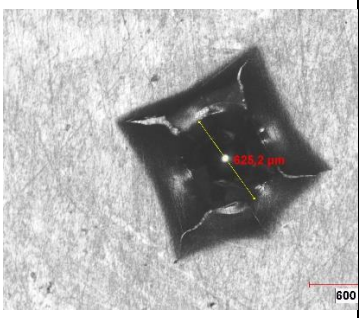
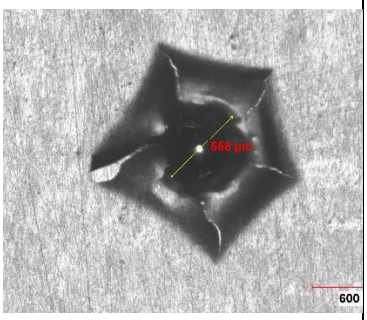
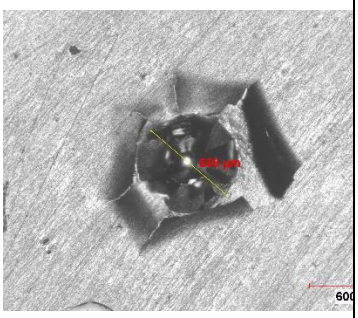
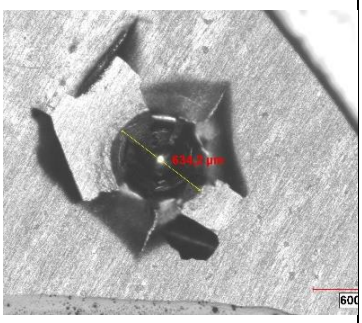
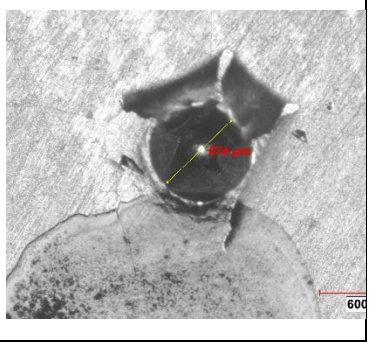


Şekil 1: VDI 3198 girinti testi yapışma kalite sınıflandırması [7]

Temas geometrisi, yoğun bir yük altında, ara yüz üzerinde aşırı kayma gerilmelerine neden olur. İyi yapışmış olan kaplamalar, bu yüklere dayanmayı başarır kayma gerilmeleri ve çevresel olarak uzatılmış delaminasyonu baskıya karşı önler. Şekil 1'de sol tarafta görülmekte olan dört girinti yüzeyleri kabul edilebilir yapışmayı gösterirken, sağ tarafta görülmekte olan iki girinti ise kabul edilmeyen yapışmayı göstermektedir. Baskının çevresinde uzun süreli delaminasyon, zayıf bir ara yüzey yapışmasını göstermekte olup, radyal çatlaklar ve zayıf delaminasyon, güçlü bir şekilde yapışan kaplamayı ama aynı zamanda da kırılgan olan kaplamaları göstermektedir [7]

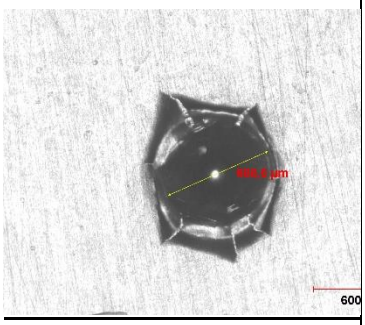
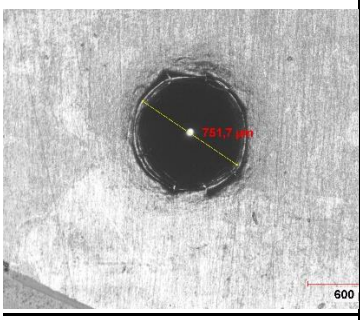
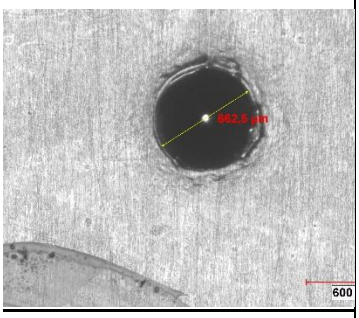
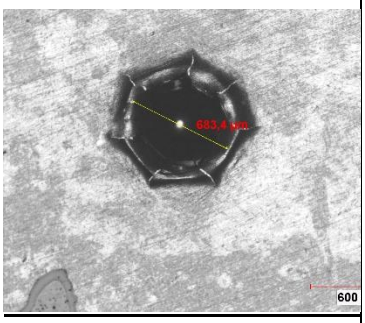
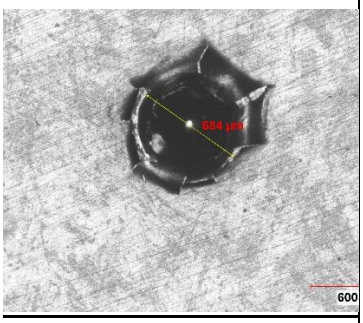
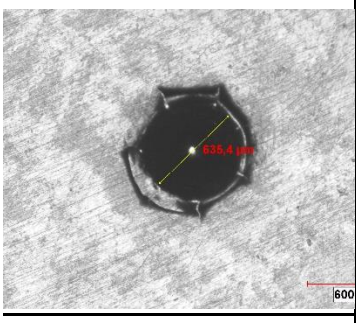
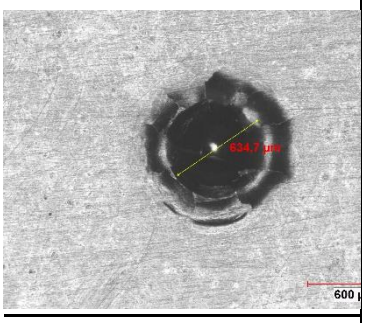
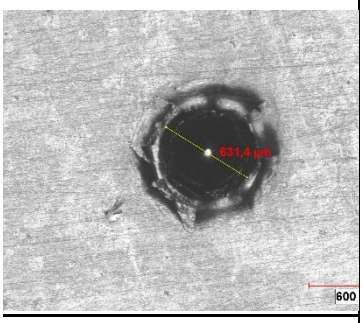
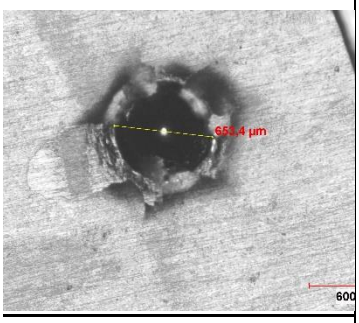
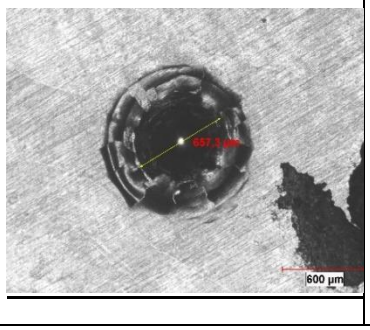
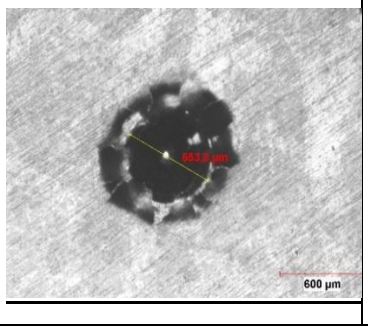
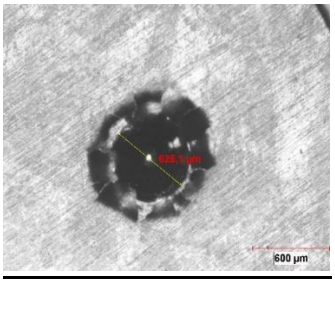
Şekil 2'de Ni-W banyosunda dört ayrı numune banyo suyu değiştirilmeden kaplanmış olup altlık malzemesi olarak kullanılan 2024 alüminyum malzeme üzerine kaplanmış ince filmin yapışma kalitesine etkisi VDI 3198 normu Rocwell-C girinti testi kullanılarak gösterilmektedir. 1. ve 2. Numuneneler de yapılmış olan girinti testlerinin optik mikroskop ile incelenmesi sonucunda yüzey üzerindeki plastik deformasyonun 3. ve 4. Numunelere göre daha az olduğu dolayısı ile 1 ve 2. Numunelerde yapışmanın 3 ve 4. Numunelere göre daha iyi olduğu görülmektedir. 1. Ve 2. Numunelerin 3. Ve 4. Numunelere göre plastik deformasyonun daha az yapışmanın ise daha fazla olmasının nedeni Ni-W banyosu içerisindeki W miktarının zamanla azalıyor olması gösterilebilir.

GM SERİSİ (Tek bir Ni-W banyosundan 4 numune)

	a	b	c
GM 1			
GM 2			
GM 3			
GM 4			

Şekil 2: Aynı Ni-W banyosundan kaplanmış olan 4 numune

GMH SERİSİ (0.025 SDS 2 PEG 0.5 hBN banyosundan 4 numune)

	a	b	c
GMH 1			
GMH 2			
GMH 3			
GMH 4			

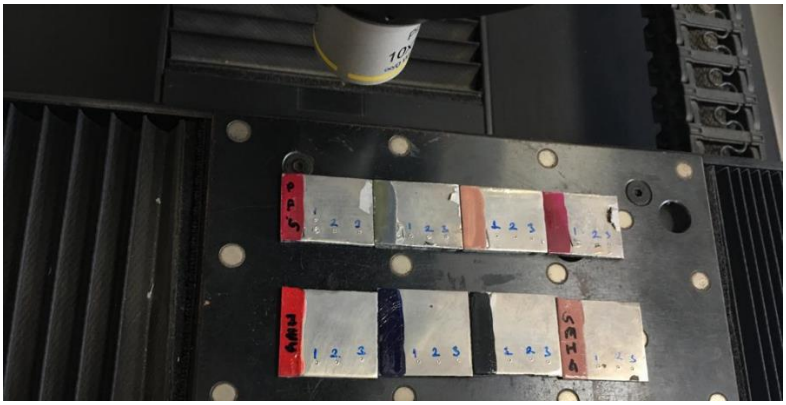
Şekil 3: Aynı Ni-W/hBN banyosundan kaplanmış olan 4 numune

Şekil 3'te Ni-W/hBN banyosunda dört ayrı numune banyo suyu değiştirilmeden kaplanmış olup altlık malzemesi olarak kullanılan 2024 alüminyum malzeme üzerine kaplanmış ince filmin yapışma kalitesine etkisi VDI 3198 normu Rocwell-C girinti testi kullanılarak gösterilmektedir. 1. ve 2. Numuneneler de yapılmış olan girinti testlerinin optik mikroskop ile incelenmesi sonucunda yüzey üzerindeki plastik deformasyonun 3. ve 4.

Numunelere göre daha az olduğu dolayısı ile 1 ve 2. Numunelerde yapışmanın 3 ve 4. Numunelere göre daha iyi olduğu görülmektedir. 1. Ve 2. Numunelerin 3. Ve 4. Numunelere göre plastik deformasyonun daha az yapışmanın ise daha iyi olmasının nedeni Ni-W/hBN banyosu içerisindeki W miktarının azalması ve aynı zamanda hBN parçacıklarının banyo içerisinde azalması ve çökelmesi gösterilebilir.

3.2 MİKROSERTLİK ÖLÇÜMÜ

Şekil 4'de görüldüğü üzere ölçümler her numune için üstten ortadan aşağıdan olmak üzere üç farklı noktan dört numune için toplam 12 noktadan alınmıştır.



Resim-1: Ölçüm yüzeyleri

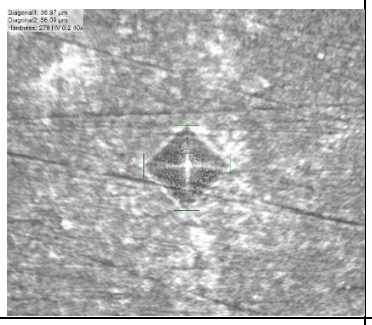
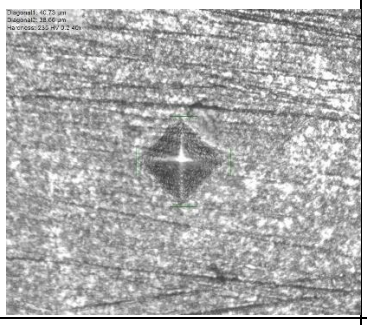
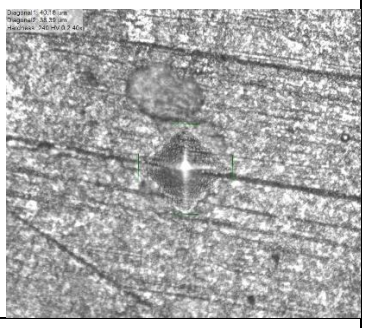
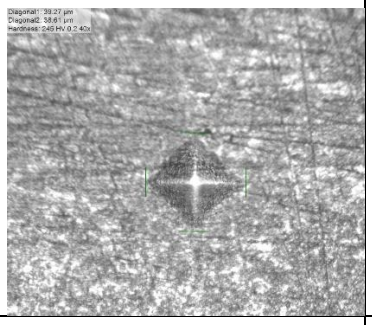
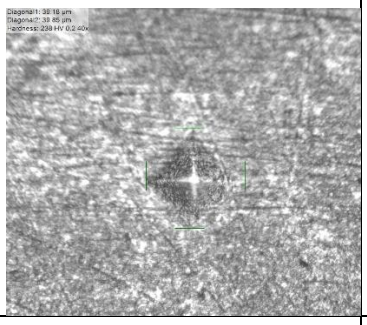
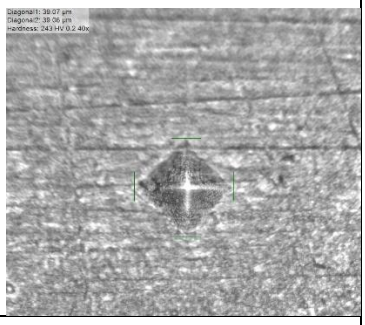
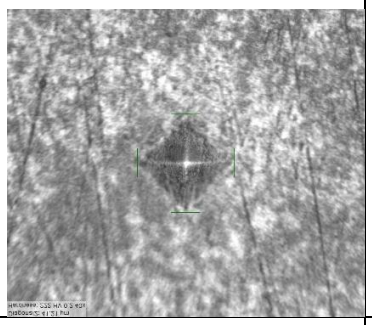
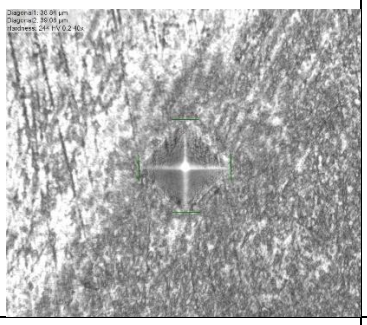
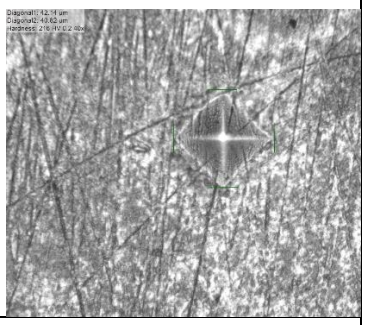
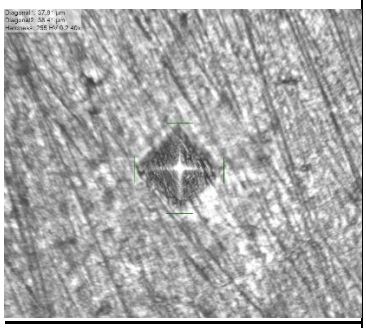
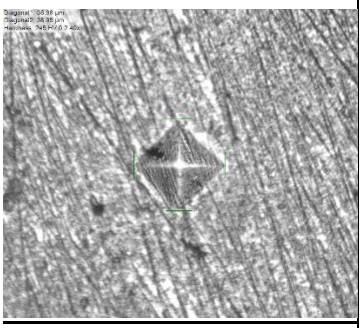
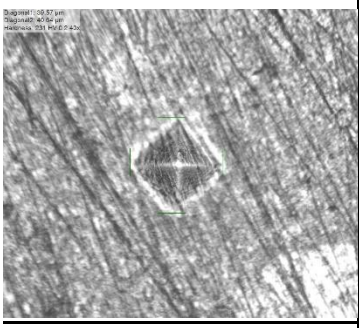
Tablo-3: Aynı Ni-W banyosundan kaplanmış olan 4 numunenin mikrosertlik değerleri

Numune İsmi	Sertlik	Ortalama Sertlik	Numune İsmi	Sertlik	Ortalama Sertlik
GM1	278	251±19	**GM3**	222	227±12
	235			244	
	240			216	
GM2	245	242±3	**GM4**	255	243±10
	238			245	
	243			231	

Şekil-4 ve tablo-III te de görüldüğü üzere en yüksek sertlik değeri 1 numaralı numunenin a noktasındadır. Bu noktada Ni-W banyosundaki W yoğunluğunun diğer noktalara göre daha çok olduğunu bu yüzden de sertliğin daha çok olduğunu söyleyebiliriz.

GM SERİSİ

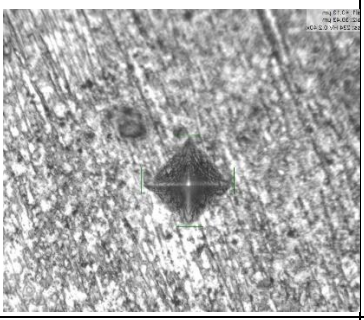
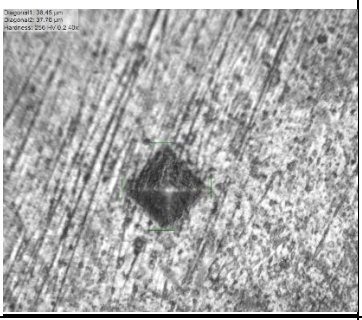
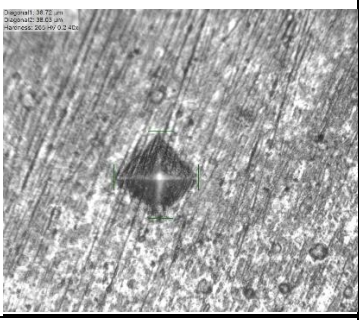
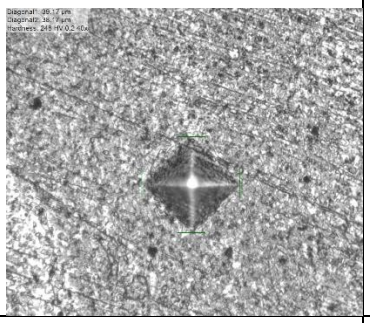
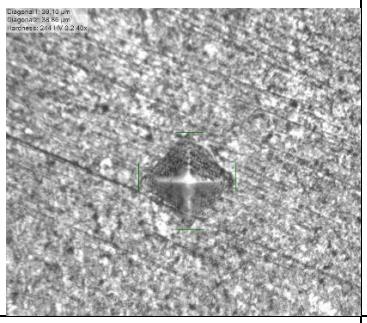
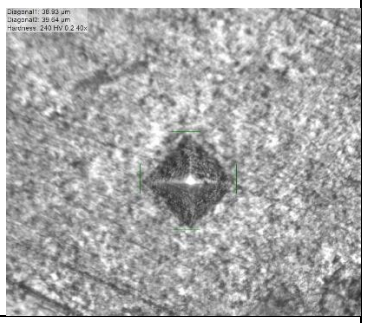
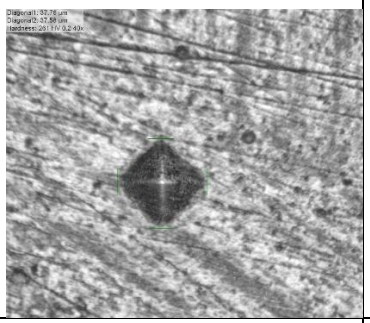
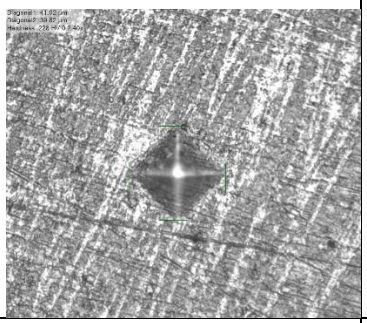
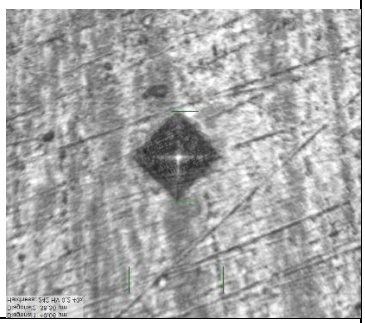
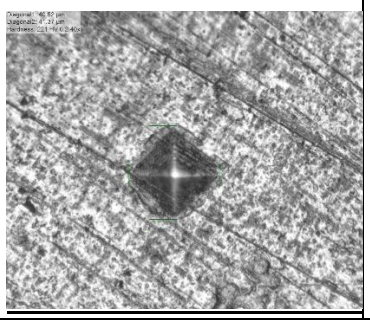
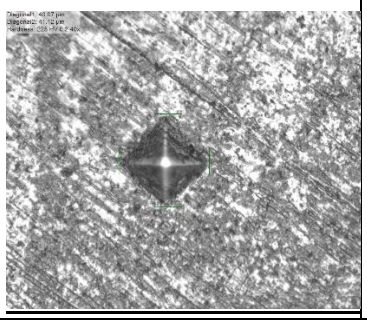
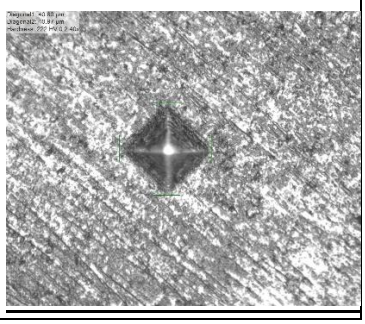
Sertlik ölçüm izleri Şekil 4'teki gibidir.

	1	2	3
GM 1			
GM 2			
GM 3			
GM 4			

Şekil-4: Aynı Ni-W banyosundan kaplanmış olan 4 numune

GMH SERİSİ (0.025 SDS 2 PEG 0.5 hBN banyosundan 4 numune)

Sertlik ölçüm izleri Şekil-5 de gösterilmiştir.

	1	2	3
GMH 1			
GMH 2			
GMH 3			
GMH 4			

Şekil-5: Aynı Ni-W/hBN banyosundan kaplanmış olan 4 numune

Tablo 4: Aynı Ni-W/hBN banyosundan kaplanmış olan 4 numunenin mikrosertlik değerleri

Numune İsmi	Sertlik	Ortalama Sertlik	Numune İsmi	Sertlik	Ortalama Sertlik
GMH1	234	252±13	**GMH3**	261	244±13
	256			228	
	265			242	
GMH2	248	244±3	**GMH4**	221	222±2
	244			225	
	240			222	

Şekil-5 ve tablo-IV te de görüldüğü üzere en yüksek sertlik değeri 1 numaralı numunenin c noktasındadır. Bu noktada Ni-W/hBN banyosundaki W ve hBN parçacıklarının yoğunluğunun diğer noktalara göre daha çok olduğunu bu yüzden de sertliğin daha çok olduğunu söyleyebiliriz. Ni banyosuna W ve hBN katılması ile sertlikliğinde artmış olduğu görülmektedir.

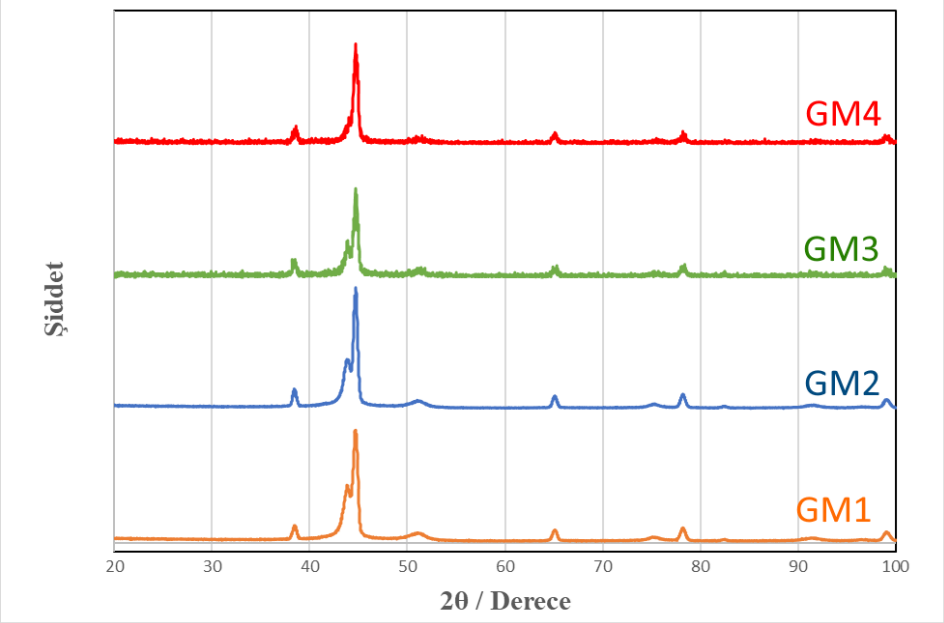
3.3 XRD

X-ışını kırınımı kaplamaların yapısal analizini ve karakterizasyonunu belirleyen bir yöntem olup, bu yöntem ile kaplama üzerine gönderilen X-ışını dalgaları kaplamanın atomik yüzeylerinden yansıyarak algılanması ve anlamlandırılması ilkesine dayanır. X-ışınlarının kristal ağdan saçılması Bragg yasası olarak adlandırılmaktadır. Bu yasaya göre kaplama yüzeyine θ açısı ile X-ışını demeti göndererek X-ışınlarından birinin üst atomik tabakadan, diğerinin ise alt atomik tabakadan yansıdığı düşünülürse, ikinci ışının birinciye göre 2a kadar daha fazla mesafe aldığı görülecektir. Sonuç olarak; 2a mesafesi gelen X-ışınının dalga boyunun tam katlarına denk gelirse iki ışın da aynı fazda olur. Bilgisayar üzerinde 2θ grafiği çizildiğinde belirli açılara karşılık pikler elde edilmektedir. Her bir pik açısından Bragg eşitliği kullanılarak atomik düzlemler arası d mesafesi ve örgü sabitleri bulunabilir ve böylece malzeme üzerindeki fazlar tanımlanabilir. Bragg eşitliği Eş. 1.1'de verilmiştir.

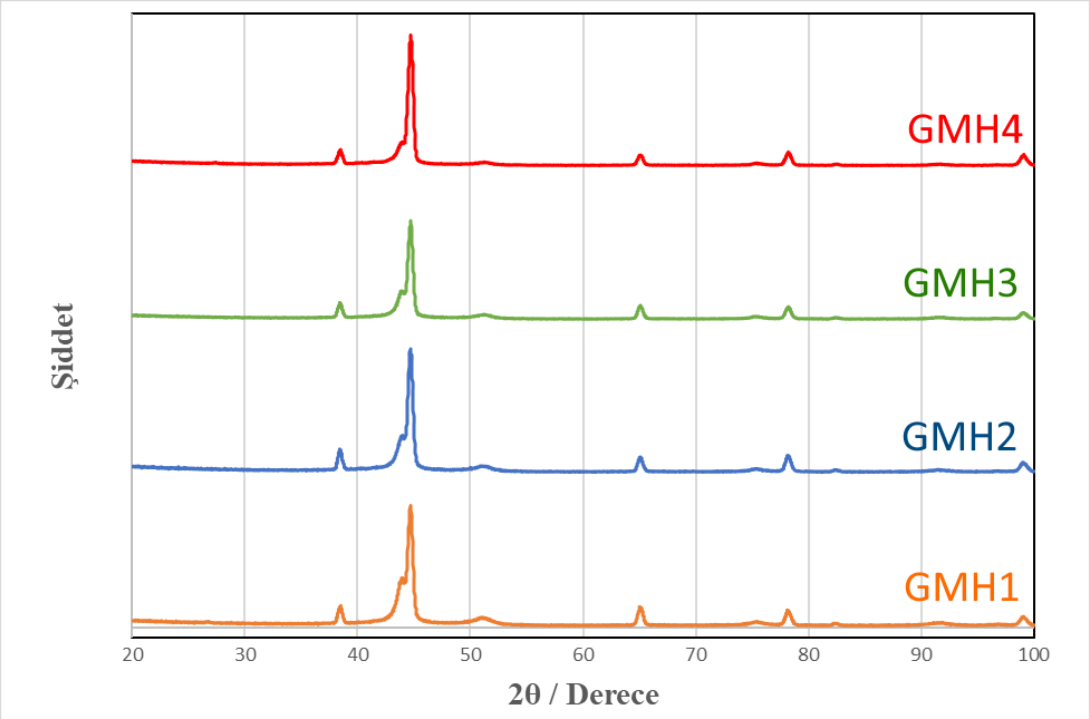
$$2\alpha = n\lambda = 2dsin\theta \qquad (1.1)$$

Burada dalgaboyu sayısı n, düzlemler arası mesafe d, gelen X-ışını ile kristal düzlem arasındaki açı θ ve dalgaboyu λ'dır.

Şekil-6'da Ni-W alaşım ve Şekil 7'de ise Ni-W/hBN kompozit kaplamalarının X-Işınım kırınım desenleri verilmiştir. Şekil-6 incelendiğinde, tek bir banyodan elde edilen 4 farklı numune içinde benzer sonuçlar elde edilmiştir. Bu durum ile bir banyodan birden fazla numune elde edilmesine rağmen, banyonun işlevselliğini devam ettirdiğini ve alaşım kaplamayı biriktirme istikrarını gösterdiğini açıklamaktadır. Kırınım desenlerinin sunduğu tepe noktaları ve elde edilen grafiklerin eşleştirilmesi sonucunda $Ni_{17}W_3$ alaşımının tepe noktaları olan 2θ = 44,71°, 51,45° ve 78,16° açılarak denk geldiği görülmektedir. Bu açılara denk gelen düzlemler sırasıyla (111), (200) ve (220)'dır. Elde edilen bu yapılar literatür ile uyum göstermektedir. [8]–[10]



Şekil-6: Aynı Ni-W banyosundan kaplanmış olan 4 numunenin XRD sonuçları

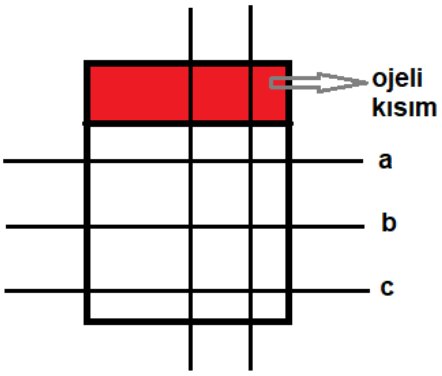


Şekil-7: Aynı Ni-W/hBN banyosundan kaplanmış olan 4 numunenin XRD sonuçları

Şekil-7'de hBN takviyesi ile elde edilen kaplamaların X-Işını kırınım desenleri görülmektedir. Elde edilen kompozit kaplamaların, alaşım kaplamalar ile benzer desenler çizdiği görülmektedir. Aynı zamanda tek bir banyodan kaplamalar elde edilmesine rağmen, banyonun kaplama işlevselliğinin devam ettiği görülmektedir. Bunun yanı sıra 44° civarlarında görülen ve en yoğun olan pikin, hBN takviyesi ile birlikte kırınımının azaldığı ve tek bir pik görünümüne yanaştığı görülmektedir.

3.4 YÜZEY PÜRÜZLÜLÜĞÜ

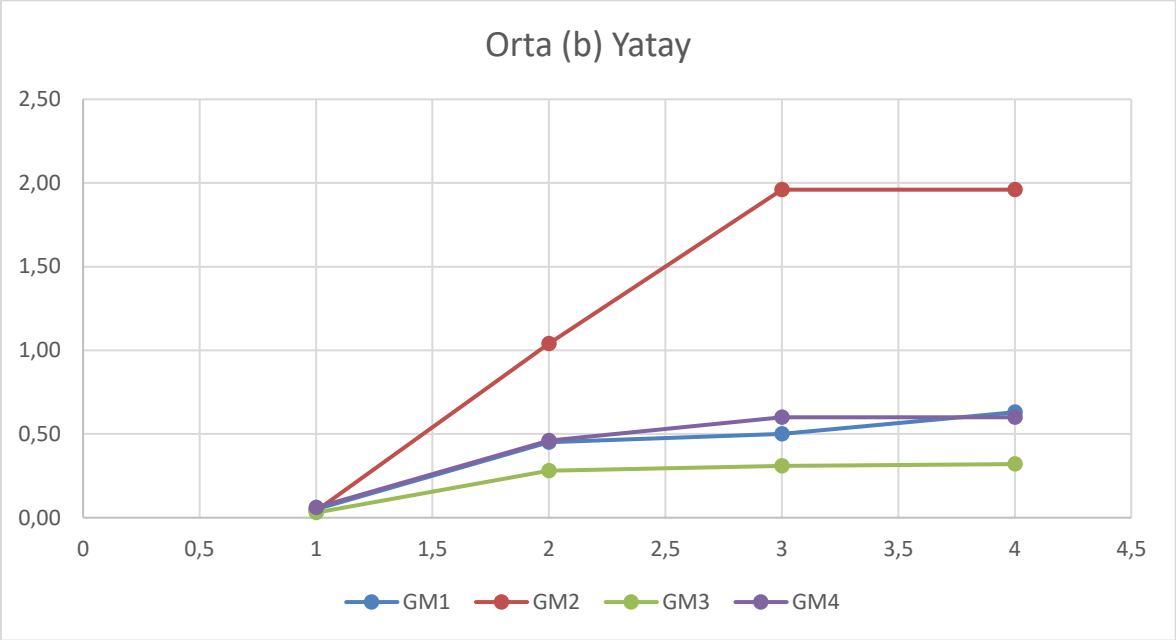
İşleyici takımın, işlenecek yüzeyin bir ucundan diğer ucuna gitmesiyle oluşan birden çok çizikli ve düzensiz kısa dalga boyu uzunluklarına pürüzlülük denmektedir. Yüzey pürüzlülüğü ölçüm cihazları yüzeyin profilini grafik olarak çizmektedirler. Yüzeyin uzun dalga boylarında olması, yüzey pürüzlülüğü ölçme parametrelerini de etkilemekte olup bu nedenle çok uzun dalga boylarının etkisi büyük önem arz etmektedir. Ra bütün ölçümlerin aritmetik ortalamasını, Rz en tepe nokta ile en derin nokta arasındaki farkı, Rt tüm ölçüm uzunluğu için maksimum yükseklik ile maksimum derinliğin toplamını ifade ederken Rq aritmetik ortalama sapmaların karekökünü ifade eder. Standartlarda açıklanmış olan parametrelerden en önemli iki parametre Ra ve Rz'dir. [11]



Resim-2: Yüzey pürüzlülüğü ölçüm noktaları

Tablo-5: Aynı Ni-W banyosundan kaplanmış olan 4 numunenin orta (b) yataydan alınmış değerlerinin tablo gösterimi

	Ra(µm)	Rz(µm)	Rmaz(µm)	Rt(µm)
GM1	0,05	0,45	0,50	0,63
GM2	0,04	1,04	1,96	1,96
GM3	0,03	0,28	0,31	0,32
GM4	0,06	0,46	0,60	0,60

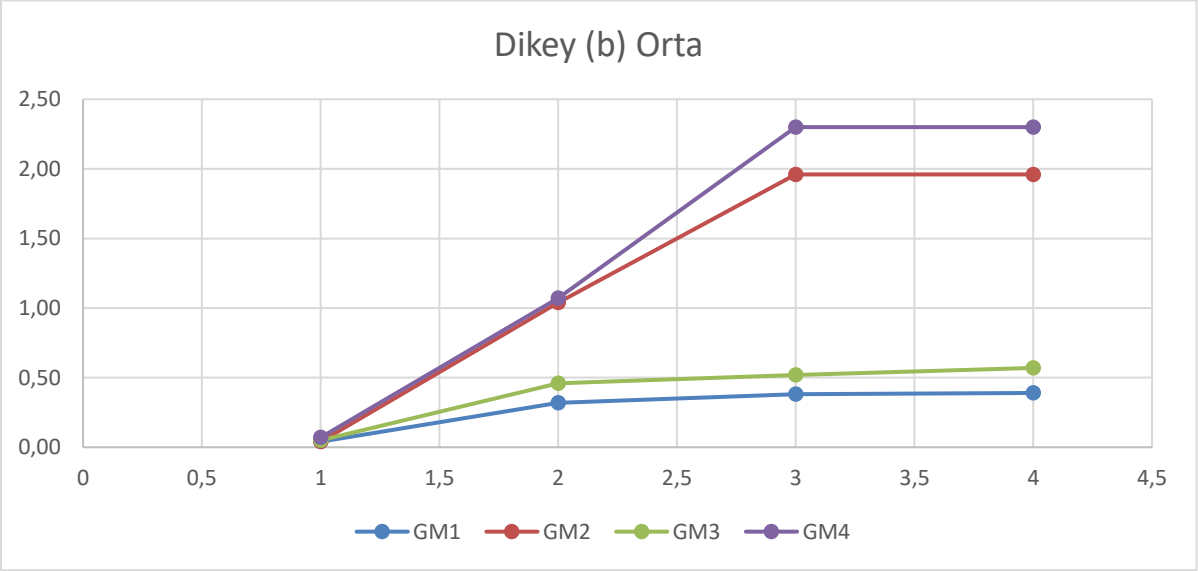


Şekil-8: Aynı Ni-W banyosundan kaplanmış olan 4 numunenin orta (b) yataydan alınmış değerleri

Aynı Ni-W banyosundan kaplanmış olan 4 numunenin orta (b) yataydan alınmış değerleri Şekil-8'de gösterilmiş olup bu değerlere göre yüzey pürüzlülük sıralaması şu şekildedir: GM2>GM4>GM1>GM3. Görüldüğü üzere birinci ve üçüncü numunenin yüzey pürüzlülük değerleri ikinci ve dördüncü numunelere göre daha düşük ve daha az pürüzlüdür.

Tablo-6: Aynı Ni-W banyosundan kaplanmış olan 4 numunenin orta (b) dikeyden alınmış değerlerinin tablo ile gösterimi

	Ra(µm)	**Rz(µm)**	**Rmaz(µm)**	**Rt(µm)**
GM1	0,04	0,32	0,38	0,39
GM2	0,04	1,04	1,96	1,96
GM3	0,05	0,46	0,52	0,57
GM4	0,07	1,07	2,30	2,30

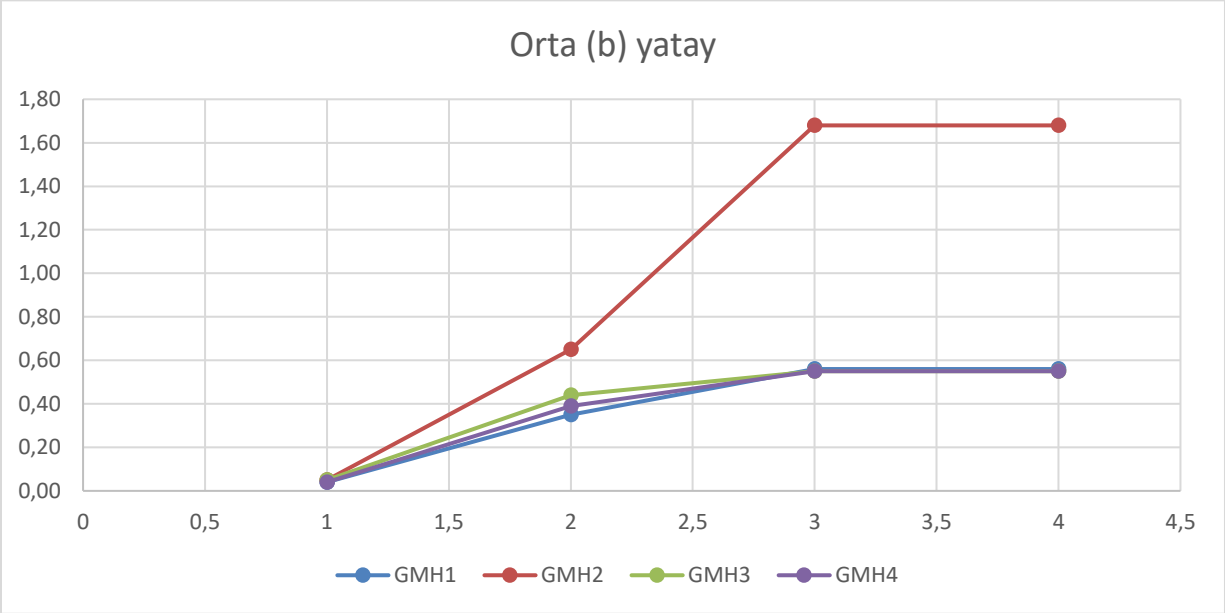


Şekil-9: Aynı Ni-W banyosundan kaplanmış olan 4 numunenin orta (b) dikeyden alınmış değerleri

Aynı Ni-W banyosundan kaplanmış olan 4 numunenin orta (b) dikeyinden alınmış değerleri Şekil-9'da gösterilmiş olup bu değerlere göre yüzey pürüzlülük sıralaması şu şekildedir: GM4>GM2>GM3>GM1. Görüldüğü üzere birinci ve üçüncü numunenin yüzey pürüzlülük değerleri ikinci ve dördüncü numunelere göre daha düşük ve daha az pürüzlüdür. Dolayısı ile numunelerin hem yatayının hem de dikeyinin orta noktalarından alınan değerlere göre birinci ve üçüncü numunelerin pürüzlülük değeri ikinci ve dördüncü numunelere göre daha iyidir.

Tablo-7: Aynı Ni-W/hBN banyosundan kaplanmış olan 4 numunenin orta (b) yataydan alınmış değerlerinin tablo ile gösterimi

	Ra(µm)	**Rz(µm)**	**Rmaz(µm)**	**Rt(µm)**
GMH1	0,04	0,35	0,56	0,56
GMH2	0,05	0,65	1,68	1,68
GMH3	0,05	0,44	0,55	0,55
GMH4	0,04	0,39	0,55	0,55

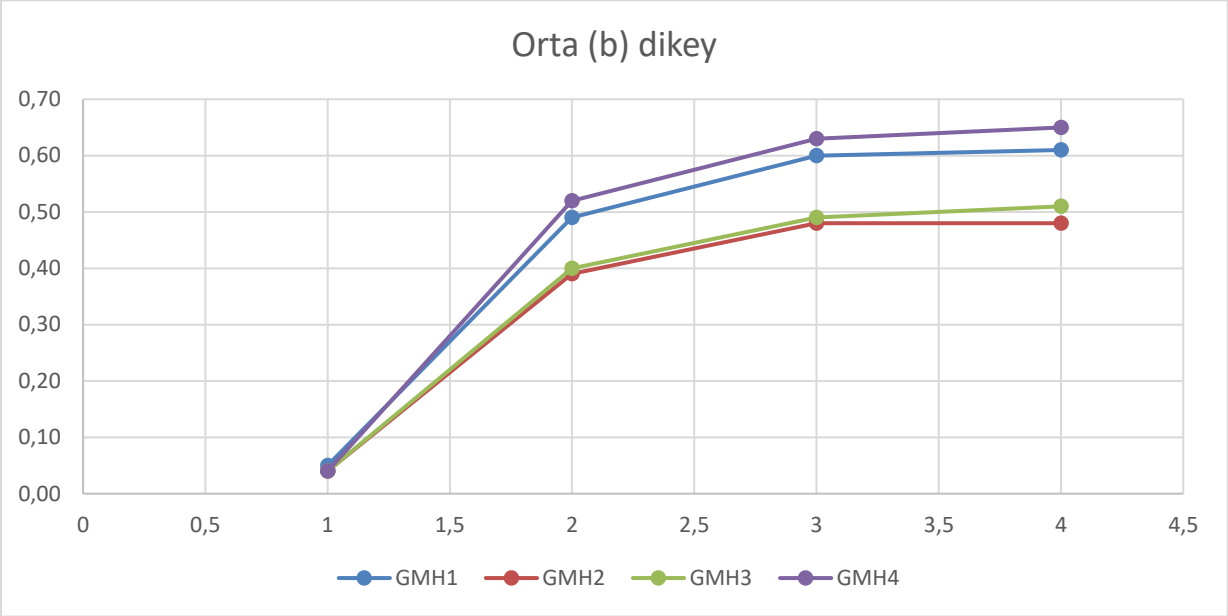


Şekil-10: Aynı Ni-W/hBN banyosundan kaplanmış olan 4 numunenin orta (b) yataydan alınmış değerleri

Aynı Ni-W/hBN banyosundan kaplanmış olan 4 numunenin orta (b) yataydan alınmış değerleri Şekil-10'da gösterilmiş olup bu değerlere göre yüzey pürüzlülük sıralaması şu şekildedir: GM2>GM3>GM4>GM1. Görüldüğü üzere birinci ve dördüncü numunenin yüzey pürüzlülük değerleri ikinci ve üçüncü numunelere göre daha düşük ve daha az pürüzlüdür.

Tablo-8: Aynı Ni-W/hBN banyosundan kaplanmış olan 4 numunenin orta (b) dikeyden alınmış değerlerinin tablo ile gösterimi

	Ra(µm)	**Rz(µm)**	**Rmaz(µm)**	**Rt(µm)**
GMH1	0,05	0,49	0,60	0,61
GMH2	0,04	0,39	0,48	0,48
GMH3	0,04	0,40	0,49	0,51
GMH4	0,04	0,52	0,63	0,65



Şekil-11: Aynı Ni-W/hBN banyosundan kaplanmış olan 4 numunenin orta (b) dikeyden alınmış değerleri

Aynı Ni-W/hBN banyosundan kaplanmış olan 4 numunenin orta (b) dikeyinden alınmış değerleri Şekil-11'de gösterilmiş olup bu değerlere göre yüzey pürüzlülük sıralaması şu şekildedir: GM4>GM1>GM3>GM2. Görüldüğü üzere üçüncü ve ikinci numunenin yüzey pürüzlülük değerleri dördüncü ve birinci numunelere göre daha düşük ve daha az pürüzlüdür. Dolayısı ile numunelerin hem yatayının hem de dikeyinin orta noktalarından alınan değerlere göre yüzey pürüzlülük değerleri değişkenlik göstermektedir.

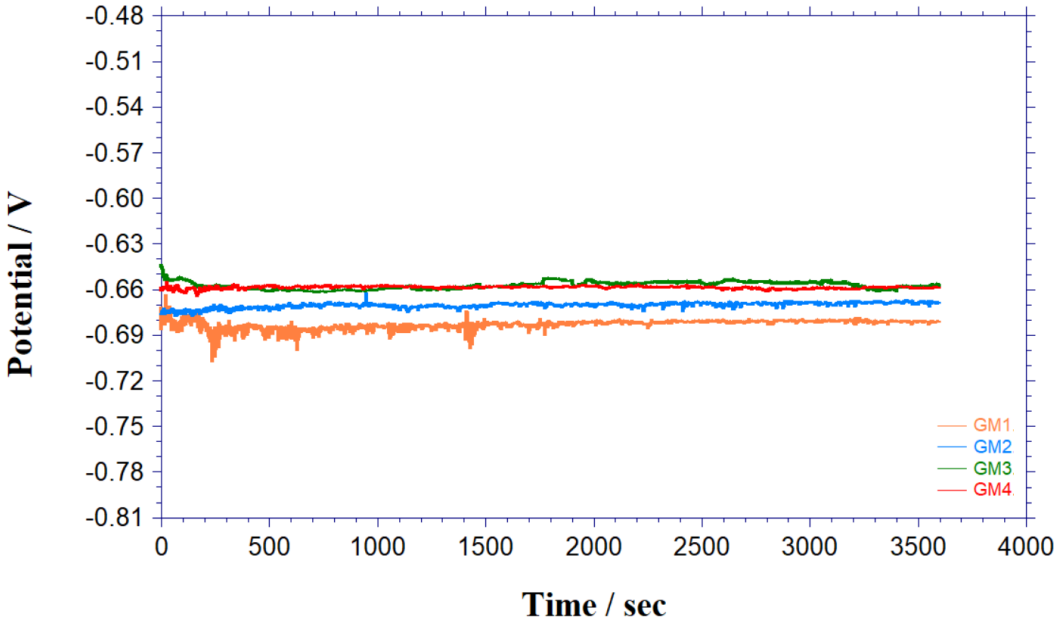
3.6. KOROZYON TESTİ

Kaplamaların korozyon performansları açık devre potansiyeli (OCP) ve Tafel ekstraspolasyon (potansiyodinamik polarizasyon eğrisi) yöntemleri ile analiz edilmiş olup bütün korozyon deneyleri %3,5 sodyum klorür (NaCl) sulu çözeltisi içerisinde uygulanmıştır.

Yapılan bu çalışmada elektrodepozisyon yöntemi kullanılarak kaplama yöntemi kullanılmıştır. Öncelikle kaplama yapılacak olan 2024 Al malzeme 2,5-2 cm olacak şekilde kesilmiştir. Kesilen 2024 Al malzemeler kaplama yüzeyinde kesimden kalan pürüzlü yüzey ve ince parçacıkların giderilmesi adına P 400 ile P1200 zımpara kağıtları ile birer dakika olacak şekilde zımparalanmış olup yüzey parlatılmıştır. Yüzey üzerindeki metal tozları önce alkol ile daha sonra da saf su ile temizlenmiştir. Daha sonra metal yüzeyi aseton ile yıkanmış tekrar saf su ile temizlenmiştir. Son olarak temizlenmiş olan 2024 Al malzeme HCl asit içerisine 10 s daldırılarak dağlanmış ve saf su ile temizlenmiştir. Böylelikle kaplama yapılacak yüzey kaplama işlemine hazır hale getirilmiştir. Kaplama yapılacak yüzeyin üst kısmı 0,5 cm olacak şekilde oje ile kapatılmış olup daha sonra Ni-W banyosu içerisine daldırılarak elektrodepolama yöntemi ile kaplanmıştır. Deneyler oda sıcaklığında ve 3 elektrotlu klasik sistemde yapılmıştır. Elektrokimyasal korozyon hücresinin tamamlayıcısı referans elektrot (RE) olarak Ag/AgCl karşıt elektrot olarak ve çalışma elektrotu (WE) olacak şekilde deney numunelerine tanımlanmıştır.

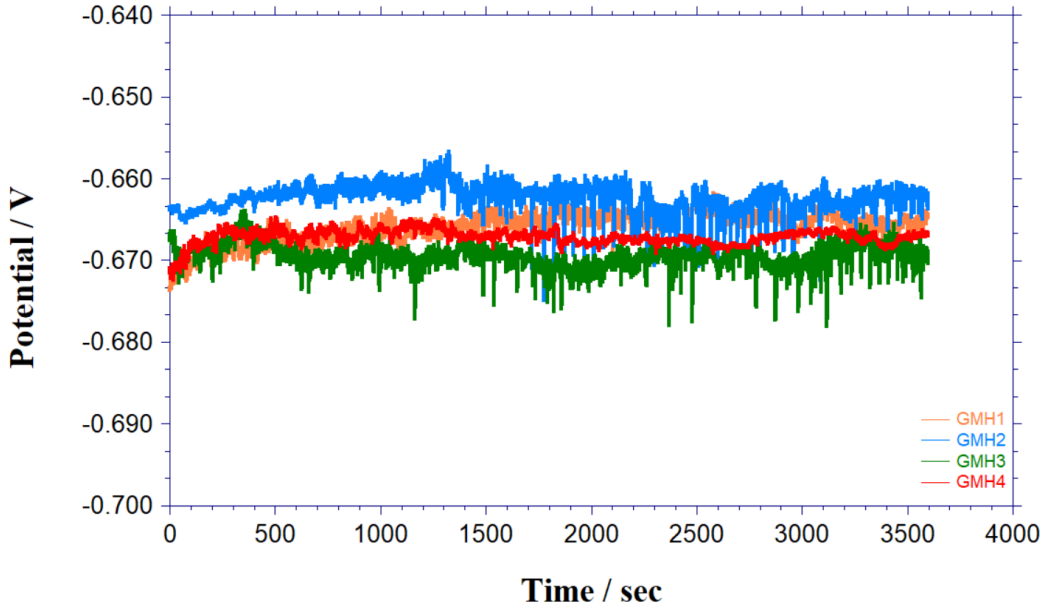
Tek bir banyodan çekilmiş olan dört ayrı numunenin OCP eğrileri Şekil-13 ve Şekil-14'te verilmiştir. OCP eğrileri ağırlıkça %3,5 NaCl çözeltisinde kararlı bir potansiyel değerleri elde edebilmek için 3600 s boyunca analiz edilmiştir. İyonik bir çözeltide kaydedilen OCP potansiyeli katodik ve anodik reaksiyonların bir denge potansiyelidir. Yani çözelti ortamı için yükseltgenme ve indirgenme aktivitelerini temsil etmektedir. Eğer çözelti ortamı korozif bir özellikte ise kaydedilen bu OCP potansiyelini korozyon potansiyeli olarak kabul edilebilir. Birbirleri ile mukayese edilen kaplamaların açık devre potansiyelleri açısından daha pozitif tarafta olanların daha negatif tarafta olanlara göre korozyona daha dirençli oldukları söylenebilir [12]

Şekil-13 incelendiğinde tüm numunelerin korozyon potansiyelleri birbirine oldukça yakın bir şekilde sıralanmıştır. Dört numunenin korozyon potansiyelleri yalnızca -0,64 V ile -0,69 V arasında yer almıştır. 3. ve 4. banyodan elde edilen numunelerin daha iyi korozyon direnci verdiği görülmektedir. Grafikte sıfıra en **uzak olan birinci** banyodan elde edilen numunenin en düşük korozyon direnci verdiği anlaşılmaktadır. Bir banyodan birden çok defa kaplama yapılması, kaplama özelliklerini kaybetmesinden ziyade kaplamanın korozyon direncini daha iyi konuma getirdiğini göstermektedir.



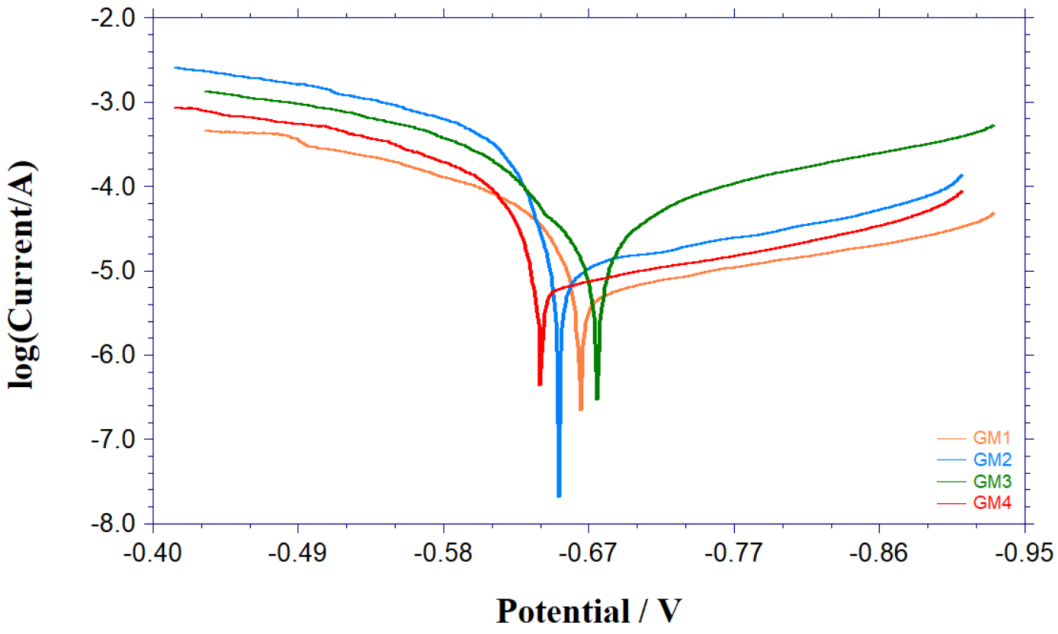
Şekil-13: Aynı Ni-W banyosundan kaplanmış olan 4 numunenin OCP eğrileri

Şekil-14 hBN ilave edilmiş banyodan üretilen numunelerin açık devre potansiyeli grafiğini göstermektedir. Grafiktende anlaşılacağı üzere korozyon potansiyelleri oldukça dar bir aralıkta sıralanmıştır. Açık devre potansiyeli ölçümlerinin ilk saniyesi ile 3600 sn arasında elde edilen grafiklerinde kaplama potansiyellerinde dikkate alınır bir artış veya azalış gözlemlenmemiştir. Bu durum kaplamanın korozyona karşı direncini koruduğunu göstermektedir. Ayrıca 4 numunenin de birbiriyle benzer karakter göstermesi bir banyodan birden fazla kaplama yapabilir olduğunu göstermektedir.



Şekil-14: Aynı Ni-W/hBN banyosundan kaplanmış olan 4 numunenin OCP eğrileri

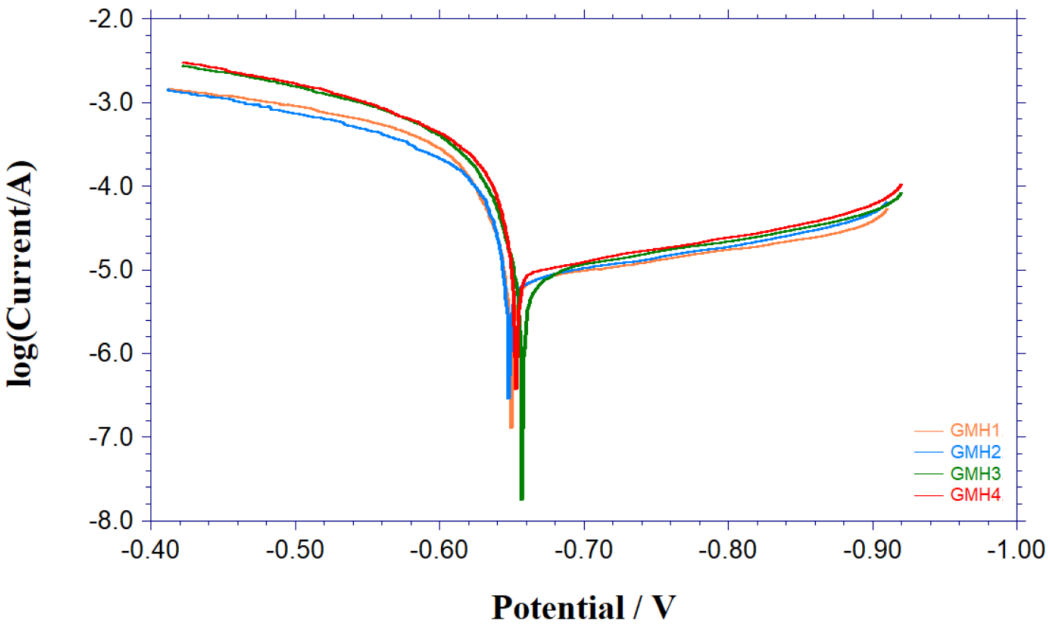
Tafel deneyleri açık devre potansiyelinin 0,25 V altından, 0,25 V üstüne kadar olan potansiyel aralığında 1 mV/s tarama hızında ve %3,5 NaCl içeren çözelti içerisinde gerçekleştirilmiştir. Numuneler Tafel ölçümü gerçekleştirilmeden önce dengeli bir potansiyel değeri elde edebilmek adına %3,5 NaCl içeren çözelti içerisinde bir saat süre ile bekletilmiştir. Şekil-15 ve Şekil-16 da Tafel ekstrapolasyon grafikleri karşılaştırma amacıyla bir arada gösterilmiştir. Şekil-15 ve Tablo-IX incelendiğinde en iyi korozyon direncini 1 numaralı numune vermiştir. Aynı şekilde Şekil-16 ve Tablo-X incelendiğinde en iyi sonucu 3 numaralı numune vermiştir.



Şekil-15: Aynı Ni-W banyosundan kaplanmış olan 4 numunenin TAFEL eğrileri

Tablo 9: Ni-W kaplamaların elektrokimyasal özellikleri

	Ecorr (mV)	Korozyon Oranı (mil/yıl)
GM1	−669	20,94
GM2	−655	37,66
GM3	−679	22,97
GM4	−643	34,86



Şekil-16: Aynı Ni-W/hBN banyosundan kaplanmış olan 4 numunenin TAFEL eğrileri

Tablo 10: Ni-W kaplamaların elektrokimyasal özellikleri

	Ecorr (mV)	Korozyon Oranı (mil/yıl)
GM1	−650	45,81
GM2	−648	56,42
GM3	−657	32,23
GM4	−653	71,00

4. Sonuçlar

Yapılan deneyler sonucunda;

1. Yapılan girinti testlerinde Ni-W ve Ni-W/hBN banyolarının banyo suyu değiştirilmeden tekrarlı yapılan numunelerinde zamanla azalan W ve hBN miktarından dolayı yüzey üzerindeki plastik deformasyonun 1. ve 2. numunede daha az yapışmanın daha iyi olduğu görülmüştür.
2. Ni-W banyosunda 1 numaralı numunenin a noktasında W yoğunluğunun diğer noktalara göre daha çok olduğu bu yüzden de sertliğin daha çok olduğunu söyleyebiliriz. Ni-W/hBN banyosunda ise 1 numaralı numunenin c noktasında en yüksek sertlik değeri görülmüş olup Ni banyosuna W ve hBN katılması ile sertliğin artmış olduğu görülmektedir.
3. Yapılan XRD görüntülemelerinde tek bir Ni-W banyosundan elde edilen 4 farklı numune içinde benzer sonuçlar elde edilmiştir. Bu durum ile bir banyodan birden fazla numune elde edilmesine rağmen, banyonun işlevselliğini devam ettirdiğini ve alaşım kaplamayı biriktirme istikrarını göstermiştir.. hBN takviyesi ile elde edilen Ni-W kaplamalarından elde edilen kompozit kaplamaların, alaşım kaplamalar ile benzer desenler çizdiği görülmüştür. Aynı zamanda tek bir banyodan kaplamalar elde edilmesine rağmen, banyonun kaplama işlevselliğinin devam ettiği de görülmüştür.
4. Aynı Ni-W banyosundan kaplanmış olan 4 numunenin yüzey pürüzlülük sıralaması göz önüne alındığında numunelerin hem yatayının hem de dikeyinin orta noktalarından alınan değerlere göre birinci ve üçüncü numunelerin pürüzlülük değeri ikinci ve dördüncü numunelere göre daha iyidir.
5. Aynı Ni-W/hBN banyosundan kaplanmış olan 4 numunenin yüzey pürüzlülük sıralaması göz önüne alındığında numunelerin hem yatayının hem de dikeyinin orta noktalarından alınan değerlere göre yüzey pürüzlülük değerleri değişkenlik göstermektedir
6. Ni-W kaplamalı dört numunenin korozyon potansiyelleri yalnızca -0,64 V ile -0,69 V arasında yer almış olup 3. ve 4. banyodan elde edilen numunelerin daha iyi korozyon direnci verdiği görülmüştür. Dolayısıyla bir banyodan birden fazla kaplama yapılması, kaplama özelliklerini kaybetmesinden ziyade kaplamanın korozyon direncini daha iyi konuma getirdiğini göstermektedir.
7. hBN ilave edilmiş banyodan üretilen numunelerin Tafel ekstrapolasyon grafikleri karşılaştırıldığında Ni-W banyosundan elde edilen kaplamaların en iyi korozyon direncini 1 numaralı numune de verdiği, aynı şekilde Ni-W/hBN banyosundan elde edilen kaplamaların ise en iyi sonucu 3 numaralı numune de verdiği görülmüştür.

Bu çalışmada yapılan Ni-W ve Ni-W/hBN tekrarlı banyolarından elde edilen ince film kaplamalı numunelerin 1 numaralı numuneler diğer numunelere göre yapışma kuvveti daha yüksek, sertliği daha fazla, korozyona daha dirençli ve W yoğunluğu daha fazladır.

Referanslar

[1] Y. D. Gamburg and G. Zangari, Theory and Practice of Metal Electrodeposition. Springer New York, 2011. doi: 10.1007/978-1-4419-9669-5.

[2] M. Demir, E. Kanca, and İ. H. Karahan, "Characterization of electrodeposited Ni–Cr/hBN composite coatings," J Alloys Compd, vol. 844, Dec. 2020, doi: 10.1016/j.jallcom.2020.155511.

[3] M. A. Farzaneh, M. R. Zamanzad-Ghavidel, K. Raeissi, M. A. Golozar, A. Saatchi, and S. Kabi, "Effects of Co and W alloying elements on the electrodeposition aspects and properties of nanocrystalline Ni alloy coatings," Appl Surf Sci, vol. 257, no. 13, pp. 5919–5926, Apr. 2011, doi: 10.1016/j.apsusc.2011.02.008.

[4] D. G. Portela, T. C. de M. Nepel, J. M. Costa, and A. F. de Almeida Neto, "Two-stages electrodeposition for the synthesis of anticorrosive Ni–W-Co coating from a deactivated nickel bath," Mater Sci Eng B Solid State Mater Adv Technol, vol. 260, Oct. 2020, doi: 10.1016/j.mseb.2020.114611.

[5] J. A. M. Oliveira, A. F. de Almeida, A. R. N. Campos, S. Prasad, J. J. N. Alves, and R. A. C. de Santana, "Effect of current density, temperature and bath pH on properties of Ni–W–Co alloys obtained by electrodeposition," J Alloys Compd, vol. 853, Feb. 2021, doi: 10.1016/j.jallcom.2020.157104.

[6] B. Li, W. Zhang, D. Li, Y. Huan, and J. Dong, "Microstructural, surface and electrochemical properties of a novel Ni–B/Ni–W–BN duplex composite coating by co-electrodeposition," Appl Surf Sci, vol. 458, pp. 305–318, Nov. 2018, doi: 10.1016/j.apsusc.2018.07.100.

[7] N. Vidakis, A. Antoniadis, and N. Bilalis, "The VDI 3198 indentation test evaluation of a reliable qualitative control for layered compounds," in Journal of Materials Processing Technology, Dec. 2003, vol. 143–144, no. 1, pp. 481–485. doi: 10.1016/S0924-0136(03)00300-5.

[8] Y. Zhang, L. Wei, S. Feng, and H. Liu, "Prefabrication of two-dimensional Ni–W/TiN films on oil-gas X52 steels by pulse electrodeposition," Journal of the Indian Chemical Society, vol. 99, no. 8, Aug. 2022, doi: 10.1016/j.jics.2022.100621.

[9] M. B. Porto, J. M. Costa, and A. F. de Almeida Neto, "Ni-W alloys and their anticorrosive properties: Ni removal efficiency from galvanic wastewater by electrodeposition," Journal of Water Process Engineering, vol. 36, Aug. 2020, doi: 10.1016/j.jwpe.2020.101250.

[10] A. Tozar and İ. H. Karahan, "A comparative study on the effect of collagen and h-BN reinforcement of hydroxyapatite/chitosan biocomposite coatings electrophoretically deposited on Ti-6Al-4V biomedical implants," Surf Coat Technol, vol. 340, pp. 167–176, Apr. 2018, doi: 10.1016/j.surfcoat.2018.02.034.

[11] H. Hüseyin BİLGİÇ et al., "S235JR ÇELİĞİ İÇİN TORNALAMA İŞLEMİ SONRASI YÜZEY PÜRÜZLÜLÜĞÜ VE KESİCİ TAKIM UÇ SICAKLIĞININ TAHMİNİ ÜZERİNE BİR ÇALIŞMA."

[12] A. Tozar and I. H. Karahan, "Structural and corrosion protection properties of electrochemically deposited nano-sized Zn-Ni alloy coatings," in Applied Surface Science, Nov. 2014, vol. 318, pp. 15–23. doi: 10.1016/j.apsusc.2013.12.020.

ISC'22 2nd International Symposium on Characterization
22-25 September 2022 Afyonkarahisar, Türkiye

Variation of Design Parameters for Micro-irrigation System Subunit Laterals by Using *LATCAD*

Gürol Yıldırım

Giresun University, Civil Engineering Department, Hydraulics Division, Giresun, Turkey.

Abstract

Micro-irrigation laterals deliver irrigation water to the plant root zones through emitters in a micro-irrigation (drip, trickle) system. Adequate analysis of micro-irrigation laterals is very important for the design and evaluation of micro-irrigation systems. Design of a lateral pipe includes the determination of the pipe length or the inside diameter, the required operating inlet pressure head and total friction head losses along the lateral assuming that the total flow rate at the inlet, characteristic of the emitter, and the acceptable level of uniformity are known previously. In this study, the forward-step method (FSM) that takes into account to the velocity head change and variation of the Reynolds number, which affects the selection of the proper friction coefficient formula to be applied along the different reaches of the lateral pipes was presented, and then, a computer program in Visual Basic 6.0 language named *LATCAD* was provided for analyzing and designing of micro-irrigation laterals. This method has the highest accuracy because only the basic equations of the hydraulics of steady pipe flow were used. In this study, variation of the operating inlet pressure head, total friction head losses and uniformity coefficients depend on the pipe lengths ranging between 25 and 250 m and the internal diameters ranging between 10 and 21 mm in zero slope condition were evaluated graphically in dimensionless form for practical purposes. These presented figures could also be used as the design charts.

Keywords: Forward-step method, Smooth pipe flow, Lateral hydraulics, Pipeline network, Software, *LATCAD*.

* Corresponding author e-mail: gurol.yildirim@giresun.edu.tr

1. Introduction

Adequate analysis of micro-irrigation lateral hydraulic is very important for the design and evaluation of the irrigation systems. One of the main tasks of the lateral hydraulic calculation, is the total friction head losses determination. In addition, the variation of the emitter outflows within limited values which defined by the uniformity coefficients is important. Because it leads to a relatively short variation in the Reynolds number range, and therefore, in a short run along the Moody's diagram. The design procedure which is based on the uniformity coefficients depending on the variation of discharge is accepted or refused. In fact, the real value of these coefficients, should be just obtained with taking into account all emitter outflows along the lateral line (Yıldırım, 2001).

The hydraulic design of a lateral or a sub main unit in a micro-irrigation system has been a problem tackled by many authors. The increasing progress in computer technology has led to the development of analytical and numerical methods of hydraulic analysis as the differential method (DM), Runge-Kutta numerical method (RKM), the energy-gradient line method (EGL), and modified EGL method, the finite-element method (FEM), the forward-step method (FSM), the successive-approximations method (SAM) and others. It has an exact solution, the forward-step calculation (Hathoot et al., 1993) applied to accurately establish the flow characteristics and also total head losses caused by friction along the lateral line. In fact, total friction head losses for micro-irrigation laterals are determined by the forward-step method, exactly, because of the kinematic head (velocity head) is taken into consideration to obtain accurate results.

Christiansen (1942) introduced the widely used friction correction factor that allows direct computation of friction head loss in a lateral. The friction correction factor (F) is a function of the number of outlets and the exponent of the velocity term in the friction formula used. The friction correction factor and its subsequent improvements were developed for fixed, periodic, or linear displacement laterals. It assumes the discharge through the lateral decreases linearly with the length of the lateral. The energy line approach is traditionally used for the

determination of the lateral pressure head profile (Wu and Gitlin, 1975; Wu and Yue, 1993). In this analytical approach, computations are considerably simplified by assuming that the emitter discharge is constant along the lateral. However, significant deviations from accurate numerical solutions in hydraulic analysis could be caused by this basic assumption of constant emitter outflow.

Warrick and Yitayew (1987, 1988), presented an alternative treatment in which the emitters are considered to be close enough that the lateral can be regarded as a homogenous system of a main tube and a longitudinal slot. This treatment includes a spatially variable discharge function. It dismissed the assumption of a uniform emitter discharge along the lateral, as suggested in methods presented by Wu and Gitlin (1975). This method, however, requires the numerical solution of a nonlinear second-order differential equation (DM).They showed that the velocity head had no significant effect on micro-irrigation lateral design, and therefore assumed a hydraulically smooth flow along the lateral pipe and disregarded the laminar flow that occurs at a downstream part of the pipe. Furthermore, they disregarded the fully turbulent flow that may occur at an upstream reach of the pipe. In addition Yitayew and Warrick (1986, 1988) presented a chart to design for trickle lateral. When the required average emitter discharge, the required uniformity of water application, and other conditions are given, a lateral length or inside diameter with operating inlet pressure head can be designed. Yitayew (1989), presented simplified approach which extension to the analytical solutions, for the determination of total friction head losses. In this approach, previously, the relative discharge values at the two boundaries (downstream and upstream end of the lateral) are computed and then total friction head losses are determined.

Hathoot et al. (1993) presented a stepwise-calculation method in forward form (FSM) for analysis and design of a micro-irrigation lateral. For the method presented in their paper, a small increment of pressure head is given at the inlet of the lateral. Based on the required average emitter discharge and the required uniformity of water application, design charts similar to that presented by Yitayew and Warrick (1988) was developed. In these charts, the relationship of the lateral length with uniformity coefficient and inlet pressure head and the relationship of the lateral inside diameter with uniformity coefficient and inlet pressure head for various lateral slope conditions and emitter characteristics can be calculated. This method has the highest accuracy because only the basic equations of the hydraulics of steady pipe flow were used. Scaloppi and Allen (1993), assuming constant outflow (linear total discharge variation along the lateral), derived pressure head distributions taking into account the effect of velocity head.

Kang and Nishiyama (1996.a) developed a method for designing single lateral and paired laterals on both flat and sloped fields to meet the required average emitter discharge and the required uniformity of water application using the finite element method (FEM). In this method the minor head loss due to a fitting (an emitter connection and riser, barb, or expansion) located at any section of pipe element is taken into account therefore, the fitting loss factor is expressed as a constant independent of the discharge of the pipe element.

Following this work, Kang and Nishiyama (1996.b) also presented the best sub-main position named “the Golden section search” is that location where the same minimum pressure exists in uphill and downhill laterals for designing of paired laterals. They used a finite-element scheme and a polynomial lateral flow rate equation, with the inlet pressure head as an independent variable, to determine pressure and flow distribution.

Valiantzas (1998) presented an analytical method which modified the energy- gradient line method (Wu and Gitlin, 1975; Wu and Yue, 1993) for direct calculation of lateral hydraulics based on the assumption that emitter outflow is spatially variable. In this study, constant discharge and variable discharge method are compared for the nine design examples which covering various combinations of design parameters and indicated that the results of variable discharge method are more accurate than other’s results.

Anwar (1999.a, 1999.b) developed a friction correction factor for laterals with outlets and outflow at the downstream end of lateral. He demonstrated the application of this friction correction factor to calculate friction head loss in tapered laterals. Following this work, Anwar (2000), two average correction factors introduced and demonstrated how these factors can be used to calculate the inlet pressure head for fixed, periodic, or linear displacement tapered laterals.

Vallesquino and Luque-Escamilla (2001) presented an alternative approach based on successive approximations scheme (SAM) for solving lateral hydraulic problems in laminar or turbulent flow. In this method

minor head losses and kinematic heads are neglected and the emitter outflow is accepted as a discrete and non constant variable event by means of Taylor polynomials used to calculate flow rates along the lateral. In addition, total head losses due to friction are calculated with a non constant logarithmic friction factor which includes relative roughness of the lateral pipe. This algorithm, allows hydraulic computation for a set of connected laterals (with different pipe line diameter, slope, flow regime, or emitter spacing) if a residual outflow is used. However, total friction head losses, water application uniformity and inlet pressure head can be hard to calculate because of the requirement an excessive calculation effort. Following this work, Vallesquino and Luque-Escamilla (2002) presented an alternative approach based on the previous iterative technique using equivalent friction factor instead of the variable friction factor along lateral for predicting friction drop and outflow variation in designing single or multi-diameter sprinkler and micro-irrigation laterals. However, each step of this algorithm was clearly analyzed and discussed by Yıldırım and Ağıralioğlu (2004.c) from important points of view. They reported that the algorithm is less efficient for predicting flow variables and it gives some deviation from the accurate numerical stepwise calculation method for different design cases.

Valiantzas (2002.a), developed a continuously variable outflow approach considering the effect of the number of outlets. In this approach, analytical expressions for determining the inlet pressure head and global statistical parameters characterizing the outflow distribution (Christiansen uniformity coefficient, pressure head variation) are developed for design and evaluation purposes. In the latest study, Valiantzas (2002.b) presented a new analytical approach based on the two previous basic assumptions for designing multi-diameter irrigation laterals. In these methods, analytical equations were presented for the case of obtaining general solution by the direct calculation.

Yıldırım and Ağıralioğlu (2004.a) developed a simplified analytical approach for designing tapered two-diameter micro-irrigation laterals based on the variable outflow approach. They presented a linear solution of the simple power equation and compared it with the previous study (Valiantzas, 2002.b) on different ground slope conditions. They reported that the linear solution yielding more accurate predictions for determining flow parameters than those of the mentioned literature for different design cases.

In the recent study, Yıldırım and Ağıralioğlu (2004.b) analyzed and classified some lateral hydraulic design methods based on the assumption of spatial variance of emitter outflow for comparative purposes from points of view such as solution methods, basic assumptions, used formulations and differences in application (Yıldırım and Ağıralioğlu, 2003.a; 2003.b). In their study, the comparison test was applied for the seven design examples with the special limited design conditions of some calculation methods, such as emitter discharge exponent, flow regime and velocity head consideration to cover various combinations of irrigation parameters, varying emitter discharge exponents and different ground slope conditions. The results were shown graphically in dimensionless form, for practical purposes.

In this study, the forward-step method (FSM) was developed by Hathoot et al. (1993) is presented. Resulting a computer program in Visual Basic 6.0 language named *LATCAD* is provided for analyzing and designing micro-irrigation laterals. According to the presented method, for a lateral pipe with equally spaced individual emitters and uniform slope the comparison test is extended for various combinations of irrigation design parameters.

Examples will be presented for the smooth pipe case and for the most commonly used values of emitter exponent (y = 0.2, 0.5 and 1.0), zero slope condition (S_0 = 0.0), and various lengths and inside diameters of the lateral. For the sake of comparison, the design curves in dimensionless form that relate the required operating inlet pressure head, the uniformity coefficients, the total friction head losses with the lateral lengths and inside diameters were developed.

2. Principles of Lateral Hydraulics

A trickle distribution system is a hydraulic structure whose design is limited by the irrigation uniformity and consequently by the friction head losses (Ağıralioğlu and Yıldırım, 2002). Design of this system depends upon a good understanding of lateral hydraulics and emitter characteristics. Hydraulically, flow in the lateral pipe is considered to be a steady, spatially varied flow with decreasing emitter outflow in the downstream direction. With decreasing discharge along the lateral, the energy gradient line decreases.

Generally, emitters are usually identical, and installed at an equal spacing on the lateral line. The flow characteristics of trickle emitters are typically described by a function of the form (Howell and Hiler, 1974; Keller and Karmeli, 1974)

$$q_n = cH_n^{\,y} \tag{1}$$

in which q_n is the outflow from an individual emitter; H_n is the pressure head in the lateral pipe at the emitter under consideration; c is the emitter coefficient that accounts for areal and discharge effects and makes the units correct. For a lateral, the spacing between successive individual emitters (s), the emitter coefficient (c), and the cross-sectional area of the lateral pipe (A), are taken as constants. The emitter discharge exponent y characterizes the flow regime and emitter type. Values of y should range from zero for a pressure-compensating emitter to 1.0 for an emitter in a laminar flow regime. The value of the discharge exponent should be close to 0.5 for emitters operating in a turbulent flow regime. The higher value of the emitter discharge exponent, the greater degree of care is required to maintain the proper pressure distribution along the lateral for the same uniformity of application (Cuenca, 1989).

Let us consider the lateral stretch as shown in Fig.1. If there are N emitters on the lateral with a common spacing S, the number of spacing will be (N – 1) and the length of the lateral is the distance between the first and last emitter, L = S (N - 1).

As shown in Fig.1, H_1 is the initial inlet pressure head, Q_1 the initial lateral discharge ($Q_1 = N\, q_{av}$) upstream from the first emitter, and q_1 the outflow of the first emitter, which may be written as

$$q_1 = c\, H_1^{\,y} \tag{2}$$

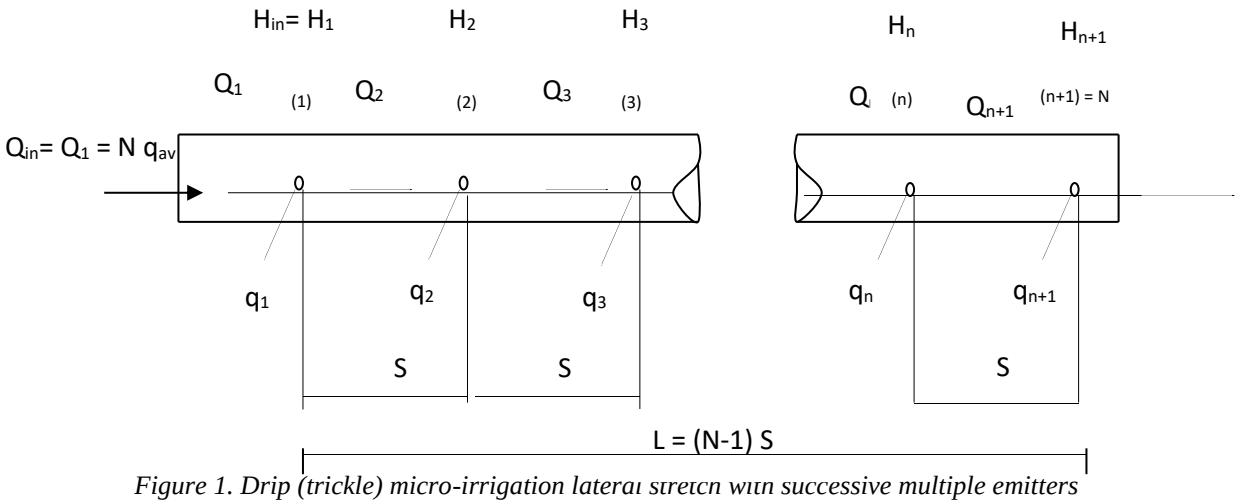


Figure 1. Drip (trickle) micro-irrigation lateral stretch with successive multiple emitters

Assuming that the outflow varies continuously in space along the lateral (the number of emitters is sufficiently large), the outflow per unit length (q) can then be described by

$$q = \left(\frac{c}{s}\right) H_n^{\,y} \tag{3}$$

If continuity is preserved along lateral, the conservation of mass is written in the general following form

$$\frac{dQ}{dx} + \frac{dA}{dt} = -q \tag{4}$$

where Q is the lateral discharge; x and t are space and time coordinates. For steady flow condition $(dA/dt = 0)$ in irrigation laterals, the continuity equation, Eq.(4), may be rewritten as follows

$$A\frac{dv}{dx} = -q \tag{5}$$

where v is the velocity of flow in the lateral pipe.

As shown in Fig.1, using the continuity equation, Eq.(5), the lateral discharge, Q_{n+1}, at the pipe reach between successive emitters (n) and (n+1), can be obtained from

$$Q_{n+1} = Q_n - q_n \tag{6}$$

The lateral discharge between the first and second emitters Q_2 can be evaluated from Eq. (6) in the special form

$$Q_2 = Q_1 - q_1 = (N\ q_{av}) - (c\ H_1^{y}) \tag{7}$$

The momentum effect resulting from decreasing the discharge in downstream direction, the conservation of momentum equation is given by the following form (Streeter and Wylie, 1979)

$$\sum F = \rho\left(Q_{n+1}V_{n+1} - Q_nV_n\right) \tag{8}$$

where $\sum F$ is the change of pressure force; ρ is the density of irrigation water; V_n and V_{n+1} are the flow velocity between successive emitters (n-1)~(n) and (n)~(n+1), respectively.

Using the conservation of momentum equation, Eq.(8), the change of pressure head, ΔH_{n+1}, due to change of momentum between successive emitters (n) and (n+1) resulting from decreasing the discharge from Q_n to Q_{n+1}, may be written as follows

$$\Delta H_{n+1} = \frac{\left(Q_{n+1}^{\ 2} - Q_n^{\ 2}\right)}{gA^2} \tag{9}$$

where g is the acceleration due to gravity.

Watters and Keller (1978) have shown that for small diameter smooth pipes used in trickle laterals, the Darcy-Weisbach friction formula can give accurate predictions for frictional losses based on conservation of energy. Therefore the following expression can be written

$$H_{fn+1} = f_{n+1}\frac{s}{D}\frac{Q_{n+1}^{\ 2}}{2gA^2} \tag{10}$$

where H_{fn+1} is the friction head loss between successive emitters (n) and (n+1); f_{n+1} is the Darcy-Weisbach friction coefficient for the pipe reach between successive emitters (n) and (n+1); D is the internal diameter of the lateral pipe.

Eq. (10) may be rewritten simplifying

$$H_{fn+1} = \frac{8S}{\Pi^2 gD^5} f_{n+1}Q_{n+1}^{\ 2} \tag{11}$$

If the lateral pipe has a uniform slope S_0 , the difference in levels of points (n) and (n+1) may be given by

$$(z_n - z_{n+1}) = \pm\ S\ S_0 \tag{12}$$

The positive sign is for laterals sloping downward and the negative for upward slopes, z_n and z_{n+1} are elevations of successive emitters (n) and (n+1) respectively, above an arbitrary datum.

Using conservation of the energy principle with Eq.(9) and Eq.(11), between successive emitters (n) and (n+1), the following form can be obtained

$$H_n + \frac{V_n^2}{2g} + z_n = H_{n+1} + \frac{V_{n+1}^2}{2g} + z_{n+1} + H_{fn+1} + \Delta H_{n+1} \quad (13)$$

where H_n and H_{n+1} are pressure head for the successive emitters (n) and (n+1); $\frac{Q_n^2}{2gA^2}$ and $\frac{Q_{n+1}^2}{2gA^2}$ are velocity head under consideration.

Solving Eq.(13) for the pressure head at the emitter (n+1), H_{n+1} is related to H_n by the following equation

$$H_{n+1} = H_n + \left(\frac{Q_n^2}{2gA^2}\right) - \left(\frac{Q_{n+1}^2}{2gA^2}\right) + (z_n - z_{n+1}) - h_{n+1} - \Delta H_{n+1} \quad (14)$$

Combining conservation of mass and momentum principles Eq.(6) and Eq.(9) with Eq.(11) and Eq.(12), into conservation of energy principle, Eq.(14), and simplifying

$$H_{n+1} = H_n + \frac{3}{2gA^2}\,[Q_n^2 - (Q_n - q_n)^2] - f_{n+1}\frac{8S}{\Pi^2 g D^5}(Q_n - q_n)^2 \pm S S_0 \quad (15)$$

For convenience, Eq.(15) is put in the form

$$H_{n+1} = H_n + B\,[Q_n^2 - (Q_n - q_n)^2] - E\, f_{n+1}(Q_n - q_n)^2 \pm S S_0 \quad (16)$$

in which

$$B = \frac{3}{2gA^2} \quad (17)$$

and

$$E = \frac{8S}{\Pi^2 g D^5} \quad (18)$$

As seen from the above hydraulic analysis, there are four basic equations in the lateral hydraulics. These equations are: 1. the emitter discharge-pressure head relationship as Eq. (1), 2. the continuity equation as Eq. (5), 3. the Darcy-Weisbach friction formula as Eq. (10), 4. the conservation of energy equation coupled with the conservation of momentum equation as Eq. (13). On the other hand, there are four unknown hydraulic variables (Q_{n+1}, q_{n+1}, H_{n+1} and H_{fn+1}) at any location of lateral (n+1), with the known previous values (Q_n, q_n, and H_n), and the other parameters (z_n, z_{n+1}, f_{n+1}, D, s, c and y). These unknown variables can be estimated using some calculation method.

3. Water Application Uniformity

One of the main tasks of the lateral hydraulic calculation is to provide a sensitive balance between the inlet pressure head, the water application uniformity, and the total frictional losses along lateral. In designing laterals, the variation of the emitter discharge within limited values, which are defined in the uniformity coefficients, namely the Christiansen's uniformity coefficient (UC) and the lower-quarter distribution uniformity coefficient (DU_{LQ}), is important, because it leads to a relatively short variation in the Reynolds number range, and therefore, in a short run along the Moody's diagram.

The design procedure, which is based on the uniformity coefficients depending on the variation of emitter discharge, is accepted or refused. In fact, the real value of these coefficients should be obtained by taking into account all emitter discharges along the lateral line (Yıldırım and Ağıralioğlu, 2001).

Obviously, individual emitters are convenient to consider expressions for emission uniformity, which is the relationship between the minimum and average emitter discharge within the system (Ağıralioğlu et al., 2000). The Christiansen's uniformity coefficient and the lower-quarter distribution uniformity are used here to express uniformity of emitter discharge throughout the system. DU_{LQ} is defined as the average discharge for the lower-quarter of the lateral divided by the overall average q_{av} (Yitayew and Warrick, 1988)

$$UC = 1 - \frac{1}{Nq_{av}} \sum_{n=1}^{n=N} |q_n - q_{av}| \quad (19)$$

and

$$DU_{LQ} = \frac{4 \times \left[\sum_{n=\frac{3N}{4}}^{n=N} (q_{low})_n \right]}{N \times q_{av}} \quad (20)$$

where q_{av}: average emitter discharge along the lateral pipe; q_n: discharge of emitter (n) and $(q_{low})_n$: discharge of the lower-quarter emitter n = 3N/4.

The uniformity of water application can also be evaluated using the emitter flow variation (V_{HM}). V_{HM} is defined by (Bralts et al., 1981; Warrick, 1983)

$$(V_{HM}) = (V_H^2 + V_M^2)^{1/2} \quad (21)$$

where V_H = effective pressure head variation at the emitters; and V_M = manufacturing variation of emitters.

4. Coefficient of Friction (*f*)

Micro-irrigation laterals are generally made of smooth materials. Flow in laterals is generally turbulent : $3000 < R \leq 10^5$, sometimes fully turbulent flow : $10^5 < R < 10^7$, exists at the upstream end of the lateral and flow becomes laminar at the downstream reach where the velocity decreases to zero. For laminar flow : $R < 2000$, the friction coefficient is given (Warrick and Yitayew, 1988; Hathoot et al., 1993)

$$f = \frac{64}{R} = \frac{64\nu}{VD} \qquad \left(R = \frac{VD}{\nu}\right) \quad (22)$$

or

$$f_n = \frac{16\Pi D\nu}{Qn} \quad (23)$$

in which R : the Reynolds number and ν : the kinematic viscosity of water.
For turbulent flow: $3000 < R \leq 10^5$, the Blasius equation can be used :

$$f = 0.316\, R^{-0.25} \quad (24)$$

or

$$f_n = 0.316 \left(\frac{\Pi D\nu}{4Q_{ni}}\right)^{0.25} \quad (25)$$

For fully turbulent flow : $10^5 < R < 10^7$, we have

$$f = 0.130\, R^{-0.172} \quad (26)$$

or

$$f_n = 0.130 \left(\frac{\Pi D\nu}{4Q_n}\right)^{0.172} \quad (27)$$

5. Software (*LATCAD*) Development

A flowchart for *LATCAD*, as given in Fig. 2, can be used to evaluate the flow characteristics along the lateral pipe and the corresponding uniformity coefficients. In practice the average emitter discharge q_{av} , the corresponding pressure head H_{av}, the flow exponent y , the number of emitters n , the spacing between emitters S, and the slope S_0 and inside diameter of the lateral pipe D are assigned in advance for a certain design. The

following algorithm is taken into account in designing of the computer program:

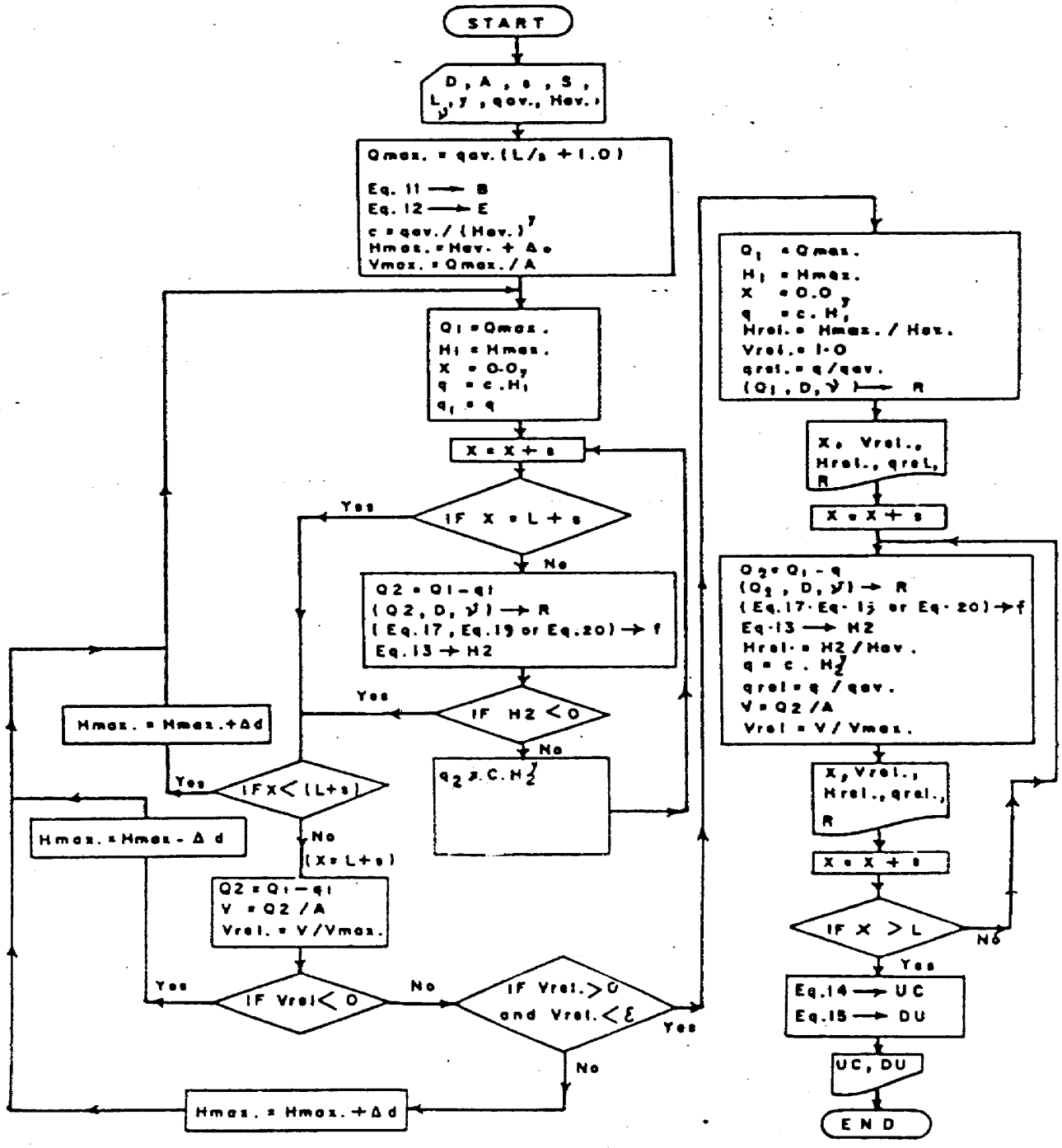


Figure 2. Flowchart for computer program (LATCAD)

6. Steps of Algorithm:

1. The initial pressure head H_{max} is first assumed by adding a reasonable head increment Δ_0 to the average head H_{av} (Initial condition).

2. The outflow of individual emitters q_i is evaluated stepwise starting from the first emitter, and in each step the corresponding lateral discharge Q_i is evaluated.

3. At each step the Reynolds number is calculated and the proper friction coefficient formula is used to evaluate the head loss due to friction and therefore the new pressure head by applying Eq. (16).
4. If Eq. (16) yields negative values of H at any emitter, this would indicate that the assumed
5. As negative values of H disappear, other conditions should be fulfilled.
6. The velocity at any reach of the lateral pipe should be positive (Boundary condition); otherwise, this would indicate that the sum of emitter outflows is greater than the initial discharge Q_{max} , which means that H_{max} should be decreased by Δ_d (Δ_d , being divided periodically by 10 on increasing or decreasing H_{max}).
7. The discharge in the lateral pipe downstream from the last emitter should be zero, which forms an important boundary condition.
8. Practically, this condition is satisfied if the relative velocity at that part becomes less than a sufficiently small quantity, ε .
9. As the proper value of H_{max} is reached, outflow, pressure head for each emitter, and the velocity at the corresponding reach of the lateral pipe are evaluated.
10. Finally, uniformity of the system is evaluated by computing UC and DU_{LQ} as given by Eq. (19) and Eq. (20) , respectively.

7. Evaluation of Design Procedure

Design procedures for a lateral pipe can be ordered in the following four steps generally (Kang and Nishiyama, 1996.a):
1. To give a series of values for the design parameter from smallest to largest.
2. To find the required operating inlet pressure head (H_{in}) that can create the required average emitter discharge, and to evaluate the total friction head losses and the uniformity of water application for each given value.
3. To plot the curves of the uniformity of water application, the required operating inlet pressure head and the total friction head losses versus the design parameter.
4. To find the solutions of the design parameter the required operating inlet pressure head and the total friction head losses from the curves plotted in the third step according to the required uniformity of water application.

8. Determination of Design Interval of the Operating Inlet Pressure Head

As seen from the above considerations, an important objective of this analysis is the proper inlet pressure head determination which can be varied within limited values in the design algorithms (boundary conditions). It means, preliminary increase in average piezometric head (Δ_0) varies ranging from minimum inlet pressure head toward maximum inlet pressure head. The design phases as follows (Yıldırım and Ağıralioğlu, 2002):

1. Determine inlet pressure head ranges (A, B) where inlet pressure head is located in. In (A, B), A : minimum inlet pressure head and B : maximum inlet pressure head.

a. Obtain minimum inlet pressure head, according to the 1. and 4. steps in the design algorithms (for H_1, if the smaller values than A are design, this would indicate that the negative value of the pressure head at any emitter would be appeared).

b. Obtain maximum inlet pressure head, according to the 1. and 5. steps in the design algorithms (for H_1, if the larger values than B are design, this would indicate that the sum of emitter outflows is greater than the initial lateral discharge Q_1, which means that, back flow occurs from downstream end toward upstream direction of lateral).

2. As the proper values of the inlet pressure head ($A \leq H_1 \leq B$) are obtained, the favorable value of H_1 should be investigated. In line with this concept, these following considerations should be taken into account:

a. For H_1, if A is selected for designing a lateral, the value of residual lateral discharge at the downstream end from the last emitter larger than acceptable small quantity, ε, either zero. Obviously, an important boundary condition doesn't keep to the right by the 5. step in the design algorithms. Whereas, the residual lateral discharge decreases from A toward B, increasingly, and then for B, it has a sufficiently small value, approximately zero.

b. In designing of a lateral, the design parameters should be determined in order to minimize of total friction drop at the end of lateral. In this respect, if A is selected, the total friction drop have major values and then,

from A toward B, have minor values, increasingly. However, if B is selected the total friction head losses are minimized.

c. In the design procedure, the water application uniformity is unknown parameter; other parameter (inlet pressure head) should be varied have the highest level of uniformity. Obviously, water application uniformity increases from A toward B, and then for B it has the highest value. As a result, the proper inlet pressure head is reached at B, total friction drop and residual flow rate are minimized whereas the water application uniformity is maximized.

9. Design Examples

In designing of the lateral pipe for a micro-irrigation system it is also assumed that the emitter outflow-pressure head relationship, average flow rate and characteristic of the emitter and acceptable level of uniformity are known a priori. It often remains to design either the pipe length or the inside diameter, the total discharge at the inlet, the pressure head at the inlet of lateral, the head loss due to friction along the lateral with the other variables known. The following are two design examples based on each concept.

Example 1. Design of Lateral Length, Operating Inlet Pressure Head and Total Friction Drop (Head Losses) Using Design Curves

It is given that the emitter outflow-pressure head relationship: $q = 3.58\ 10^{-7}\ H^{0.5}$, average flow rate of emitter : $q_{av} = 4\ lh^{-1}$ ($1.111\ 10^{-6}\ m^3s^{-1}$), spacing between successive interior emitters: S = 1.0 m, design uniformity coefficient : UC = 0.95, the inside diameter of lateral : D = 14 mm, the kinematic viscosity of water at 20 ^{0}C $\nu = 1.01\ 10^{-6}\ m^2s^{-1}$. The values that must be determined are : (1) Length of lateral, (2) the pressure head at the lateral inlet, (3) the frictional head loss along lateral.

Solution: On the basis of the forward-step method discussed, the values of the inlet pressure H_{in}, the frictional head loss H_f and the uniformity coefficients UC, DU_{LQ} are evaluated for various pipe lengths ranging between 25 and 250 m (D = 0.014 m). In each calculation the values of design parameters are obtained from output of *LATCAD* and plotted in dimensionless form for practical purpose which could also be used as a design chart (Figure 3.a, 3.b, 3.c, 3.d). From Figure 3.b and for design uniformity coefficient UC = 0.95; length of the lateral, L = 125 m is found. On the other hand, from Figure 3.a and for L = 125 m; we have relative pressure head at the inlet, $H_{in}/H_{av} = 1.26$. From the emitter outflow-pressure head relationship we find:

$$H_{av} = \left(\frac{q_{av}}{c}\right)^{\frac{1}{y}} = \left(\frac{1.11110^{-6}}{3.5810^{-7}}\right)^{\frac{1}{0.5}} = 9.631\ \text{m.}$$

Resulting: $H_{in} = 1.26*9.631 = 12.135$ m is found. From Figure 3.c and for L = 125 m; we have relative friction drop, $H_F/H_{in} = 0.326$ and then the frictional head loss along the lateral, $H_F = 0.326*12.135 = 3.956$ m is found. For the second uniformity design parameter DU_{LQ} ,from Figure 3.d and for L = 125 m ; $DU_{LQ} = 0.915$ is found.

The same example was solved by Warrick and Yitayew (1988.b) using differential method based on numerical solution of a nonlinear second-order differential equation and also more accurate analytical forward-step method developed by Hathoot et al. (1993). The results were presented here for the sake of comparison.
Differential method gives L = 126 m, $H_{in} = 12.49$ m, $H_F = 3.841$ m and $DU_{LQ} = 0.925$ whereas Yitayew's (1989) head loss equation which extension of the basic analytical solution gives L = 125 m, $H_{in} = 12.536$ m and $H_F = 3.883$ m. However, Hathoot et al. (1993) give: L = 129 m, and $H_{in} = 12.69$ m.

The difference between two basic solution may be attributed to this cause: In the FSM variation of the Reynolds number along the lateral pipe is considered whereas in DM the Blasius equation is used along of full lateral also including the last downstream length at the end of lateral in which flow is actually laminar. It is worthy to note that the results of computer program are in close agreement with those of other researcher's.

Example 2. Design of Lateral Inner Diameter, Operating Inlet Pressure Head and Total Friction Drop (Head Losses) Using Design Curves

Design the following parameters for design uniformity coefficient UC = 0.95 and the lateral length L = 150 m using the same data given in Example 1: (1) the inside diameter of the lateral, (2) the pressure head at the lateral inlet, (3) the frictional head loss along lateral.

Solution: The values of the inlet pressure H_{in}, the frictional head loss H_f and the uniformity coefficients UC, DU_{LQ} are evaluated for various pipe internal diameters ranging between 10 mm and 21 mm (L = 150 m). In each calculation the values of design parameters are obtained from output of *LATCAD* and plotted in dimensionless form for practical purpose which could also be used as a design chart (Figure 4.a, 4.b, 4.c, 4.d). From Figure 4.b and for design UC = 0.95; inside diameter of the lateral, D = 16.4 mm is found. On the other hand, from Figure 4.a and for D = 16.4 mm; we have relative pressure head at the inlet, H_{in}/H_{av} = 1.195. From the emitter outflow-pressure head relationship we find,

$$H_{av} = \left(\frac{q_{av}}{c}\right)^{\frac{1}{y}} = \left(\frac{1.11110^{-6}}{3.5810^{-7}}\right)^{\frac{1}{0.5}} = 9.631 \text{ m.}$$

Resulting: H_{in} = 1.195*9.631 = 11.51 m is found. From Figure 4.c and for D = 16.4 mm ; we have relative friction drop, H_F/H_{in} = 0.277 and then the frictional head loss along the lateral, H_F = 0.277*11.51 = 3.188 m is found. For the second uniformity design parameter DU_{LQ}, from Figure 4.d and for D = 16.4 mm; DU_{LQ} = 0.925 is found.

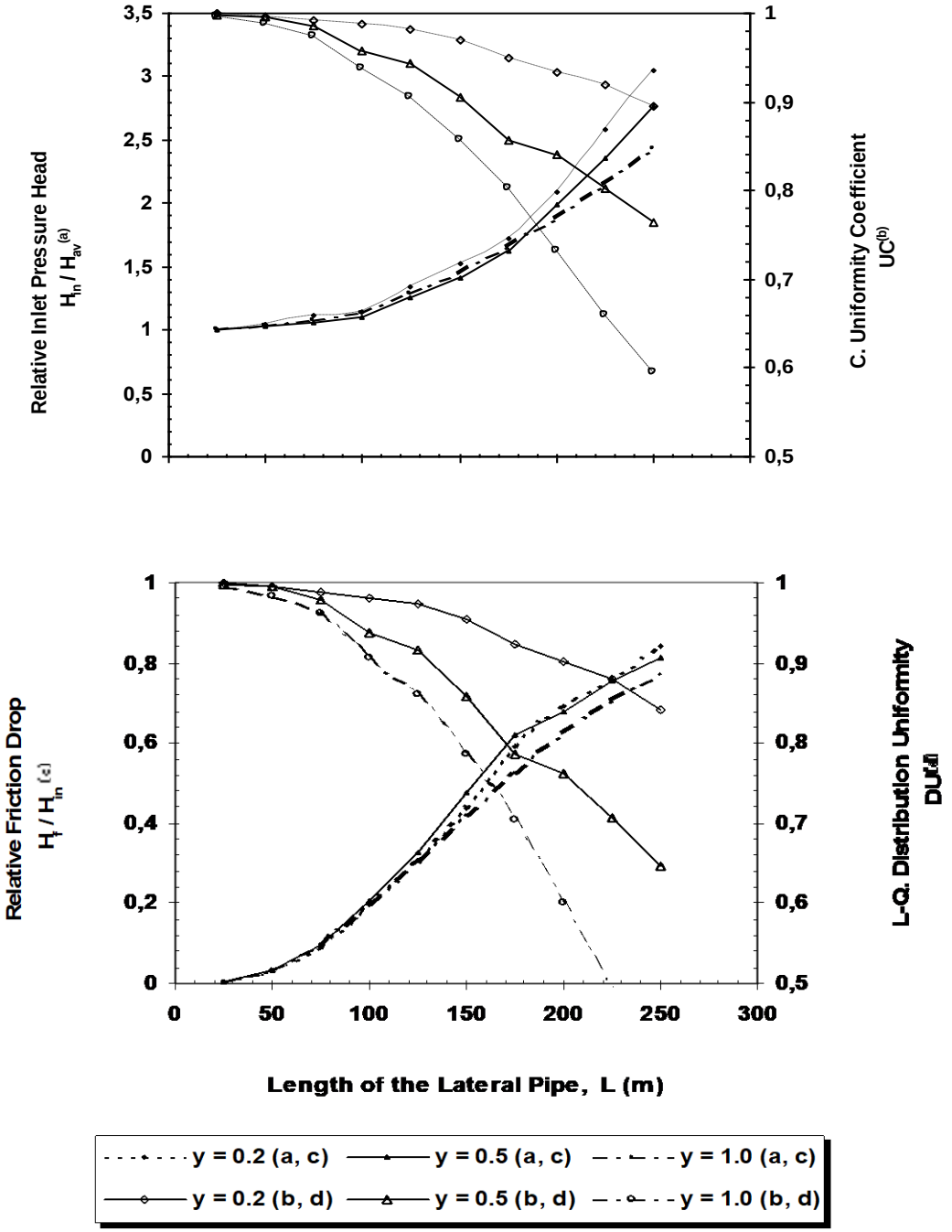


Figure 3 (a, b) Variation of Relative Inlet Pressure Head and Christiansen Uniformity Coefficient with Lateral Length (c, d) Variation of Relative Friction Drop and Lower-Quarter Distribution Uniformity Coefficient with Lateral Length

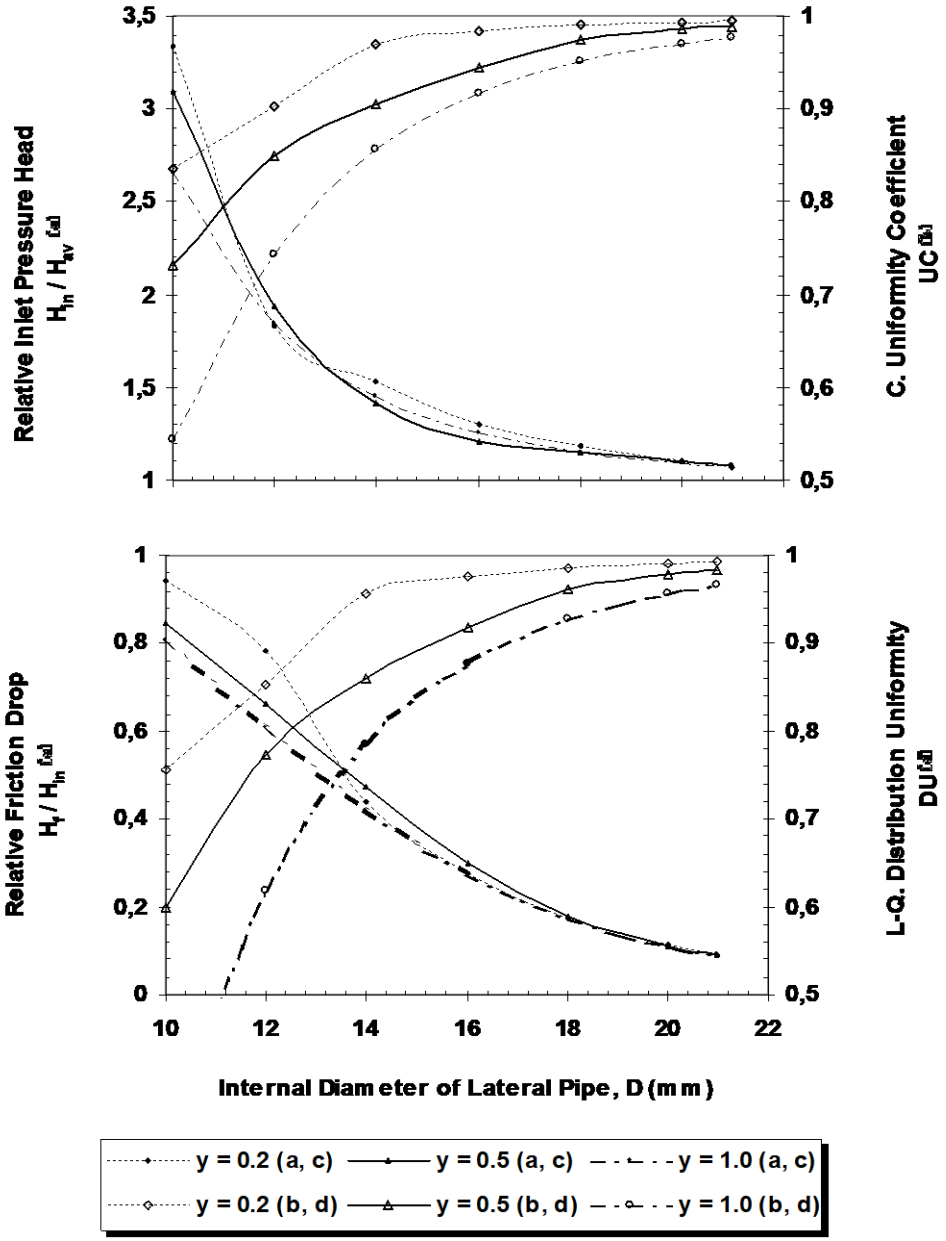


Figure 4 (a, b) Variation of Relative Inlet Pressure Head and Christiansen Uniformity Coefficient with Internal Diameter of Lateral (c, d) Variation of Relative Friction Drop and Lower-Quarter Distribution Uniformity Coefficient with Internal Diameter of Lateral

10. Summary and Conclusions

A lateral is a hydraulic structure whose design is limited by the irrigation uniformity, and consequently, by the friction head losses. These facts are very important because it should be provided that the variation of the emitter outflows within limited values which are defined uniformity coefficients. In addition, head loss due to friction at the end of lateral should be estimated, correctly.

In this study the principles of micro-irrigation lateral hydraulic based on the forward-step method was presented and a computer program was developed for this purpose. In this method, the design of the lateral pipe with equally spaced individual emitters and uniform slope is aimed so that hydraulic criteria are suitable and the uniformity coefficient is desired. In designing of a lateral by computer program, for a lateral length and inside diameter, firstly, the inlet pressure head is appointed, and then the friction drop along lateral and level of uniformity of the system are determined.

On the other hand, effects of design parameters on discharge distribution for consistent designing due to various combinations of the lateral length and the inside diameter can be experienced. In addition, hydraulic design criteria for lateral pipes in detail are presented. The design examples for verification the design criteria are also presented. Results obtained from covering various combinations of irrigation design parameters are plotted for three emitter characteristics and zero-slope condition graphically in dimensionless form for practical purposes. These presented figures could also be used as the design charts. For different design applications, the results of computer program based on the forward-step method has the higher accuracy and sensitivity rather than the results of other analytical and numerical methods, because only the basic equations of the hydraulics of stead pipe flow were used in each part of lateral which divided by the emitters.

References

Ağıralioğlu, N., Eren, R.H. and Yıldırım, G. (2000). "Investigation of Water Resources for Landscape Irrigation in Istanbul Region", *Technical Report*, Technical University of Istanbul, Civil Engineering Department, Istanbul.

Ağıralioğlu, N., and Yıldırım, G., (2002). "Determining Water Requirements for Landscape Irrigation in Istanbul Region", *Proc., International Conference On Water Resources Management in Arid Regions*, Kuwait Institute for Scientific Research, Kuwait.

Anwar, A.A. (1999.a). "Factor G for Pipelines with Equally Spaced Multiple Outlets and Outflow." *Journal of Irrigation and Drainage Eng., ASCE*, 125(1), 34-39.

Anwar, A.A. (1999.b). "Adjusted Factor G_a for Pipelines with Multiple Outlets and Outflow." *Journal of Irrigation and Drainage Eng., ASCE*, 125(6), 355-359.

Anwar, A.A. (2000). "Inlet Pressure for Horizontal Tapered Laterals." *Journal of Irrigation and Drainage Eng., ASCE*, 126(1), 57-63.

Bralts, V.F., Wu, I.P., and Gitlin, H.M. (1981). "Manufacturing Variation and Drip Irrigation Uniformity." *Trans. ASAE*, 24(1), 1234-1240.

Christiansen, J.E. (1942). "Irrigation by Sprinkling." *California Agricultural Experimental Station Bulletin* 670, Univ. of California, Davis, California.

Cuenca, R.H. (1989). "Irrigation Systems Design: An Engineering Approach". *Prentice Hall*, New Jersey.

Hathoot, H.M., Al-Amoud, A.I. and Mohammad, F.S. (1993). "Analysis and Design of Trickle Irrigation Laterals ", *Journal of Irrigation and Drainage Eng., ASCE*, 119(5), 756-767.

Howell, T.A. and Hiler, E.A. (1974). "Trickle Irrigation Lateral Design." *Trans. ASAE*, 17(5), 902-908.

Kang, V. and Nishiyama, S., (1996.a). "Analysis and Design of Micro-irrigation Laterals", *Journal of Irrigation and Drainage Eng., ASCE*, 122(2), 75-82.

Kang, V. and Nishiyama, S., (1996.b). " Design of Micro-irrigation Sub-main Unit", *Journal of Irrigation and Drainage Eng., ASCE*, 122(2), 83-89.

Keller, J. and Karmeli, D. (1974). " Trickle Irrigation Design Parameters." *Trans. ASAE*, 17(4), 678-683.

Scaloppi, E. J., and Allen, R. G. (1993). "Hydraulics of Irrigation Laterals: Comparative Analysis", *Journal of Irrigation and Drainage Eng., ASCE*, 119(1), 91-115.

Streeter, V.L. and Wylie, B.E., (1979). *Fluid Mechanics*, New York : Mc Graw-Hill.

Valiantzas, J. D., (1998). "Analytical Approach for Direct Drip Lateral Hydraulic Calculation", *Journal of Irrigation and Drainage Eng., ASCE*, 124(6), 300-305.

Valiantzas, J. D., (2002.a). "Continuous Outflow Variation Along Irrigation Laterals: Effect of the Number of Outlets", *Journal of Irrigation and Drainage Eng., ASCE*, 128(1), 34-42.

Valiantzas, J.D., (2002.b). "Hydraulic Analysis and Optimum Design of Multidiameter Irrigation Laterals." *Journal of Irrigation and Drainage Eng., ASCE*, 128(2),78-86.

Vallesquino, P., and Luque - Escamilla, P. L., (2001). "New Algorithm for Hydraulic Calculation in Irrigation Laterals", *Journal of Irrigation and Drainage Eng., ASCE*, 127(4), 254-260.

Vallesquino, P., and Luque-Escamilla, P.L., (2002). "Equivalent Friction Factor Method for Hydraulic Calculation in Irrigation Laterals." *Journal of Irrigation and Drainage Eng., ASCE*, 128(5), 278-286.

Yıldırım, G., (2001). "Computer Aided Design of Trickle Laterals", *MS thesis*, Istanbul Technical University, Institute of Science and Technology, Civil Engineering Department, Hydraulic Division, , Istanbul.

Yıldırım, G., and Ağıralioğlu, N., (2001). "Computer Aided Design of Lateral Pipes in Drip Irrigation", *Proc., 1st International Symposium On Water Resources and Environmental Impact Assessment*, 267-279, Istanbul.

Yıldırım, G., and Ağıralioğlu, N., (2002). "Variation of Total friction Head Losses and Uniformity Coefficients Based on Inlet Pressure Head in Trickle Irrigation Laterals", *Proc., International Conference On Water Resources Management in Arid Regions*, Kuwait Institute for Scientific Research, Kuwait.

Yıldırım, G., and Ağıralioğlu, N., (2003.a). Discussion of "New Algorithm for Hydraulic Calculation in Irrigation Laterals" by Pedro Vallesquino and Pedro L. Luque-Escamilla, *Journal of Irrigation and Drainage Eng., ASCE*, 129(2), 142-144.

Yıldırım, G., and Ağıralioğlu, N., (2003.b). Discussion of "Continuous Outflow Variation Along Irrigation Laterals: Effect of the Number of Outlets" by John D. Valiantzas, *Journal of Irrigation and Drainage Eng., ASCE*, 129(5), 382-386.

Yıldırım, G., and Ağıralioğlu, N., (2004.a). "Linear Solution for Hydraulic Analysis of Tapered Microirrigation Laterals", *Journal of Irrigation and Drainage Eng., ASCE*, 130(1), 78-87.

Yıldırım, G., and Ağıralioğlu, N., (2004.b). "Comparative Analysis of Hydraulic Calculation Methods in Design of Microirrigation Laterals". *Journal of Irrigation and Drainage Eng., ASCE*, (press in May/June, 2004 issue).

Yıldırım, G., and Ağıralioğlu, N., (2004.c). Discussion of "Equivalent Friction Factor Method for Hydraulic Calculation in Irrigation Laterals" by Pedro Vallesquino and Pedro L. Luque-Escamilla, *Journal of Irrigation and Drainage Eng., ASCE* (in press).

Wu, I. P., and Gitlin, H. M. (1975). "Energy Gradient Line for Drip Irrigation Laterals", *Journal of Irrigation and Drainage Eng., ASCE*, 101(4), 323-326.

Wu, I.P., and Yue, R. (1993). "Drip Lateral Design Using Energy Gradient Line Approach." *Trans. ASAE*, 36(2), 389-394.

Yitayew, M. and Warrick, A.W., (1986). "Velocity Head Consideration for Trickle Laterals", *Journal of Irrigation and Drainage Eng., ASCE*, 113(4), 611-615.

Yitayew, M. and Warrick, A.W., (1988) "Trickle Lateral Hydraulics-II : Design and Examples", *Journal of Irrigation and Drainage Eng., ASCE*, 114(2), 289-300.

Yitayew, M., (1989). "Head Loss in Manifolds or Trickle Lateral: Simplified Approach", *Journal of Irrigation and Drainage Eng., ASCE*, 115(4), 739-743.

Warrick, A.W. (1983). "Interrelationships of Irrigation Uniformity Terms." *J. Irrig. and Drain. Engrg., ASCE*, 109(31), 317-332.

Warrick A.W., and Yitayew M., (1987). "An analytical Solution for Flow in a Manifold ", *Advances in Water Resources, ASCE*, 10, June, 58-63.

Warrick A.W., and Yitayew M., (1988) "Trickle Lateral Hydraulics-I: Analytical Solution", *Journal of Irrigation and Drainage Eng., ASCE*, 114(2), 281-288.

Watters, G. Z., and Keller, J. (1978). "Trickle Irrigation Tubing Hydraulics" presented at *the Summer Meeting of ASAE*, Utah State University, Logan, Utah, Paper No.78-2015.

İnşaat Sektöründe Yeni Bir Yalıtım Malzemesinin Geliştirilmesi

Atila Gürhan Celik, İbrahim Günes

[1]Giresun Üniversitesi, Mühendislik Fakültesi, İnşaat Mühendisliği Bölümü, 28200, Giresun/Türkiye

Özet

Bu çalışmada; Tekstil katı atıklarının büyük fiziksel ve kimyasal birikimi ve bozunması, atık yönetimi gibi fikirlerin geri dönüştürülmesi ve yeniden kullanılması gibi çevreci yaklaşımlar sağlanmıştır. Bu nedenle tekstil katı atıklarının yalıtım malzemelerine dönüştürülerek geri dönüşümüne katkı sağlanması planlandı. Deneysel çalışmada ısı ve ses iletkenlik değerleri EPS kontrol örneğine göre daha iyi sonuçlar vermiştir. En ideal yalıtım malzemesi 0.031 (W/mK) en iyi ısıl iletkenlik değerleri ile üretilmiştir.

Anahtar kelimeler: EPS, XPS, geri dönüşüm, kompozit malzeme, yalıtım malzemesi.

Development of a New Insulatıon Materıal In the Constructıon Industry

Abstract

In this study; Environmentalist approaches such as large physical and chemical accumulation and degradation of textile solid wastes, recycling and reuse of ideas such as waste management have been ensured. Therefore, it was planned to contribute to the recycling of textile solid wastes by converting them into insulation materials. In the experimental study, heat and sound conductivity values showed better results than the EPS control sample. The most ideal insulation material was produced with the best thermal conductivity values of 0.031 (W/mK).

Keywords: EPS, XPS, recycling, composite material, insulation material.

1. Giriş

İnşaat sektöründe yalıtım; yapının kendi bünyesi ve dışarıdan gelecek zararlı etkilere karşı korumak için alınan önlemlerdir. Bunun yanında, başta plastik olmak üzere petrol türevi maddelerin doğada çürüme döngüsü yavaş gerçekleştiğinden dolayı çevre kirliliğinin de önüne geçilmiş olacaktır. Sağladığı bu avantajları ile geri dönüşüm ve yeniden kullanım dünya üzerinde canlı hayatın devam etmesi adına vazgeçilmemesi gereken olgulardır. Bu nedenle birçok bilim adamı ve üretici, mamul malzemelerin yapısında kullanılan hammaddelerin geri dönüşümü için süreçler geliştirmekte veya onların yeniden kullanımı için endüstri sahaları oluşturmaktadırlar. Bu amaçla yapılan çalışmalarda, tekstil üretim ve kullanım atıklarının, geri kazanımı, çevresel ve ekonomik etkilerini incelemiştir. Tekstil endüstrisinin gıda, tarım, hayvancılık gibi alanlarla karşılaştırılması ve ne kadar büyük bir paya sahip olduğunun tespiti hakkında sayısal veriler sunulmuştur(1). Yapılan diğer bir çalışmada, dokuma kumaş atığını ve ikincil atığını ısı izolasyonu malzemesi olarak kullanmı araştırılmıştır. Sonuçlara göre, dokuma kumaş atığının ve dokuma kumaş ikincil atığının çift duvar uygulamalarında ısıl yalıtım özellikleri %56 ve %30 destekleyerek fayda sağladığını tespit etmişlerdir(2). Paiva ve ark., ısı yalıtımı malzemesi olarak tekstil alt atıklarını incelemiştir. Kullanılan tekstil alt atıkları yatak endüstrisinden elde edilmiş malzemelerin kompozit haline getirilerek ısı iletkenlik katsayısının hesaplanması deneylerini başarıyla gerçekleştirilmiş ve %33lük bir termal ısı savunması başarılı bir şekilde gerçekleştirilen bir kompozit ürün elde edilmiştir (3). Dissanayake ve ark., tekstil atıklarını kullanarak sıkıştırılmış panel üretimi ve yalıtım özellikleri incelemiştir, sentetik materyaller (naylon,

spandex, poliüretan) kullanılarak sıkıştırılmış kalıplama işlemi uygulanarak termik iletkenlik testine tabii tutulmuştur sonuç olarak; en iyi ısı yalıtımını veren kombinasyon %40 poliüretan parçalarıyla karıştırılmış %60 naylon kumaş parçaları olarak görülmüştür (4). Silika aerojellerin ısı ve ses izolasyon malzemesi olarak kullanılması amacıyla aerojellerin bulunduğu malzemelerin daha kompakt bir bütün yapı oluşturdukları için ısı ve ses absorbe işlemlerinin çok daha iyi hatta 0,02W/mK gibi çok çok ufak değerlere sahip iletkenlik katsayıları tespit edilmiştir (5). Bu çalışmada; tekstil katı atıklarının büyük fiziksel ve kimyasal birikimi ve bozulmaları, atık yönetimi gibi fikirleri geri kazanım ve yeniden kullanım gibi çevreci yaklaşımların doğması sağlanmıştır. Geri dönüşüm, yeniden değerlendirilebilme olanağı olan atıkların çeşitli işlemlerden geçerek üretim sürecine yeniden dahil edilmiştir.

2. Materyal ve Metot

2.1. Materyal

2.1.1. Tekstil Atık Malzemesi

Atık pamuk lifi, atık yün lifi, kumaş parçaları ve polyester kumaş ana hammadde olarak kullanılmıştır. Defibrasyon yöntemi ile işlenerek kullanıma hazır hale getirilmiştir.

2.1.2. Bağlayıcı

Kompozit malzeme üretimi için döküm tipi polyester reçine kullanılmıştır.

2.1.3. Alev Geciktirici

Alev geciktirici olarak Fire-0 alev almazlık solüsyonu kullanılmıştır. Fire-O doğal malzemeden üretilmiş, insan sağlığına zararı bulunmayan, çevre sağlığı bakımından risk taşımayan ve yasaklı malzeme içermeyen bir üründür. Bunun yanında duman oksijen ve azot bakımından %20 -25 daha zengindir. Dolayısı ile yangın anında alev almazken dumanının boğucu etkisi yarı yarıya azaltılmıştır.

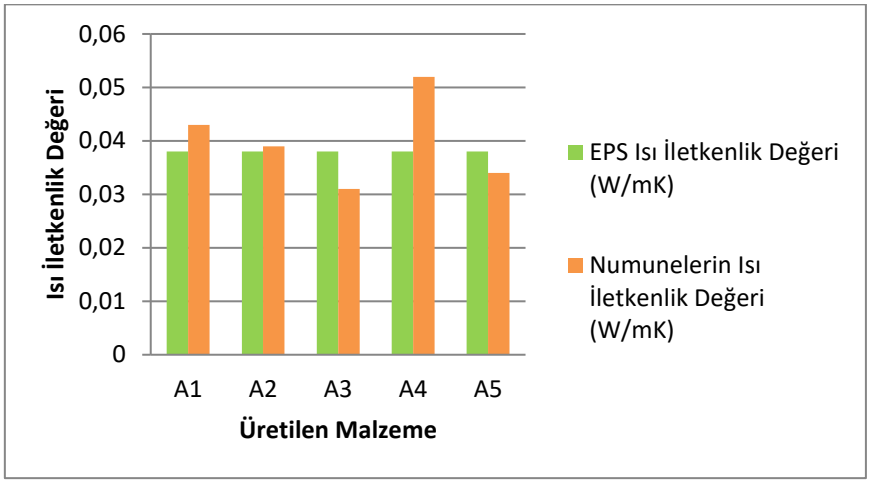
2.2.Metod

Hammaddelerin numunelerin öncelikle elle ayrıştırılması ve karışım yüzdelerinin ağırlıkça belirlenmesi işlemi gerçekleştirilmiştir. Numuneler (A1-5) olarak sınıflandırılmış ve Fire-0 Alev Almazlık Solüsyonu ve EPOXY (Kompozit malzeme üretimi için döküm tipi polyester reçine) ile karıştırılmıştır. 5cm*60cm*120 cm boyuta sahip kalıplarda şekillendirilmiştir. 5 ayrı ürün reçetesi hazırlanmıştır. Numuneler kalıba alınarak 300 bar pres basıncına sahip makineyde sıkıştırılmıştır. Presin ardından numuneler 24 saat kalıbın içerisinde bekletilmiştir. Son olarak üretilen plaka 80°C fırında 3 saat süreyle bekletilerek kürleme işlemi gerçekleştirilmiştir. Ürünler üzerinde ısı ve ses yalıtım testleri yapılmış ve ticari ürün olan EPS (Genişletilmiş Polistiren Köpük) ile karşılaştırılmıştır.

3. Deneysel Sonuçlar

3.1. Isı İletim Katsayısı Deneyi(W/mK)

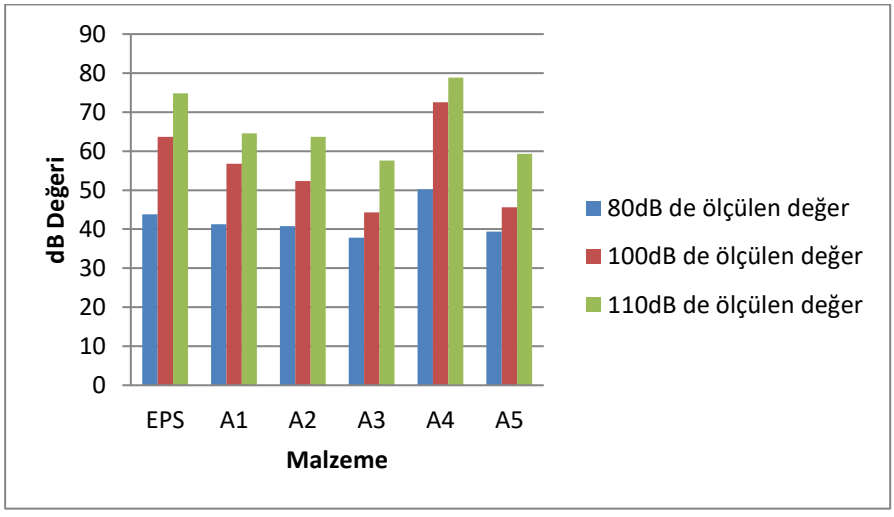
Deneylerde TLS-100 cihazı kullanılmıştır. Elde edilen veriler Şekil 1’de verilmektedir.



Şekil 1'e göre; geliştirilen ürünlerden elde edilen ısı iletkenlik değerleri sırayla A1=0,043W/mK, A2=0,039, A3=0,031, A4=0,052, A5=0,034 olarak bulunmuştur. Numunelerden elde edilen ısı iletim değerlerine göre; A3 ve A5 numaralı olanlar EPS den daha iyi yalıtım sonuçları sunmuştur. Ayrıca tüm reçeteler yalıtım malzemesi olarak kullanılabilir değerlere sahiptir.

3.2. Ses Geçirgenlik Deneyi(dB)

Ses Ölçüm Cihazı olarak PCE-428-KIT-N model kullanılmıştır. Gürültü ölçüm cihazı, test sinyalinin ne kadar sürdüğünü kaydeder. Ölçüm prosedürü DIN EN ISO 3382'de belirtilen standartlara göre yapılmıştır. Çalşımadan elde edilen veriler Şekil 2'de verilmiştir.



Şekil 2'de görüldüğü üzere, ölçüm yapılan tüm yüzeylerde gürültü seviyelerinin ortalaması birbirine yakın olup A3 ve A5 numunelerden en iyi sonuçlar elde edilmiştir. Kaynak tarafında gürültü seviyesinin 110 dB olması durumunda ise en az ölçülen ses şiddeti 57,6 dB ile A3 malzemede gerçekleşmiştir. Deneyler sonucunda taş yünü ve tekstil katı atıklarından üretilen numuneler gibi lifli malzemelerin ses yalıtımı açısından diğer yalıtım

malzemelerinden daha etkin olduğu görülmektedir. EPS kapalı gözenekli ve düşük yoğunluk nedeniyle önemli bir akustik özellik göstermez.

4. Sonuç ve Öneriler

Çalışmanın sonuçları aşağıda verilmiştir;

- Ses geçirgenliği bakımından; A3 ve A5 olarak isimlendirilen numuneler açık ara üretilen ses şiddetini ciddi manada absorbe edebilmiştir. Kaynak tarafında gürültü seviyesinin 110 dB olması durumunda ise en az ölçülen ses şiddeti 57,6 dB ile A3 malzemede gerçekleşmiştir. Deneyler sonucunda taş yünü ve tekstil katı atıklarından üretilen numuneler gibi lifli malzemelerin ses yalıtımı açısından diğer yalıtım malzemelerinden daha etkin olduğu görülmektedir.
- ısı iletkenlik değerleri sırayla A1=0,043W/mK, A2=0,039, A3=0,031, A4=0,052, A5=0,034 olup endüstriyel kullanılan yalıtım malzemelerinin bazılarından daha yüksek ısı iletkenlik katsayısına sahiptir.
- EPS ve A3 numuneleri kıyaslanmıştır. EPS in 90°C'ye ulaştığında yapısal anlamda tamamen bozulduğu görülmüştür ancak A3 numunesinde bozulmaların başladığı, ayrışımların numunenin ortasından köşelere doğru gerçekleştiği tespit edilmiştir.
- Bu çalışma geri dönüşüm noktasında ülkemize fayda sağlayacağı, ürün doğallığı, üretim maliyet düşüklüğü sayesinde avantajlar sunacağı değerlendirilmektedir.

Kaynaklar

[1] Ş.Altun., "Tekstil Geri Kazanım Sektörü Raporu", Uşak TSO, 2014.
[2] Briga-Sa, A., Nascimento, D., Teixeira, N., Pinto, J., Caldeira, F., Varum, H., Paiva, A., "Textile Waste as an Alternative Thermal Insulation Building Material Solution", Construction and Building Materials, 2012, 38, 156.
[3] A. Paiva, H. Varum, F. Caldeira, A. Sá, D. Nascimento, N. Teixeira, "International Conference on Petroleum and Sustainable Development" IPCBEE 2011, vol. 26.
[4] D.G.K. Dissanayake, D.U. Weerasinghe, K.A.P. Wijesinghe, K.M.D.M.P. Kalpage., " Developing a compression moulded thermal insulation panel using postindustrial textile waste" Waste Management, Volume 79, September 2018, Pages 356-361.
[5] Huang, L, "Feasibility of using silica aerogel as insulation for buildings" KTH, School of Industrial Engineering and Management (ITM), thesis, 2012, p. 91.

Investigation of Shear Wall Effect on Dynamic Parameters of Reinforced Concrete Building

Sertaç Tuhta[1*]

[1*] Ondokuz Mayıs Üniversitesi, Mühendislik Fakültesi, İnşaat Mühendisliği Bölümü, Samsun, Türkiye, (ORCID: 0000-0003-2671-6894), stuhta@omu.edu.tr

Öz

Günümüzde betonarme yapıların kullanımı dünyada oldukça popülerdir. Betonarme yapıların diğer tüm yapı türleri gibi deprem etkilerinden etkilendiği bilinmektedir. Bu duruma ek olarak betonarme yapılar da diğer tüm nesneler gibi çevresel titreşimlerden etkilenir. Tüm bu etkilerden dolayı betonarme yapılar zamanla taşıma gücünü kaybedebilir. Bu durumda yapının çökmesi gibi çok tehlikeli sonuçlara neden olmaktadır. Bu tür sorunları çözmek için kanıtlanmış çeşitli güçlendirme yöntemleri mevcuttur. Perde duvarların kullanımı da bu güçlendirme yöntemlerinden birisidir. Perde duvar ile güçlendirme yönteminin oldukça yaygın kullanıldığı birçok çalışmada görülmüştür. Bu çalışmada, örnek bir betonarme binada perde duvarların etkileri, sonlu elemanlar yöntemi kullanılarak ve modal analiz yapılarak ortaya konmuştur. Özellikle ilk 5 modun yapı titreşim periyotları ve serbest titreşim modu şekilleri detaylı olarak ele alınmıştır. Böylece perde duvarlar ile güçlendirmenin yapının rijitliği üzerindeki olumlu etkisi daha net ortaya konmuştur. Tüm bu sonuçlar ışığında betonarme yapıların güçlendirilmesinde perde duvar ile güçlendirme yönteminin kullanılabilir olduğu görülmektedir.

Anahtar Kelimeler: Betonarme yapılar, Perde duvarlar, Sonlu elemanlar metodu, Dinamik parametreler, Güçlendirme

Investigation of Shear Wall Effect on Dynamic Parameters of Reinforced Concrete Building

Abstract

Today, the use of reinforced concrete structures is very popular in the world. It is known that reinforced concrete structures are affected by earthquake effects like all other building types. In addition to this situation, reinforced concrete structures are affected by environmental vibrations like all other objects. Due to all these effects, reinforced concrete structures may lose their bearing capacity over time. In this case, it causes very dangerous results such as collapse of the structure. Various proven retrofit methods are available to solve such problems. The use of shear walls is one of these retrofit methods. It has been proven in many studies that the shear walls reinforcement method is quite common. In this study, the effects of shear walls in a sample reinforced concrete building are revealed by making modal analysis using the finite element method. In particular, the structure vibration periods and free vibration mode shapes of the first 5 modes are discussed in detail. Thus, the positive effect of shear walls on the rigidity of the structure has been more clearly demonstrated. In the light of all this results, the method of shear walls can be used in the reinforcement of reinforced concrete buildings.

Keywords: RC structures, Shear walls, Finite element method, Dynamic parameters, Retrofitting

1. Introduction

Shear walls are vertical load-bearing elements whose thickness in the plan is quite large compared to their height, and their task is to transfer the horizontal and vertical loads from the floors and beams to the ground and to limit the horizontal drift of the structures, especially under the influence of lateral loads such as earthquakes and winds. In the Turkish Building Earthquake Code, shear walls are called vertical structural elements with a ratio of at least 6 to the thickness of their long sides. Vertical loads, that is, constant loads, which are the weight of the building, and human, machine, etc. occurring in the building. Columns generally provide sufficient strength for welded live loads. Shear walls, which have large cross-sections compared to columns, of course, greatly increase the resistance of structures against vertical loads. However, the main purpose in the use of shear walls is to increase the strength and rigidity of the structure against lateral loads. Shear walls in different country regulations; Planar vertical elements created in FEMA 356 to serve to meet the horizontal loads in reinforced concrete structures, elements supported by other structural elements in Eurocode 8 and whose cross-sectional length to thickness ratio is greater than four, in ACI 318, V, M and N effects caused by earthquake effects on structures. Structural elements designed to meet the effects of combinations are defined in IBC 2000 as structural elements designed to meet horizontal loads parallel to its plane. The main task of curtains is to carry horizontal loads and limit the horizontal displacement of the structure. With its relatively high lateral stiffness, the shear walls are effective in meeting the moment and shear forces caused by the earthquake and in keeping the storey drifts under control. Shear walls are very important criteria in earthquake design and they are effective elements in terms of rigidity, strength and ductility in the structure.

Researchers have carried out many studies using both the finite element method and the reinforcing methods. There are many other studies by the authors using the finite element method before. In this study, studies [1], [2], [3], [4], [5], [6], [7], [8], [9] on the use of the finite element method were used. With all this knowledge, this new study has been carried out.

Researchers have conducted studies [10], [11], [12], [13], [14], [15], [16], [17], [18] about shear walls which also contributing to this study.

The aim of this study is to examine the effects of retrofit with shear walls on dynamic parameters in reinforced concrete building. There may be a need for a retrofit method without architectural disadvantages or excessive dead load increments. In such cases, the retrofit method with shear wall is also known to be an option. For this reason, it is very important to reveal the effect of shear wall on dynamic parameters.

2. Material and Method

In this study, A reinforced concrete building model was created and modal analysis was carried out with the finite element method. The reinforced concrete building model was retrofitted with shear walls and a retrofitted model building model was created for comparison. In the application of the finite element method, the SAP2000 package program, which is used in the field of academic and engineering applications all over the world, was used.

2.1. The Model of Reinforced Concrete Building

The model 5-storey reinforced concrete building with two spans of 6 meters in x and y directions, and a floor height of 3 meters. The columns of the model reinforced concrete building are sized as 40x50 cm. The beams of the model reinforced concrete building are sized as 30x50 cm. The slabs are sized to be 20 cm reinforced concrete. The concrete class used is C30 in Turkish Standarts. Reinforcement steel used is S420 class in Turkish Standarts.

By designing the building as symmetrical and simple, it is aimed to reveal the result of the retrofit to be applied more clearly. The spans are therefore taken equal.

The 3D finite element model in SAP2000 package software of the model reinforced concrete building is given in Figure 1.

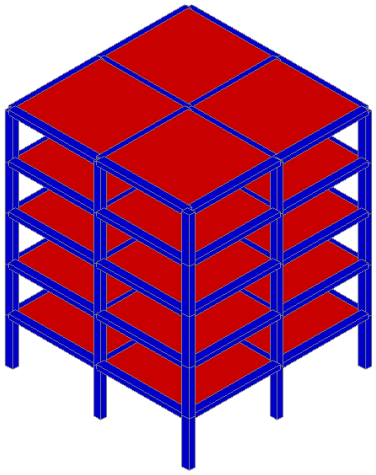


Figure 1. The model reinforced concrete building's 3D view

2.2. The Model of Retrofitted Reinforced Concrete Building

A 20x150 cm shear wall was added to only two openings of the building. The shear wall was applied throughout all floors. The shear wall is reinforced concrete. The 3D finite element model in SAP2000 package software of the retrofitted model reinforced concrete building given in Figure 2.

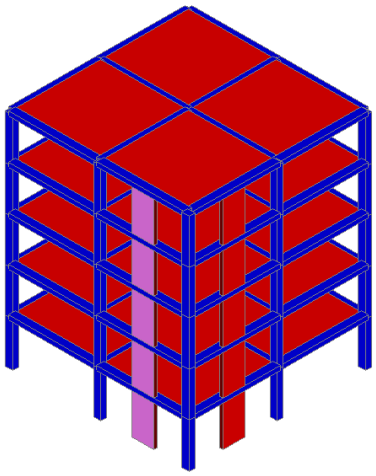


Figure 2. The retrofitted reinforced concrete building's 3D view

3. Result and Discussion

Model reinforced concrete building and retrofitted model reinforced concrete building were analysed separately. The modal analysis results of each model are shared under separate headings. The results include the analysis results of the first five modes. Mode shape and period values are taken into consideration for each mode. The parameters obtained for both models were compared for each mode separately. During the analysis, the SAP2000 package software, which is a finite element method software, was used.

3.1. Analysis Results of Model Reinforced Concrete Building

The model reinforced concrete building was analysed without retrofitting. When the first five modes are examined, the results obtained are presented in figure 3,4,5,6,7 as period values and mode shapes for each mode.

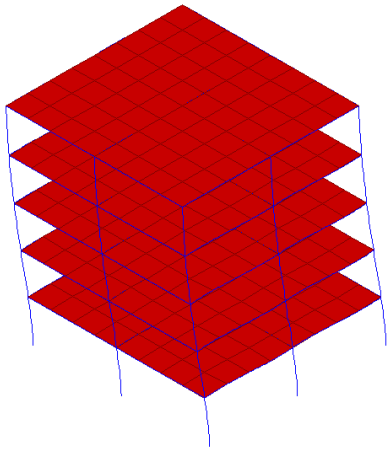


Figure 3. 1. Mode shape (T = 0.83 s)

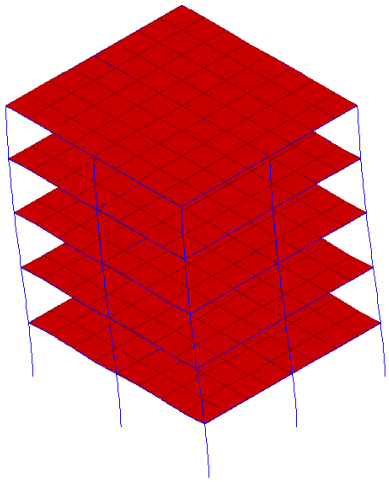


Figure 4. 2. Mode shape (T = 0.76 s)

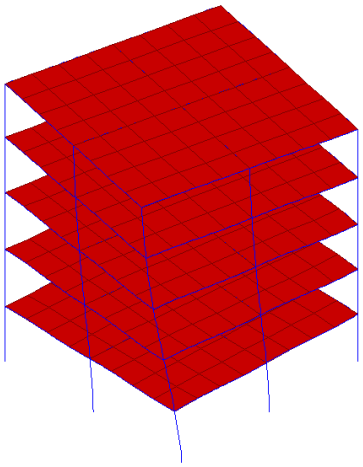


Figure 5. 3. Mode shape (T = 0.64 s)

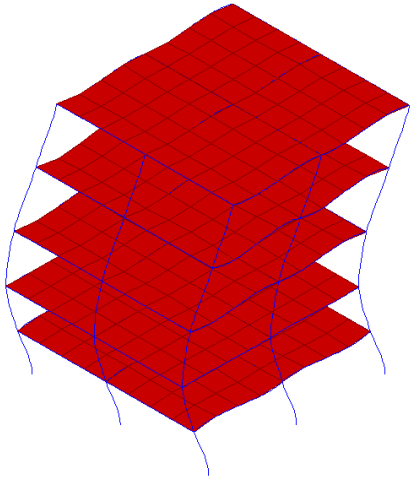


Figure 6. 4. Mode shape (T = 0.25 s)

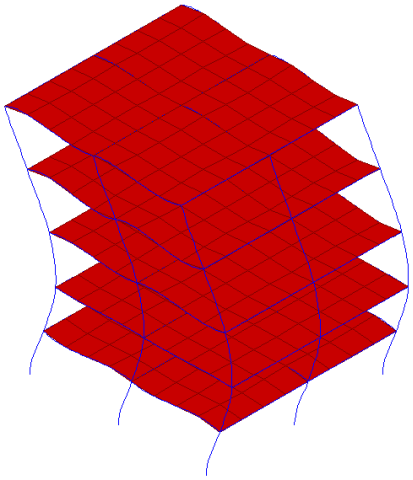


Figure 7. 5. Mode shape (T = 0.23 s)

3.2. Analysis Results of Retrofitted Model Reinforced Concrete Building

The model reinforced concrete building was analysed with reinforcing by shear walls. When the first five modes are examined, the results obtained are presented in figure 8,9,10,11,12 as period values and mode shapes for each mode.

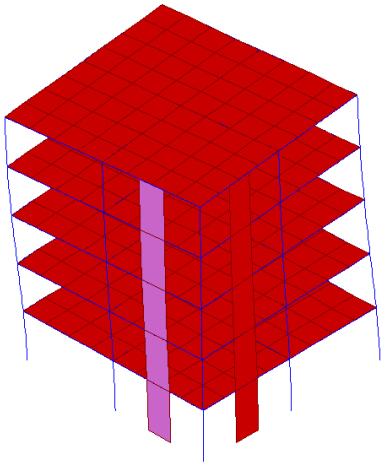


Figure 9. 1. Mode shape (T = 0.74 s)

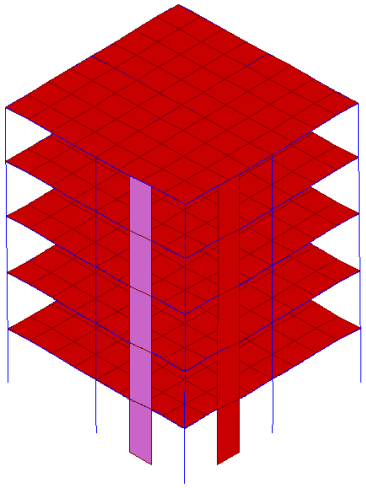


Figure 10. 2. Mode shape (T = 0.58 s)

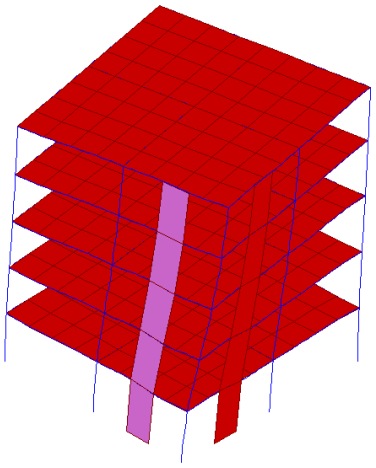


Figure 11. 3. Mode shape (T = 0.37 s)

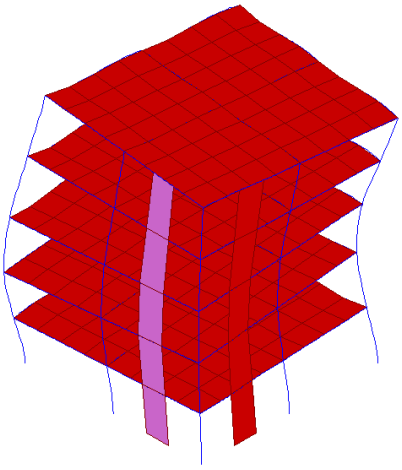


Figure 12. 4. Mode shape (T = 0.23 s)

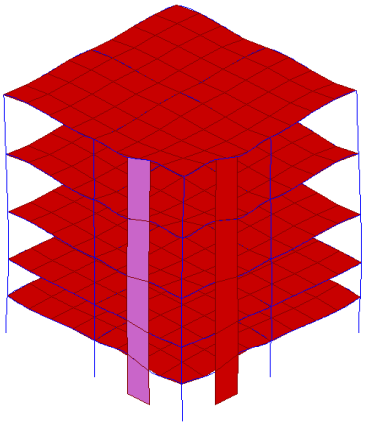


Figure 13. 5. Mode shape (T = 0.17 s)

3.3. Comparison of Analysis Results

The comparison of period values of the model reinforced concrete building and retrofitted model reinforced concrete building is given in Table 1.

Table 1. Comparison of period values

Mode	**1**	**2**	**3**	**4**	**5**
Non-Retrofitted	0.83	0.76	0.64	0.25	0.23
Retrofitted	0.74	0.58	0.37	0.23	0.17
Difference (s)	0.09	0.18	0.27	0.02	0.06
Difference (%)	10.84	23.68	42.19	8.00	26.09

The comparison of mode shapes of the model reinforced concrete building and retrofitted model reinforced concrete building is given in Table 2.

Table 2. Comparison of mode shapes type

Mode	**1**	**2**	**3**	**4**	**5**
Non-retrofitted	Translational	Translational	Torsional	Translational	Translational
Retrofitted	Translational	Translational	Torsional	Translational	Translational

4. Conclusions

In the mode 1, the period difference between non-retrofitted model and retrofitted model status was obtained as 0.09 s. The effect of period retrofitting with shear walls as a percentage was determined as 10.84.

In the mode 2, the period difference between non-retrofitted model and retrofitted model status was obtained as 0.18 s. The effect of period retrofitting with shear walls as a percentage was determined as 23.68.

In the mode 3, the period difference between non-retrofitted model and retrofitted model status was obtained as 0.27 s. The effect of period retrofitting with shear walls as a percentage was determined as 42.19.

In the mode 4, the period difference between non-retrofitted model and retrofitted model status was obtained as 0.02 s. The effect of period retrofitting with shear walls as a percentage was determined as 8.00.

In the mode 5, the period difference between non-retrofitted model and retrofitted model status was obtained as 0.06 s. The effect of period retrofitting with shear walls as a percentage was determined as 26.09.

When the mod shapes were examined, no mod shape type changes were observed with the retrofit with shear wall. However, it has been observed clearly that the mode shapes move more rigidly with the retrofit.

In the light of all these results, significant decrease in periods was detected in first five modes. Thus, it is clearly seen that the rigidity of the structure increases by strengthening the model reinforced concrete building with shear walls. In the 1st mode, in other words, there is a decrease of 10.84 percent in the dominant period value. In addition, there is a large decrease of 42.19 percent in the period value in the 3rd mode. It has been observed that the 3rd mode shape is the torsional mode shape. The fact that this effect is in the form of a torsion mode is an indication that this retrofitting also reduces the effects of torsion. Of course, it should be taken into account that the design of the structure and retrofitting is very important in obtaining the data in this way. Incorrect model

selection and faulty retrofit designs can make data more unreliable. In the light of all this obtaining information, the retrofit method with shear walls may be used in reinforced concrete buildings.

References

[1] Ziada, M., Tuhta, S., Gençbay, E. H., Günday, F., & Tammam, Y. (2019). Analysis of Tunnel Form Building Retrofitted with CFRP using Finite Element Method. International Journal of Trend in Scientific Research and Development, 3(2), 822–826.

[2] Tuhta, S., Günday, F., & Pehlivan, N. C. (2019). Investigation of Cfrp Retrofitting Effect on Masonry Dome on Bending Moment Using Finite Element Method. International Journal of Innovatıons in Engineering Research and Technology, 6(6), 18–22.

[3] Tuhta, S., Günday, F., & Alihassan, A. (2020). The Effect of CFRP Reinforced Concrete Chimney on Modal Parameters Using Finite Element Method. International Journal of Innovations in Engineering Research and Technology, 7(2), 1–6.

[4] Tuhta, S., Günday, F., & Köroğlu, E. (2021). The Effect of TMD on The Periods and Mode Shapes of The Reinforced Concrete Building by Finite Element Analysis. JournalNx, 7(12), 5–13.

[5] Bakkour, F., Tuhta, S., & Günday, F. (2022). Determination of Modal Parameters of Reinforced Concrete Box Culvert Retrofitted with GFRP Using Finite Element Method. International Journal of Innovations in Engineering Research and Technology, 9(4), 1–9.

[6] Kasimzade, A.A., Tuhta, S., Günday, F. & Aydın, H. (2021). Obtaining Dynamic Parameters by Using Ambient Vibration Recordings on Model of The Steel Arch Bridge. Periodica Polytechnica Civil Engineering, 65(2), 608-618.

[7] Hammoud, M. A., Tuhta, S., & Günday, F. (2022). Determination of Modal Parameters of Reinforced Concrete Tunnel Retrofitted with CFRP using Finite Element Method. International Journal of Innovations in Engineering Research and Technology, 9(4), 10–18.

[8] Kasimzade A.A., Structural Design and Analysis Based on FEM with SAP2000 in the Light of Current Codes (is included education and finite element analysis software on a DVD-QR code), Nobel Publication, December 2021, p. 342.

[9] Kasimzade A.A., Finite Element Method foundation and Application to Structural Analysis (is included education and finite element analysis software on a DVD-QR code), Nobel Publication, June 2018, p. 818.

[10] White, M.W., & Dolan, J.D (1995). Nonlinear Shear-Wall Analysis. Journal of Structural Engineering, 121(11), 1629-1635.

[11] Chandurkar, P.P., & Pajgade, P.S. (2013). Seismic Analysis of RCC Building with and Without Shear Wall. International Journal of Modern Engineering Research, 3(3), 1085-1810.

[12] Geol R. K., & Chopra, A. K. (1998). Period Formulas for Concrete Shear Wall Buildings. Journal of Structural Engineering, 124(4), 426-433.

[13] Toko, H., & Chiaki, M. (2003). Experimental Study on Steel Shear Wall with Slits, Journal of Structural Engineering, 129(5), 586-595.

[14] Martinelli, P., & Filippou, F.C. (2000). Simulation of the shaking table test of a seven-story shear wall building. Earthquake Engng. Struct. Dyn, 38(5), 587-607.

[15] Patel, N., & Jamle, S. (2019). Use of Shear Wall Belt at Optimum Height to Increase Lateral Load Handling Capacity in Multistory Building: A Review. International Journal of Advanced Engineering Research and Science, 6(4), 310-314.

[16] El-Dakhakhni, W., & Ashour, A. (2017). Seismic Response of Reinforced-Concrete Masonry Shear-Wall Components and Systems: State of the Art, Journal of Structural Engineering, 143(9).

[17] Harne, V.R. (2014). Comparative Study of Strength of RC Shear Wall at Different Location on Multi-storied Residential Building, International Journal of Civil Engineering Research, 5(4), 391-400.

[18] Lu, X., Xie, L., Guan, H., Huang, Y., & Lu, X. (2015). A shear wall element for nonlinear seismic analysis of super-tall buildings using OpenSees, Finite Elements in Analysis and Design, 98(2015), 14-25.

Mineral Katkılı Betonların Fiziksel Özellikleri

Atila Gürhan Celik, İbrahim Günes

[1]Giresun Üniversitesi, Mühendislik Fakültesi, İnşaat Mühendisliği Bölümü, 28200, Giresun/Türkiye

Özet

Bu çalışmada, beton üretiminde mineral katkısı olarak silis dumanı kullanılmıştır. Ünye Çimento Fabrikasında üretilen Portland kompozit çimento (PC) üzerinde fiziksel deneyler yapılmıştır. Bağlayıcı malzeme olarak PC(CEM I 42,5R) ve mineral katkılı çimento kullanılarak üretilen betonların performans özellikleri araştırılmıştır. Yapılan çalışma sonucunda; Katkılı betonun hidratasyon ısısı ve kılcal geçirgenlik değerleri incelenmiştir. Portland çimentosu ve mineral katkılı harçların fiziksel özellikleri karşılaştırılmıştır.

Anahtar kelimeler: Kolemanit, Basınç dayanımı, Hidrasyon, Portland çimentosu.

Physical Properties Of Mineral-Added Concretes

Abstract

In this study, silica fume was used as a mineral additive in concrete production. Physical experiments were carried out on Portland composite cement (PC) produced in Ünye Cement Factory. The performance properties of concretes produced by using PC(CEM I 42.5R) and mineral-added cement as binder material were investigated. As a result of the study; The heat of hydration and permeability absorption values of the reinforced concrete were investigated. The physical properties of Portland cement and mineral-added mortars were compared

.Keywords: Colemanite, Compressive strength, Hydration, Portland cement.

2. Giriş

Silika dumanı yapısı gereği genellikle pürüzsüz bir yüzeye, küresel ve camsı özelliklere sahiptir. Bu fonksiyonları sayesinde betondaki (1-2) hava boşluklarını rahatlıkla doldurabilir. Silis dumanı katkısı, diğer puzolanlar gibi yeni C-S-H jellerinin oluşumunu sağlarken, ince silika dumanı taneleri agrega-macun ara yüzeyini sıkılaştırarak ve güçlendirerek betonun mukavemetini arttırır. Öte yandan, belirli bir işlenebilirlik için su ihtiyacını (3) artırmak gibi olumsuz etkileri de vardır. Silis dumanı ilavesi ile 28 günlük basınç dayanımında %20-50'ye varan bir artış elde edilebilir(4). Beton üretiminde kullanılan silis dumanı, çimento taneleri arasındaki karışım suyunun yerini alır, granülometriyi iyileştirir ve serbest su miktarını artırarak olumlu etki yapar (5-6). Silis dumanının betonun işlenebilirliği ve basınç dayanımı üzerindeki etkisi iki farklı çimento kullanılarak araştırılmıştır. S/C oranını 0.25-0.45 arasında değiştirdikleri çalışmalarında, silika dumanının işlenebilirlik üzerindeki etkisinin, su/bağlayıcı oranındaki %10 veya daha az silis dumanı kullanımı azalmasıyla daha belirgin hale geldiğini bildirmişlerdir (7).

2. Materyal ve Metot

2.1. Materyal

2.1.1. Çimento

Çalışmalarda, gerek çimento kimyasal ve fiziksel özelliklerinin belirlenmesi ve gerekse beton deneylerinde Göltaş Çimento Fabrikası'nda üretilen BC ve PC(CEM I 42,5R) tipi çimento kullanılmıştır.

2.1.2. Agrega

Bu çalışmada kullanılan agregalar 0-2mm, 2-4mm, 4-8mm 8-16 16-22,4 ve 22,4- 32 tane boyutuna sahip olacak şekilde gruplandırılmışlardır. TS 802'ye uygun olarak maksimum dane boyu 22,4 mm alınmıştır.

2.1.3. Karışım Suyu

Yapılan çalışmada karışım suyu olarak Giresun ilinde şehir şebeke suyu kullanılmıştır. Kullanılan suyun ilgili standartlarda yer alan özellikleri sağlamasına dikkat edilmiştir.

2.1.5. Süper Akışkanlaştırıcı Katkı Maddesi

Glenium51'in geleneksel süperakışkanlık verici katkı maddesi kullanılmıştır. Bu süper akışkanlaştırıcının en öenmli özelliği çimento dağılımının etkinliğini büyük ölçüde arttırmasıdır.

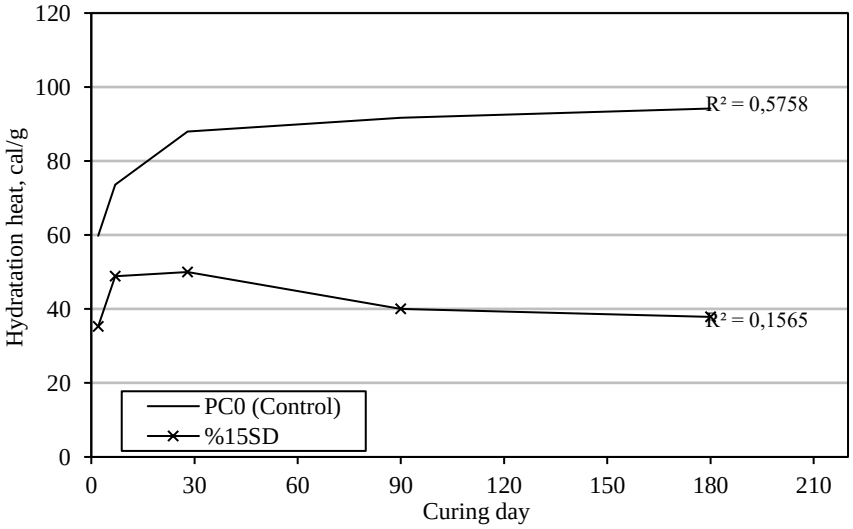
2.2.Metod

Deneysel çalışmalar Giresun Üniversitesi İnşaat laboratuvarlarında gerçekleştirilmiştir. Ürün olarak Ünye Çimento Fabrikası PC kullanılarak beton numuneleri üretilmiştir. Puzolan olarak kullanılan SD, çimentoya ağırlıkça %15 oranında ilave edilerek beton üretimi gerçekleştirilmiştir. Harç karışımları 150x150x150 mm'lik kalıplarda kimyasal katkı kullanılmadan üretilmiştir. Numuneler 24 saat sonra kalıptan çıkarılmış ve musluk suyunda 20 ^{0}C'de (2, 7, 28, 90, 180) kürlenmiştir. Numuneler üzerinde fiziksel deneyleri (hidratasyon ısısı, geçirgenlik) değerleri incelenmiştir. Hidratasyon ısısı ölçümleri MC-CAL izotermal kalorimetre cihazı kullanılarak yapılmıştır.

3. Deneysel Sonuçlar

3.1. Hidratasyon Isısı(cal/gr)

Beton harçların hidratasyon ısısı değeri önemli fiziksel özelliğidir. Özellikle kütle betonlarında kullanılması gereken çimentoların 7 günde en fazla 60 cal/g ve 28 günde de an fazla 70 cal/g civarında toplam hidratasyon ısısına sahip olmaları talep edilir.

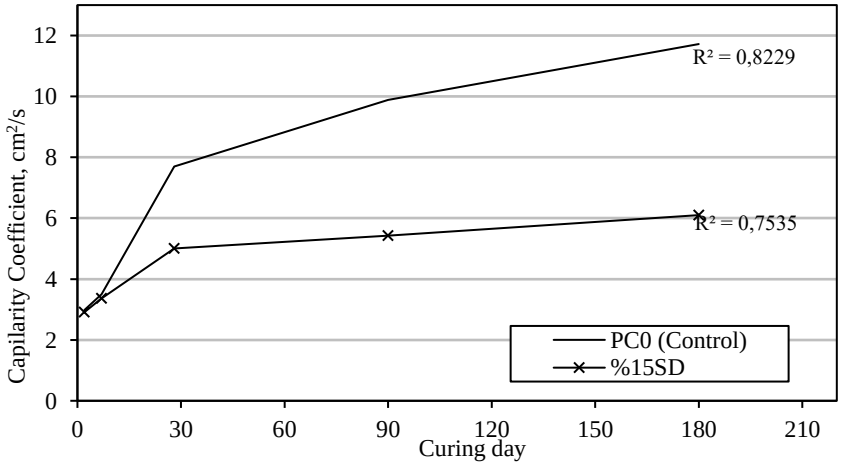


Şekil 1. Harçların hidratasyon ısısı değerleri

Şekil 1' de %15SD ve PC(CEM I 42,5R) içeren çimentoların hidratasyon ısılarının karşılaştırılması verilmektedir. Grafikten görüldüğü üzere, SD katkılı harçların hidratasyon ısısı PC harçlara kıyasla %40.5 daha düşük çıkmıştır.

3.2. Kılcallık Katsayısı(cm^3/s)

Beton harçlarının kılcallık katsayılarını belirlemek için testler yapılmıştır. Şekil 2'de görüldüğü gibi 15SD katkılı betonların kılcallık katsayı değerleri referans betonlara göre en iyi sonucu vermekte olup, 28, 90 ve 180 gün sonunda 5.0, 5.43 ve 6.1 cm^2/s elde edilmiştir. Kürlenme süresi arttıkça kılcallık katsayısı artar.



Şekil 2. Kürlenme süresine bağlı olarak farklı çimento harçlarının kılcallık katsayıları.

4. Sonuç ve Öneriler

Çalışmanın sonuçları aşağıda verilmiştir;

- 15SD katkılı harçların hidratasyon ısısı PC harçlara kıyasla %40.5 daha düşük çıkmıştır.
- Birim ağırlık, PC harçlar SD katkılı harçlara kıyasla daha düşük bulunmuş olup %3.3 oranında azalmıştır.

- 15SD katkılı betonların kılcallık katsayı değerleri referans betonlara göre en iyi sonucu vermekte olup, 28, 90 ve 180 gün sonunda 5.0, 5.43 ve 6.1 cm^2/s elde edilmiştir. Kürlenme süresi arttıkça kılcallık katsayısı artar.
- Mikroyapı olarak SD katkısı ile açığa çıkan CH miktarının azaldığı değerlendirilmektedir. Ayrıca, SD'nin zamanla kalan CH' ı bağladığı, gözenekleri tıkadığı geçirimsizliği arttırdığı düşünülmektedir.
- %15SD harçlarından üretilen beton, durabilite açısından baraj, beton yol, tünel vb. olarak kullanılabilir.

Kaynaklar

[1] Keçeci, A.,Effects of Using Silica Fume on Concrete Compressive Strength and Adherence in Self-Compacting Concrete, Konya University, Graduate School of Education Departments, Master Thesis, 2018.

[2]T, Uygunoglu,., I.B. Topçu, A.G. Çelik., Use of waste marble and recycled aggregates in self-compacting concrete for environmental sustainability, Journal of Cleaner Production 84(1), pp. 691-700, 2014.

[3] Yeğinobalı, A., Its Use in Concrete with Silica Fume and Cement. Turkish Cement Manufacturers Association. Ankara, 64s, 2002.

[4] Özcan, F., Atiş, C. D., Carbonation and shrinkage properties of mortars produced with silica fume, Ömer Halisdemir University, Journal of Engineering Sciences, Volume 6, Issue 2, 634-64128. 2017.

[5] Xiaofeng, C. et al., Role of silica fume in compressive strength of cement paste, mortar and concrete, ACI Materials Journal, Detroit, 89(4), 375-388. 1993.

[6] Duval, R., Kadri, E.H., Influence of Silica Fume on the Workability and the Compressive Strength of High-Performance. Concretes. Cement and Concrete Research, 533-547. 1998.

[7] Celik A G and Cakal G O., Characterization of espey colemanite and variation of its physical properties with temperature. Physicochem. Prob. Miner. Proces. 52: 66 – 76. 2016.

ISC'22 2nd International Symposium on Characterization
22-25 September 2022 Afyonkarahisar, Türkiye

Power Law Friction Factor Equation for Commercial Pipeline Hydraulic Design Accounting Local Pressure Losses Using *MathCAD*

Gürol Yıldırım

Giresun University, Civil Engineering Department, Hydraulics Division, Giresun, Turkey.

Abstract

The paper presents a design procedure improved by using power law friction factor, which provides accurate solutions for three types of pipe design problems (Types A, B and C) with considering effect of local losses. The parameters introduced in the power law are related with the type and size of commercial pipes, thus several dimensionless physical numbers by a suitable combination of the variables for the solution of Type B and Type C problems, are also introduced. For solution of the general case of a Type B problem (sloping pipe with pumping power), user-friendly the *MathCAD* procedure, which produces a consistent framework for analyzing and solving common piping-system applications, was also carried out. In order to prove degree of accuracy of the present technique, several design examples are examined for three types of commercial pipes, and for a wide range of uniform pipe slope, and the results are shown in the design curves. The curves employed have practical importance to quickly determine the values of required variables for a given pipe slope. The present technique gives an opportunity to compare the results of the proposed method with those of obtained from the existent literature, in profession practice.

Keywords: Water distribution networks; Pipeline design; Commercial pipes; Pipe hydraulics; Pressurized flows; Steady-state analysis; Software; Power law equation, Math*CAD*.

* Corresponding author e-mail: gurol.yildirim@giresun.edu.tr

1. Introduction

Analysis and design problem of water distribution networks has been and will continue to be a main subject of the hydraulic engineering. Three types of design problems of single-lined commercial pipes arise with the existing solution techniques: optimization of the pump power (Type A), determining of discharge (Type B), and design of the smallest pipe size or pipe length (Type C) (Yıldırım 2006, 2008a,d).

The conventional estimation method requires lengthy iterative process since the friction factor is a function of relative roughness of the pipe and Reynolds number, even for a single-lined set of pipes and even without considering local losses. However, with progress in technology and solution techniques, automated methods which provide accurate and convenient alternatives to the manual methods, have become available for solving different pipe-flow problems (Larock et al. 2000, Finnemore and Franzini 2002).

The Colebrook-White (C-W) equation (Colebrook and White 1937, Colebrook 1939) has been widely used to estimate the friction factor for turbulent fluid flow in rough pipes.

However this equation, which relates the friction factor to pipe roughness and Reynolds number (R), is implicit for the friction factor (*f*). Recognizing the implicit nature of the CW equation, *f* versus R charts were constructed early on (Moody 1944) that allowed for a graphical estimation of *f* when R and pipe roughness were known. Since then, several approximations of the C-W equation that are explicit in the friction factor have been proposed (Moody 1947, Churchill 1977, Jain 1976, Swamee and Jain 1976, Zigrang and Sylvester 1982, Haaland 1983, Keady 1998, Sonnad and Goudar 2004, 2006, Ozger and Yıldırım 2008, Yıldırım and Özger 2009, Yıldırım 2008b,c, Yıldırım 2009a,b,c).

Recently, for practical use and easy manipulation of a simple design of single-lined pipes with neglecting local losses (Yıldırım 2007, 2008a), the friction factor of the power law have been suggested by Yoo and Singh (2004). Following this work, Yoo and Singh (2005) have also proposed two methods for estimating the friction factor of commercial pipes; one combining the zero velocity points and the other combining the friction factors of the smooth and rough parts of the pipe.

The aim of this paper is to present an accurate design procedure with considering effect of local losses, for three design cases of commercial pipes, on the basis of the power form friction factor. The proposed technique is suitable for analysis and design problems of single-lined pipeline networks, and produces simple but exact solutions for routine engineering applications.

2. Analysis of Commercial Pipeline Design Problems

The design problems of commercial pipelines with uniform slope can be analyzed in three main categories: In the Type A problems, the required parameters are pump power (P_W) and/or friction or total energy loss (h_f, h_T); and initially known parameters are pipe slope (s), pipe diameter (D), pipe length (L), discharge (Q), and material type of the commercial pipe (galvanized-iron, wrought-iron, tar-coated cast-iron, PVC, concrete etc.). In the Type B problems, the values required are Reynolds number (R), velocity (V) or Q and/or h_f, h_T; known parameters are P_W, and pipeline properties (pipe type, s, D, and L); and for the Type C problems, the required parameters are D or L, and/or h_f, h_T; known parameters are pipe type, s, Q, and P_W.

Each of three types of design problems can be analyzed in their subclasses depending on the existent/no existent design cases are: neglecting or considering local losses, h_l, horizontal (s = 0) or sloping pipe and, with or no pumping power, P_W. Table 1 synthesizes the three types of design problems (A, B and C) and their subclasses (A_1, A_2, A_3, $A_{1\text{-}3}$, $A_{2\text{-}3}$; B_1, B_2, B_3, $B_{1\text{-}3}$, $B_{2\text{-}3}$; C_1, C_2, C_3, $C_{1\text{-}3}$, $C_{2\text{-}3}$) with corresponding equations. Note that in this table, the design parameters; h_l, s, and P_W are represented with corresponding dimensionless physical numbers (M, N and J), respectively, which will be defined in the next section.The problems in the categories A and B are analysis problems. Analysis of the Type A problems is direct, without iteration, even if any type of friction factor equation is used. However, iteration may be required for the Type B problems. Type C is a sizing problem, which normally requires more assumptions and more iterative computations to solve.

Table 1. General Types of Commercial Pipeline Design Problems with Their Subclasses

Problem Type	Known Quantities	Required Parameters	Related Eqs.
A	Discharge (Q), pipeline properties	Pumping power (P_W) and/or friction/total energy loss (h_f, h_T)	**(1)~(9)**
B	P_W, pipeline properties	Reynolds number (R), velocity (V) or discharge (Q) and/or h_f, h_T	**(10)~(13)**
C	Pipe slope (s), pipe type, Q, P_W	Smallest pipe size (D) or pipe length (L) and/or h_f, h_T	**(14) ~(18)**

Subclasses:	Existent Design Cases:	No Existent Design Cases:
A, B, C	s (N), h_l (M), P_W (J)	-
A_1, B_1, C_1	h_l (M), P_W (J)	s (N)
A_2, B_2, C_2	p = -1; s (N), h_l (M)	P_W (J)
A_3, B_3, C_3	s (N), P_W (J)	h_l (M)
$A_{1\text{-}3}$, $B_{1\text{-}3}$, $C_{1\text{-}3}$	P_W (J)	s (N), h_l (M)
$A_{2\text{-}3}$, $B_{2\text{-}3}$, $C_{2\text{-}3}$	p = -1; s (N)	h_l (M), P_W (J)

Note: Pipeline properties include the pipe diameter or length (D or L), uniform pipe slope (s), and pipe type; p: slope indicator (p = 0, -1, and 1; for zero, downhill and uphill slope, respectively); h_l: local loss; M, N and J are dimensionless physical numbers related to the parameters h_l, s and, P_W, respectively; the subscripts of subclasses illustrate existent design cases; (1): horizontal pipe case, (2): attractive pipe flow case (with no pumping power), and (3): design case with neglecting local losses, respectively.

In recent years, preprogrammed equation solvers have become available on certain more advanced programmable scientific calculators and in some spread sheet and mathematics software packages like *MathCAD*, *Matlab* or *Excel*. Effective instruction in hydraulic design and piping system analysis has been the subject of several recent publications (Huddleston et al. 2004, Huddleston 2002, Jewell 2001, Gottfried 2000, Hodge and Taylor 2002, Weiss and Gulliver 2001, Yıldırım 2006). Note that, the December 2001 issue of the *Journal of Hydraulic Engineering* was devoted to the topic of teaching hydraulic design. Consequently, to avoid tedious trial-and-error procedure the automated solution techniques can be easily applied for the solution of both the types of pipe design problems (Types B and C) (Larock et al. 2000, Finnemore and Franzini 2002).

3. Governing Power Law Equation

The governing design formulation of a single-lined pressurized pipe with uniform slope can be expressed in the general form:

$$P_W = \gamma Q H_P \tag{1}$$

$$H_P = h_T + psL \tag{2}$$

$$h_T = h_f + h_l = (k_f + k_l)\frac{V^2}{2g}; \qquad k_f = f\frac{L}{D} \tag{3}$$

where $P_{W(Kgms^{-1})}$ = pump power in which a unit conversion factor can be applied to this result to express the power, horsepower (*HP*) or kilowatts (*kW*); γ = specific weight of fluid (Kgm^{-3}); Q = discharge (m^3s^{-1}); H_P = total pumping head (m); h_T , h_f and h_l = total, friction and local energy losses, respectively (m); k_f and k_l = pipe friction loss and total local loss coefficients, respectively; V = mean velocity in the pipe cross-section (ms^{-1}); D and L = pipe diameter and length, respectively (m); $V^2/2g$ = kinetic head (m); s = pipe slope assuming to be uniform along the pipeline; p = slope indicator which is taken 0, -1 and 1; for zero, downhill, and uphill slope cases, respectively; and f = Darcy-Weisbach friction factor.

4. Power Form Friction Factor (*f*) Formula

Yoo and Singh (2004) have developed new sets of pipe friction factor equations with neglecting local losses in the form of a power law that allows explicit solutions for three types of pipe design problems. They have compared the results of the power law with those of the Colebrook-White (C-W) and Hazen-Williams (H-W) equations; thus have reported that the overall error of the power law is 5.89%, while that of the C-W equation is 11.24%, and that of the H-W is 15.25%.

The power law friction factor for commercial pipes is given by (Yoo and Singh 2004):

$$f = \alpha R^{\beta}; \qquad \alpha = \omega\left(\frac{D}{D_0}\right)^{\zeta} \tag{4}$$

$$R = \frac{VD}{\nu} = \frac{4Q}{\pi D\nu}; \qquad V = \frac{4Q}{\pi D^2} \tag{5}$$

where α, ω, β and ζ = empirical constants of power law friction factor as a function of pipe sizes (small: D < 25 mm; medium: 25 mm < D < 1 m; and large: D > 1 m) and pipe type (galvanized-iron, wrought-iron, tar-coated cast-iron and PVC); R = Reynolds number; D_0 = base diameter (= 1 m); and ν = kinematic viscosity of water ($\cong 10^{-6}\, m^2s^{-1}$).

5. Methodology

5.1. Head Loss and/or Pump Power Problem (Type A)

Combining Eqs. (4) and (5) into Eq. (3) for the pipe friction loss, finally the h_f can be deduced in the power form:

$$h_f = KQ^{2+\beta} \tag{6}$$

$$K = \frac{\omega(4/\pi)^{2+\beta}}{2g\nu^{\beta}D_0^{\zeta}} \frac{L}{D^{5+\beta-\zeta}} \tag{7}$$

where K = dimensional unit conversion factor which can be applied to express the h_f in meter ($s^{2+\beta}/m^{3\beta+5}$).

Resulting, general form of a type A problem (considering local losses) can be directly solved by Eq. (1) with Eqs. (2) and (3).

For a simple design case of neglecting local losses (Type A_3), the P_W can be computed from:

$$P_W = \sigma\gamma QL \quad (h_l = 0) \tag{8}$$

$$\sigma = s' + ps; \qquad s' = \frac{h_f}{L} = \frac{KQ^{2+\beta}}{L} \tag{9}$$

where σ = dimensionless constant which is summation of the friction slope, s', and the uniform pipe slope, s; s' = the friction slope or the slope of the energy-grade line (m/m); p and s = slope indicator and uniform pipe slope, respectively, defined in the previous section.

5.2. Discharge or Velocity Problem (Type B)

In order to determine the discharge (or velocity) through the pipeline, new dimensionless physical numbers will be introduced in this section. For the solution of a Type B problem, the general governing equation, Eq. (1) is restated in terms of the Reynolds number, substituting the power law friction factor given by Eq. (2) into Eq. (1) then yields:

$$MR^3 + \alpha R^{3+\beta} + 2pN^2R - \frac{8}{\pi}J^3 = 0 \tag{10}$$

$$M = k_l\frac{D}{L}; \qquad N = \frac{(gs)^{1/2}D^{3/2}}{\nu}; \quad J = \frac{1}{\nu}\left(\frac{P_W gD^2}{\gamma L}\right)^{1/3} \tag{11}$$

where M, N and J = dimensionless physical numbers (Yoo and Singh 2004). Noting that in Eq. (4), one unknown is R when the discharge or velocity is the required one parameter; then, the other physical numbers can be determined depending on the initially known quantities.

For a simple design case of a pumping power on a horizontal pipeline and neglecting local losses (Type $B_{1\text{-}3}$: $s = 0$, $N = 0$; $h_l = 0$, $M = 0$), the Reynolds number, R_J is directly computed from (Yoo and Singh 2004):

$$R_J = \lambda_J J^{\delta_J}; \qquad \lambda_J = \left(\frac{8}{\pi\alpha}\right)^{1/(3+\beta)}; \qquad \delta_J = \frac{3}{3+\beta} \tag{12}$$

For the case of a downhill sloping pipe with no pumping power and neglecting local losses (Type $B_{2\text{-}3}$: p = -1, $P_W = 0$, $J = 0$; and $h_l = 0$, $M = 0$), the Reynolds number, R_N is given by

$$R_N = \lambda_N N^{\delta_N}\ ;\quad \lambda_N = \left(\frac{-2p}{\alpha}\right)^{1/(2+\beta)}\ ;\qquad \delta_N = \frac{2}{2+\beta} \tag{13}$$

5.3. Sizing (Pipe Diameter or Length) Problem (Type C)

In order to design of pipe diameter, D, a new dimensionless physical number, S_D in relation with the discharge is also introduced. Rearranging Eq. (1) with Eq. (2), in terms of S_D, then yields (with D_0 = 1 m):

$$\left(\frac{\pi^2}{8}\right) T^5 {S_D}^4 - \omega\left(\frac{4}{\pi}\right)^{\beta} {S_D}^{\zeta-(1+\beta)} {S_{0D}}^{-\zeta} - k_l {S_L}^{-1} = 0 \tag{14}$$

$$T = \frac{g^{1/5}}{\nu}\left(\frac{P_W Q^2}{\gamma L} - psQ^3\right)^{1/5}\ ;\quad S_D = \frac{\nu D}{Q} = \frac{4}{\pi R}\ ;\quad S_{0D} = \frac{\nu D_0}{Q}\ ;\qquad S_L = \frac{\nu L}{Q} = \frac{4L}{\pi D R} \tag{15}$$

where T, S_D, S_{0D} and S_L = dimensionless physical numbers (Yoo and Singh 2004); and g = acceleration due to gravity (ms^{-2}).

For the Type C problems, all physical numbers except for S_D (for this case, S_L is a known parameter) are determined using the initially known values; and the S_D can be easily determined by using one of the user-friendly software packages mentioned above.

As a special case, when the local losses are neglected (Type C_3: $h_l = 0$, $M = 0$), then yields:

$$S_D = \lambda_T T^{\delta_T} \quad (h_l = 0)\ ;\quad \lambda_T = \left[\frac{\omega}{2}\left(\frac{4}{\pi}\right)^{2+\beta} {S_{0D}}^{-\zeta}\right]^{1/(5+\beta-\zeta)}\ ;\ \delta_T = \frac{5}{[\zeta-(5+\beta)]} \tag{16}$$

The similar derivative procedure presented above can be followed to determine the pipe length, L (the D is a known parameter, for this case) by introducing another physical number, S_L:

$$S_L = \frac{4}{\pi}\left(\frac{2{J_L}^3 - k_l R^2}{\alpha R^{3+\beta} + 2pN^2 R}\right) \tag{17}$$

$$J_L = \frac{1}{\nu}\left(\frac{4gP_W D}{\gamma\pi R}\right)^{1/3}\ ;\quad \text{or}\quad J_L = \left(\frac{gP_W D^2}{\gamma Q \nu^2}\right)^{1/3} \tag{18}$$

where J_L = dimensionless physical number. Noting that, Eq. (17) with Eq. (18) can be directly used without needing iterative procedure.

6. Computational Application

In order to present the practicability the proposed design equations, an original example (Larock et al. 2000), for the Type B problem of a downhill sloping pipe case (with no pumping power), is selected herein.

A tar-coated cast-iron pipe connects two reservoirs having a difference in water surface level of only 6.1 m. Length of the pipeline is 365 m and has a diameter of 0.46 m (= 18 *in.*). a) determine the discharge when only pipe friction is considered; b) determine the change of discharge computed when local losses for a sharp-edged entrance, a fully open gate valve near the pipe exit, and the pipe exit itself are also considered; c) determine the new discharge for the case of the gate valve in part (b) were only 1/4 open.

a) This is a Type $B_{2\text{-}3}$ problem (p = -1: $h_l = 0$, $M = 0$ and $P_W = 0$, $J = 0$); so, Eq. (13) can be directly used as the following steps:

The empirical parameters (ω, ζ, β) for tar-coated cast-iron pipe of medium size (25 mm < D = 0.46 m < 1 m): ω = 0.071, ζ = -0.255, and β = -0.13 (Table 1 of Yoo and Singh 2004).

From Eq. (4): $\alpha = 0.071\times(0.46/1)^{-0.255} = 0.0865$

Slope of the pipeline, $s = \frac{6.1}{365} = 0.0167$ (p = -1; downhill slope)

From Eq. (11): $N = \frac{(9.81\times 0.0167)^{1/2}\,0.46^{3/2}}{10^{-6}} = 1{,}26325.1$

From Eq. (13): $\lambda_N = \left(\frac{-2\times(-1)}{0.0865}\right)^{1/(2-0.13)} = 5.3615$; $\delta_N = \frac{2}{(2-0.13)} = 1.0695$

Then finally, $R_N = 5.3615\times 126325.1^{1.0695} = 1{,}532250$ is obtained.

From Eq. (5): $Q = \frac{\pi D\nu}{4} R = \frac{\pi\times 0.46\times 10^{-6}}{4}\times 1{,}532250 = 0.554\ m^3s^{-1}$

and therefore, V = 3.33 ms^{-1}.

From Eq. (4): $f = 0.0865\times 1{,}532250^{-0.13} = 0.0136$

From Eq. (6) with Eq. (7): $K = \frac{0.071\times(4/\pi)^{(2-0.13)}}{2\times 9.81\times 10^{-6(-0.13)}\times 1.0^{-0.255}}\times\frac{365}{0.46^{(5-0.13+0.255)}} = 18.425$ then finally, $h_f = 18.425\times 0.554^{2-0.13} \cong 6.1$ m ($s' = 0.0167$), is computed.

b) This is a Type B_2 problem (p = -1: $h_l \neq 0$, $M \neq 0$ and P_W = 0, J = 0); the local loss coefficients for a sharp-edged entrance and pipe exit; $k_{ent.}$ = 0.5 and $k_{ex.}$ = 1.0, and for fully open gate valve, k_{valve} = 0.2 (Larock et al. 2000, Table 2.5). Therefore, the total local loss coefficient, $k_l = (0.5+1.0+0.2) = 1.7$ is found.

From Eq. (11): $M = 1.7\times\frac{0.46}{365} = 2.142\times 10^{-3}$

From Eq. (10): $(2.142\times 10^{-3})\times R^3 + 0.0865\times R^{2.87} - (3.189\times 10^{10})\times R = 0$

Using *MathCAD Equation-Solver*: $R = 1.415\times 10^6$ then, Q = 0.511 m^3s^{-1} and V = 3.1 ms^{-1} are computed. This result indicates that, the discharge has decreased by 0.043 m^3s^{-1}, a bit under 8%, as a consequence of considering local losses. Using Eqs. (3)~(7), one can obtain the following results:

f = 0.0137, h_f = 5.25 m and $h_l = 1.7\times 3.1^2/(2\times 9.81) = 0.82$ m (h_T = 6.1 m).

c) Similar procedure presented in part (b) is repeated except for the gate valve is only 1/4 open. For this case, the valve loss coefficient has increased from 0.2 to 17.0 (Larock et al. 2000, Table 2.5) since it will cause more head loss than the pipe friction term. Replacing 0.2 in part (b) by 17.0 (k_l = 18.5, M = 0.0233), we recomputed and find the values: Using *MathCAD Equation-Solver*, $R = 9.15\times 10^5$ then, Q = 0.33 m^3s^{-1}, and V = 1.98 ms^{-1}, f = 0.0145, h_f = 2.32 m and h_l = 3.69 m (h_T = 6.1 m). It is remarkable result from the analysis, a decrease of about one third from the discharge computed in part (b).

7. Design Examples in Engineering Practice

In the following, two design examples for different series pipe-flow problems (Types B_3 and C_3) with a general design case (sloping pipe with pumping power) will be presented, respectively.

7.1. Example 1 (Type B_3: Uphill Sloping Pipe)

It is required to supply the water from the reservoir at elevation 410.4 m to another reservoir at elevation 433.2 m with a pump of effective power 58.5 *kW*. Length of the line of a tar-coated cast-iron pipe ($\omega = 0.071$, $\zeta = -0.255$, and $\beta = -0.13$) is 1824 m, and has a diameter of 0.46 m (= 18 *in.*) with neglecting local losses, compute the discharge in the pipeline.

This is a Type B_3 problem, and computation is done in the following steps:

$s = (433.2 - 410.4)/1824 = 0.0125$ (p = 1.0, uphill slope)

From Eq. (11): M = 0, N = 109,251.2 and J = 189,328.3 are computed and substituted into Eq. (10), then finally we obtain: $0.0865R^{2.87} + 2.387\times10^{10}R - 1.728\times10^{16} = 0$

Using *MathCAD Equation-Solver:* $R = 5.9\times10^{5}$ then, Q = 0.213 m^3s^{-1} and V = 1.28 ms^{-1}, f = 0.0154 and h_f = 5.1 m and therefore, $s' = 5.11/1824 = 2.8\times10^{-3}$, are computed. It should be noted, in order to check the accuracy of the results obtained from the computation, Eqs. (8) and (9) can be directly used as follows: $\sigma = s' + ps = 2.8\times10^{-3} + 1.0\times0.0125 = 0.0153$; then finally $P_w = 0.0153\times1000\times0.213\times1824/102 = 58.5\,kW$ ($H_P = 5.1 + 1.0\times0.0125\times1824 \cong 28.0$ m).

On the basis of the algorithm discussed, the computations of Example 1 are also extended to cover three types of a commercial pipe (tar-coated cast-iron, galvanized-iron and wrought-iron) of medium size (25 mm < D = 0.46 m < 1 m), and for various slope combinations; then the results are shown in Figs. 1, 2 and 3. The empirical parameters of power form friction factor by Eq. (4), for three pipe types are (Yoo and Singh 2004): tar-coated cast-iron: $\omega = 0.071$, $\zeta = -0.255$, and $\beta = -0.13$ ($\alpha = 0.0865$); galvanized-iron: w = 0.034, $\zeta = -0.282$, and $\beta = -0.08$ ($\alpha = 0.0423$); and wrought-iron: w = 0.067, $\zeta = -0.135$, and $\beta = -0.12$ ($\alpha = 0.0744$).

The design curves in Figs. 1, 2 and 3 have a practical importance to quickly determine the values of design parameters for a given pipe slope. It should be noted for Figs. 1 and 2, the slope ranges in percent are indicated on the axis of x (starting from 0% to $\pm$10%); and the values of the design parameters for different downhill (on dotted line) and uphill (on straight line) slope ranges, are individually represented on the first axis and secondary axis of y, respectively.

Fig. 1.a, 1.b and 1.c illustrate the variation of discharge, Q, total pumping head, H_P, and head loss due to friction, h_f, , respectively; whereas Fig. 2.a and 2.b show the values of friction factor, f and Reynolds number, R, versus different ranges of downhill and uphill slopes. On the other hand, the values of pumping power, P_W, for three pipe types and for different ranges of uphill slope are also plotted in Fig. 3.

As shown in Figs. 1 and 2, for the three pipe types, as the down slope increases the discharge, the Reynolds number, and the head loss due to friction increase (with decreasing the f); whereas the total pumping head decreases. In other word, the values of Q, R, and h_f decrease (with increasing the f); whereas the values of H_P increase with increasing the upslope.

Examination of the results indicated that (Figs. 1 and 2) for the three pipe types, variation of the Q, R, h_f , and H_P coincides except for a little change, for a wide range of pipe slope; whereas as the upslope increases more deviation for the values of friction factor (Fig. 2.a) is observed.

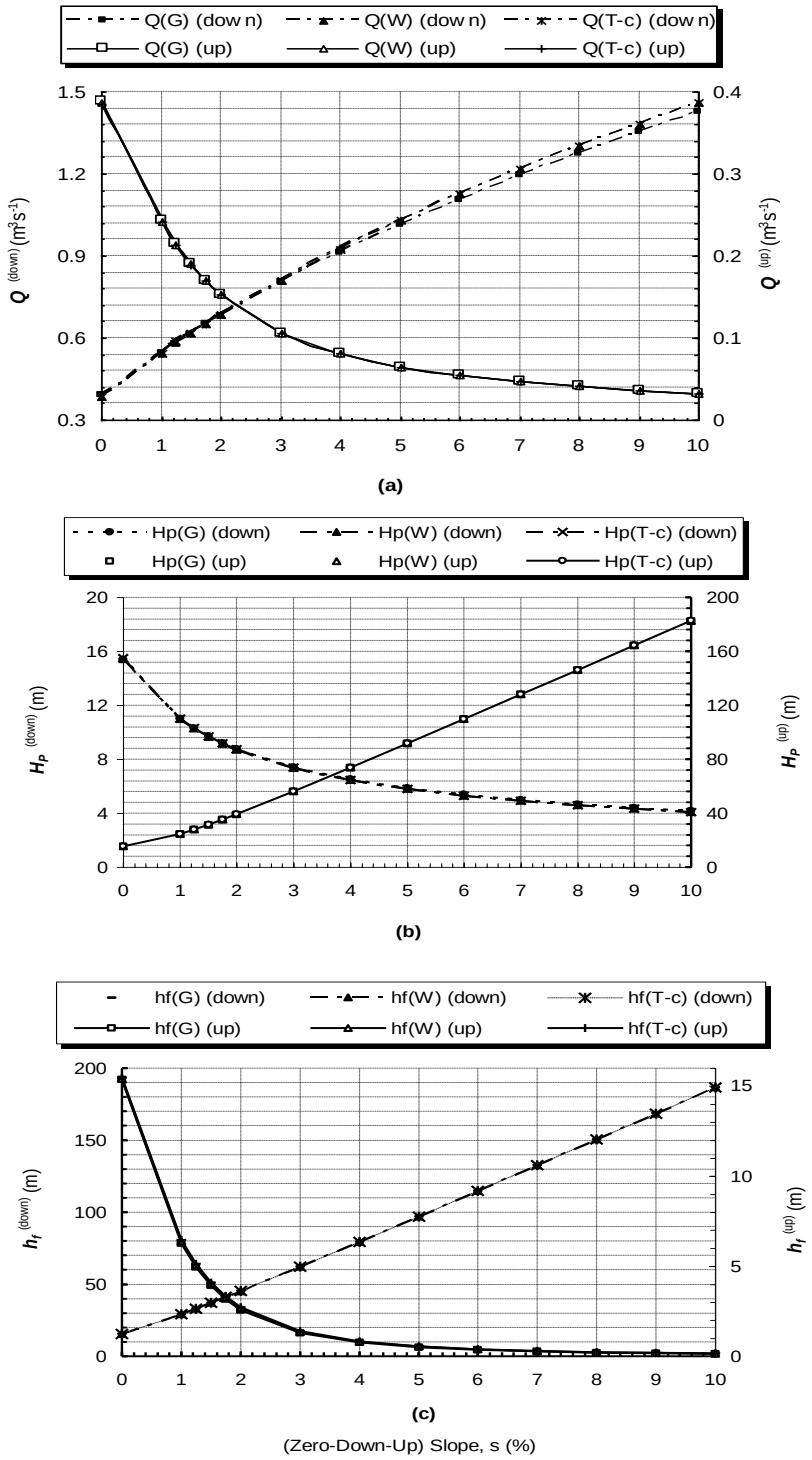


Figure 1. Results for the Design Variables [(a):Discharge, Q, (b): Total Pumping Head, H_P , and (c): Head Loss due to Friction, h_f] for Different Pipe Slopes (s = 0% ~ s = ±10%), and for Three Types of Commercial Pipe [G: Galvanized-iron, W: Wrought-iron, and T-c: Tar-coated cast-iron], Using Data of Example 1 (s = 1.25%, uphill slope).

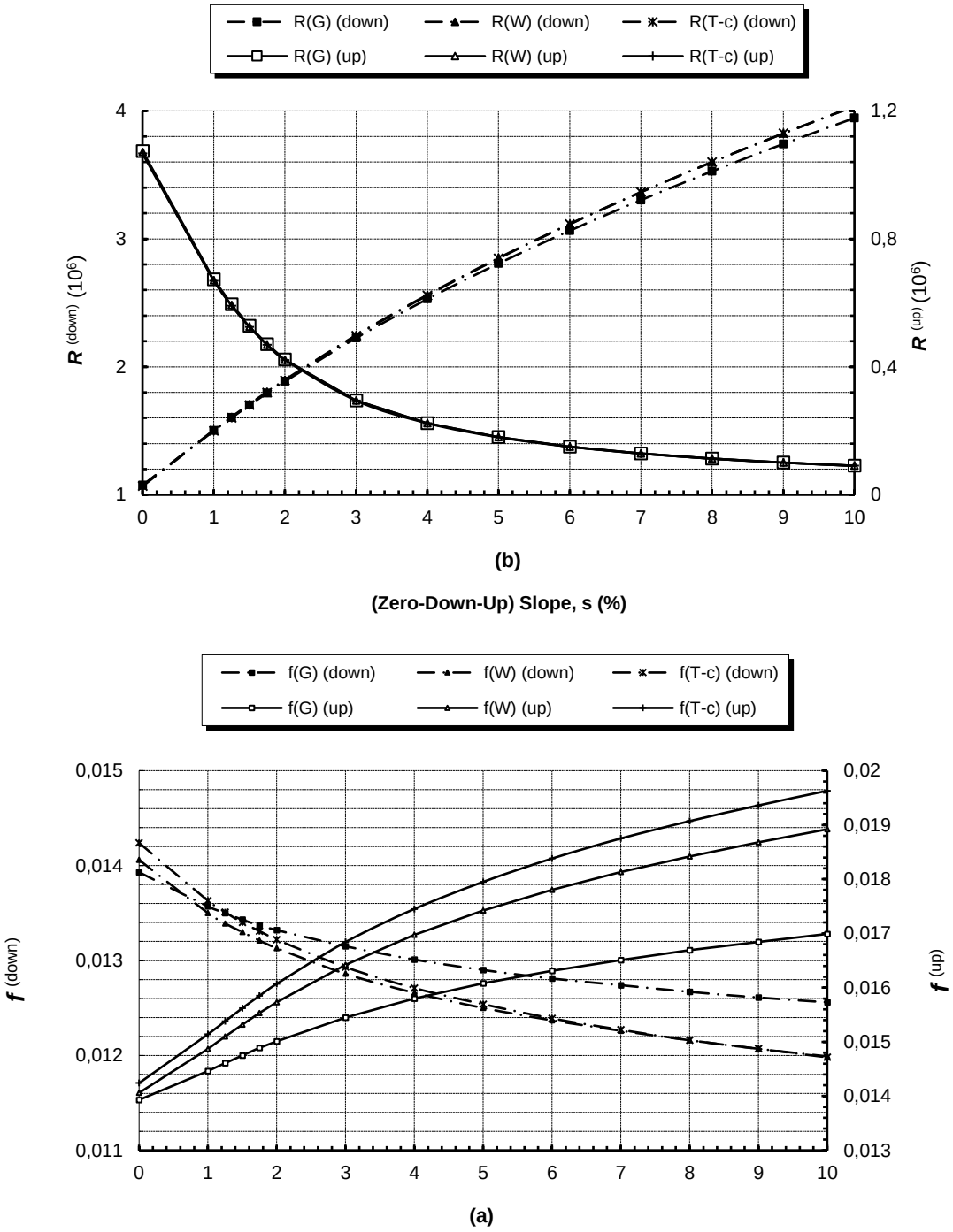


Figure 2. Results for (a): Friction Factor, f , and (b): Reynolds Number, R; for Different Pipe Slopes (s = 0% ~ s = ±10%), and for Three Types of Commercial Pipe [G: Galvanized-iron, W: Wrought-iron, and T-c: Tar-coated cast iron], Using Data of Example 1 (s = 1.25%, uphill slope).

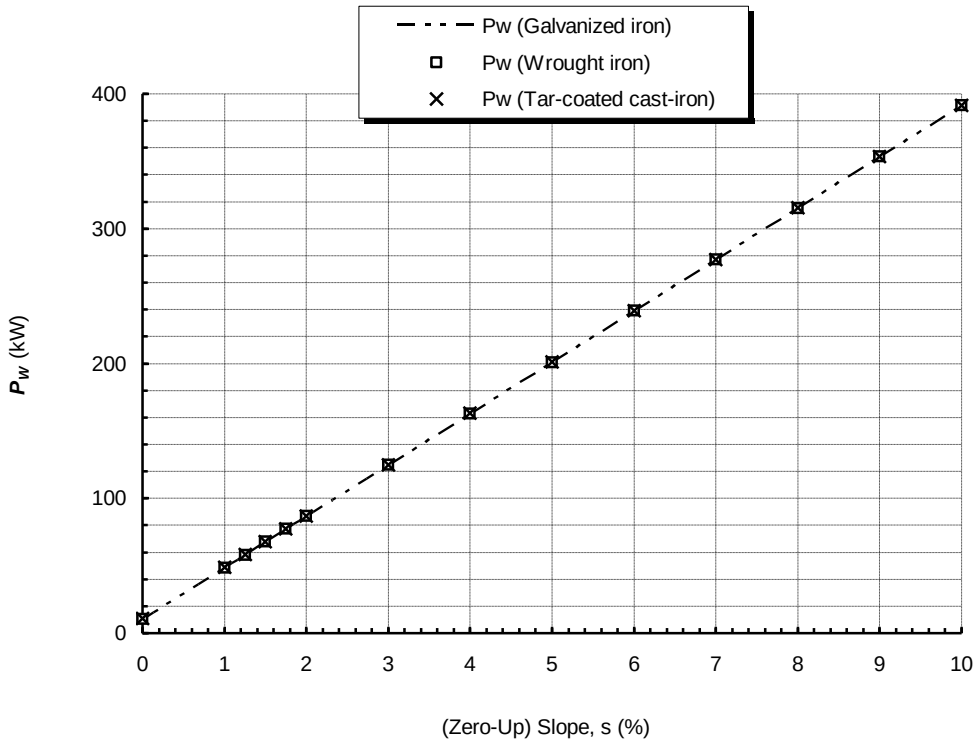


Figure 3. Results for Pumping Power (kW), P_W, for Different Uphill Slope Ranges (s = 0%~s = ± 10%), and for Three Types of Commercial Pipe [G: Galvanized-iron, W: Wrought-iron, and T-c: Tar-coated cast iron], Using Data of Example 1 (s = 1.25%, uphill slope).

7.2. Example 2 (Type C_3: Uphill Sloping Pipe)

The data of an original design problem presented by Yoo and Singh (2004) are selected herein, for the sake of comparison: the elevation difference between two reservoirs is 5 *m*, and the total pipe length including the equivalent length for secondary loss is 2 *km*. It is required to supply the water from the reservoir located below to the reservoir located above with the discharge of 0.2 m^3s^{-1} with a pump of effective power 10 *kW*. Compute the minimum diameter of tar-coated cast-iron pipe.

This is a Type C_3 problem, and the computation steps are presented:

1. $s = 5/2000 = 0.0025$ (p = 1.0, uphill slope);

2. From Eq. (15):

$$T = \frac{9.81^{1/5}}{10^{-6}} \times \left(\frac{10 \times 102 \times 0.2^2}{1000 \times 2000} - 1.0 \times 0.0025 \times 0.2^3 \right)^{1/5} = 82,405.6 ; \qquad S_{0D} = \frac{10^{-6} \times 1.0}{0.2} = 5 \times 10^{-6} ;$$

3. From Eq. (16):

$$\lambda_T = \left[\frac{0.071}{2} \times \left(\frac{4}{\pi} \right)^{2-0.13} \times (5 \times 10^{-6})^{0.255} \right]^{1/(5-0.13+0.255)} = 0.31 ; \qquad \delta_T = \frac{5}{[-0.255-(5-0.13)]} = -0.976 ;$$

$$S_D = 0.31 \times 82936.5^{-0.976} = 4.94 \times 10^{-6} ;$$

4. Then finally from Eq. (15):

$$D = \frac{S_D Q}{\nu} = \frac{4.94\times10^{-6}\times0.2}{10^{-6}} = 0.99 \cong 1.0 \text{ m};$$

5. From Eq. (6) with Eq. (7):

K = 1.887 therefore, $h_f = 1.887\times0.2^{2-0.13} = 0.093$ m (f = 0.0141); $s' = 0.093/2000 = 4.65\times10^{-5}$;

6. To check the results from Eqs. (8) and (9):

$\sigma = 4.65\times10^{-5} + 1.0\times0.0025 = 2.55\times10^{-3}$; $P_W = 2.55\times10^{-3}\times1000\times0.2\times2000/102 =$ 10 *kW*.

Moreover, the present example can be restated assuming the pipe length L, is a required parameter, and the pipe diameter (D = 1.0 m) with the remaining parameters (Q = 0.2 m^3s^{-1}, s = 0.0025, P_W = 10 *kW*) are initially known, for this case. The computation steps by using Eqs. (17) and (18) are:

1. $R = \frac{4Q}{\pi D\nu} = \frac{4\times0.2}{\pi\times1.0\times10^{-6}} = 254,648$; $\alpha = \omega\left(\frac{D}{D_0}\right)^{\xi} = 0.071\times\left(\frac{1.0}{1.0}\right)^{-0.255} = 0.071$;

$$N = \frac{(gs)^{1/2}D^{3/2}}{\nu} = \frac{(9.81\times0.0025)^{1/2}\times1.0^{3/2}}{10^{-6}} = 156,604.6;$$

2. $J_L = \frac{1}{\nu}\left(\frac{4gP_W D}{\gamma\pi R}\right)^{1/3} = \frac{1}{10^{-6}}\times\left(\frac{4\times9.81\times10\times102\times1.0}{1000\times\pi\times254,648}\right)^{1/3} \cong 36,848$;

$$S_L = \frac{4}{\pi}\left(\frac{2J_L^{\,3}}{\alpha R^{3+\beta} + 2pN^2R}\right) = \frac{4}{\pi}\times\left(\frac{2\times36,848^3}{0.071\times254,648^{3-0.13} + 2\times1.0\times156,604.6^2\times254,648}\right) \cong 0.01 \quad (k_l = 0);$$

3. $L = \frac{S_L Q}{\nu} = \frac{0.01\times0.2}{10^{-6}} = 2000$ m.

On the basis of the algorithm discussed, the data of Example 2 (Type C) are also applied for a wide range of pipe slope (starting from 0% to $\pm$1%), only for a pipe type of tar-coated cast-iron, and the complete results for the pipe diameter, are shown in Fig. 4.a. Furthermore, the values of the pipe length for different slope ranges, using the same data except for D = 0.4 m (Q = 0.2 m^3s^{-1}, s = 0.0025, P_W = 10 *kW*), with Eqs. (17) and (18), are also shown in Fig. (4.b).

Fig. 4.a illustrates that, as the down slope increases the pipe diameter decreases whereas the pipe length increases (dotted lines). In other word, the pipe diameter increases and the pipe length decreases (straight lines) with increasing the up slope (Fig. 4.b).

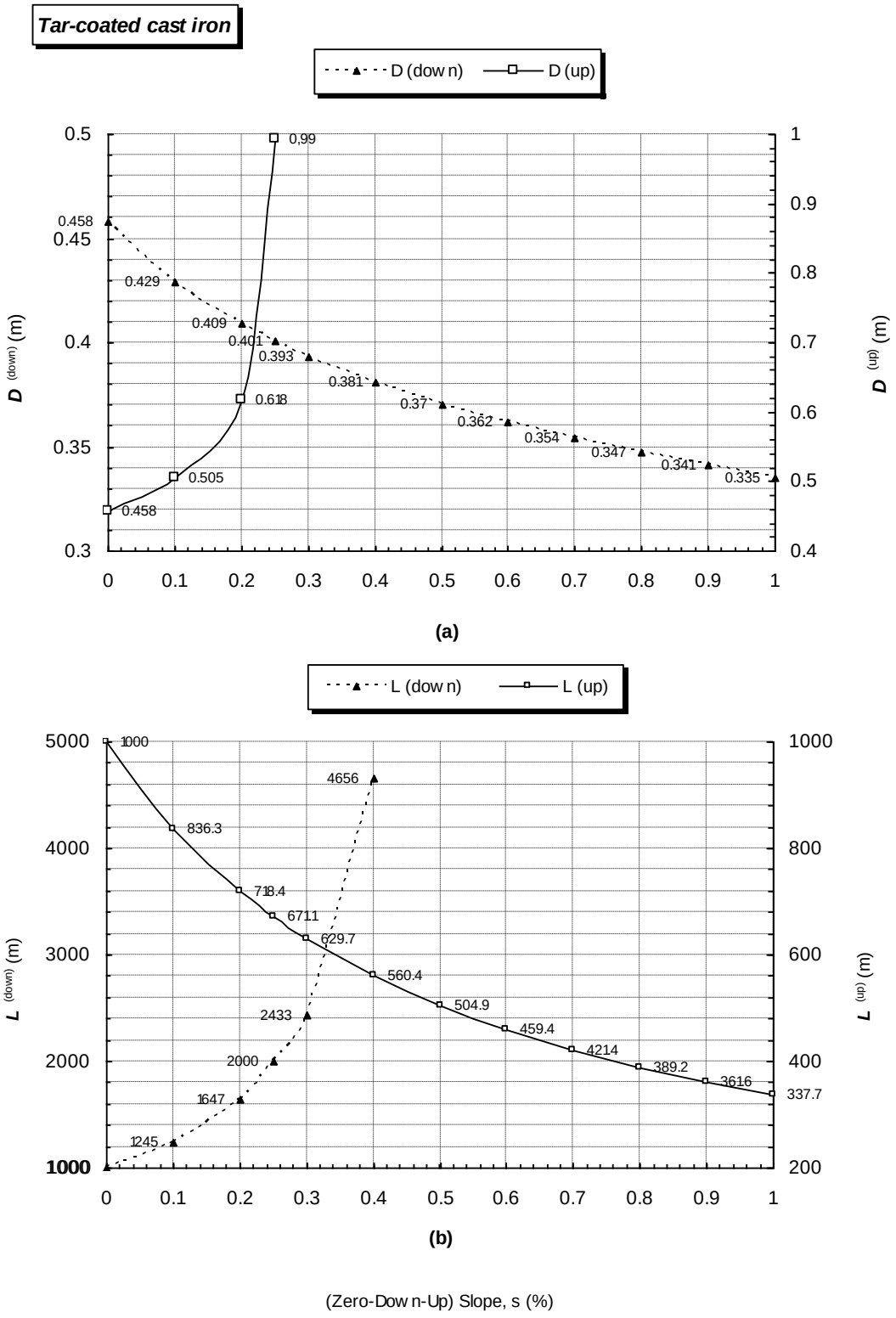


Figure 4. Results for (a): Pipe Diameter, D, and (b): Pipe Length, L; for Different Pipe Slopes (s = 0% ~ s = ± 1%), and only for Tar-coated Cast-iron Pipe, Using Data of Example 2 (s = 0.25%, uphill slope).

8. Summary and Conclusions

An accurate design procedure is developed by using power form friction factor, for three design cases of single-lined commercial pipelines. General equations improved in this procedure provide accurate solutions for the general case of three types of design problems with considering effect of local losses. The user-friendly *MathCAD* procedure was also carried out for solving general case of a Type B problem.

The proposed technique is applied on several design examples for three types of commercial pipes and for a wide range of uniform pipe slope, thus the results are shown in the design curves, for practical purpose. The curves employed give an opportunity to compare the complete results of the proposed method with those of obtained from the existent literature. It can be concluded that the software based-design technique is simple, easy to apply but sufficiently accurate in comparison with the traditional trial-and-error procedures, for different types of design problems of commercial pipelines, in routine hydraulic engineering applications.

9. Notation

The following symbols with dimensions are used in this paper:

D = pipe diameter [L];

D_0 = base diameter (= 1 *m*) [L];

f = Darcy-Weisbach friction factor;

g = acceleration due to gravity [LT^{-2}];

h_T = total head losses [L];

h_f = head loss due to friction [L];

h_l = head loss due to localized disruption of the flow [L];

H_P = total pumping head [L];

J = dimensionless physical numbers [Eq. (11)];

J_L = dimensionless physical number [Eq. (18)];

K = dimensional unit conversion factor [Eq. (7)] [$T^{2+\beta} L^{-(3\beta+5)}$].

k_f = pipe friction loss coefficient;

k_l = total local loss coefficient;

L = pipe length [L];

M = dimensionless physical numbers [Eq. (11)];

N = dimensionless physical numbers [Eq. (11)];

P_W = pump power [KLT^{-1}];

p = slope indicator which is taken 0, -1 and 1; for zero, downhill, and uphill slope cases;

Q = discharge [L^3T^{-1}];

R = Reynolds number;

R_J = R for the design case of $B_{1\text{-}3}$ [Eq. (12)];

R_N = R for the design case of $B_{2\text{-}3}$ [Eq. (13)];

s = uniform pipe slope;

s' = the friction slope or the slope of the energy-grade line;

S_D = dimensionless physical number [Eq. (15)];

S_{0D} = dimensionless physical number [Eq. (15)];

S_L = dimensionless physical number [Eq. (15)];

T = dimensionless physical number [Eq. (15)];

V = mean velocity in the pipe cross-section [LT^{-1}];

α = empirical constant of power law friction factor [Eq. (4)];

β = empirical constant [Eq. (4)];

γ = specific weight of fluid [KL^{-3}];

ω = empirical constant [Eq. (4)];

ζ = empirical constant [Eq. (4)];

λ_J = empirical constant [Eq. (12)];

λ_N = empirical constant [Eq. (13)];

λ_T = empirical constant [Eq. (16)];

δ_J = empirical constant [Eq. (12)];

δ_N = empirical constant [Eq. (13)];

δ_T = empirical constant [Eq. (16)];

σ = dimensionless constant [Eq.(9)];

ν = kinematic viscosity of water [L^2T^{-1}];

ε = absolute roughness of the pipe [L];

ε/D = relative roughness.

References

Colebrook, C. F. (1939). "Turbulent flow in pipes, with particular reference to the transition region between the smooth and rough pipe laws." *J. Inst. Civil Engrs., London*, 11, 133-156.

Colebrook, C. F., and White, C. M. (1937). "Experiments with fluid friction in roughened pipes." *Proc. Royal Society, Series A Math. & Phys. Sci*., 161(904), 367-381.

Churchill, S. W. (1977). "Friction factor equation spans all fluid-flow regimes." *Chem. Eng*., 84(24), 91-92.

Finnemore, E. J., and Franzini, J. B. (2002). Fluid mechanics with engineering applications. *Mc-Graw-Hill, 10th ed.*, 268-282.

Haaland, S. E. (1983). "Simple and explicit formulas for the friction factor in turbulent pipe flow." *J. Fluids Eng*., 105, 89-90.

Hodge, B. K., and Taylor, R. P. (2002). "Piping-system solutions using *Mathcad*." *Comput. Appl. Eng. Educ.*, 10(2), 59-78.

Huddleston, D. H. (2002). "Spreadsheet tools utilized to introduce computational field simulation concepts to undergraduate engineering students." *Comput. Educ. J*., 12(1), 6-11.

Huddleston, D. H., Alarcon, V. J., and Chen, W. (2004). "Water distribution network analysis using *Excel*." *J. Hydraulic Engrg., ASCE*, 130(10), 1033-1035.

Jain, A. K. (1976). "Accurate explicit equations for friction factor." *J. Hydraulic Div., ASCE*, 102(5), 674-677.

Jewell, T. K. (2001). "Teaching hydraulic design using equation solvers." *J. Hydraulic Engrg., ASCE*, 127(12), 1013-1021.

Keady, G. (1998). "Colebrook-White formula for pipe flows." *J. Hydraulic Engrg., ASCE*, 124(1), 96-97.

Larock, B. E., Jeppson, R. W., and Watters, G Z. (2000). Hydraulics of pipeline systems. *CRC Press LLC, Florida*.

Moody, L. F. (1944). "Friction factors for pipe flow." *Trans. ASME*, 66, 671-684.

Moody, L. F. (1947). "An approximate formula for pipe friction factors." *Trans. ASME*, 69, 1005-1006.

Ozger, M. and Yıldırım, G. (2009). "Determining turbulent flow friction coefficient using adaptive neuro-fuzzy computing technique." *Advances Eng. Software* 40: 281-287.

Sonnad, J. R., and Goudar, C. T. (2004). "Constraints for using Lambert W function-based explicit Colebrook-White equation." *J. Hydraulic Engrg., ASCE*, 130(9), 929-931.

Sonnad, J. R., and Goudar, C. T. (2006). "Turbulent flow friction factor calculation using a mathematically exact alternative to the Colebrook-White equation." *J. Hydraulic Engrg., ASCE*, 132(8), 863-867.

Swamee, P. K., and Jain, A. K. (1976). "Explicit equations for pipe-flow problems." *J. Hydraulic Div., ASCE*, 102(5), 657-664.

Weiss, P. T., and Gulliver, J. S. (2001). "What do students need in hydraulic design projects?" *J. Hydraulic Engrg., ASCE*, 127(12), 984-991.

Yıldırım, G. (2006). "Hydraulic analysis and direct design of multiple outlets pipelines laid on flat and sloping lands*." J. Irrig. Drain .Engrg., ASCE*, 132(6), 537-552.

Yıldırım, G. (2007a). "An Assessment of Hydraulic Design of Trickle Laterals Considering Effect of Minor Losses." *Irrig. and Drain. (ICID Journal)* 56(4), 399-421.

Yıldırım, G. (2007b). "Analytical Relationships for designing multiple outlets pipelines*." J. Irrig. Drain. Engrg., ASCE*, 133(2), 140-154.

Yıldırım, G. (2008a). "Determining inlet pressure head incorporating uniformity parameters for multioutlet plastic pipelines." *J. Irrig. Drain .Engrg., ASCE*, 134(3), 341-348.

Yıldırım, G. (2008b). "Discussion of "Turbulent flow friction factor calculation using a mathematically exact alternative to the Colebrook-White equation. By Sonnad and Goudar" *J. Hydraulic Engrg., ASCE*, 134(8), 1185-1186.

Yıldırım, G. and Özger, M. (2009). "Neuro-fuzzy approach in estimating Hazen-Williams friction coefficient for small-diameter polyethylene pipes." *Advances in Engineering Software* 40: 593-599.

Yıldırım, G. (2009a). "Computer-Based Analysis of Explicit Approximations to the Implicit Colebrook-White Equation in Turbulent Flow Friction Factor Calculation." *Advances in Engineering Software* (in press).

Yıldırım, G. (2009b). "Simplified procedure for hydraulic design of small-diameter plastic pipes." *Irrig. Drain. (ICID J.)* 58(3):209-233.

Yıldırım, G. (2009c). "Discussion of "Simplified Method for Sizing Laterals with Two or More Diameters" by Muluneh Yitayew" *J. Irrig. and Drain. Eng., ASCE* (in press).

Yoo, D. H. and Singh, V. P. (2004). "Explicit design of commercial pipes with no secondary losses." *J. Irrig. Drain Engrg., ASCE*, 130(5), 437-440.

Yoo, D. H. and Singh, V. P. (2005). "Two methods for the computation of commercial pipe friction factors." *J. Hydraulic Engrg., ASCE*, 131(8), 694-704.

Zigrang, D. J., and Sylvester, N. D. (1982). "Explicit approximations to the solution of Colebrook's friction factor equation." *AIChE J*., 28, 514-515.

Enantiyoselektif Michael Reaksiyonu İçin Diazadioksokaliks[2]Aren[2]Triazin Bazlı Kiral Organokatalizörler

Ummu Ozgun[1*], Abdulkadir Sirit[2*]

[1*] Necmettin Erbakan University, Institute of Science, Department of Chemistry, Konya, Türkiye, (ORCID: 0000-0002-5682-3001), ummu.vural@gmail.com

[2*] Necmettin Erbakan University, Ahmet Kelesoglu Faculty of Education, Department of Chemistry, Konya, Türkiye, (ORCID: 0000-0002-6427-2991), asirit42@hotmail.com

Öz

Kiral bileşiklerin seçici olarak oluşmasını sağlayan sentez şekline asimetrik sentez denilmektedir. Asimetrik sentez organik kimyada beşeri ve tarımsal sanayiinde ve gıdadaki katkı maddelerinin üretiminde hayati önem taşımaktadır. Çünkü organik kimyada asimetrik bir molekülün farklı diastereomerleri ya da enantiyomerleri vardır ve bunlar genellikle farklı biyolojik aktivite gösterirler. Bu çalışmada feniletilaminin her iki enantiyomerik formu kullanılarak diazadioksokaliks[2]aren[2]triazin bazlı yeni bir organokatalizör sentezlenmiş ve katalitik aktivitesini belirlenmek üzere Michael katılması tepkimesinde katalizör olarak denenmiştir. Sentezlenen bu katalizör varlığında asetil asetonun *trans*-β-nitrostirene enantiyoselektif katılmasında optimum şartlar belirlenmiştir. Çalışma süresince reaksiyonların tamamı İTK (İnce Tabaka Kromatografi) ile izlenmiş, sentezlenen maddeler kolon kromatografi ile saflaştırılmıştır. Saflaştırılan ürünlerin yapıları FTIR, ^{1}H NMR ve ^{13}C NMR teknikleriyle aydınlatılmış ve optikçe aktif maddelerin çevirme açıları ölçülmüştür.

Anahtar Kelimeler: Organokataliz, Asimetrik sentez, Diazadioksokaliks[2]aren[2]triazin, Stereoselektivite, Michael katılması.

Chiral Diazadioxocalix[2]Arene[2]Triazine-Based Organocatalysts For Enantioselective Michael Reactions

Abstract

Asymmetric synthesis is an organic synthesis that allows the selective formation of chiral compounds. Asymmetric synthesis in organic chemistry is vital in the human/agricultural pharmaceutical industry and the production of nutritional additives. Because in organic chemistry, different diastereomers or enantiomers of a molecule often have other biological activities. A new diazadioxocalix[2]arene[2]triazine-based organocatalyst was synthesized using both enantiomeric forms of phenylethylamine. In the presence of this synthesized catalyst, optimum conditions were determined for the enantioselective addition of acetylacetone to *trans*-β-nitrostyrene. During the study, all of the reactions were followed with TLC and the synthesized substances were made pure by column chromatography. The purified products were illuminated by FTIR, ^{1}H NMR and ^{13}C NMR techniques and the rotation angles of the optically active compounds were measured.

Keywords: Organocatalysis, Asymmetric synthesis, Diazadioxocalix[2]arene[2]triazine, Stereoselectivity, Michael addition

1. Introduction

Chiral compounds are very important structures found in all living systems, from single-celled organisms to the most complex ones [1], [2]. Most of the useful chemicals, such as human drugs, pesticides, and nutritional additives, besides catalysts used in asymmetric synthesis, consist of chiral compounds [3], [4].

Organocatalysis used in the synthesis of chiral materials has emerged as an extremely important method. Organocatalysts have been used for a long time as chiral tools to support various asymmetric reactions in addition to enzymes, biocatalysts, and chiral metal complexes. [5], [6].

Organocatalysts provide many advantages such as widespread applicability, environmental compatibility, reusability, high efficiency, high selectivity and simplicity in use [7], [8]. Therefore, the synthesis and use of effective chiral catalysts is a rapidly developing research area in synthetic organic chemistry.

The Michael addition reaction between nitroolefins and 1,3-dicarbonyl compounds is one of the most productive reactions used to form carbon-carbon bonds. Optically active γ-nitro carbonyl structures formed as a result of these reactions are precious resources that can be used to create a variety of pharmaceuticals [9] – [11].

These substances, which play a crucial role as chiral building components in organic and medicinal chemistry, can be converted into various functional groups such as amines, aldehydes, ketones, nitrile oxides, oximes, carboxylic acids and hydroxyl amines very easily [12].

Due of growing interest in this field, List and Barbas independently made and reported organocatalytic studies using L-proline. Then, very high efficiency and enantiomeric excess chiral organcatalysts were obtained for chiral michael addition [13], [14]. The most common examples are urea and thiourea-derived bifunctional organocatalysts [15], chiral diamines [16], Cinchona-based catalysts [17], chiral pyrrolidine-type diamines [18], L-proline derivatives [19], chiral guanidines [20].

As a member of the supramolecules, calixarenes are very good platforms for the synthesis of artificial host molecules, as they can be used in numerous application areas [21], [22]. Calixarenes are composed of phenolic structures bonded together by methylene bridges and substituted at the para position. In heteroatom bridged calixarenes, a new calixarene derivative, the aromatic groups in the structure are connected to each other by heteroatom bridges, unlike methylene bridges [23]- [25]. These new generation heteroatom bridged calixarenes may have different chemical and structural properties such as caviyt size, molecular recognition, and host-guest interaction [26]- [28].

In our previous studies, we synthesized squaramide-based chiral calixarenes, chiral calixarenes containing different chiral amine groups, and tetraoxacalix[2]arene[2]triazine-based chiral catalysts containing different chiral amine groups. Then, we tested the catalytic efficiency of these catalysts in various asymmetric addition reactions [29]- [32].

Herein, we report the synthesis both enantiomeric forms of Diazadioxocalix[2]Aren[2]Triazine-based chiral catalyst and the optimum conditions of these catalysts in the Michael reaction of acetylacetone to *trans-β*-nitrostyrene. To our knowledge, the catalytic application of Diazadioxocalix[2]Aren[2]Triazine-based chiral catalyst derivatives for stereoselective Michael reactions has been synthesized for the first time.

2. Materials and Methods

2.1. Synthesis and Use of Catalysts

2.1.1. Procedure for the Synthesis of 3a/3b

Heteroatom bridged calix[2]arene[2]triazine was synthesized in accordance with the procedure published by Wang et al. [33], [34].

To the obtained solution of diazadioxocalix[2]arene[2]triazine (1) (0.5 mmol) prepared in THF(20 mL) was added the solution of (*R*)–phenylethylamine(2a)/(*S*)–phenylethylamine(2b) (1.1 mmol) and diisopropyl ethylamine (DIPEA, 2.2 mmol) prepared in THF (20 mL) at room temperature. 24-26 hours were spent to reflux the mixture. When the reaction was finished, the solvent was removed under reduced pressure. Finally, the impure product was purified by flash chromatography (hexane/EtOAc) over silica gel. The pure product (3a/3b) was obtained.

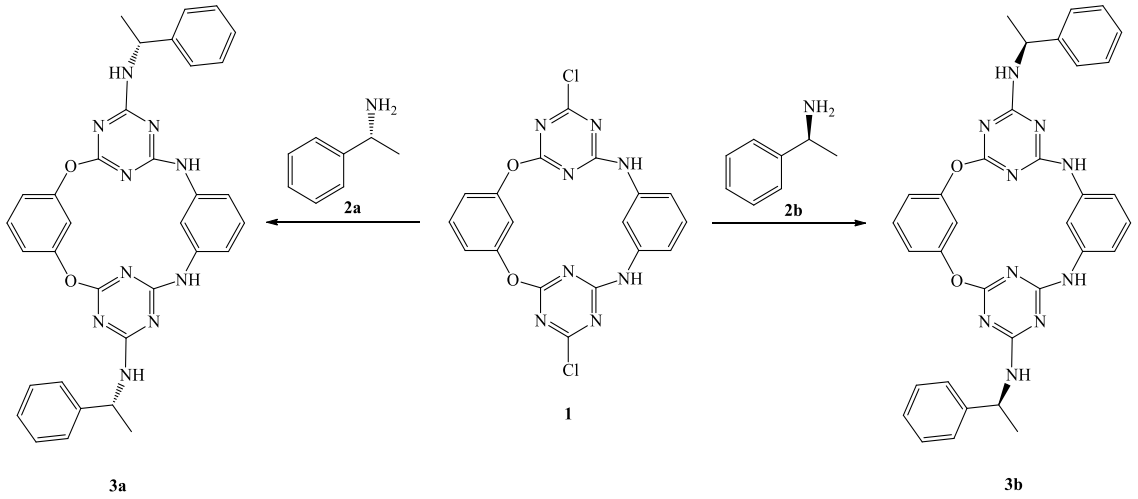


Figure 1. Procedure for the synthesis of heteroatom-bridged calixaromatic-based chiral catalysts 3a and 3b

(3a): Crystalline Solid, 72% yield, $[\alpha]_D^{25}$ =+11.45 (*c*=1.0, $CHCl_3$), mp.: 219-221 °C; (3b): Crystalline Solid, 74% yield, $[\alpha]_D^{25}$ =-11.57 (*c*=1.0, $CHCl_3$), mp.: 220-222 °C; FTIR (cm^{-1}): 3258, 1572, 1484, 1370; ^{1}H NMR (400 MHz, $CDCl_3$): δ 7.41-7.38 (m, 2H), 7.36-7.30 (m, 4H), 7.28-7.25 (m, 2H), 7.15-7.11 (m, 2H), 6.79-6.71 (m, 4 H), 6.58-6.52 (m, 4H), 5.42 (q, 2H, *J* = 6.9 Hz), 1.63 (d, 6H, *J* = 6.9 Hz), NH signals were not observed.; ^{13}C NMR (100 MHz, $CDCl_3$): δ 165.4, 160.4, 152.2, 142.4, 138.3, 132.3, 129.9, 128.7, 127.3, 125.9, 118.7, 116.5, 111.5, 49.8, 22.7; Anal. Calcd. for $C_{34}H_{30}N_{10}O_2$ (%): C, 66.88; H, 4.95; N, 22.93. Found(%): C, 66.77; H, 4.81; N, 22.87.

2.1.2. Procedure for the synthesis of analog compound 8a/8b

Analog substances (8a/8b) containing (*R*)–phenylethylamine(2a)/(*S*)–phenylethylamine(2b) were synthesized following the procedure published by Genc et al. [31].

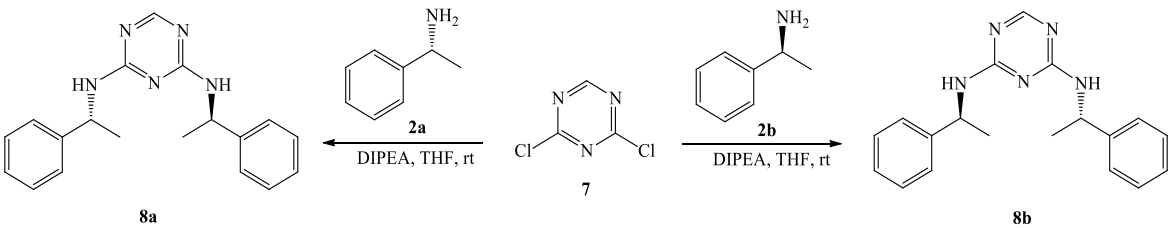
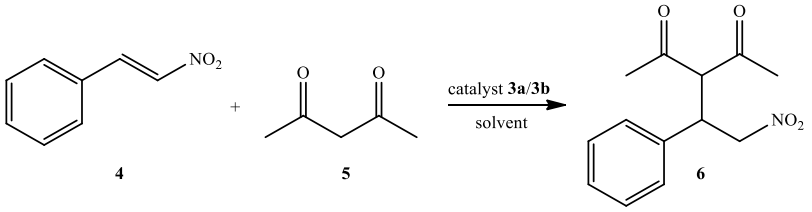


Figure 2. Preparation of chiral analogues 8a/8b

3. Results and Discussion

In order to reach the target molecule, we first prepared Diazadioxocalix[2]Aren[2]Triazine with certain steps using suitable starting materials [33], [34]. To synthesize the targeted molecule, Diazadioxocalix[2]Aren[2]Triazine (1) and (*R*)–phenylethylamine(2a)/(*S*)–phenylethylamine(2b) (2eq.) and diisopropylethylamine (DIPEA) reacted efficiently in THF at room temperature. As a result of this reaction, chiral 3a/3b substances shown in Figure 1 were obtained. These obtained materials were characterized by methods such as FTIR, ^{1}H NMR and ^{13}C NMR.

Table 1. Michael addition between 5 and 4 catalyzed by 3a to 3b in different solvents



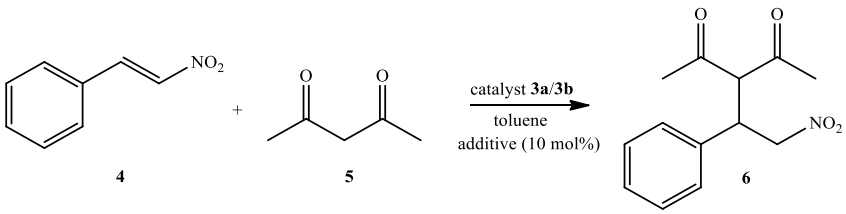
Entry[a]	Catalyst	Solvent	Time (d)	Yield (%)[b]	*ee* (%)[c]
1	**3a**	Toluene	4	94	95 (*R*)
2	**3b**	Toluene	4	96	96 (*S*)
3	**3a**	THF	4	93	87 (*R*)
4	**3b**	THF	4	92	85 (*S*)
5	**3a**	CH_3CN	4	87	87 (*R*)
6	**3b**	CH_3CN	4	85	83 (*S*)
7	**3a**	Et_2O	4	92	94 (*R*)
8	**3b**	Et_2O	4	93	93 (*S*)
9	**3a**	CCl_4	2	92	88 (*R*)
10	**3b**	CCl_4	2	93	91 (*S*)
11	**3a**	1,4-dioxane	2	89	83 (*R*)
12	**3b**	1,4-dioxane	2	82	82 (*S*)
13	**3a**	DMF	4	87	87 (*R*)
14	**3b**	DMF	4	86	86 (*S*)
15	**3a**	$CHCl_3$	4	94	83 (*R*)
16	**3b**	$CHCl_3$	4	96	86 (*S*)
17	**3a**	Acetone	4	93	87 (*R*)
18	**3b**	Acetone	4	92	88 (*S*)
19	**3a**	CH_2Cl_2	4	87	93 (*R*)
20	**3b**	CH_2Cl_2	4	85	93 (*S*)
21	**3a**	*i*-PrOH	4	92	92 (*R*)
22	**3b**	*i*-PrOH	4	93	90 (*S*)

[a] Reaction conditions: *trans-β*-nitrostyrene (1 eq.), acetylacetone (2 eq.) and 3a/3b (10 mol%), 0.25mL solvent.
[b] Yields were obtained after flash chromatography.
[c] Results were determined using HPLC. Configuration and retention time was determined by being compared with the literature data.

The obtained diazadioxocalix[2]arene[2]triazine-based compounds were used as catalysts in Michael addition, which is an enantioselective reaction, in order to learn the catalytic efficiency of them. The reaction of *trans-β*-nitrostyrene with acetylacetone is shown in Table 1. The synthesized catalysts (3a/3b) were put to the test in this reaction, and the results are reported in Table 1. The various solvents were tested to determine the most suitable solvent to be used in Michael addition. The highest yield and enantiomeric excess were obtained in the presence of toluene (entry 1,2).

Various additives (acid, base, etc.) were added to the reaction at the rate of 10%, and the effect on yield and enantiomeric excess was observed. However, as seen in Table 2, it was observed that the additives added to the reaction did not increase the yield or enantiomeric excess in the reactions.

Table 2. Additive effect of the 3a and 3b catalyzed Michael addition of 5 to 4



Entry[a]	Catalyst	Additive	Time (d)	Yield (%)[b]	*ee* (%)[c]
1	**3a**	None	4	94	95 (*R*)
2	**3b**	None	4	96	96 (*S*)
3	**3a**	AcOH	4	51	86 (*R*)
4	**3b**	AcOH	4	55	83 (*S*)
5	**3a**	DMAP	5	68	79 (*R*)
6	**3b**	DMAP	5	68	77 (*S*)
7	**3a**	PhCOOH	4	63	83 (*R*)
8	**3b**	PhCOOH	4	68	84 (*S*)
9	**3a**	*p*-TsOH	4	75	87 (*R*)
10	**3b**	*p*-TsOH	4	70	85 (*S*)
11	**3a**	Pyridine	5	69	76 (*R*)
12	**3b**	Pyridine	5	71	75 (*S*)

[a] Reaction conditions: *trans-β*-nitrostyrene (1 eq), acetylacetone (2 eq), additive (10 mol%) and 3a/3b (10 mol%), 0.25mL toluene.
[b] Yields were obtained after flash chromatography.
[c] Results were determined using HPLC. Configuration and retention time was determined by being compared with the literature data.

The same reaction was carried out at -20 ºC and 0ºC with toluene, as shown in Table 3. But it was seen that both the yield and enantiomeric excess decreased. The experiments revealed that room temperature was the ideal temperature for this process (Table 3, entries 1-6).

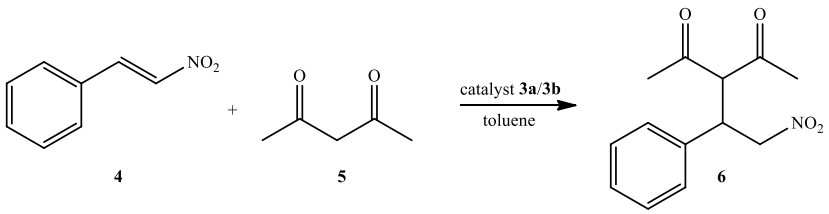
We then added recycled catalysts (3a/3b) to the Michael reaction and observed the results. The results obtained showed a decrease in yield and enantiomeric excess (Table 3, entries 7 and 8).

To investigate the effect of the amount of catalyst on the addition reaction, this time we added 15 mol% catalyst to the reaction and observed the results. The results indicated that there was no increase in yield and enantiomeric excess with increasing the amount of catalyst. (Table 3, entries 9 and 10).

We suppose that the heteroatom-bridged, bulky, and chiral amine-bonded calixarene platform is highly important for generating high yields and high enantiomeric excess in Michael products. To confirm this, we synthesized the monomeric analog substance using suitable starting materials (Figure 2). We used these synthesized analog structures as catalysts for Michael addition. The results showed that Michael reactions resulted in low yields and enantioselectivity in the presence of analogues catalysts (Table 3, entries 11 and 12).

All our experimental studies showed that catalysts containing bulky heteroatom bridged calixarene platform are highly effective on enantioselective addition reactions.

Table 3. Enantioselective Michael addition catalyzed by 3a, 3b and 8a, 8b in toluene



4 5 6

Entry[a]	Catalyst	Temp.(°C)	Time (d)	Yield (%)[b]	*ee* (%)[c]
1	**3a**	-20	5	85	86 (*R*)
2	**3b**	-20	5	82	84 (*S*)
3	**3a**	0	4	89	88 (*R*)
4	**3b**	0	4	87	89 (*S*)
5	**3a**	r.t.	4	94	95 (*R*)
6	**3b**	r.t	4	96	96 (*S*)
7[d]	**3a**	r.t.	4	90	93 (*R*)
8[d]	**3b**	r.t	4	88	91 (*S*)
9[e]	**3a**	r.t.	2	95	94 (*R*)
10[e]	**3b**	r.t	2	84	95 (*S*)
11	**8a**	r.t.	4	40	25 (*R*)
12	**8b**	r.t	4	35	21 (*S*)

[a] Reaction conditions: *trans-β*-nitrostyrene (1 eq), acetylacetone (2 eq) and 3a/3b or 8a/8b (10 mol%), 0.25mL toluene.
[b] Yields were obtained after flash chromatography.
[c] Results were determined using HPLC. Configuration and retention time was determined by being compared with the literature data.
[d] Recycled catalyst was used in the reaction.
[e] Reaction was performed with 15 mol% catalyst.

The results showed that were the ideal conditions toluene solvent, 10 mol% catalyst loading, room temperature, a four-day reaction period, and no additives.

Studies to determine the catalytic activity of these catalysts continue under optimum conditions obtained in the Michael reaction of acetylacetone with substituted and unsubstituted aromatic nitrostyrene derivatives. The yields and enantioselectivities obtained as a result of these experiments will be reported.

4. Conclusion

As a result, a new class of chiral calixarene based on Diazadioxocalix[2]arene[2]triazine was developed, and optimum conditions for enantioselective Michael addition were investigated. All Michael products obtained in the study were analyzed by HPLC using chiral columns. Studies are continuing to determine the catalytic efficiency of these synthesized catalysts in the Michael reaction of acetylacetone with substituted and unsubstituted aromatic nitrostyrene derivatives under optimum conditions.

5. Acknowledge

The Necmettin Erbakan University Research Foundation provided financial support for this study (BAP-211451001).

References

[1] M. S. Taylor and E. N. Jacobsen, "Asymmetric Catalysis by Chiral Hydrogen-Bond Donors," *Angew. Chem. Int. Ed*., vol. 45, Feb., pp. 1520–1543, 2006.

[2] X. Yu and W. Wang, "Hydrogen-bond-mediated asymmetric catalysis," *Chem. Asian. J*., vol. 3, Mar., pp. 516-532, 2008.

[3] B. T. Kumpuga and S. Itsuno, "Synthesis of chiral polyesters of cinchona alkaloid catalysts for enantioselective Michael addition of anthrone to nitroalkenes," *J. Catal.*, vol. 361, Mar., pp. 398–406, 2018.

[4] B. J. V. Verkuijl, A. J. Minnaard, J. G. Vries and B. L. Feringa, "Chiral Separation of Underivatized Amino Acids by Reactive Extraction with Palladium-BINAP Complexes, " *J. Org. Chem.*, vol. 74, pp. 6526–6533, 2009.

[5] S. Bertelsen and K. A. Jørgensen, "Organocatalysis—after the gold rush," *Chem. Soc. Rev*., vol. 36, pp. 2178–2189, 2009.

[6] H. Pellissier, "Asymmetric organocatalysis," *Tetrahedron*, vol. 63, pp. 9267–9331, 2007.

[7] C. Xie, Z. Lu, W. Zhou, J. Han and Y. Pan, "A facile organocatalyzed Michael addition of pyrazolines to α,β-unsaturated carbonyl compounds," *Tetrahedron Lett.*, vol 53, Dec., pp. 6650–6653, 2012.

[8] Z. Yacob, A. Nan and J. Liebscher, "Proline-Functionalized Magnetic Core-Shell Nanoparticles as Efficient and Recyclable Organocatalysts for Aldol Reactions," *Adv. Synth. Catal*., vol. 354, Nov., pp. 3259–3264, 2012.

[9] S. B. Tsogoeva, "Recent Advances in Asymmetric Organocatalytic 1,4-Conjugate Additions," *Eur. J. Org. Chem*., vol. 2007, Apr., pp. 1701-1716, 2007.

[10] S. R. Harutyunyan, T. D. Hartog, K. Geurts, A. J. Minnaard and B. L. Feringa, "Catalytic Asymmetric Conjugate Addition and Allylic Alkylation with Grignard Reagents," *Chem. Rev.*, vol. 108, Aug., pp. 2824-2852, 2008.

[11] Y. Zhang and W. Wang, "Recent advances in organocatalytic asymmetric Michael reactions," *Catal. Sci. Technol*., vol. 2, Oct., pp. 42-53, 2012.

[12] O. M. Berner, L. Tedeschi and D. Enders, "Asymmetric Michael additions to nitroalkenes," *Eur. J. Org. Chem.*, Vol. 2002, pp. 1877-1894, 2002.

[13] N. Mase, K. Watanabe, H. Yoda, K. Takabe, F. Tanaka and C. F. Barbas, "Organocatalytic direct Michael reaction of ketones and aldehydes with *β*-nitrostyrene in brine," *J. Am. Chem. Soc*., vol. 128, pp. 4966-4967, 2006.

[14] E. Tsandi, C. G. Kokotos, S. Kousidou, V. Ragoussis and Kokotos G. "Sulfonamides of homoproline and dipeptides as organocatalysts for Michael and Aldol reactions," *Tetrahedron*, vol. 65, pp. 1444-1449, 2009.

[15] S. B. Tsogoeva and S. Wei, "Highly enantioselective addition of ketones to nitroolefins catalyzed by new thiourea–amine bifunctional organocatalysts," *Chem. Commun*., vol. 13, Feb., pp. 1451-1453, 2006.

[16] O. Andrey, A. Alexakis and G. Bernardinelli, "Asymmetric Michael addition of *α*-hydroxyketones to nitroolefins catalyzed by chiral diamine," *Org. Lett*., vol. 5, Jul., pp. 2559-2561, 2003.

[17] J. X. Ye, D. J. Dixon and P. S. Hynes, "Enantioselective organocatalytic Michael addition of malonate esters to nitro olefins using bifunctional cinchonine derivatives," *Chem. Commun*., vol. 35, Aug., pp. 4481-4483 2005.

[18] B. Ni, Q. Zhang and A. D. Headley, "Pyrrolidine-based chiral pyridinium ionic liquids (ILs) as recyclable and highly efficient organocatalysts for the asymmetric Michael addition reactions," *Tetrahedron Lett*., Vol. 49, Feb., pp. 1249-1252, 2008.

[19] L. Q. Gu and G. Zhao, "4,4′-disubstituted-l-proline catalyzes the direct asymmetric Michael addition of aldehydes to nitrostyrenes," *Adv. Synth. Catal*., vol. 349, pp. 1629-1632, 2007.

[20] M. Terada, H. Ube and Y. Yaguchi, "Axially chiral guanidine as enantioselective base catalyst for 1,4-addition reaction of 1,3- dicarbonyl compounds with conjugated nitroalkenes," *J. Am. Chem. Soc*., vol. 128, pp. 1454-1455, 2006.

[21] C. D. Gutsche, *Calixarenes: An Introduction*, 2nd edn, Cambridge, UK, The Royal Society of Chemistry, Thomas Graham House, 2008.

[22] S. B. Nimse and T. Kim, "Biological applications of functionalized calixarenes," *Chem. Soc. Rev*., vol. 42, Oct., pp. 366-386, 2013.

[23] M.-X. Wang, "Heterocalixaromatics, new generation macrocyclic host molecules in supramolecular chemistry," *Chem. Commun*., vol 38, pp. 4541-4551, 2008.

[24] M.-X. Wang, "Nitrogen and oxygen bridged calixaromatics: synthesis, structure, functionalization, and molecular recognition," *Acc. Chem. Res.*, vol. 45, pp. 182-195, 2011.

[25] W. Maes and W. Dehaen, "Oxacalix[n](het)arenes," *Chem. Soc. Rev*., vol. 37, pp. 2393-2402, 2008.

[26] S. Li, D.-X. Wang, Q.-Q. Wang, Y.-F. Ao, D.-X. Wang and M.-X. Wang, "Oxacalix[2]arene[2]triazine derivatives with halogen bond donors: synthesis, structure, and halide binding in the solid state," *Cryst. Growth Des*., vol. 16, Aug., pp. 5460-5465, 2016.

[27] S. Pan, D.-X. Wang, L. Zhao and M.-X. Wang, "Synthesis and functionalization of inherently chiral tetraoxacalix[2]arene[2] pyridines," *Org. Lett*., vol. 14, pp. 6254-6257, 2012.

[28] S. Pan, D.-X. Wang, L. Zhao and M-X Wang, "Synthesis and conformational structures of functionalized tetraoxacalix[2]arene[2] triazines," *Tetrahedron*, vol. 68, pp. 9464-9477, 2012.

[29] U. Vural, M. Durmaz and A. Sirit, "A novel calix[4]arene-based bifunctional squaramide organocatalyst for enantioselective Michael addition of acetylacetone to nitroolefins," *Org. Chem. Front*., vol. 3, pp. 730-736, 2016.

[30] H. N. Genc and A. Sirit, "Novel efficient bifunctional calixarene thiourea organocatalysts: synthesis and application in the direct enantioselective Aldol reactions," *Tetrahedron Asymmetry*, vol. 27, pp. 201-207, 2016.

[31] H. N. Genc, U. Ozgun and A Sirit, "Chiral tetraoxacalix[2]arene[2]triazine-based organocatalysts for Enantioselective Aldol reactions," *Tetrahedron Letters*, vol. 60, pp. 763–1768, 2019.

[32] H. N. Genc, U. Ozgun and A Sirit, "Design, synthesis and application of chiral tetraoxacalix[2]arene[2]triazine-based organocatalysts in asymmetric Michael addition reactions," *Chirality*, vol.31, Apr., pp. 293-300, 2019.

[33] M.-X. Wang and H.-B. Yang. "A general and high yielding fragment coupling synthesis of heteroatom-bridged calixarenes and the unprecedented examples of calixarene cavity fine-tuned by bridging heteroatoms," *J Am. Chem. Soc*., vol. 126, pp. 15412-15422, 2004.

[34] H.-B. Yang, D.-X. Wang, Q.-Q. Wang and M.-X. Wang, "Efficient functionalizations of heteroatom-bridged calix[2]arene[2]triazines on the larger rim," *J. Org. Chem.*, vol. 72, Apr., pp. 3757-3763, 2007.

Comparative study on TiAlN and TiCN Coatings Tribological Performance for Dental Implant Drills

Seda ATAŞ BAKDEMİR[1,2*], Doğuş ÖZKAN[1], Cenk TÜRKÜZ[3], Serdar SALMAN[2,4]

[1*] National Defence University, Turkish Naval Academy, Tuzla/İstanbul, Turkey (ORCID: 0000-0003-1601-2033), sabakdemir@dho.edu.tr

[2] Marmara University, Metallurgy and Materials Engineering, Göztepe/İstanbul, Turkey (ORCID: 0000-0002-3044-4310), dozkan@dho.edu.tr

[3] Titanit Ultrahard Coatings Company, Güngören/İstanbul, Turkey (ORCID: 0000-0002-4447-7287), cenk.turkuz@titanit.com.tr

[4] National Defence University, Beşiktaş /İstanbul, Turkey (ORCID: 0000-0002-9184-3876), ssalman@marmara.edu.tr

Öz

Kemik delme, birçok cerrahi proseste kullanılan temel ve yaygın bir işlem adımıdır. Delme işlemindeki termal özellikler, kemiğe verilen termal hasarı ve ameliyat sonrası iyileşme süresini doğrudan etkilemektedir. Aynı zamanda, ısı oluşumuna neden olan sıcaklık artışı, implant bölgesindeki kemik dokusunun termal yaralanması ile sonuçlanarak implant başarısızlığına neden olmaktadır. İmplant tedavisinin başarısı, kullanılan malzemelerin kimyasal, mekanik ve yüzey özellikleri, hazırlanma tekniği ve birincil stabilitesi gibi farklı parametrelere bağlı olan osseointegrasyon ile belirlenmektedir. Bu çalışmada, farklı karakterizasyon yöntemleri kullanılarak kortikal kemik delme işlemi sırasında termal nekrozu azaltmak ve tribolojik özellikleri geliştirmek için alternatif bir kaplama türü sunmak için üzere deneysel bir araştırma yapılmıştır. Kaplamalar PVD katodik ark yöntemi ile üretilmiş ve XRD analizi, taramalı elektron mikroskobu kullanılarak kaplamaların morfolojisi ve kimyasal bileşimi incelenmiştir. Kaplamalar, kuru kayma durumunda aşınma direncinin yanı sıra sertlik ve yapışma mukavemeti gibi mekanik özellikler açısından da analiz edilmiştir. Elde edilen sonuçlar, TiCN kaplamanın benzer mekanik özellikler sergilediğini ancak sürtünme katsayısı değerinin belirgin şekilde farklı olduğunu ve en yüksek aşınma direncine sahip olduğunu göstermektedir.

Anahtar Kelimeler: Aşınma Direnci, Dental İmplant Matkabı, Kemik Sıcaklığı, Koruyucu Kaplamalar, Otoklav Sterilizasyonu.

Comparative study on TiAlN and TiCN Coatings Tribological Performance for Dental Implant Drills

Abstract

Bone drilling is an essential and common step of procedure in many forms of surgery. The thermal characteristics in the drilling process directly affect thermal damage to the bone and postoperative healing time. In the same time, the temperature increment causing to heat generation results in thermal injury of the bone tissue to the implant site resulting into implant failure. The success of implant treatment is determined by osseointegration, which in turn depends on different parameters, such as the chemical, mechanical, and surface characteristics of the used materials, the preparation technique, and primary stability. In this study, an experimental investigation was conducted to present an alternative coating type to reduce thermal necrosis and enhance tribological properties during cortical bone drilling using different characterization methods. The coatings were produced by PVD cathodic arc method and the morphology, chemical composition and phase of coatings were investigated by using

X-ray diffraction, scanning electron microscopy. The coatings were analysed in terms of mechanical properties such as their hardness and adhesion strength besides wear resistance at dry sliding condition. The obtained results show that TiCN coating exhibits similar mechanical properties but their friction of coefficient value is markedly different and have the highest wear resistance.

Keywords: Wear Resistance, Dental Implant Drill, Bone Temperature, Protective Coatings, Autoclave Sterilization.

1. Introduction

The endosseous implant applications have grown in importance in dentistry with the advancement of biomaterials [1]. As a result, there has been an increase in research into implant materials, structures, shapes, surface properties, and biocompatibility. The most critical factor in implant success is osseointegration, which is defined as the bond between bone and implant body [2]. The selection of the most appropriate method for drilling the bone and preventing the formation of thermal necrosis and microcracks during bone drilling is a critical step in minimally traumatic implant preparation. The preservation of the original bone tissue has a significant benefit for the healing process following the application. In vivo studies were used to determine the destructive effect of excessive heating, and the threshold temperature for thermal necrosis is specified as 47°C for 1 minute. The parameters of the dental drill have a direct impact on the temperature produced during drilling [3]. Heat generation during drilling is affected by a variety of factors, including drill design, material, diameter, lifetime, surface treatment, drilling forces, cooling system, sterilization methods, and bone dependent properties such as cortical thickness, bone density, and patient health [4]. Continuous drilling causes wear and sharpness loss, reducing cutting efficiency and raising the temperature with each bur application. The drilling system must be designed to avoid thermal increments without the use of a cooling system in order to prevent bone necrosis [5]. Coating is a common way to improve the mechanical properties and corrosion resistance of dental drills. Although stainless steel is the most commonly used material for dental drills, ceramics and coated stainless steels, such as diamond-like carbon-coated stainless steel, have been researched [6], [7], on the other hand, are appealing for high-speed cutting tools and rotating parts. Furthermore, previous researches have shown that coated drills produce a better surface finish and hole accuracy (TiN, TiCN, TiAlN and TiSiN) [8].Dental drills are designed with small details and long kink planes. The freewheeling of dental drills during the process leaves contaminants (such as saliva, blood, or other biological fluids) on the surface and channels. The goal of autoclave sterilization is to kill microbes by using saturated water vapor at high pressure and temperature inside an enclosed chamber. The autoclave is the most common and safest sterilization method, but it has some drawbacks, including a high corrosion risk and a lengthy process time [9]. Implant site preparation is an important step in determining the successful osseointegration of a dental implant, and drill wear plays a significant role in this. Using PVD methodology, this study evaluates the tribological performance of AlTiN and TiCN coatings for dental drills. The abrasive wear resistance of these coatings on 440M steel substrate was investigated for this purpose using alumina balls at various loads. Furthermore, the effect of autoclave sterilization on corrosion properties is investigated.

2. Material and methods

The metallographic polished 440M stainless steel (5x20 mm diameter) were coated with AlTiN and TiCN by using cathodic arc-PVD deposition system in the Titanit Ultrahard Coating Company. Before deposition, the substrates were polished to mirror surface and then ultrasonically cleaned in acetone and ethanol. Crystallographic orientations of the coatings were determined using Bruker X-ray diffraction (XRD) with CuK_{α} radiation. The overall thickness and chemical composition of the coatings was explored by SEM/EDS analysis. The coating thickness were determined through the Calotest whereas hardness and elastic modules were measured via nanoindentation tests. Additionally, scratch and Daim-Benz tests were employed to characterize adhesion behavior of the coatings to substrates. The diamond Berkovich tip with a 0.2 mm radius were used to generate 10 mm long

scratches by increasing the load from 0 to 100 N with a 10 mm/min scratching speed. The critical loads (Lc), were determined by optical microscope examinations of the scratch.

Wear and friction tests were performed by using a commercial tribometer (UTS-10/20) with reciprocating module. The total sliding distance was 50 meters with a sliding speed of 50 mm/s and stroke was 5 mm under the 1 and 2 N loads. The Alumina balls (Al_2O_3) with 6 mm diameter were selected as counter surface due to their chemical inertness. The hardness and elastic modulus of the balls were 16 GPa and 350 GPa, respectively.

Wear scar profiles and wear volumes were obtained through optical profilometer analysis for tested samples. The wear rates of the samples were found by using Archard's wear rate formula (see Eq. 1), where V is the wear volume (mm^3), S is the total sliding distance (m) and F is the normal load (N) [10]. Tribometer tests were conducted with three reputations for each coating.

$$K = \frac{V}{F \times S} \quad (1)$$

After autoclave sterilization (OT-12 Nüve) at different cycle time, the corrosion resistance of coatings were evaluated by means of optical microscope examination.

3. Results and Discussion

Fig. 1(a) and (b) show the XRD patterns of TiCN and AlTiN coatings, respectively. The XRD pattern of TiAlN coating shows some weak peaks of AlTiN (111) and AlTiN (220) phases whereas AlTiN (200) peak was determined in high intensity. XRD patterns confirm that TiAlN coating has both TiN and AlN phases that isomorphic FCC lattices, with only small differences in the values of their parameters [11]. The XRD data of TiCN coating shows that the intensities of (111) were high and that it was the dominant reflection beside the (220) plane. This results can be attributed to that the (111) direction is the fastest growing one in cubic system [12]. Due to the solid solution model of TiCN coating, the reflections of TiCN coatings are generally in between the TiC and TiN reflections that belong to an FCC lattice. [13]. The presence of carbon in the TiN structure decreases the angle of diffraction pattern.

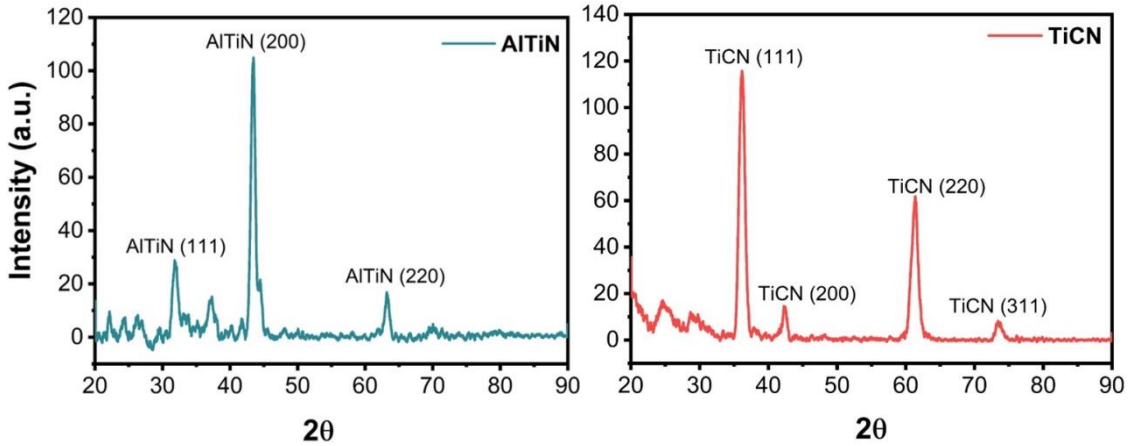


Figure 1. X-ray diffraction patterns of TiCN and AlTiN coatings.

Figure 2 shows the morphology and coating thickness of AlTiN and TiCN coatings. The coating thickness was calculated to be between 1.5 and 2 µm. The coatings have a dense structure, and small droplets can be seen on the coating surface. Additionally, Figure 2 shows SEM/EDS the chemical composition of the deposited coatings.

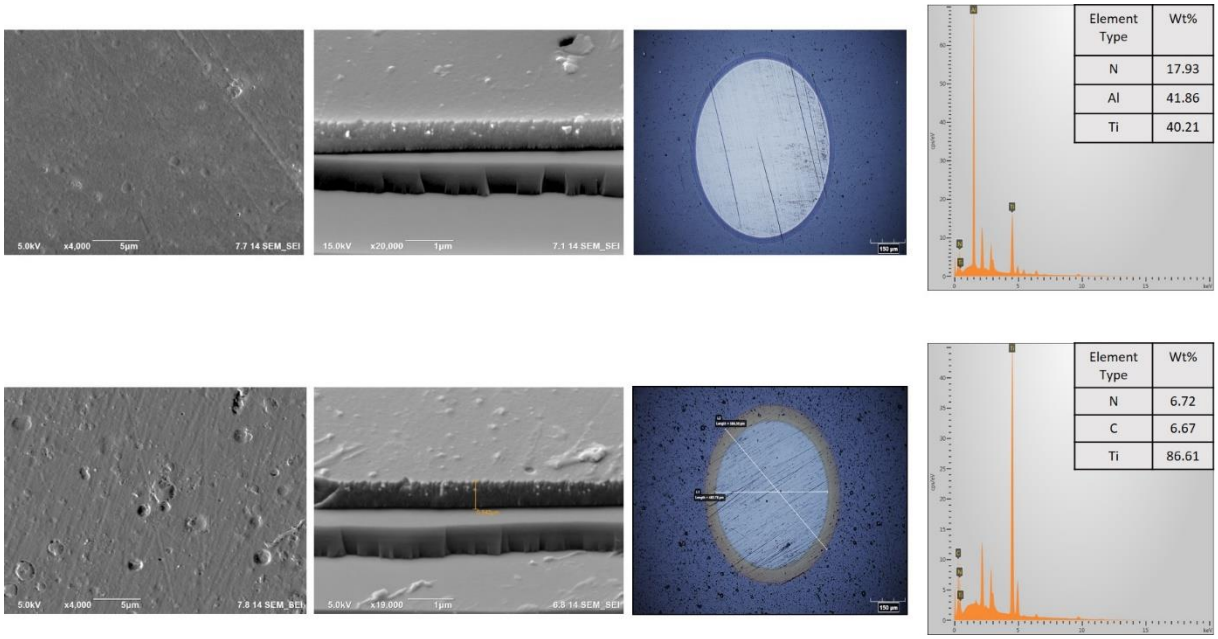


Figure 2. SEM images of surface/cross section and calotest of AlTiN and TiCN coatings.

Figure 3 shows optical microscope images of the scratch and Rockwell adhesion results. The first crack in the AlTiN coating occurs at 44 N, and the first crack in the TiCN coating occurs at 48 N, as shown in Figure 3. Both Lc1 and Lc2 of the TiCN coating are greater than those of the AlTiN coating, indicating that the TiCN coating has better adhesion than the AlTiN coating. According to the Rockwell adhesion image, TiCN coating has micro-sized flaking when compared to AlTiN coating. However, the level of coating deformation is acceptable for both coatings as HF1-HF2, and this situation is compatible with the critical load value. The absence of deformation indicates that the coatings have good properties to resist fractures and deformations, as well as high adhesion to 440M stainless steel [14]. TiCN and AlTiN coatings have hardness values of 3400 HV and 3300

HV, respectively.

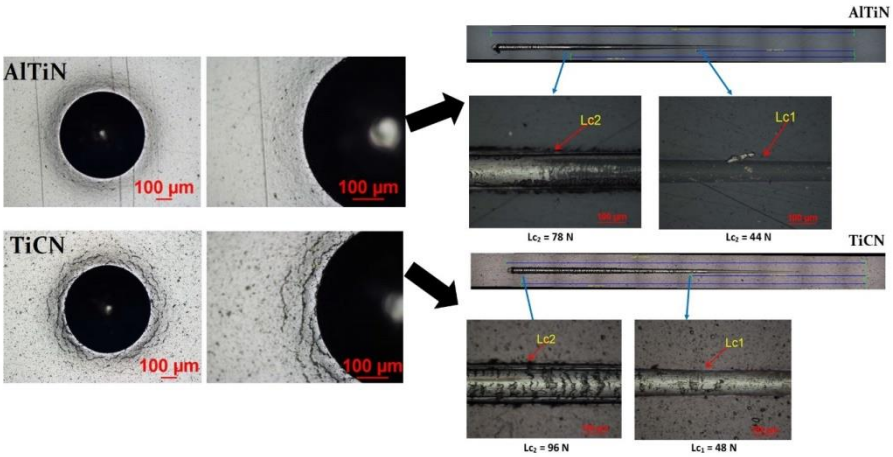


Figure 3. Rockwell indents and scratch track of coatings.

Dry sliding tests with 1N and 2N loads were used to simulate the wear behavior of TiCN, AlTiN coatings and bare steel. Figure 4 displays the coefficient of friction regime vs sliding distance curves. The following gradation can

be achieved by averaging the COFs values at 1N and 2N loads: TiCN (0.21), AlTiN (0.95), 440M stainless steel (1.05). After 20m of sliding distance, the AlTiN coating and bare steel reach a steady state regime with a rapid increase in value. The cause of the sharp increase during this first period was attributed to wear particles that occur in the adjacent zone. The higher COFs value of AlTiN coating could be attributed to aluminum oxid

which generated in the sliding process and could cause brittle failure [15].

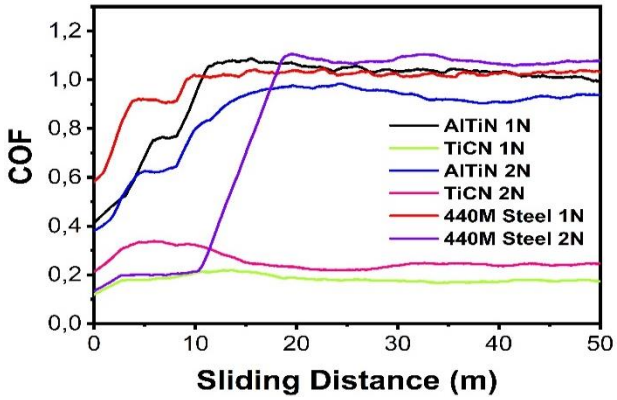


Figure 4. Friction coefficient of AlTiN and TiCN coatings and bare steel as function of sliding distance.

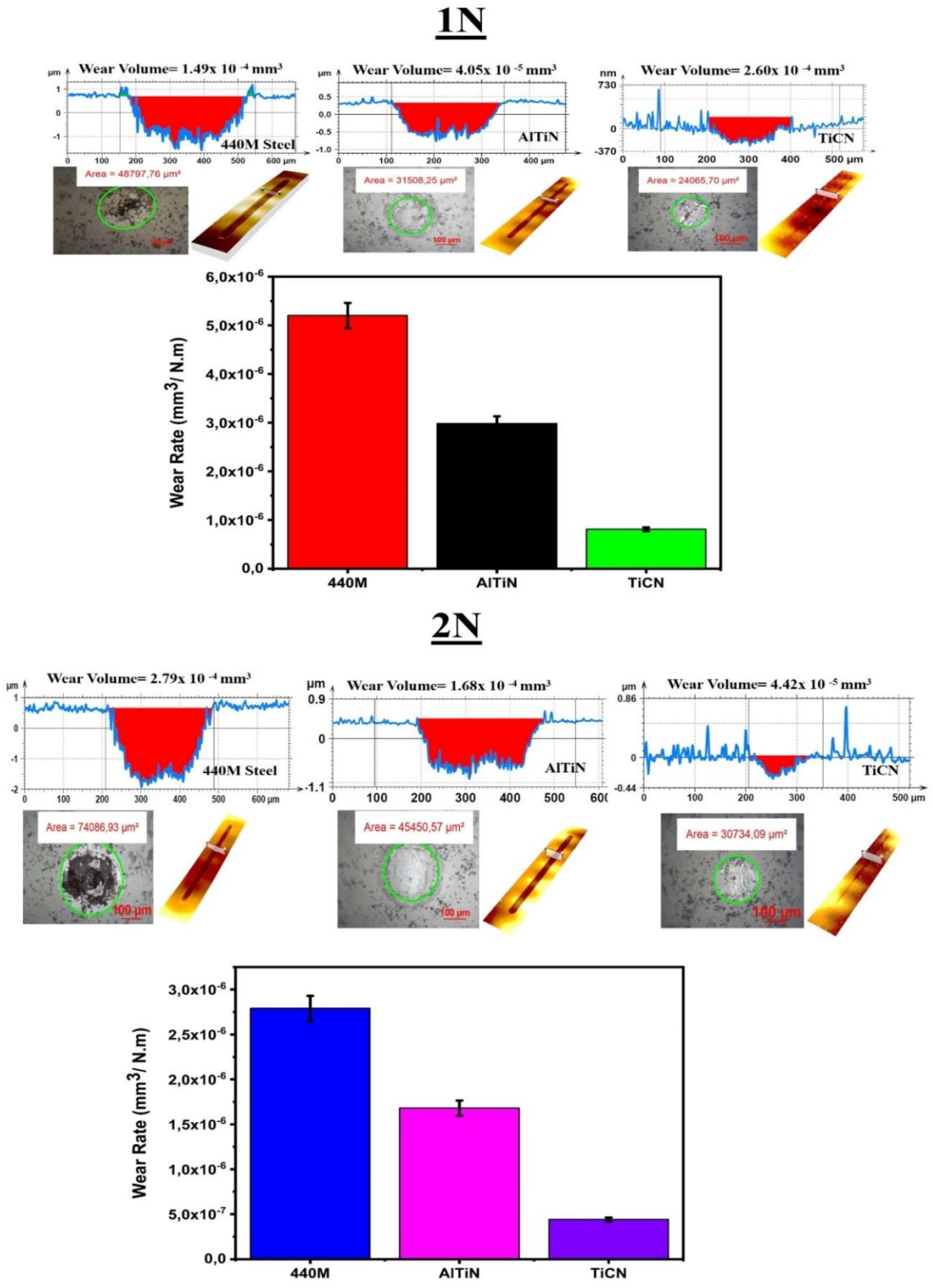


Figure 5. The sectional morphologies of wear scar and wear rates of the coatings, optical microscope images of the corresponding balls at 1N and 2N loads.

This situation, however, cannot be said to be valid for TiCN coating because it demonstrated a stable regime with the exception of a slight fluctuation at the start of the wear test at 2N load. The graphite in the TiCN coating acts as a lubricant by forming a transfer film on the sliding surface. As a result, this coating has a lower friction

coefficient and a lower wear volume [16]. Due to the low content of residual graphite in TiCN coatings, its distinct signal was not obtained in the XRD result.

Figure 5 shows the wear rate and depth of coatings, and the results were consistent with the friction coefficient regime represented in Figure 4. The wear rates showed that the AlTiN coating had lower wear resistance than the TiCN coating. When the sectional depth and 3D view of wear scars were considered, it is clear that TiCN coating has the smoothest wear scar and micro roughness, whereas AlTiN coating had relatively larger grooves. The poor wear behavior of the AlTiN coating was caused by a brittle failure mechanism that produces a third body in the tribological system [17].

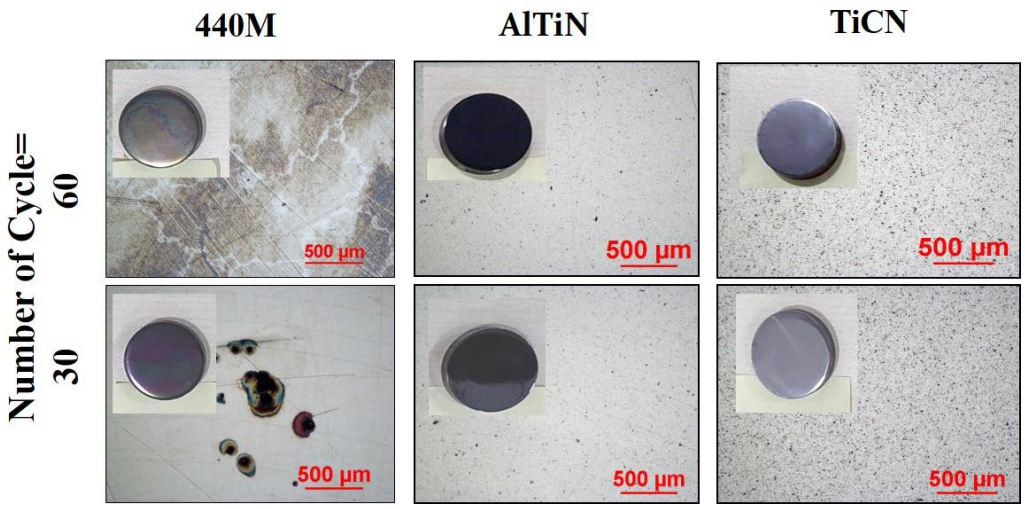


Figure 6. The photographs and optical image of coatings and 440M stainless steel after autoclave sterilization at 30 and 60 cycles time.

The surface examinations were done following the autoclave sterilization (see Figure 6). For dental drills, a high sterilization resistance surface to autoclave processing is required. Although AlTiN and TiCN coatings provided us with sterilization resistance while also protecting the surface from corrosion, 440M steel is not as successful. While corrosion initiation was observed in bare steel, it was not observed in coated samples, indicating that both coatings were resistant to autoclave sterilization.

4. Conclusion

The main wear mechanism observed during drilling was discovered to be a complex combination of abrasive, adhesive, and thermal wear. These findings demonstrated that surface modification with PVD hard thin film coatings is an effective method for extending dental implant drill lifetime and reducing necrosis with lower bone temperature during drilling procedures. The presence of graphite particles in the TiCN coating may improve solid lubricity and source wear resistance. As a result, when compared to uncoated steel, the COFs and wear rates of coated samples were significantly decreased in dry sliding conditions, with the TiCN coating providing the best wear resistance. Our findings showed that a new alternative surface coating (TiCN) improved the performance of dental implant drills by reducing the increase in bone temperature. It is also a promising corrosion resistance alternative because it can be autoclave sterilized in 60 cycles with no change in the surface.

5. Acknowledge

The authors thank to the support of the Scientific and Technical Research Council of Turkey, for the funded project, Project no 3200170 and Titanit ultra hard PVD coatings company in Turkey.

References

[1] F. Parnia, J. Yazdani, V. Javaherzadeh ve S. Maleki Dizaj, «Overview of Nanoparticle Coating of Dental Implants for Enhanced Osseointegration and Antimicrobial Purposes,» *Journal of Pharmacy & Pharmaceutical Sciences,* cilt 20, pp. 148-160, 2017.

[2] S. K. Mishra ve R. Chowdhary, «Heat Generated by Dental Implant Drills During Osteotomy—a review: heat generated by dental implant drills,» *Journal of Indian Prosthodontic Society,* cilt 14, no. 2, pp. 131-143, 2014.

[3] G. Marenzi, J. C. Sammartino, G. Quaremba, V. G. Graziano, A. El Hassanin, M. E. Qorri, G. Sammartino ve V. Iorio-Siciliano, «Clinical Influence of Micromorphological Structure of Dental Implant Bone Drills,» *BioMed Research International,* 2018.

[4] B. Bullon, E. F. Bueno, M. Herrero, A. Fernandez-Palacin, J. V. Rios, P. Bullon ve F. J. Gil, «Effect of irrigation and stainless steel drills on dental implant bed heat generation,» *Journal of Materials Science: Materials in Medicine,* cilt 26, no. 2, 2015.

[5] S. Li, L. Shu, T. Kizaki, W. Bai, M. Terashima ve N. Sugita, «Cortical bone drilling: A time series experimental analysis of thermal characteristics,» *Journal of Manufacturing Processes,* cilt 64, pp. 606-619, 2021.

[6] D. Tur, K. Giannis, E. Unger, M. Mittlböck, X. Rausch-Fan ve G. D. Strbac, «Thermal effects of various drill materials during implant site preparation—Ceramic vs. stainless steel drills: A comparative in vitro study in a standardised bovine bone model,» *Clinical Oral Implants Research,* cilt 32, no. 2, pp. 154-166, 2021.

[7] N. Ariharan, C. G. Sriram, N. Radhika, S. Aswin ve S. Haridas, «A comprehensive review of vapour deposited coatings for cutting tools: properties and recent advances,» *The International Journal of Surface Engineering and Coatings,* cilt 100, no. 5, pp. 262-275, 2021.

[8] M. Aamir, A. Davis, W. Keeble, U. Koklu, K. Giasin, A. Vafadar ve M. Tolouei-Rad, «The Effect of TiN-, TiCN-, TiAlN-, and TiSiN Coated Tools on the Surface Defects and Geometric Tolerances of Holes in Multi-Spindle Drilling of Al2024 Alloy,» *Metals,* cilt 11, p. 1103, 2021.

[9] J. Sazaki ve S. Imazato, «Autoclave sterilization of dental handpieces: A literature review,» *Journal of Prosthodontic Research,* cilt 64, no. 3, 2019.

[10] L. Shan, Y. Wang, J. Li, H. Li, X. Wu ve J. Chen, «Shan, L., Wang, Y., Tribological behaviours of PVD TiN and TiCN coatings in artificial seawater,» *Surface and Coatings Technology,* no. 226, pp. 40-50, 2013.

[11] F. Komarov , V. Konstantinov, A. Kovalchuk, S. Konstantinov ve H. Tkachenko, «The effect of steel substrate pre-hardening on structural,mechanical, and tribological properties of magnetron sputtered TiN and TiAlN coatings,» *Wear,* cilt 352, no. 353, pp. 92-101, 2016.

[12] K. Kuptsov, P. Kiryukhantsev-Korneev, A. Sheveyko ve D. Shtansky, «Comparative study of electrochemical and impact wear behavior of TiCN, TiSiCN,TiCrSiCN, and TiAlSiCN coatings,» *Surface & Coatings Technology,* no. 216, pp. 273-281, 2013.

[13] J. Caicedo, C. Amaya, L. Yate, M. Gómez, G. Zambrano, J. Alvarado-Rivera, J. Munoz-Saldana ve P. Prieto, «TiCN/TiNbCN multilayer coatings with enhanced mechanical properties,» *Applied Surface Science,* p. 5898–5904, 2010.

[14] Z. Zhang, L. Zhang, H. Yuan, M. Qui, X. Zhang, B. Liao, F. Zhang ve X. Ouyang, «Tribological Behaviors of Super-Hard TiAlN Coatings Deposited by Filtered Cathode Vacuum Arc Deposition,» *Materials,* cilt 15, p. 2236, 2022.

[15] L. Aihua, D. Jianxin, C. Haibing, C. Yangyang ve Z. Jun, «Friction and wear properties of TiN, TiAlN, AlTiN and CrAlN PVD nitride coatings,» *International Journal of Refractory Metals and Hard Materials,* cilt 31, pp. 82-88, 2012.

[16] P. Mi, J. He, Y. Qin ve K. Chen, «Nanostructure reactive plasma sprayed TiCN coating,» *Surface & Coatings Technology,* 2017.

[17] L. Aihua, D. Jianxin, C. Haibing, C. Yangyang ve Z. Jun, «Friction and wear properties of TiN, TiAlN, AlTiN and CrAlN PVD nitride coatings,» *Int. Journal of Refractory Metals and Hard Materials,* cilt 31, pp. 82-88, 2012.

2343 Kodlu Çelik Dökümü Sonrası Atık Haline Gelen Hassas Döküm Kumunun Şamot Refrakter Üretiminde Kullanımı

Veysel Murat BOSTANCI[1*], Tuba BAHTLI [2]

[1*] Necmettin Erbakan Üniversitesi, Makine Mühendisliği Anabilim Dalı, Konya, Türkiye, (ORCID: 0000-0001-9704-6467), vmuratb@hotmail.com

[2] Necmettin Erbakan Üniversitesi, Metalurji ve Malzeme Mühendisliği, Konya, Türkiye, (ORCID: 0000-0001-5682-6280), taksoy@erbakan.edu.tr

Öz

Döküm sektöründe önemli bir yere sahip olan hassas dökümün sağladığı büyük avantajların yanında hazırlanan kalıbın tekrar kullanılamaması hem depolama maliyeti hem de çevresel problem oluşturması açısından dezavantajlara sahiptir. Hassas döküm atık kumuna yapılan x-ışını difraktometre (XRD) analizi sonucu, malzemenin alüminasilikat esaslı olduğu ve seramikler için değerli bir mineral olan zirkon mineralini içerdiği tespit edilmiş ve şamot refrakter tuğla üretiminde kullanılabilirliğinin araştırılmasına karar verilmiştir. Yapılan bu çalışmada, 2343 kodlu çelik dökümünde kullanılan ve atık haline gelen hassas döküm kalıbı toz haline getirilerek %5, %10 ve %20 oranlarında şamot refrakterlere ilave edilmiş, refrakterlerin fiziksel, mekanik ve ısıl şok direnci testleri yapılmıştır. Testler sonucu atık malzemenin içindeki zirkon varlığı ile birlikte mukavemet ve ısıl özelliklerinde iyileşmeler meydana gelmiştir. Üretim sonrası atık girdisinin malzemede yeni bir faz oluşturup oluşturmadığını anlamak adına XRD analizi yapılmıştır. Ayrıca taramalı elektron mikroskobu (SEM) ile malzemelerin mikroyapı analizleri yapılmıştır.

Elde edilen veriler doğrultusunda atık girdisinin şamot refrakter malzeme üretimi için maliyet düşürücü ve aynı zamanda mukavemet ve ısıl özellikleri artırıcı etkisi olduğu gözlenmiştir.

Anahtar Kelimeler: Şamot, Hassas döküm, Atık, Refrakter, Mekanik özellikler, Isıl şok.

Use of Precision Casting Sand, Coded 2343, Which Becomes Waste After Steel Casting, In the Production of Fireclay Refractory

Abstract

In addition to the great advantages of precision casting, which has an important place in the casting industry, the reuse of the prepared mold has disadvantages in terms of both storage cost and environmental problems. As a result of X-ray diffractometer (XRD) analysis performed on precision casting waste sand, it was determined that the material is aluminosilicate-based and contains zircon mineral, a valuable mineral for ceramics, and it was decided to investigate its usability in fireclay refractory brick production. In this study, the precision casting mold used in 2343 coded steel casting and turned into waste was pulverized and added to the fireclay refractories at the rates of 5%, 10% and 20%, and physical, mechanical and thermal shock resistance tests of the refractories were carried out. As a result of the tests, there were improvements in strength and thermal properties with the presence of zircon in the waste material. XRD analysis was performed in order to understand whether waste input creates a new phase in the material after production. In addition, the microstructure analyzes of the materials were made with scanning electron microscopy (SEM). In line with the data obtained, it was observed that the waste input had a cost-reducing effect for the production of fireclay refractory material, as well as increasing the strength and thermal properties.

Keywords: Chamotte, Precision casting, Waste, Refractory, Mechanical properties, Thermal shock.

1. Introduction

Investment casting is a casting process used for the production of complex and precision casting products (1). Although the process always has advantages such as leading to development and innovation, it is a time-consuming and labor-intensive process (2). The process includes applying a coating layer of ceramic material onto the wax pattern assembly. Zircon based materials are used as the first layer and silica based materials are used as the secondary layer. Colloidal silica traditionally has been used as the binder material (3). However, the silica concentration in the slurry plays an important role in developing the required surface properties (4). In a particular case, sodium silicate can be used as a slurry as it increases the strength of the shell mold and reduces the overall production time (5).

Refractories are used for any high temperature production. Due to their stability and chemical inertness at high temperatures, they are often used in alumina, silica, magnesia, zirconia, chromium, etc. They are produced from materials in combination or alone (6,7).Among them, alumina-silica group refractories are widely used and classified as chamotte (fire clay) refractories and high alumina refractories according to their physical and chemical structures (8).

Fireclay refractories are produced from natural clay (rich in silica) that can withstand temperatures above 19 with a PCE (pyrometric cone equivalent) value without disintegration, deformation, cracking, softening or melting. Typical compositions of fire clay bricks are SiO_2 (<78%) and Al_2O_3 (<44%), these refractories mainly consist of kaolinite clay minerals ($Al_2O_3 \cdot 2SiO_2 \cdot 2H_2O$). As a result, these refractories are generally used in power generation blast furnaces, chimney linings, boilers, glass tank kilns and pottery kilns; and also for production of cast refractories such as sleeves, nozzles, stoppers and tuyeres (6,7,9).

As a result of X-ray diffractometer (XRD) analysis performed on precision casting waste sand, it was determined that the material was aluminosilicate-based and contains zircon mineral, which is a valuable mineral for ceramics, and its usability in the production of fireclay refractory bricks was investigated in this study.

2. Material and Method

The XRF analysis results of Chamotte, Bauxite raw materials and precision casting waste sand (PCWS) used in experimental studies are given in Table 1. The results of the analysis show that raw materials and precision casting waste sand are generally composed of Al_2O_3 and SiO_2. Each of the impurities in the raw material are around 3% maximum.

Table 1. XRF data of raw materials and precision casting waste sand

	2343- PCWS	Chamotte 1-3mm	Chamotte 0-1mm	Chamotte Powder	Bauxite 1-3mm
Al_2O_3	37,24	33,67	28,53	33,63	71,81
SiO_2	54,16	61,48	66,82	59,96	22,99
Fe_2O_3	1,44	1,66	1,54	2,46	2,09
TiO_2	2,44	2,84	2,52	2,99	2,80
CaO	0,33	0,35	0,59	0,96	0,31
ZrO_2	3,85	0,00	0,00	0,00	0,00
Na_2O	0,26	0,00	0,00	0,00	0,00

Cr_2O_3	0,07	0,00	0,00	0,00	0,00
P_2O_5	0,09	0,00	0,00	0,00	0,00
K_2O	0,06	0,00	0,00	0,00	0,00
HfO_2	0,06	0,00	0,00	0,00	0,00

The phases in the waste material are seen in the XRD analysis results (Figure 1). Generally current phases are mullite ($3Al_2O_3.2SiO_2$), quartz (SiO_2), cristobalite (SiO_2), zircon ($ZrSiO_4$) and corundum (Al_2O_3) phases.

Table 2. Composition recipes for the production of chamotte refractory bricks

	1-3 mm Chamotte (%)	0-1 mm Chamotte (%)	-63 µm Chamotte (%)	1-3 mm Bauxite (%)	-63 µm PCWS (%)	Binding Clay (%)	Totanine (%)
Reference	20	15	20	35	0	10	3
%5 2343 PCWS	20	15	15	35	5	10	3
%10 2343 PCWS	20	15	10	35	10	10	3
%20 2343 PCWS	20	15	0	35	20	10	3

The compositions indicated in Table 2 were mixed in the Necmettin Erbakan University Metallurgical and Materials Engineering Department laboratory, after mixing in the mixer, i) 125 cm^3 square prism (Figure 3.1), ii) 35 bar (40 MPa) by applying pressure, refractory materials in the form of rods of 25 mm x 25 mm x 150 mm were shaped by applying 25 bar (40 MPa) pressure by the Hursan brand press. The shaped materials were sintered at 1250°C for 4 hours by using a heating rate of 5°C/min in the MSE Brand ATM_ELV_1700_12_(CH) model high temperature furnace. After the sintering process, x-ray diffractometry (XRD) analysis, physical (density and open pore) and mechanical tests of the materials were performed. Strength, toughness and elastic modulus values of materials were examined by mechanical tests. Then, the thermal shock test was applied to determine the resistance of the materials to thermal shock. In addition, the microstructure and fracture surface analyzes of the produced refractories were carried out by scanning electron microscope (SEM).

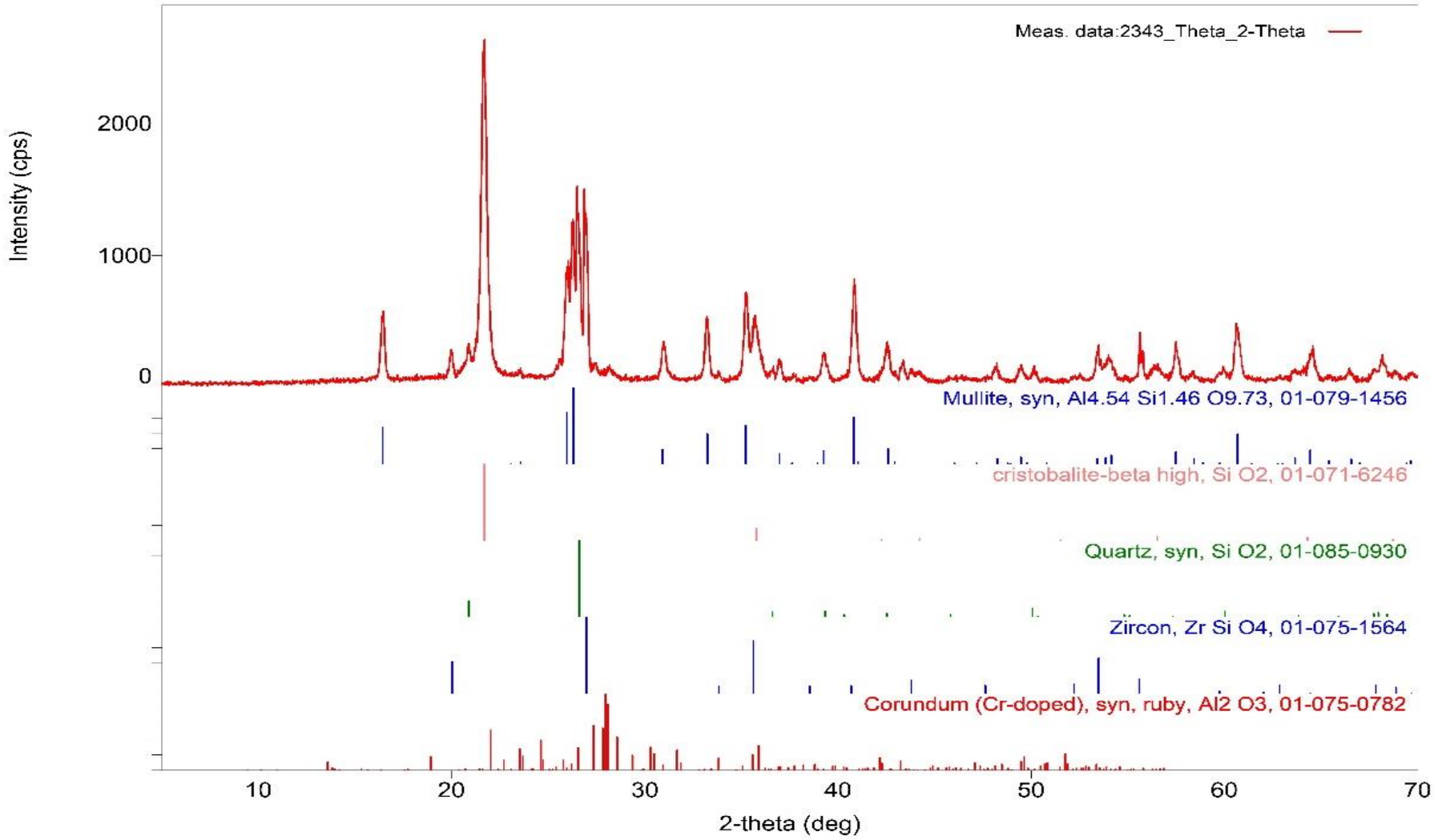
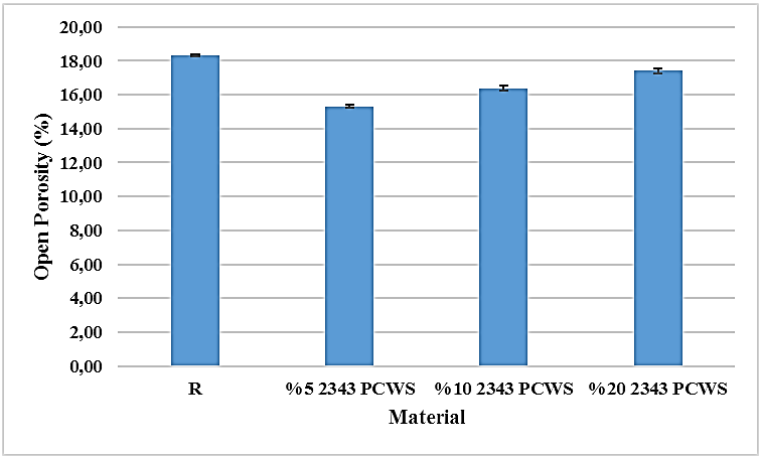


Figure 1. XRD analysis result of precision casting waste sand

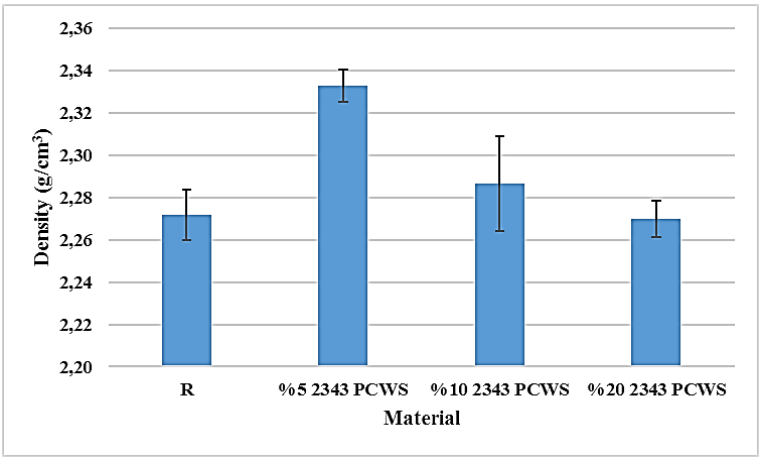
3. Results & Discussion

3.1. Results of Physical Tests

The % open porosity and density values of produced fireclay refractory materials determined by using the Archimedes principle were shown in Figure 2.



(a)



(b)

Figure 2. a) % open pore and b) density graph of reference and chamotte refractories produced by using 2343 steel precision casting waste sand

While the highest density and the lowest open porosity values were obtained in the material with 5% 2343 PCWS, it was observed that the values were close to the reference material when the amount of additive was 20%. Density values higher than the reference were achieved in 5% and 10% 2343 PCWS added materials. The density of the zircon mineral in the waste sand is higher than the fireclay material (d_{zircon}: 4.7 g/cm^3 > $d_{chamotte:}$ 1.9-2.35 g/cm^3) and the filling of the pores as a result of the use of the waste with a size below 63 microns could be shown as the reasons for the increase in density (10,11).

3.2. Results of Mechanical Tests

3.2.1. Cold Crushing Strength (CCS)

The cold crushing strength values of reference fireclay refractory and compositions produced by using 2343 steel precision casting sand wastes were given in Figure 3.

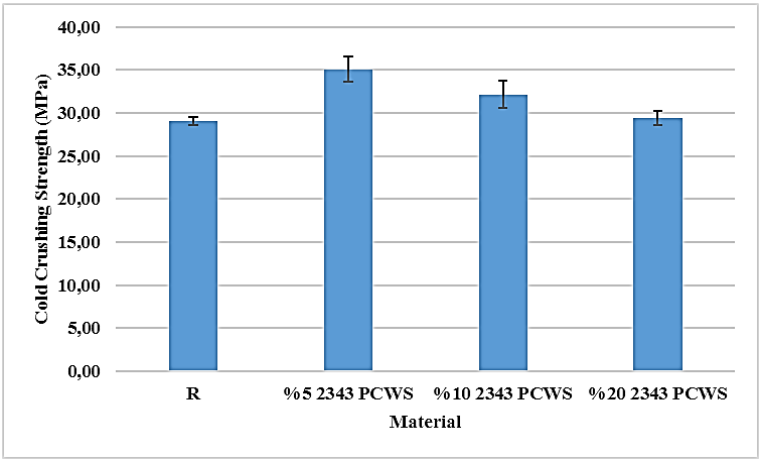


Figure 3. The cold crushing strength graph of reference and chamotte refractories produced using 2343 precision casting sand waste

The highest CCS value was reached in the 5% PCWS added fireclay material that has the highest density. It was determined that the CCS values increased with the increase in density and the density value was effective on CCS. When the studies on this subject are examined, it has been observed that the addition of zircon increases the density and reduces the open porosity, and the addition of zircon also increases the cold compression strength (11). The addition of zirconia powder leads to a five-fold increase in mechanical strength at room temperature (12). In the study in which alumina-silica systems were examined, it was stated that the mullite phase provides strength in ceramic bodies (13). It is desirable that alkali, alkaline earth oxides and iron oxide-containing compounds (K_2O, Na_2O, CaO, Fe_2O_3) used for the binding phase in refractories should be used as low as possible. The high amount of those type of oxides adversely affects high temperature properties such as refractoriness under load, flexural strength at high temperature-HMOR (14). According to results obtained, it is thought that the increased Fe_2O_3 and TiO_2 percentages came from the investment casting waste sand in the fireclay refractory recipe composition have a negative effects on the strength of the produced fireclay refractory.

3.2.2. 3-Point Bending Test

The 3-point bending test results for each produced and sintered composition such as a 25mm x 25mm x 150mm (width x length x height) square prism were given in Figure 4-6. When the bending strength results were examined, it was seen that similar graphics were obtained with the CCS test. It can be said that density has an effect on strength. Elastic modulus and toughness graphs of the produced materials are given in Figure 5. According to graphics, the toughness and elastic modulus values of PCWS added materials were also higher than the reference due to the presence of zircon grains. The toughness increasing mechanism of zircon is a known method and because of this feature, it has supported the increase of toughness.

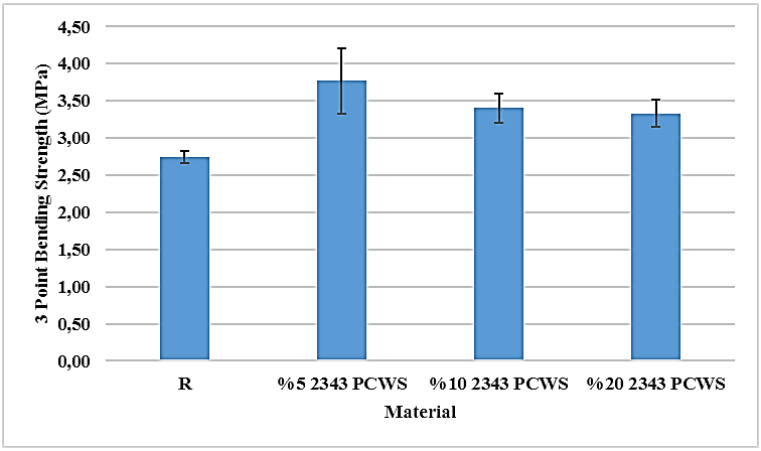
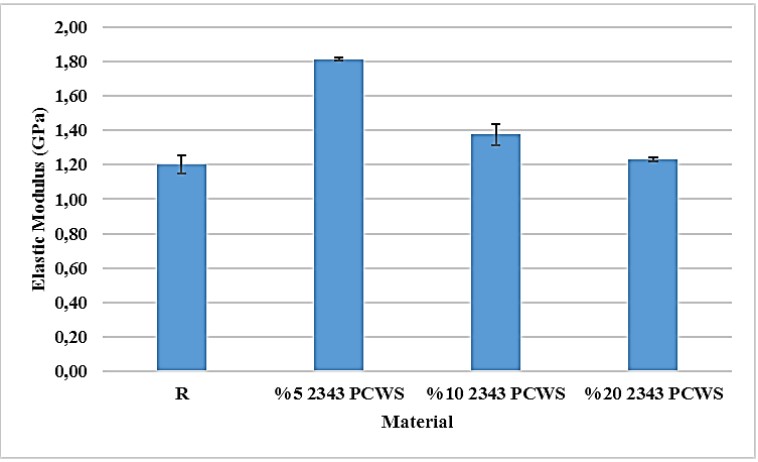
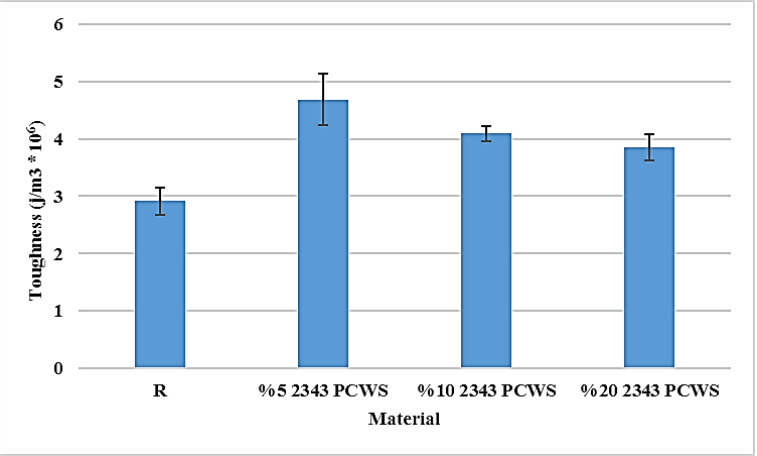


Figure 4. 3-point flexural strength graph of reference and chamotte refractories produced by using 2343 precision casting sand waste



(a)



(b)

Figure 5. Elastic modulus and Toughness graph of the reference and chamotte refractories produced by using 2343 precision casting sand waste

3.3. Results of XRD Analysis of Produced Fireclay Refractory Materials

When the XRD analyzes were examined, it was seen that the mullite ($3Al_2O_3.2SiO_2$), cristobalite (SiO_2), quartz (SiO_2), corundum (Al_2O_3), titanium dioxide (TiO_2) and iron oxide (Fe_2O_3) phases were found in the content of the pure reference material. When PCWS-doped refractories were examined, it could be seen that mullite ($3Al_2O_3.2SiO_2$), cristobalite (SiO_2), quartz (SiO_2), corundum (Al_2O_3), zircon ($ZrSiO_4$), beta cristobalite (β-SiO_2), iron oxide (Fe_2O_3) and rutile (TiO_2) phases appeared. No new phase formation was observed due to precision casting sand wastes.

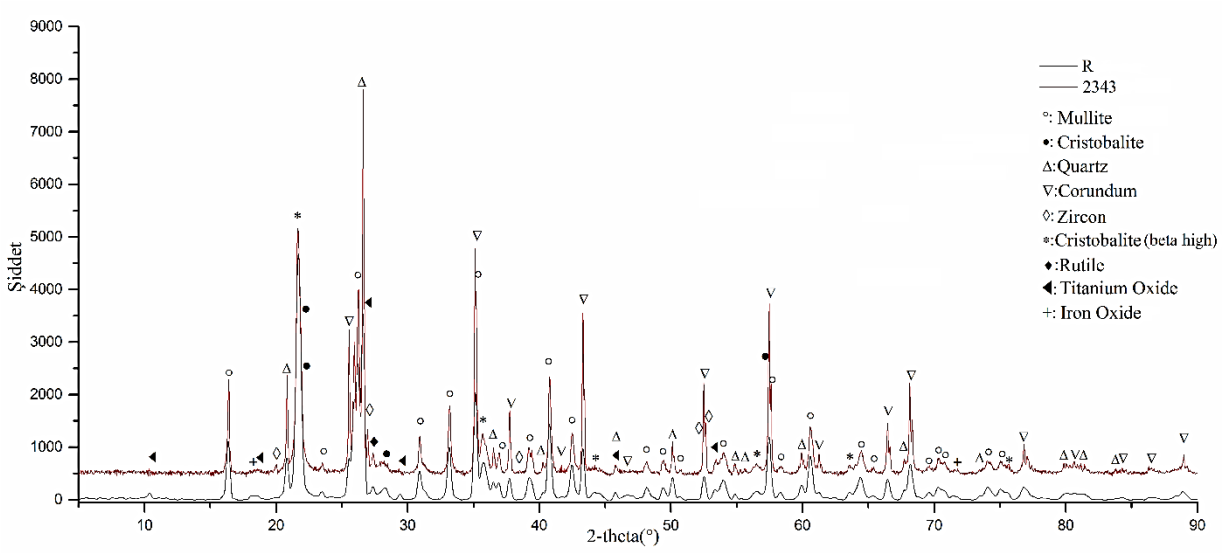
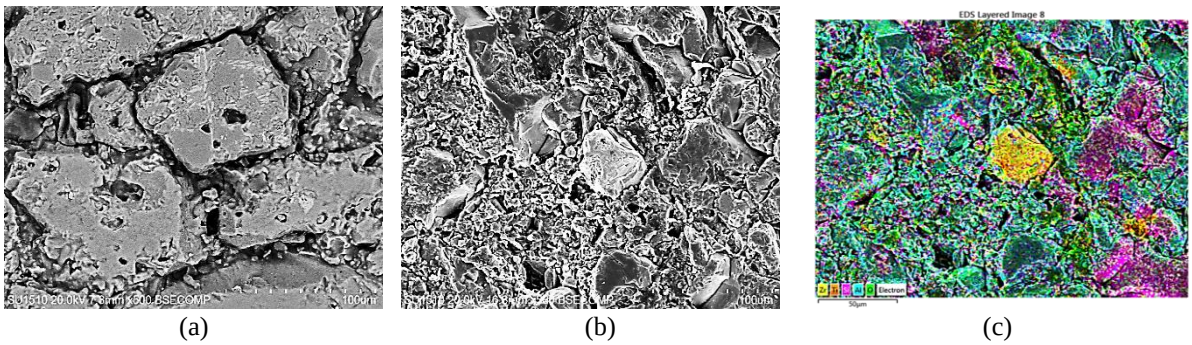


Figure 6. XRD analysis result of reference and PCWS 2343 added chamotte refractory materials

3.4. SEM Microstructure Analysis Results



(a) (b) (c)

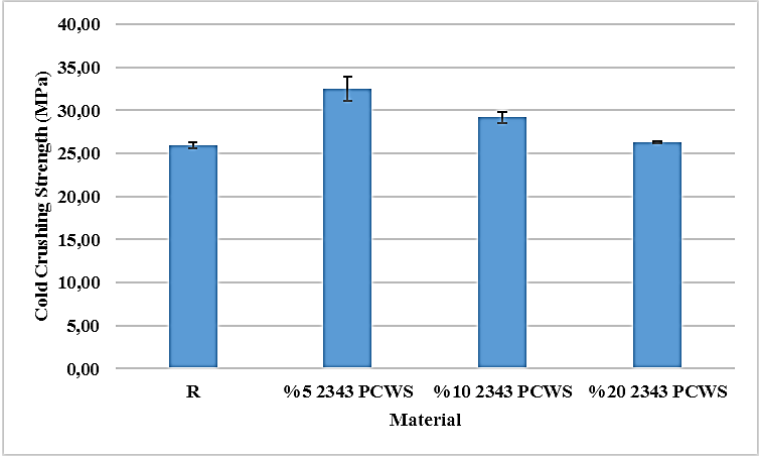
Figure 7. Microstructure analyzes of a) reference, b) PCWS 2343 doped composition and c) mapping of PCWS 2343 doped composition

The microstructure images of the materials were given in Figure 7. In Figure 7.c, the zircon in the structure was shown in yellow. When the microstructure image of the PCWS added refractory material was examined, it was seen that there were smaller grains than the reference material. It is thought that the small grain size compared

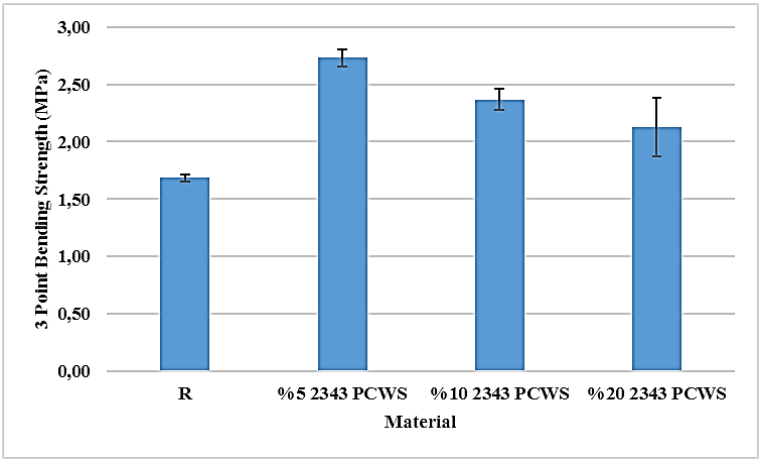
to the reference material, the toughness with the presence of zircon, as well as the presence of microcracks and porosities cause an increase in toughness, and therefore it has better mechanical properties than the reference material. However, as the amount of used waste increases, larger cracks form without preventing crack propagation and then negatively affect the physical and mechanical properties of the material.

3.5. Thermal Shock Test Results

The graphs obtained after the thermal shock test were shown in Figure 8. When the results of CCS and 3-point bending tests were examined, a general decrease in strength occurred. The reason for this situation could be the formation of new cracks in the material after thermal shock.



(a)

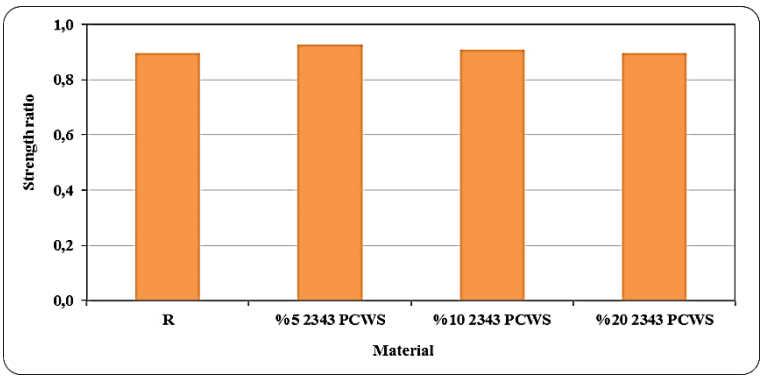


(b)

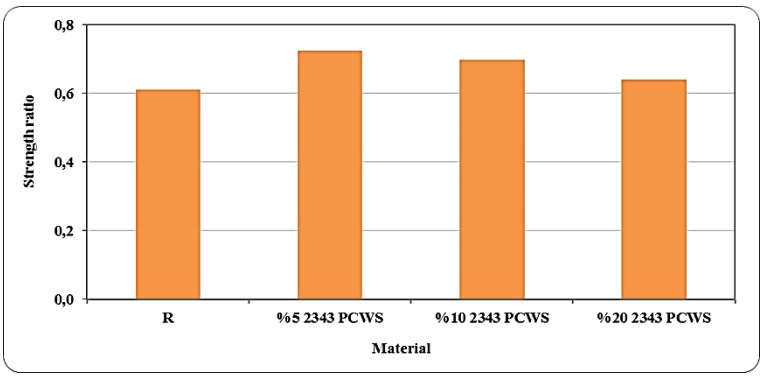
Figure 8. Graphs of a) CCS and b) 3-point bending tests after thermal shock for reference and chamotte refractories produced by using 2343 precision casting sand waste

The strength ratio shows how long the strength is preserved after thermal shock test. In chamotte refractory materials produced by using 5%, 10% and 20% waste, the strength ratio values were generally close and/or high than this of reference. Strength ratio graphs were shown in Figure 9. The resistance of zircon to thermal shock and

the energy absorption by crack bridging of microcracks after shock can be explained as the reason for the increase in the strength ratio.



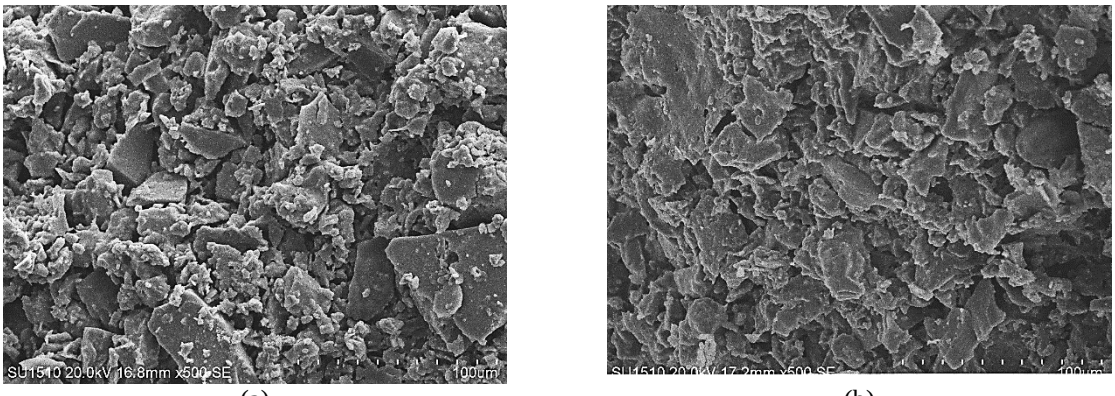
(a)



(b)

Figure 9. Strength ratio graphs of reference and chamotte refractories produced by using 2343 precision casting sand waste after a) CCS and b) 3 point bending tests.

3.6. Fractured Surface Analysis Results

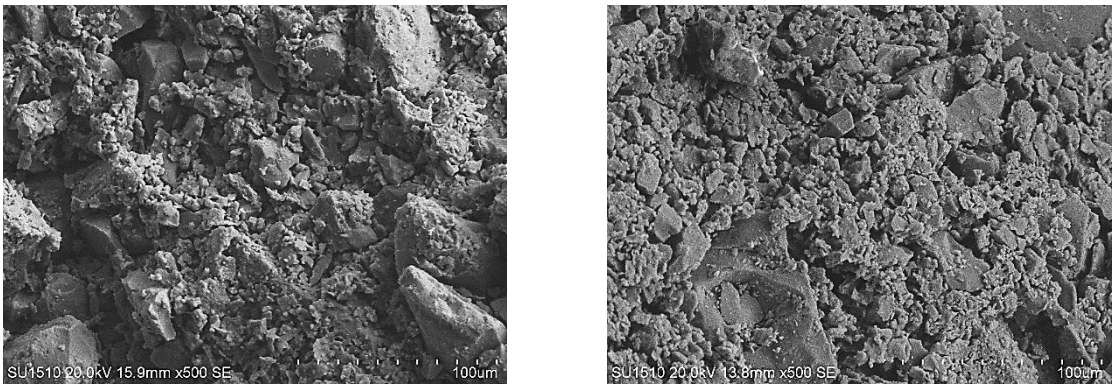


(a) (b)

Figure 10. Broken surface analysis images of the compositions produced as reference a) before and b) after thermal shock

In Figure 10, fracture surface analysis images of the pure material were given. In the reference chamotte refractory, while transgranular fracture was dominant in general, it was seen that this situation became more dominant after

thermal shock. Small grains had intergranular fractures. It was also seen that there were coarser grain structures than PCWS added material.



(a) (b)

Figure 11. Broken surface analysis images of the chamotte rafratory produced with PCWS 2343 additive a) before and b) after thermal shock

In Figure 11, when the fracture surface images of the PCWS added material were examined, both transgranular and intergranular fractures were observed before and after the shock. It was also seen that the much more intergranular fracture was observed than this of reference chamotte refractory.

4. Results

According to the results of this study, especially in 5% PCWS added material, the increase in strength was approximately 20% in CCS and approximately 32% in 3-point bending compared to the reference. And also, the increase of toughness value of this refractory was an approximately 50% than this of reference. Due to advantages: i) reduction in production cost with the use of precision casting waste sand, which has become an environmental problem and has storage problems, as raw material input in fireclay refractory production; ii) an increase in strength and toughness of refractories with the zircon mineral comes from waste, it can be said that the use of PCWS in fireclay brick production will be beneficial.

References

[1] A. Sata ve M. Sutaria, "Scope of investment castings supported by survey of foundries in rajkot cluster", *Indian Foundry J.*, c. 60, ss. 42–46, 2014.

[2] S. Jones ve C. Yuan, "Advances in shell moulding for investment casting", *J. Mater. Process. Technol.*, c. 135, ss. 258–265, 2003.

[3] P. R. Jhonson ve S. Eliot, "Investment casting and the the method of making the same", 4966225, 1990.

[4] Y. meng Wei, K. hui Hu, ve Z. gang Lu, "Effect of SiO2 concentration in silica sol on interface reaction during titanium alloy investment casting", *China Foundry*, c. 15, ss. 23–30, 2018.

[5] L. G. Znamenskii, O. V. Ivochkina, ve A. S. Varlamov, "Acceleration of the formation on the sodium silicate binder in investment casting", *Mater. Sci. Forum*, c. 946 MSF, ss. 673–677, 2019.

[6] A. Andrews, E. Nsiah-Baafi, S. K. Y. Gawu, ve P. A. Olubambi, "Synthesis of high alumina refractories from lithomargic clay", *Ceram. Int.*, c. 40, ss. 6071–6075, 2014.

[7] A. Andrews, J. Adam, ve S. K. Y. Gawu, "Development of fireclay aluminosilicate refractory from lithomargic clay deposits", *Ceram. Int.*, c. 39, ss. 779–783, 2013.

[8] ASTM, "Standard Classification of Fireclay and High-Alumina Refractory Brick", 2021. [Çevrimiçi]. Available at: https://www.astm.org/c0027-98r18.html.

[9] *Materials Handbook*. London: Springer London, 2008.

[10] R. Ceylantekin ve C. Aksel, "MgO-Spinel kompozit refrakterlere ZrSiO4 ilavesinin korozyon davranışına etkisi", *Anadolu Üniversitesi Bilim ve Teknol. Dergisi-A Uygulamalı Bilim. ve Mühendislik*, c. 11, sayı 2, ss. 103–114, 2010.

[11] W. Meng, C. Ma, T. Ge, ve X. Zhong, "Effect of zircon addition on the physical properties and coatability adherence of MgO-2CaO·SiO2-3CaO·SiO2 refractory materials", *Ceram. Int.*, c. 42, sayı 7, ss. 9032–9037, 2016, doi: 10.1016/j.ceramint.2016.02.140.

[12] C. Aksel, M. Dexet, N. Logen, F. Porte, F. L. Riley, ve F. Konieczny, "The influence of zircon in a model aluminosilicate glass tank forehearth refractory", *J. Eur. Ceram. Soc.*, c. 23, sayı 12, ss. 2083–2088, 2003, doi: 10.1016/S0955-2219(03)00025-6.

[13] D. Michel, L. Mazerolles, ve R. Portier, "Directional solidification in the alumina-silica system: microstructure and interfaces", *Ceram. Trans.*, c. 6, ss. 435–437, 1990.

[14] M. S. Başpınar, "Mullit Refrakterlerde Bağlayıcı Fazın Optimizasyonu", Anadolu Üniversitesi, 2005.

Image Processing Based Path Planning and Tracking of Differential Drive Robot

Syed Sajjad Ali
Manager Industrial Operations
Atlas Group of Companies, Pakistan
Sajjad.Ali@adl.atlas.pk

Abstract

Since industries are demanding Robotic Process Automation (RPA) to digitalize its operations and become global market competitive. This research is contribution to autonomous human-free industry environment through differential drive path planning robot. A visual localization of a static environment has developed for differential drive robot using a camera and one ultrasonic sensor is integrated for real time obstacle detection. This combined arrangement is simple and give satisfactory results in path planning and traversing from a given position to final destination. A modified A* search algorithm is developed whereby the path is planned considering the diagonal motion that allows smooth movement of robot at corners. The planned path is traversed based on the PID control of orientation error of robot with respect to the next coordinate in planned path. On a low level, an ultrasonic sensor is continuously checking for real time obstacle that was absent during path planning so as to generate new path if any found.

1. Introduction

Since the beginning of the development of machine vision, researchers have realized its importance in the robotics field, as it provides a useful tool for both the environment detection and decision making during the automation process. At the same time, path planning for robots influences many in the robotics and automation process and it has remained active for both methodology research and system implementation [1].Path planning is an essential part in the automation process of a system that moves in the environment while avoiding obstacles and respecting various constraint[5][6].

For a robot to carry out its navigation form its position to destination, it must know the environment around it. It's better described as in "Given partial knowledge about its environment and a goal position or series of positions, navigation encompasses the ability of the robot to act based on its knowledge and sensor values so as to reach its goal positions as efficiently and reliably as possible." [2]. There are three main aspects in this research, i.e. map extraction to find navigable regions, path planning and tracking of the planned path along with avoiding real-time obstacles. The extraction of navigable region is based on the color based extraction of environment using openCV library [3]. The path planning algorithm revolves around A* path planner [4] having the ability to find paths diagonally.

Tracking of the planned path is done using PID algorithm using kinematics of Differential Drive robot. A simple circular differential drive robot has been selected with an ultrasonic sensor on its front. A wireless connection has been established using Bluetooth technology between robot and the controller.

2. System Model

The hardware of the system consisted of a camera mounted on a rod supported by two stands. The camera is adjusted onto the rod so that the environment captured is horizontally straight and not oblique. The robot consists of an ultrasonic sensor for checking any real time obstacles. The physical layout of the system is shown in figure 1.

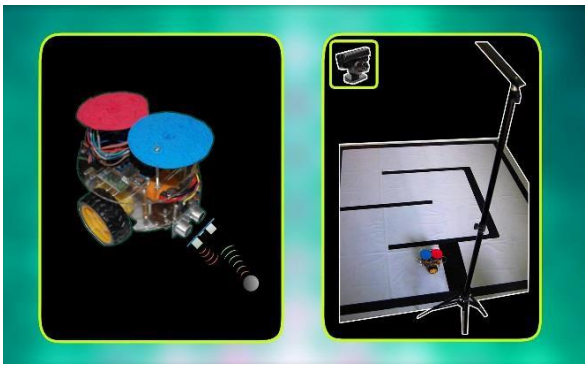


Figure 1 Hardware Setup of the System

The map data is gathered by camera along with location of robot and goal that has to be reached. The path is then planned which is later used by PID algorithm to compute right and left wheel velocities for the robot's navigation. The system model is shown in figure 2.

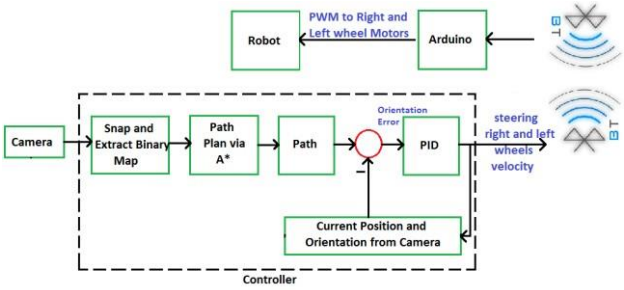


Figure 2 Complete block diagram of System Model

Thus, our system encompasses three main components,data for planning path using vision, planning the route and tracking that route. The complete system flowchart gives a better overview in figure 3.

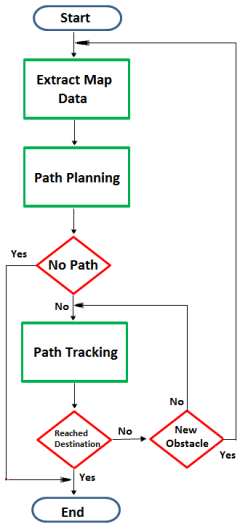


Figure 3 Flowchart of Overall System

3. Map Extraction

The map data is gathered using camera which is mounted on a rod supported by two stands thus providing the static environment's information. The following information is gathered from camera:

Location of robot and destination.

Identification of navigable region and the regions that have to be avoided.

Thresholding of environment so as to get the map information in binary.

The detailed information is given in flowchart in figure 4.

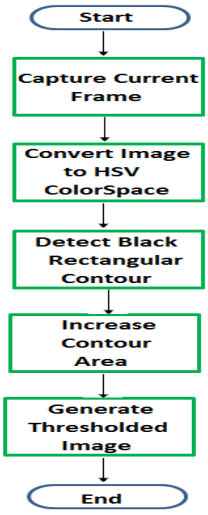


Figure 4 Flow chart of processing image for Contour Area enlargement

The image thresholding is by first converting the image into 60x60 image and averaging out the colors in pixel. If the average color is less than 40, it's considered the region to be navigable since white color has low HSV values, otherwise the region is regarded as blockade

4. Path Planning

The path planning algorithm used is A* search algorithm. A* path planner is modified to search for all the possible neighboring 8 cells and determines the shortest path based on the minimum cost. The cost is computed based on the Manhattan Distance that allows the computations to become faster by eliminating the ambiguities of floating point computation and computation times of floating point by avoiding Euclidean Distance. The flowchart of algorithm is shown in figure 5.

The cost function of algorithm is given in equation 1.

$$f(n) = g(n) + h(n) \quad (1)$$

Where f (n) is the cost function. g (n) is the number of grids moved from starting position. h(n) is the distance between the current position (ax, ay) and endpoint (bx, by) (Manhattan Distance) mathematically computed as:

$$M.H = |ax - bx| + |ay - by| \quad (2)$$

Graphically, the algorithm's working is shown below in figure 6. The green point is robot's current position while the red one is the endpoint

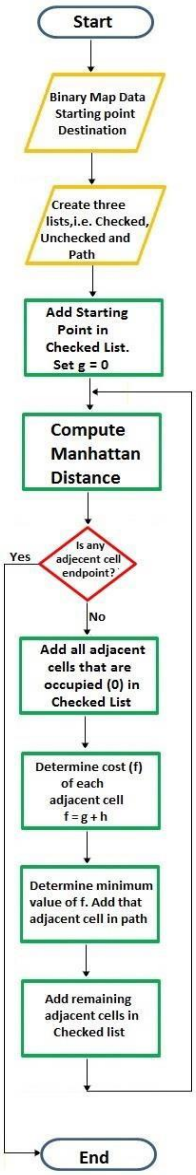


Figure 5 Algorithm for A Path Planner*

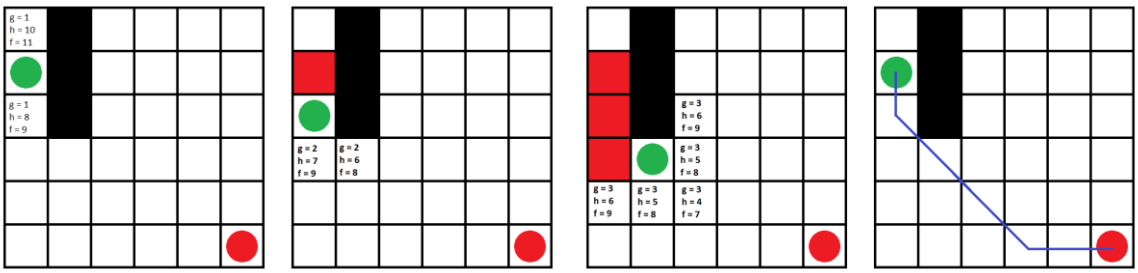


Figure 6 Graphical representation of A Algorithm*

5. Path Tracking

Once the path has been planned, now a PID controller is used to track that path based on the current position and the orientation of robot based on vision data. To ensure path is followed, nearest coordinate in planned path is selected and the orientation error is computed based on the next coordinate selected (goal) and the robot's current orientation. The equation that determines error is given in equation 3.

$$\theta = \tan^{-1}\frac{(oriented_x)(goal_y)-(oriented_y)(goal_x)}{(oriented_x)(goal_x)+(oriented_y)(goal_y)} \quad (3)$$

This $\theta$is used to compute angular velocity $\omega$by taking time derivative (last orientation error minus current divided by sampling time) of θ. This $\omega$is now used with differential drive model to determine the velocities of right and left wheel. The equations governing velocities calculation are given in equation 4 and 5.

$$V = (R + L/2) \quad (4)$$

$$V = (R - L/2) \quad (5)$$

The block diagram for path tracking is shown in figure 7.

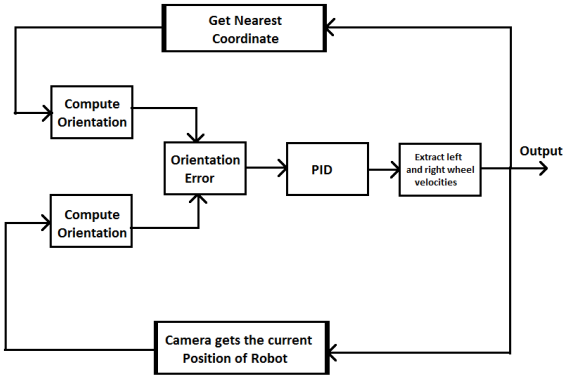


Figure 7 Block Diagram of Path Tracking of robot using PID controller

6. Simulation Results

Path planning was simulated on a small 6x6 map by giving the map data in binary format as

```
m = [[1,0,1,1,1,1],
     [ 1,0,1,1,1,1],
     [ 1,0,1,1,1,1],
     [ 1,1,1,1,1,1],
     [ 1,1,1,1,0,1],
     [ 1,1,1,1,1,1]]
```

Its graphical representation is shown in figure 6. The path planned by A* algorithm is also shown in figure 5. On the other hand, the tracking of robot was simulated using python and differential drive robot's kinematic model. The result of the tracking is shown in figure 8.

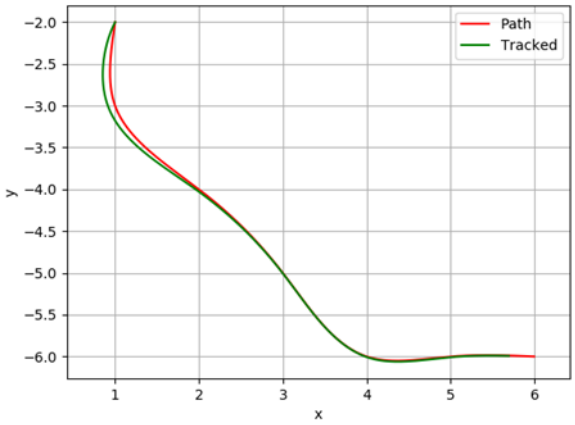


Figure 8 Simulation of path tracking based on differential drive robot's kinematics

Since the model used was of differential drive and it works on Instantaneous Centre of Curvature (ICC), the robot's motion is just like an arc and thus introducing errors between the path generated and the tracked path

Table 1 Comparison between Planned Coordinates and the Tracked Coordinates in Simulation

Planned Coordinates (x,y)	Tracked Coordinates (x,y)	Error (Distance)
(1.0, -2.0)	(1.0, -2.0)	0.0
(1.0, -3.0)	(0.85, -3.0)	0.15
(2.0, -4.0)	(1.95, -4.0)	0.05
(3.0, -5.0)	(3.0, -5.0)	0.0
(4.0 -6.0)	(4.0, -6.0)	0.0

7. Hardware Results

The thresholding of image to get binary data introduced noise because the binary information depends on the average color pixels and the intensity of light in the environment introduces color distortion perceived by vision system, thus adding extra non navigable region. The tracking of the planned path was successfully achieved with the robot oscillating around corners. The maximum deviation of about 10.2cm. Moreover, any real time obstacle detected by ultrasonic sensor, sends the request of preplanning the path that introduces delay due to planning of new path that takes about 7 seconds. Moreover, the sampling time for controller introduced the delay of 200 milliseconds to get the robot's current position and orientation due to image processing.

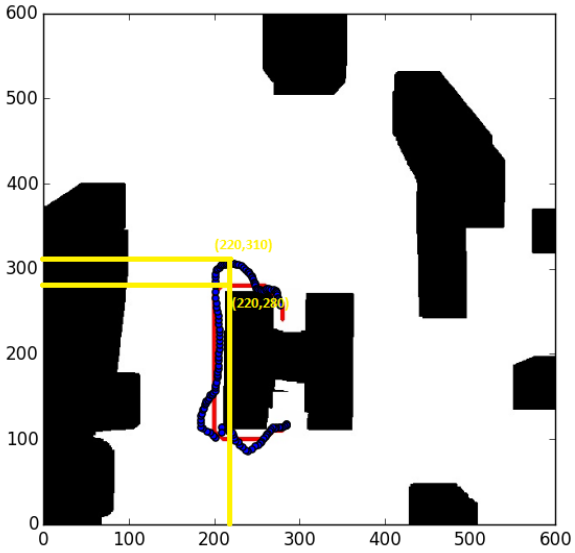


Figure 9 Blue dots represent the path along with the robot traversed while the red line represents the planned path

Table 2 Comparison between Planned Coordinates and the Tracked Coordinates in Hardware

Planned Coordinates (x,y)	Tracked Coordinates (x,y)	Error (pixels)
(250, 100)	(250, 85)	15.0
(200, 100)	(210, 100)	10.0
(200, 120)	(185, 120)	15.0
(200, 200)	(205, 200)	5.0
(220, 280)	(220, 310)	30.0

Thus practically, the tracking of the planned path was found to be satisfactorily accurate due to feedback of robot's position after every sampling time. This accuracy introduced delay of about 300ms rendering the system slow

8. Conclusion

Image processing based path planning and tracking of a differential drive robot is developed and found correct. The implementation of 8 point A* path planner was successfully achieved. The hardware integration scheme was also successful but it succumbed to environmental light intensity as it distorts the camera results. Moreover, the feedback of robot's position in the environment introduced large time delays of about 200 milliseconds rendering the robot to navigate very slowly.

9. References

[1] A. Mohammeda, L. Wanga,*, R.X. Gao, “Integrated image processing and path planning for robotic sketching.” 8th CIRP Conference on Intelligent Computation in Manufacturing Engineering.

[2] D. S. Roland Seigwart, Illah R. Nourbakhsh, “Introduction to Autonomous Mobile Robots.” The MIT Press, 2nd ed., 2011.

[3] https://opencv.org [4]http://theory.stanford.edu/~amitp/GameProgramming/AStarComparison.html

[5] Souissi, O., Benatitallah, R., Duvivier, D., Artiba, A., Belanger, N., & Feyzeau, P. (2013, October). Path planning: A 2013 survey. In Industrial Engineering and Systems Management (IESM), Proceedings of 2013 International Conference on (pp. 1-8). IEEE.

[6] Souissi, O., Benatitallah, R., Duvivier, D., Artiba, A., Belanger, N., & Feyzeau, P. (2013, October). Path planning: A 2013 survey. In Industrial Engineering and Systems Management (IESM), Proceedings of 2013 International Conference on (pp. 1-8). IEEE.

An Internet of things for Data security using Artificial Intelligence

Arham Iqbal khan, Syed Sajjad Ali
Department of Electronic Engineering
University of Engineering and Technology Karachi, Pakistan
arhamiqbal @cloud.neduet.edu.pk

ABSTRACT

Security and privacy of user data become substantial by using Internet of Things (IoT) applications in almost every aspect of human life. Threats are emerging at an impulsive rate retained the current privacy and security measure a big question mark. Artificial Intelligence is currently playing an emergent role in enlightening the traditional cyber security, both the resource limitation and the networking of IoT devices are still great hazards. Several protective approaches are using in Iot application but Machine language caught the attention at most because of its extensive features make it more appropriate for Iot Environment. Machine learning as a subdivision of artificial intelligence smartly monitors the Iot devices and resolve the attack. This paper contributes to a detailed analysis of attacks and its solution using machine learning on the basis of security and privacy.



Figure: 1 Research Paper Flow

I. INTRODUCTION

Visualize earth a place to live in where our electric kettle synchronized with our timepieces to offer immaculately fresh Tea as long as u wakeup, and communicate the room blinds when to get unfolded primarily on the basis of previous inclinations. Our fridges ask a web-based store to deliver us various groceries to be needed with checking the meal plan calendar, where our vehicles automatically cover up themselves as the rain started based on forecasted weather. Where the intelligent mirrors which can scan us and tell us about the potential health problem. Even though a decade ago these are only thriving in technical movies and can be called a product of the intelligent science fiction authors but the latest development in engineering and technological sector permitting the nightmare of Internet of thing to turn out to be a reality.

The theory of IoT says that each device can interact with each other through networks and makes an intelligent decision based on data collected by every device. Internet of Things connects various devices, sensors, data, processing, and connectivity solutions, as a consequence of actionable intelligence and benefits, from the most straightforward to essentially the most advanced application. .In a nutshell IoT needs all potential objects to work together on the web to offer a secure and comfortable life for humans.

Two devices in each millisecond are associated with the web. This connectivity and the massive explosion of IoT gadgets have enhanced the volume of data traffic. Because of this connectivity, challenges like Non-trust worthy connection take place, as Internet connectivity is among the major hurdle. . IOT involves enormous data sharing

between the connecting devices which made the Storage and Security a great concern .another pinching issue is user privacy. Data verification and authentication of devices makes the data security and information protection at higher risk.

Particularly for IoT data safety and protection with the limitation of conventional approaches highlighted the necessity to handle the innovative security technologies. Artificial intelligence appeared as a promising technological solution which has been used in various applications [3]. Machine learning (ML) caught tremendous attention in the area of artificial intelligence because of Its idea and strategies possess been extensively used to unravel advanced issues in lots of engineering applications. Machine learning came out as an optimistic approach to report the attacks in IoT. [1,2]

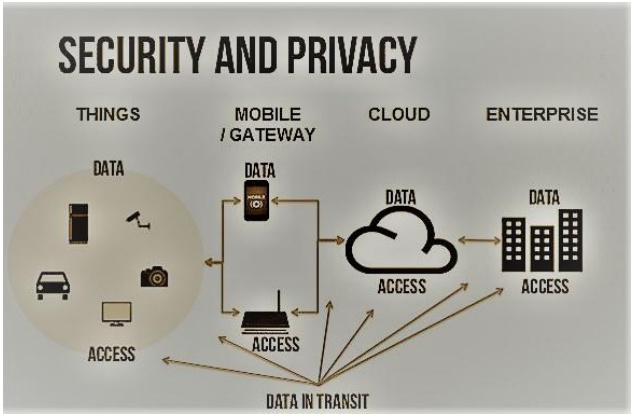
In this paper, we present a detailed introduction to the Internet of Things (Section I), classification of IoT threats based on security and privacy (Section II) classification of different machine learning algorithms in IoT(Section III). Machine learning as a solution for security and privacy threats in IoT(Section IV). Finally, we concluded our research paper (Section V). The research flow of this paper is depicted in the figure1.

II. THREATS IN IOT

IoT signifies to a network where all the physical entities can interact with each other by means of internet[5]. Existing sources of end devices made the IoT attacks different as compared to Traditional Networks[6]As a tremendous increment in connecting smart devices and gadgets to the network Over the time, safeguarding the IoT devices from the vulnerable threats is gradually becoming uncovered. Complex attributes and characteristic versatile landscape of IoT devices forced them to prone to various security threats. An easy access the network and the Motility of sensitive data are the main contributors which need to be retrenched and monitored which aims to Completely devastated the Privacy of the network. These circumstances indicate the maturity of IoT deployed network as being not developed completely.

IoT devices have constrained memory and computational control and less protected protocols are used such as Zigbee.in contrast with the traditional Internet, which contains influential servers with an enhanced multi-layer security structure which isn't supervised by a real-time IoT framework.IoT devices have diverse information and configurations, make it extremely challenging to form a standard security protocol[7] All these obstacles put IoT at risk of various security and privacy threats.as the size of the network increases, The chances of an attack in a network will be increased.

IoT devices have limited computational resources that reduce their ability to deal with advanced threats. In short, IoT susceptibilities are classified as definite and general, vulnerabilities such as discharging of batteries, regularization, and trustworthy connections are definite to IoT devices, and vulnerabilities inherited to the internet fall on the general category. We discuss some of the threats mostly encountered in IoT and classify the threats mainly on the basis of their security and privacy .



SECURITY THREATS IN IOT

security is basically a state of being protected from any mishap. Security threat targets the inaccessibility of the network and affects the data integrity by manipulating it, misroute the data packets, and makes wrong decisions. In IoT, data can be anything, such as user identification, or a multimedia conversation between two individuals .any unauthorized revelation of sensitive information may end up in a violation of confidentiality, integrity, and availability of the network. We elaborate on some of the security threat found in IoT.

- **DENIAL OF SERVICE (DOS) THREAT**

A Denial-of-Service(DOS) Threat is among one of the notorious cyber-attack strategy referred as Security attack which is responsible for Inaccessibility of the network for the legitimate user node .As a DOS threat is behindhand in the network to take the user in the wrong direction by taking an inappropriate decision. The main motive of DOS attacks in IoT framework is to send excessive request simultaneously to bombarded the server by data flooding .

- **MITM ATTACK**

Mitm is the abbreviation of Man[3] in the middle attack, computed as advanced attacks in the history of cyber security [9]. Spoofing and eavesdropping may be classified as MiTM threats .The accused node camouflages as a device, by creating a long winded connection to other devices without their consent and Subtly transfers and conceivably modifies the communication between the two devices who accept that they are having straightforward connections

- **MALWARE**

Malware is an acronym for malicious software. Several program planned stealthily to invade and harm the client security .Malware referred as a collaboration of distinctive attacks such as as spyware key logger, adware and worms. [10 11].In presence of such attacks, the complex information of IoT communication may be revealed, transformed, or even may not be available to the users. Many IoT security ruptures have been reported recently, which have disturbed the access to popular websites

A. PRIVACY THREAT IN IOT

Privacy refers to a state of mind where an individual is not bothered by others. Attacks on the confidentiality of the user data are stated as privacy attacks. Sniffing and inference attacks are few of the known privacy threat witnessed in IoT framework. Hewlett Packard, in his report on Privacy problem in IoT 2015[24]having an in-depth research Primarily focus on the privacy contractions faced and reported as a tremendous privacy distress at the maximal percentage of 80% and least chances of being safe in IoT

- **DATA PRIVACY ATTACK**

the privacy attacks threaten data confidentiality generally categorized as Active Privacy Attacks (APA) and Passive Privacy Attacks (PPA). Attacks that are responsible for manipulating the data are categories as Active Privacy Attacks such as Denial of Service (DOS) attacks, jamming, and spoofing. Whereas, Passive Privacy Attacks caused by re-identification and data leakage such as Eavesdropping and traffic analysis.

- **PERFORMANCE BASED ATTACKS**

The privacy attack targets on the accessibility of sensitive data such as decryption keys can be categorized into internal Privacy Attacks (IPA) and External Privacy Attacks (EPA). Attacks that are responsible for misrouting, packet dropping, eavesdropping, and data alteration is categories as Internal Privacy Attacks. Whereas, External privacy Attacks caused by network congestion and resource exhaustion .examples are DoS attacks

III. Overview of machine learning Techniques

The machine learning Techniques come forward as a solution to the present safety mechanism in the IoT network. We further classified the machine learning algorithm to a supervised, unsupervised, and reinforcement learning algorithm. In this section, we overview some of the significant techniques in detail.

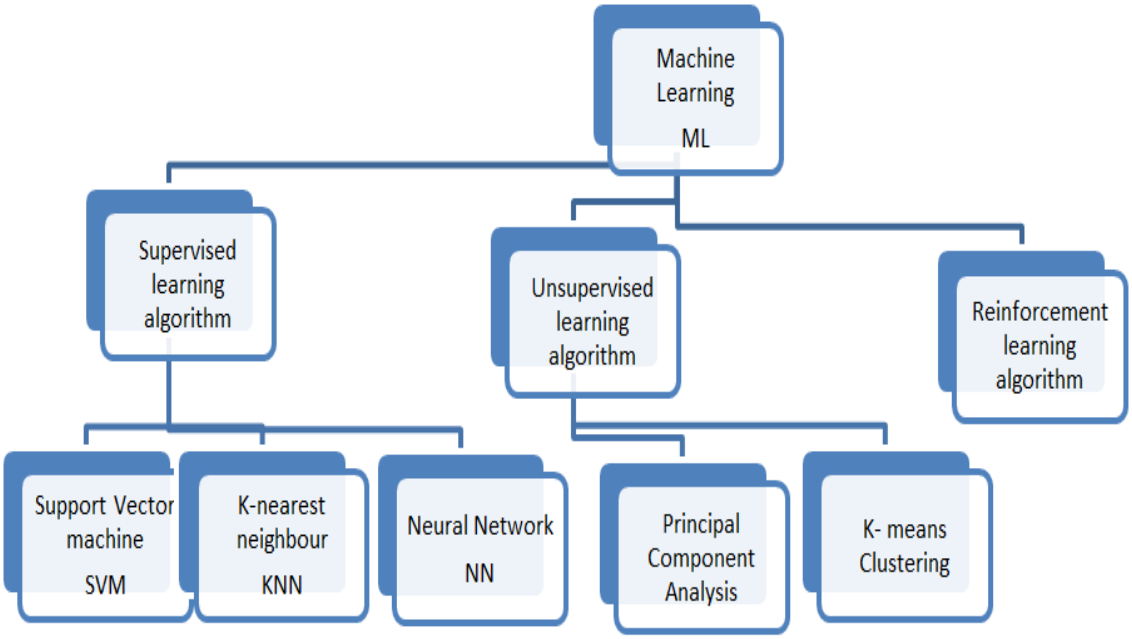


Figure: 2 Overview of Machine learning Algorithms

A. SUPERVISED LEARNING TECHNIQUES

Supervised machine learning is a method of learning functions where machine learns by training data with identified outcomes .supervised machine learning further classified on the basis of Classification and regression among various groups but mostly classification is being used. Some of the main supervised learning techniques are stated.

❖ SUPPORT VECTOR MACHINE(SVM)

SVM is a supervised learning algorithm contributes to one of the highest performance algorithm in term of accuracy estimation .SVM is utilized in both of the cases of classification as well as regression problems for solving security issues in IoT but primary commitment is for classification model. SVM is broadly utilized for detection of distinctive patterns and classification in plenty of application as a main ingredient such as Bioinformatics.

❖ K-NEAREST NEIGHBOUR ALGORITHM(KNN)

K-Nearest Neighbor is a simple supervised learning algorithm used for both classification cased and regression problems and give inaccurate results in case of larger datasets. Prediction based on likeliness of the absent node can be achievable by using Euclidian formula in term of similarity fashion of the neighboring node

- NEURAL NETWORKS (NN)

Neuron network is a combination of input, hidden and output layer is a series of the algorithm that attempts to recognize the relationship in a data set by replicating the human brain.it is used to solve nonlinear and complex problems. Neural networks are applied in the industrial sector from financial service to forecasting and in scam exposure as well.

B. UNSUPERVISED LEARNING ALGORITHM

Unsupervised learning algorithms used unlabeled data to train the algorithm.it is a pattern detection technique and grouped the data based on their similarities measures as Clusters. Unsupervised learning is more complex and unpredictable as compared to a supervised learning algorithm. We present some of the unsupervised learning algorithms

- **K-MEANS ALGORITHM**

K mean algorithm is an unsupervised learning technique where the Input data collected together in form of clusters based on their similarities patterns. We represent the mean point or centroid as the Kth term. And classified each data set to its nearest mean point and revise the mean points by taking their average points of the node in each cluster accordingly .this process will be repeated for a particular time until the clusters are formed.

- **PRINCIPLE COMPONENT ANALYSIS**

Principle component analysis is an unsupervised learning algorithm used to decompose the progressive data set into compact size because of lesser data requirements.it is most commonly used in the area of Image compression, face recognition, and prediction in machine learning.

C. Reinforcement learning algorithm

Reinforcement learning algorithm is a machine learning practice where agents learn to behave in an environment by performing actions and found rewards based on their performance .both input and corresponding output are unknown and predict based on their experience and it's generally called a surrounding friendly algorithm.

IV. MACHINE LEARNING AS A SOULTION FOR SECURITY AND PRIVACY IN IoT

We summarized this section with the different mechanisms applied to machine learning (ML) as a solution for securing IoT and keeping their privacy intact in Iot environment.

A. SECURITY SOLUTIONS IN IOT

- **COUNTER DOS ATTACKS**

Raj and Kulkarni[15] analysis of Dos attacks used to be detected by a supervised learning algorithm named as Support Vector Machine and Neural Network.SVM and NN are mainly influenced by the rate of collision and the rate of arrival to training the machines. To calculate the chances of DOS attacks, both rates have been sent by the nodes. In NN, As a result of a smaller threshold in comparison of the given probability indicates a typical sign of DOS attack.so in the case, it completely shut down until the attack is terminated. In terms of Accuracy, SVM is better in contrast to NN to detect the order in a limited period.

Gurulakshmi, A. Nesarani [16] design a systematic approach for Mirai attacks which causes huge data congestion at the server. He proposed to detach a boundary between a regular and anomalous flow based on classification model, which is responsible for predicting prior abnormality in traffic flow. Network traffic is distributed among two distinctive classes on the contrary to the DDoS attack. Two classification algorithms SVM and KNN are used in this approach.

Kolika et al. [17] conduct a comparative performance assessment of various machine learning techniques in term of enhancing the safety in IoT networks .severe Supervised and unsupervised learning techniques involved for

instance Naive Bayes(NB), Random Forest(RF), Bagging(B), and Radial Basis Function (RBF). SVM embark the position in term of highest accuracy achievable among all.

- **COUNTER MAN IN THE MIDDLE ATTACK**

Cañedo and A. Skjellum Proposed a strategically solution for the attacks as counter man in the middle utilizing Artificial Neural Network for protection [18]A five layered wise structure consist of three input neurons utilized with two concealed layers. Input layers hold the sensitive data comprise of device authentication and the sensor value with the time delay and two hidden neurons in term of Programming. The anticipated Neural Network structure is responsible for monitoring the strength of the node .they set criteria for predicting false information that I the targeted data diverge from the data expected an error is occurred

- **MALWARE Detection by SVM ALGORITHM**

Kim M. & Choi[19], make use of Support Vector Machine (SVM), a supervised learning algorithm for detecting Malware by reviewing various mechanisms based on signature, behavior, and taint-analysis.SVM compete for the rest of the techniques in term of malware detection with the highest accuracy. For Instance, in a behavioral detection system, statistics on the device is observed for detecting anomalous configurations and ML techniques to evaluate the data.

- **MALWARE Detection by using RF ALGORITHM**

Alam & Vuong [20], used Random Forest, a supervised learning algorithm for detection of various malware attacks in android In terms of checking the accuracy for classifying the application based on behavioral changes and termed as Malicious or Benign accordingly. By taking 48,919 data points as a reference with 42 features each, observe the detection accuracy of RF elements such as the total no of trees involved, depth of an individual tree, random features .and resulted in less than one percent of error and the highest accuracy is achieved in that case.

Security Threats	Machine learning algorithm
Dos Attack	• Support Vector Machine [15] • Neural Network [15]
Mirai attack	• Support Vector Machine [16] • K-Nearest Neighbor[16]
Man in the middle attack	• Artificial Neural Network [18]
Malware detection	• Support Vector Machine [19] • Random Forest (20)

Table I : Iot Security solutions using ML algorithms

B. PRIVACY SOLUTIONS IN IoT

- **PRIVACY IN VANET**

Zhang et al. [21] highlighted the need for privacy safeguard mechanisms in VANET. Vehicle node generally adapted a cooperative environment for learning causing privacy problems., it can be an easy target for a malicious node to obtain sensitive data because of restricted computational and memory resources. In this paper, the author introduces a solution for the privacy issues in applying the machine learning algorithm by using collaborative IDS and the concept of dynamic differential privacy for securing data set.

❖ ANOMALY DETECTION USING CLASSIFICATION

Jatti, Kannan, Alisha, Vijayalakshmi & Sinha [22]design an IoT device for securing women from any mishap by a real time transmission of statistics such as physiological data and position of the body specifies either the wearer is in danger or in safe zone. Input data is transmitted in a form of galvanic skin response and body temperature to determine the position of the body. The reason is that when an individual is confronted with a risky circumstance, emission of Adrenalin influences various organs in the human body and resulted in severe sweating and elevated blood levels measure by an electro dermal response.clasifier investigate the information and decide whether the person in safe mode or in jeopardy.

❖ ACCESS CONTROL USING REINFORCEMENT LEARNING

In order to improvise the system and take over the access control issues raised in IoT framework, the sensitive data has been scattered at the edges instead of being placed at a centralized position which causes the damage as a whole in case of single malicious node. Machine learning is used extensively to cope up and progress the access control policy by using Reinforcement Algorithm and introduce a model of "Smart Contract" which is a code design in order to grant denial or accessibility option upon any request and a token will be issues to the one who is accessible in the premises of IoT domain.

Cases	Proposed Solutions
VANET privacy	Collaborative IDS[21]
Anomaly detection	Classification [22]
Access Control	Reinforcement Learning Algorithm [23]

Table 2: IoT Privacy solution using ML algorithms

V. CONCLUDED REMARKS

This research paper has covered an apothegmatic review of Internet of things and the attacks mostly encountered in IoT in term of security and privacy concern. Being a subset of artificial intelligence and well-known among network as Machine learning , an encouraging solution to the protection in IoT framework by using its techniques on a classified scale of privacy and security. As IoT being an irradiated technology with an explosive growth ,security loophole is still an existing hazard. Resource constraint problem of IoT device and limited computation obstruct the adoption of various solutions profound in Iot Networks. A lot of challenges Machine learning have to deal with in between high level security and lower complexity of IoT.

ACKNOWLEDGEMENT

I am very much thankful to my course teacher Dr.Irfan Ahmed for being so cooperative and to get us familiarized with the world of research with such an informative activity.

References

[1]M. A. Alsheikh, S. Lin, D. Niyato, and H.-P. Tan, "Machine learning in wireless sensor networks: Algorithms, strategies, and applications," IEEE Commun. Surv. Tutor., vol. 16, no. 4, pp. 1996–2018, 2014.

[2]I. Butun, S. D. Morgera, and R. Sankar, "A survey of intrusion detection systems in wireless sensor networks," IEEE Commun. Surv. Tutor., vol. 16, no. 1, pp. 266–282, 2014.

[3] M. S. Mahdavinejad, M. Rezvan, M. Barekatain, P. Adibi, P. Barnaghi, and A. P. Sheth, "Machine learning for Internet of Things data analysis: A survey," Digit. Commun. Netw., vol. 4, no. 3, pp. 161–175, Aug. 2018, DOI: 10.1016/J.DCAN.2017.10.002.

[4] Z. Imran, Tasneem Y., Rwan M., Fadi A., "Internet of Things (IoT) Security: Current Status, Challenges and Countermeasures", International Journal for Information Security Research (IJISR), Volume 5, Issue 4, December 2015

[5] Fatima Hussain, Syed Ali Hassan, Rasheed Hussain, and Ekram Hossain. 2020. Machine Learning for Resource Management in Cellular and IoT Networks: Potentials, Current Solutions, and Open Challenges. IEEE Communications Surveys & Tutorials c (2020), 1–1.

[6] Qi Jing, Athanasios Vasilakos, Jiafu Wan, Jingwei Lu, and Dechao Qiu. 2014. Security of the Internet of Things: Perspectives and challenges. Wireless Networks 20 (11 2014), 2481–2501

[7] I. Makhdoom, M. Abolhasan, J. Lipman, R. P. Liu, and W. Ni. 2019. Anatomy of Threats to the Internet of Things. IEEE Communications Surveys Tutorials 21, 2 (Secondquarter 2019), 1636–1675

[8] I. Brass, L. Tanczer, M. Carr, M. Elsden, and J. Blackstock. 2018. Standardizing a moving target: The development and evolution of IoT security standards. Living in the Internet of Things: Cybersecurity of the IoT - 2018. 1–9

[9] Dan Swinhoe. 2019. What is a man-in-the-middle attack? How MITM attacks work and how to prevent them. (2019). https://www.csoonline.com/article/3340117/ what-is-a-man-in-the-middle-attack-how-MITM-attacks-work-and-how-to-prevent-them.html [122] Z. Tan, A. Jamdagni, X. He, P. Nanda, and R. P. Liu. 2014. A System for Denial-of-Service Attack D

Malware is usually stated as a virus, spyware, worm, trojan horse, rootkit, or malvertising [10, 11].

[10] I. Makhdoom, M. Abolhasan, J. Lipman, R. P. Liu, and W. Ni. 2019. Anatomy of Threats to the Internet of Things. IEEE Communications Surveys Tutorials 21, 2 (Secondquarter 2019), 1636–1675.

[11] Benjamin Zi Hao Zhao, Muhammad Ikram, Hassan Jameel Asghar, Mohamed Ali Kaafar, Abdelberi Chaabane, and Kanchana Thilakarathna. 2019. A Decade of Mal-Activity Reporting: A Retrospective Analysis of Internet Malicious Activity Blacklists. In Proceedings of the 2019 ACM Asia Conference on Computer and Communications Security. 193–205.

[12] Hewlett Packard. (2015). Internet of things research study. Retrieved March 10, 2016, from http://www8.hp.com/h20195/V2/GetPDF.aspx/4AA5-4759ENW.pdf

[13] Zanolli, L. (2015, March 23). Welcome to Privacy Hell, Also Known as The Internet of Things. Retrieved March 24, 2016, from http://www.fastcompany.com/3044046/tech-forecast/welcome-toprivacy-hell-otherwise-known-as-the-internet-of-things

[14] Schectman, J. (2015, January 28). Internet of Things Opens New Privacy Litigation Risks. Retrieved March 24, 2016, from http://blogs.wsj.com/riskandcompliance/2015/01/28/internet-of-thingsopens-new-privacy-litigation-risks

[15] A. B. Raj, M. V. Ramesh, R. V. Kulkarni, and T. Hemalatha, "Security enhancement in wireless sensor networks using machine learning," in Proc of IEEE HPCC-ICESS, 2012

[16] K.Gurulakshmi, A.Nesarani "Analysis of IoT Bots against DDOS attack using Machine learning algorithm" Proceedings of the 2nd International Conference on Trends in Electronics and Informatics (ICOEI 2018) IEEE Conference Record: # 42666; 2018

[17] K. RT, S. T. Selvi, and K. Govindarajan, "Ddos detection and analysis in sdn-based environment using support vector machine classifier," in 2014 Sixth International Conference on Advanced Computing (ICoAC), pp. 205–210, Dec 2014

[18] J. Cañedo and A. Skjellum, "Using machine learning to secure IoT systems," in Proc. of 14th Annual Conference on Privacy, Security, and Trust (PST), 2016.

[19] Ham, H. S., Kim, H. H., Kim, M. S., & Choi, M. J. (2014). Linear SVM-based android malware detection for reliable IoT services. Journal of Applied Mathematics, 2014

[20] Alam, M. S., & Vuong, S. T. (2013, August). Random forest classification for detecting Android malware. In Green Computing and Communications (Green-Com), 2013 IEEE, and Internet of Things (iThings/CPSCom), IEEE International Conference on and IEEE Cyber, Physical and Social Computing (pp. 663-669). IEEE.

[21] Tao Zhang and Quanyan Zhu. 2018. Distributed Privacy-Preserving Collaborative Intrusion Detection Systems for VANETs. IEEE Transactions on Signal and Information Processing over Networks 4, 1 (2018), 148–161.

[22] Jatti, A., Kannan, M., Alisha, R. M., Vijayalakshmi, P., & Sinha, S. (2016, May). Design and development of an IOT based wearable device for the safety and security of women and girl children. In Recent Trends in Electronics, Information & Communication Technology (RTEICT), IEEE International Conference on (pp. 1108-1112). IEEE.

[23] A. Outchakoucht, E.-S. Hamza, and J. P. Leroy, "Dynamic Access Control Policy based on Blockchain and Machine Learning for the Internet of Things," Int. J. Adv. Comput. Sci. Appl., vol. 8, no. 7, pp. 417–424, 2017.

Axial Dynamics of Elastic Deformable Supported Nonlocal Rods Using A Higher-Order Nonlocal FEM

Hayri Metin Numanoğlu[1*], Furkan Şen[2]

[1] Giresun University, Civil Engineering Department, Division of Mechanics, Giresun, Turkey

[2] Giresun University, Civil Engineering Department, Division of Construction, Giresun, Turkey

Abstract

A higher-order (three-node) finite element formulation of nonlocal free vibration is studied for axial nanorods under elastic deformable boundary condition. According to this, stiffness and mass matrices are obtained by applying weighted residual-based finite element formulation (NL-FEM) to the equation of motion of rod element. By adding elastic boundary condition to NL-FEM, nonlocal nondimensional frequency parameters of clamped-axial spring attached nanorods are presented. Detailed discussions of numerical results are performed.

Keywords : Axial rod, Elastic support, Finite element, Free vibration, Nonlocal elasticity.

* Corresponding author e-mail : metin_numanoglu@hotmail.com

1. Introduction

Thanks to advances in nano-electro-mechanical systems technology (NEMS), we observe important changes in many devices and equipment today. Low weight, low volume, high mechanical strength, and high durability are examples of this. The reason of development in NEMS technology is the discovery of important properties of materials such as carbon nanotube, boron nitride nanotube, silica carbide nanotube, nanorod, nanowire, graphene, etc.

It is very important to accurately analyze the mechanical behavior of structural elements such as nanobeams, nanorods, and nanoplates that may be involved in NEMS organization. Because the correct mechanical analysis of these systems allows their correct design. Classical theories cannot reflect reality about mechanical behavior of nano scaled structural elements. In order to overcome this problem, different mathematical formulations based on the nano size effect are presented. The nonlocal elasticity theory [1] is a higher-order elasticity theory developed in this context.

Vibration analyses of simple [2-5] and shear deformation [6-9] axial nanorods with various boundary conditions have been studied by nonlocal elasticity theory. Also, the dynamics of nanorods with different end attachments are investigated [4,8-12]. On the other hand, Adhikari et al. [13,14] searched the axial dynamics of nonlocal rods via the finite element method. Numanoğlu [15] formulated the free vibrations of nanorods and nanobeams with tip attachment by employing finite elements. On the other hand, forced [16] and free [17] vibrations of cracked nanorods have been also examined. A spectral element method in free vibration of axial nanorods was given by Narendar and Gopalakrishnan [18]. Additionally, studies on the torsional vibration of nanorods are also available in the scientific literature. For example, a new

nonlocal stress model has been considered for torsional vibration of circular rods [19]. Numanoğlu and Civalek [20] presented a nonlocal finite element formulation for free vibration of attached circular nanorods embedded in elastic medium. Torsional static and dynamic behaviors of nanorods embedded in elastic medium were investigated with analytical solution by Arda and Aydoğdu [21].

The development of a finite element formulation for the nonlocal axial free dynamics of nanorods that have elastic spring attachment is mentioned in this study. According to this, nonlocal equation of motion is obtained. Then, by solving the nonlocal equation of motion with a three-node finite element formulation, the nondimensional frequencies of nanorods are calculated under different parameters. The results are discussed and the importance of the results in nano mechanics is emphasized.

2. Nonlocal Dynamics of Axial Nanorods

In Eringen's nonlocal theory, the constitutive equation of elastic solids is given as follows [1]:

$$\left(1-\left(e_0 a\right)^2 \frac{\partial^2}{\partial x^2}\right)\sigma^{nl} = \sigma^c \tag{1}$$

where σ^{nl} is nonlocal stress and σ^c defines classical stress. e_0 is an experimentally determined constant for atomic material, a is the internal characteristic length of atomic material.

The displacement components of axial rod depicted in Fig. 1 are written as:

$$u(x,t)=u\,,\quad v(x,t)=0\,,\quad w(x,t)=0 \tag{2}$$

in which, u is the axial displacement component. Since the Poisson's effect is neglected in the simple axial rod, the lateral and transverse displacement components are $v = w = 0$. On the other hand, the strain and stress components are defined as follows:

$$\varepsilon_{xx} = \frac{1}{2}\left(\frac{\partial u}{\partial x}+\frac{\partial u}{\partial x}\right)=\frac{\partial u}{\partial x}\,,\quad \varepsilon_{xy}=\varepsilon_{xz}=\varepsilon_{yz}=\varepsilon_{yy}=\varepsilon_{zz}=0\,,$$
$$\sigma_{xx} = E\frac{\partial u}{\partial x}+\mu\rho\frac{\partial^3 u}{\partial x\partial t^2}-\frac{\left(e_0 a\right)^2}{A}\frac{\partial f}{\partial x}\,,\ \sigma_{xy}=\sigma_{xz}=\sigma_{yz}=\sigma_{yy}=\sigma_{zz}=0 \tag{3}$$

where ε_{xx} and σ_{xx} are nonlocal axial strain and nonlocal axial stress, respectively.

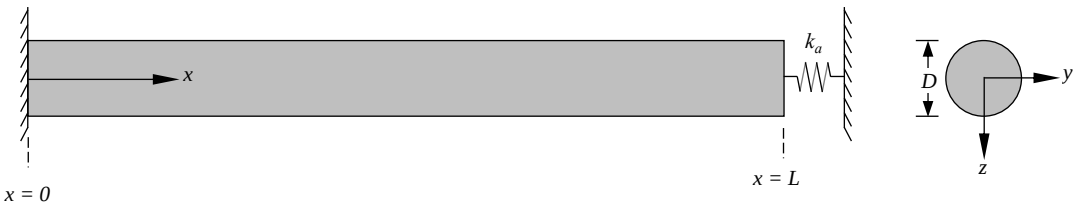


Figure 1. Schematic representation of axial nanorod with clamped-spring attached boundary condition**.**

The nonlocal equation of motion is obtained via the variational principle. According to this:

$$\delta\int_{t_1}^{t_2}\left[U-\left(T+W\right)\right]\mathrm{d}t=0 \tag{4}$$

where U is the strain energy, T is the kinetic energy, and W is the work of the external force. Also, t is the time. δ indicates the variation symbol. Energy expressions are as follows:

$$\begin{aligned}U&=\int_V\left(\sigma_{xx}\varepsilon_{xx}+\sigma_{yy}\varepsilon_{yy}+\sigma_{zz}\varepsilon_{zz}+2\sigma_{xz}\varepsilon_{xz}+2\sigma_{xz}\varepsilon_{xz}+2\sigma_{xy}\varepsilon_{xy}\right)+\frac{1}{2}\sum_{i=1}^{n}k_{a,i}\left[u\left(x_i,t\right)\right]^2\\&=\frac{1}{2}\int_0^L\left(EA\left(\frac{\partial u}{\partial x}\right)^2+\left(e_0a\right)^2\rho A\frac{\partial^3u}{\partial x\partial t^2}\frac{\partial u}{\partial x}-\left(e_0a\right)^2\frac{\partial f}{\partial x}\frac{\partial u}{\partial x}\right)\mathrm{d}x+\frac{1}{2}k_a\left[u\left(L,t\right)\right]^2\end{aligned} \tag{5}$$

$$T=\frac{1}{2}\int_V\rho\left[\left(\frac{\partial u}{\partial t}\right)^2+\left(\frac{\partial v}{\partial t}\right)^2+\left(\frac{\partial w}{\partial t}\right)^2\right]\mathrm{d}V=\frac{1}{2}\int_0^L\rho A\left(\frac{\partial u}{\partial t}\right)^2\mathrm{d}x \tag{6}$$

$$W=\int_0^L fu\mathrm{d}x \tag{7}$$

where E is modulus of elasticity, A is cross-section area, ρ is mass of unit volume, f is the external axial excitation. Additionally, k_a denotes the stiffness of spring attachment, and V is the volume. As seen in Fig. 1, the attachment is assumed at $x = L$ end of rod.

By substituting the first variations of Eqs. (5)-(7) into Eq. (4), the following expressions are attained for $\delta u \neq 0$ and $\delta u(L,t) \neq 0$ boundaries, respectively:

$$EA\frac{\partial^2u}{\partial x^2}+\left(e_0a\right)^2\rho A\frac{\partial^4u}{\partial x^2\partial t^2}-\left(e_0a\right)^2\frac{\partial^2f}{\partial x^2}-\rho A\frac{\partial^2u}{\partial t^2}+f=0 \tag{8}$$

$$EA\frac{\partial u\left(L,t\right)}{\partial x}+\left(e_0a\right)^2\rho A\frac{\partial^3u\left(L,t\right)}{\partial x\partial t^2}-\left(e_0a\right)^2\frac{\partial f}{\partial x}=-k_au\left(L,t\right) \tag{9}$$

where Eqs. (8) and (9) express the equation of motion and the dynamic equilibrium of the attached tip, respectively. Since the free vibration problem is examined, $f = 0$. The solution of Eq. (8) is investigated with the following expression:

$$u\left(x,t\right)=U\left(x\right)e^{\mathbf{i}\omega t} \tag{10}$$

Substituting this expression into Eq. (8), the following partial differential equation is obtained:

$$\frac{\mathrm{d}^2U}{\mathrm{d}x^2}+\eta^2U=0 \tag{11}$$

Where,

$$\eta^2 = \frac{\omega^2 \rho}{E - \omega^2 \left(e_0 a\right)^2 \rho} \tag{12}$$

The analytical solution of Eq. (11) can be written as follows [4,12]:

$$U = C_1 \cos \eta x + C_2 \sin \eta x \tag{13}$$

in which, ω is natural frequency of free vibration. The boundary condition for clamped end is as follows:

$$U(0) = 0 \tag{14}$$

If Eqs. (9) and (14) are used in Eq. (13), the frequency equation of a nonlocal axial rod with clamped-axial spring attached can reached as follows [4]:

$$\eta L \cot \eta L = -\left(1 + \left(e_0 a\right)^2 \eta^2\right) \beta_k \tag{15}$$

Where,

$$\beta_k = \frac{k_a}{k_r} = \frac{k_a L}{EA} \tag{16}$$

where k_r defines the axial stiffness of rod. β_k means stiffness ratio of attachment.

3. Nonlocal Finite Element Method

A nonlocal finite element formulation (NL-FEM) is introduced for the other solution of size-dependent vibration problem investigated in this study. According to this, the average weighted residue is formulated as follows:

$$\mathrm{I} = \int_0^{L_e} h \left(EA \frac{\partial^2 u}{\partial x^2} + \left(e_0 a\right)^2 \rho A \frac{\partial^4 u}{\partial x^2 \partial t^2} - \rho A \frac{\partial^2 u}{\partial t^2} \right) \mathrm{d}x \tag{17}$$

in which, I is the average weighted residual and h is the weighting function. L_e expresses the length of finite element. Other expressions for rearrangement of Eq. (17) are defined as follows:

$$u = \varphi \mathbf{d}\,, \quad \frac{\partial u}{\partial x} = \mathrm{D}^{\mathrm{k}} u = \mathbf{B}\mathbf{d}\,, \quad h = \varphi^{\mathrm{T}} \tag{18}$$

where d is the displacement of axial finite element. Additionally, φ explains the shape function. In this study, three-node finite element is employed and shape function is defined as below [9]:

$$\varphi = \begin{bmatrix} 2\xi^2 - 3\xi + 1 & -4\xi^2 + 4\xi & 2\xi^2 - \xi \end{bmatrix} \tag{19}$$

where $\xi = x/L_e$ defines the nondimensional longitudinal coordinate. x and L_e indicate the longitudinal coordinate and finite element length, respectively. The three-node finite element is depicted in Fig. 2.

Using Eq. (18) into Eq. (17) yields the following equation:

$$\int_0^{L_e} EA\left(\mathbf{B}^{\mathrm{T}}\mathbf{B}\right)\mathbf{d}\mathrm{d}x+\int_0^{L_e}\left(e_0a\right)^2\rho A\left(\mathbf{B}^{\mathrm{T}}\mathbf{B}\right)\ddot{\mathbf{d}}\mathrm{d}x+\int_0^{L_e}\rho A\left(\varphi^{\mathrm{T}}\varphi\right)\ddot{\mathbf{d}}\mathrm{d}x=0 \tag{20}$$

This expression is presented as follows in closed matrix notation

$$\left(K\right)\mathbf{d}+\left(M_c+M_{nl}\right)\ddot{\mathbf{d}}=0 \tag{21}$$

In which, the following expressions are valid [15]:

$$K=\int_0^{L_e} EA\left(\mathbf{B}^{\mathrm{T}}\mathbf{B}\right)\mathrm{d}x=\frac{EA}{L_e}\begin{bmatrix}7&-8&1\\-8&16&-8\\1&-8&7\end{bmatrix} \tag{22}$$

$$M_c=\int_0^{L_e}\rho A\left(\varphi^{\mathrm{T}}\varphi\right)\mathrm{d}x=\frac{\rho AL_e}{6}\begin{bmatrix}4&2&-1\\2&16&2\\-1&2&4\end{bmatrix} \tag{23}$$

$$M_{nl}=\int_0^{L_e}\left(e_0a\right)^2\rho A\left(\mathbf{B}^{\mathrm{T}}\mathbf{B}\right)\mathrm{d}x=\frac{\left(e_0a\right)^2\rho A}{L_e}\begin{bmatrix}7&-8&1\\-8&16&-8\\1&-8&7\end{bmatrix} \tag{24}$$

where, K, M_c, and M_{nl} represent the axial stiffness, classical mass, and nonlocal mass matrices, respectively. For the displacement of finite element, the eigenvalue problem arising from an operation as in Eq. (10) is reduced according to the geometric boundary conditions and natural frequencies of nonlocal rod are reached. For the boundary conditions of rod considered in this study, the clamped end is the reason for the reduction. On the other hand, the stiffness of axial spring attachment is added to the stiffness matrix of the last finite element (*n*th element) in the finite element mesh of rod [9,15]:

$$\left[K_{e=n}\right]=\left[K\right]+\left[K_A\right] \tag{25}$$

where k_a is the stiffness matrix for axial spring attachment.

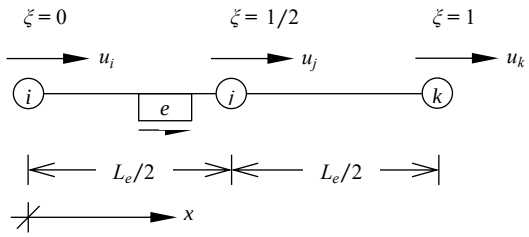


Figure 2. Demonstration of three-node finite element.

4. Numerical Results and Discussions

Within the scope of numerical results, the nondimensional frequencies of nonlocal clamped-elastic spring attached axial nanorods are calculated under the following parameters [15]: Elasticity modulus E = 1 TPa, unit volume weight $\rho = 2300\,\mathrm{kg/m^3}$, diameter of circular cross-section d = 5 nm and length L = 20 nm. Nondimensional frequencies are formulated as:

$$\overline{\omega}_i = \omega_i L\sqrt{\frac{E}{\rho}} \tag{26}$$

where i is mode number.

A comparison study about the first four modes nonlocal nondimensional frequencies of clamped-elastic spring attached axial nanorods is given in Table 1. According to this, for the stiffness ratio β_k = 10, the analytical results from [4] are compared with the calculated NL-FEM results for four different finite element numbers. Firstly, it should be noted that the values computed for $e_0a/L = 0$ present the classical elasticity results. Generally, the nonlocal parameter reduces the nondimensional frequencies. As mode number increases, it is understood that the atomic parameter more decreases the nondimensional frequencies. These reveal that the atomic size effect on nanoscale axial structural elements is important.

As seen in Table 1, the finite element results are in great accordance with the analytical values. When low finite element numbers are considered, the difference between the NL-FEM and analytical results rises with the increment of mode number. This difference diminishes by increasing the finite element number. Moreover, the difference between analytical and NL-FEM results is lower for the analyses under nonlocal parameter. This inference indicates that the higher-order shape function based-nonlocal finite element formulation developed in this study is quite useful.

Table 1. Convergence of NL-FEM for nondimensional frequencies of clamped-spring attached nanorods (β_k = 10).

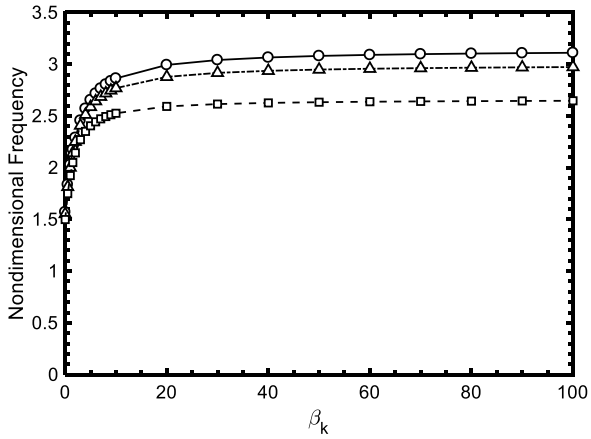
e_0a/L	Mode	Ref. [1]	NL-FEM Results			
			n = 100	n = 20	n = 10	n = 2
0	1	2.86277	2.86277	2.86277	2.86278	2.86877
	2	5.76056	5.76056	5.76058	5.76093	5.80618
	3	8.70831	8.70831	8.70851	8.71128	10.33821
	4	–	11.70268	11.70354	11.71562	17.93790
0.25	1	2.37560	2.37560	2.37560	2.37561	2.37967
	2	3.34527	3.34527	3.34528	3.34537	3.35162
	3	3.67332	3.67332	3.67334	3.67360	3.76741
	4	–	3.80829	3.80832	3.80883	6.94186

In Fig. 3, The variations of nonlocal vibration frequencies in response to the increment of stiffness ratio are plotted for the first four modes of clamped-spring attached nanorod. If the

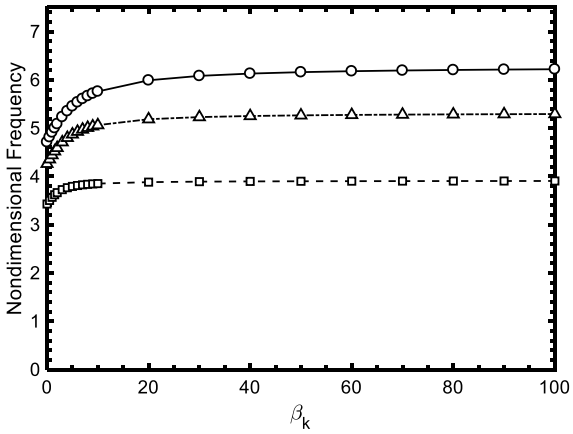
stiffness ratio is equal to 0, since there is no attachment, nanorod is axial cantilever (clamped-free). Generally, the nonlocal frequencies increase as the stiffness ratio of attachment increases. Lower values of stiffness ratio raise more the nondimensional frequencies. If the stiffness ratio increases further, the vibration behavior of nonlocal axial nanorod approaches the nanorod with clamped at both ends. On the other hand, it can be said that the nonlocal parameter reduces the frequencies more as the mode number increases. Also, the nonlocal parameter is more effective for higher stiffness ratio values. Finally, it should be added that the effect of stiffness ratio on the nondimensional frequencies is low in high values of mode number and nonlocal parameter.

5. Conclusions

In this study, a nonlocal finite element formulation (NL-FEM) for free vibration analysis of axial nanorods with clamped-elastic spring boundary condition is presented. By using NL-FEM, nondimensional frequency parameters of nanorod model are calculated under different parameters such as nonlocal parameter, attachment stiffness ratio, mode number, and numerical results are discussed. Since nanorods have a wide range of use in nano-electro-mechanical systems technology, it is important to understand the mechanical behavior of nanorods. The results obtained by using NL-FEM developed for this purpose reveal that the atomic size dependency must be taken into consideration in nanorods. Additionally, the high accuracy of NL-FEM shows that the formulation can be used to solve many problems in nonlocal structural mechanics.



(a)



(b)

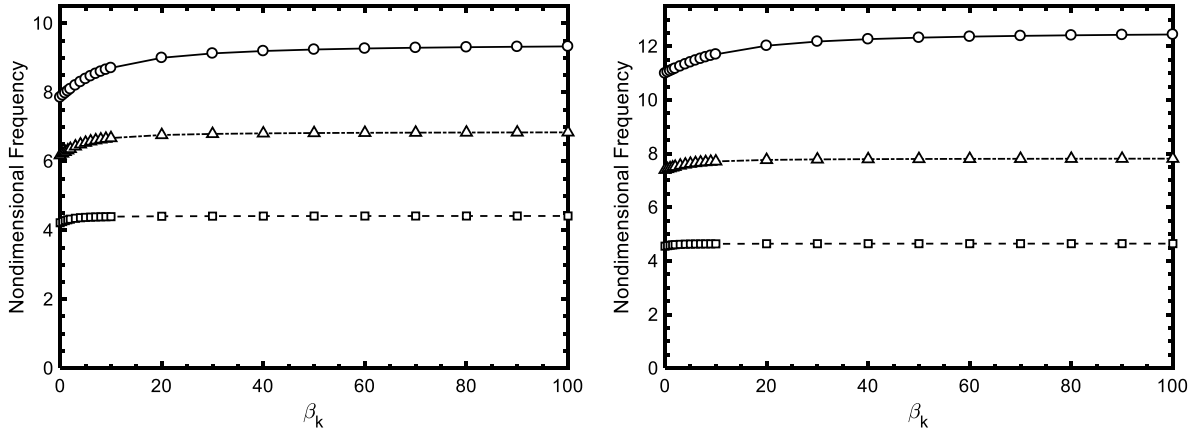


Figure 3. Variation of nondimensional frequencies of clamped-spring attached nanorods according to the increment of stiffness ratio **(a)** First mode **(b)** Second Mode **(c)** Third mode **(d)** fourth mode (–○–: $e_0a/L = 0$, –△–: $e_0a/L = 0.1$, –□–: $e_0a/L = 0.2$).

References

[1] A. C. Eringen, Linear theory of nonlocal elasticity and dispersion of plane waves, International Journal of Engineering Science, vol. 10, pp. 425-435, 1972.

[2] M. Aydoğdu, Axial vibration of the nanorods with the nonlocal continuum rod model, Physica E: Low-Dimensional Systems and Nanostructures, vol. 41, pp. 861-864, 2009.

[3] M. Aydoğdu, A nonlocal rod model for axial vibration of double-walled carbon nanotubes including axial van der Waals force effects, Journal of Vibration and Control, vol. 21, 2015.

[4] H. M. Numanoğlu, B. Akgöz, and O. Civalek, On dynamic analysis of nanorods, International Journal of Engineering Science, vol. 130, pp. 33-50, 2018.

[5] X. Zhu and L. Li, On longitudinal dynamics of nanorods, International Journal of Engineering Science, vol. 120, pp. 129-145, 2017.

[6] X. F. Li, Z. B. Shen and K. Y. Lee, Axial wave propagation and vibration of nonlocal nanorods with radial deformation and inertia. ZAMM Journal of Applied Mathematics and Mechanics, vol. 97, pp. 602-616, 2017

[7] D. Z. Karličić, S. Ayed and E. Flaieh, Nonlocal axial vibration of the multiple Bishop nanorod system, Mathematics and Mechanics of Solids, vol. 24, pp. 1668-1691, 2019.

[8] M. Ö. Yayli, Axial vibration analysis of a Rayleigh nanorod with deformable boundaries, Microsystem Technologies, vol. 26, pp. 2661-2671, 2020.

[9] Ö. Civalek and H. M. Numanoğlu, Nonlocal finite element analysis for axial vibration of embedded love–bishop nanorods, International Journal of Mechanical Sciences, vol. 188, pp. 105939, 2020.

[10] B. Uzun, U. Kafkas and M.Ö. Yaylı, Axial dynamic analysis of a Bishop nanorod with arbitrary boundary conditions, ZAMM Journal of Applied Mathematics and Mechanics, vol. 100, e202000039, 2020.

[11] T. Murmu and S. Adhikari, Nonlocal vibration of carbon nanotubes with attached buckyballs at tip, Mechanics Research Communications, vol. 38, pp. 62-67, 2011.

[12] H. M. Numanoğlu, Vibration analysis of beam and rod models of nanostructures based on nonlocal elasticity theory, B. Sc. Thesis, Akdeniz University, Antalya, 2019, (In Turkish).

[13] S. Adhikari, T. Murmu and M. A. McCarthy, Frequency domain analysis of nonlocal rods embedded in an elastic medium, Physica E: Low-dimensional Systems and Nanostructures, vol. 59, pp. 33-40, 2014.

[14] S. Adhikari, T. Murmu and M. A. McCarthy, Dynamic finite element analysis of axially vibrating nonlocal rods, Finite Elements in Analysis and Design, vol. 630, pp. 42-50, 2013.

[15] H. M. Numanoğlu, Dynamic analysis of nano continuous and discrete structures based on nonlocal finite element formulation (NL-FEM), M. S. Thesis, Akdeniz University, Antalya, 2019, (In Turkish).

[16] Ş. D. Akbaş, Axially forced vibration analysis of cracked a nanorod, Journal of Computational Applied Mechanics, vol. 50, pp. 63-68, 2019.

[17] H. M. Numanoğlu and O. Civalek, Novel size-dependent finite element formulation for modal analysis of cracked nanorods, Materials Today Communications, vol. 31, pp. 103545, 2022.

[18] S. Narendar and S. Gopalakrishnan, Spectral Finite Element Formulation for Nanorods via Nonlocal Continuum Mechanics, vol. 78, 061018, 2011.

[19] C. W. Lim, C. Li and L. Yu, Free torsional vibration of nanotubes based on nonlocal stress theory. Journal of Sound and Vibration, vol. 331, pp. 2798-2808, 2012.

[20] H. M. Numanoğlu and O. Civalek, On the torsional vibration of nanorods surrounded by elastic matrix via nonlocal FEM, International Journal of Mechanical Sciences, vol. 161-162, pp. 105076, 2019.

[21] M. Arda and M. Aydoğdu, Torsional statics and dynamics of nanotubes embedded in an elastic medium, Composite Structures, vol. 114, pp. 80-91, 2014.

Cape Town, Güney Afrika'dan toplanan atık kehribar renkli şişe camları üzerinde karakterizasyon çalışmaları

Recep KURTULUŞ[1*] , Taner KAVAS[2]

[1*] Afyon Kocatepe Üniversitesi, Mühendislik Fakültesi, Malzeme Bilimi ve Mühendisliği Bölümü, Afyonkarahisar, Türkiye , (ORCID: 0000-0002-3206-9278),

rkurtulus@aku.edu.tr

[2] Afyon Kocatepe Üniversitesi, Mühendislik Fakültesi, Malzeme Bilimi ve Mühendisliği Bölümü, Afyonkarahisar, Türkiye (ORCID: 0000-0003-1070-8451),

tkavas@aku.edu.tr

Öz

Bu araştırmada, Cape Town, Güney Afrika, sokak çöp kutusundan toplanan atık kehribar renkli ambalaj şişe camı, farklı teknikler kullanılarak kapsamlı bir şekilde karakterize edildi. Bu doğrultuda başarılı olmak için, cam tozları, ilk olarak yıkama (su-sabun karışımı), kurutma (fırında 110 ºC'de), kırma (el çekiçiyle), öğütme (alümina bilyeli öğütme) ve eleme (149 mikronun altında) aşamaları takip edilerek elde edilmiştir. Bu işlemlerden sonra elde edilen tozlar, X-ışını floresansı (XRF), X-ışını kırınımı (XRD), Fourier transform kızılötesi (FT-IR), spektrofotometre (UV-Vis) ve Arşimet prensibini içeren karakterizasyon tekniklerinde kullanılarak, fiziksel, kimyasal ve optik özellikler anlaşıldı. XRF sonuçları, atık camın ticari kehribar camına benzer tipik bir kimyasal bileşime sahip olduğunu göstermiştir. Ayrıca, XRD desenleri amorf bir yapı sergilerken, FT-IR spektrumu esas olarak Si-O-Si bağlanma tipini belirledi. Öte yandan, cam yoğunluğu 2.5110 g/cm^3 değerine eşit olup, diğer ambalaj cam türlerine benzer bir değere sahiptir. Optik özellikler bağlamında, iletim spektrumu, geleneksel soda-kireç-silika (SLS) camına kıyasla ışık iletimi için daha düşük bir yüzde ortaya çıkardı. Bu çalışmanın bir sonucu olarak, yazarlar atık kehribar renkli ambalaj şişe camında geniş bir özellik yelpazesi ortaya çıkardılar.

Anahtar Kelimeler: Atık cam, Kehribar cam, Ambalaj camı, Karakterizasyon, Atık yönetimi

Characterization studies on waste amber-colored bottle glass collected from Cape Town, South Africa

Abstract

In this investigation, the waste amber-colored container bottle glass collected from Cape Town, South Africa, street trash box was comprehensively characterized using different techniques. To succeed in this direction, the glass powders were initially obtained by neatly following the washing (water&soap mixture), drying (at 110 ºC in an oven), breaking (using a hand-hammer), milling (alumina ball milling), and sieving (under 149 microns) steps. After these processes, the obtained powders were employed in characterization techniques, including X-ray fluorescence (*XRF*), X-ray diffraction (*XRD*), Fourier transform infrared (*FT-IR*), spectrophotometer (*UV-Vis*), and Archimedes' principle (ρ_{glass}), to understand its physical, chemical, and optical properties. The *XRF* results showed that the waste glass has a typical chemical composition to that of commercial amber glass. Further, the

XRD patterns demonstrated an amorphous structure while the *FT-IR* spectrum ascertained mainly Si-O-Si bonding type. On the other hand, the ρ_{glass} equaled 2.5110 g/cm^3, which has an ordinary value compared to other container glass types. In the context of optical properties, the transmission spectrum revealed a lower percentage for light transmission when compared to a traditional flint soda-lime-silica (SLS) glass. As a result of this study, the authors unveiled a wide range of properties in waste amber-colored container bottle glass.

Keywords: Waste glass, Amber glass, Container glass, Characterization, Waste management

1. Introduction

Glass science and engineering have been ever-developing to serve humankind's necessities [1]. From light bulbs to kitchenware or from optical fibers to smart-technology displays, glass materials have been surrounding people's daily lives with ultimate satisfaction owing to their significant advantages [2]. Specifically, the advancements in glassware such as bottles or jars pave the way for safely protecting foods and drinks insomuch that product shelf-life has been either extended or preserved taste. From this perspective, glass materials will continue to interest many application areas.

Packaging glass was used commercially at the beginning of the 1900s. In earlier times, flint-colored glass articles, including bottles or jars, had widely been fabricated. After some time, different colored-glass products like green, amber, or emerald were developed to serve the needs [3]. In particular to ultraviolet-sensitive foods or drinks, colored-glass wares were preferred. If one digs into the chemical composition of the mentioned packaging glass type, one can see that soda-lime-silica (SLS) has been dominantly favored. In this SLS glass, typical glass composition can be given as follows: (70 - 72)SiO_2 + (14 – 16)Na_2O + (8 – 12)CaO + (2 - 4)MgO + (1 - 2)Al_2O_3 [4]. The stated glass composition may vary company-to-company based on cost, raw material availability, glass product type, etc.; nevertheless, the intended SLS glass composition has occurred in these ranges. Depending upon color demand, the coloring agents such as iron oxide, manganese oxide, chromium oxide, or the like may be modified as a minor constituent.

In view of colored-glass objects, amber-colored ones have extensively been manufactured in the beverage field. This preference aims to preserve the beverage's taste, gaseous, and texture against ultraviolet (UV) light [5]. In addition to the beverage field, pharmaceutical applications necessitate amber-colored glass packaging articles to protect medicine. Preventing UV light transmission throughout the glass medium ensures a safe shelf-life for medical purposes. Therefore, amber-colored glass products take great importance for many essential application areas.

Based upon the given essentiality of amber-colored glass, the present investigation intends to characterize waste amber-colored container bottle glass collected from Cape Town, South Africa. This waste glass contained a milk and beverage mixture with a special domestic plant called marula. The collected waste glass was subjected to some characterization analyses, including X-ray fluorescence (XRF), X-ray diffraction (XRD), Fourier transform infrared (FT-IR), spectrophotometer (UV-Vis), and Archimedes' principle. The findings were thoroughly presented in the below-given parts, accordingly.

2. Materials and Methods

After collecting the waste glass from Cape Town, South Africa, the glass powders were initially obtained by neatly following the washing (water&soap mixture), drying (at 110 ºC in an oven), breaking (using a hand-hammer), milling (alumina ball milling), and sieving (under 149 microns) steps. **Figure 1** shows the waste glass and the glass powders accordingly.



Figure 1. Image of waste amber-colored glass (left) and glass powder (right).

After these processes, the obtained powders were employed in different characterization techniques. The X-ray fluorescence (XRF) technique was used via Rigaku ZSX Primus to determine chemical composition. The X-ray diffraction (XRD) analysis was performed using Bruker D8 Advance with 30 mA, 40 kV, and 0.02 scan speed, and 10-80 degrees range conditions to observe structure. For detecting bonds in the glass network, Fourier transform infrared (FT-IR) method was implemented via Perkin Elmer UATR Two Device between 4000 and 400 cm^{-1} range. In addition to the physical and chemical property determinations, the optical properties were identified by performing a UV-Vis spectrophotometer practice using Spectrum Instruments SP-UV-300 device in the range of 190 and 1100 nm. Lastly, glass density(ρ_{glass}) was calculated via Equation 1 after applying Archimedes' principle.

$$\rho_{glass} = \frac{m_{air}}{m_{air} - m_{liquid}} \rho_{water} \quad (1)$$

where m_{air} and m_{liquid} represent the sample's weight in air and demineralized water, respectively, while ρ_{water} is the density of water used (0.992 g/cm^3).

3. Results and Discussions

According to the XRF analysis, the glass's chemical composition was found as given below:

$$73.76SiO_2 + 2.08Al_2O_3 + 0.75Fe_2O_3 + 9.69CaO + 1.19MgO + 0.36K_2O + 11.97Na_2O + 0.03Cr_2O_3 + 0.17SO_3$$

The glass composition we found shows parallelity compared to the literature studies, such as Refs [6] and [7]. Nothing but minor changes can be seen among the mentioned studies for amber glass composition.

Archimedes' principle was carried out to calculate the glass density value. The result showed that the waste amber-colored bottle glass equaled 2.5110 g/cm^3, which has an ordinary value compared to other container glass types [8], [9].

The crystallographic knowledge was gained from the XRD technique, and the patterns are drawn as revealed in **Figure 2**. It is apparent that no sharp peak is visible; instead, a hump-like shape is visible between 15 and 35 degrees. Such a finding is very acceptable and can be verified with literature findings [10]. Therefore, one can say that an amorphous structure was found in the waste amber-colored glass article.

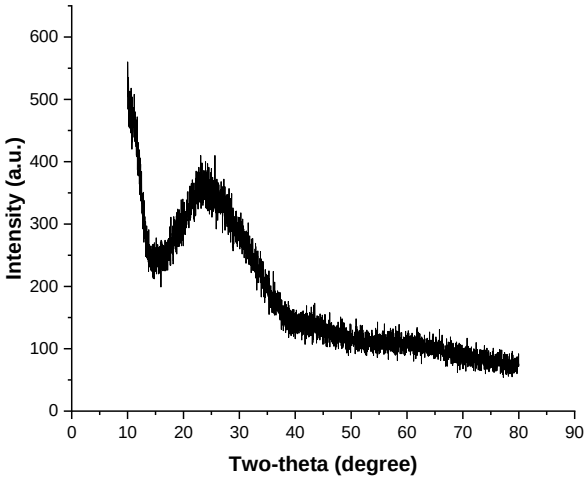


Figure 2. The XRD patterns for the waste amber-colored bottle glass.

The FT-IR spectrum was recorded to understand the bond types in the waste amber-colored bottle glass, and the related spectrum is demonstrated as given in **Figure 3**. The peaks around 3700 and 3600 1/cm can be assigned to forming O-H bonds. Besides that, the peaks that formed 3000 and 2700 1/cm range may be attributed to the C-H bonds, this is because the plate on the device was cleaned out using acetone. On the other hand, some peaks around 1500 1/cm might occur due to Si-OH bonds. In addition to Si-containing bonds, one can observe a sharp peak around 1100 1/cm, which can be referred to as Si-O-Si and/or Si-O bonds [11], [12]. Lastly, some peaks after 1100 1/cm may be associated with the formations of Si-O-A bonds where A notifies Na, Ca, and K elements. In conclusion, the FT-IR spectrum revealed bonding types for the intended glass system.

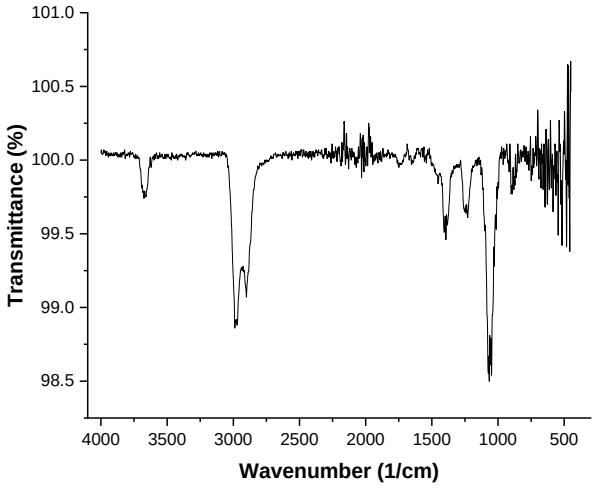


Figure 3. The FT-IR spectrum for the waste amber-colored bottle glass.

The transmission versus wavelength spectrum is plotted in **Figure 4** to display the optical properties. In the visible light range (400 and 700 nm), one can see a sharp peak, having a transmission value of around 35%. This value is somehow low, and UV light partially penetrates throughout the glass body.

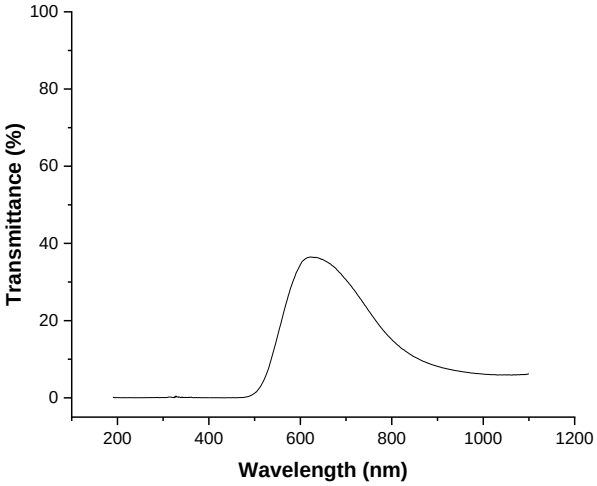


Figure 4. The transmission vs wavelength spectrum for the waste amber-colored bottle glass.

On the other hand, **Figure 5** graphs the same spectrum for an ordinary flint SLS glass. Apparently, the transmission percentage is much higher than waste amber-colored glass, namely around 80% between the 400 and 700 nm range.

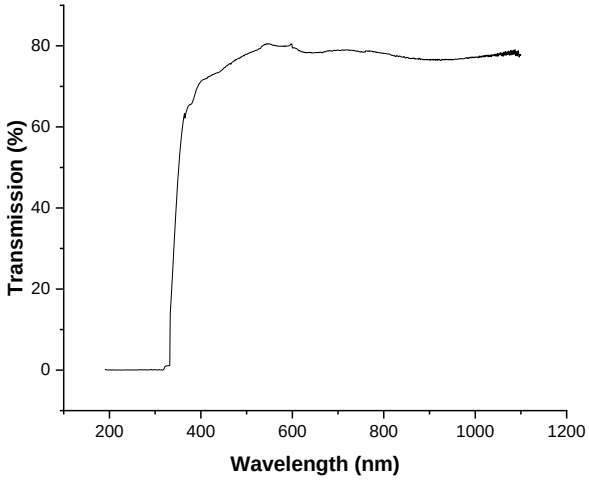


Figure 5. The transmission vs wavelength spectrum for ordinary flint SLS glass.

Lastly, **Figure 6** shows the comparison among the intended waste amber glass, ordinary amber glass (collected from Afyonkarahisar, Turkey), and conventional SLS glass. It seems that the intended glass has lower transmission than those given despite it has been categorized together with the ordinary amber glass. Therefore, we can conclude that amber-colored glass is more resistant to UV light than flint and ordinary amber color.

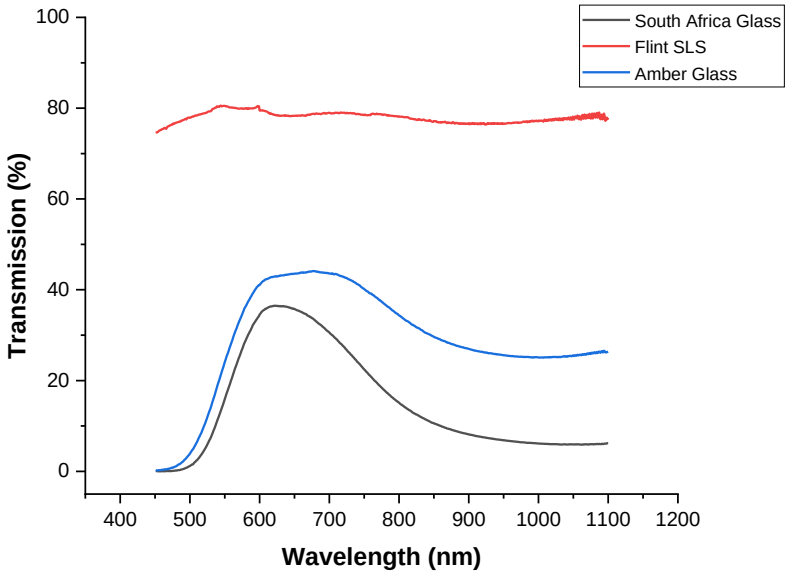


Figure 6. The transmission vs wavelength spectrum for intended waste amber glass, ordinary amber glass, and flint SLS glass.

4. Conclusions

The below-listed findings can be pointed out:

- The glass's chemical composition was found as $73.76SiO_2 + 2.08Al_2O_3 + 0.75Fe_2O_3 + 9.69CaO + 1.19MgO + 0.36K_2O + 11.97Na_2O + 0.03Cr_2O_3 + 0.17SO_3$

- The result showed that the waste amber-colored bottle glass equaled 2.5110 g/cm^3.

- One can say that an amorphous structure was found in the waste amber-colored glass article.

- FT-IR spectrum revealed O-H, C-H, Si-OH, Si-O-Si, Si-O, and Si-O-A (A: Na, Ca, K) bond types in the waste amber-colored glass.

- In the visible light range (400 and 700 nm), one can see a sharp peak, having a transmission value of around 35%. However, an ordinary flint SLS glass has 80% transmission in the same range. The intended waste amber glass has lower transmission than those given despite it has been categorized together with the ordinary amber glass. Therefore, we can conclude that amber-colored glass is more resistant to UV light than flint color.

- Eventually, this investigation may be regarded as an alternative characterization study to highlight the properties of waste amber-colored container bottle glass collected from Cape Town, South Africa.

5. Acknowledge

The authors would like to thank Res. Asst. Mustafa Gursoy and Res. Asst. Ibrahim Celik for bringing the waste amber-colored container bottle glass from their South Africa visit.

References

[1] A. K. Varshneya and J. C. Mauro, *Fundamentals of inorganic glass making*. 2019.

[2] J. E. Shelby, *Introduction to Glass Science and Technology*, no. Second Edition. 2005.

[3] M. Testa, O. Malandrino, M. R. Sessa, S. Supino, and D. Sica, "Long-term sustainability from the perspective of cullet recycling in the container glass industry: Evidence from Italy," *Sustainability (Switzerland)*, vol. 9, no. 10. 2017, doi: 10.3390/su9101752.

[4] J. D. Musgraves, J. Hu, and L. Calvez, *Springer Handbook of Glass*. 2019.

[5] F. Report, "Protection from Lightstrike in Lightweight Glass Beer Bottles," no. September, 2008.

[6] C. Bragança, S. & Bergmann, "Use of glass waste in the red clay-wares processing.," *ResearchGate*, no. June 2014, 2020.

[7] R. Kurtuluş, M. S. Buriahi, S. A. M. Issa, H. O. Tekin, T. Kavas, and E. Kavaz, "Physical, structural, mechanical and radiation shielding features of waste pharmaceutical glasses doped with Bi2O3," *Optik (Stuttg).*, vol. 261, Jul. 2022, doi: 10.1016/J.IJLEO.2022.169108.

[8] R. Kurtulus, T. Kavas, I. Akkurt, and K. Gunoglu, "An experimental study and WinXCom calculations on X-ray photon characteristics of Bi2O3- and Sb2O3-added waste soda-lime-silica glass," *Ceram. Int.*, vol. 46, no. September, pp. 21120–21127, 2020, doi: 10.1016/j.ceramint.2020.05.188.

[9] R. Kurtuluş and T. Kavas, "An Investigation on Usability of Waste Container Glass with Gd2O3 and La2O3 Addition in Radiation Shielding Applications," 2019.

[10] M. Flood *et al.*, "Glass Fines: A review of cleaning and up-cycling possibilities," *Journal of Cleaner Production*, vol. 267. Elsevier Ltd, 10-Sep-2020, doi: 10.1016/j.jclepro.2020.121875.

[11] L. de Siqueira, T. M. B. Campos, S. E. A. Camargo, G. P. Thim, and E. S. Trichês, "Structural, crystallization and cytocompatibility evaluation of the 45S5 bioglass-derived glass-ceramic containing niobium," *J. Non. Cryst. Solids*, vol. 555, p. 120629, Mar. 2021, doi: 10.1016/J.JNONCRYSOL.2020.120629.

[12] R. Kurtuluş, T. Kavas, E. Kavaz, H. O. Tekin, and Y. Kurucu, "Synthesis and characterization of waste CRT glasses through physical, optical and structural properties: A comprehensive study on recycling," *Optik (Stuttg).*, vol. 248, no. October, p. 168167, 2021, doi: 10.1016/j.ijleo.2021.168167.

ISC'22 2nd International Symposium on Characterization
22-25 September 2022 Afyonkarahisar, Türkiye

Nonlocal Natural Frequencies of Shear Deformable Functionally Graded Nanobeams Via Nonlocal FEM

Musa Demir[1], Furkan Şen[2], Hayri Metin Numanoğlu[3*]

[1] Giresun University, Mechanical Engineering Department, Division of Thermodynamics, Giresun, Turkey

[2] Giresun University, Civil Engineering Department, Division of Construction, Giresun, Turkey

[3] Giresun University, Civil Engineering Department, Division of Mechanics, Giresun, Turkey

Abstract

In this research, the atomic size-dependent free vibration analysis of nanobeams made of functionally graded material (FGM) is carried out. The free vibration of nanobeam is formulated according to the nonlocal Timoshenko beam theory. The classical mixing rule is used as functionally grading. A finite element formulation based on the atomic size effect (NL-FEM) is developed to solve the equation of motion. Nondimensional natural frequencies of shear deformable FGM nanobeams are calculated for different parameters by using NL-FEM and numerical results are discussed.

Keywords : Clamped nanobeam, Finite element, Functionally graded material, Free vibration, Nonlocal elasticity.

* Corresponding author e-mail : metin_numanoglu@hotmail.com

1. Introduction

Functionally graded materials (FGM) are materials in which physical and mechanical properties of material (e.g. elasticity modulus, shear modulus, unit volume weight) change according to a continuous mathematical equation. Materials with different properties form a new material type that has stronger properties. Since the material properties constantly change, the stress concentrations are minimized. Therefore, FGMs have superior properties compared to the conventional laminated composite materials. FGMs have uses in the fields such as chemical industry, materials engineering, aerospace engineering, mechanical engineering, automotive engineering [1].

Important results such as the discovery of nano scaled materials and the development of imaging technology at this scale have accelerated research on nano-electro-mechanical systems (NEMS) technology. Many of devices used today are the result of NEMS technology. In order for these systems to have the desired properties and functionality, it is quite important to know

the strength of nano scaled homogeneous or composite structures that are the members of system under mechanical forces. The analysis of mechanical characteristics of nano scaled structures with classical theories gives nonsensical results compared to experimental results. In addition to this, the demands of experimental approaches such as high cost, high expertise, and long processes make difficulties to researchers. To overcome these problems, the classical theory of elasticity has been reinforced with the size effect of nanostructure. The atomic size dependent elasticity theories provide a great practicality in the investigation of mechanical characteristics of nano scaled structures.

It can be stated that the nonlocal elasticity theory [2] is the most popular higher-order elasticity theory in the scientific literature. According to this theory, an experimental material constant and characteristic atomic length of nano structure should be considered for the mechanical analysis. The mechanical analysis of nanostructures with nonlocal elasticity theory have had a wide field of study in the scientific literature. It can be said that the bending, vibration, and buckling analyses of nanomaterials modelled like bending rods are an important example in this point [3-9]. Differently from these, free vibration [10] and statics [11] of nano scaled metallic materials were also investigated. Additionally, the nonlocal dynamics of discrete structures such as nano scaled frame was focused [13,14]. On the other hand, bending, vibration, and buckling of nanobeams were analyzed by nonlocal finite element method (NL-FEM) [15-22].

Various studies have been performed on the nonlocal mechanics of functionally graded composite nanobeams. Nejad and Hadi [23] formulated the free vibration of Euler-Bernoulli FGM nanobeams. Ghadiri and Jafari [24] examined the vibration of shear deformable nanobeams under mass attachment at the tip. Thermal effects in the vibration of FGM nanobeams were also investigated [25]. Also, vibration, buckling, and bending behaviors in FGM nanobeams were studied via different nonlocal beam theories [26-28]. Moreover, the nonlinear vibration of FGM nanobeams was also expressed with nonlocal Euler-Bernoulli beam theory [29]. Furthermore, finite element formulations were presented to search the nonlocal mechanical behavior of FGM nanobeams [30-32].

Considering that composite nanobeams may take part in NEMS structures, it should be expressed that to analyze the nonlocal mechanics of nanobeams made of FGM is important. In some cases, shear deformations of nanobeams also become important. With this motivation, this study examines the free vibration behavior of FGM nanobeams formulated with nonlocal Timoshenko beam theory. Firstly, the equation of motion is obtained by using variational algebra. The equation of motion is solved by using NL-FEM. Then, the nondimensional frequencies are computed via NL-FEM and the results are discussed. Finally, the inferences obtained from discussion of numerical results are given.

2. FGM Model

Two different FGM nanobeam models are given in Fig. 1. It will be assumed that the nanobeam structure has functionally grading according to classical mixture rule. So that,

$$P(z) = P_L V_L + P_U V_U \tag{1a}$$

$$V_U = \left(\frac{z}{h}+\frac{1}{2}\right)^k,\ V_L = 1-\left(\frac{z}{h}+\frac{1}{2}\right)^k \tag{1b}$$

where $P(z)$ is the effective material property. P_L and P_U are any physical or mechanical properties of lower and upper surfaces, respectively. Also, V_L and V_U denote the volume diffractions of materials on the lower and upper surfaces, respectively. H is the height of rectangular section and z is the transverse coordinate. On the other hand, k refers to the functionally grading index. According to these equations, the mechanical and physical properties of FGM are formulated as follows:

$$E(z) = (E_U - E_L)\left(\frac{z}{h}+\frac{1}{2}\right)^k + E_L \tag{2a}$$

$$G(z) = (G_U - G_L)\left(\frac{z}{h}+\frac{1}{2}\right)^k + G_L \tag{2b}$$

$$\rho(z) = (\rho_U - \rho_L)\left(\frac{z}{h}+\frac{1}{2}\right)^k + \rho_L \tag{2c}$$

$$G_U = \frac{E_U}{2(1+\upsilon_U)},\ G_L = \frac{E_L}{2(1+\upsilon_L)} \tag{2d}$$

where E, G, ρ, and υ denote the elasticity modulus, shear modulus, volume of unit mass, and Poisson's ratio, respectively.

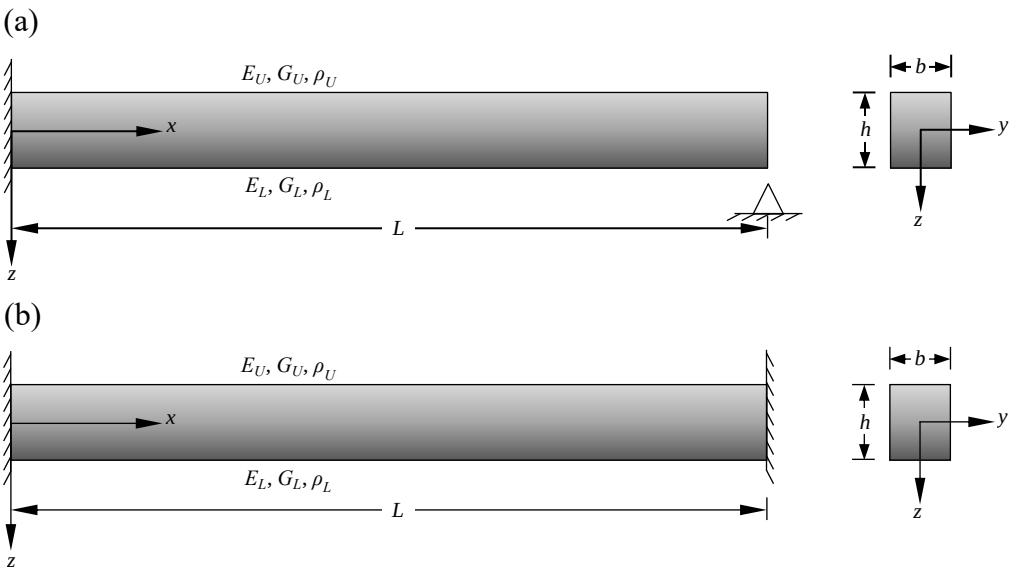


Figure 1. FGM Nanobeam with different boundary conditions (a) Clamped-simply supported boundary condition (b) Clamped-Clamped boundary condition.

3. Nonlocal Vibration of FGM Nanobeam

The nonlocal elasticity theory formulates the relationship between the classical stress s_{ij} and the nonlocal stress σ_{ij}:

$$\left(1-\left(e_0 a\right)^2 \frac{\partial^2}{\partial x^2}\right)\sigma_{ij} = s_{ij} \tag{3}$$

in which, e_0 is the experimental material constant and a is the internal characteristic length.

In this study, free vibration of FGM nanobeams is investigated by considering Timoshenko beam theory, which is the fundamental shear deformable beam formulation. In this beam theory, the displacement field is defined as:

$$u = -z\varphi = -z\frac{\partial w_b}{\partial x},\ v = 0,\ w = w_b + w_s \tag{4}$$

where u is the axial, v is the lateral and w is the transverse displacement. w_b and w_s express bending and shear displacements, respectively. Additionally, φ explains for section rotation. On the other hand, nonzero strain and stress components can be computed as:

$$\varepsilon_{xx} = -z\frac{\partial \varphi}{\partial x},\ \varepsilon_{xz} = \frac{1}{2}\left(\frac{\partial w}{\partial x} - \varphi\right),$$
$$\sigma_{xx} = E(z)\varepsilon_{xx} = -E(z)z\frac{\partial \varphi}{\partial x},\ \sigma_{xz} = G(z)\varepsilon_{xz} = -\frac{1}{2}G(z)\left(\frac{\partial w}{\partial x} - \varphi\right) \tag{5}$$

In which, while ε_{xx} and ε_{xz} denote axial and shear strains, respectively, σ_{xx} and σ_{xz} indicate the axial and shear stresses, respectively. Also, the classical bending moment and classical shear force, which are internal forces consist of classical stresses, are presented as follows:

$$M_c = -D_1\frac{\partial^2 w_b}{\partial x^2},\ V_c = k_s S_1\frac{\partial^2 w_s}{\partial x} \tag{6}$$

where D_1 and S_1 mean the bending and shear stiffnesses of FGM nanobeam, respectively. On the other hand, k_s is known as the shear correction coefficient.

The nonlocal free vibration equation of motion of FGM nanobeam is obtained with the help of variational algebra. Accordingly, the first variation of potential energy of nanobeam is equal to zero the at the time interval (t_1, t_2):

$$\delta\int_{t_1}^{t_2}\left[U - (T + W)\right]\mathrm{d}t = 0 \tag{7}$$

where d is the variation symbol. U is the internal strain energy, T is the kinetic energy, and W is the work potential. Energy expressions are written as follows:

$$U = \frac{1}{2}\int_V\left(\sigma_{xx}\varepsilon_{xx} + 2\sigma_{xz}\varepsilon_{xz}\right) = \frac{1}{2}\int_0^L\left[D_1\left(\frac{\partial \varphi}{\partial x}\right)^2 + S_1\left(\frac{\partial w}{\partial x} - \varphi\right)^2\right]\mathrm{d}x$$
$$= \int_0^L\left[-M\frac{\partial \varphi}{\partial x} + V\left(\frac{\partial w}{\partial x} - \varphi\right)\right]\mathrm{d}x \tag{8}$$

$$T=\frac{1}{2}\int_V \rho(z)\left[\left(\frac{\partial u}{\partial t}\right)^2+\left(\frac{\partial v}{\partial t}\right)^2+\left(\frac{\partial w}{\partial t}\right)^2\right]\mathrm{d}V=\frac{1}{2}\int_0^L\left[I_2\left(\frac{\partial \varphi}{\partial t}\right)^2+I_0\left(\frac{\partial w}{\partial t}\right)^2\right]\mathrm{d}x \tag{9}$$

$$W=\int_0^L fw\mathrm{d}x \tag{10}$$

In which,

$$D_1=\int_A E(z)z^2\mathrm{d}A,\ S_1=\int_A G(z)\mathrm{d}A,\ I_0=\int_A \rho(z)\mathrm{d}A,\ I_2=\int_A \rho(z)z^2\mathrm{d}A \tag{11}$$

where I_0 and I_2 indicate the zeroth- and second- order mass inertias, respectively. After substituting Eqs. (8)-(10) into Eq. (7), equilibrium equations are obtained as a result of several mathematical operations for variations of different deformations as follows:

$$\delta\varphi\neq 0:\quad \frac{\partial M}{\partial x}-V=-I_2\frac{\partial^2\varphi}{\partial t^2} \tag{12}$$

$$\delta w\neq 0:\quad \frac{\partial V}{\partial x}=I_0\frac{\partial^2 w}{\partial t^2}-f \tag{13}$$

On the other hand, the relation between shear and bending displacements in a functionally graded shear deformable nonlocal beam is given as the following form:

$$w_s=-\frac{1}{kS_1}\left(D_1\frac{\partial^2 w_b}{\partial x^2}-I_2\frac{\partial^2 w_b}{\partial t^2}+(e_0a)^2 I_2\frac{\partial^4 w_b}{\partial x^2\partial t^2}\right) \tag{14}$$

By using Eqs. (3), (6) and (12)-(14), the equation of motion is attained as a result of several mathematical operation as follows:

$$\begin{aligned}&D_1\frac{\partial^4 w_b}{\partial x^4}-\frac{I_0I_2}{kS_1}\frac{\partial^4 w_b}{\partial t^4}-I_0\frac{\partial^2 w_b}{\partial t^2}-\frac{(e_0a)^4 I_0I_2}{kS_1}\frac{\partial^8 w_b}{\partial x^4\partial t^4}+\frac{2(e_0a)^2 I_0I_2}{kS_1}\frac{\partial^6 w_b}{\partial x^2\partial t^4}\\&-\frac{(e_0a)^2 I_0D_1}{kS_1}\frac{\partial^6 w_b}{\partial x^4\partial t^2}+(e_0a)^2 I_2\frac{\partial^6 w_b}{\partial x^4\partial t^2}+\frac{I_0D_1}{kS_1}\frac{\partial^4 w_b}{\partial x^2\partial t^2}+(e_0a)^2 I_0\frac{\partial^4 w_b}{\partial x^2\partial t^2}\\&+I_2\frac{\partial^4 w_b}{\partial x^2\partial t^2}-(e_0a)^2\frac{\partial^2 f}{\partial x^2}+f=0\end{aligned} \tag{15}$$

4. Finite Element Formulation

This study focuses on solution of Eq. (15) via finite elements. For free vibration, f is equal to 0. Accordingly, first, the average weighted residue is expressed as:

$$\mathrm{I}=\int_0^{L_e} h\left(D_1\frac{\partial^4 w_b}{\partial x^4}-\frac{I_0I_2}{kS_1}\frac{\partial^4 w_b}{\partial t^4}-I_0\frac{\partial^2 w_b}{\partial t^2}-\frac{(e_0a)^4 I_0I_2}{kS_1}\frac{\partial^8 w_b}{\partial x^4\partial t^4}+\frac{2(e_0a)^2 I_0I_2}{kS_1}\frac{\partial^6 w_b}{\partial x^2\partial t^4}\right.$$
$$-\frac{(e_0a)^2 I_0D_1}{kS_1}\frac{\partial^6 w_b}{\partial x^4\partial t^2}+(e_0a)^2 I_2\frac{\partial^6 w_b}{\partial x^4\partial t^2}+\frac{I_0D_1}{kS_1}\frac{\partial^4 w_b}{\partial x^2\partial t^2}+(e_0a)^2 I_0\frac{\partial^4 w_b}{\partial x^2\partial t^2}$$
$$\left.+I_2\frac{\partial^4 w_b}{\partial x^2\partial t^2}\right)\mathrm{d}x=0 \tag{16}$$

where I and h are known as the average weighted residue and weighting function, respectively. Other equations are given for rearrangement of Eq. (16) as follows:

$$w_b=\varphi\mathbf{w}\,,\ \frac{\partial w_b}{\partial x}=\mathrm{D}^{\mathrm{k}}w_b=\mathbf{B}\mathbf{w}\,,\ h=\varphi^{\mathrm{T}} \tag{17}$$

It should be noticed that the equation of motion is formulated only in terms of bending displacements. Therefore, the known finite element formulation for the beam without shear deformation can be used in the solution [21,22]:

$$\varphi^{\mathrm{T}}=\begin{Bmatrix} 1-3\xi^2+2\xi^3 \\ -L_e\left(\xi+2\xi^2-\xi^3\right) \\ 3\xi^2-2\xi^3 \\ -L_e\left(\xi^2-\xi^3\right)\end{Bmatrix} \tag{18}$$

in which, $\xi=x/L_e$ is called as the nondimensional axial coordinate. x is the longitudinal coordinate. L_e denotes the length of finite element. After Eqs. (17) and (18) are used into Eq. (16), by performed the partial integration process, the eigenvalue formulation is reached as the following form:

$$\det\left(\left[K\right]_{n\times n}-\omega^2\left[M^0\right]_{n\times n}+\omega^4\left[M^1\right]_{n\times n}\right)=0 \tag{19}$$

where K, M_0, and M_1 denoting the global matrices of FGM nanobeam, define the stiffness matrix, simple mass matrix, and higher order mass matrix, respectively. Mass matrices are written as:

$$M^0=M_1+M_2+M_3+M_4+M_5+M_6 \tag{20}$$

$$M^1=M_7+M_8+M_9 \tag{21}$$

The stiffness and mass matrices can be formulated as follows:

$$K=\int_0^{L_e} D_1\left(\mathbf{B}'^{\mathrm{T}}\mathbf{B}'\right)\mathrm{d}x\,,\ M_1=\int_0^{L_e} I_0\left(\varphi^{\mathrm{T}}\varphi\right)\mathrm{d}x\,,\ M_2=\int_0^{L_e}\frac{2(e_0a)^2 I_0I_2}{kS_1}\left(\mathbf{B}^{\mathrm{T}}\mathbf{B}\right)\mathrm{d}x\,,$$

$$M_3 = \int_0^{L_e} (e_0 a)^2 I_2 \left(\mathbf{B}'^{\mathrm{T}}\mathbf{B}'\right)\mathrm{d}x,\ M_4 = \int_0^{L_e} \frac{I_0 D_1}{kS_1}\left(\mathbf{B}^{\mathrm{T}}\mathbf{B}\right)\mathrm{d}x,\ M_5 = \int_0^{L_e} (e_0 a)^2 I_0 \left(\mathbf{B}^{\mathrm{T}}\mathbf{B}\right)\mathrm{d}x,$$
$$M_6 = \int_0^{L_e} I_2 \left(\mathbf{B}^{\mathrm{T}}\mathbf{B}\right)\mathrm{d}x,\ M_7 = \int_0^{L_e} \frac{I_0 I_2}{kS_1}\left(\varphi^{\mathrm{T}}\varphi\right)\mathrm{d}x,\ M_8 = \int_0^{L_e} \frac{(e_0 a)^4 I_0 I_2}{kS_1}\left(\mathbf{B}'^{\mathrm{T}}\mathbf{B}'\right)\mathrm{d}x \tag{22}$$
$$M_9 = \int_0^{L_e} \frac{(e_0 a)^2 I_0 D_1}{kS_1}\left(\mathbf{B}'^{\mathrm{T}}\mathbf{B}'\right)\mathrm{d}x$$

5. Numerical Results and Discussion

In this section, nondimensional frequencies of free vibration of shear deformable FGM nanobeams and are presented by using nonlocal finite element formulation for clamped-clamped (C-C) and clamped-simply supported (C-S) boundary conditions. Discussions of numerical results are also given. According to this, the nondimensional frequency is formulated as follow:

$$\overline{\omega}_i = \omega_i L^2 \sqrt{\frac{\rho_U A}{E_U I}} \tag{23}$$

It is considered that the FGM nanobeam is consist of fully silicon on the upper surface and fully aluminum on the lower surface. Material properties are taken as [29]: Modulus of elasticity, $E_U = 210$ TPa, $E_L = 70$ TPa; weight of unit volume, $\rho_U = 2370$ kg/m^3, $\rho_L = 2700$ kg/m^3; Poisson's ratio: $v_U = 0.24$, $v_L = 0.3$. On the other hand, the height and thickness of rectangular section are taken as $h = 1$ nm and $b = 2$ nm, respectively. Finally, the length of the beam is $L = 20$ nm.

In order to demonstrate the accuracy of nonlocal finite element formulation presented in the study, the values from a reference study and the nonlocal finite element results are compared in Table 1 for the first three modes nondimensional frequencies of homogeneous nanobeams. Firstly, nondimensional frequencies decreases under the nonlocal parameter. Also, it is observed that the nondimensional frequencies increase as the mode number increases. At higher modes, the nonlocal parameter is more effective in reducing nondimensional frequencies. Additionally, the nondimensional frequencies of C-C nanobeams are higher than C-S nanobeams. Moreover, it is understood that the nonlocal parameter more affects C-C nanobeams. On the other hand, the comparative results are in great agreement. Therefore, it can be stated that the finite element formulation is useful.

In Table 2, first three modes nondimensional frequencies of nonlocal shear deformable FGM nanobeams are compared for three different functionally grading indexes. Accordingly, when the results of homogeneous nanobeams are considered, the functionally grading index reduces nondimensional frequencies. As the FG index increases, the atomic parameter more decreases the frequencies. Therefore, it should be stated that the nonlocal parameter must be taken into account on the dynamics of functionally graded composite nanobeams.

Table 1. Convergence of NL-FEM for nondimensional frequencies of homogeneous nanobeams.

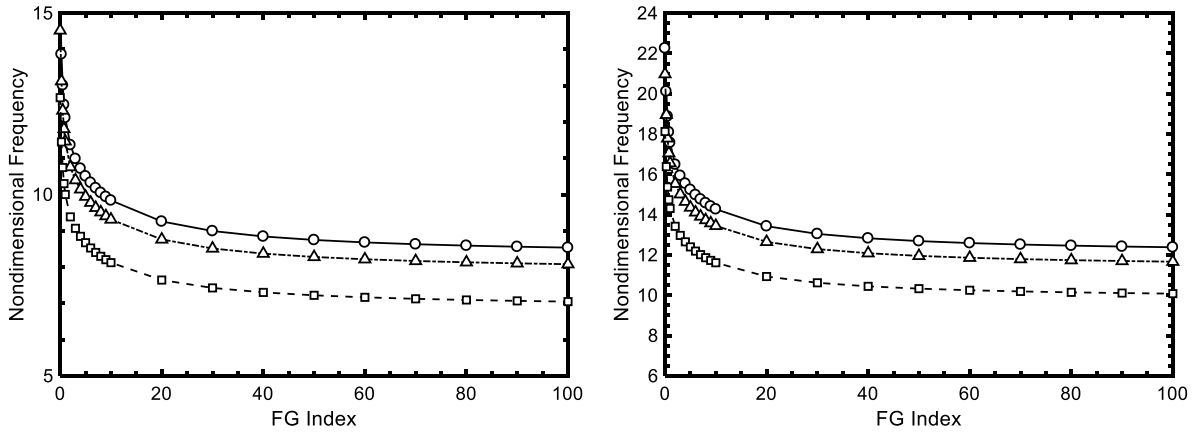
e_0a/L	Mode	C-S Boundary Condition				C-C Boundary Condition			
		Ref. [22]	NL-FEM Results			Ref. [22]	NL-FEM Results		
			n = 16	n = 14	n = 12		n = 16	n = 14	n = 12
0	1	15.34282	15.34286	15.34288	15.34294	22.25679	22.25691	22.25699	22.25717
	2	49.07729	49.07858	49.07949	49.08136	60.50259	60.50502	60.50672	60.51023
	3	100.34216	100.35361	100.36162	100.37802	116.17257	116.19042	116.20289	116.22840
0.2	1	12.66770	12.66773	12.66775	12.66780	18.12197	18.12208	18.12217	18.12234
	2	29.68057	29.68143	29.68204	29.68328	35.39543	35.39721	35.39844	35.40097
	3	45.78807	45.79359	45.79743	45.80523	51.59952	51.60895	51.61545	51.62859

Table 2. First three modes nondimensional frequency parameters of functionally graded nanobeams for different functionally grading indexes (n = 16).

e_0a/L	Mode	C-S Boundary Condition			C-C Boundary Condition		
		k = 0.01	k = 0.1	k = 10	k = 0.01	k = 0.1	k = 10
0	1	15.26768	14.64830	9.839333	22.14811	21.24967	14.27276
	2	48.86064	46.88422	31.42558	60.23891	57.80291	38.73650
	3	99.97721	95.95089	64.10973	115.76121	111.10096	74.21273
0.1	1	14.45090	13.86471	9.31235	20.86960	20.02328	13.44605
	2	40.79651	39.14698	26.23149	49.56762	47.56526	31.85137
	3	71.50415	68.62701	45.82464	81.32999	78.06235	52.06941
0.2	1	12.60622	12.09496	8.12257	18.03607	17.30509	11.61569
	2	29.55371	28.35929	18.99666	35.25309	33.83044	22.63730
	3	45.63215	43.79707	29.23286	51.44417	49.37980	32.90875

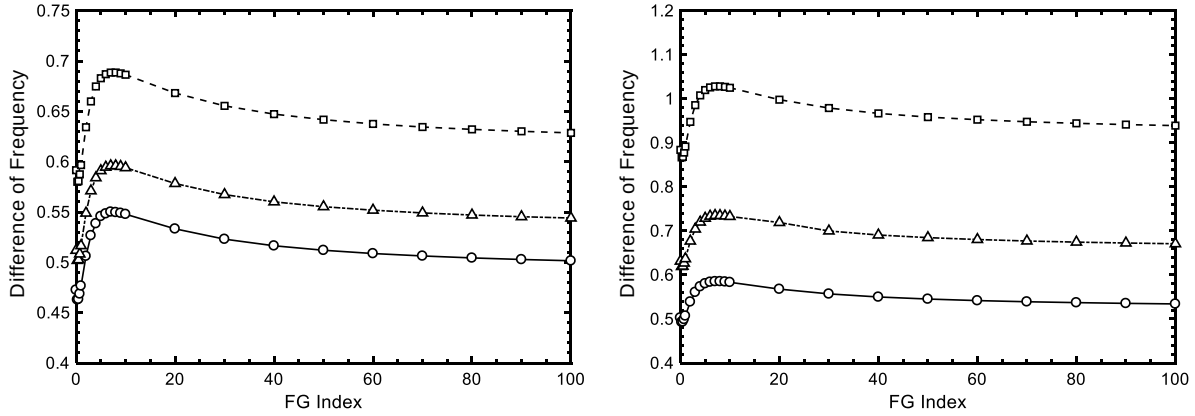
The variations of nondimensional frequencies of shear deformable FGM nanobeams in response to the increment in FG index are depicted in Fig. 2. The most important inference obtained here is that FG index is effective on nondimensional frequencies. Also, while FG index is low, atomic parameter more reduces the frequencies. The effect of atomic parameter does not change much at higher values of FG index.

The variations of nondimensional frequency differences of FGM nanobeams according to the increment of FG index is given in Fig. 3. Here, the difference of frequencies is defined as the percentage that shear deformation reduces the natural frequency of FGM nanobeam according to the beam theory without shear deformation (Euler-Bernoulli Beam Theory). The frequency difference increases at lower values of FG index. Therefore, the shear deformation effect becomes important here. However, the importance of shear deformation decreases as the difference parameter diminishes after a certain value of FG index. On the other hand, it is seen that the difference parameter rises with an increment in atomic parameter. Therefore, it should be noted that the shear deformation effect at the nanoscale is quite important.



(a) (b)

Figure 2. Variations of first mode nondimensional frequencies of FGM nanobeams according to the increment of functionally grading index **(a)** C-S **(b)** C-C (–○–: $e_0a/L = 0$, –△–: $e_0a/L = 0.1$, –□–: $e_0a/L = 0.2$).



(a) (b)

Figure 3. Differences of first mode nondimensional frequencies of FGM nanobeams according to the increment of functionally grading index **(a)** C-S **(b)** C-C (–○–: $e_0a/L = 0$, –△–: $e_0a/L = 0.1$, –□–: $e_0a/L = 0.2$).

6. Conclusions

Since nanocomposites as well as nano scaled homogeneous beams can be utilized in NEMS organizations, mechanical behaviors of nanocomposites must be determined by performing mechanical analyses according to higher-order elasticity theories. For this purpose, free vibration of functionally graded shear deformable nanobeams is examined in this study. A nonlocal finite element formulation (NL-FEM) is developed to solve the equation of motion. With the help of NL-FEM, the nondimensional frequencies of FGM nanobeams are calculated and numerical results are discussed. According to this, the atomic size effect must be considered in the nanostructure, because frequencies calculated by classical theory do not reflect the

accurate mechanical behavior. Additionally, in nonlocal mechanical analysis, it has been understood that shear deformation of nanocomposites is more important than classical elasticity theory.

References

[22] B. Akgöz, Static and dynamic analyses of one- and two- dimensional microstructures based on higher-order elasticity theores, PhD Thesis, Akdeniz University, Antalya, 2016. (In Turkish).

[23] A. C. Eringen, Linear theory of nonlocal elasticity and dispersion of plane waves, International Journal of Engineering Science, vol. 10, pp. 425-435, 1972.

[24] M. Aydogdu, A general nonlocal beam theory: Its application to nanobeam bending, buckling and vibration, Physica E: Low-dimensional Systems and Nanostructures, vol. 41, pp. 1651-1655, 2009.

[25] H.T. Thai, A nonlocal beam theory for bending, buckling, and vibration of nanobeams, International Journal of Engineering Science, vol. 52, pp. 56–64, 2012.

[26] S. Thai, H.T. Thai, T.P. Vo and V.I. Patel, A simple shear deformation theory for nonlocal beams, Composite Structures, vol. 183, pp. 262-270, 2018.

[27] A. Benzair, A. Tounsi, A. Besseghier, H. Heireche, N. Moulay, and L. Boumia, The thermal effect on vibration of single-walled carbon nanotubes using nonlocal Timoshenko beam theory, Journal of Physics D: Applied Physics, vol. 41, 225404. 2008.

[28] Z.B. Shen, X.F. Li, L.P. Sheng, G.J. Tang, Transverse vibration of nanotube-based micro-mass sensor via nonlocal Timoshenko beam theory, Computational Materials Science, vol. 53, pp. 340-346, 2012.

[29] K. Mercan, H.M. Numanoğlu, B. Akgöz, Ç. Demir, Ö. Civalek, Higher-order continuum theories for buckling response of silicon carbide nanowires (SiCNWs) on elastic matrix, Archive of Applied Mechanics, vol. 87, pp. 1797-1814, 2017.

[30] H.M. Numanoğlu, Cross-section effect on the deflections of simply supported Timoshenko nanobeams using nonlocal elasticity, Journal of Characterization, vol. 2, pp. 134-146, 2022.

[31] H.M. Numanoğlu, K. Mercan and Ö. Civalek Frequency and mode shapes of Au nanowires using the continuous beam models, International Journal of Engineering and Applied Sciences, vol. 9, pp. 55-61, 2017.

[32] H.M. Numanoğlu and Ö. Civalek, Elastic beam model and bending analysis of silver nanowires, International Journal of Engineering and Applied Sciences, vol. 10, pp. 13-20, 2018.

[33] S.C. Pradhan, Nonlocal finite element analysis and small scale effects of CNTs with Timoshenko beam theory, Finite Elements in Analysis and Design, vol. 50, pp. 8-20, 2012.

[34] H.M. Numanoğlu and Ö. Civalek, On the dynamics of small-sized structures, International Journal of Engineering Science, vol. 145, 103164, 2018.

[35] H.M. Numanoğlu, Examination of how size-effect modifies the stiffness and mass matrices of nanotrusses/nanoframes, International Journal of Engineering and Applied Sciences, vol. 13, pp. 155-165, 2021.

[36] Ç. Demir, K. Mercan, H.M. Numanoğlu and Ö. Civalek, Bending response of nanobeams resting on elastic foundation, Journal of Applied and Computational Mechanics, vol. 4, pp. 105-114, 2018.

[37] B. Uzun, H.M. Numanoğlu, Ö. Civalek, Free vibration analysis of BNNT with different cross-sections via nonlocal FEM, Journal of Computational Applied Mechanics vol. 49, pp. 252-260, 2018.

[38] H.M. Numanoğlu, K. Mercan and Ö. Civalek, Finite element model and size dependent stability analysis of boron nitride and silicon carbide nanowires/nanotubes, Scientia Iranica, vol. 26, pp. 2079-2099, 2019.

[39] Ç. Demir and Ö. Civalek, A new nonlocal FEM via Hermitian cubic shape functions for thermal vibration of nano beams surrounded by an elastic matrix, Composite Structures, vol. 168, pp. 872-884, 2017.

[40] H.M. Numanoğlu, Thermal vibration of zinc oxide nanowires by using nonlocal finite element method, International Journal of Engineering and Applied Sciences, vol. 12, pp. 99-110, 2020.

[41] Ç. Demir and Ö. Civalek, On the analysis of microbeams, International Journal of Engineering Science, vol. 121, pp. 14–33, 2017.

[42] H.M. Numanoğlu, H. Ersoy, O. Civalek and A.J.M. Ferreira, Derivation of nonlocal FEM formulation for thermo-elastic Timoshenko beams on elastic matrix, Composite Structures, vol. 273, 114292, 2021

[43] H.M. Numanoğlu, H. Ersoy, B. Akgöz and Ö. Civalek, A new eigenvalue problem solver for thermo-mechanical vibration of Timoshenko nanobeams by an innovative nonlocal finite element method, Mathematical Methods in the Applied Sciences, vol. 45, pp. 2592-2614, 2022.

[44] M.Z. Nejad and A. Hadi, Non-local analysis of free vibration of bi-directional functionally graded Euler–Bernoulli nano-beams, International Journal of Engineering Science, vol. 105, pp. 1-11, 2016.

[45] M. Ghadiri and A. Jafari, A nonlocal first order shear deformation theory for vibration analysis of size dependent functionally graded nano beam with attached tip mass: An exact solution, Journal of Solid Mechanics, vol. 10, pp. 23-37, 2018.

[46] F. Ebrahimi and E. Salari, Thermo-mechanical vibration analysis of nonlocal temperature-dependent FG nanobeams with various boundary conditions, Composites Part B: Engineering, vol. 78, pp. 272-290. 2015.

[47] F. Ebrahimi and M.A. Barati, A nonlocal higher-order shear deformation beam theory for vibration analysis of size-dependent functionally graded nanobeams, Arabian Journal of Geosciences, vol. 41, pp. 1679-1690, 2016.

[48] O. Rahmani, V. Refaeinejad and S.A.H. Hosseini, Assessment of various nonlocal higher order theories for the bending and buckling behavior of functionally graded nanobeams, Steel and Composite Structures, vol. 23, pp. 339-350, 2017.

[49] O. Rahmani and O. Pedram, Analysis and modeling the size effect on vibration of functionally graded nanobeams based on nonlocal Timoshenko beam theory. International Journal of Engineering Science, 77: 55-70. 2014.

[50] R. Nazemnezhad and S. Hosseini-Hashemi, Nonlocal nonlinear free vibration of functionally graded nanobeams, Composite Structures, vol. 110, pp. 192-199, 2014.

[51] M.A. Eltaher, S.A. Emam and F.F. Mahmoud, Free vibration analysis of functionally graded size-dependent nanobeams. Applied Mathematics and Computation, vol. 218, pp. 7406-7420, 2012.

[52] M.A. Eltaher, A. Khairy, A.M. Sadoun and F.A. Omar, Static and buckling analysis of functionally graded Timoshenko nanobeams, Applied Mathematics and Computation, vol. 229, pp. 283-295, 2014.

[53] A.I. Aria and M.I. Friswell, A nonlocal finite element model for buckling and vibration of functionally graded nanobeams, Composites Part B: Engineering, vol. 166, pp. 233-246. 2019.

Portland Çimentolu Alternatif Polipropilen Elyaf Katkılı Beton

Atila Gürhan Celik, İbrahim Günes

[1]Giresun Üniversitesi, Mühendislik Fakültesi, İnşaat Mühendisliği Bölümü, 28200, Giresun/Türkiye

Özet

Bu çalışmada, polipropilen lif karışımları hazırlanmış ve betona katkı maddesi olarak kullanılan polipropilen lif ve süper akışkanlaştırıcı eklenmiştir. Polipropilen lifler izotaktik polipropilenden üretilir. Kalınlıkları 50 mikron ile 100 mikron arasında değişmektedir. Filamentli lif bir katman olarak kullanılır. 165 ºC'de erime özelliği gösterir, ancak malzeme 100 ºC'ye kadar kendi özelliğini koruyabilir. Beton harçlarında genellikle %0.3-1.5 tercih edilir. Elde edilen numunelerin su emme, yoğunluk ve birim ağırlık değerleri sertleşmiş beton için incelenmiştir.

Anahtar kelimeler: Polipropilen, Beton, Su emme, Yoğunluk, Birim ağırlık

Alternatıve Polypropylene Fıber Addıtıve Concrete wıth Portland Cement

Abstract

In this study, polypropylene fiber mixtures were prepared and polypropylene fiber and super plasticizer used as an additive were added in the concrete. Polypropylene fibers are produced from isotactic polypropylene. Their thickness varies between 50 microns and 100 microns. The filamentous fiber is used as a layer. It shows melting property at 165 ºC, but the material can maintain its own property up to 100 ºC. Generally, 0.3-1.5% is preferred in concrete mortars.The water absorption, density and unit weight values of the obtained samples were investigated for the hardened concrete.

Keywords: Polypropylene, Concrete, Water absorption, Density, Unit weight

3. Giriş

Beton dünya çapında endüstri olarak en çok tüketim sağlanan inşaat malzemelerinden biridir. Beton tasarımlara uygulama kolaylığı, uzun vadede kullanılabilirliği, sağlamlığı açılarından oldukça fazla tercih edilen bir yapı malzemesidir. Ülkemizde de katlı yapıların artışı ile beton tüketiminin arttığı göz ile görülmektedir. Betonlara çeşitli katkı malzemeleri eklenerek beton dayanımı artışı sağlanmaktadır. Betonun temel bileşenlerini yanı sıra kimyasal katkılara ek olarak farklı miktarlarda liflerin eklenmesiyle elde edilen bir çeşit güçlendirilmiş kompozit yapı malzemesine lifli beton denir. Beton içerisinde belirli oranlarda kullanımı birçok fizikomekanik özelliklerinde onarım sağlayabilmektedir (1). Bu amaçla bir çok çalışma yapılmıştır. Yapılan çalışmada; çimento olarak CEM I 42.5 R tipte Portland kullanılmıştır. 7 ve 28 günlük numunelerin basınç dayanımları ve eğilme dayanımları incelenmiştir. Eğilme dayanımı incelendiğinde ise lif katkılı betonlarda 7. Ve 28. Günlerde bir artış gözlenmiştir. 28. Günde eğilmedeki artış oranı 7. Gündeki artış oranına göre daha az olduğu gözlenmektedir. Eğilmede gözlenen bu artışlar beton içerisinde aderansın çok iyi bir şekilde sağlandığının bir göstergesidir (2). Aghabaglou, ve ark. yaptığı bir başka çalışma ise, CEMI 42,5 portland çimentosu kullanılmıştır. Lif içermeyen şahit numune ve yanında %0,4, %0,8 ve %1 oranlarında polipropilen lif katkılı lifler ile 4 farklı karışım hazırlanmıştır. Tüm bu karışımlarda su/çimento oranı, çimento dozajı ve çökme değerleri sabit tutulmuştur. Çökme miktarının istenen miktarda olması için yüksek oranda su azaltıcı katkı kullanılmıştır. Şahit numunede azaltıcı katkı 4 kg/m^3 iken diğer lifli oranlarda 8 kg/m^3 olarak alınmıştır (3). Kırca, ve ark. yaptıkları çalışmada; polipropilen lif kullanımı ile beyaz çimento harcında oluşan erken yaşlardaki büzülme deformasyonlarına etkisini incelemişlerdir. Çalışmalarında BPÇ 42.5/85 çimentosu kullanmışlardır.18mm boyunda propilen lifler 1.29 gram kadar kullanmışlardır (4). Diğer bir çalışmada; lif eklenen betonların kırılma tokluğuna etkilerini incelemiştir. Çimento olarak PÇ 42,5 kullanılmıştır. C20 betonu hedeflenmiştir. Kullanılacak ve agreganın %60' ı mıcır, %40' ı kumdur. Dmax =16 mm alınmıştır. Şahit

numunelerle aynı ortam ve koşullarda polipropilen lifli beton hazırlanmıştır. Hacimce %0.5-1- 1.5 oranında polipropilen lif eklenmiştir. Beton çekme dayanımında önemli artışlar tespit edilmiştir(5).

Bu çalışmada betona Polipropilen lif katkı olarak seçilmiştir. Polipropilen lif eklemekteki amaç betonunun fiziko-mekanik özelliklerini iyileştirmek ve dış etkenlere karşı betona bir savunma sunmaktır.

2. Materyal ve Metot

2.1. Materyal

2.1.1. Çimento

Çimsa fabrikasının çimentolarından CEM I 42,5 R - Portland Çimento kullanılmıştır.

2.1.2. Agrega

Bu çalışmada kullanılan agregalar 0-2mm, 2-4mm, 4-8mm 8-16 16-22,4 ve 22,4- 32 tane boyutuna sahip olacak şekilde gruplandırılmışlardır. TS 802'ye uygun olarak maksimum dane boyu 22,4 mm alınmıştır ve granülometri eğrisine uygun olarak karışıma eklenmiştir.

2.1.3. Polipropilen Lif

Polipropilen olarak M12 tipi kullanılmıştır. Özellikleri Çizelge 1' de verilmiştir.

Çizelge 1. Polipropilen Lif Özellikleri

Özellik	M12
Uzunluk	12
Çap (µ)	38
Yoğunluk kg/lt	0.91
Gerilme Dayanımı	411 N / mm²
Kalınlık	0,0268 mic

2.1.4. Karışım Suyu

Yapılan çalışmada karışım suyu olarak Giresun ilinde şehir şebeke suyu kullanılmıştır. Kullanılan suyun ilgili standartlarda yer alan özellikleri sağlamasına dikkat edilmiştir.

2.1.5. Süper Akışkanlaştırıcı Katkı Maddesi

Glenium51'in geleneksel süperakışkanlık verici katkı maddesi kullanılmıştır. Bu süper akışkanlaştırıcının en öenmli özelliği çimento dağılımının etkinliğini büyük ölçüde arttırmasıdır. Bir diğer olumlu sonucu ise, belirli beton işlenebilirliğinin daha az su Polikarboksilik eter esaslı olan bu yeni kuşak süperakışkanlaştırıcı (20°C"de) 1,07- 1,012 g/cm³ özgül ağırlığında olup kahverengi renkte sıvı ve homojen haldedir.

2.2.Metod

Söz konusu materyaller kullanarak farklı gruplarda beton numuneleri hazırlanmıştır. Şahit (%0 polipropilen) ve çimentonun %1, %2, %4 oranlarında polipropilen lif katkısı eklenerek ana numuneler oluşturulmuştur. Polipropilen lif içeriği oranını belirtecek şekilde PP0, PP1,PP2 ve PP4 olarak isimlendirilmiştir. Beton tasarımında C18/22 beton üretmek için 0-5mm (kum) , 5-12mm (ince taneli) ,ve 12-22,4 mm (iri taneli) agrega grupları sırasıyla %54, %14 ve %32 oranlarında kullanılmıştır. Karışım suyu 180 lt, su/çimento oranı 0,70, hava içeriği

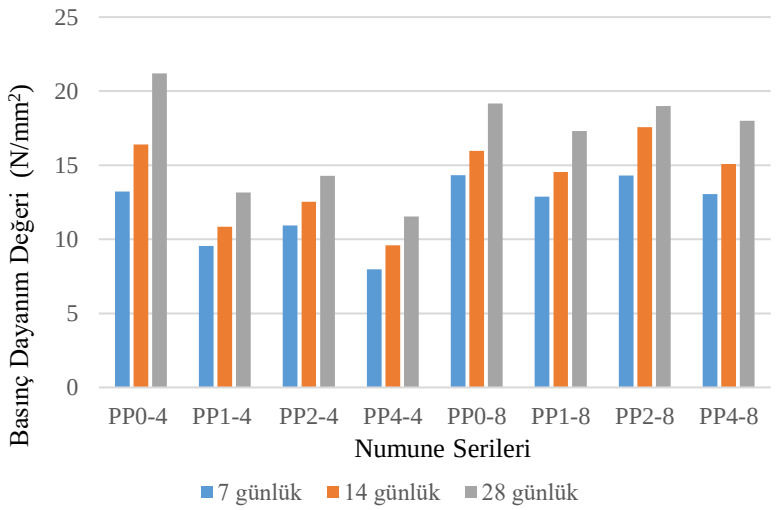
%1,8 ve çökme miktarları 6 cm olarak belirlenmiştir. Her beton grubu için üçer adet 15×15×15 cm boyutunda toplam 24 adet küp numune hazırlanmıştır.

3. Deneysel Sonuçlar

3.1. Mekanik Deneyler

3.1.1. Basınç Dayanımı

Kontrol Numunesi olan PP0-4, PP0-8 (%0 polipropilen içeren ve sırası ile %0,4- %0,8 oranında süper akışkanlaştırıcı içeren) serileri ve diğer polipropilen katkılı numuneler PP1-4,PP1-8, PP2-4,PP2-8, PP4-4,PP4-8 serileri 7,14 ve 28 günlük kür sürelerinden sonra pres cihazı ile basınç deneyine tabi tutulmuştur. Elde edilen sonuçlar karşılaştırıldığında, şahit numunelerde %0,4 (PP0-4 serisi) oranında kullanılan süper akışkanlaştırıcı katkı maddesi %0,8 oranında kullanılan numunelere (PP0-8 serisi) göre daha dayanımı yüksek çıktığı görülmüştür(Şekil1).



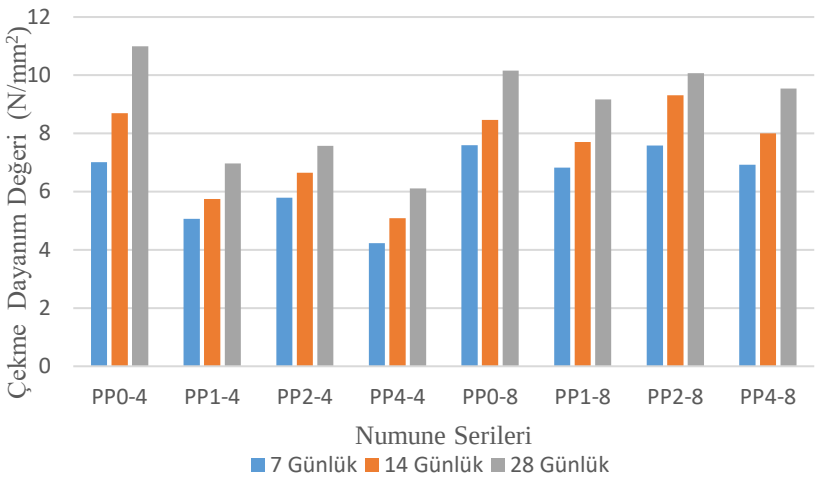
Şekil 1. Numunelerin basınç dayanım değerleri

3.1.2. Çekme Dayanımı

Kontrol Numunesi olan PP0-4, PP0-8 (%0 polipropilen içeren ve sırası ile %0,4- %0,8 oranında süper akışkanlaştırıcı içeren) serileri ve diğer polipropilen katkılı numuneler PP1-4,PP1-8, PP2-4,PP2-8, PP4-4,PP4-8 serileri 7,14 ve 28 günlük kür sürelerinden sonra pres cihazı ile basınç deneyine tabi tutulmuştur.

Yapılan incelemeler ışığında şahit numunelerinde 28 günlük basınç dayanım değeri yüksek olduğundan çekme dayanım değeri de yüksek gözükmektedir. Şahit numuneler kendi içinde değerlendirildiğinde çekme dayanımı %0,8 oranında süper akışkanlaştırıcı kullanılan numuneler %0,4 süper akışkanlaştırıcı kullanılan numunelere kıyasla çekme dayanımının düştüğü gözlenmektedir. Kontrol numuneleri haricinde polipropilen kullanılan numunlerde ise süper akışkanlaştırıcının %0,8 oranında kullanıldığı durumlarda daha iyi sonuçlar elde edilmiştir.

En iyi çekme dayanımı sonucu ise PP2-8 olan numune serisinde yani kullanılan polipropilen oranı %2 ve kullanılan süper akışkanlaştırıcı oranı %0,8 olan numune serisinde görülmüştür (Şekil 2).



Şekil 2. Numunelerin çekme dayanım değerleri

4. Sonuç ve Öneriler

Çalışmanın sonuçları aşağıda verilmiştir;

- Polipropilen lif katkılı ve şahit numuneler incelendiğinde ve dayanım sonuçları kıyaslandığında, şahit numunelerde (PP0) %0,8 oranındaki süper akışkanlaştırıcı %0,4 oranındaki süperakışkanlaştırıcının kullanımına göre daha düşük dayanımlı sonuçlar elde edilmiştir.
- Polipropilen kullanılan numunelerde en yüksek dayanım PP2 yani %2 oranda polipropilen kullanımı söz konusu olan numunlerde görülmüş ve en az dayanıma sahip olan PP4(%4 oranında polipropilen içeren) numunesi olmuştur. Bu durumda basınç dayanımı için en ideal kullanım %2 oranında polipropilen lif ve %0,8 oranında süper akışkanlaştırıcının birlikte kullanımıdır.
- Çekme dayanımı; polipropilen lif kullanılan numune gruplarında %2 polipropilen içerikli ve %0,8 süper akışkanlaştırıcı katkılı beton grubu (PP2-8) daha başarılı bulunmuştur.
- Bu çalışma sonucunda polipropilen katkısının betonun basınç dayanıma çok fazla etkisinin olmadığı fakat çekme dayanımını arttırdığı ve polipropilen lif ve katkı dozunun iyi ayarlanması gerektiği tespit edilmiştir.

Kaynaklar

[1] Sanjudn M.A. , Bentur A. ve Andrade C. “Effect of polypropylene fibre reinforced mortars on steel reinforcement corrosion induced by carbonation” Materials and Structures, 1998. s. 343-349.
[2] Güçlüer K., Demir İ., ve Günaydın O., “Polipropilen Lif Katkılı Betonların Mekanik Özelliklerinin İncelenmesi” Adıyaman Cıvıltech , 2019.
[3] Aghabaglou A. M., “ Polipropilen Lif Kullanımı Oranının Beton Karışımlarının Dayanıma Etkisi” XX. Ulusal Mekanik Kongresi, Bursa Uludağ Üniversitesi, 2017.
[4] Kırca Ö. ve Şahin M. “Polipropilen Lif Kullanımının Beyaz Beton Dayanıklılığına Etkisi” İMO.
[5] Bahadır B., “Liflerin Beton Kırılma Tokluğuna Etkileri” Sakarya, Sakarya Üniversitesi, 2007.

Requirements for specialists in the Industry 4.0 environment: problems and solutions

Mahmudova Rasmiyya Sharif

[1*] Institute of Information Technology, Departmant of Training Innovation Center, Baku, Azerbaijan (ORCID: 0000-0002-5816-9373), rasmahmudova@gmail.com

Abstract

The new industrial revolution is changing human life and activities beyond recognition. The development of digital technologies, the application of cyber-physical systems and the use of artificial intelligence lead to an increase in the standard of living of certain groups of the population, and economic growth in several areas of the economy. At the same time, it brings a number of problems.

An important condition for ensuring competitive activity of the enterprise in the environment of Industry 4.0 is human capital - training of qualified personnel with digital skills.

The article examines the advantages and disadvantages of the application of digital technologies in the industry 4.0 environment, the problems that arise, and ways to overcome these problems. Existing approaches for defining a list of new skills and habits in terms of the requirements for specialists now and in the near future are analyzed and summarized. Suggestions and recommendations are given for developing these skills and habits.

Keywords: Industry 4.0, Digital competencies, Human capital

1. Introduction

Artificial intelligence, robotics, internet of things, 3D printing, nanotechnologies, quantum computing, big data – these are all technological realities that form the basis of the fourth industrial revolution. These technologies are designed to provide humanity with everything it needs, including ensuring the security of the individual, society and the state.

The application of digital technologies leads to job losses. According to the forecast of the World Economic Forum, millions of people in several countries of the world will face the threat of losing their jobs as a result of the application of robots in the future.

An important condition for ensuring competitive activity of the enterprise in the environment of Industry 4.0 is human capital - training of qualified personnel with digital skills. On the other hand, the content of the most required skills and habits has changed significantly in recent years, and new training methods have appeared. This requires constant updating of programs designed for personnel training and skill development.

Application of cyber-physical systems in industrial enterprises, management of production processes and other processes with computer programs requires ensuring high level of cyber security. Currently, in the modern digital world, cybercrime is the main threat factor for the development of the world economy. Previously, there was an opinion that strong software development and technical methods were sufficient to prevent unauthorized access to information resources. However, it is not possible to ensure information security only with software and technical means. The solution of information security problems also depends on the culture of people and their behavior in relation to information.

Research shows that the majority of security breaches are caused by human error. Therefore, enterprises should prepare their employees in a better way in order to increase the level of information security of their resources and increase the resistance of employees to cyber threats.

2. The essence and possible consequences of Industry 4.0

Today we are on the threshold of the 4th industrial revolution. The project Industry 4.0 was one of the 10 "Projects of the Future" identified by the German government as part of the "High-Tech Strategy 2020" Action Plan [1].

The concept of Industry 4.0 was proposed in Germany in 2011. Its essence lies in the combination of real and virtual labor organization systems, as well as in the integration of people with digitally controlled intelligent machines that widely use the Internet and information technologies. Production is characterized by automation, computerization and robotization. All devices in the production line interact with each other and shape an intelligent system.

The main components of Industry 4.0 are cyber-physical systems, the Internet of Things, IOS and intelligent systems. Smart products are sub-components of cyber-physical systems. The intelligent systems are estimated to be the main components for the successful development of society.

The 4th industrial revolution leads to a strong connection between the real and virtual world in cyber-physical systems, that is, the new industrial concept called Industry 4.0 means the integration of IT devices and solutions into production processes to increase production efficiency and flexibility. Industry 4.0 specifies new directions for changes in production and management, and at the same time affects various aspects of society.

Economic initiatives related to Industry 4.0 are gradually increasing. The propagation of Industry 4.0 is causing changes in many areas of society and economy. The range of changes is quite wide and it is impossible to list them all, or even to define them completely. Against the background of ongoing changes, the question arises: what are the social expectations of the 4th industrial revolution?

The changes taking place are changing the structure of the labor market. This is due to the fact that new technologies allow the automation of a large part of the processes, resulting in the reduction of jobs [2]. Second, new technologies create new opportunities for business, which, in turn, means the creation of new jobs.

Industry 4.0. affects the complete transformation of the industry in three directions:

- Digitization of production, i.e., data management systems and production scheduling;
- Automation, i.e., a system of data collection from production lines through multiple machines;
- Integration of production sites in a complex supply chain, i.e., automatic data sharing.

Any industrial revolution is not only accompanied by technical innovations, nevertheless, gradually covers all spheres of society and leads to fundamental cultural and social changes [3].

As a result of the introduction of new technologies, the automation of labor and the increase of productivity are expected. Technological development and the possibilities of artificial intelligence can completely destroy a number of professions and lead to an increase in unemployment.

The new technical reality put forward strict demands on specialists, namely, having knowledge in the field of ICT, mathematics and finance along with the main profession. The usefulness and efficiency of a person in the labor market will depend on his/her ability to think critically, creatively approach the problem solving, his/her initiative, ability to constantly adapt and adopt new skills and approaches in various contests.

3. Digital skills for Industry 4.0

As a result of the impact of the 4th industrial revolution, we are witnessing the changes in employment conditions and requirements for professional skills. The key component for the successful implementation of Industry 4.0 technologies in enterprises and the expansion of opportunities for future activity is the employees'

skills. G20 analyst report predicts the demand for non-standard analytical skills related to creativity, problem solving, communication, teamwork and entrepreneurship to increase.

The guarantee of successful implementation of Industry 4.0 in enterprises is the acquisition of new knowledge and skills by employees and their constant self-development. Therefore, each enterprise must define specific digital skills specific to the enterprise in the future.

Talent and skills are the main driving force behind the successful implementation of Industry 4.0. Advanced manufacturing concept can be realized with the help of skilled and well-trained workforce. The success of Industry 4.0 depends not only on technologies, but also on people [4].

One of the nine main pillars forming the basis of Industry 4.0 is additive manufacturing. Additive manufacturing is considered to be one of the most innovative technologies. This is of great interest to industrial enterprises, educational institutions and public authorities. In this regard, training the workforce and preparing it for new realities is one of the most central tasks.

EU countries implement numerous projects to increase the qualifications and develop the digital skills of not only employees, but also the general population, i.e., citizens, teachers, students, and various professions. For example, "Digital Competencies for Citizens (DigComp)", "Digital Competencies for Consumers (DigCompConsumers)", "Competencies for Entrepreneurs (EntreComp)", etc. [5].

The DigComp model of digital competencies envisages competencies in five areas [6]:

1. Literacy in the field of information and data (searching information, extracting and storing the necessary out of the information found, etc.);
2. Communication and cooperation (interacting, communicating and participating in the life of society using digital technologies, etc.);
3. Competencies for digital content creation (creating and editing digital content in various formats, being aware of and applying copyright and licensing);
4. Competencies in the field of security (risks and threats in the digital environment, protection of devices and data, awareness of security measures, data privacy, knowledge of the impact of digital technologies on the environment and its prevention);
5. Solving emerging problems (using digital tools to apply innovations to processes and products).

The World Economic Forum analysts believe that the following competencies that are important for successful operation in the conditions of the 4th industrial revolution are [7]: complex problem solution; critical thinking; creativity; people management; coordination skills (interaction); emotional intelligence; reasoning and decision making; service-oriented (customer-orientated); ability to negotiate; cognitive flexibility.

The fundamental skills model of the digital economy developed by Burning Glass [8] includes four blocks. The model develops a list of fundamental skills.

Table 1. Fundamental skills model of the digital economy

Human Skills	Domain Knowledge	Digital Building Block Skills	Business Enabler Skills
Critical thinking, creative approach, analytical analysis, communication and cooperation	Strategy, economics, marketing, communications/public relations, talent development/human resource management, research and development/product development;	Data analysis, Big Data and data management, software development, ensuring information security	Project management, decision making, data visualization and communication.

In this model, skills are divided into three levels: primary skills; basic skills; special skills.

4. Conclusion

The introduction of Industry 4.0 technologies leads to a number of changes. Digitization and automation of production affects the nature of the organization of work in enterprises and the employment of population. As a result of automation, the following changes are observed:

- Reduction of some jobs;
- Change in the nature of works performed;
- Creation of new jobs;
- Inconsistency between required and offered skills;
- Change of working conditions (remote work).

The importance of the skill mismatch problem is also shown in international studies. Lack of basic skills is the third most important factor preventing the increase in the enterprise performance [9].

For the successful implementation of Industry 4.0 technologies, employees must have appropriate qualifications. It is extremely important to have a flexible system capable to perform training, upgrading and retraining of personnel within the enterprise. For this, enterprises should perform the following activities:

1. Preparing and systematizing the list of digital skills important for the enterprise (general and specific skills);
2. Employees' digital knowledge and skills should be assessed and the necessary knowledge and skills should be determined according to the assessment results;
3. A training program should be prepared and constantly updated, allowing to acquire the required knowledge and skills;
4. A budget should be allocated for training and the training process should be managed;
5. New training methods (open educational resources, virtual reality, games, etc.) should be applied in the training process.

Thus, for the successful implementation of digital technologies, employees must have the appropriate skills. Retraining and increasing the qualification of the existing labor force is one of the important conditions for future economic growth and increasing the stability of society.

References

[1] Li Da Xu, Eric L. Xu & Ling Li (2018) Industry 4.0: state of the art and future trends, International Journal of Production Research, 56:8, 2941-2962, DOI: 10.1080/00207543.2018.1444806.

[2] Gutorovich O.V. The fourth industrial revolution and its possible consequences. Discourse. 2018;4(6):11-17. (In Russ.) https://doi.org/10.32603/2412-8562-2018-4-6-11-17

[3] Polevaya M.V. Human resourse management in the context of global changes. Moscow: Prometey, 2019, 236 p. (In Russ.).

[4] Accenture Consulting. (2017). **Manning the mission for advanced manufacturing**. Retrieved from https://www.accenture.com/il-en/_acnmedia/PDF-50/Accenture-Manning-Mission-Advanced-Manfacturing.pdf.

[5] Ryazantseva M.V. Developing digital competences as a labour productivity growth source. Ekonomika. Nalogi. Pravo = Economics, taxes & law. 2019;12(6):77-85. (In Russ.). DOI: 10.26794/1999-849X-2019-12-6-77-85.

[6] DigComp 2.1. The Digital Competence Framework for Citizens. With Eight Proficiency Levels and Examples of Use. Available at: http:// publications.jrc.ec.europa.eu/repository/bitstream/JRC106281/web-digcomp2.1pdf.

[7] The 10 Skills You Need in the Fourth Industrial Revolution. Available at: https://www. weforum.org/agenda/2016/01/the-10-skills-youneed-to-thrive-in-the-fourth-industrial-revolution.

[8] The New Foundational Skills of the Digital Economy. Developing the Professionals of the Future. Available at: https://www.burning-glass.com/wp-ontent/uploads/New_ Foundational_Skills.pdf.

[9] CEOs' curbed confidence spells caution. 22nd Annual Global CEO Survey. URL: https://www.pwc.com/gx/en/ceo-agenda/ ceosurvey/2019/gx.html.

Effect of Silane Treatment on the Mechanical Properties of Cellulose Nanocrystal (CNC) Based Polymer Composites

S. Bahar Baştürk[1*], Seçil Çelik Erbaş[1], Fatih Acer[1]

[1*] Manisa Celal Bayar University, Engineering Faculty, Metallurgy and Materials Engineering Department, Manisa, Turkey, (ORCID: 0000-0002-4027-1935), bahar.basturk@cbu.edu.tr

[1] Manisa Celal Bayar University, Engineering Faculty, Metallurgy and Materials Engineering Department, Turkey, (0000-0001-6029-7190:), secil.celik@cbu.edu.tr

[1] Manisa Celal Bayar University, Engineering Faculty, Metallurgy and Materials Engineering Department, Turkey, (ORCID:0000-0002-5997-5115), fatihacer4566@gmail.com

Abstract

In recent years, cellulose nano crystal (CNC) can be characterized as an appropriate reinforcement material for nanocomposites due to its characteristic properties such as lightness and high surface area/volume ratio. In this study, 1% wt. CNC was introduced into epoxy via conventional casting method to produce composite samples. Furthermore, CNC was modified with (3-Glycidoxypropyl) trimethoxysilane (GPTMS) and the composites consisted of that powder were prepared for 1% wt. concentration as well. Structural characterizations of pristine and silanized CNC were performed using attenuated total reflectance-Fourier Transform Infrared Spectroscopy (ATR-FTIR). The spectrum clearly indicates that CNC was successfully treated with GPTES. Tensile and flexural responses of those structures were determined to reveal the effect of silanization. Based on the test results, GPTES presence led to the increase of tensile and flexural strength values as 16% and 50%, respectively as compared with unmodified CNC/epoxy composites. However, elastic modulus and flexural modulus parameters of modified composites were slightly lower (approximately 10.5-11%) than the pristine CNC based structures. Although silane treatment promoted improved strength values, neat epoxy still exhibited better mechanical properties. This situation can be attributed to the particle size of modified CNC. It is highly probable that grinded CNC was no longer a nano-size powder, therefore its positive effects could not be observed in mechanical tests.

Keywords: Cellulose nanocrystal (CNC), CNC/epoxy composite, Mechanical properties

1. Introduction

Cellulose-based nanomaterials are known as environmentally friendly/ecological reinforcement materials because of easy decomposition in nature, carbon neutral characteristics and recyclability properties. Due to the aforementioned reinforcement features, it attracts the attention of researchers working in the field of materials science. Cellulose nanocrystal (CNC) particles contribute to the mechanical and thermal properties at a high level when used as a reinforcing element in a polymer-based matrix [1]. Since the matrix has a hydrophobic character and the reinforcement shows a hydrophilic character, the optimum distribution between those components is more difficult as compared to other nanoparticles. This situation limits the industrial use of cellulose nanocrystals in commercial applications. The moisture problem caused by the hydrophilic character is a factor that reduces the reinforcement properties of composite materials [2]. The cellulose nanomaterial additive between 2% and 5%, which will be reinforced into the epoxy resin, shows comparable properties with the epoxy composites reinforced with 15%, 20% glass fiber/volume ratio, with its high hardness and specific strength values [3]. In the literature,

there are many studies on the use of cellulose nanocrystal (CNC) reinforcement in different matrices at different rates.

León et al. investigated the mechanical properties of ABS nanocomposites formed by reinforcing modified cellulose nanocrystal particles to ABS at certain rates and reached the result of an increase in Young's modulus and yield stress values when compared to pure ABS. The 1% concentration by mass was determined as the optimum value and it was seen that the modification of nanoparticles exhibited a positive effect. At 0.25% wt. concentration, the storage modulus value determined by DMA achieved the highest value, and no change was observed in the glass transition temperature (T_g) for ABS [4].Nascimento et al. investigated the mechanical and thermal properties of cellulose nanocrystal reinforced epoxy matrix composites by dispersing 4%, 5.5%, and 7% wt. CNC particles in epoxy resin. Thermal properties such as thermal stability, glass transition temperature and degree of conversion were measured by thermal gravimetric analysis (TGA) and differential scanning calorimetry (DSC). In the microstructural examinations conducted on the fracture surfaces with transmission electron microscopy (TEM), a decrease in the impact resistance was observed due to the non-homogeneous distribution of the CNCs. There was no significant change in the tensile and bending modulus when compared to neat epoxy. Scanning electron microscopy (SEM) analysis revealed a difference in the fracture mechanism of epoxy, revealing that CNCs increased the elastic modulus with its reinforcement properties. However, CNC also acted as a defect, which accelerated the fracture. Many researchers have stated that the lack of reinforcement occurs due to the particle agglomeration. That agglomeration can be attributed to the non-homogeneous dispersion as a result of hydrophilic behavior of CNCs in the epoxy matrix [5]. Roszowska-Jarosz et al. investigated the effect of low-doped nanocellulose material on the improvement of the mechanical properties in epoxy composites. They focused on three different rates as 0.5%, 1.0%, 1.5% wt. As a result of the test results, it was determined that the impact strength increased between 70-90%, the resistance to brittle fracture improved by 70% and the bending stress at break increased by 15% when compared to the pure epoxy sample [6].

The primary motivation for our work is to produce composites using eco-friendly CNC as the reinforcement component. For this purpose, the CNC obtained entirely from bio-based natural resources, was reinforced with epoxy and its tensile and flexural properties were investigated for 1% wt. concentration. Furthermore, silane modified CNC was integrated with epoxy for the same percentage and the performance of resultant composites were compared with the neat CNC based composites and pure epoxy.

2. Materials and Methods

In this study, epoxy supplied from Duratek™ (with DTE 1200 resin and DTS 2110 hardener components) and cellulose nanocrystal (CNC) purchased from Nanografi™ (10-20 nm width and 300-900 nm length) were used as the matrix and particle reinforcement constituents, respectively for composite preparation. To improve the compatibility between hydrophobic epoxy and hydrophilic CNC, silane surface modification was conducted based on the procedure referred in [7] and [8]. According to this process, a calculated quantity of 3-glicidyloxy-propyltrimethoxy silane (GPTMS) was added into 100 ml ethanol/water mixture (80/20 V/V). Concentrated acetic acid was added to the mixture until the pH was 5 and stirred at room temperature for 30 min. CNC (4 wt %) was added to deionized water and mixing with homogenizatör (25,000 rpm) for 5 min. After this process, mixture was sonicated for 30 min. The CNC dispersion was added slowly into the silane mixture under stirring at room temperature. The reaction was stirred for 12 h. After the reaction was completed, ethanol was evaporated and the product was dried in an oven at 50 ^{0}C for 4 days. The dired products were grinded using an agate mortar and washed with ethanol for three times to remove unreacted silane. Finally, the samples were dired in an oven at 80 ^{0}C. This product were prepared as GPTMS / CNC with 5:1 wt/wt and 12 reaction time.

To emerge the silane modification outcomes, Fourier transform infrared spectroscopy (FT-IR) characteristics were evaluated with Jasco™ FT/IR-6700 equipment over 400-4000 cm^{-1} zone at room temperature.In order to reveal the effects of silane treatment on the mechanical properties, only 1% wt. CNC concentration was tested during this study. Experimental preperation steps are given as seen in Figure 1. Epoxy resin (component-A) was firstly mixed with the required amount of CNC powder manually. Dual mixing, which is the combination of sonication and magnetic stirring, was applied to that two-phase solution for about 20-30 minutes subsequently. After the addition of DTS 2110 hardener, the resultant mixture were stirred for 5 minutes and cast into silicon molds for specimen manufacturing. Both tensile and flexural test specimens cured at room temperature for 48 hours and post-curing process was applied at 80 °C for 8 hours.

Two different groups of samples were produced in the context of this study: 1 % wt. neat CNC/epoxy and 1% wt. silanized CNC/epoxy composites. Neat epoxy samples were also produced to compare its mechanical performance with modified and unmodified CNC based composites. Tensile and flexural tests of the whole structures were carried out via Schimadzu™ AG 50 kN universal test system. The crosshead speed of tensile test was determined as 1 mm/min according to ASTM D638-99 standard. The three-point bending apparatus was used for flexural test and based on ASTM D790-03 standard, the respective crosshead speed was determined as 1.5 mm/min. Three samples for each category were evaluated and average values were expressed with standard deviations.

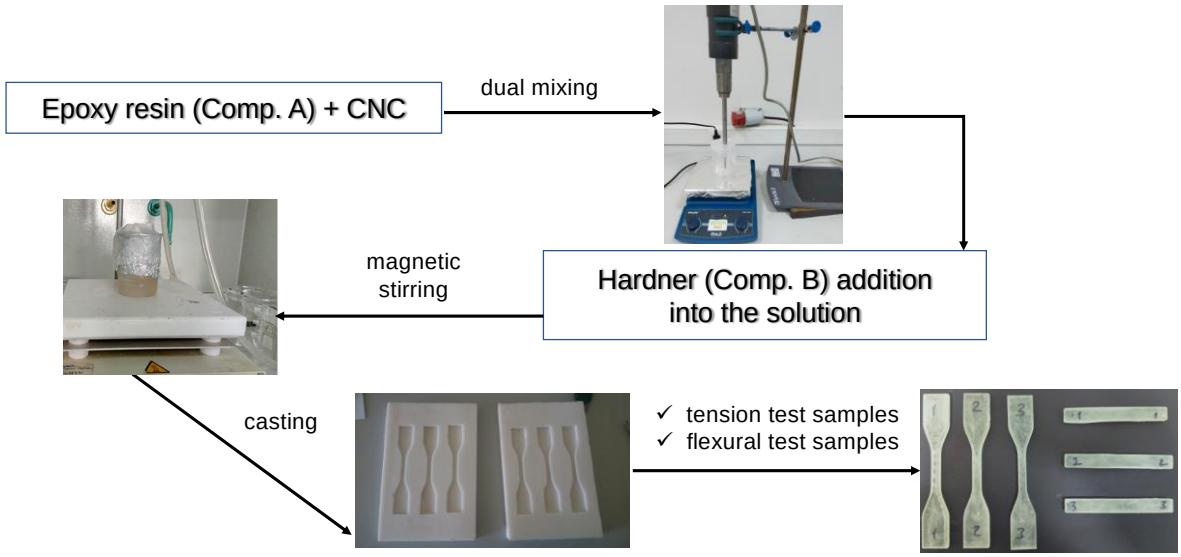


Figure 1. Preparation stages of CNC/epoxy composites

3. Results and Discussions

Structural characterizations of pristine and silanized CNC were performed using attenuated total reflectance-Fourier Transform Infrared Spectroscopy (ATR-FTIR) and shown in Figure 2. The peaks observed around 2871 and 2898 cm^{-1} corresponds to C-H stretching in the spectra of both CNC and treated CNC. There is also a peak at 2933 which belong to C-H stretching in treated CNC. The absorbance peaks in the range 3330-3334 cm^{-1} are attributed to the stretching of the OH groups of cellulose. The decrease in peak intensity indicates that most of the OH groups are silanized. Generally, the spectrum clearly indicates that CNC is successfully treated with GPTMS.

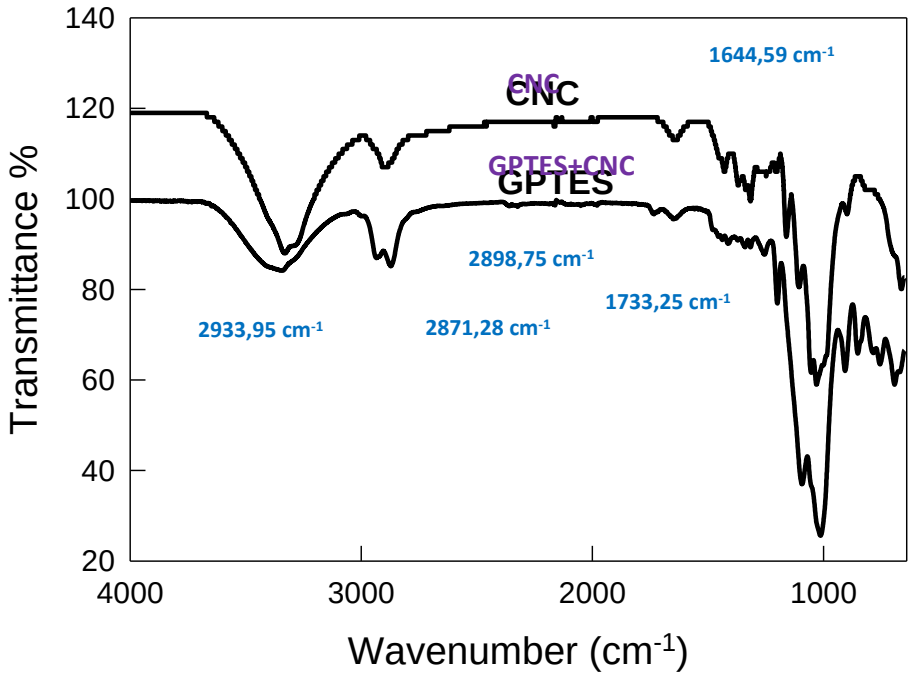
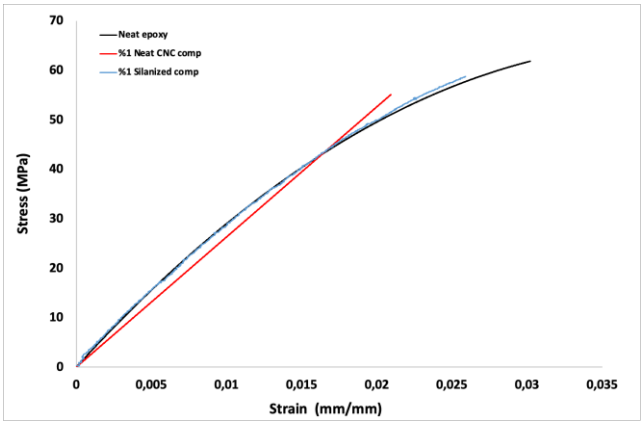
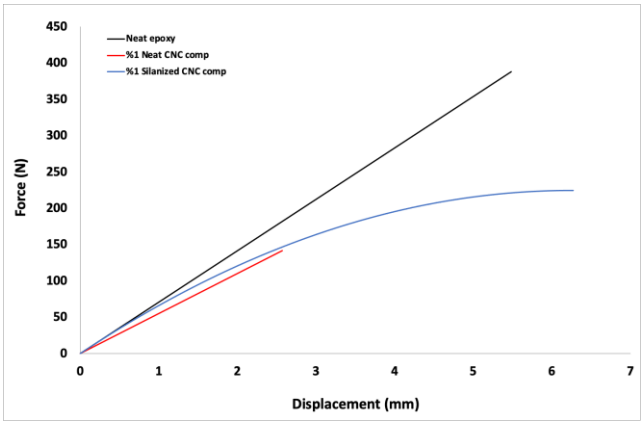


Figure 2. FTIR spectrum of CNC and Silanized CNC

Representative tensile and flexural test graphs of host matrix (epoxy) and prepared composites are shown in Figure 3(a) and 3(b), respectively. The parameters obtained from those tests are also given in Table 1. It is appearent that neat epoxy exhibited a ductile characteristic with a particular plasticity. As seen in Figure 3(a), addition of neat CNC leads to emergence of the brittleness and reduction of ductility while the average ultimate tensile strength (σ_{UTS}) value of composites decreased. Silane tratment promoted the strength magnitude, which is the indication of improved stress transfer between epoxy and CNC. When the average elastic modulus (E) values of three set of samples are compared, it is observed that surface modification negatively influenced that parameter and declined it. Similar type of behavior was also seen in the flexural test results. The presence of silanized CNC caused to 13% decrese of flexural modulus while the neat CNC/epoxy composites just led to the 2% reduction for the same parameter. Flexural strength of silanized CNC/epoxy samples are ~35% higher than the other composite group. However, none of the composites could attain the strength of pure epoxy under out of plane loading.



(a)



(b)

Figure 3. (a) Tension test graph, (b) flexural test graph of neat epoxy and CNC based composites.

Table 1. Mechanical test results of neat epoxy and CNC based composites

Sample ID	**Tensile Strength (MPa)**	**Tensile Modulus (GPa)**	**Flexural Strength (MPa)**	**Flexural Modulus (GPa)**
Neat epoxy	60.8±6.24	3.08±0.22	145.8±16.1	3.58±0.19
%1 neat CNC/epoxy comp.	50.7±10.33	3.05±0.31	83±34.86	3.51±0.24
%1 silanized CNC/epoxy comp.	58.5±3.30	2.77±0.18	125.2±14.07	3.13±0.43

4. Conclusions

In this study, neat CNC and silan treated CNC based polymer composites were successfully manufactured. Epoxy was choosen as the matrix material and the composites were prepared with traditional casting technique. Both tensile and flexural responses of composites were determined and compared with pure epoxy. The modification effect of silane was verified via FT-IR analysis. Based on the test results, it is observed that tensile and flexural strength values of silanized CNC/epoxy composites were higher than unmodified CNC based counterparts. However, modulus values obtained from the same tests decreased with the presence of silane surface agent. Although stress transfer became more effective in the modified composites, stiffness magnitudes slightly reduced and none of the composites could achieve the performance of neat epoxy. This situation can be ascribed to the particle size of modified CNC. It is highly probable that after grinding process, the resultant CNC was no longer a nano-size powder. For that reason, unexpected results obtained from mechanical tests could be attributed to this possibility.

References

[1] S. Eyley, W. Thielemans, "Surface modification of cellulose nanocrystals," *The Royal Society of Chemistry: Nanoscale*. Vol. 6, no. 14, pp. 7764-7779, 2014.

[2] M.A. Azizi Samir, F. Alloin, and A. Dufresne, "A. Review of recent research into cellulosic whiskers, their properties and their application in nanocomposite field," *Biomacromolecules*, vol. 6, no. 2, pp. 612-626, 2005.

[3] A.K. Mohanty, A. Wibowo, M. Misra, and L.T. Drzal, "Effect of process engineering on the performance of natural fiber reinforced cellulose acetate biocomposites," *Composites Part A: Applied Science and Manufacturing*, vol. 37, pp. 363-370, 2004.

[4] R. Díaz de León, E. Guzmán, R. López González, A. Díaz Elizondo, I. Magaña, G. Neira, A. Castañeda Facio, L. Valencia, "Surface modification of cellulose nanocrystals with lactone monomers via plasma-induced polymerization and their application in ABS nanocomposites," *Polymers*, vol. 13, pp. 2699, 2021.

[5] N.R. Nascimento, I.F. Pinheiro, G.F. Alves, L.H.I. Mei, J.C. Macedo Neto, and A.R. Morales, "Role of cellulose nanocrystals in epoxy-based nanocomposites: mechanical properties, morphology and thermal behavior," *Polímeros: Ciência e Tecnologia*, vol. 31 no. 3, 2021.

[6] M. Roszowska-Jarosz, J, Masiewicz, M. Kostrzewa, W. Kucharczyk, W. Zurowski, J. Kuci´nska-Lipka, and P. Przybyłek, "Mechanical properties of bio-composites based on epoxy resin and nanocellulose fibres," *Materials*, https:// doi.org/10.3390/ma14133576, 2021.

[7] H.M. Tizazu, H. Tesfaalem, L. Malin, "Hydrophobic functionalization of cellulose nanocrystals for enhanced corrosion resistance of polyurethane nanocomposite coatings," *Applied Surface Science*, vol. 540, pp. 148299, 2021.

[8] J. Zaihan, R. Rafeadah, M.A. Mohamad Nasir, W.S. Hashim, A. Ishak, "A high strength green nanocomposites based on wood veneer nanocrystalline cellulose and epoxy resin polymer," *Materials Science and Engineering*, vol. 368, pp. 012007, doi:10.1088/1757-899X/368/1/012007, 2018.

About intelligent software system and development method for the intelligent interface

Shafagat MAHMUDOVA[1*]

[1]Institute of Information Technology of ANAS, Baku, Azerbaijan, (ORCID: 0000-0003-1817-0756), shafagat@gmail.com

Abstract

An intelligent software system refers to any software using artificial intelligence to analyze and interpret data or to communicate with systems and people. The article substantiates the relevance of the issue and highlights existing problems. The following factors are taken into consideration when assessing the problems of intelligent software system designing: easy data collection, low cost of developing intelligent systems, availability of experts and necessary resources (computers, program developers, software, etc.). A model is developed for the intelligent interface. The competency of the expert group is formed and evaluated, and experiments are conducted. The results obtained are satisfactory. The developed method can be beneficial for everyone.

Keywords: Software system, Intelligent, Intelligent interface, Expert group.

1. Introduction

Intelligent System (IS) is a creative hardware or software system capable to skillfully solve problems related to a specific subject area, so that knowledge is stored in the memory of such systems. Intelligent systems are explored by a group of scientists called "artificial intelligence". However, many researchers, namely psychologists, educators, point out the negative features (for example, cyber-addiction, etc.) of the application of intelligent systems; they believe that a different type of personality, i.e., a person belonging to the cyber world, is formed being affected by intelligent systems [1].

Intelligent systems also suffer from the security issues of a person's private life and provision of data security. Based on the above, it is possible to draw appropriate conclusions in accordance with the study of theoretical and technological intellectual systems. The purpose of this work is to study the stages, components and technological aspects of intelligent software systems, to analyze the application aspects of intelligent systems. The stages, components, trends, etc. indicated in the conceptual model for the design of intelligent software systems are studied and the characteristics of each of them are determined [2].

Synthesis refers to coordination and construction. The term was first introduced in 1845 by the German scientist Kim Adolf German.

The issue of synthesis in decision-making becomes its part when the alternative variants have a complex multi-element structure; and in this case, the combination of different subdivisions of certain elements occurs in a single variant. Synthesis involves procedures for analyzing solutions. These issues can be classified for many traits [3].

Available approaches to the development of decision support software system are grouped as follows:

- Approaches based on the mathematical methods of decision-making theory and the artificial intelligence;
- Systems building with expert data, mathematical modeling and data structure based on mathematical methods [4].

2. Materials and Method

Creating intelligent systems is a complex process. It consists of many stages. One of the main stages here is the design of intelligent software systems.

Designing intelligent software systems is an iterative and evolutionary process involving a group of experts. This includes creating a system on the subject area, involving specialists with knowledge in the field of artificial intelligence, high-level engineers, analysts and programmers with engineering knowledge. Depending on the size and complexity of the work, the group may involve three to six people [5].

The following factors should be considered when assessing the problems when designing intelligent software systems: easy data collection, the cost of developing intelligent systems, the availability of experts and necessary resources (computers, programmers, software, etc.).

Following the analysis of the problem area and determination of the feasibility of implementing an intelligent system in this area, the system is designed directly [6].

There are different views on determining the number of stages in the design of intelligent systems. This is particularly associated to the functions of future intelligent system, the scope of use, the availability of advanced tools, and so forth.

One of the ways to increase the technical efficiency in solving problems arising when studying the features of software systems is the use of artificial intelligence methods in the design and synthesis of the Intelligent Information Measurement System (IIMS). Optimization of the intelligent decision-making procedures in accordance with the selected criteria to choose the optimal mode parameters of measurements depending on the measurement situation refers the efficiency and accuracy of measurements [7].

The general theory of the basic methodological systems for solving the synthesis problem of the IIMS structure includes the artificial intelligence and fuzzy set methods.

The main goal of solving the synthesis problem of the IIMS structure is to develop a universal structure of the intelligent system and achieve a reliable result, increase the efficiency of the system functionality [8].

The main issues in the ISS synthesis are as follows (Figure 1):

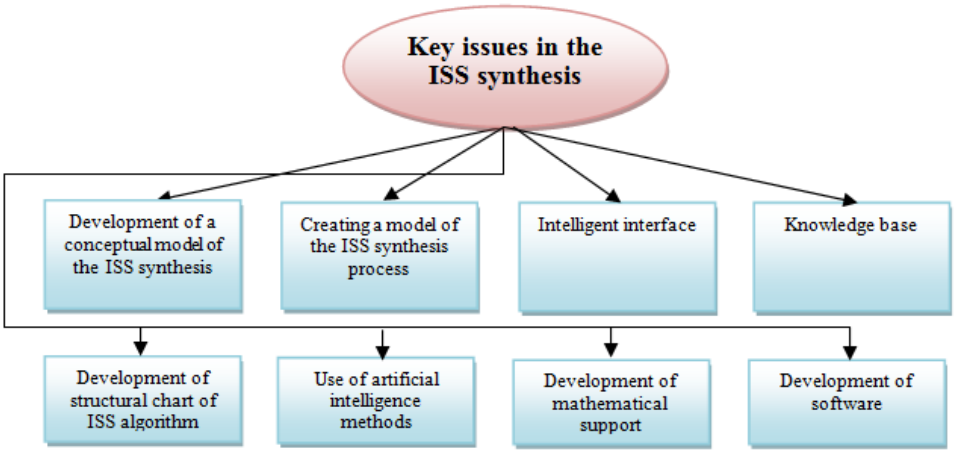


Figure 1. Key issues in the ISS synthesis

3. Conclusions

Designing intelligent software systems is one of the most important issues. The article developed a conceptual model for designing intellectual software systems. The novelty of this work was that the stages required for design and their characteristics were concentrated in the developed model. The synthesis of ISS was concluded to be one of the most pressing issues. The creation and use of such systems saves costs and makes the program run faster and more efficiently. In the future, more efficient results can be achieved using newer technologies.

References

[1] Babak, V.F. and Ryzhenko, I.N. 2002. *Sovershenstvovaniye metodologii proyektirovaniya informatsionnykh sistem.* Moskva: GOU VPO, 2002
[2] Bourque, P. and Fairley, R.E. *Guide to the Software Engineering Body of Knowledge (SWEBOK))*. Los Alamitos: IEEE Computer Society.(http://www.Swebok.org), 2014
[3] Ostroukh, A.V. *Intellektual'nyye sistemy*. Krasnoyarsk: Nauchno-innovatsionnyy tsentr, 2015.
[4] Dolinina, ON., Kushnikov, VA., Pechenkin, VV. and Rezchikov AF. (2019). "The Way of Quality Management of the Decision Making Software Systems Development", *Software engineering and algorithms in intelligent systems*, (https://doi.org/10.1007/978-3-319-91186-1_11)
[5] Mahmudova Sh. "Development of a conceptual model for intelligent software system designing". *Review of information engineering and applications*. vol. 9, no. 1, pp. 12-22, 2022.
[6] "Chto takoye baza znaniy" August. 06, 2022. [Online]. Available: https://www.atlassian.com/ru/itsm/knowledge-management/what-is-a-knowledge-base
[7] T. M. Zubkova, Ye. N. Natochaya. "Proyektirovaniye interfeysa programmnogo obespecheniya s ispol'zovaniyem elementov iskusstvennogo intellekta", Software & Systems, tom 30, № 1, str. 5-11, 2017
[8] Sovetov, B.YA*Modelirovaniye sistem*: M.: Vyssh, 2005.

Susuz Boraks Katkısının Alüminyum Malzemelerin Vickers Sertlik ve İz Modülü Değerlerine Etkisinin İncelenmesi ve Eniyilenmesi

Şenol ŞAHİN[1], Ayşegül BODUR YILMAZ[2*], Orçun YÖNTEM[3]

[1] Kocaeli Üniversitesi, Mühendislik Fakültesi, Makina Mühendisliği Bölümü, Kocaeli, Türkiye, (ORCID: 0000-0002-7823-2245), sensah@kocaeli.edu.tr

[2*] Kocaeli Üniversitesi, Fen Bilimler Enstitüsü, Makina Mühendisliği A.B.D., Kocaeli, Türkiye, (ORCID: 0000-0003-1456-1282), aysegul.bodur@kocaeli.edu.tr

[3] Kocaeli Üniversitesi, Fen Bilimleri Enstitüsü, Makine Mühendisliği A.B.D., Kocaeli, Türkiye – Toyotetsu Otomotiv, (ORCID: 0000-0001-7149-9169), yontemo@toyotetsu.com.tr

Öz

Bu çalışmada matris malzemesi olarak hafifliği, dayanımı ve fonksiyonel olması özellikleriyle ön plana çıkan alüminyum malzemesi (Al) ve katkı malzemesi olarak ise bor mineralinin bir çeşidi olan susuz boraks (SB) maddesi kullanılarak alüminyum matrisli kompozit malzeme üretimi gerçekleştirilmiştir. Bu kapsamda alüminyum malzemenin Vickers sertlik ve İz modülü değerlerini artırmak için farklı ağırlıkça oranlarda susuz boraks farklı alüminyum serileri ile karıştırılarak toz metalurjisi yöntemiyle üretilmiş ve deney tasarım yöntemiyle kompozit malzemenin sertlik ve iz modülü değerlerinin eniyilemesi çalışması gerçekleştirilmiştir. Taguchi deney tasarım yöntemi kullanılarak gerçekleştirilen çalışmada kompozit malzeme özelliklerine etkisi olduğu düşünülen alüminyum serisi (saf, 1050, 5754), susuz boraks katkı oranı (%1, %2.5, %5), sinterleme sıcaklığına ısıtma hızı (5°C/dak, 10°C/dak, 20°C/dak) ve sinterleme sıcaklığında bekleme süresi (5dak, 10dak, 20dak) kontrol faktörleri olarak seçilmiş ve bu faktörlerin üç seviyesine bağlı olarak Taguchi L9 ortogonal deney dizini oluşturularak kompozit malzeme üretimleri gerçekleştirilmiştir. Al/SB kompozit malzemelerin BS EN ISO 14577-1 standardına göre Vickers sertliği (HV) ve İz modülü (E_{IT}) değerleri ölçümleri gerçekleştirilerek faktör ve seviyelerinin etkileri araştırılmıştır.

Anahtar Kelimeler: Alüminyum, İz Modülü, Susuz Boraks, Sertlik, Toz Metalurjisi

Investigation and Optimization of the Effect of Anhydrous Borax Additive on the Vickers Hardness and Indentation Modulus Values of Aluminum Materials

Abstract

In this study, aluminum material (Al), which stands out with its lightness, strength and functional properties, was used as the matrix material and anhydrous borax (SB), a type of boron mineral, was used as an additive material to produce aluminum matrix composite material. In this context, to increase the Vickers hardness and indentation modulus of the aluminium material, anhydrous borax was mixed with different aluminium series in different weight ratios and produced by powder metallurgy, and the optimisation of the hardness and indentation modulus values of the composite material was carried out by the design of experiments method. In the study carried out

using Taguchi experimental design method, aluminum series (pure, 1050, 5754), anhydrous borax additive ratio (1%, 2.5%, 5%), heating rate to sintering temperature (5ºC/min, 10ºC/min, 20ºC/min) and waiting time at sintering temperature (5min, 10min, 20min), which are considered to have an effect on composite material properties, were selected as control parameters, and composite material productions were carried out by creating Taguchi L9 orthogonal array depending on three levels of these parameters. Vickers hardness and Indentation modulus values of Al/SB composite materials were measured according to BS EN ISO 14577-1 standard and the effects of factors and levels on composite material properties were investigated.

Keywords: Aluminium, Anhydrous Borax, Indentation Modulus, Hardness, Powder Metallurgy

1. Giriş

Kompozitler, en az iki farklı malzemenin bir araya gelmesiyle oluşan, matris ve takviye olarak adlandırılan bileşenlerin bir arayüz oluşturarak bir araya geldiği ve tek bir malzeme gibi davrandığı ileri teknolojik malzeme grubudur. Teknoloji geliştikçe malzemelerden beklenen özellikler de değişmiş ve birçok sektörde yüksek kimyasal ve mekanik dayanıma sahip ancak hafif malzemelere olan talebin artması kompozitlere olan ilgiyi artırmıştır [1,2].

Hafifliğin giderek önem kazandığı otomotiv sektöründe alternatif malzeme arayışlarıyla birlikte alüminyum malzemelere yönelim başlamış ve mekanik özellikleri iyileştirmek için alüminyumun matris olarak kullanıldığı metal matrisli kompozitler tercih edilmeye başlanmıştır [3,8]. Metal matrisli kompozitlerin üretiminde tercih edilen takviye malzemeleri, iyi mekanik özelliklere ve yüksek sertlik değerlerine sahip seramik malzemelerdir. Metal matrisli kompozitlerin üretiminde tercih edilen bir diğer önemli takviye malzemesi olan bor karbür (B_4C), elmas ve kübik bor nitrürden (cBN) sonra bilinen en sert malzemedir [4]. Yüksek erime sıcaklığına, kimyasal kararlılığa ve yüksek sertlik değerlerine sahip B_4C minerali, düşük yoğunluk değerlerine ve iyi mukavemet özelliklerine sahip bir alüminyum matris içinde kullanarak yüksek mukavemet ve iyi aşınma özelliklerine sahip bir kompozit malzeme geliştirmek amaçlanmaktadır [5, 6]. Özellikle otomotiv, havacılık ve savunma gibi sektörler hem hafif hem de rijit malzemelere ihtiyaç duymaktadır. Ancak üretimde kullanılan malzemeler beklenen performansı göstermediğinde üretim verimsizlikleri, kalite sorunları ve sonuç olarak müşteri memnuniyetsizliği gibi durumlar kaçınılmaz olarak ortaya çıkmaktadır. Bu kapsamda hem beklenen malzeme özelliklerini hem de ürün kalitesini artırmak için geliştirilen farklı yöntemler mevcuttur. 1980'den sonra özellikle ürün geliştirmede kullanılan Taguchi yöntemi, yapılan deneysel çalışmaları tasarlayarak en az süre, maliyet ve enerji ile en fazla bilgiyi elde etmek için geliştirilmiş yöntemlerden biridir. Birçok farklı üretim ortamında optimum üretim koşullarının yaratılmasında, özellikle de daha az denemeyle daha etkili sonuçlar elde edilmesinde etkili bir araç olduğu kanıtlanmıştır [7].

Bu çalışmada matris malzemesi olarak alüminyum (Al) ve katkı malzemesi olarak ise bor mineralinin bir çeşidi olan susuz boraks (SB) maddesi kullanılarak alüminyum matrisli kompozit malzeme üretimi gerçekleştirilmiştir. Nihai ürünün (kompozit malzemenin) mekanik özelliklerine, SB katkı oranının ve üretim parametrelerinin etkileri birlikte değerlendirilerek, Vickers sertliğini ve İz modülünü artırmaya yönelik en etkili katkı oranının ve üretim parametrelerinin saptanması ve Alüminyum/Susuz boraks (Al/SB) kompozit malzeme geliştirilmesi amaçlanmıştır. Zaman ve maliyetten tasarruf edebilmek için ise araştırmada deneysel çalışma tam faktöriyel deney düzeneği yerine Taguchi deneysel tasarım yöntemi ile gerçekleştirilmiş ve elde edilen Taguchi ortogonal dizine göre toz metalurjisi yöntemiyle Al/SB kompozitlerin üretimleri gerçekleştirilmiştir.

2. Materyal ve Metod

2.1. Alüminyum Serileri

Kompozit malzemelerin üretimi için matris malzemesi olarak, 2.70 g/cm^3 yoğunluk ve 660ºC ergime sıcaklığına sahip saf alüminyum (%99.8 Al), 2.80 g/cm^3 yoğunluk ve 640ºC ergime sıcaklığına sahip 1050 serisi

ve 2.66 g/cm^3 yoğunluk ve 568ºC ergime sıcaklığına sahip 5754 serisi Al malzemeler, elek altı 1.8 mm tane boyutlarında kullanılmıştır.

2.2. Susuz Boraks

Kompozit malzemelerin üretimi için katkı malzemesi olarak, Eti Maden A.Ş.'den temin edilen, yoğunluğu 2,37 g/cm^3 ve ergime sıcaklığı 742,5ºC olan ticari ismi Etibor-68 ($Na_2B_4O_7$) minerali öğütülerek, elek altı 20 µm tane boyutlarında kullanılmıştır.

2.3. Taguchi Deney Tasarım Yönteminin Uygulanması

Üretilen kompozitlerin Vickers sertlik ve İz modülü değerlerini eniyilemek ve üretim parametrelerinin optimum seviyelerini belirlemek için Taguchi deneysel tasarım yöntemi kullanılmıştır. Toz metalurjisi yöntemiyle üretilen ürünün kalitesini ve mekanik özelliklerini etkilediği düşünülen kontrol faktörleri (parametreleri) ve her bir faktör için ise üç farklı seviye belirlenmiştir. Kontrol faktörü olarak belirlenen üretim parametrelerine ek olarak, SB katkı maddesinin farklı yüzde ağırlık oranlarının da etkisini araştırmak için, SB katkı oranı da kontrol faktörü olarak belirlenmiştir (bkz. Tablo 1).

Tablo 1. Kontrol faktörleri ve seviyeleri

Faktörler		**Seviye 1**	**Seviye 2**	**Seviye 3**
Malzeme (Al serisi)	A	Saf Al	1050	5754
SB oranı (% ağırlık)	B	1	2.5	5
600ºC sinterleme sıcaklığına ısıtma hızı (ºC/dak)	C	5	10	20
600 ºC sinterleme sıcaklığında bekleme süresi (dak)	D	5	10	20

Belirlenen faktör ve seviyelerine bağlı olarak Taguchi L9 ortogonal dizisi seçilmiş (bkz. Tablo 2) ve üretimler ortogonal diziye uygun olarak gerçekleştirilmiştir. Her bir deney düzeneği için en az 3 adet numune üretilmiş ve numuneler üzerinden 5 farklı ölçüm alınarak Vickers sertlik değeri ve iz modülü değerleri belirlenmiştir.

Vickers sertliği ve iz modülü değerlerinin ölçümlerinin ardından elde edilen deneysel veriler kullanılarak bu değerleri eniyileyen parametreleri belirlemek için ''en büyük en iyi'' (bkz. Denklem 1) yöntemine uygun olarak sinyal/gürültü (S/G) oranları incelenmiştir.

$$S/G = -10 \cdot \log\left(\frac{1}{n}\sum_{i=1}^{n}\frac{1}{yi^2}\right) \quad (1)$$

Burada y_i = ölçülen i. gözlem değerini, n = gözlem sayısını temsil etmektedir.

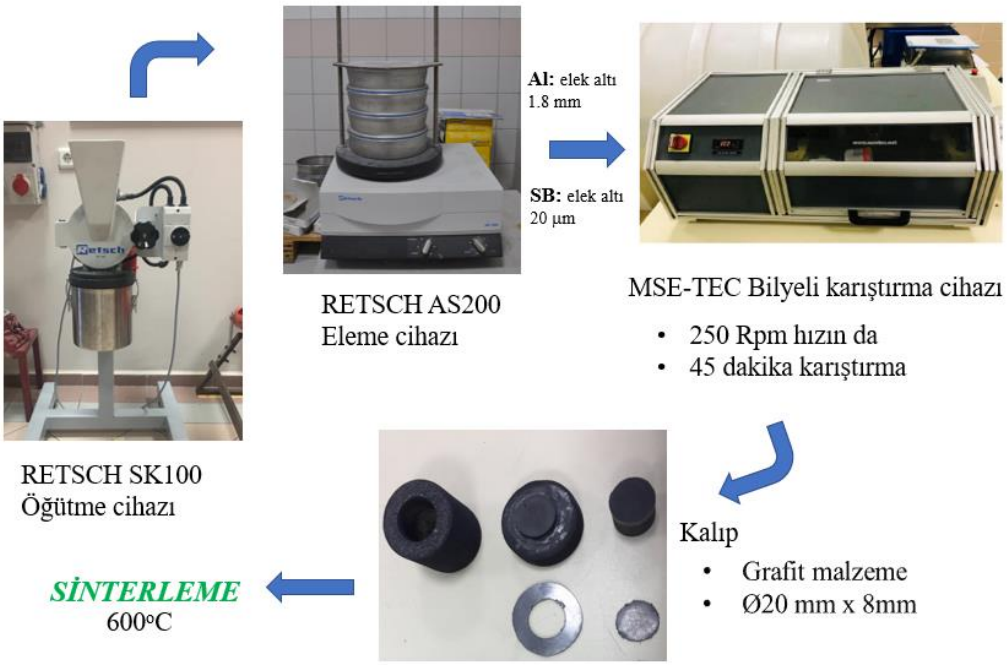
Ayrıca belirlenen faktörlerin her bir yanıt değişkeni üzerindeki anlamlılık değeri (P değeri) ve etki yüzdeleri varyans analizi (ANOVA) ile belirlenmiştir.

Tablo 2. L9 Ortogonal dizi için deneysel koşullar

Deney numarası	Faktörler			
	Malzeme (Al serisi)	SB oranı (% ağırlık)	Isıtma hızı (°C/dak)	Bekleme süresi (dak)
1	Saf	1	5	5
2	Saf	2.5	10	10
3	Saf	5	20	20
4	1050	1	10	20
5	1050	2.5	20	5
6	1050	5	5	10
7	5754	1	20	10
8	5754	2.5	5	20
9	5754	5	10	5

2.4. Kompozit Malzeme Üretimi

Üretim öncesi gerçekleştirilen ön hazırlık aşamasında (bkz. Şekil 1) alüminyum malzemeler ve SB ayrı ayrı olacak şekilde önce tane boyutlarını küçültmek için RETSCH marka SK100 model cihazda öğütme, ardından numuneleri tane boyutlarına göre ayırmak için RETSCH marka AS200 model cihazda eleme işlemine tabi tutulmuşlardır. Farklı yüzde ağırlık oranında Al/SB kompozit karışımlar, homojen bir karışım elde etmek için, MSE-TEC marka karıştırma cihazı kullanılarak içinde nikel bilye bulunan cam kavanoz içerisinde, devir hızı 250 rpm ve karıştırma süresi 45 dakika olan karıştırma parametrelerinde hazırlanmıştır. Ardından Al/SB kompozit malzemeleri, DIEX marka VS50 model indüksiyon fırınında, iç çapı 20 mm olan grafit kalıpta hem sabit 50 MPa uygulama basıncı (sıkıştırma) altında hem de sabit 600°C sinterleme sıcaklığında fakat farklı sinterleme sıcaklığına ısıtma hızlarında ve farklı sinterleme sıcaklığında bekleme sürelerinde elde edilmiştir.



Şekil 1. Kompozit malzeme üretimi ön hazırlık aşamaları

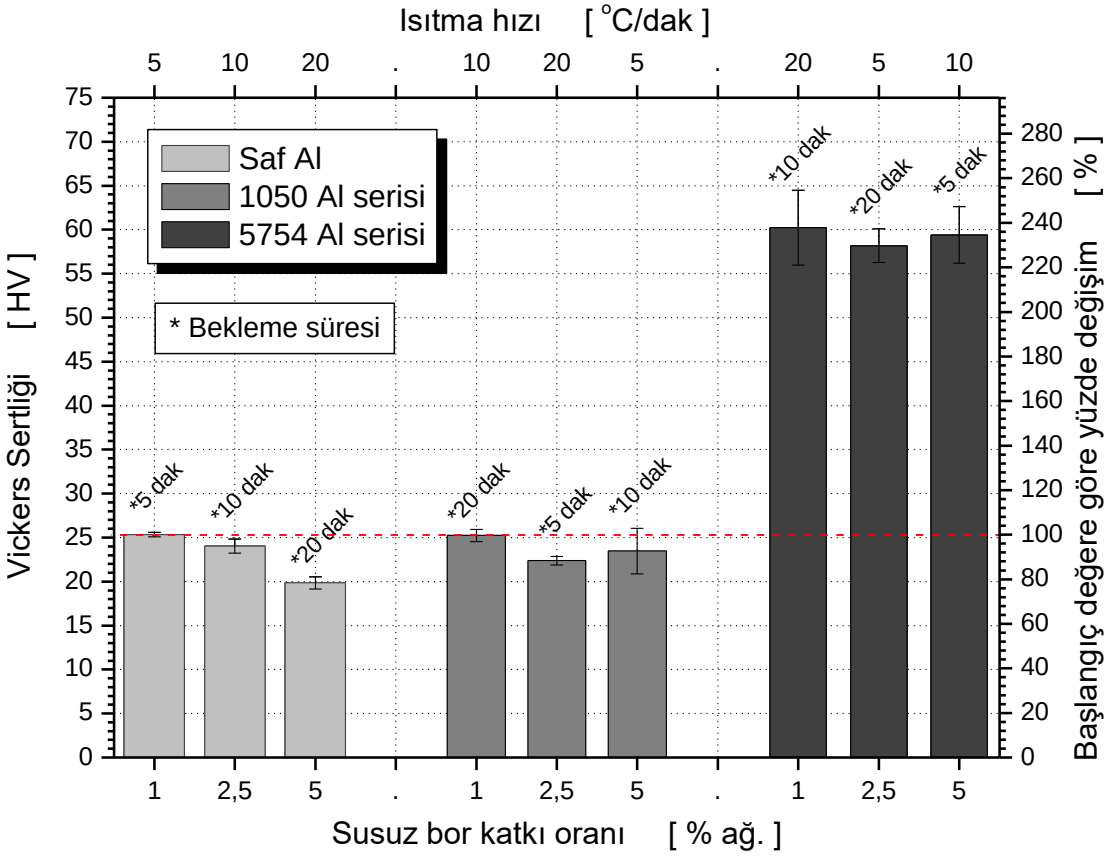
2.5. Vickers Sertlik ve İz Modülü Ölçümü

Vickers sertlik ve İz modülü testleri 1 kg yük altında BS EN ISO 14577-1-2015 standardına göre Tübitak Ulusal Metroloji Enstitüsünde bulunan Zwick BZ2.5/TS1S marka enstrümente sertlik ölçme cihazında, her bir grup için 5'er adet tekrarlı ölçüm olacak şekilde gerçekleştirilmiştir.

3. Bulgular ve Tartışma

3.1. Vickers Sertlik Değeri

Elde edilen deneysel veriler kullanılarak oluşturulan, kompozit malzemelerin Vickers Sertlik değerleri karşılaştırmalı olarak Şekil 2'de grafikleştirilmiştir. Şekil 2 incelendiğinde ağırlıkça %1 SB katkılı 5754 serisi kullanılarak üretilen kompozit malzemenin sertlik değerinin referans olarak belirlenen ağırlıkça %1 SB katkılı saf Al malzemeye kıyasla yaklaşık %130 daha yüksek olduğu tespit edilirken SB katkı oranının, farklı alüminyum serileri kendi arasında incelediğinde, Vickers sertlik değeri üzerinde kayda değer bir etki göstermediği görülebilmektedir.

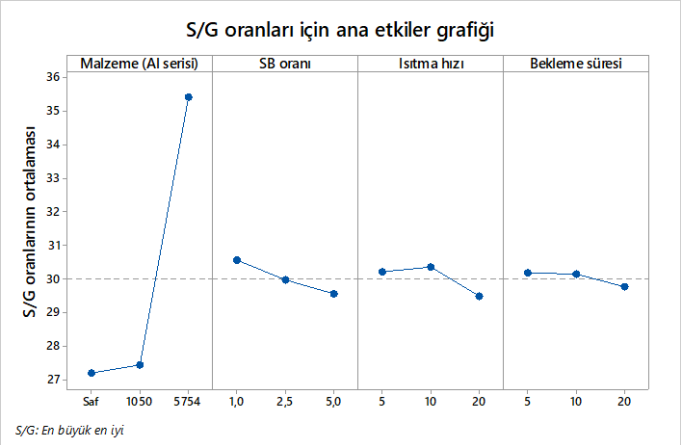


Şekil 2. Al/SB kompozit malzemelerin Vickers sertlik değerleri değişim grafiği

S/G oranı tablosu (bkz. Tablo 3) ve grafiği (bkz. Şekil 3) incelendiğinde Vickers sertliği üzerinde en etkili parametrenin en büyük fark değerine sahip faktör olan Malzeme (Al serisi) olduğu belirlenmiştir. Diğer faktörler incelendiğinde ise sırasıyla etki sırasına göre SB oranı, ısıtma hızı ve bekleme süresi faktörlerinin etkili olduğu tespit edilmiştir. Vickers sertlik değerini eniyileyen (en yüksek yapan) faktör seviyeleri ise 5754 serisi, %1 SB oranı, 10°C/dak ısıtma hızı ve 5dak bekleme süresi olduğu belirlenmiştir.

Tablo 3. Al/SB kompozitlerin Vickers sertlik değerleri S/G oranları yanıt tablosu

Seviye	Malzeme (Al Serisi)	Susuz bor	Isıtma hızı	Bekleme süresi
1	27,20	**30,55**	30,21	**30,17**
2	27,43	29,96	**30,36**	30,14
3	**35,42**	29,55	29,49	29,75
Fark	8,22	1,00	0,87	0,42
Sıra	1	2	3	4



Şekil 3. Al/SB kompozitlerin Vickers sertlik değerleri S/G oranları ana etkiler grafiği

Vickers sertlik değeri için %95'lik bir güven düzeyi ile gerçekleştirilen ANOVA sonuçları verilen Tablo 4 incelendiğinde bekleme süresi faktörü (P>0,05) dışındaki diğer faktörlerin P değerlerinin 0,05'ten küçük olması nedeniyle Vickers sertliği üzerinde önemli bir etkiye sahip olduğu belirlenmiştir. Ayrıca malzeme (Al serisi) faktörünün Vickers sertlik değeri üzerindeki toplam etkinin %97.91'ini oluşturduğu da tespit edilmiştir.

Varyans analizi sonrası elde edilen regresyon denklemi aşağıda verilmiş olup, modelin R^2 değeri ise Tablo 5'te bulunmaktadır. %98.77 çıkan R^2 değeri, seçilen kontrol faktörlerinin kompozit malzemenin Vickers sertlik değerindeki değişimi açıklamak için uygun ve yeterli olduğunu göstermektedir.

Tablo 4. Al/SB kompozitlerin Vickers sertlik değerleri için ANOVA

Faktörler	Serbestlik Derecesi (DF)	Kareler Toplamı (SS)	Etki yüzdesi (%)	F-Değeri	P-Değeri
Malzeme (Al serisi)	2	12883,0	**97,91**	1429,90	0,000
SB Oranı (%)	2	59,7	0,45	6,63	0,004
Isıtma hızı (°C/dak)	2	34,2	0,26	3,80	0,032
Bekleme süresi (dak)	2	19,6	0,15	2,17	**0,129**
Hata	36	162,2	1,23		
Toplam	44	13158,7	100,00		

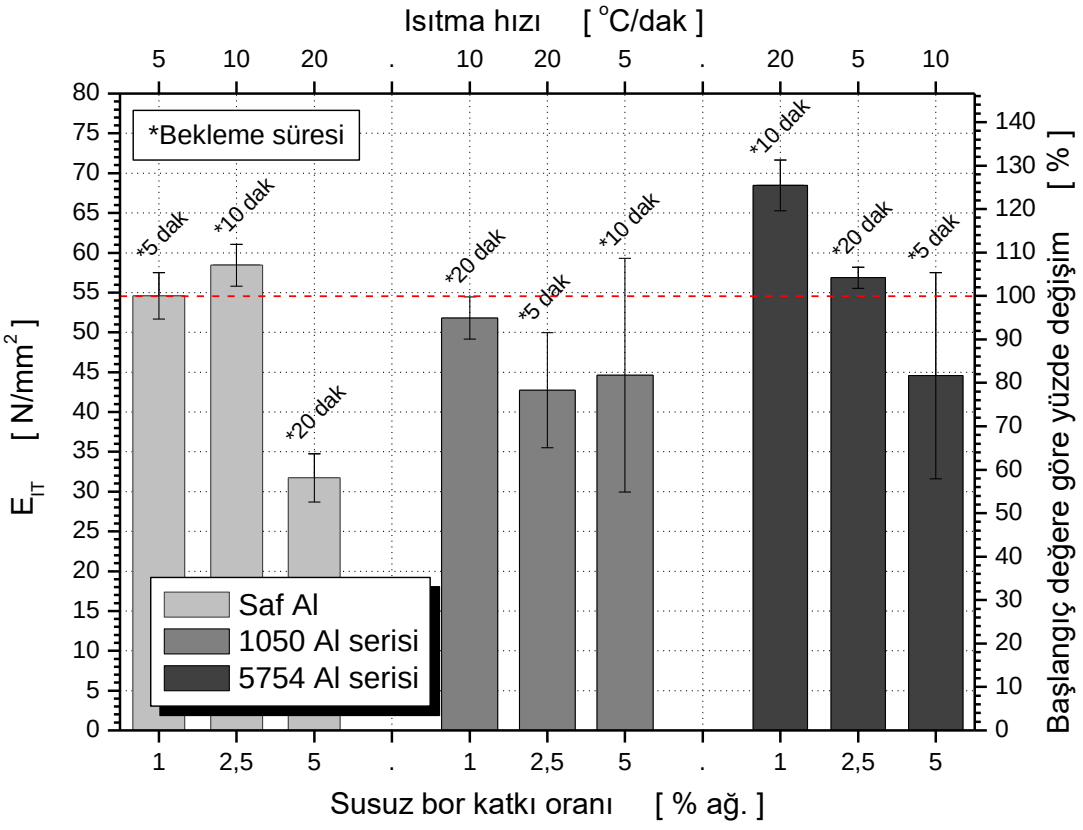
Vickers Sertlik Regresyon Denklemi = 35,341 - 12,277 Malzeme (Al serisi)_Saf - 11,649 Malzeme (Al serisi)_1050 + 23,926 Malzeme (Al serisi)_5754 + 1,589 SB oranı_1,0 - 0,485 SB oranı_2,5 -1,104 SB oranı_5,0 + 0,317 Isıtma hızı_5 + 0,874 Isıtma hızı_10 - 1,191 Isıtma hızı_20 + 0,356 Bekleme süresi_5 + 0,569 Bekleme süresi_10 - 0,925 Bekleme süresi_20

Tablo 5. Model Özeti

R-sq	R-sq (adj)	R-sq(pred)
%98,77	%98,49	%98,07

3.2. İz Modülü Değeri

Elde edilen deneysel veriler kullanılarak oluşturulan, kompozit malzemelerin İz modülü değerleri karşılaştırmalı olarak Şekil 4'te grafikleştirilmiştir. Şekil 4 incelendiğinde %1 SB katkılı 5754 serisi kullanılarak üretilen kompozit malzemenin iz modülü değerinin referans olarak belirlenen %1 SB katkılı saf Al malzemeye kıyasla yaklaşık %25 daha yüksek olduğu tespit edilirken SB katkı oranının, farklı alüminyum serileri kendi arasında incelediğinde, iz modülü üzerinde önemli bir etkiye sahip olduğu görülebilmektedir.



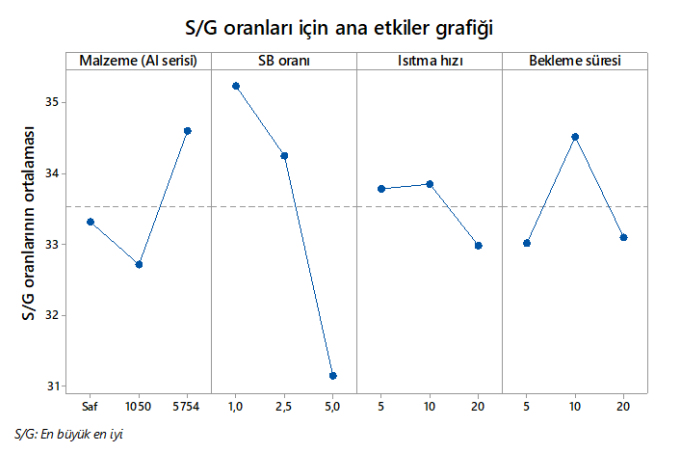
Şekil 4. Al/SB kompozitlerin İz modülü değerleri değişim grafiği

S/G oranı tablosu (bkz. Tablo 6) ve grafiği (bkz. Şekil 5) incelendiğinde İz modülü üzerinde en etkili parametrenin en büyük fark değerine sahip faktör olan SB oranı olduğu belirlenmiştir. Diğer faktörler

incelendiğinde ise sırasıyla etki sırasına göre malzeme (Al serisi), bekleme süresi ve ısıtma hızı faktörlerinin etkili olduğu tespit edilmiştir. İz modülü değerini eniyileyen (en yüksek yapan) faktör seviyeleri ise 5754 serisi, %1 SB oranı, 10°C/dak ısıtma hızı ve 10 dak bekleme süresi olduğu belirlenmiştir.

Tablo 6. Al/SB kompozitlerin İz Modülü S/G oranları yanıt tablosu

Seviye	Malzeme (Al Serisi)	SB Oranı	Isıtma hızı	Bekleme süresi
1	33,32	**35,22**	33,78	33,00
2	32,71	34,25	**33,85**	**34,51**
3	**34,58**	31,14	32,98	33,09
Fark	1,88	4,08	0,86	1,50
Sıra	2	1	4	3



Şekil 5. Al/SB kompozitlerin İz Modülü S/G oranları ana etkiler grafiği

İz modülü için %95'lik bir güven düzeyi ile gerçekleştirilen ANOVA sonuçları verilen Tablo 7 incelendiğinde ısıtma hızı faktörü (P>0,05) dışındaki diğer faktörlerin P değerlerinin 0,05'ten küçük olması nedeniyle İz modülü üzerinde önemli bir etkiye sahip olduğu belirlenmiştir. Ayrıca SB oranı faktörünün İz modülü üzerindeki toplam etkinin %38.72'sini oluşturarak en yüksek etkiye sahip olduğu da tespit edilmiştir.

Tablo 7. Al/SB kompozitlerin İz Modülü için ANOVA

Faktörler	Serbestlik Derecesi (DF)	Kareler Toplamı (SS)	Etki yüzdesi (%)	F-Değeri	P-Değeri
Malzeme (Al serisi)	2	894,00	13,65	8,40	0,001
SB Oranı (%)	2	2536,60	**38,72**	23,83	0,000

Isıtma hızı (°C/dak)	2	176,10	2,69	1,65	**0,205**
Bekleme süresi (dak)	2	1028,70	15,70	9,66	0,000
Hata	36	1916,00	29,25		
Toplam	44	6551,40	100,00		

Varyans analizi sonrası elde edilen regresyon denklemi aşağıda verilmiş olup, modelin R^2 değeri ise Tablo 8'de bulunmaktadır. %70.75 çıkan R^2 değeri, kompozit malzemenin İz modülü değerinin değişimi için seçilen kontrol faktörlerinin yanı sıra farklı faktörlerin de etkili olduğunu ve/veya yapılan deney sayısını artırmak gerektiğini göstermektedir.

İz Modülü Regresyon Denklemi = 50,42 - 2,18 Malzeme (Al serisi)_Saf - 4,04 Malzeme (Al serisi)_1050+ 6,21 Malzeme (Al serisi)_5754 + 7,86 SB oranı_1,0 + 2,26 SB oranı_2,5 - 10,11 SB oranı_5,0 - 3,13 Bekleme süresi_5 + 6,76 Bekleme süresi_10 - 3,63 Bekleme süresi_20 + 1,60 Isıtma hızı_5 + 1,18 Isıtma hızı_10 - 2,79 Isıtma hızı_20

Tablo 8. Model Özeti

R-sq	R-sq (adj)	R-sq(pred)
%70,75	%64,26	%54,30

4. Sonuçlar

Vickers sertlik değerini ve İz modülünü birlikte eniyileyen parametrelerin sırasıyla 5457 alüminyum serisi, %1 SB katkı oranı, 10°C/dak sinterleme sıcaklığına ısıtma hızı ve 10 dak sinterleme sıcaklığında bekleme süresi olduğu tespit edilmiştir.

Farklı Al serisi malzemeler kullanılarak üretilen Al/SB kompozitlerin Vickers sertlik değerinin;

- İlave edilen SB katkısından kısmen etkilendiği,
- En etkili faktörün malzeme (Al serisi) olduğu,
- Sinterleme sıcaklığına ısıtma hızının ise bir etkisinin olmadığı,
- Saf malzemeye kıyasla (%1 SB), 5754 Al serisi ile yapılan üretimin (%1 SB) Vickers sertlik değerinin yaklaşık %130 daha yüksek olduğu tespit edilmiştir.

Farklı Al malzemeler kullanılarak üretilen Al/SB kompozitlerin İz modülü değerinin;

- İlave edilen SB katkısından güçlü oranda etkilendiği,
- En etkili faktörün SB katkı oranı olduğu,
- Sinterleme sıcaklığında bekleme süresinin ise bir etkisinin olmadığı,
- Saf malzemeye kıyasla (%1 SB), 5754 Al serisi ile yapılan üretimin (%1 SB) İz modülü değerinin yaklaşık %25 daha yüksek olduğu tespit edilmiştir.

İlgili konudaki gelecekte yapılabilecek çalışmalarda; susuz boraks partikül boyunun azaltılması/artırılması ve SB katkı oranlarının azaltılması/artırılması ve farklı üretim parametrelerinin de etkisinin incelenmesi önerilmektedir.

5. Teşekkür

Bu çalışma Kocaeli Üniversitesi, Fen bilimleri Enstitütsü, Makine Mühendisliği Anabilim Dalı, Yükseköğretim Kurulu (YÖK) 611576 tez numaralı, "*Toz metalurjisi ile üretilen alüminyum matrisli kompozitlerde bor minerali ilavesinin mekanik özelliklere etkisinin deneysel tasarım yöntemleri ile incelenmesi*" isimli yüksek lisans tezi kapsamında hazırlanmıştır.

Kaynaklar

[1] Petersson, H., "Carbon Fiber Composite Materials in Modern Day Automotive Production Lines: A Case Study", Proceedings of the ASME 2013 International Mechanical Engineering Congress & Exposition IMECE2013, San Diego, California, USA, 2013.

[2] V. V. Reddy, R. K. Mandava, V. R. Rao, S. Mandava, "Optimization of dry sliding wear parameters of Al 7075 MMC's using Taguchi method", Materials Today: Proceedings vol 62, pp. 6684–6688, 2022

[3] D. Uzun, "Alüminyum Matrisli Bor Karbür Takviyeli Sermet Kompozit Malzeme Üretimi Ve Karakterizasyonu", Gazi Üniversitesi, Fen Bilimleri Enstitüsü, Yüksek Lisans Tezi, Ankara, 2011.

[4] E. Karaçay, "Bor Karbür Üretimi ve Karakterizasyonu", Gazi Üniversitesi, Fen Bilimleri Enstitüsü, Yüksek Lisans Tezi, Ankara, 2008.

[5] K. Shirvanimoghaddam, "Boron Carbide Reinforced Aluminium Matrix Composite:Physical, Mechanical Characterization And Mathematical Modelling", *Materials Science and Engineering*, Vol. 658, pp.135-149, 2016

[6] A.A. K. Sai, M.Chandrasekaran, T.V.Kumar, R.Pugazhenthi, "Study the enhanced mechanical properties of Al/B4C metal matrix composite", *Materials Today: Proceedings*, doi.org/10.1016/j.matpr.2022.06.465, April 2022

[7] A. Bodur., Ş. Şahin. ve Y. Şahin, "Polipropilen Talk/Kolemanit Hibrit Kompozit Malzemelerin Eğilme Mukavemetinin Deneysel Tasarım Yöntemi İle Eniyilenmesi", 3. Uluslararası Mühendislik Mimarlık ve Tasarım Kongresi, Başiskele, Kocaeli, Türkiye, 2018

[8] Ş. Şahin, A. Bodur Yılmaz, "Basınçsız Döküm Yönteminin Susuz Boraks Katkılı Alüminyum Alaşımlı Kompozit Malzemenin Mekanik Özelliklerine Etkisinin İncelenmesi" 10th International Automotive Technologies Congress OTEKON 2020, Bursa, Türkiye, 6-7 Septebmer 2021

[9] S.K. Tamang, D. Devi, M. Seenivasan, N. Gopalsamy, "Optimization of surface roughness using Taguchi technique for aluminium metal matrix composite", *Materials Today: Proceedings* vol. 62, pp 2029–2033, 2022

The Effect of Steel Strip on Dynamic Parameters of Steel Structure

Furkan Günday[1*]

[1*] Giresun Üniversitesi, Mühendislik Fakültesi, İnşaat Mühendisliği Bölümü, Giresun, Türkiye, (ORCID: 0000-0003-2979-9373), furkan.gunday@giresun.edu.tr

Öz

Depremlerin yapılar üzerindeki yıkıcı etkileri bilinmektedir. Ayrıca çevresel etkilerin ve titreşimlerin zararlı etkileri de göz ardı edilmemelidir. Bu gereksinimlerinde yapı tasarımlarında değişiklik ve gelişmelere neden olduğu bilinmektedir. Yapıyı etkileyecek etkileri en aza indirmek için çeşitli çalışmalar ve uygulamalar mevcuttur. Çelik yapılar geçmişten günümüze popüleritesini arttırmış bir yapı türüdür. Özellikle homojen malzeme yapısı ile depreme dayanıklı yapı tasarımında çelik yapı ön plana çıkmaktadır. Ancak çelik yapılarda bu gibi olumsuz etkilere bağlı olarak güçlendirme ihtiyacı ortaya çıkabilir veya tasarım zorlukları olabilir. Bu durumda daha az kütle ile daha fazla yük taşıma prensibine bağlı kalabilmek için çelik şeritlerle güçlendirme yönteminin kullanılması daha mantıklı düşünülebilir. Çelik şeritlerle güçlendirme yönteminin yapı üzerine nispeten küçük bir kütle artışı ile yapının rijitliğini arttırdığı birçok çalışmada kanıtlanmıştır. Bu çalışmada, sonlu elemanlar yöntemi kullanılarak modal analiz yapılarak örnek model bir çelik yapıda çelik şerit takviyesinin etkileri ortaya konmuştur. Özellikle ilk 5 modun yapı titreşim periyotları ve serbest titreşim modu şekilleri detaylı olarak ele alınmıştır. Böylece çelik şerit kullanımının çelik yapının rijitliğine olumlu etkisi daha net bir şekilde ortaya konmuştur. Tüm bu çalışmalar sonucunda çelik yapılarda çelik şerit ile güçlendirme yönteminin kullanılabilirliği öngörülmüştür.

Anahtar Kelimeler: Çelik yapılar, Çelik şerit, Sonlu elemanlar metodu, Dinamik parametreler, Güçlendirme

The Effect of Steel Strip on Dynamic Parameters of Steel Structure

Abstract

The destructive effects of earthquakes on structures are known. In addition, the harmful effects of environmental vibration and effects should not be ignored. This requirement is known to cause changes and developments in building designs. There are various studies and applications to minimize the effects that will affect the structure. Steel structures are a type of building that has increased its popularity from past to present. Especially with its homogeneous material structure, steel structure comes to the fore in earthquake resistant building design. However, in steel structures, depending on the effects, the need for reinforcement may arise or there may be design difficulties. In this case, it may be considered more logical to use the reinforcement method with steel strips in order to adhere to the principle of carrying more load with a lower mass. It has been proven in many studies that the reinforcement method with steel strips increases the rigidity of the structure by placing a relatively small mass on the structure. In this study, the effects of steel strip reinforcement in a sample steel structure are revealed by making modal analysis using the finite element method. In particular, the structure vibration periods and free vibration mode shapes of the first 5 modes are discussed in detail. Thus, the positive effect of the use of steel strip the rigidity of the steel structure has been more clearly demonstrated. As a result of all these studies, the reinforcement method with steel strip may be used in steel structures.

Keywords: Steel structures, Steel strip, Finite element method, Dynamic parameters, Reinforcement

1. Introduction

Strip steel or cold rolled strip is a steel product that is produced from a hot rolled strip that has been pickled. The coil is then reduced by a single stand cold roll steel mill straight away or reversing mill or in a tandem mill consisting of several single stands in a series. The strip is reduced to approximately final thickness by cold-rolling directly, or with the inclusion of an annealing operation at some intermediate thickness to facilitate further cold reduction or to obtain mechanical properties desired in the finished product. High carbon strip steel requires additional annealing and cold reduction operations. The coil is then slit to the desired width through the process of roll slitting. Stainless steel strip is the extension product of strip steel, usually long and narrow stainless steel strips are manufactured to meet the demands of various industrial and mechanical areas. According to the processing method, the stainless steel strip can be divided into cold rolled stainless steel strip and hot rolled stainless steel strip. The final product typically consists of cold rolled steel that has been cut into strips of a specific widths and coiled or oscillate coiled for delivery, frequently interleaved with paper or another material which protects the surface finish of the material and assists in retaining oil or some other rust prevention solution. This product is often later stamped to form a part from the strip steel. An example of a steel strip is given in figure 1.



Figure 1. Steel strips

Researchers have carried out many studies using both the finite element method and the reinforcing methods. There are many other studies by the authors using the finite element method before. In this study, studies [1], [2], [3], [4], [5], [6], [7] on the use of the finite element method were used. With all this knowledge, this new study has been carried out.

Researchers have conducted studies [8], [9], [10], [11], [12], [13], [14], [15], [16] about steel strips which also contributing to this study.

The aim of this study is to examine the effects of reinforcement with steel strips on dynamic parameters in steel structures. There may be a need for a retrofit method without architectural disadvantages or excessive dead load increments. In such cases, the reinforcement method with steel strips is also known to be an option. For this reason, it is very important to reveal the effect of steel strips on dynamic parameters.

2. Material and Method

In this study, A steel structure model was created and modal analysis was carried out with the finite element method. The steel structure model was reinforced with steel strips and a reinforced model structure model was created for comparison. In the application of the finite element method, the SAP2000 package program, which is used in the field of academic and engineering applications all over the world, was used. In addition, the steel material used was taken according to ANSI/AISC 360-10 standards.

2.1. Description of Model Steel Structure

The model steel structure is a 6-storey steel structure with two spans of 6 m each in the x and y directions, with a floor height of 3 meters. Columns and beams are dimensioned as 25x25x1 cm steel box profile. The slabs are sized to be 2 cm steel plate.

By designing the building as symmetrical and simple, it is aimed to reveal the result of the reinforcement to be applied more clearly. The profile and dimensions of the columns and beams are therefore chosen the same. Also, the spans are therefore taken equal.

The 3D finite element model in SAP2000 package software of the model steel structure is given in Figure 2.

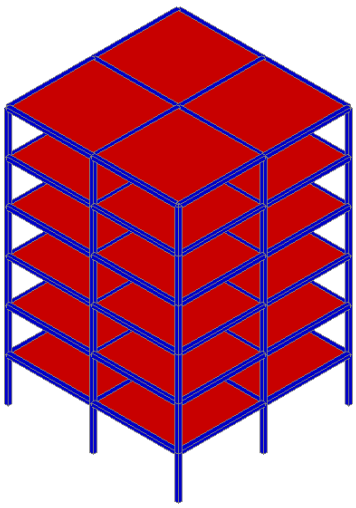


Figure 2. The model steel structure's 3D view

2.2. Description of Reinforced Model Steel Structure

Strip elements were applied to one span of the structure in the x and y directions. The strip element is 10 cm wide and 1 cm thick and made of steel. The 3D finite element model in SAP2000 package software of the reinforced model steel structure is given in Figure 3.

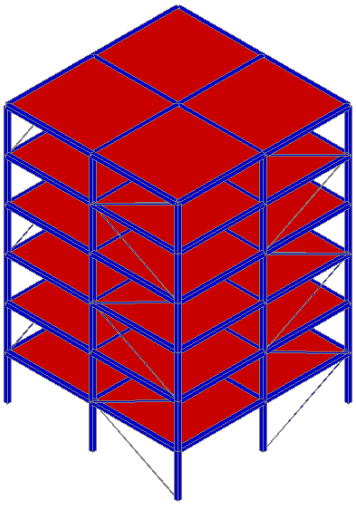


Figure 3. The reinforced model steel structure's 3D view

3. Result and Discussion

Model steel structure and reinforced model steel structure were analysed separately. The modal analysis results of each model are shared under separate headings. The results include the analysis results of the first five modes. Mode shape and period values are taken into consideration for each mode. The parameters obtained for both models were compared for each mode separately. During the analysis, the SAP2000 package software, which is a finite element method software, was used.

3.1. Analysis Results of Model Steel Structure

The model steel structure was analysed without reinforcing. When the first five modes are examined, the results obtained are presented in figure 4,5,6,7,8 as period values and mode shapes for each mode.

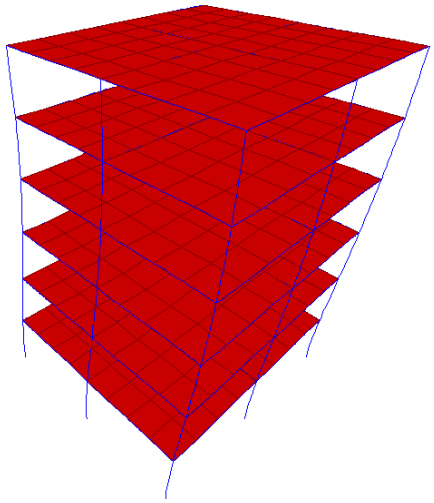


Figure 4. 1. Mode shape (T = 0.97 s)

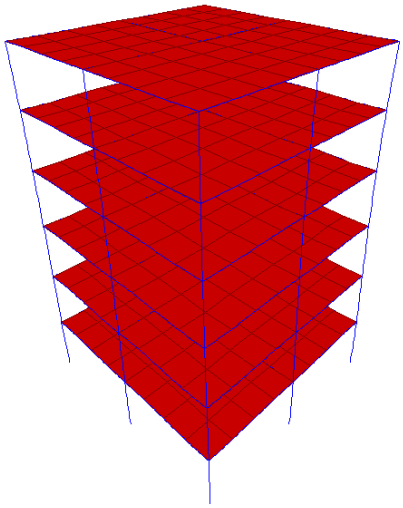


Figure 5. 2. Mode shape (T = 0.72 s)

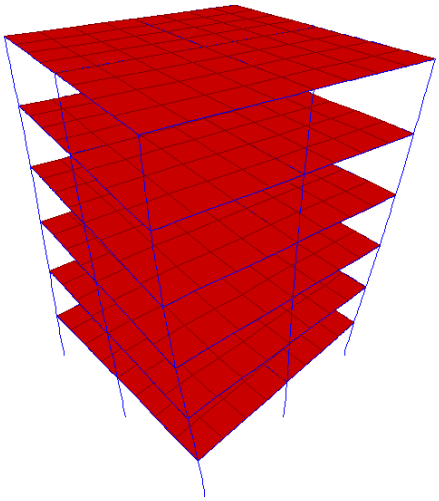


Figure 6. 3. Mode shape (T = 0.31 s)

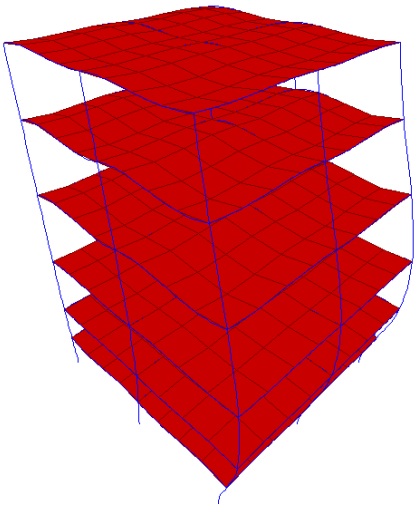


Figure 7. 4. Mode shape (T = 0.24 s)

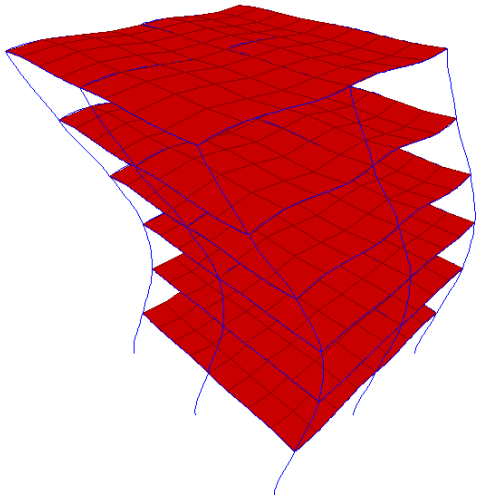


Figure 8. 5. Mode shape (T = 0.19 s)

3.2. Analysis Results of Reinforced Model Steel Structure

The model steel structure was analysed with reinforcing by steel strips. When the first five modes are examined, the results obtained are presented in figure 9,10,11,12,13 as period values and mode shapes for each mode.

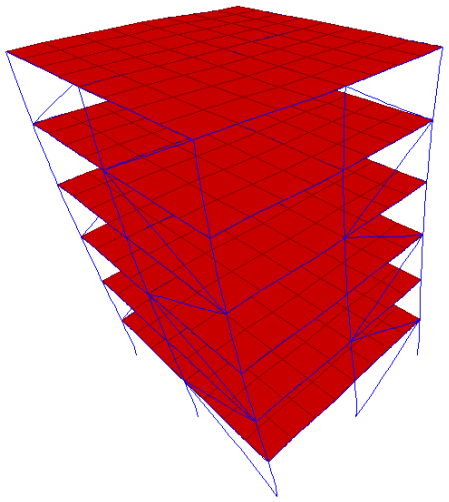


Figure 9. 1. Mode shape (T = 0.56 s)

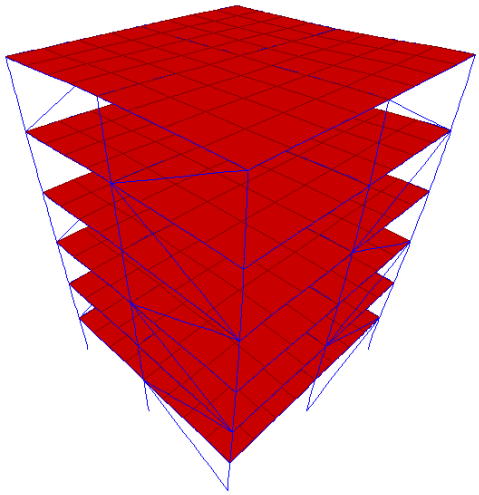


Figure 10. 2. Mode shape (T = 0.37 s)

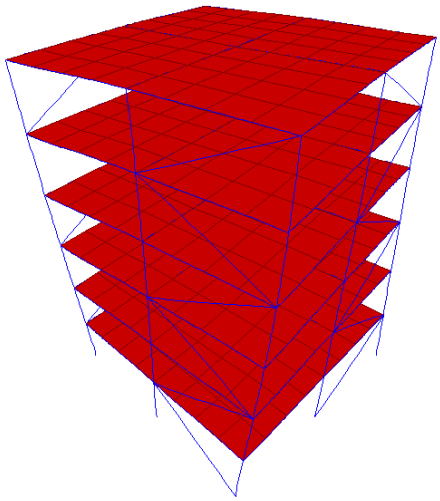


Figure 11. 3. Mode shape (T = 0.24 s)

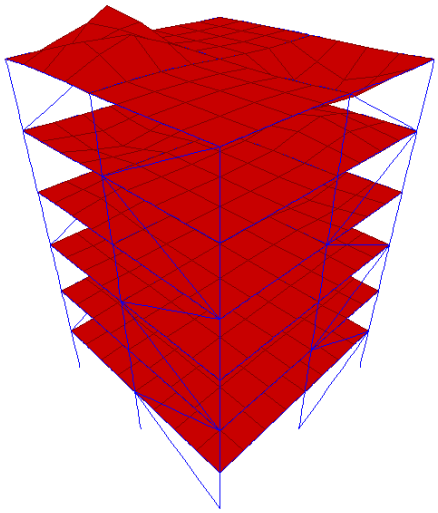


Figure 12. 4. Mode shape (T = 0.20 s)

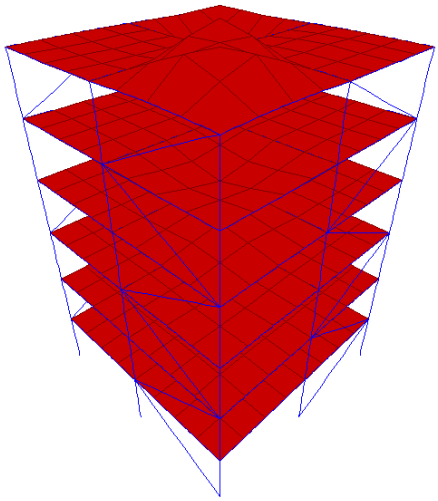


Figure 13. 5. Mode shape (T = 0.12 s)

3.3. Comparison of Analysis Results

The comparison of period values of the model steel structure and reinforced model steel structure is given in Table 1.

Table 1. Comparison of period values

Mode	**1**	**2**	**3**	**4**	**5**
Non-Reinforced	0.97	0.72	0.31	0.24	0.19
Reinforced	0.56	0.37	0.24	0.20	0.12
Difference (s)	0.41	0.35	0.07	0.04	0.07
Difference (%)	42.27	48.61	22.58	16.67	36.84

The comparison of mode shapes of the model steel structure and reinforced model steel structure is given in Table 2.

Table 2. Comparison of mode shapes type

Mode	**1**	**2**	**3**	**4**	**5**
Non-reinforced	Translational	Translational	Torsional	Translational	Translational
Reinforced	Translational	Translational	Torsional	Translational	Translational

4. Conclusions

In the mode 1, the period difference between non-reinforced model and reinforced model status was obtained as 0.41 s. The effect of period retrofitting with steel strips as a percentage was determined as 42.27.

In the mode 2, the period difference between non-reinforced model and reinforced model status was obtained as 0.35 s. The effect of period retrofitting with steel strips as a percentage was determined as 48.61.

In the mode 3, the period difference between non-reinforced model and reinforced model status was obtained as 0.07 s. The effect of period retrofitting with steel strips as a percentage was determined as 22.58.

In the mode 4, the period difference between non-reinforced model and reinforced model status was obtained as 0.04 s. The effect of period retrofitting with steel strips as a percentage was determined as 16.67.

In the mode 5, the period difference between non-reinforced model and reinforced model status was obtained as 0.07 s. The effect of period retrofitting with steel strips as a percentage was determined as 36.84.

When the mod shapes were examined, no mod shape type changes were observed with the reinforcement with steel strips.

In the light of all these results, it is clearly seen that the rigidity of the structure increases by strengthening the model steel structure with steel strips. In the 1st mode, in other words, there is a decrease of 42.27 percent in the dominant period value. In addition, there is a large decrease of 48.61 percent in the period value in the 2nd mode. A significant increase in stiffness was observed. Of course, it should be taken into account that the design of the structure and reinforcement is very important in obtaining the data in this way. Incorrect model selection and faulty retrofit designs can make data more unreliable. In the light of all this obtaining information, the reinforcement method with steel strip may be used in steel structures.

References

[1] Ziada, M., Tuhta, S., Gençbay, E. H., Günday, F., & Tammam, Y. (2019). Analysis of Tunnel Form Building Retrofitted with CFRP using Finite Element Method. International Journal of Trend in Scientific Research and Development, 3(2), 822–826.

[2] Tuhta, S., Günday, F., & Pehlivan, N. C. (2019). Investigation of Cfrp Retrofitting Effect on Masonry Dome on Bending Moment Using Finite Element Method. International Journal of Innovatıons in Engineering Research and Technology, 6(6), 18–22.

[3] Tuhta, S., Günday, F., & Alihassan, A. (2020). The Effect of CFRP Reinforced Concrete Chimney on Modal Parameters Using Finite Element Method. International Journal of Innovations in Engineering Research and Technology, 7(2), 1–6.

[4] Tuhta, S., Günday, F., & Köroğlu, E. (2021). The Effect of TMD on The Periods and Mode Shapes of The Reinforced Concrete Building by Finite Element Analysis. JournalNx, 7(12), 5–13.

[5] Bakkour, F., Tuhta, S., & Günday, F. (2022). Determination of Modal Parameters of Reinforced Concrete Box Culvert Retrofitted with GFRP Using Finite Element Method. International Journal of Innovations in Engineering Research and Technology, 9(4), 1–9.

[6] Kasimzade, A.A., Tuhta, S., Günday, F. & Aydın, H. (2021). Obtaining Dynamic Parameters by Using Ambient Vibration Recordings on Model of The Steel Arch Bridge. Periodica Polytechnica Civil Engineering, 65(2), 608-618.

[7] Hammoud, M. A., Tuhta, S., & Günday, F. (2022). Determination of Modal Parameters of Reinforced Concrete Tunnel Retrofitted with CFRP using Finite Element Method. International Journal of Innovations in Engineering Research and Technology, 9(4), 10–18.

[8] Huang, B., Bathurst, R. J., & Allen, T. M. (2012). LRFD Calibration for Steel Strip Reinforced Soil Walls. Journal of Geotechnical and Geoenvironmental Engineering, 138(8), 922-933.

[9] Zhai, Z., Guo, W., Yu, Z., Hu, Y., & Ma, C. (2021). Seismic performance assessment of steel strip dampers equipped in high-rise steel frame. Journal of Constructional Steel Research, 2021(177).

[10] Yi, L., Li, G. & Jiang, M. (2017). An End-to-End Steel Strip Surface Defects Recognition System Based on Convolutional Neural Networks. Steel Research International, 88(1600068).

[11] Song, K., & Yan, Y. (2013). A noise robust method based on completed local binary patterns for hot-rolled steel strip surface defects. Applied Surface Science, Part B, 285(2013), 858-864.

[12] Watanabe, Y., Kenmochi, K., Yarita, I., Izumi, Y., & Shibata, S. (1992). Analysis of Vibration for Sendzimir Mill in Cold Rolling of Stainless-Steel Strips. Tetsu-to-Hagane, 78(10), 1554-1560.

[13] Yarita, I., Furukawa, K., Seino, Y., Takimoto, T., Nakazato, Y., & Nakagawa, K. (2019). An Analysis of Chattering in Cold Rolling for Ultrathin Gauge Steel Strip, Transactions of the Iron and Steel Institute of Japan, 18(1), 1-10.

[14] Chen, R. Y., & Yuen, W. Y. D. (2000). A Study of the Scale Structure of Hot-Rolled Steel Strip by Simulated Coiling and Cooling. Oxidation of Metals, 53(2000), 539–560.

[15] Lee, C-H., Ju, Y.K., Min, J-K., Lho, S-H., & Kim, S-D. (2015). Non-uniform steel strip dampers subjected to cyclic loadings. Engineering Structures, 99(2015), 192-204.

[16] Manesh, H.D., & Taheri, A.K. (2004). Study of mechanisms of cold roll welding of aluminium alloy to steel strip, Materials Science and Technology, 20(8), 1064-1068.

The effect of an aluminum alloy on its fluidity when alloyed with a lithium-fluorine-containing compound

Tursunbaev Sarvar[1*], Turakhodjayev Nodir[2]

[1*] PhD student, Tashkent State Technical University, Tashkent, Uzbekistan, (ORCID: 0000-0003-2516-3597), tursunbayev88@bk.ru

[2]Professor, Tashkent State Technical University, Tashkent, Uzbekistan, (ORCID: 0000-0003-2411-3487), nod18tur@gmail.com

Abstract

The article considers the effect of lithium fluorine compound on the fluidity property of aluminum alloy liquid. The experiments were carried out by adding lithium fluorine as alloying elements in the mass fraction. In this case, the lithium fluoride compound is included in the charge during the melting of aluminum in an amount from 5% to 15%. In the experiments, samples were taken using a resistance furnace. Based on the conducted experiments, a graph of the relationship was drawn up, on which the authors' conclusions were drawn.

Keywords: fluidity, lithium, fluorine, AK7, D16, furnace, temperature

1. Introduction

Currently, a lot of aluminum alloy parts are used in the world in the field of mechanical engineering. One of the pressing problems in aluminum alloys today is that the alloy does not have sufficient flow properties and is typical for gas pores in parts[1]. Aluminum alloy parts are made by liquefying aluminum by adding elements such as Si, Si, Mg, Zn, Mn, Ni, Fe, Ti individually or in a certain combination.Other similar additives to aluminum alloys, such as Ni, Cr, Sa, Na, Be, Ti, Ce, Nb, Li, are added in small quantities as elements that improve the properties of the alloy.These elements are physical, chemical and mechanical properties allow to obtain a wide range of aluminum alloys[2].Aluminum alloys are considered much more durable, but at the same time light.This has been added to the aluminum alloy as an element that leaches the lithium-fluorine compound in our research work to enhance its strength and casting properties[3].

2. Materials and methods

Lithium fluoride compound is a binary chemical compound of lithium and fluorine and is a lithium salt of hydrofluoric acid. Under normal conditions-white powder or transparent colorless crystal, a non-hygroscopic, insoluble compound in cold water. It is a substance soluble in nitrate and hydrofluoric acids[4-5]. In the research work, a resistance furnace was used to obtain samples. (Fig. 1). The technical characteristics of the furnace are given in the table below (Table 1).

The samples were poured into sand-clay molds.The composition of sand-clay forms consists of: 85% quartz sand, 11% bentadine clay, 4% water.In this composition, a molding mixture was prepared and mixed in a mixer until the same mass was obtained.The finished mass was placed in pre-prepared flasks, and the molds for namana were pressed and prepared. Our experiments were carried out by setting the oven to 750 °C.

Table 1. Technical classification of the oven

1.	Capacity	1400 Vt
2.	Metal mass entering the crucible	3 kg
3.	Maximum temperature	1100 °C
4.	Dimensions of gabarite	485x700x950
5.	Current voltage	220 V



Figure 1.Resistance furnace.

3. Experments

To compare the samples, first of all, an aluminum alloy of the AK7 brand was poured, without the addition of a lithium-fluoride compound. In order for the samples to be of the same mass, the charges were measured on a scale before crucifixion and loaded into an equal number of crucibles for the charge. Each sample was taken from 130 grams. In the next step, a lithium fluoride compound was added to aluminum alloy wrapped in aluminum foil. In this case, a lithium fluoride compound in the amount of 5% of the total mass was added to the first sample, 10% i was added to the second sample, and a lithium fluoride compound in the amount of 15% was added to the third sample[6]. To test the fluidity of non-ferrous metals in the first place for casting samples, a spiral sample (Curie sample) sand-clay molds were prepared [7] (fig.2).



a *b* *c*

Figure 2. The process of pouring sand-clay mixture into the sample.

a - casting process; b - spiral sample; s - cast sample.

4. Results

The samples were separated from the molds after they were poured into the molds. Below are examples of studies of aluminum grade AK7 (Fig.3).

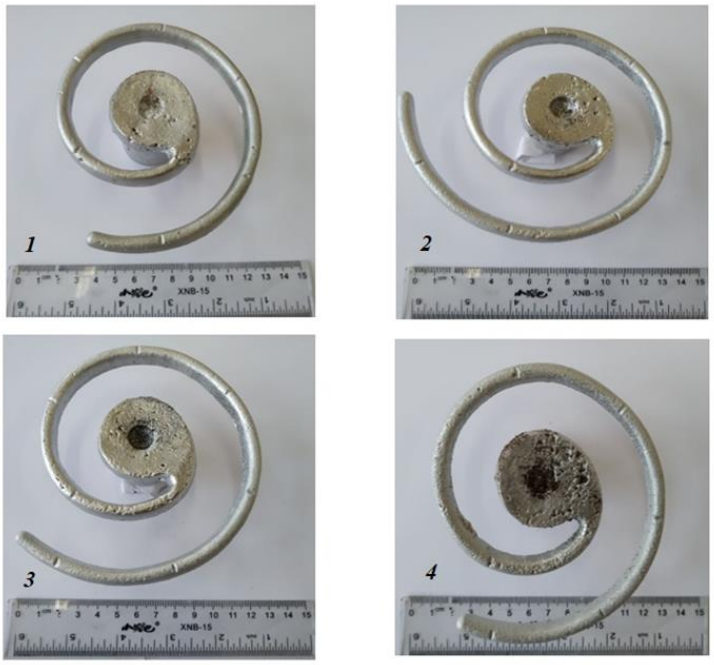


Figure 3. Cast samples.

1-AK 7; 2-lithium fluorine with the addition of 5% of the sample; 3-lithium fluorine with the addition of 10% of the sample; 4-lithium fluorine with the addition of 15% of the sample.

The second stage of the experiment presented above was carried out. At the next stage, a lithium-fluorine compound was introduced into the D16 aluminum alloy. The experiments were carried out in the order given above. At this stage, experiments were carried out with a mass fraction of ham of 5%, 10% and 15%. The cast samples were separated from the molds and the length of the spiral of the samples was determined. The following are examples of studies on aluminum grade D16 (Fig.4)

Measurement results for the AK7 brand: measurement results the length of the sample made of AK7 aluminum without the addition of lithium fluoride was 354 mm, the length of the sample with the addition of lithium fluoride 5% 463 mm, the length of the sample with the addition of lithium fluoride 10% 391 mm, the length of the sample with the addition of lithium fluoride 15% was 298 mm.

Measurement results for grade D16: measurement results the length of the sample made of grade D16 aluminum without the addition of lithium fluoride was 341 mm, the length of the sample with the addition of lithium fluoride 5% was 434 mm, the length of the sample with the addition of lithium fluoride 10% was 404 mm, the length of the sample with the addition of lithium fluoride 15% was 273 mm.

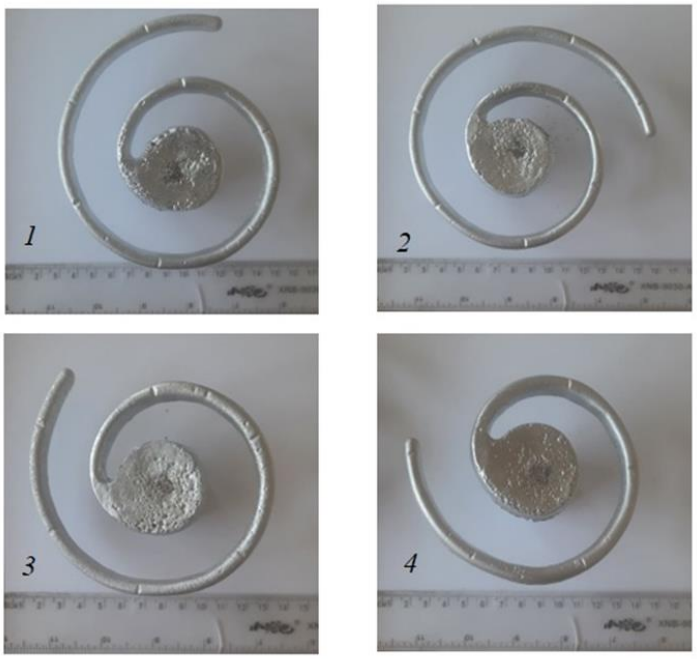


Figure 4. Cast samples.

1- D16; 2-lithium fluorine with the addition of 5% of the sample; 3-lithium fluorine with the addition of 10% of the sample; 4-lithium fluorine with the addition of 15% of the sample.

Based on the measurement results, a graph of the dependence of the helical fluidity of the lithium fluorine compound was compiled. (Fig.5).

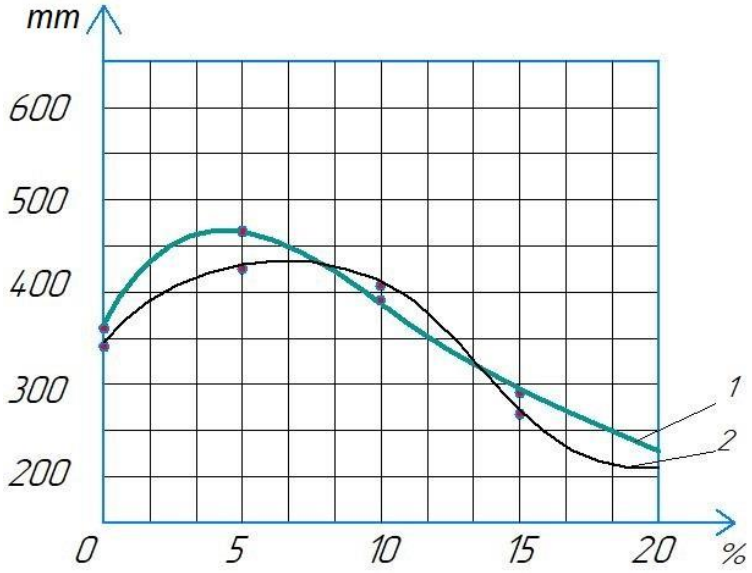


Figure 5. Graph of the dependence of fluidity on the amount of lithium fluorine.

Line 1 is AK7; Line 2 is D16.

4. Conclusion

From the experiments carried out, it can be concluded that the yield strength increases to a certain extent compared to samples without the addition of lithium-fluoride compound added to aluminum alloys of the AK7 and D16 grades as a leaching element. In this case, it is recommended to add the most optimal amount of the additive in an amount of 4-5% I of the total mass. As you can see from the graph above, the best result is achieved by adding 4-5%. Fluorine casting allowed to increase the fluidity of AK7 grade aluminum alloy by a maximum of 30-31%, and the fluidity property of D16 grade aluminum alloy by a maximum of 26-28%.

5. Acknowledge

I express my gratitude to Muhammed İhsan ÖZGÜN, a researcher at Nekmettin Erbakan University, who helped in the preparation of the conference article.

References

[1]. Nodir, T., Sarvar, T., Kamaldjan, K., Shirinkhon, T., Shavkat, A., & Mukhammadali, A. (2022). THE EFFECT OF LITHIUM CONTENT ON THE MASS OF THE PART WHEN ALLOYED WITH LITHIUM ALUMINUM. *International Journal of Mechatronics and Applied Mechanics*, *2022*(11), 52–56. https://doi.org/10.17683/ijomam/issue11.7

[2]. Tursunbaev, S., Umarova, D., Kuchkorova, M., & Baydullaev, A. (2022). Study of machining accuracy in ultrasonic elliptical vibration cutting of alloyed iron alloy carbon with a germanium. *Journal of Physics: Conference Series*, *2176*(1). https://doi.org/10.1088/1742-6596/2176/1/012053

[3]. Li, Y., Wang, J., Wu, R., Wei, Z., Ji, Q., Zhong, F., Zhang, S., Yang, Z., Wang, J., Jin, S., Xu, L., & Hou, L. (2022). Effects of Al, Y, and Zn Additions on the Microstructure and Mechanical Properties of Mg−3Li Alloy. *Advanced Engineering Materials*, *24*(8). https://doi.org/10.1002/adem.202101502

[4]. Tursunbaev, S., Turakhodjaev, N., Turakhujaeva, S., Ozodova, S., Hudoykulov, S., & Turakhujaeva, A. (2022). Reduction of gas porosity when alloying A000 grade aluminum with lithium fluoride. *IOP Conference Series: Earth and Environmental Science*, *1076*(1). https://doi.org/10.1088/1755-1315/1076/1/012076

[5]. Cisko, A. R., Jordon, J. B., Avery, D. Z., McClelland, Z. B., Liu, T., Rushing, T. W., ... & Garcia, L. (2019). Characterization of fatigue behavior of Al-Li alloy 2099. Materials Characterization, 151, 496-505. Cisko A. R. et al. Characterization of fatigue behavior of Al-Li alloy 2099 //Materials Characterization. – 2019. – Т. 151. – С. 496-505.

[6]. Tian-Zhang, Z., Long, J., Yong, X., & Shi-Hong, Z. (2020). Anisotropic yielding stress of 2198 Al–Li alloy sheet and mechanisms. Materials Science and Engineering: A, 771, 138572.

[7]. Turakhodjaev, N., Akramov, M., Turakhujaeva, S., Tursunbaev, S., Turakhujaeva, A., & Kamalov, J. (2021). Calculation of the heat exchange process for geometric parameters. *International Journal of Mechatronics and Applied Mechanics*, *1*(9), 90–95. https://doi.org/10.17683/IJOMAM/ISSUE9.13

Çimento Fabrikası Emisyon Ölçümlerinde Ölçüm Belirsizlikleri İçin Yeni Yaklaşımlar

Arslan Can MARTOĞLU[1*], Andaç AKDEMİR[2]

[1*] Etibakır A.Ş. Cerrattepe Maden İşletmesi, Artvin, Türkiye , (ORCID: 0000-0002-4463-1125), arslancanmartoglu@gmail.com

[2] Ondokuz Mayıs Üniversitesi, Mühendislik Fakültesi, Çevre Mühendisliği Bölümü, Samsun, Türkiye, (ORCID: 0000-0002-7592-4449), aakdemir@omu.edu.tr

Öz

Çimento üretim sektörünün; iklim değişikliği, ekosistem kalitesi, insan sağlığı ve kullanılan kaynaklar üzerindeki olumsuz etkilerini en aza indirmek için çimento üretim sürecinin çevresel etkilerinin değerlendirilmesi oldukça önemlidir. Özellikle sera gazı salınımının izlemesinde, ölçüm belirsizlikleri ve kullanılan metotlar önem kazanmıştır. Bu çalışma kapsamında geleneksel hammadde, geleneksel yakıt, geri kazanılan alternatif hammadde ve geri kazanılan alternatif yakıt kullanımı sonucunda, başta iklim değişimine neden olan karbondioksit gibi kirleticilerin ortaya çıkma potansiyellerinin hesap temelli yöntemlerle belirlenmesi ve belirsizlik bileşenlerinin ortaya çıkarılması amaçlanmıştır.

Anahtar Kelimeler: Belirsizlik, Çimento, Sera gazı, Simülasyon

NEW APPROACHES TO MEASUREMENT UNCERTAINTY IN CEMENT FACTORY EMISSION MEASUREMENTS

Abstract

It is very important to evaluate the environmental effects of the cement production process in order to minimize the negative effects of the cement production sector on climate change, ecosystem quality, human health and the resource used. Measurement uncertainties and the methods used have gained importance especially in monitoring greenhouse gas emissions. In this study, it is aimed to determine the potentials of pollutants such as carbon dioxide, which cause climate change as a result of the use of conventional raw materials, conventional fuel, recycled alternative raw materials and recycled alternative fuels, by computational methods and to reveal the uncertainty components.

Keywords: Uncertainty, Cement, Greenhouse gas, Simulation

1. Giriş

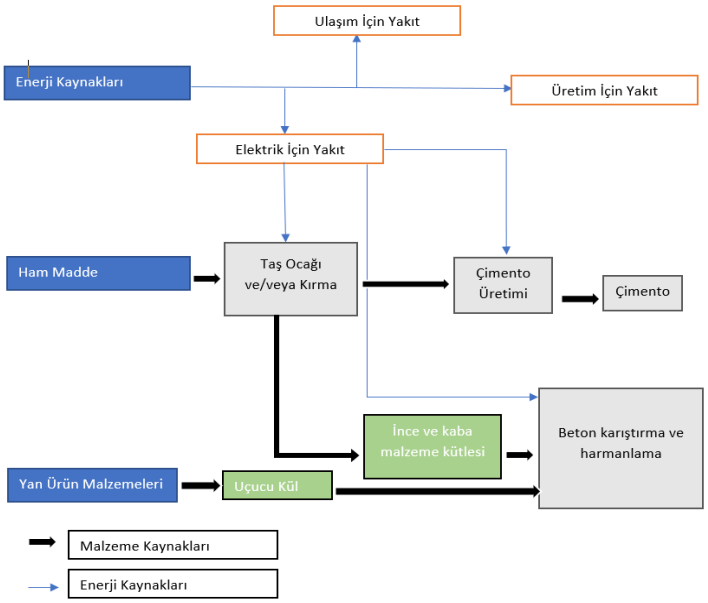
Çimento üretimi hem doğrudan hem de dolaylı olarak karbondioksit (CO_2) yayar (CSI, 2005; Worrell ve diğerleri, 2001). Doğrudan CO_2 emisyonları esas olarak çimento üretim sürecindeki kimyasal reaksiyonlardan (esas olarak kireçtaşı kalsinasyonundan) kaynaklanan CO_2 emisyonlarını ve çimento üretimi için fosil yakıt kullanımından kaynaklanan CO_2 emisyonlarını içerir (CSI, 2005, 2011; Worrell ve diğerleri, 2001). Dolaylı CO_2 emisyonları esas olarak çimento üretimi için elektrik tüketiminden veya daha spesifik olarak "çimento üreticileri tarafından tüketilen elektriğin harici üretiminden" kaynaklanmaktadır (CSI, 2011). Fosil yakıt yanmasından kaynaklanan doğrudan CO_2 emisyonları ve elektrik tüketiminden kaynaklanan dolaylı CO_2 emisyonları genellikle enerji ile ilgili CO_2 emisyonları olarak kabul edilirken, çimento yapımındaki kalsinasyon işleminden kaynaklanan doğrudan CO_2 emisyonları genellikle çimento prosesi CO_2 emisyonları olarak adlandırılır.

Günümüzde, sanayileşme ve kentleşme nedeniyle, yoğun miktarda enerji kullanan, kaynak tüketen ve karbon

emisyonu yüksek bir sektör olan çimento imalatında önemli bir artış meydana gelmiştir. Toplam küresel insan faaliyetleri sonucu karbondioksit (CO_2) emisyonlarının yaklaşık %7'si ve toplam sera gazı emisyonlarının %3'ü çimento üretiminden kaynaklanmaktadır. Çimento üretiminden kaynaklanan CO_2 emisyonlarını tahmin etmek için sıklıkla kullanılan iki tür hesaplama yöntemi vardır: Girdi (hammadde veya farin miktarı) yöntemi ve çıktı (klinker üretimi miktarı) yöntemi.

Girdi yöntemi, çimento üretimi için tüketilen hammaddelerin hacmine ve karbonat içeriğine dayalı kalsinasyon CO_2 emisyonlarını hesaplar (CSI, 2005, 2011).

Çimento, agrega, su ve uygulanabilir olduğunda katkı maddeleri ve/veya takviye lifleri gibi birçok malzemeden oluşan beton, günümüzde sudan sonra insanlar tarafından en çok kullanılan ikinci malzemedir (Monteiro ve diğerleri, 2017). Çimento ve beton gibi kompozitlerinin mevcut üretimi, küresel antropojenik sera gazı emisyonlarının yaklaşık %8-9'u (Miller ve diğerleri, 2016), dünya çapında enerji kullanımının %2-3'ü ve küresel su çekilmesinin %1-2'si ile sonuçlanmaktadır (Miller ve diğerleri, 2018). Çeşitli faktörlerden hareketle, geçmiş çalışmalar, hem tesisler arasında hem de zaman içinde çimento üretiminden kaynaklanan CO_2 ve hava kirletici emisyonlarında değişkenlik olduğunu göstermiştir (Chen ve diğerleri, 2010, Von Bahr ve diğerleri, 2003). Beton ve diğer yapı malzemelerinin üretiminden kaynaklanan sera gazı emisyonları ve hava kirletici emisyonlarının, kullanılan enerji ve hammadde kaynaklarının güçlü bir fonksiyonu olduğu gösterilmiştir (Gursel ve diğerleri, 2016, Su ve diğerleri,2016, Van Den Heede ve De Belie, 2012). Şekil.1' de beton üretiminde farklı üretim aşamalarıyla ilişkili ortak malzeme ve enerji akışlarını temsil eder. Dikkate alınan prosesler arasında hammadde alımı ve hazırlanması, çimento üretimi, uygun olduğunda nakliye kullanımı, uçucu kül kullanımı ve bu bileşenler kullanılarak betonun harmanlanması yer almaktadır.



Şekil:1 Beton üretiminin süreç akış diyagramı.

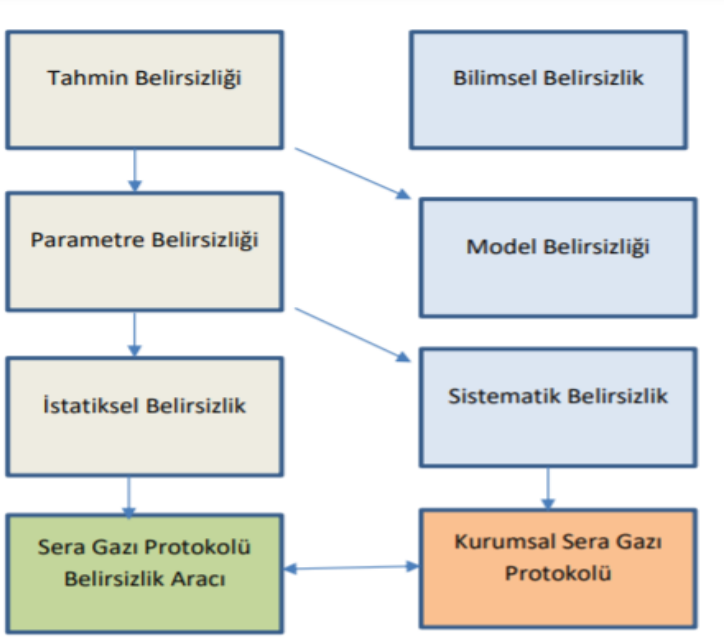
Betonun çevresel etki değerlendirmelerinde, çeşitli göstergeler, veri belirsizliğini ve değişkenliğini karşılaştırmalara dahil etme ihtiyacını ortaya koymuştur.

Klinkere dayalı çıktı yöntemi, üretilen klinkerin hacmine, bileşimine ve ayrıca hammaddelerdeki organik karbondan kaynaklanan atık toz ve CO_2 emisyonlarına dayalı kalsinasyon CO_2 emisyonlarını hesaplar (CSI, 2005). Klinker bazlı çıktı yöntemi, Uluslararası İklim Değişikliği Paneli (IPCC) tarafından ulusal sera gazı envanter hesaplamaları için Katman 2 yöntemi olarak benimsenmiştir. IPCC Katman 1 yöntemi ise çimento üretim verilerinden klinker üretimini tahmin etmektedir (IPCC, 2006).

2. Materyal ve Metod

Belirsizlik tahminleri, CO_2 emisyon envanterinin önemli bir unsurudur. Bu tür bilgiler, gelecekte envanterlerin doğruluğunu artırma çabalarını kolaylaştıran bir araç olarak kabul edilecektir. Çimento klinker üretim tesislerinden yayılan CO_2 miktarlarının belirsizlik analizi, Avrupa Birliği Resmi Gazetesinde (29.1.2004) sunulan kılavuza (IPCC) göre belirli katmanlar dikkate alınarak geliştirilmiştir *(Commission Decision of 29 January 2004).*

Sera gazı envanterleriyle ilgili belirsizlikler (*GHG belirsizlik protokolü).* Şekil.2.'de görüldüğü gibi gruplandırılmıştır. Bilimsel belirsizlik; emisyon ve uzaklaştırma süreçleri hakkında eksik bilimsel bilgi ile ilgili belirsizliktir. Örneğin, farklı sera gazlarının emisyon tahminlerini birleştirmek için kullanılan küresel ısınma potansiyeli değerleriyle ilişkili doğrudan ve dolaylı emisyon faktörlerinin çoğu, önemli bilimsel belirsizlikleri içerir. Tahmin belirsizliği ise miktar belirleme yöntemleriyle ilişkili belirsizlikleri oluşturur ve sera gazı emisyonlarının nicelleştirildiği her zaman ortaya çıkar. Bu nedenle, tüm emisyon veya giderim tahminleri, tahmin belirsizliği ile ilişkilidir.



Şekil 2: Sera Gazı Envanterleriyle İlişkili Belirsizlik Türleri

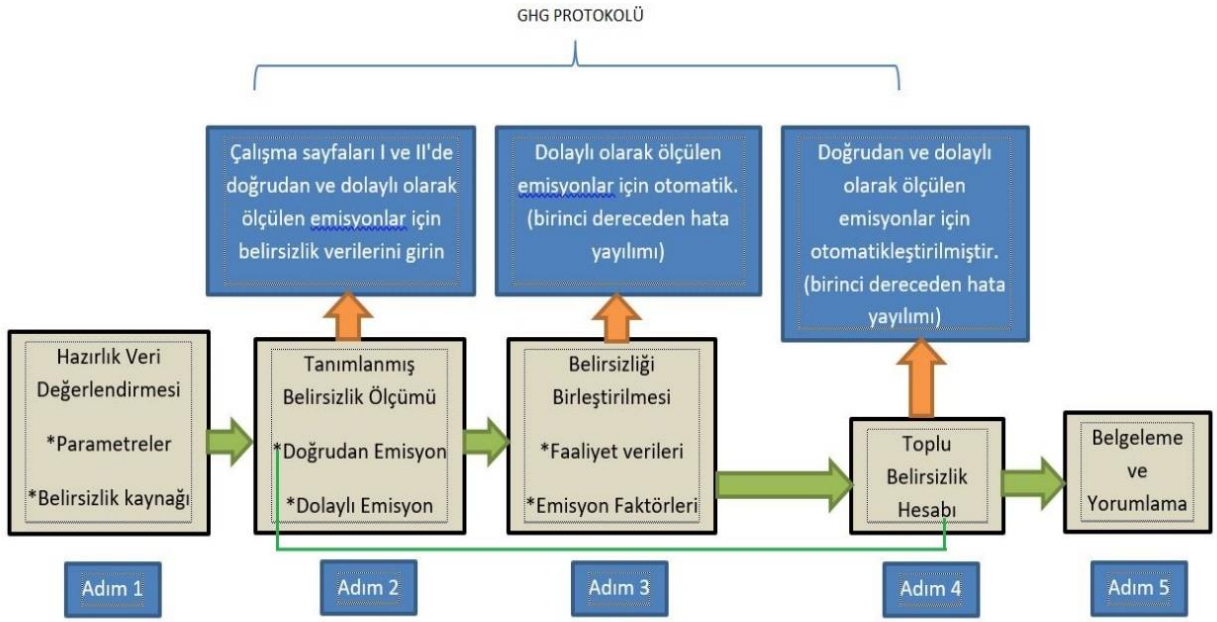
(GHG belirsizlik protokolü)

Tahmin belirsizliği; model belirsizliği ve parametre belirsizliği olarak iki sınıfa ayrılır. Model belirsizliği çeşitli parametreler ve sera gazı emisyonlarını tahmin etmek için kullanılan matematiksel denklemlerle ilişkili belirsizliği (yani istatistiksel, stokiyometrik veya diğer modeller) ifade eder. Örneğin, model belirsizliği, yanlış bir matematiksel modelin kullanılması veya modelde uygun olmayan parametreler (yani girdiler) nedeniyle ortaya çıkabilir. Parametre belirsizliği ise bir emisyon tahmininde kullanılan parametrelerin örneğin faaliyet verileri, emisyon faktörleri veya diğer parametreler gibi sayısallaştırılmasıyla ilgili belirsizliği ifade eder. Ayrıca parametre belirsizliği de iki belirsizlik yöntemi ile kontrol edilir: Bunlardan ilki istatistiksel belirsizlikler olarak adlandırılır ve örnek verilerin rastgele değişkenliğinden kaynaklanan belirsizlik olarak tanımlanır. İkinci belirsizlik sistematik Belirsizliklerdir ve tahmin sürecinde meydana gelen sistematik önyargılarla ilişkili belirsizlikleri (örneğin temsili olmayan numunelere dayalı emisyon faktörleri, hatalı ölçüm ekipmanı, vb.) anlatır.

Parametre belirsizlik aralıkları hakkında yeterli bilgi toplandığında ve parametre belirsizliği bilgilerini tamamen nicel bir yaklaşım kullanarak birleştirmek istenildiğinde, iki ana matematiksel teknik seçeneği vardır; birinci dereceden hata yayılım Yöntemi (Gauss Yöntemi) ve Monte Carlo Simülasyonuna dayalı yöntemlerdir.

3. Bulgular ve Tartışma

Birinci dereceden hata yayılım tekniği kullanılarak Sera gazı muhasebesindeki istatistiksel belirsizliklerin değerlendirilmesi için izlenecek süreç beş adımdan oluşmaktadır.



Şekil 3: Sera gazı envanterleri için parametre belirsizliğini tahmin etme ve toplama süreci (GHG belirsizlik protokolü)

3.1.Parametre Belirsizliğini Tahmin Etme ve Toplama Süreci

3.1.1. Hazırlık Verileri Değerlendirmesi (1. Adım)

Herhangi bir belirsizlik değerlendirmesinde olduğu gibi, sera gazı emisyonlarının tahmin edilen ile tanımlanan ve ölçülen belirsizliklerin olası nedenlerinin neler olduğu açıkça belirtilmelidir.

Sera gazı emisyonları doğrudan veya dolaylı olarak ölçülebilir. Dolaylı yaklaşım genellikle bir tahmin modelinin (faaliyet verileri ve emisyon faktörü gibi) kullanılmasını içerirken, doğrudan yaklaşım atmosfere verilen emisyonların bir tür ölçüm cihazı (örneğin, sürekli emisyon monitörü) tarafından ölçülmesini gerektirir.

3.1.2. Kaynak Düzeyinde İstatistiksel Belirsizliklerin Ölçülmesi (2. Adım)

Sera gazı envanterleri bağlamındaki istatistiksel belirsizlik, genellikle, emisyonun beklenen ortalama değerinin yüzdesi olarak ifade edilen bir belirsizlik aralığı verilerek sunulur. Bu aralık, belirsiz bir miktarın altında yatan değerin, belirli bir olasılık için bulunduğu düşünülen "güven sınırları" hesaplanarak belirlenebilir.

İstatistiksel t-testini kullanarak örnek verilerden belirli parametrelerin belirsizlik aralığının hesaplama aşamasında;

Parametre belirsizlikleri, örnekleme aralıklarından, örnekler arasındaki varyasyonlardan ve cihaz kalibrasyonundan bir parametrenin güven aralığını hesaplamak için istatistiksel yöntemler kullanılarak da tahmin edilebilir. Örnek verileri kullanarak belirsizlik aralığının hesaplanması için basit bir istatistiksel yöntemi açıklarsak; t istatistiği kullanılarak bir güven aralığı tahmini, doğrudan ölçülen emisyonların belirsizliklerinin yanı sıra dolaylı ölçümler (faaliyet verileri ve emisyon faktörleri) ile ilişkili belirsizliklerin tahmini için uygulanabilir.

'n'' ölçümlü bir numune için burada sunulan yöntem beş aşama gerektirir:

1- Güven düzeyi seçimi: Emisyonun gerçek değerinin belirlenen belirsizlik aralığı içinde yer alma olasılığını belirler. Doğa bilimlerinde ve teknik deneylerde %95 veya %99,73 güven düzeylerinin seçilmesi genellikle standart uygulamadır. IPCC, aralık tanımı için uygun bir düzey olarak %95'lik bir güven düzeyi önerir. Kullanılan güven düzeyi her zaman rapor edilmelidir.

2- t faktörünün belirlenmesi: Tahmin edilecek standart hata bir ''t'' dağılımını takip eder. Bu, Tablo 1 kullanılarak yapılabilir.

Tablo 1: %95 ve %99,73 güven düzeyi için t-faktörleri (GHG belirsizlik protokolü)

Ölçüm sayısı (n)	**Güvenlik düzeyi için t faktörü**	
	%95	%99,73
3	4,30	19,21
5	2,78	6,62
8	2,37	4,53
10	2,26	4,09
50	2,01	3,16
100	1,98	3,08
∞	1,96	3,00

3- Örnek ortalamasının (x) ve örnek standart sapmasının (s) hesaplanması:

n farklı ölçüme sahip bir numune için;

$$\bar{x} = \frac{1}{n}\sum_{k=1}^{n} x_k \quad \textbf{(1)}$$

$$s = \sqrt{\frac{1}{n-1}\sum_{k=1}^{n}(x_k - \bar{x})^2} \quad \textbf{(2)}$$

4- $\frac{s \cdot t}{\sqrt{n}}$ değerinin hesaplanması **(3)**

5- Ortaya çıkan aralığın hesaplanması: $\left[\bar{x} - \frac{s \cdot t}{\sqrt{n}}; \bar{x} + \frac{s \cdot t}{\sqrt{n}}\right]$ **(4)**

(T. Dimitris, 2007; E. Sadıkhov at al.1995)

3.1.3. Dolaylı Olarak Ölçülen Tek kaynaklı Emisyonlar İçin Belirsizliklerin Birleştirilmesi (3.Adım)

Dolaylı ölçüm durumunda, belirsizlikler faaliyet verileri ve emisyon faktörü ile ilgilidir. Bu parametrelerdeki belirsizlik aralığını ölçmenin birkaç yolu vardır:

- Bir veya birkaç örnek veri seti üzerinde istatistiksel testler yapılması.
- Özellikle aktivite verileri için kullanılan herhangi bir ölçüm ekipmanının cihaz hassasiyetini belirlenmesi.
- Kullanılan verilerin belirsizlik aralığının bir tahminini vermek için uzmanlara danışılması.
- Üçüncü el belirsizlik aralıklarının kullanılması.

Dolaylı olarak ölçülen emisyonlar tipik olarak bir faaliyet faktörü ile bir emisyon faktörünün çarpılmasıyla hesaplanır. Örneğin: Satın alınan elektrik, CO_2 /kWh üretim faktörü ile çarpılır.

Belirsizliği sayısal olarak karakterize edersek iki veya daha fazla faktörün çarpımı için güven aralığının hesaplanmasında kareler toplamı yaklaşımı kullanılabilir. Bu yaklaşım, yalnızca belirsizliklerin normal bir dağılım izlemesi ve bireysel belirsizliklerin %60'ın altında olması durumunda geçerlidir. Çarpımın göreli güven aralığı (artı veya eksi yüzde), her bir faktörün göreli (yüzde) güven aralıklarının karelerinin toplamının kareköküdür.

Belirsizliği çarpılması:

(A +/- a%) X (B +/- b%) = C +/- c% ile $c = \sqrt{a^2 + b^2}$ **(5)**

3.1.4. Tek Kaynakların Toplamları ve Alt Toplamları İçin Belirsizliğin Ölçülmesi (4. Adım)

Bir envanterdeki tek kaynaklar için parametre belirsizliği değerlendirilirse, ağırlıklı ortalama yaklaşımını kullanarak ara toplamlar ve toplamlar için belirsizlik tahminleri belirlenebilir.

Toplamsal belirsizlik, aşağıda özetlenen bir hesaplama yöntemi kullanılarak tahmin edilebilir.

Belirsizliklerin eklenmesi :

(C +/- c%) + (D +/- d%) = E +/- e% $e = \frac{\sqrt{(C \times c)^2 + (D \times d)^2}}{E}$ **(6)**

Sayısal belirsizlikler, her parametrenin veya tahminin göreli ağırlığını ayarlamak için mutlak değerler kullanılarak, kareler toplamı teknikleri kullanılarak birleştirilir (J.Ke ve diğerleri, 2013).

Örnek: Bir envanter, 110 ± %4 ve 90 ± %24 ton olarak hesaplanan iki CO2 kaynağına sahiptir. Envanter toplamı, aşağıdaki belirsizlikle birlikte 200 tondur:

$u = \frac{\sqrt{4.4^2 + 21.6^2}}{110 + 90} = \frac{22.04}{200} \approx \pm 11\%$ **(7)**

3.1.5. Belirsizlik Değerlendirmesini Belgeleme ve Yorumlama (5. Adım)

Bununla birlikte, toplanan verilerin ve bir bütün olarak envanterin kalitesinde gerçek gelişmeleri göstermek için süreç boyunca bulguları dikkatli bir şekilde belgelemek ve yorumlamak adına adımlar atılmazsa, tüm bu çabalar çok az fayda sağlayabilir. Belirsizlik değerlendirme çabalarının, genel kalite yönetim sisteminin uygulanmasıyla bütünleştirilmesi, bu sorunun çözülmesine yardımcı olacaktır.

Bir belirsizlik değerlendirmesinin nicel kısmından elde edilen sonuçlar belgelenirken, bir özet ölçeği kullanılarak sıralanabilir. Tablo 2'de rastgele olmasına rağmen tipik bir ölçek verilmiştir. Bu değerler, tahmin edilen veya ölçülen değerin yüzdesi olarak, gerçek değerin muhtemelen mevcut olduğu nicel güven aralıklarına dayanmaktadır.

Tablo 2: Sera Gazı Protokolü belirsizlik aracında kullanılan Veri Doğruluğu derecesi ve karşılık gelen aralıklar (GHG belirsizlik protokolü)

Veri doğruluğu	Ortalama Değer Yüzdesi olarak aralık
Yüksek	+/- % 5
İyi	+/- % 15
Orta	+/- %30
Kötü	% 30'dan fazla

4. Sonuçlar

Betona yönelik küresel taleplerin yoğun oluşu, üretimiyle ilişkili çevresel etkileri de gün geçtikçe artırmaktadır. Bu etkilerin farkında olarak, akademi, endüstri, sivil toplum kuruluşları ve hükümetler tarafından çok sayıda azaltma stratejisi araştırılmaktadır. Yine de, bu önlemlerden elde edilen çevresel faydaların raporlanmasında tutarlılık sorunları ve önlemlerin uygulanması halinde arzu edilen azalmaların meydana gelme olasılığı konusunda netlik eksikliği bulunmaktadır. Beton üretiminden kaynaklanan sera gazı emisyonlarının değerlendirilmesindeki belirsizlik ve değişkenlik, diğer bilinen hava kirletici (yani NO_X, SO_X, VOC, CO, Pb, PM_{10} ve $PM_{2.5}$) emisyonlarından daha düşüktür. Fakat CO, Pb, PM_{10} ve $PM_{2.5}$ emisyonları için temel belirsizliğin yüksek düzeyde oluşu, güvenilirlik, tamlık, zamansal, coğrafi ya da teknolojik korelasyonlardan kaynaklanan sınırlı veri değişkenliği olduğu durumlarda bile metreküp beton başına emisyonlara büyük oranda katkıda bulunur.

Veri değişkenliği ve belirsizliği olsa bile, ortaya çıkma olasılığı yüksek olan sera gazı emisyonlarında kayda değer azalmalara yol açabilecek, karbon yakalama ve dopalama kullanımı ya da mümkün olduğu ölçüde yüksek klinker içerikli Porland çimento kullanımının sınırlandırılması gibi yöntemlerin kullanılması da mümkündür. Porland çimento kullanımının sınırlandırılması, diğer hava kirletici emisyonlarda faydalı azalmalara yol açabilir; ancak kullanılan enerji kaynaklarına bağlı olarak karbon yakalama ve dopalama, hava kirletici emisyonlarda artışlara neden olabilir.

Hem veri değişkenliğinin hem de veri belirsizliğinin, beton üretimiyle ilişkili sera gazı ve hava kirletici emisyonları üzerindeki etkilerinin incelenmesinde son yıllarda yoğun çalışmalar yapılmaktadır. Bu veri değişkenlikleri ve belirsizlikleri için kullanılan en yaygın iki yöntemden biri olan Monte Carlo Simülasyon Yöntemi; herhangi bir olasılık dağılımı, aralığı ve korelasyon yapısına sahip belirsizliklerin, uygun şekilde nicelleştirilmeleri koşuluyla birleştirilmesine izin verir. Bu yöntem, belirli ve kesin olmayan girdilerin olması durumunda ve bir fonksiyonla hesaplanabilecek bir dağılıma sahip olunduğunda kullanılabilir ve rastgele sayıları baz alarak tahmini sistemler

modellenir. Bu yöntemin kullanılabilmesi için teorik eğitimin yanında örneğin C veya C++ gibi bilimsel çalışmalarda sıklıkla kullanılan programları iyi derecede bilmek gerekmektedir. Monte Carlo tekniği, tek kaynakların belirsizliğini tahmin etmenin yanı sıra belirsizlikleri toplamak için de kullanılabilen güçlü bir belirsizlik hesaplama yöntemidir. Diğer bir yaygın belirsizlik hesaplama yöntemi olan Gauss Yöntemi'ne Sera Gazı Protokolü Belirsizlik aracı olarak birinci dereceden hata yayılımlarını kullanır. Ancak bu yöntem yalnızca belirli varsayımlar yerine getirildiğinde uygulanabilmektedir. Bunlardan ilki, her parametredeki hatalar normal dağılımlı olmalıdır. Tahmin edici işlevinde hiçbir yanlılık olmamalıdır. Tahmin edilen parametreler korelasyonsuz olmalıdır ve her parametredeki bireysel belirsizlikler, ortalamanın %60'ından az olmalıdır.

Netice itibari ile belirsizliklerin tüm bileşenlerin doğru yöntemlerle belirlenmesi ve bunun ölçüm sonuçlarına katkısının tespit edilmesi özellikle sera gazı ve diğer kirleticilerin sürekli izlenmesinde kullanılan SEOS sistemlerinin verimliliğini arttırmak için önemli bir unsurdur.

Kaynaklar:

1) World Business Council for Sustainable Development, GHG Protocol guidance on uncertainty assessment in GHG inventories and calculating statistical parameter uncertainty, https://ghgprotocol.org/sites/default/files/ghg-uncertainty.pdf

2) T. Dimitris, "Uncertainty Analysis of CO_2 Emissions from Cement Production" Proc. of the 3rd IASME/WSEAS Int. Conf. on Energy, Environment, Ecosystems and Sustainable Development, Agios Nikolaos, Greece, July 24-26, 2007 17,p:172-177. https://www.researchgate.net/publication/235410701_Uncertainty_Analysis_of_CO2_Emissions_from_Cement_Production

3) E. Sadıkhov, R. Kangı, S. Uğur, Ölçüm Belirsizliği,Ulusal Meteoroloji Enstitüsü,UME-95-014, Kasım 1995, Gebze/Kocaeli, https://www.ume.tubitak.gov.tr/sites/images/ume/ume-95-014.pdf

4) IPCC/OECD/IEA (1997) Revised 1996 IPCC Guidelines for National Greenhouse Gas Inventories. The Reference Manual. Intergovernmental Panel on Climate Change, Organisation for Economic Co-operation and Development, and International Energy Agency. Download at http://www.ipcc-nggip.iges.or.jp/public/gl/invs1.htm

5) IPCC (Intergovernmental Panel on Climate Change), 2006. 2006 IPCC Guidelines for National Greenhouse Gas Inventories. < http://www.ipcc-nggip.iges.or.jp/public/2006gl/ >

6) CSI (Cement Sustainability Initiative), 2005. CO_2 Accounting and Reporting Standard for the Cement Industry, Version 2.0. < http://www.wbcsdcement.org >.

7) CSI (Cement Sustainability Initiative), 2011. CO_2 and Energy Accounting and Reporting Standard for the Cement Industry, Version 3.0. < http://www.wbcsdcement.org/pdf/tf1_co2%20protocol%20v3.pdf >.

8) T. Wu, S. T. Ng, J. Chen, " Deciphering the CO_2 emissions and emission intensity of cement sector in China through decomposition analysis" Journal of Cleaner Production 352 (2022) 131627.

9) J. Ke, M. McNeil, L. Price, N. Z. Khanna, N. Zhou, "Estimation of CO_2 Emissions from China's Cement Production:Methodologies and Uncertainties" Energy Policy, Volume 57, Pages 172–181, June 2013.

10) Worrell, E., Price, L., Martin, N., Hendriks, C., Ozawa Meida, L., 2001. Carbon dioxide emissions from the global cement industry. Annual Reviews of Energy & the Environment 26 (8), 303-329.

11) Commission Decision of 29 January 2004, Establishing guidelines for the monitoring and reporting of greenhouse gas emissions pursuant to Directive 2003/87/EC of the European Parliament and of the Council, *Official Journal of the European Union*, 2004.

12) Monteiro P J M, Miller S A and Horvath A 2017 Towards sustainable concrete Nat. Mater. 16 698–9.

13) Miller S A, Horvath A and Monteiro P J M 2016 Readily implementable techniques can cut annual CO2 emissions from the production of concrete by over 20% Environ. Res. Lett. 11 074029

14) Miller S A, Horvath A and Monteiro P J M 2018 Impacts of booming concrete production on water resources worldwide Nat. Sustain. 1 69–76

15) Chen C, Habert G, Bouzidi Y and Jullien A 2010 Environmental impact of cement production: detail of the different processes and cement plant variability evaluation J. Clean. Prod. 18 478–85

16) Von Bahr B, Hanssen O J, Vold M, Pott G, Stoltenberg-Hansson E and Steen B 2003 Experiences of environmental performance evaluation in the cement industry. Data quality of environmental performance indicators as a limiting factor for benchmarking and rating J. Clean. Prod. 11 713–25

17) Gursel A P, Maryman H and Ostertag C 2016 A life-cycle approach to environmental, mechanical, and durability properties of "green" concrete mixes with rice husk ash J. Clean. Prod. 112 823–36

18) Su X, Luo Z, Li Y and Huang C 2016 Life cycle inventory comparison of different building insulation materials and uncertainty analysis J. Clean. Prod. 112 275–81

19) Van Den Heede P and De Belie N 2012 Environmental impact and life cycle assessment (LCA) of traditional and 'green' concretes: literature review and theoretical calculations Cem. Concr. Compos. 34 431–42

20) S.A. Miller, "The role of data variability and uncertainty in the probability of mitigating environmental impacts from cement and concrete", Environ. Res. Lett. 16 (2021) 054053. https://iopscience.iop.org/article/10.1088/1748-9326/abe677.

The Effect of Stud Walls on Dynamic Characteristics of Steel Building

Sertaç Tuhta[1*]

[1*] Ondokuz Mayıs Üniversitesi, Mühendislik Fakültesi, İnşaat Mühendisliği Bölümü, Samsun, Türkiye, (ORCID: 0000-0003-2671-6894), stuhta@omu.edu.tr

Öz

Günümüzde dünyada çelik yapıların kullanımı artmaktadır. Çelik yapıların diğer tüm bina türleri gibi deprem etkilerinden etkilendiği bilinmektedir. Bu duruma ek olarak çelik yapılar da diğer tüm nesneler gibi çevresel titreşimlerden etkilenir. Tüm bu etkilerden dolayı çelik yapılar zamanla taşıma gücünü kaybedebilir. Bu durumda yapının çökmesi gibi çok tehlikeli sonuçlara neden olur. Bu tür sorunları çözmek için kanıtlanmış çeşitli güçlendirme yöntemleri mevcuttur. Dikme duvarların kullanımı bu güçlendirme yöntemlerinden biridir. Dikme duvar güçlendirme yönteminin oldukça yaygın olduğu birçok çalışmada kanıtlanmıştır. Bu çalışmada, sonlu elemanlar yöntemi kullanılarak modal analiz yapılarak örnek bir çelik binada pervazların (dikme duvar) etkileri ortaya konmuştur. Özellikle ilk 5 modun yapı titreşim periyotları ve serbest titreşim modu şekilleri detaylı olarak ele alınmıştır. Böylece dikme duvarların yapının rijitliği üzerindeki olumlu etkisi daha net bir şekilde ortaya konmuştur. Tüm bu sonuçlar ışığında çelik yapıların güçlendirilmesinde dikme duvar yöntemi kullanılabilir.

Anahtar Kelimeler: Çelik yapılar, dikme (pervaz) duvarlar, Sonlu elemanlar metodu, Dinamik parametreler, Güçlendirme

The Effect of Stud Walls on Dynamic Characteristics of Steel Building

Abstract

Today, the use of steel structures is increase in the world. It is known that steel structures are affected by earthquake effects like all other building types. In addition to this situation, steel structures are affected by environmental vibrations like all other objects. Due to all these effects, steel structures may lose their bearing capacity over time. In this case, it causes very dangerous results such as collapse of the structure. Various proven retrofit methods are available to solve such problems. The use of stud walls is one of these retrofit methods. It has been proven in many studies that the stud walls reinforcement method is quite common. In this study, the effects of stud walls in a sample steel building are revealed by making modal analysis using the finite element method. In particular, the structure vibration periods and free vibration mode shapes of the first 5 modes are discussed in detail. Thus, the positive effect of stud walls on the rigidity of the structure has been more clearly demonstrated. In the light of all this results, the method of stud walls can be used in the reinforcement of steel buildings.

Keywords: Steel buildings, Stud walls, Finite element method, Dynamic parameters, Retrofitting

1. Introduction

The wall studs form the vertical upright portion of a wall frame. The top and sole plates of the frame are fitted to the floor and ceiling and the wall studs are added, evenly spaced along the length of the wall. The vertical portion of the wall studs forms the top of a rigid frame. Since the wall studs only take up the top portion of the

wall, any distance between them is purely the physical space needed for the frame. Also called overhead braces, wall anchors are used to secure the wall studs to the studs of the adjoining wall, thus creating the wall frame. The development of the stud wall system has improved structures resistance to earthquakes. It is a system that has only recently begun to be used in the construction industry in comparison to other traditional seismic reinforcement elements. Bolting holds stud walls to beams that are nailed to the columns. Its purpose is to provide energy consumption, boost system stiffness, and withstand all lateral loads. It lessens earthquake-related damage. Conventional steel beams, on the other hand, are made of steel plates with welded-on connections and are susceptible to buckling and fracture during an earthquake. The stud wall system is generally preferred over traditional beams as it does not involve a lot of structural elements. In other words, there is very less material involved. Stud wall system is also preferred by contractors, as they save on building cost. Other systems, such as tension (wire rope) system and cold-formed steel stud wall system, however, are used widely in structures.

Steel beams and columns are made of steel plates, which are welded together to form steel beams. Steel beams are not easy to install, as they are brittle. The reinforcements that are placed in between the plate and beam, known as tension members, help provide a sufficient amount of lateral support to the foundation during an earthquake. Stud walls are different from the foundation walls, because the stud wall system does not sit on the ground. Depending on the height of the foundation, various types of stud wall systems can be implemented. Stud wall schematic drawing is given in Figure 1.

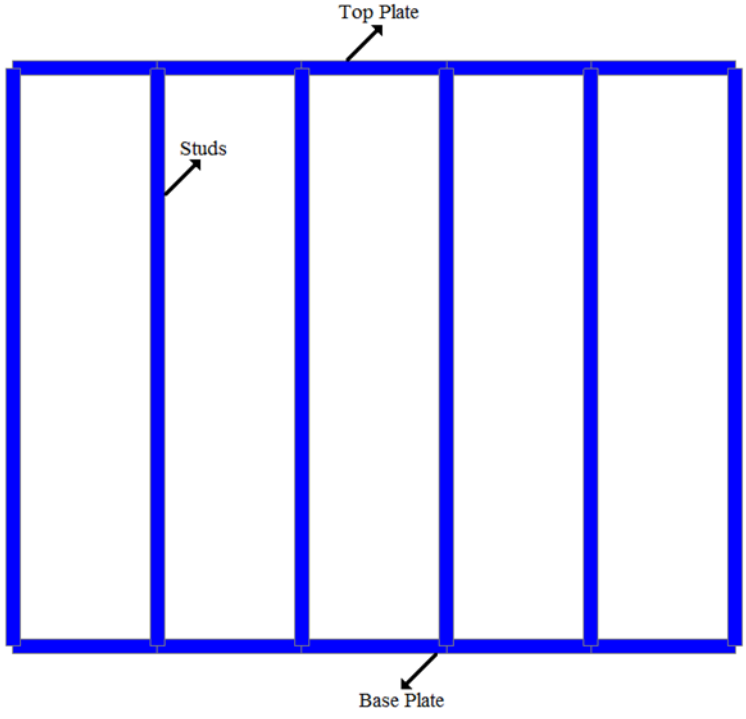


Figure 1. Stud wall schematic drawing

Researchers have carried out many studies using both the finite element method and the reinforcing methods. There are many other studies by the authors using the finite element method before. In this study, studies [1], [2], [3], [4], [5], [6], [7], [8], [9] on the use of the finite element method were used. With all this knowledge, this new study has been carried out.

Researchers have conducted studies [10], [11], [12], [13], [14], [15], [16], [17], [18], [19] about stud walls which also contributing to this study.

The aim of this study is to examine the effects of retrofit with stud walls on dynamic characteristics in steel building. There may be a need for a retrofit method without economical disadvantages or excessive dead load increments. In such cases, the retrofit method with stud wall is also known to be an option. For this reason, it is very important to reveal the effect of stud wall on dynamic characteristics.

2. Material and Method

In this study, A steel building model was created and modal analysis was carried out with the finite element method. The steel building model was retrofitted with stud walls and a retrofitted model building model was created for comparison. In the application of the finite element method, the SAP2000 package program, which is used in the field of academic and engineering applications all over the world, was used.

2.1. The Model of Reinforced Steel Building

It is a 5-storey steel building with two spans in x and y directions (6 m) and a floor height of 4 meters. Columns and beams are 20x25x1 cm box profile, floor thickness is 2 cm steel plate.

By designing the building as symmetrical and simple, it is aimed to reveal the result of the retrofit to be applied more clearly. The spans are therefore taken equal.

The 3D finite element model in SAP2000 package software of the model steel building is given in Figure 2.

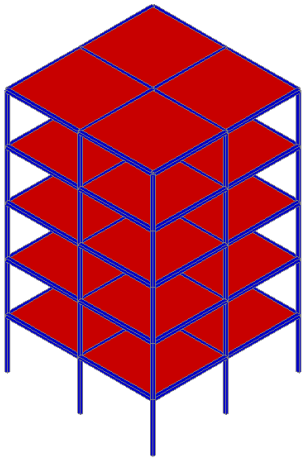


Figure 2. The model steel building's 3D view

2.2. The Model of Retrofitted Steel Building

A stud wall was applied to one of the openings in the x and y directions of the building. Stud wall measures 10x10x0.5 cm at 1m intervals and is made of steel. The 3D finite element model in SAP2000 package software of the retrofitted model steel building given in Figure 3.

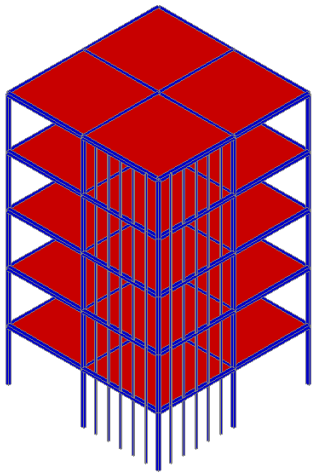


Figure 3. The retrofitted steel building's 3D view

3. Result and Discussion

Model steel building and retrofitted model steel building were analysed separately. The modal analysis results of each model are shared under separate headings. The results include the analysis results of the first five modes. Mode shape and period values are taken into consideration for each mode. The parameters obtained for both models were compared for each mode separately. During the analysis, the SAP2000 package software, which is a finite element method software, was used. The steel material used was taken according to ANSI/AISC 360-10 standards.

3.1. Analysis Results of Model Steel Building

The model steel building was analysed without retrofitting. When the first five modes are examined, the results obtained are presented in figure 4,5,6,7,8 as period values and mode shapes for each mode.

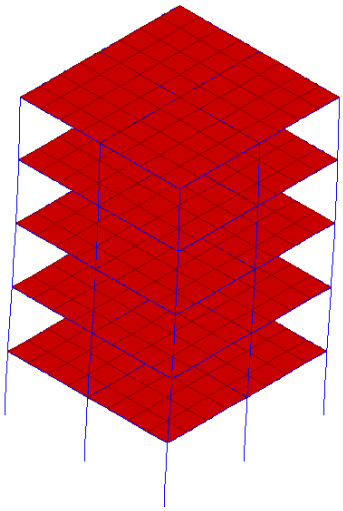


Figure 4. 1. Mode shape (T = 1.45 s)

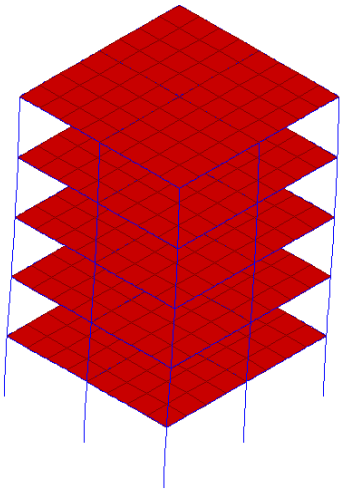


Figure 5. 2. Mode shape (T = 1.35 s)

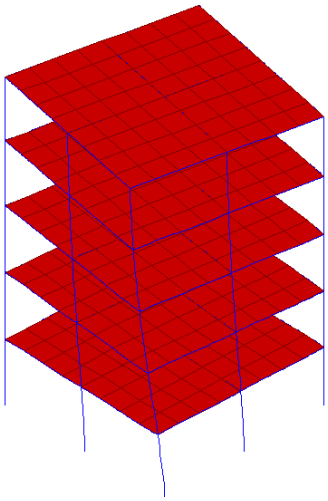


Figure 6. 3. Mode shape (T = 1.02 s)

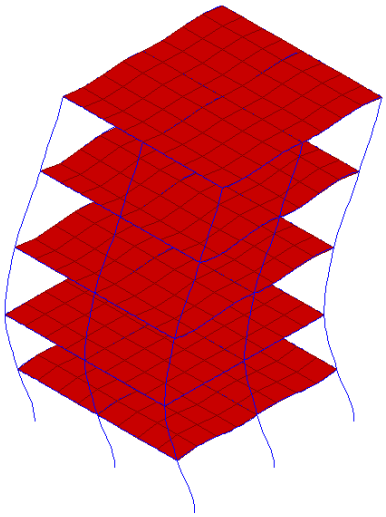


Figure 7. 4. Mode shape (T = 0.46 s)

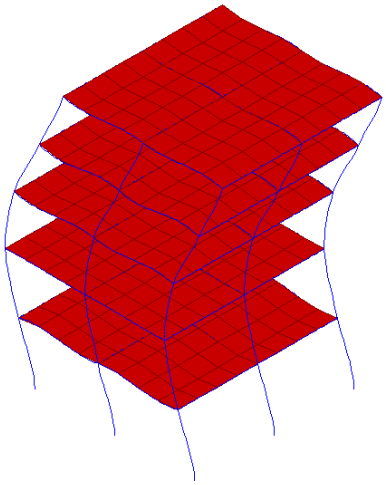


Figure 8. 5. Mode shape (T = 0.42 s)

3.2. Analysis Results of Retrofitted Model Steel Building

The model steel building was analysed with reinforcing by stud walls. When the first five modes are examined, the results obtained are presented in figure 9,10,11,12,13 as period values and mode shapes for each mode.

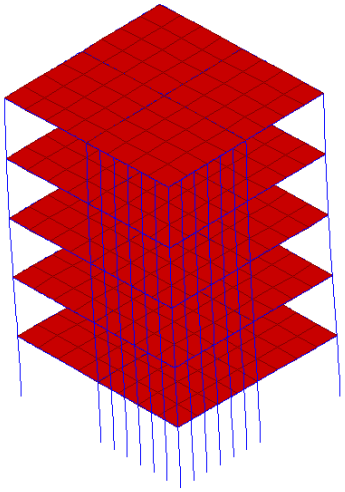


Figure 9. 1. Mode shape (T = 1.38 s)

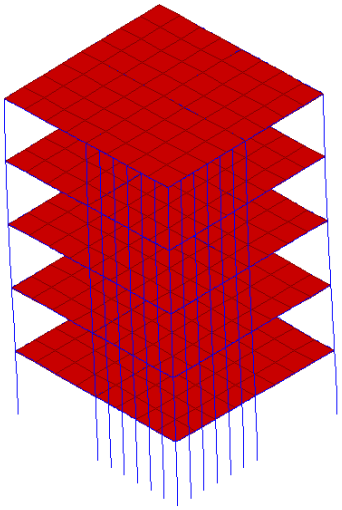


Figure 10. 2. Mode shape (T = 1.29 s)

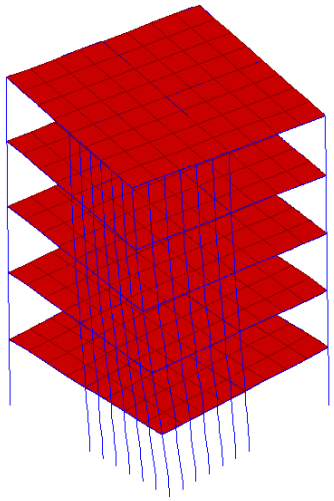


Figure 11. 3. Mode shape (T = 0.95 s)

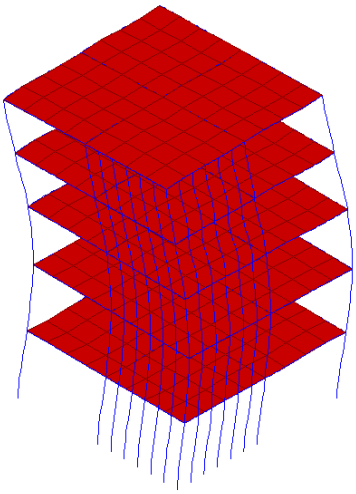


Figure 12. 4. Mode shape (T = 0.44 s)

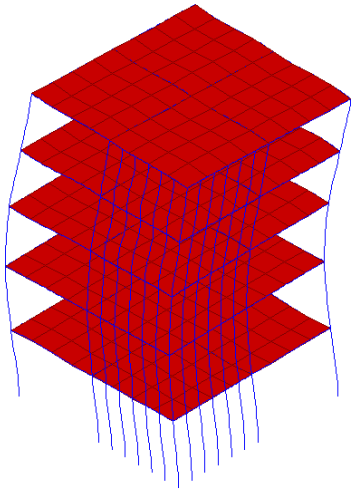


Figure 13. 5. Mode shape (T = 0.40 s)

3.3. Comparison of Analysis Results

The comparison of period values of the model steel building and retrofitted model steel building is given in Table 1.

Table 1. Comparison of period values

Mode	**1**	**2**	**3**	**4**	**5**
Non-Retrofitted	1.45	1.35	1.02	0.46	0.42
Retrofitted	1.38	1.29	0.95	0.44	0.40
Difference (s)	0.07	0.06	0.07	0.02	0.02
Difference (%)	4.83	4.44	6.86	4.35	4.76

The comparison of mode shapes of the model steel building and retrofitted model steel building is given in Table 2.

Table 2. Comparison of mode shapes type

Mode	**1**	**2**	**3**	**4**	**5**
Non-retrofitted	Translational	Translational	Torsional	Translational	Translational
Retrofitted	Translational	Translational	Torsional	Translational	Translational

4. Conclusions

In the mode 1, the period difference between non-retrofitted model and retrofitted model status was obtained as 0.07 s. The effect of period retrofitting with stud walls as a percentage was determined as 4.83.

In the mode 2, the period difference between non-retrofitted model and retrofitted model status was obtained as 0.06 s. The effect of period retrofitting with stud walls as a percentage was determined as 4.44.

In the mode 3, the period difference between non-retrofitted model and retrofitted model status was obtained as 0.07 s. The effect of period retrofitting with stud walls as a percentage was determined as 6.86.

In the mode 4, the period difference between non-retrofitted model and retrofitted model status was obtained as 0.02 s. The effect of period retrofitting with stud walls as a percentage was determined as 4.35.

In the mode 5, the period difference between non-retrofitted model and retrofitted model status was obtained as 0.02 s. The effect of period retrofitting with stud walls as a percentage was determined as 4.76.

When the mod shapes were examined, no mod shape type changes were observed with the retrofit with stud wall. However, it has been observed clearly that the mode shapes move more rigidly with the retrofit.

In the light of all these results, decrease in periods was detected in first five modes. Thus, it is seen that the rigidity of the structure increases by strengthening the model steel building with stud walls. In the 1st mode, in other words, there is a decrease of 4.83 percent in the dominant period value. In addition, there is a large decrease of 6.86 percent in the period value in the 3rd mode. It has been observed that the 3rd mode shape is the torsional mode shape. The fact that this effect is in the form of a torsion mode is an indication that this retrofitting also reduces the effects of torsion. Of course, it should be taken into account that the design of the structure and retrofitting is very important in obtaining the data in this way. Incorrect model selection and faulty retrofit designs can make data more unreliable. In the light of all this obtaining information, the retrofit method with stud walls may be used in steel buildings.

References

[1] Ziada, M., Tuhta, S., Gençbay, E. H., Günday, F., & Tammam, Y. (2019). Analysis of Tunnel Form Building Retrofitted with CFRP using Finite Element Method. International Journal of Trend in Scientific Research and Development, 3(2), 822–826.

[2] Tuhta, S., Günday, F., & Pehlivan, N. C. (2019). Investigation of Cfrp Retrofitting Effect on Masonry Dome on Bending Moment Using Finite Element Method. International Journal of Innovatıons in Engineering Research and Technology, 6(6), 18–22.

[3] Tuhta, S., Günday, F., & Alihassan, A. (2020). The Effect of CFRP Reinforced Concrete Chimney on Modal Parameters Using Finite Element Method. International Journal of Innovations in Engineering Research and Technology, 7(2), 1–6.

[4] Tuhta, S., Günday, F., & Köroğlu, E. (2021). The Effect of TMD on The Periods and Mode Shapes of The Reinforced Concrete Building by Finite Element Analysis. JournalNx, 7(12), 5–13.

[5] Bakkour, F., Tuhta, S., & Günday, F. (2022). Determination of Modal Parameters of Reinforced Concrete Box Culvert Retrofitted with GFRP Using Finite Element Method. International Journal of Innovations in Engineering Research and Technology, 9(4), 1–9.

[6] Kasimzade, A.A., Tuhta, S., Günday, F. & Aydın, H. (2021). Obtaining Dynamic Parameters by Using Ambient Vibration Recordings on Model of The Steel Arch Bridge. Periodica Polytechnica Civil Engineering, 65(2), 608-618.

[7] Hammoud, M. A., Tuhta, S., & Günday, F. (2022). Determination of Modal Parameters of Reinforced Concrete Tunnel Retrofitted with CFRP using Finite Element Method. International Journal of Innovations in Engineering Research and Technology, 9(4), 10–18.

[8] Kasimzade A.A., Structural Design and Analysis Based on FEM with SAP2000 in the Light of Current Codes (is included education and finite element analysis software on a DVD-QR code), Nobel Publication, December 2021, p. 342.

[9] Kasimzade A.A., Finite Element Method foundation and Application to Structural Analysis (is included education and finite element analysis software on a DVD-QR code), Nobel Publication, June 2018, p. 818.

[10] Belal, M. F., Serror, M. H., Mourad, S. A., & Saadawy, M. M. E. (2020). Numerical study of seismic behavior of light-gauge cold-formed steel stud walls. Journal of Constructional Steel Research, 174, 106307.

[11] Serrette, R., & Ogunfunmi, K. (1996). Shear resistance of gypsum-sheathed light-gauge steel stud walls. Journal of Structural Engineering, 122(4), 383-389.

[12] Restrepo, J. I., & Bersofsky, A. M. (2011). Performance characteristics of light gage steel stud partition walls. Thin-Walled Structures, 49(2), 317-324.

[13] Moghimi, H., & Ronagh, H. R. (2009). Performance of light-gauge cold-formed steel strap-braced stud walls subjected to cyclic loading. Engineering Structures, 31(1), 69-83.

[14] Iuorio, O., Macillo, V., Terracciano, M. T., Pali, T., Fiorino, L., & Landolfo, R. (2014). Seismic response of Cfs strap-braced stud walls: Experimental investigation. Thin-Walled Structures, 85, 466-480.

[15] Fülöp, L. A., & Dubina, D. (2004). Performance of wall-stud cold-formed shear panels under monotonic and cyclic loading: Part I: Experimental research. Thin-Walled Structures, 42(2), 321-338.

[16] Fiorino, L., Terracciano, M. T., & Landolfo, R. (2016). Experimental investigation of seismic behaviour of low dissipative CFS strap-braced stud walls. Journal of Constructional Steel Research, 127, 92-107.

[17] Mpilias, N., Rajabipour, A., Rodeghiero, B., & Bazli, M. (2022). Lateral load capacity of the common steel stud wall framing braced bays in Australia's Northern Territory, Case Studies in Construction Materials, 17, e01275.

[18] Ibrahim, Y. E., Hameed, A., Qazi, A. U., Rasool, A. M., Latif, M. F., & Qureshi, M. U. (2021). Experimental response of cold-formed steel stud shear wall with hardboard sheathing under seismic loading. Case Studies in Construction Materials, 15, e00574.

[19] Bao, W., Jiang, J., Shao, Y., & Liu, Y. (2019). Experimental study of the lateral performance of a steel stud wall with a semi-rigid connected frame. Engineering Structures, 183, 677-689.

Borlu Çimento Harçlarının Fizikomekanik Özellikleri

Atila Gürhan Celik, İbrahim Günes

[1]Giresun Üniversitesi, Mühendislik Fakültesi, İnşaat Mühendisliği Bölümü, 28200, Giresun/Türkiye

Özet

Bu çalışmada, Göltaş Çimento Fabrikası'nda (Isparta, Türkiye) üretilen Bor çimentosu ve Portland kompozit (PC) çimentosu üzerinde mekanik ve fiziksel deneyler yapılmıştır. Bağlayıcı malzeme olarak PC (CEM I 42,5R) ve BC(Borlu çimento) kullanılarak üretilen betonların performansları araştırılmıştır. Yapılan çalışmalar sonucunda, 180 günlük kür sonunda BC ve PC harçların basınç dayanımı ve hidratasyon ısısı BA' dan %8,7 ve PC'den %82 daha düşük bulunmuştur.

Anahtar kelimeler: Boron cement, Compressive strength, Hydration, Portland cement.

Investigation Physicomechanical Properties of Boron Cement Mortars

Abstract

In this study, mechanical and physical experiments are carried out on Boron cement and Portland composite (PC) cement produced in Göltaş Cement Plant (Isparta, Turkey). The performances of concretes manufactured by using PC (CEM I 42,5R) and Boron cement as binding material are investigated. As a result of the studies performed, the compressive strength of the mortars with BC and PC mortars at the end of 180 days of curing, respectively, and the hydration heat is 8.7% lower than BA and 82% lower than PC.

Keywords: Polypropylene, Concrete, Water absorption, Density, Unit weight

4. Giriş

Çimento, kalker ve kil karışımının yüksek sıcaklıkta ısıtıldıktan sonra öğütülmesi ile elde edilen hidrolik bir bağlayıcıdır. Çimento bağlayıcılık görevini su ile tepkimeye girdikten sonra kazandığı için hidrolik bağlayıcı olarak adlandırılır (1). Normal portland klinkerinde dört ana faz mevcuttur ve klinkerleşme sıcaklığı yaklaşık 1400-1450°C'dir: Temel faz Alit'in (C_3S) yanısıra, Belit (β-C_2S), Celit (C_3A) ve Brownmillerit (C_4AF) minerallerinden oluşur. Belit çimentolarının esasını C_2S fazı oluşturur. Kristal yapılarına göre değişen dört belit modifikasyonu mevcuttur. γ-C_2S: pasif hidrolik özelliğe sahiptir ve mukavemet vermez, β-C_2S: erken dayanımı düşük ancak ileri yaşlarda alit ile aynı mukavemete ulaşır, α' - C_2S: reaktif veya aktif belit olarak adlandırılır ve α - C_2S: reaktif veya aktif belit - yüksek sıcaklık formasyonu olarak bilinmektedir (2-5). Bor atığının klinkere ilave edilerek elde edilen çimentoların priz süreleri, basınç dayanımları, çekme dayanımları ve radyasyon geçirgenlikleri ölçülmüş ve portland çimentosu ile mukayese edilmiştir. Beton örnekler üzerinde yapılan mekanik ve fiziksel testler sonucunda %5 atık ilavesine kadar mukavemet değerleri portland çimentosu ile elde edilen örneklerden yüksek bulunmuştur. %5 atık katkısından sonra mukavemet değeri giderek azalmaktadır (6). Yapılan araştırmalarda, endüstriyel üretim sonrasında elde edilen klinkerler üzerinde yapılan mineralojik analizler sonucunda, borlu klinkerin, %6,5 kolemanit ihtiva eden hammaddenin fırına girmesinden itibaren elde edildiği görülmüştür. Optimum koşullara %10 kolemanit ihtiva eden hammadde ile ulaşılmıştır[7]. Bu çalışmada, PC ve BA harçlardan imal edilen betonların performans özellikleri araştırılmıştır.

2. Materyal ve Metot

2.1. Materyal

2.1.1. Çimento

Çalışmalarda, gerek çimento kimyasal ve fiziksel özelliklerinin belirlenmesi ve gerekse beton deneylerinde Göltaş Çimento Fabrikası'nda üretilen BC ve PC(CEM I 42,5R) tipi çimento kullanılmıştır.

2.1.2. Agrega

Bu çalışmada kullanılan agregalar 0-2mm, 2-4mm, 4-8mm 8-16 16-22,4 ve 22,4- 32 tane boyutuna sahip olacak şekilde gruplandırılmışlardır. TS 802'ye uygun olarak maksimum dane boyu 22,4 mm alınmıştır.

2.1.3. Karışım Suyu

Yapılan çalışmada karışım suyu olarak Giresun ilinde şehir şebeke suyu kullanılmıştır. Kullanılan suyun ilgili standartlarda yer alan özellikleri sağlamasına dikkat edilmiştir.

2.1.5. Süper Akışkanlaştırıcı Katkı Maddesi

Glenium51'in geleneksel süperakışkanlık verici katkı maddesi kullanılmıştır. Bu süper akışkanlaştırıcının en öenmli özelliği çimento dağılımının etkinliğini büyük ölçüde arttırmasıdır.

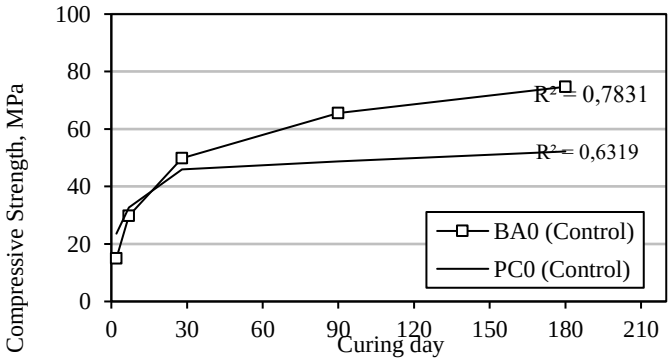
2.2.Metod

Deneysel çalışmalar Ulusal Bor Araştırma Enstitüsü laboratuvarlarında gerçekleştirilmiştir. Ürün olarak Göltaş Çimento Fabrikası PC ve BA kullanılarak beton numuneler üretilmiştir. Harç karışımları 150x150x150 mm kalıplarda ve kimyasal katkı kullanılmadan üretilmiştir. Örnekler 24 saat sonra kalıptan çıkarılarak şebeke suyunda 20 0C sıcaklıkta (2, 7, 28,90 ve 180) kürlenmiştir. Örnekler üzerinde fizikomekanik deneyleri gerçekleştirilmiştir. Hidratasyon ısısı ile ilgili yapılan ölçümler ASTM C1702□29□ standardına uygun olarak MC-CAL izotermal kalorimetre cihazı kullanılarak gerçekleştirilmiştir.

3. Deneysel Sonuçlar

3.1. Basınç Dayanımı

Şekil 1'de BC ve PC harçlarının basınç dayanımı sonuçları 180 güne kadar sunulmuştur. BC sonuçları ilk 7 gün hariç tüm kürleme çağlarında PC'den daha yüksek olduğu tespit edilmiştir.

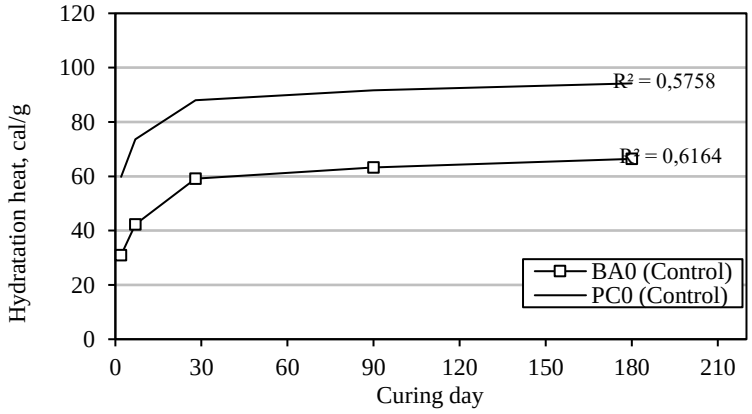


Şekil 1. Harçların basınç dayanım değerleri

BC karışımların erken dayanımının düşük geç dayanımlarının zamanla arttığı görülmüştür. BC harçların dayanımları, 28, 90 ve 180 gün kür süresine bağlı olarak sırasıyla 49.9, 65.6 ve 74.7 MPa olarak elde edilmiştir.

3.2. Hidratasyon Isısı(cal/gr)

Beton harçların hidratasyon ısısı değeri önemli fiziksel özelliğidir. Özellikle kütle betonlarında kullanılması gereken çimentoların 7 günde en fazla 60 cal/g ve 28 günde de an fazla 70 cal/g civarında toplam hidratasyon ısısına sahip olmaları talep edilir.

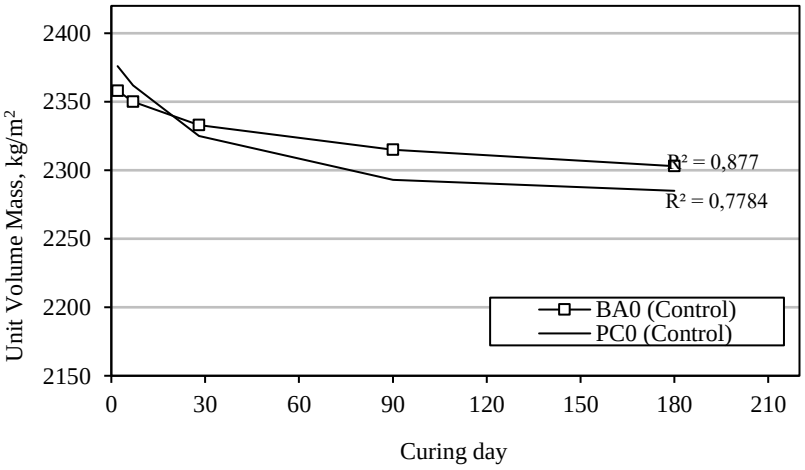


Şekil 2. Harçların hidratasyon ısısı değerleri

Şekil 2' de BC ve PC(CEM I 42,5R) içeren çimentoların hidratasyon ısılarının karşılaştırılması verilmektedir. Grafikten görüldüğü üzere, BA katkılı harçların hidratasyon ısısı PC harçlara kıyasla %88 daha düşük çıkmıştır.

3.3. Birim Hacim Ağırlık(kg/m^3)

Birim ağırlık test sonuçları, 180 gün sonunda iyi ve en düşük birim ağırlığın PC katkılı beton harçlardan elde edildiğini (2285kg/m^3) göstermektedir (Şekil 3). Ayrıca, kür süresinin artması ile beton harçların BHA değerlerinin düştüğü belirlenmiştir. Hafiflik özelliği, beton ve inşaat sektörü için en önemli özelliklerden biridir.



Şekil 3. Harçların birim hacim ağırlık değerleri

4. Sonuç ve Öneriler

Çalışmanın sonuçları aşağıda verilmiştir;

- BC katkılı harçların 28 günlük hidratasyon ısısı (59.1 cal/g) ve PC (88.2 cal/g) bulunmuştur. BC harçların hidratasyon ısısı değeri PC' ye göre %88 daha düşük çıkmıştır.
- Birim ağırlık, PC harçlar BA harçlara kıyasla daha düşük bulunmuş olup %3.3 oranında azalmıştır.
- BC karışımların dayanımları, 28, 90 ve 180 gün kür süresine bağlı olarak sırasıyla 49.9, 65.6 ve 74.7 MPa olarak elde edilmiştir. Bu harçların dayanımları 180 günlük kürleme sonunda karşılaştırıldığında BC betonlar PC^ ye kıyasla % 38,6 daha yüksek çıkmıştır.
- BC harçlarından üretilen betonların durabilite yönünden kütle betonu uygulamalarında kullanılmasının avantajlı olacağı sonucuna varılmıştır.
- Borlu çimento harçlara farklı miktarlarda puzolan ve mineral katkılar takviye edilerek çalışmalar yapılmalıdır.

Kaynaklar

[1] P. C. Hewlet, "Lea's Chemistry of Cementand Concrete", Fourth Edition, London, 1998.
[2] S. Türk, G. Gürbüz, T. Ertün, A. Yeginobali, Heat of hydration and shrinkage properties of boron containing active belite cements, International RILEM-JCI Seminar on Concrete Durability and Service Life Planning: Curing, Crack Control, Performance in Harsh Environments, RILEM Publications SARL, pp:397- 404, 2006.
[3] Patent, TR 2006 07669 Çelik A.G, Soylu F, İnger E, Ertün T, Gürbüz G and Türk S. Colemanite-Added Portland Cement and Production Method (Turkish Type Cement), 2006.
[4] A. Gies, D. Knöfel, Influence of alkalies on the composition of belite-richcement clinker sand the technological properties of the resulting cements, Cem. Concr. Res. vol.16, pp. 411-422, 1986.
[5] Celik A G and Cakal G O Characterization of espey colemanite and variation of its physical properties with temperature. *Physicochem. Prob. Miner. Proces.* 52: 66 – 76, 2016.
[6] Chunmeng J, Linhua J, Xinjun T, Jingwei G and Hongqiang C Impact of calcium leaching on mechanical and physical behaviors of high belite cement pastes. Constr. Build. Mater. 286: 122983, 2021.
[7] Slater C S Hydraulic cement and method of producing same, US patent-3, 861-928, 1975.

Production of Antibacterial Powders

Büşra Alomar [1*], Atilla Evcin[2]

[1] Basankul Ariha, Idlib/Syria

[2] Afyon Kocatepe University, Materials Science and Engineering Department, Afyonkarahisar, Türkiye

Abstract

In this study, researchers were carried out on the production of antibacterial ceramic coatings, which can contribute to the development of human health and the environment, and also attract the product market in different directions. The aim of the study was to produce anti-bacterial powders by wet chemical method and to add these powders to the operating conditions and to test the final products for bacteria. Characterization of the produced powders was done by XRD. Studies were carried out on the production of tiles with antibacterial properties by adding the antibacterial powders to the business glaze. As a result of antibacterial tests, it has been seen that the powders have antibacterial properties.

Keywords: Antibacterial, hydroxyapatite, silver, cupper, zinc

1. Introduction

The environment we live in is the environment in which we are in contact with microorganisms, which are among the most important factors that cause diseases. Due to the pandemic in recent years, interest in antibacterial products is increasing. An increase has been observed in studies on metal-added products, especially with antibacterial effect. The effectiveness of metals such as silver, copper and zinc against bacteria has been known since ancient times. Glass, ceramics, polymers and composites containing this metal and its oxides are widely studied materials [1-11].

This study aimed to examine the preparation and antibacterial activity of glazed ceramic tiles consists of metal (Ag, Cu, Zn) doped hydroxyapatite powder by sol-gel method. The obtained powders were investigated by X-ray Diffraction(XRD). The antibacterial activity of the metal-doped glaze was studied against Gram-negative Escherichia coli.

2. Materials and Method

The experimental study was carried out in three stages. In the first step, silver, copper and zinc ions were dissolved in water and added to the $Ca(OH)_2$ (calcium hydroxide) solution for the production of metal ion doped hydroxy apatite by wet chemical method. H_3PO_4 (phosphoric acid) solution was dropped on it and mixed with a magnetic stirrer. The pH values of the suspensions prepared by adding metal salts (0.01 mol) in container was controlled by continuous mixing. The precipitate formed as a result of mixing and adding phosphoric acid in stoichiometric ratio was dried at 120 °C. Metal ion doped hydroxyapatite structure was investigated by XRD (X-Ray Diffraction) analysis of the milled powders. Antibacterial powders prepared in the second stage were added to the wall tile production glaze in different proportions (1%, 2% and 3% w).



Figure 1. Experimental setup.

The wall tiles in the size of (20X20X7) mm produced in the ceramic plant are fed to the production line for engop application after drying in the range of 200ºC inlet temperature and 70ºC outlet temperature in order to be resistant to tape applications. The tiles taken from the tape were reduced to 10X10 size before the glaze suspension was applied. The liter weight of the glaze suspension taken from the enterprise was determined as 1935 g/L. The liter weight was reduced to 1700 g/L so that the antibacterial powder could be thoroughly mixed and applied easily on the tile. After providing the appropriate liter weight, Cu-Zn-Ag containing antibacterial powder was added to the glaze suspension at 1%, 2%, 3% and mixed in a jet mill for 30 minutes. Prepared glaze suspensions were poured 7 grams on each tile with a pistol in the glazing unit. After the glazed tiles were dried in an oven at 225ºC for 30 minutes, they were placed in the oven to be fired for 60 minutes.

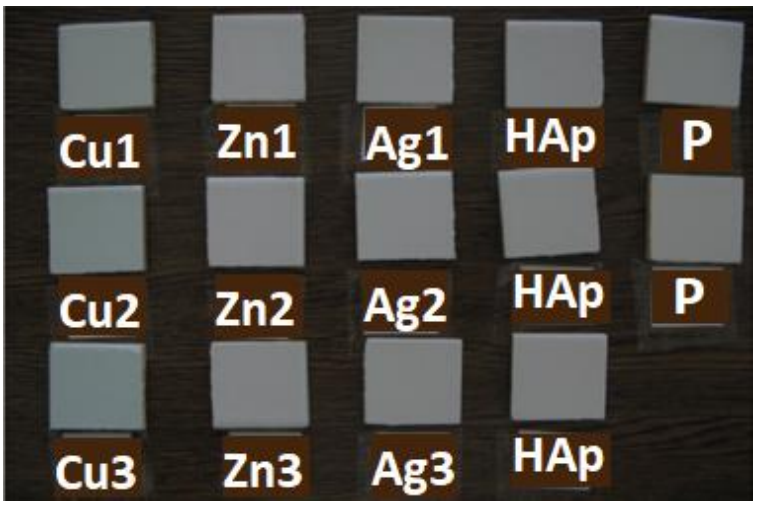


Figure 2. Glazed tiles with antibacterial powder..

Antibacterial Test

The number of E. coli (25922) bacteria was determined by the smear plate method using Baird Parker agar. First of all, E. coli (25922), the bacteria to be used in the analysis, were grown in nutrient broth for 24 hours

at 37°C. After inoculation of 105 cfu/mL bacteria per cm^2 on each sample surface, it was spread homogeneously on the surface with a sterile pipette. The medium to be used in the analyzes was sterilized in an autoclave at 121°C under 1 atmosphere pressure for 20 minutes and then cooled to room temperature. After incubation, the number of bacteria in cm2 of the samples was calculated by counting the black colored colonies with a white zone around them larger than 0.5 mm.

Antibacterial properties of samples prepared using the agar disc diffusion method were also tested. Agar disc diffusion method, Biswas et al. (2014) from the study by and some modifications were made (Biswas et al. 2014). After the microorganism to be tested was activated on Miller Hinton agar, one lop was taken and planted in 5 mL Caso broth. Incubation was performed at 37°C at 180 rpm until the McFarland standard of 0.5 was reached. A bacterial suspension containing 1-1.5x107 cells was prepared with 0.85% w/v NaCl. Add 100 µL of the prepared bacterial suspension to petri dishes and use a drigalski spatula spread on Miller Hinton agar. It was waited for 15 minutes for the agar to dry. After this process, the prepared membrane with a diameter of 6 mm was placed on agar. After this process, the petri dishes were incubated flat at 37°C for 24 hours. It was determined whether they formed a zone or not [12].

3. Results and Discussion

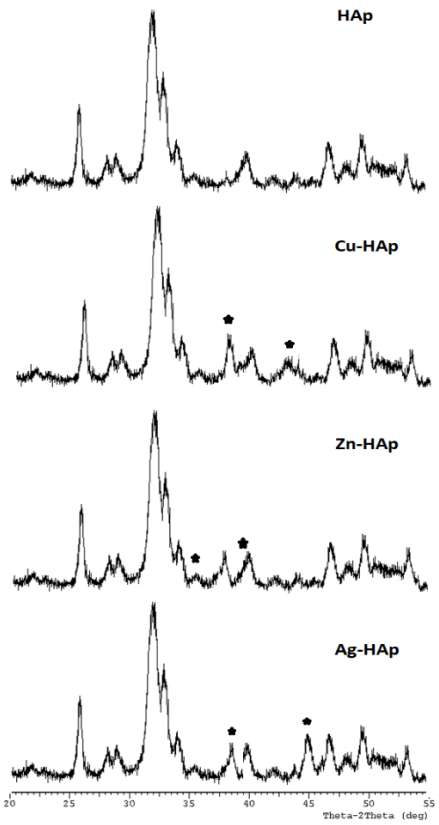


Figure 2. XRD analysis of powder

As can be seen in Figure 2, the xrd diagram of pure and metal-added powders is shown. Metal ion doping is evident as a result of XRD analysis. When the literature is compared, the results obtained are similar [13-20].

Antibacterial test results are shown in the Table 1. From Table 1, as the metal ion concentration increases, its antibacterial activity increases. Accordingly, the most effective metal ion is silver, followed by copper and zinc.

When the zone diameters are examined, it is seen that the antibacterial tendency is the same. There are also studies with similar results in the literatüre [21-24].

Table 1. Antibacterial tests

Substance	Amount %w	Bacterial amount (kob/cm^2)	Zone diameter (mm)
P	-	5.10^5	-
HAp	1	$2x10^4$	4
	2	$6x10^3$	6
	3	$1x10^3$	7
Cu-HAp	1	$1x10^2$	11
	2	$0.5x10^2$	12
	3	10	15
Zn-HAp	1	$1x10^3$	8
	2	$6x10^2$	10
	3	$0.4x10^2$	12
Ag-HAp	1	-	15
	2	-	17
	3	-	19

4. Conclusions

Metal ion added antibacterial powders were produced by sol-gel method.The expected result was obtained in XRD analysis and Ag-Hap, Cu-Hap and Zn-Hap powders were produced. These produced powders are added to the wall tile glaze in different proportions to produce tiles for antibacterial properties. Antibacterial test were examined by the smear plate method and dick diffusion method. As a result of bacterial analysis, its effectiveness against e-coli was observed. According to these results, it is expected that the use of antibacterial powder-added glazed tiles will have positive results in terms of health, especially in environments with communal life.

.

References

[1] Morones, J.R., Elechiguerra, J.L., Camacho, A., Holt, K., Kouri, J.B., Ramírez, J.T., Yacaman, M.J., 2005. The Bactericidal Effect of Silver Nanoparticles. Nanotechnology 16, 2346-2353.

[2] Mukhtar, H.A., Tia, E.K., John, A.B., Charles, W.B., Jeremy, W.H., 2011. Adsorption and photocatalytic degradation of human serum albuminon TiO2 and Ag-TiO2 films. Journal of Photochemistry and Photobiology A: Chemistry 222, 123-131.

[3] N. Baheiraeia, F. Moztarzadeha, M. Hedayati, Antibacterial Ag/SiO2 Thin Film on Glazed Ceramic Tiles Prepared by Sol-gel Method, 18th Iranian Conference on BioMedical Engineering, 14-16 December 2011, Tehran, Iran

[4] S.G. Yeo, C.H. Ahn, I.S. Kim, Y.B. Park, Y.H. Park, S.B. Kim, Antimicrobial effect of tea extract from green tea, oolong tea and black tea, J. Korean. Soc. Food. Nutr. 24 (1981) 293–298.

[5] Feng, Q.L., Wu, J., Chen, G.Q., Cui, F.Z., Kim, T.N., Kim. J.O., 2000. A Mechanistic Study of the Antibacterial Effect of Silver I ons onEscherichia Coli and Staphylococcus Aureus. Journal of Biomedical Materials Research Part 52, 662-668

[6] T.N. Kim, Q.L. Feng, J.O. Kim, J. Wu, H. Wang, G.C. Chen, F.Z. Cui, Antimicrobial effects of metal ions (Ag+, Cu2+, Zn2+) in hydroxyapatite, J. Mater. Sci. Mater. Med. 9 (1998) 129–134.

[7] Harikishorea, M. & M, Sandhyarani & Venkateswarlu, Dr & Nellaippana, T.A. & Rameshbabua, N.. (2014). Effect of Ag Doping on Antibacterial and Photocatalytic Activity of Nanocrystalline TiO2. Proceedia Materials Science. 6. 10.1016/j.mspro.2014.07.071.

[8] B.O. Jung, Y.M. Lee, J.J. Kim, Y.J. Choi, K.J. Jung, S.J. Chung, The antimicrobial effect of water soluble chitosan, J. Korean. Ind. Eng. Chem. 10 (1999) 660–665.

[9] S.Q. Sun, B. Sun, W. Zhang, D. WANG, Preparation and antibacterial activity of Ag–TiO2 composite film by liquid phase deposition (LPD) method, J. Bull. Mater. Sci. 31 (2008) 61–66.

[10] Liu, Hairong & Chen, Cu & Song, Li & Ye, Reifang & Lu, Jianying & Li, Huiping. (2008). Ag-Doped Antibacterial Porous Materials with Slow Release of Silver Ions. Journal of Non-Crystalline Solids. 354. 1314-1317. 10.1016/j.jnoncrysol.2007.02.098.

[11] Pham, Dinh-Chuong & Nguyen, Thi Hiep & Ngoc, Uyen & Le, Trang & Tran, Tuong & Nguyen, Dai Hai. (2018). Preparation, Characterization and Antifungal Properties of Chitosan-Silver Nanoparticles Synergize Fungicide Against Pyricularia oryzae. Journal of Nanoscience and Nanotechnology. 18. 10.1166/jnn.2018.15400.

[12] Özcan, B. , Kır, E. , Bezir, N. Ç. , Sardohan Köseoğlu, T. , Özmen, İ. & Evcin, A. (2022). Gümüş Nitrat Katkılı Modifiye Nanofiber Membranların Hazırlanması, Karakterizasyonu ve Antibakteriyel Özellikleri . Afyon Kocatepe Üniversitesi Fen Ve Mühendislik Bilimleri Dergisi , 22 (1) , 57-67 . DOI: 10.35414/akufemubid.866861

[13] Ruíz-Baltazar, Álvaro & Reyes-López, Simón & Silva-Holguin, Pamela & Larrañaga, Daniel & Estevez, Miriam & Perez-Campos, Ramiro. (2018). Novel biosynthesis of Ag-hydroxyapatite: Structural and spectroscopic characterization. Results in Physics. 9. 10.1016/j.rinp.2018.03.016.

[14] Audita, Rahmania & Khoirunisa, & Hasna, Azizah & Zahra, & Nugroho, Bambang & Hidayat, Habibi & Fatimah, Is. (2021). Composite of Polylactic Acid/Chitosan/Ag-Hydroxyapatite Synthesized Using Turmeric Leaves Extract-Mediated Silver Nanoparticleand Snail Shell as Antibacterial Material. EKSAKTA Journal of Sciences and Data Analysis. 21. 116-123. 10.20885/EKSAKTA.vol2.iss1.art14.

[15] Carmen Steluta Ciobanu, Florian Massuyeau, Liliana Violeta Constantin, Daniela Predoi. Structural and physical properties of antibacterial Ag-doped nano-hydroxyapatite synthesized at 100A degrees C. Nanoscale Research Letters, 2011, 6, pp.1. 10.1186/1556-276X-6-613.hal-00849703

[16] Jemal, Jihène & Tounsi, Hassib & Chaari, Kamel & Petitto, Carolina & Delahay, Gérard & Djemel, Samir & Ghorbel, A.. (2014). NO reduction with NH3 under oxidizing atmosphere on copper loaded hydroxyapatite. Applied Catalysis B: Environmental. s 113–114. 255–260. 10.1016/j.apcatb.2011.11.045.

[17] K. Poovendran, K.S. Joseph Wilson, M.S. Revathy, A. Ayeshamariam, K. Kaviyarasu, Functionalization effect of HAp with copper (Cu) having excellent dielectric applications, Surfaces and Interfaces, Volume 19, 2020, https://doi.org/10.1016/j.surfin.2020.100474.

[18] El-Aal MA, Ali HM, Ibrahim SM. Cu-Doped 1D Hydroxyapatite as a Highly Active Catalyst for the Removal of 4-Nitrophenol and Dyes from Water. ACS Omega. 2022 Jul 21;7(30):26777-26787. doi: 10.1021/acsomega.2c03106. PMID: 35936455; PMCID: PMC9352244.

[19] Predoi, Daniela & Iconaru, Simona Liliana & Deniaud, Aurélien & Chevallet, Mireille & Michaud-Soret, Isabelle & Buton, Nicolas & Prodan, Alina. (2017). Textural, Structural and Biological Evaluation of Hydroxyapatite Doped with Zinc at Low Concentrations. Materials. 10. 229. 10.3390/ma10030229.

[20] Swamiappan, Sathiskumar & Sekar, Vanaraj & Devaraj, Sabarinathan & Preethi, Kathirvel. (2018). Evaluation of Antibacterial and Antibiofilm activity of Synthesized Zinc-Hydroxyapatite composites from Labeo rohita fish scale waste. Materials Research Express. 5. 10.1088/2053-1591/aaae10.

[21] Mosaad, Kareem & Shoueir, Kamel & Dewidar, Montasser. (2021). Fabrication of Multifunctional Wound Dressing Composite Biomaterials Composed of Ag/Mg-Hydroxyapatite Doped Electrospun Poly (Vinyl Alcohol) Nanofibers for Skin Tissue Regeneration. Journal of Cluster Science. 10.1007/s10876-021-02195-1.

[22] A. Mariappan, P. Pandi, K.R. Beula Rani, Rajeswarapalanichamy, K. Neyvasagam, Study of the photocatalytic and antibacterial effect of Zn and Cu doped hydroxyapatite, Inorganic Chemistry Communications, Volume 136, 2022, 109128, https://doi.org/10.1016/j.inoche.2021.109128.

[23] R.-J. Chung, M.-F. Hsieh, K.-C. Huang, L.-H. Perng, F.-I. Chou, T.-S. Chin, Fong-In Chou, Tsung-Shune Chin Anti-Microbial Hydroxyapatite Particles Synthesized by a Sol-Gel Route J. Sol-Gel Sci. Technol., 33 (2) (2005), pp. 229-239

[24] H. Alioui, O. Bouras, J.-C. Bollinger Toward an efficient antibacterial agent: Zn- and Mg-doped hydroxyapatite nanopowders J. Environ. Sci. Health Part A, 54 (4) (2019), pp. 315-327.

ISC'22 2nd International Symposium on Characterization
22-25 September 2022 Afyonkarahisar, Türkiye

Fabrication of Durable Hydrophobic coating on Glass Substrate

Atilla Evcin[1]

[1] Afyon Kocatepe University, Materials Science and Engineering Department, Afyonkarahisar, Turkiye

Abstract

Sol-gel method has attracted the attention of researchers in recent years. There is no alternative to the sol-gel method in obtaining high purity and correct compositions. The biggest problem seen in coatings is the inability to provide sufficient adhesion on the substrate. For this reason, studies have focused on the production of durable films. In this study, silane-based solutions containing high molecular weight carboxylic acid and saturated fatty acid that adhere well to the glass surface were used. The coating was characterized in terms of its physical properties and morphology. After coating, a surface with high hydrophobicity was obtained.

Keywords: silane, hydrophobic, glass, coating, sol-gel

Corresponding Author e-mail : evcin@aku.edu.tr

1. Introduction

Sol-gel method is a method of obtaining powder or film by hydrolysis and condensation reactions by using a compound containing an active ingredient (alkoxide or metal salts) as a starting material, forming a stable sol system in solution [1-5].

Thin Film coating methods include electrolytic coating, electroless coating, sol-gel process, physical vapor deposition (PVD), chemical vapor deposition (CVD), chemical deposition, plasma spray, etc. There are many methods such as These methods have advantages and disadvantages. Thin coatings are very thin layers of metal, glass or substrate for functionalization such as crystals, ceramics. Generally, it can be oxide-containing (SiO2, TiO2, MgF2, Au, Al etc.) as well as metallic or metal-based coatings. It can be modified with the thickness and number of layers so that the surface has properties such as scratching, conductivity, hydrophobicity, color, reflection, anti-reflection, and dirt-repellent [6-8].

2. Materials and Method

3-(*GlycidoxyPropyl*)*TriMethoxySilane* (GPTMS), 1H, 1H, 2H, 2H-Perfluorooctyltrimethoxysilane (FAS), Calcium stearate were used as precursors. All chemicals were analytical grade and used as received.

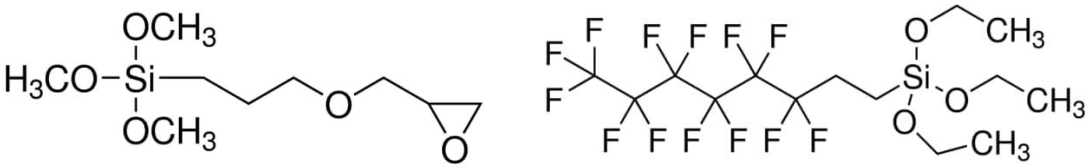


Figure 1. Molecular and structural formula of precursors [9]

The glass substrate was cleaned ultrasonically using acetone, ethanol and deionized water (Fig 2). After cleaning substrate was dried at ambient temperature.



Figure 2. Cleaning of glass substrate

The cleaned glasses were dried in a vacuum oven. The prepared sols were sprayed on the surface at 2 bar pressure with a gun with a nozzle opening of 0.8 mm. It was then kept at 200 °C for 30 min.

The hydrophobicity and surface morphology of the thin films were performed using contact angle measurements and scanning electron microscopy (SEM), respectively. Water contact angle measurements were analyzed using static sessile drop method at ambient temperature using Attention theta lite. Morphology was performed by using *LEO* 1430 VP model SEM (Fig 3-4).

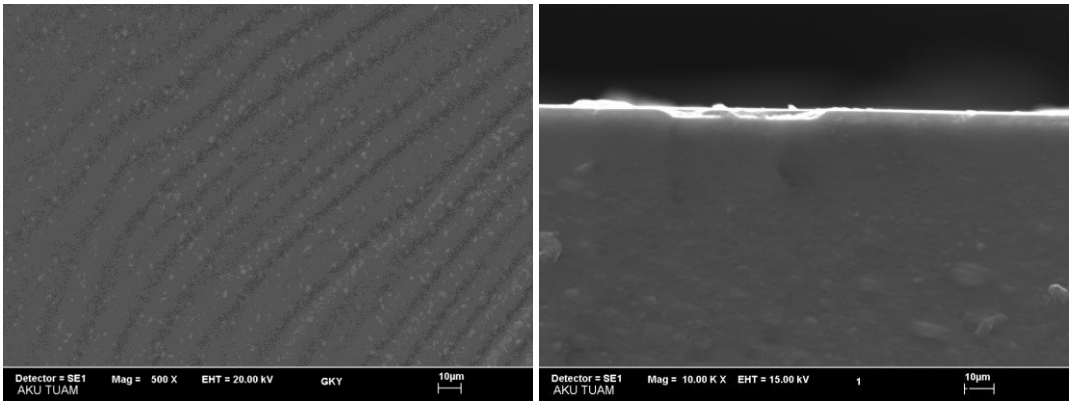


Figure 3. SEM image of glass surface and cross section

It can be seen from Figure 3 that the coating is homogeneous and the roughness is low. It is clear from the section that the coating thickness is about 10 microns.

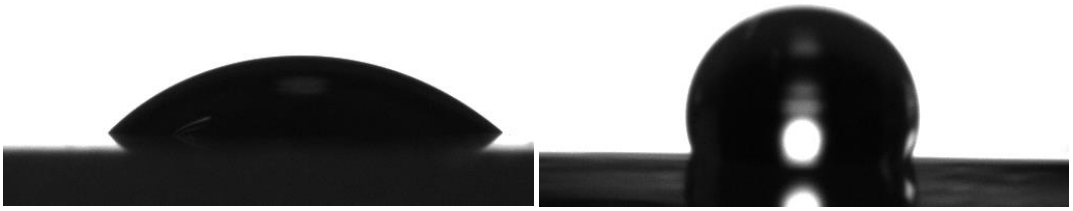


Figure 4. Contact angle of bare and coated glass

In Figure 4, uncoated glass has a contact angle of 54 degrees, while solution-coated glass containing GPTMS, FAS and Ca-stearate has a contact angle of 128 degrees.

3. Conclusion

As a result, the desired hydrophobic coating is obtained. The coating is homogeneous and its thickness is around 10 microns. It can be easily used in applications where a hydrophobic surface is required.

References

[1] Sakka, Sumio. (2013). Sol–Gel Process and Applications. 10.1016/B978-0-12-385469-8.00048-4.

[2] Katiyar, N. Kumar, P. Srivastava, R.K. Shukla, A. Srivastava, Structural andphysical parameters of sol-gel spin coated ZnO thin films: Effect of sol concentration,Materials Today: Proceedings, 2020

[3] C.J. Brinker, G.W. Scherer, SOL-GEL SCIENCE: The Physics and Chemistry ofSol-Gel Processing, ACADEMIC PRESS, INC.

[4] Pierre A.C. (1998). Introduction to Sol–Gel Processing.Kluwer, Boston

[5] Wang, Xuanze. (2020). Preparation, synthesis and application of Sol-gel method.

[6] Kumar, Amit & Singh, Rajeev & Bahuguna, Gaurav. (2016). Thin Film Coating through Sol-Gel Technique. Research Journal of Chemical Sciences. 6. 65.

[7] Cruz M.R.A., Zarzoza G.O., Castanon G.A.M. andMartínez J.R. (2012). Thin films from different materialsobtained by the Sol-Gel method: study of the morphologythrough Atomic Force Microscopy (AFM). CurrentMicroscopy Contributions to Advances in Science andTechnology, 1370-1376.

[8] Znaidi L. (2010). Sol–gel-deposited ZnO thin films: Areview. Materials Science and Engineering B, 174, 18-30.

[9] https://www.sigmaaldrich.com

Microstructural Investigations In Increasing The Durability Of Cold Forging Dies (U8 Steel) By The Method Of Double Heat Treatment

Darob M. Berdiev [1], Ravshan K. Toshmatov[2], Muhammed İhsan Özgün [3]

[1*] Tashkent State Technical University named after I. Karimova, Department of Metallurgy and Material Engineering, Tashkent, Uzbekistan, (ORCID: 0000-0003-1154-2115), miozgun@erbakan.edu.tr

[2*] Tashkent State Technical University named after I. Karimova, Department of Metallurgy and Material Engineering, Tashkent, Uzbekistan, (ORCID: 0000-0001-9113-9953), ravshan_iqtisod@mail.ru

[3] Necmettin Erbakan University Department of Metallurgy and Material Engineering, Konya, Türkiye, (ORCID: 0000-0003-0048-3439), miozgun@erbakan.edu.tr

Abstract

Microstructure studies aim to find optimum heat treatment regimes that provide the maximum possible fine austenite grain after heat treatment of the tool. For research, samples were prepared from steel U8 (C80U, European Norm) with a diameter of 20 mm and a height of 5 mm. This ensured the commensurability of the samples' cross-section with the heat-treated tool's cross-section. Thermal treatment of models, as already mentioned, consisted of the following: heating in a salt bath to temperatures of 820, 900, 1000, 1100, 1150, 1200, and 1260 ºC; the heating time was 5 minutes. The formation of a martensitic structure after the first hardening and cooling was carried out in the water with a transfer to quenching oil. Hardened samples had intermediate tempering at 200, 300, 350, and 450 ºC. Some of the pieces were not subjected to intermediate tempering. The point of view of achieving the minimum grain size of austenite, pre-hardening at 1100 ºC, intermediate tempering at 200, 350, and 450 ºC is preferable.

Keywords: Austenite, Heat Treatment, Microstructure, Martensite, Reheating,

1. Introduction

Generally, traditional, accepted methods of heat-treating metal goods provide them with high mechanical qualities. U8 (C80U, European norm) quality steels are preferred as unalloyed cold work tool steel [1]. U8 quality tool steels are heat treated to obtain a structure with maximum wear resistance. Therefore, it is essential to minimize the amount of residual austenite that may exist in the structure during heat treatment or to develop a heat treatment process to reduce the grain size in the structure. When the transformation graphs are examined in steels containing more than 0.7% carbon, it does not seem possible to transform martensite below 0 °C completely. (Figure 1) 8[2].

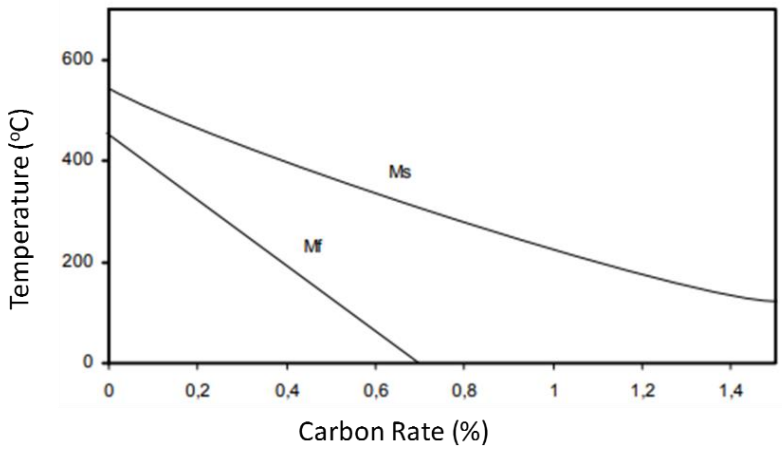


Figure 1. Variation of M_s (start) and M_f (finish) temperatures depending on the carbon ratio of the steel [2]

Keeping the presence of residual austenite in the structure to a minimum will reduce strength at a micro scale and thus the possibility of damage will be significantly reduced. Complete removal of residual austenite is completely removed by subzero treatment. It is required to lower the temperature to a specific intermediate value, wait for the part temperature to reach that homogeneity, and then continue cooling to prevent thermal damage during cooling in high-section parts. Subzero operation is then carried out at the processing temperature and waiting time chosen under the material's intended qualities [3]. However, depending on the part geometry and size, distortion and micro-scale crack formation can occur in subzero operations. Therefore, a two-stage heat treatment regime was investigated to obtain a temper martensite structure containing residual austenite reduced to fine grain size to impart a certain strength.

2. Materials and Methods

To find the optimum heat treatment regimes that provide the maximum possible fine austenite grain after heat treatment was selected U8 grade steel to observe the austenitic grains. For research, samples were prepared from steel U8 with a diameter of 20 mm and a height of 5 mm. This ensured the commensurability of the cross section of the samples with the cross section of the heat-treated tool. Through heat treatment, a temper martensitic structure was created.

Thermal treatment of samples, consisted of the following: heating in a salt bath to temperatures of 820, 900, 1000, 1100, 1150, 1200, 1260 ºC; the heating time was 5 minutes. To ensure the formation of a martensitic structure after the first hardening, cooling was carried out in water with transfer to oil.

Hardened samples had intermediate tempering at temperatures of 200, 300, 350, 450 ºC. Some of the samples were not subjected to intermediate tempering.

Reheating of all samples was also carried out in a salt bath to a temperature of 820 ºC. The heating time was 5 minutes. Cooling was carried out in the mode of precipitation along the boundaries of the austenite grains of the troostite network (nitrate bath with a temperature of 180 ºC). After etching of thin sections (made from the indicated samples) with a 4% solution of nitric acid in ethyl alcohol, as well as with a saturated solution of nicranic acid in ethyl alcohol, as well as with a saturated solution of nicranic acid with additives of detergents, the austenite grain size was calculated according to GOST 5639-65.

3. Results

The measurement results are shown in the graph in Figure 2. It has been established that, in comparison with furnace heating, the size of the austenite grain in all cases is 1–2 points finer [4].

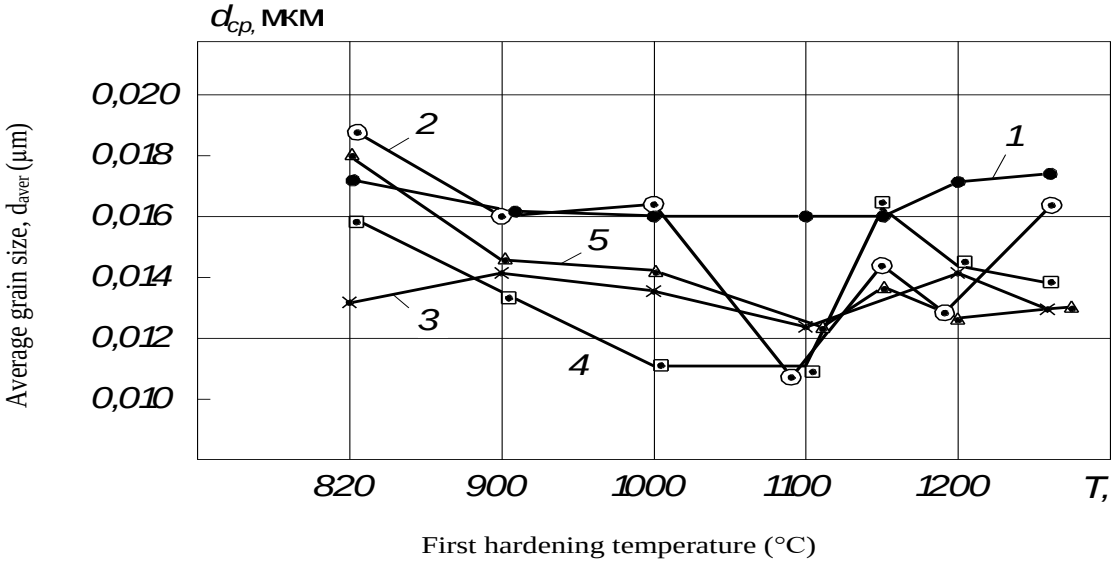


Figure 2. Change in the average diameter of the austenite grain of steel U8 after final heat treatment depending on the temperature of pre-hardening and tempering.

Interim leave: 1 – no; 2 – 450 ºC; 3 – 200 ºC; 4 – 300 ºC; 5 – 350 ºC.

It can also be argued that the first hardening from a heating temperature of 1100 ºC provides an additional reduction in grain size by 1-2 points. The optimal intermediate tempering temperature will be 200 º, 350 º and 450 ºC, ensuring the stability of the grain size in the region of the first hardening temperatures of 1100-1150 ºC. Thus, the results of measuring the size of the austenite grain during heating in a salt bath differ significantly from those obtained during furnace heating [5]. The microstructure was studied on special samples of steel U8 subjected to the same heat treatment regimes as for studying the size of the austenite grain. The difference was that the second hardening was carried out with cooling in water with transfer to a saltpeter bath with a temperature of 180 ºC. Thus, for microstructural studies, the heat treatment regimes fully corresponded to the heat treatment regimes of the tool. The microstructure micrographs are shown in Figure 3 and Figure 4.

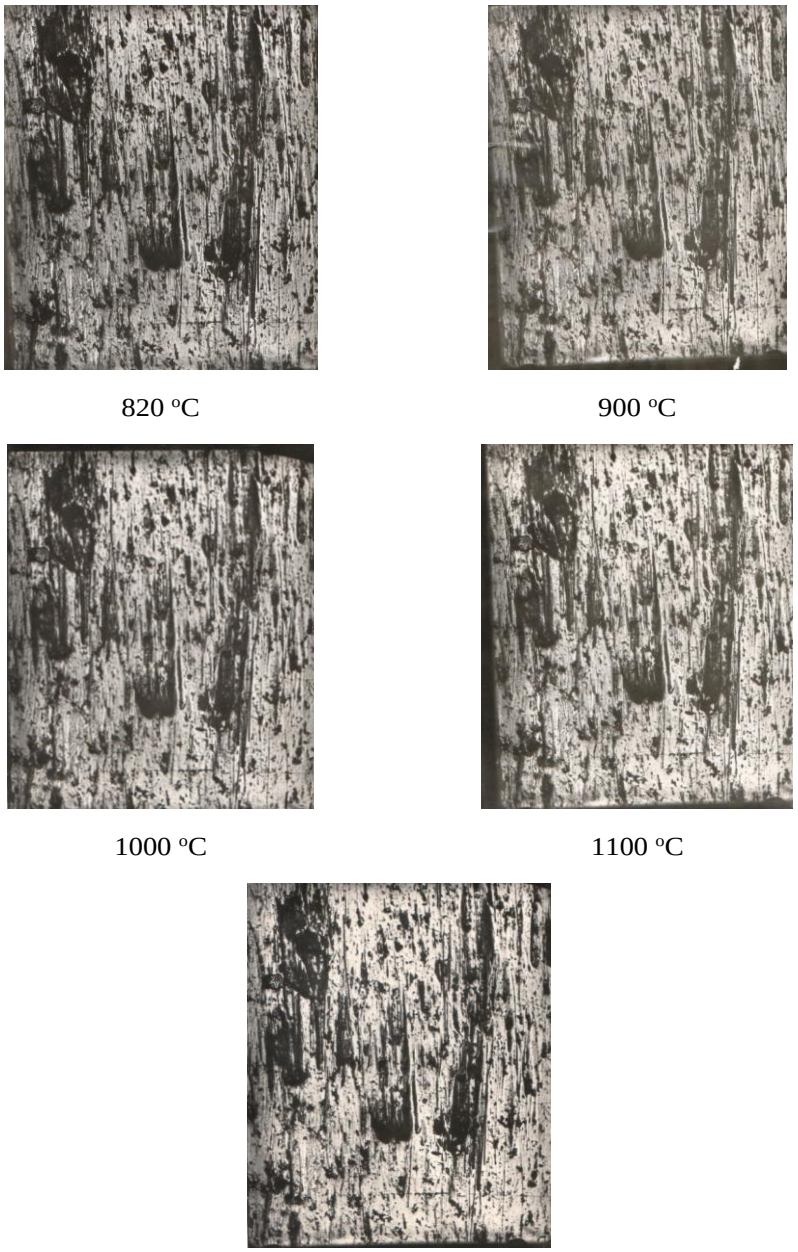


Figure 3. Microstructure of steel U8 after hardening from different heating temperatures

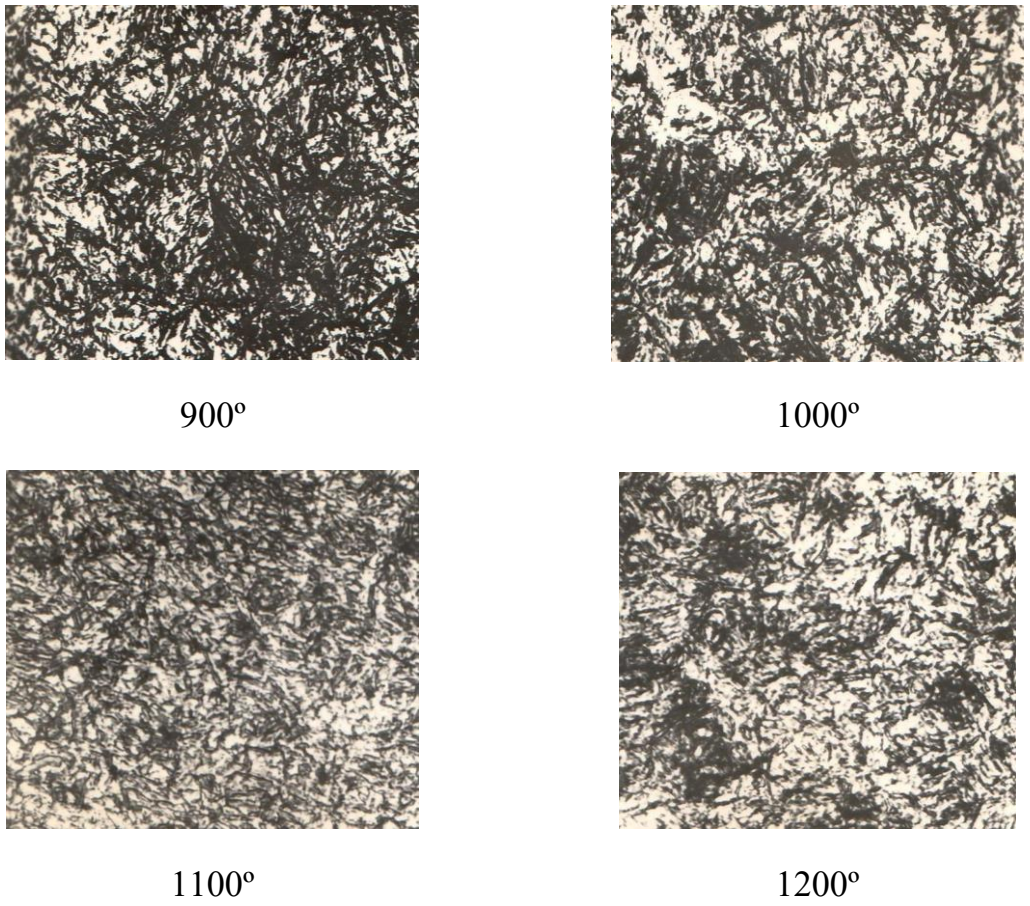


Figure 4. Microstructure of steel U8 at 500 magnification after the first hardening from different temperatures, intermediate tempering 450 ºC, second hardening from a temperature of 820 ºC

4. Discussion and Conclusion

As the result of the study shows that the first hardening and high temperatures contribute to the growth of austenite grains and martensite needles (up to 1 point at a heating temperature of 1260 ºC).

The second quenching from a temperature of 820 ºC after an intermediate tempering of 450 ºC ensures the production of fine acicular martensite, and the finest acicular martensite occurs if the first quenching was carried out from a temperature of 1100 ºC (see Fig. 4). No undissolved particles of cement were found, which also indicates the complete transfer of carbon into a solid solution.

Thus, from the point of view of achieving the minimum grain size of austenite, pre-hardening at 1100 ºC, intermediate tempering at 200, 350 and 450 ºC is preferable.

References

[1] D. M. Berdiev, A. A. Yusupov, M. Umarova and T. Ibodullaev, "Improving wear resistance of steel products to unconventional heat treatment methods," *International Journal of Scientific & Technology Research*, vol. 9, pp. 2504-25094, 2020.

[2] B. Uluğ, "Sıfıraltı/kreojenik Isıl İşlemin 100cr6 ve 8620 Kalite Çeliklerin Özellikleri Üzerine Etkisi," PhD. Thesis, İstanbul Techninal University, İstanbul, Türkiye, 2006.

[3] A. Stojko, "Sub-zero Treatment of Tool Steels," M. S. thesis, Technical University of Denmark, Copenhagen, Denmark, 2001.

[4] D. M. Berdiev and R. K. Toshmatov, "Osobennosti fazovyx i strukturnnyx prevrasheniy konstruksionnnyx staley pri netraditsionnnyx rejimax termicheskoy obrabotki [Features of phase and structural transformations of structural steels under unconventional modes of heat treatment]," *Vestnik mashinostroeniya = Bulletin of Mechanical Engineering*, vol. 10, pp. 63-65, 2020.

[5] D. M. Berdiev and R. K. Toshmatov, "Phase and Structural Transformations of Structural Steels in Nontraditional Heat Treatment," *Russian Engineering Research*, vol. 41, no. 1, pp. 46-48, 2021.

Investigation of Deformation Induced Martensitic Transformation and Powder Morphology of 304 Stainless Steel as a Function of Milling Time

Ahmet B. BATIBAY[1*] and Hasan KOTAN[1]

[1*] Necmettin Erbakan University, Department of Metallurgical and Materials Science, Konya, TÜRKİYE (ORCID: 0000-0002-0163-5097), abbatibay@erbakan.edu.tr

Abstract

In this study, 304 stainless steel was nanostructured by mechanical alloying from elemental powders. Effect of severe plastic deformation induced during high energy mechanical alloying on phase transformation and particle morphology was investigated as a function of milling time from 15 minutes up to 30 hours. The microstructural evolution of the as-milled powders was characterized by means of X-ray diffraction (XRD) and scanning electron microscopy (SEM) techniques. A mathematical model adopted from literature was utilized to estimate the martensite percentage as a function of milling time. It was found that the austenite-to-martensite phase transformation was triggered in the early stage of milling reaching to about 20% after 2.5 hours milling. The martensite percentage was determined as around 90% after 7.5 hours of milling and remained above 90% up to 30 hours of room temperature milling. Electron microscopy analysis of the milled powders suggested that average particle size increased with increasing milling time. That is, as-received particle sizes of Fe, Cr, and Ni were 15 μm, 50 μm, and 150 μm, respectively. Average particle size of milled powders changes with increasing milling time. The results have revealed that austenite in as-received powder partially transformed to martensite phase during mechanical milling. Furthermore, while the austenite-to-martensite phase ratio increased with increasing milling time, the equilibrium structure was not achieved after milling up to 30 hours resulting in dual-phased steels. Also, result show that while phase transformation was completed before 10 hours of milling grain size reduction continued up to 30 hours milling.

Keywords: Mechanical alloying, deformation induced phase transformation, martensite, austenite, stainless steels.

Deformasyona Bağlı Martensitik Dönüşümün Ve 304 Paslanmaz Çeliğin Toz Morfolojisinin Öğütme Süresinin Bir Fonksiyonu Olarak İncelenmesi

Öz

Bu çalışmada, 304 paslanmaz çelik, elementel tozlardan mekanik alaşımlama ile nano yapılandırılmıştır. Yüksek enerjili mekanik alaşımlama sırasında oluşan şiddetli plastik deformasyonun faz dönüşümü ve parçacık morfolojisi üzerindeki etkisi, 15 dakikadan 30 saate kadar öğütme süresinin bir fonksiyonu olarak incelenmiştir. Öğütülmüş tozların mikroyapısal gelişimi X-ışını kırınımı (XRD) ve taramalı elektron mikroskobu (SEM) teknikleri ile karakterize edilmiştir. Öğütme süresinin bir fonksiyonu olarak martenzit yüzdesini tahmin etmek için literatürden uyarlanan matematiksel bir model kullanılmıştır. Östenit-martenzit faz dönüşümünün öğütmenin erken aşamasında tetiklendiği ve 2,5 saatlik öğütmeden sonra yaklaşık %20'ye ulaştığı bulunmuştur. Martenzit yüzdesi 7,5 saatlik öğütmeden sonra yaklaşık %90 olarak belirlenmiş ve oda sıcaklığında 30 saatlik öğütme sonrası %90'ın üzerinde kalmıştır. Öğütülmüş tozların elektron mikroskobu analizi, ortalama partikül boyutunun artan öğütme süresi ile arttığını göstermiştir. Yani alınan Fe, Cr ve Ni'nin partikül boyutları sırasıyla 15 μm, 50 μm ve 150 μm idi. Öğütülmüş tozların ortalama partikül boyutu, artan öğütme süresiyle değişir. Sonuçlar, mekanik öğütme sırasında toz halindeki östenitin kısmen martenzit fazına dönüştüğünü ortaya koymuştur. Ayrıca, östenit-martenzit faz oranı artan öğütme süresiyle artarken, 30 saate kadar öğütme sonrasında denge yapısına ulaşılamamış ve çift

fazlı çelikler ortaya çıkmıştır. Ayrıca, sonuçlar faz dönüşümünün 10 saatlik öğütmeden önce tamamlanmış olmasına rağmen tane boyutundaki küçülmenin 30 saatlik öğütmeye kadar devam ettiğini göstermektedir.

Anahtar Kelimeler: Mekanik Alaşımlama, Deformasyon Kaynaklı Faz Dönüşümü, Martenzit, Östenit, Paslanmaz Çelik

1. Introduction

Austenitic stainless steels have been widely used in many industries such as chemical, nuclear, petrochemical and food industries mainly because of their excellent corrosion resistance, high ductility, excellent weldability and biocompatibility [1-3]. Therefore, it is without a doubt that they are very important as engineering materials. However, austenitic stainless steels are in general of rather low-yield strength and need to strengthen for more advanced engineering applications.

Conventionally, there are various reported ways to strengthen stainless steels [4-7]. More recently strengthening through nanostructuring has been adopted in part due to the success of implementing various severe plastic deformation techniques [8, 9]. For example, nanocrystallized stainless steels obtained using surface mechanical attrition treatments (SMAT) [10] have been examined to reveal the grain size of 316L stainless steels can be refined down to nanometer range (20 nm). A. Etienne et al. [11] have demonstrated that ultrafine-grained 316 and 304 austenitic stainless steels can be prepared by high-pressure torsion. High energy mechanical milling is also a well-established route for producing nanocrystalline stainless steels at the finest length scale, microstructures consisting of an average grain size less than 15 nm have been reported [12].

Nevertheless, the drawback of grain refinement is that nanocrystalline materials in general are metastable, regardless of the technique that they are prepared with [13-17] for the following reason. In nanocrystalline materials, the total volume fraction of grain boundaries and triple junctions can be greater than 50% [18, 19]. In addition, severe plastic deformation techniques used to synthesized nanocrystalline steels are characterized by extremely high strain rate and therefore, creation of a high density of lattice defects such as point defects, dislocations, interstitials, and stacking faults [14, 20, 21]. This high volume fraction of non-equilibrium defects leads to a large increase in the total free energy of the material and the reduction of this free energy provides a strong driving force for grain growth and restructuring of the microstructure [17, 22-26] as observed for many systems including pure Fe [27-30], binary Fe-Ni [31] and Fe-Cr [32] steels. Knowing that the composition of stainless steels is optimized by adding substantial amounts of Cr and Ni with regard to strength and/or resistance to corrosion at elevated temperatures [33, 34] nanostructured stainless steels should be successfully stabilized against temperature in order to prevent loss of function under application at elevated temperatures. Thus, it is of interest to study the thermal stability and inherent grain growth of synthesized nanocrystalline steels as a result of high temperature exposure.

Phase transformation from austenite to martensite during plastic deformation has been studied for differrent austenitic steels including stainless steels, high manganese steels and nickel alloys [35-40]. Significant ductility enhancement has been informed in these steels, naming them as ‘transformation induced plasticity’ (TRIP) steels [41].

The main aim of this work is to study the microstructural evolutions of 304 steels as a function milling time. Specifically we plan to investigate the martensitic phase transformation and powder morphology. The results have revealed that after 2.5h milling time martensitic transformation can be rapidly increased. The microstructural evolution has also revealed that the volume fraction of retained martensite increased with increasing milling time, the austenite phase did not completely transform to the martensite phase even after 30 hours milling time resulting in a dual-phase structure with the dominant martensite phase.

2. Materials and Methods

The material used in this study was a commercial iron powder, nickel powder and chromium powder purchased from Alfa Aesar. For mechanical milling, appropriate masses were mixed with hardened steel balls and sealed in a hardened steel vial under vacuum prior to milling. A ball-to-powder mass ratio of 10:1 with a powder charge of 5.1g was loaded into the vial and milled 0 to 30 hours. The microstructure was characterized using X-ray diffraction (XRD). Phase ratio was measured using the formula [11]. Powder morphology was obtained using

Scanning Electron Microscope (SEM). X-ray diffraction analysis of as-milled powders were performed with a GNR X-ray diffractometer using CuKα (λ = 0.1542) radiation.

$$f_{\alpha'} = 1 - \frac{0.65(I_{311_\gamma} + I_{220_\gamma})}{I_{211_{\alpha'}} + 0.65(I_{311_\gamma} + I_{220_\gamma})} \quad [11]$$

3. Results and Discussion

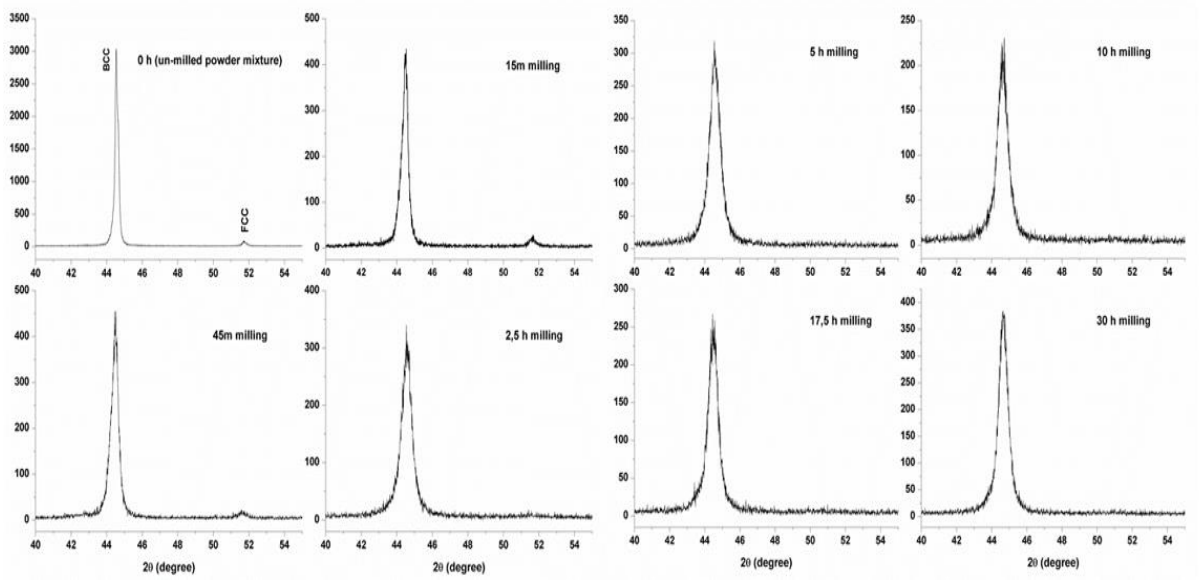


Figure 1. XRD analysis of as milled powders

Fig. 1 presents the XRD patterns showing the structure of stainless steels before and after mechanical milling. The unmilled XRD pattern clearly indicated a mixture of BCC and FCC phases coming from Fe – Cr - Ni. The BCC and FCC phases appear in mixed and as milled powders. The figure shows that the high-energy ball milling pattern at a 15m and 45m milling time contained the same BCC and FCC phases. But a high-energy ball milling pattern at a 2,5h milling time included the same BCC with reduced intensity of peaks, and FCC peaks disappeared, meaning that deformation-induced phase deformation occurred. A comparison of the spectra before and after milling shows i) the sharp crystalline diffraction peaks of the mixed powder broadened as a result of refinement of crystalline size as well as accumulation of internal stress due to the high number of defects and non-equilibrium grain boundaries, ii) a significant reduction in the intensity ratio of the austenite-to-martensite diffraction peaks suggests a significant increase in the fraction of martensite phase as a result of the mechanical milling process. Dual phase consisting of austenitic and martensite were reported for austenitic stainless steels after ball milling [12, 42] or other severe plastic deformation techniques [10, 43, 44]. It is well documented that during severe plastic deformation, metastable austenitic stainless steels (i.e., 304 and 316) are susceptible to martensite transformation, resulting in a dual-phase [45-47]. This is explained by [1] that the structure of the metastable austenite stainless steel is transformed to only some degree by severe plastic deformation so that a mixed austenite-martensite structure is developed.

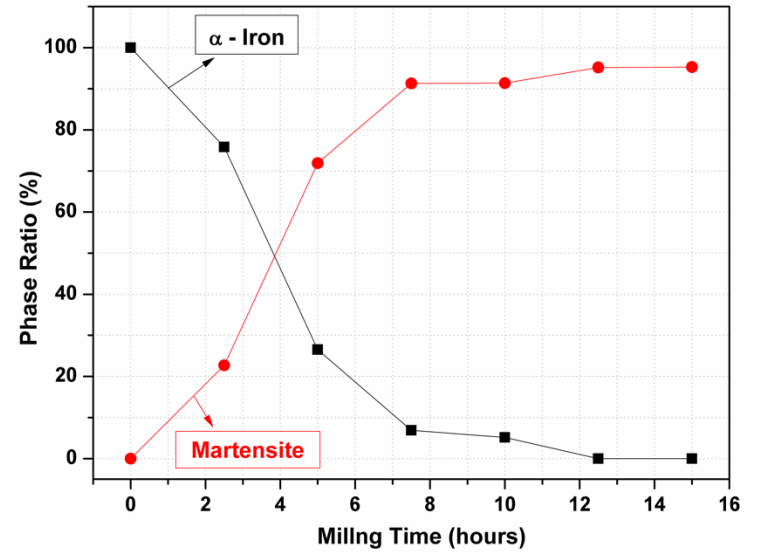


Figure 2. Phase ratio of as milled powders as a function milling time

Figure 2 can be seen the phase ratio of as milled powders as a function of milling time. Phase transformation ratio was measured using the formula in the literature [11]. The volume fraction of α'-martensite can be calculated using the following equation [43]. (311)γ, (220)γ and (211)α' reflections were used for calculation [11]. After 2,5 hours milling time transformation can be rapidly increased. As the milling time increases, alpha iron to martensite transformation increases. Nevertheless, austenite phase did not completely transform to martensite phase after the milling process is complete. The calculations indicate that the initial martensite percentage in the as milled powder increased from 0% to around 90% after 30 hours milling time. According to the results shown in Fig. 2, the mixed powder has around 0% martensite and this percentage increased to 90% after 30 hours mechanical milling due to incurring extensive plastic deformation. The obtained martensite percentage is consistent but is higher than some reported steels produced by other severe plastic deformation techniques [4, 48].

Changes in particle size and particle morphology as a function of milling time can be obtained in Figure 3. Average particle size less than 50 μm after 150 minutes milling. Particle size increases as the milling time increases. This trend could be due to the mechanical attrition mechanism in which particles cold-welded and fractured during milling. The trend of changing particle size from 0 to 30 h increase with increasing milling time.

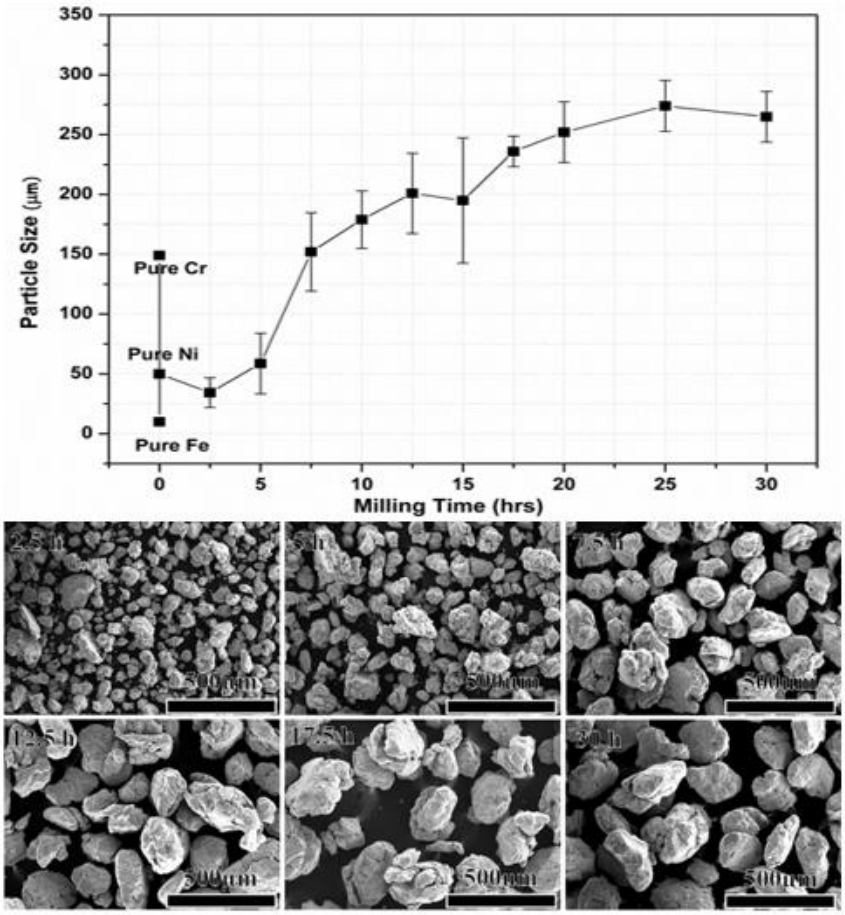


Figure 3. Particle size of as milled powders as a function milling time

4. Conclusion

This study concerns the deformation-induced martensitic transformation as a function of milling time. For this purpose, different milling times for 304 stainless steels were synthesized by mechanical alloying from elemental powders at room temperature. The experimental results showed that an almost complete deformation-induced martensitic phase transformation was obtained after 2.5 hours of milling time. After 30 hours milling is done, as milled powders have approximately 90% martensite in the microstructure. The austenite/martensite phase ratio increases for as milled powders as the milling time increases. XRD studies demonstrated that the martensitic transformation from the initial austenitic phase to the martensitic phase depends on milling time. The reported research may present an important contribution to a better understanding of mechanically alloyed 304 stainless steels.

5. Acknowledgement

The authors wish to thank BITAM for electron microscopy and crystallographic investigations.

References

[1] W. F. Smith, Structure and properties of engineering alloys. USA: McGraw-Hill, 1993.

[2] K. H. Lo, C. H. Shek, and J. K. L. Lai, "Recent developments in stainless steels," (in English), Materials Science & Engineering R-Reports, vol. 65, no. 4-6, pp. 39-104, May 29 2009.

[3] N. R. Baddoo, "Stainless steel in construction: A review of research, applications, challenges and opportunities," (in English), Journal of Constructional Steel Research, vol. 64, no. 11, pp. 1199-1206, Nov 2008.

[4] M. H. Enayati, M. R. Bafandeh, and S. Nosohian, "Ball milling of stainless steel scrap chips to produce nanocrystalline powder," (in English), Journal of Materials Science, vol. 42, no. 8, pp. 2844-2848, Apr 2007.

[5] F. Forouzan, A. Najafizadeh, A. Kermanpur, A. Hedayati, and R. Surkialiabad, "Production of nano/submicron grained AISI 304L stainless steel through the martensite reversion process," (in English), Materials Science and Engineering a-Structural Materials Properties Microstructure and Processing, vol. 527, no. 27-28, pp. 7334-7339, Oct 25 2010.

[6] H. W. Huang, Z. B. Wang, J. Lu, and K. Lu, "Fatigue behaviors of AISI 316L stainless steel with a gradient nanostructured surface layer," (in English), Acta Materialia, vol. 87, pp. 150-160, Apr 1 2015.

[7] B. Radiguet, A. Etienne, P. Pareige, X. Sauvage, and R. Valiev, "Irradiation behavior of nanostructured 316 austenitic stainless steel," (in English), Journal of Materials Science, vol. 43, no. 23-24, pp. 7338-7343, Dec 2008.

[8] Y. T. M. Umemoto, J. Li, K. Tsuchiya, "Nanocrystalline structure in steels produced by various severe plastic deformation processes," Materials Science Forum, vol. 503-504, pp. 11-18, 2006.

[9] S. V. Dobatkin, J. Zrnik, and I. Mamuzic, "Nanostructures by severe plastic deformation of steels: Advantages and problems," (in English), Metalurgija, vol. 45, no. 4, pp. 313-321, Oct-Dec 2006.

[10] T. Roland, D. Retraint, K. Lu, and J. Lu, "Enhanced mechanical behavior of a nanocrystallised stainless steel and its thermal stability," (in English), Materials Science and Engineering a-Structural Materials Properties Microstructure and Processing, vol. 445, pp. 281-288, Feb 15 2007.

[11] A. Etienne, B. Radiguet, C. Genevois, J. M. Le Breton, R. Valiev, and P. Pareige, "Thermal stability of ultrafine-grained austenitic stainless steels," (in English), Materials Science and Engineering a-Structural Materials Properties Microstructure and Processing, vol. 527, no. 21-22, pp. 5805-5810, Aug 20 2010.

[12] M. H. Enayati and M. R. Bafandeh, "Phase transitions in nanostructured Fe-Cr-Ni alloys prepared by mechanical alloying," (in English), Journal of Alloys and Compounds, vol. 454, no. 1-2, pp. 228-232, Apr 24 2008.

[13] T. R. Malow and C. C. Koch, "Thermal stability of nanocrystalline materials," (in English), Metastable, Mechanically Alloyed and Nanocrystalline Materials, Pts 1 and 2, vol. 225, pp. 595-604, 1996.

[14] C. Suryanarayana and C. C. Koch, "Nanocrystalline materials - Current research and future directions," (in English), Hyperfine Interactions, vol. 130, no. 1-4, pp. 5-44, 2000.

[15] C. Suryanarayana, "Structure and Properties of Nanocrystalline Materials," (in English), Bulletin of Materials Science, vol. 17, no. 4, pp. 307-346, Aug 1994.

[16] M. H. F.J. Humphreys, Recrystallization and related annealing phenomena. Oxford, UK: Elsevier, 2004.

[17] C. C. Koch, "Optimization of strength and ductility in nanocrystalline and ultrafine grained metals," (in English), Scripta Materialia, vol. 49, no. 7, pp. 657-662, Oct 2003.

[18] H. Gleiter, "Nanostructured Materials," (in English), Advanced Materials, vol. 4, no. 7-8, pp. 474-481, Jul-Aug 1992.

[19] C. Suryanarayana, "The structure and properties of nanocrystalline materials: Issues and concerns," (in English), Jom-Journal of the Minerals Metals & Materials Society, vol. 54, no. 9, pp. 24-27, Sep 2002.

[20] C. Suryanarayana, "Recent developments in nanostructured materials," (in English), Advanced Engineering Materials, vol. 7, no. 11, pp. 983-992, Nov 2005.

[21] C. C. Koch, "Structural nanocrystalline materials: an overview," (in English), Journal of Materials Science, vol. 42, no. 5, pp. 1403-1414, Mar 2007.

[22] J. H. Driver, "Stability of nanostructured metals and alloys," (in English), Scripta Materialia, vol. 51, no. 8, pp. 819-823, Oct 2004.

[23] M. Hillert, "On Theory of normal and abnormal grain growth," Acta Metall., vol. 13, no. 3, p. 227, 1965.

[24] R. Kirchheim, "Reducing grain boundary, dislocation line and vacancy formation energies by solute segregation II. Experimental evidence and consequences," (in English), Acta Materialia, vol. 55, no. 15, pp. 5139-5148, Sep 2007.

[25] F. Liu and R. Kirchheim, "Nano-scale grain growth inhibited by reducing grain boundary energy through solute segregation," (in English), Journal of Crystal Growth, vol. 264, no. 1-3, pp. 385-391, Mar 15 2004.

[26] J. Weissmuller, "Alloy Effects in Nanostructures," (in English), Nanostructured Materials, vol. 3, no. 1-6, pp. 261-272, 1993.

[27] K. A. Darling, B. K. VanLeeuwen, C. C. Koch, and R. O. Scattergood, "Thermal stability of nanocrystalline Fe-Zr alloys," (in English), Materials Science and Engineering a-Structural Materials Properties Microstructure and Processing, vol. 527, no. 15, pp. 3572-3580, Jun 15 2010.

[28] T. R. Malow and C. C. Koch, "Grain growth in nanocrystalline iron prepared by mechanical attrition," (in English), Acta Materialia, vol. 45, no. 5, pp. 2177-2186, May 1997.

[29] T. R. Malow and C. C. Koch, "Mechanical properties, ductility, and grain size of nanocrystalline iron produced by mechanical attrition," (in English), Metallurgical and Materials Transactions a-Physical Metallurgy and Materials Science, vol. 29, no. 9, pp. 2285-2295, Sep 1998.

[30] K. A. Darling, R. N. Chan, P. Z. Wong, J. E. Semones, R. O. Scattergood, and C. C. Koch, "Grain-size stabilization in nanocrystalline FeZr alloys," (in English), Scripta Materialia, vol. 59, no. 5, pp. 530-533, Sep 2008.

[31] H. Kotan, K. A. Darling, M. Saber, R. O. Scattergood, and C. C. Koch, "Thermal stability and mechanical properties of nanocrystalline Fe-Ni-Zr alloys prepared by mechanical alloying," (in English), Journal of Materials Science, vol. 48, no. 24, pp. 8402-8411, Dec 2013.

[32] M. Saber, H. Kotan, C. C. Koch, and R. O. Scattergood, "Thermal stability of nanocrystalline Fe-Cr alloys with Zr additions," (in English), Materials Science and Engineering a-Structural Materials Properties Microstructure and Processing, vol. 556, pp. 664-670, Oct 30 2012.

[33] C. Sun et al., "Superior radiation-resistant nanoengineered austenitic 304L stainless steel for applications in extreme radiation environments," (in English), Scientific Reports, vol. 5, Jan 15 2015.

[34] R. Diederichs, S. Trute, and W. Bleck, "Modelling of the high-temperature ductility properties during solidification of austenitic stainless steel," (in English), Steel Research International, vol. 77, no. 6, pp. 423-429, Jun 2006.

[35] Angel, Tryggve. "Formation of martensite in austenitic stainless steels effects of deformation, temperature, and composition." J. Iron and Steel Inst. 177, 165-174, 1954.

[36] Ludwigson, D. C., and J. An Berger. "Plastic behaviour of metastable austenitic stainless steels." J Iron Steel Inst 207.1, 63-69, 1969.

[37] Olson, Gregory B., and Morris Azrin. "Transformation behavior of TRIP steels." Metallurgical Transactions A 9.5, 713-721, 1978.

[38] Remy, L., and A. Pineau. "Twinning and strain-induced FCC→ HCP transformation in the Fe-Mn-Cr-C system." Materials science and engineering 28.1, 99-107, 1977.

[39] Jang, Jae-Myeong, et al. "Effects of annealing conditions on microstructure and mechanical properties of low carbon, manganese transformation-induced plasticity steel." Metals and Materials International 15.6, 909-916, 2009.

[40] Kwon, Ki Hyuk, et al. "In-situ neutron diffraction analysis on deformation behavior of duplex high Mn steel containing austenite and ε-martensite." Metals and Materials International 18.5, 751-755, 2012.

[41] Zackay, Victor F., et al. "The enhancement of ductility in high-strength steels." ASM Trans Quart 60.2, 252-259, 1967.

[42] A. Szymanska, D. Oleszak, A. Grabias, M. Rosinski, K. Sikorski, J. Kazior, et al., "Phase transformations in ball milled AISI 316L stainless steel powder and the microstructure of the steel obtained by its sintering," Reviews on Advanced Materials Science, vol. 8, pp. 143-146, Dec 2004.

[43] J. Manjanna, S. Kobayashi, Y. Kamada, S. Takahashi, and H. Kikuchi, "Martensitic transformation in SUS 316LN austenitic stainless steel at RT," Journal of Materials Science, vol. 43, pp. 2659-2665, Apr 2008.

[44] M. Shirdel, H. Mirzadeh, and M. H. Parsa, "Estimation of the kinetics of martensitic transformation in austenitic stainless steels by conventional and novel approaches," Materials Science and Engineering a-Structural Materials Properties Microstructure and Processing, vol. 624, pp. 256-260, Jan 29 2015.

[45] V. Seetharaman and R. Krishnan, "Influence of the Martensitic-Transformation on the Deformation-Behavior of an Aisi-316 Stainless-Steel at Low-Temperatures," Journal of Materials Science, vol. 16, pp. 523-530, 1981.

[46] A. K. De, D. C. Murdock, M. C. Mataya, J. G. Speer, and D. K. Matlock, "Quantitative measurement of deformation-induced martensite in 304 stainless steel by X-ray diffraction," Scripta Materialia, vol. 50, pp. 1445-1449, Jun 2004.

[47] S. S. M. Tavares, D. Gunderov, V. Stolyarov, and J. M. Neto, "Phase transformation induced by severe plastic deformation in the AISI 304L stainless steel," Materials Science and Engineering a-Structural Materials Properties Microstructure and Processing, vol. 358, pp. 32-36, Oct 15 2003.

[48] D. S. Leem, Y. D. Lee, J. H. Jun, and C. S. Choi, "Amount of retained austenite at room temperature after reverse transformation of martensite to austenite in an Fe-13%Cr-7%Ni-3%Si martensitic stainless steel," Scripta Materialia, vol. 45, pp. 767-772, Oct 10 2001.

Antibacterial and Hydrophobic TiO2 coating on wall tiles by the sol-jel method

Abdullah Alawadhi [1] , Atilla Evcin[2] and Gökhan Akarca[3]

[1] Sana'a, Yemen

[2] Afyon Kocatepe University, Materials Science and Engineering Department, Afyonkarahisar, Turkiye

[3] Afyon Kocatepe University, Food Engineering Department, Afyonkarahisar, Turkiye

Abstract

In this study, tiles coated with TiO2 were produced by spraying method for anti-fogging, water-free and antibacterial applications. At the beginning of the study, the surface of the tiles was cleaned with cleaning solutions. The tiles were dried at room temperature and calcined at 980˚C for 1 hour. The samples were sprayed with the prepared coating solution and left to dry at room temperature. The coating solution was characterized by DTA/TG, and FTIR. The coated samples were characterized by contact angle measurement, SEM and antibacterial test. Antibacterial and hydrophobic tiles were produced successfully.

Keywords : Sol-gel, hydrophobic, antibacterial, photocatalytic effect

Corresponding Author e-mail : al3wadhiabdullah@gmail.com

1. Introduction

Nature has revealed the best solutions to problems. The properties of the surfaces are improved by imitating the lotus flower, which grows in a highly polluted swamp, biomimetic. Lotus leaves have this feature because of the nanobumps on the surface (Fig 1.). The surface of lotus leaf shows the superhydrophobic effect. Lotus plant (white water lily) grows in muddy and dirty environments. Despite this, the leaves of the plant are always clean. Because the plant shakes its leaves and pushes the dust particles towards certain points when the smallest dust particles come on it [1-5].

Coating is a way of protecting the surface of the different materials as ceramic, glass, metal, clay, wood, and cementitious from pollutant, dust. self-cleaning coating can be achieved by modifying the surface to have super-hydrophobic, super-hydrophilic, and photocatalytic properties. This feature of the lotus plant has opened the way for researchers to design a new building surface [6-8]. Thereupon, the researchers started to work on building surfaces, such as the leaves of the lotus, that clean the dirt on them by using rain water.



Figure 1. Lotus effect

Water Repellent Feature Means; The fact that the water does not stay on the surface has a slippery effect on the surface and means that the water easily leaves the surface without leaving any stains. It has a similar feature to each other with its self-cleaning feature [9-11]. Self-Cleaning; That is, it means that the dirt disappears from the surfaces without cleaning it manually, for example, as a result of a chemical or photocatalytic function. "Self-cleaning" is often mistakenly used in association with Nano technology, but what is really meant is "Lotus result" or "easy-to-clean" is. Self-cleaning coatings utilized in different diciplines such as the materials, chemistry, aerospace, medicine, defence, military, physics etc [11-12]. TiO2 coating and TiO2-derived materials have been discovered to understand the fundamental principles of self-cleaning with hydrophilic and hydrophobic surfaces [13-17]. The aim of the this study is to show the titania coating obtained films which significantly affect the coating morphology, hydrophobicity, structural and antibacterial properties.

2. Material and Method

20x20 mm wall tiles were dipped in cleaning solutions before coating. They were immersed in 5% NaOH, 5% HCl, deionized water, acetone, ethyl alcohol and deionized water, respectively, for one minute. After drying in the oven, it was taken into a desiccator.

(3-Glycidoxypropyl)trimethoxysilane (GLYMO, C9H20O5Si, 236.34 g/mol), Titanium tetrapropoxide (TTIP, C12H28O4Ti, 284,215 g/mol), 3-Aminopropyltrimethoxysilane (3-APTES, H2N(CH2)3Si(OC2H5)3 , 221,37 g/mol), nitric acid (HNO3, 63,01 g/mol), Ethanol (C2H5OH, 46 g/mol) Butyl glycol (BG, CH3(CH2)3OCH2CH2OH , 118,17 g/mol) and hydrochloric acid (HCI, 36,5 g/mol) were used precursor.

Table 1. Coating solution

Component	W, g
GLYMO	2,36
TTIP	2,48
3-APTES	2,21
C2H5OH	50
BG	0,12
HCI	pH:4

Ceramic substrate surfaces were coated with the obtained solutions using the spray coating technique. Solvents with low boiling points such as ethanol and isopropanol were used at the beginning of the spray applications. The nozzle diameter of the spray gun used was 0.8 mm, and the coating process was carried out by spraying the coating solution at 3 bar pressure on the tile surface at a distance of 20 cm. A homogeneous coating was obtained by coating the surface in a single layer in a controlled manner.

3. Results and Discussion

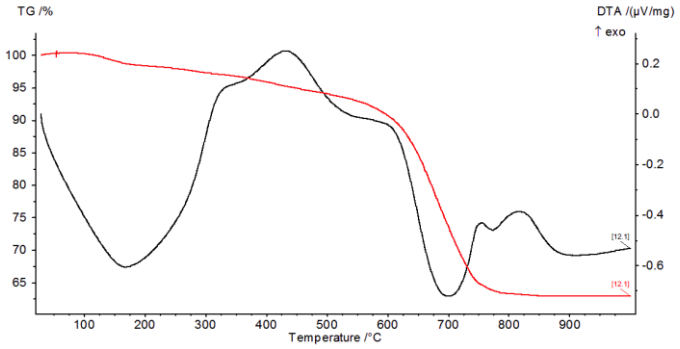


Figure 2. DTA/TG analysis of coating solution.

DTA/TG analyzes of the coating solution are given in Figure 2. From the TG analysis of the coating solution, the weight loss up to 180oC, due to the removal of adsorbed water. and ethanol. The DTA curve shows two exothermic peaks at approximately 310 ±C and 460 ±C, respectively. The lower exotherm corresponds to an oxidative decomposition, while the next one is believed to signify a phase transition from amorphous TiO2 to crystalline anatase

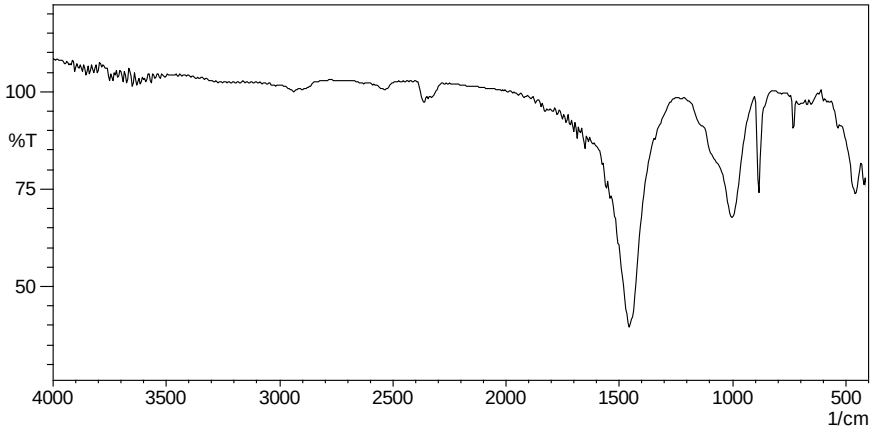


Figure 3. FTIR analysis of coating solution.

FT-IR analysis was performed to identify the structure of silane based coating solution by Spectrophotometer (Perkin Elmer spectrum two). As shown in Figure 2, the band at ~1040 cm^{-1} which is characteristic for –Si–O–C bond is observed. Sharp bands, at 1500 cm^{-1} which are for –C=(O)–NH–. [18-19]

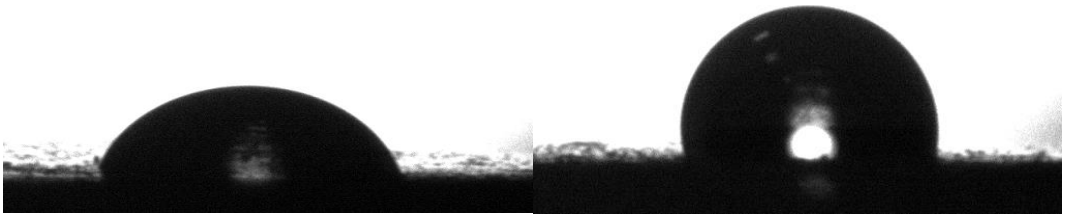


Figure 4. Contact angles measurement of surface.

Static contact angle measurement was used to characterizethe hydrophobicity of the coatings (Fig 4.). Contact angle measurements were determined by using Attention Theta Lite. Contact angle of uncoated tile is 56° and contact angle of coated tile is 110 °. Contact angles obtained with the new silane coating formulation were comparable with the literatüre [20-23].



Figure 5. Antibacterial test of coated tiles.

The bactericidal activity of the pure tile and coated tile was evaluated in vitro using a spread plate method. Fig. 5 shows the photos of colony forming units of viable E.coli for control ($1x10^5$ kob/cm^2) and antibacterial tile ($2x10^2$ kob/cm^2). The bactericidal activities of the films were evaluated by the inhibition of growth of Gram-negative bacteria E. Coli [24-27].

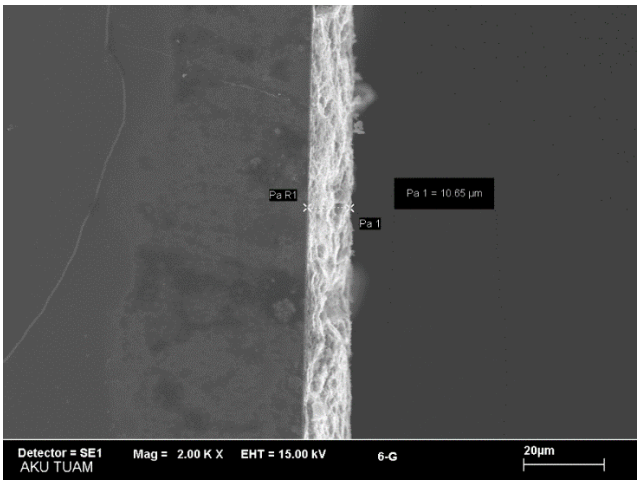


Figure 6. Cross section SEM image of coated tiles.

Figure 6 shows that the coating thickness is approximately 10 µm and its homogeneity is high. As a result of the study, an antibacterial, hydrophobic homogeneous surface was obtained by sol-gel method.

References

[1] Yamamoto, Minehide & Nishikawa, Naoki & Mayama, Hiroyuki & Nonomura, Yoshimune & Yokojima, Satoshi & Nakamura, Shinichiro & Uchida, Kingo. (2015). Theoretical Explanation of the Lotus Effect: Superhydrophobic Property Changes by Removal of Nanostructures from the Surface of a Lotus Leaf. Langmuir : the ACS journal of surfaces and colloids. 31. 10.1021/acs.langmuir.5b00670.

[2] Mueller, Felix & Michel, Werner & Schlicht, Volker & Tietze, Andrea & Winter, Patrick. (2007). Self-Cleaning Surfaces Using the Lotus Effect. 10.1016/B978-044451664-0/50024-3.

[3] Carbone, Giuseppe & Mangialardi, Luigi. (2005). Hydrophobic properties of a wavy rough substrate. The European physical journal. E, Soft matter. 16. 67-76. 10.1140/epje/e2005-00008-y.

[4] Shahda, Merhan & Elmokadem, Ashraf & elhafeez, Prof. (2014). Biomimicry Levels as an Approach to the Architectural Sustainability.

[5] Raindrops falling on the leaf are directed towards these points and it is provided to sweep the dust there.

[6] Miranda, Wederley & Carellos, Felipe & Silva, Gabriel & Cunha, João & Uchôas Stumpf, Laura & Moraes, Marcelo & Paixão, Rayenne & Cerqueira, Vitor. (2017). Coating Processes. 10.13140/RG.2.2.31195.21284.

[7] Fotovvati, Behzad & Namdari, Navid & Dehghanghadikolaei, Amir. (2019). On Coating Techniques for Surface Protection: A Review. 3. 10.3390/jmmp3010028.

[8] Fopp-Spori, Doris. (2010). Structural Influences on Self-cleaning Surfaces. 10.3929/ethz-a-006193586.

[9] Yasuyuki Takata , Sumitomo Hidaka & Takashi Uraguchi (2006) Boiling Feature on a Super Water-Repellent Surface, Heat Transfer Engineering, 27:8, 25-30, DOI: 10.1080/01457630600793962

[10] Hosseinpour Chermahini, Dr. Siavash & Eslamian, Saeid & Singh, Vijay & Dalezios, Nicolas & Ostad-Ali-Askari, Kaveh. (2018). New Trends in Self-Cleaning Materials for Different Purposes. Advances in Civil Engineering. 1. 149-158.

[11] Hosseini, Saeideh. (2020). Self-Cleaning surfaces for different purposes: Review of production methods and future prospects. Conference: 9th International Conference & Exhibition on Materials Science & Metallurgical Engineering (iMat2020) At: Iran-Tehran

[12] Prathapan, Ragesh & Venkatesan, Anand Ganesh & Nair, Shantikumar & Nair, Sreekumaran. (2014). A review on 'self-cleaning and multifunctional materials'. Journal of Materials Chemistry A: Materials for Energy and Sustainability. 2. 14773-14797. 10.1039/c4ta02542c.

[13] Yusliza, Yusuf & Abdollah, Mohd Fadzli Bin. (2019). Superhydrophilicity of laser surface textured TiO2 coating for self- cleaning surfaces.

[14] Xie, T. H., & Lin, J. (2007). Origin ofphotocatalytic deactivation of TiO2 film coated onceramic substrate. The Journal of PhysicalChemistry C, 111(27), 9968-9974

[15] Yaghoubi, H., Taghavinia, N., & Alamdari, E. K.(2010). Self cleaning TiO2 coating onpolycarbonate: surface treatment, photocatalyticand nanomechanical properties. Surface andcoatings technology, 204(9-10), 1562-1568

[16] Malnieks, Kaspars & Mezinskis, Gundars & Ilona, Pavlovska. (2016). Effect of Different Dip-Coating Techniques on TiO2 Thin Film Properties. Key Engineering Materials. 721. 128-132. 10.4028/www.scientific.net/KEM.721.128.

[17] Abbas, Mudassar & Iftikhar, Hina & Malik, Mumtaz & Nazir, Ahsan. (2018). Surface Coatings of TiO2 Nanoparticles onto the Designed Fabrics for Enhanced Self-Cleaning Properties. Coatings. 8. 35. 10.3390/coatings8010035.

[18] Atilla EVCİN, Harun GÜNEY and Nalan Çiçek BEZİR , Sol-gel Preparation of Silane-based Titania Hybrid Composite Thin Film , *International Journal of Computational and Experimental Science and ENgineering (IJCESEN) Vol. 7-No.1 (2021) pp. 25-28*

]19] Halbus, Ahmed & Horozov, Tommy & Paunov, Vesselin N. (2019). Self-grafting copper oxide nanoparticles show a strong enhancement of their anti-algal and anti-yeast action. Nanoscale Advances. 1. 10.1039/C9NA00099B.

[20] Abbas, Mudassar & Iftikhar, Hina & Malik, Mumtaz & Nazir, Ahsan. (2018). Surface Coatings of TiO2 Nanoparticles onto the Designed Fabrics for Enhanced Self-Cleaning Properties. Coatings. 8. 35. 10.3390/coatings8010035.

[21] Burunkaya, Esin & Kiraz, Nadir & Kesmez, Ömer & Asilturk, Meltem & Çamurlu, H. & Arpaç, Ertuğrul. (2010). Sol–gel synthesis of IPTES and D10H consisting fluorinated silane system for hydrophobic applications. Journal of Sol-Gel Science and Technology. 56. 99-106. 10.1007/s10971-010-2281-y.

[22] Lal, Manjari & Chhabra, Vishal & Ayyub, Pushan & Maitra, Amarnath. (1998). Preparation and characterization of ultrafine TiO2 particles in reverse micelles by hydrolysis of titanium di-ethylhexyl sulfosuccinate. Journal of Materials Research. 13. 1249-1254. 10.1557/JMR.1998.0178.

[23] Bayan, Ekaterina & Lupeiko, Timofey & Volkova, Maria & Kostenikova, Anna & Pustovaya, Larisa & Fedorenko, Aleksey. (2018). Hydrothermal Two-Step Synthesis of Titanate Nanotubes. 10.1007/978-3-319-78919-4_6.

[24] Hajkova, Pavlina & Spatenka, Petr & Krumeich, Joerg & Exnar, Petr & Kolouch, Ales & Matousek, Jindrich & Kocí, P.. (2009). Antibacterial effect of silver modified TiO 2 /PECVD films. European Physical Journal D - EUR PHYS J D. 54. 189-193. 10.1140/epjd/e2009-00087-7.

[25] De Falco, Gianluigi & Porta, Amalia & Del Gaudio, Pasquale & Commodo, Mario & Minutolo, Patrizia & D'Anna, Andrea. (2016). Antimicrobial Activity of TiO2 Coatings Prepared by Direct Thermophoretic Deposition of Flame-Synthesized Nanoparticles. MRS Advances. 2. 1-6. 10.1557/adv.2016.665.

[26] Mungkalasiri, Jitti & Bedel, Laurent & Emieux, Fabrice & Cara, Aurelia & Freney, Jean & Maury, F. & Renaud, François. (2014). Antibacterial properties of TiO2–Cu composite thin films grown by a one step DLICVD process. Surface and Coatings Technology. 242. 187–194. 10.1016/j.surfcoat.2013.08.039.

[27] Evcin, A., Çoşkun, B. & Akarca, G. A closer look at silane-based anti-bacterial coatings on polycarbonate: synthesis and characterizations. *Int. J. Environ. Sci. Technol.* **19**, 11741–11748 (2022). https://doi.org/10.1007/s13762-022-03954-x

Controlled Drug Release with Diatomite

Zeynep Özkan[1*], Hakan Çiftçi[2]

[1*] Afyon Kocatepe University, Institute of Science, Nanoscience and Nanotechnology, Afyonkarahisar, Turkey, (ORCID: 0000-0003-2793-157X), zeyyozkan26@gmail.com

[2] Afyon Kocatepe, Faculty of Engineering, Departmant of Mining Engineering, Afyonkarahisar, Turkey, (ORCID: 0000-0001-7910-7350), hakanciftci86@gmail.com

Abstract

This study was focused on the beneficiation of raw diatomite ore, characterization, and the drug release performance of the beneficiated diatomite. For this purpose, first of all, raw diatomite was enriched by calcining at 550°C for 4 hours. Then, diphenhydramine hydro chloride (DPH) drug, which was used as an active ingredient, was loaded onto calcined diatomite by adsorption technique. Finally, the DPH release profile of diatomite was investigated as a function of time. According to the data obtained, it was determined that the surface area of the diatomite increased from 21.7 m^2/g to 75.1 m^2/g with the calcination process. In addition, in drug release studies, it was determined that the obtained formulation showed a release for 60 minutes and released 88% of DPH.

Keywords: Diatomite, Diphenhydramine Hydrochloride, Drug Release.

1. Introduction

The selection of a suitable and effective drug carrier depends on its biocompatibility, loading capacity, release rate, safety, and cost of production [1]. Micro- and nano-scale drug delivery systems have greatly influenced the pharmaceutical industry by minimizing the disadvantages such as short plasma half-life, poor stability, and side effects of the active substance [2]. In the last decade, porous silica-based micro and nanoparticles have received much attention in pharmaceutical applications. For example, natural nano-porous silicates such as diatomite and natural zeolite are highly environmentally and cost-effective compared to synthetic porous silica-based materials [1,3].

Diatomaceous earth, also known as diatomite, is a fossil material of sedimentary origin, formed over centuries by the siliceous skeleton (frustule) of single-celled micro-algae in water, deposited at the bottom of lakes or found in marine environments. Diatomite morphology consists of particles of different sizes from 2 µm to 2 mm, and the structure has a large surface area of up to 200 m^2/g [4]. Diatomite, the main component of which is amorphous silica, is of interest to researchers in many areas due to its widespread availability, and its superior properties such as high thermochemical stability, low density, high absorption capacity, non-toxicity, and excellent biocompatibility. For this reason, diatomite may be particularly promising for its use as a drug delivery system. According to Jelena et al. (2015), in vitro drug release studies in phosphate buffer showed that diclofenac sodium loaded on modified diatomite released over 8 hours, further indicating the potential safety of diatomite in them in vivo toxicity test results on mice [5]. Ruggiero et al. (2014) incubated different concentrations of chemically modified diatomite nanoparticles into cancer cells and observed homogeneous distribution of nanoparticles in the cytoplasm and nucleus in imaging analysis [6].

In this study, firstly, raw diatomite was beneficiated by calcining and then characterized. Then, dihenhydramine (DPH) active agent was loaded on calcined diatomite. Finally, the drug release profiles of DPH were investigated.

2. Materials and Method

2.1. Materials

The raw diatomite used in this study was collected from the Seydişehir-Konya-Turkey region. Diphenhydramine hydrochloride (DPH) was used as active agent and purchased from Sigma-Aldrich. Hydrochloric acid and sodium chloride was used to prepare simulated stomach liquid and purchased from Merck.

2.2. Methods

2.2.1. Characterization

X-ray diffraction (XRD) spectras were obtained using a Shimadzu XRD-6000 instrument with Cu-Ka radiation at a wavelength of **λ**:1.54184 Å. The samples were scanned in the 2-70º angle range. For this, the raw samples were ground using a ring mill and then dried at 105ºC for 24 hours. The specific surface areas of the raw and calcined diatomite samples were calculated by the Brunauner-Emmett-Teller (BET) equation, which is based on the calculation of the amount of gas required to cover the sample surface with a single molecular layer. The size distribution of the pores was obtained from the desorption isotherm data using the Barrett, Joyner and Halenda (BJH) method. For this, Micromeritics brand Gemini VII 2390t model device based on nitrogen gas adsorption technique in liquid nitrogen environment at -196ºC was used.

2.2.2. Drug Loading

Acetic acid solution (2%) containing 1000 mg/L of active ingredient (DPH) was prepared firstly. Drug carrier system were prepared by calcining of raw diatomite for 4 hours at 550 ºC. The ratio of active ingredient and carrier material was kept constant as 1/10. For this, 2500 g of calcined diatomite was added in 250 mL DPH solution. The prepared dispersion was slowly stirred using a magnetic stirrer at 25ºC for 24 hours. The resulting mixture was dried in an oven at 55ºC for 24 hours and then ground using a ring mill.

2.2.3. Drug Release

The release study of drug-loaded formulations was performed with the USP apparatus I basket method. Firstly, the formulations containing 25 mg of diphenhydramine HCl were weighed and filled into hard gelatin capsules. The working speed was set at 50 rpm and the temperature at 37°C. Vessels were filled with 900 mL of pH 1.2 acidic medium. At the specified time intervals (5. 15. 30. 45. 60. 75. 90. 120. 150. 180. min) 1 mL sample was taken and transferred to vials by filtering through a membrane filter (pore size of 0.2 µm). Fresh medium and vessels were made up to the same amount. Samples were analyzed in HPLC device at 227 nm. The study was performed in triplicate for each formulation.

3. Results and Discussion

3.1. Characterization of Diatomite

The XRD spectrum was analyzed to investigate the crystal structure of diatomite (Figure 1). The broad diffraction peak observed at 2θ=22° was assigned to the amorphous silica of the characteristic diatomite structure.

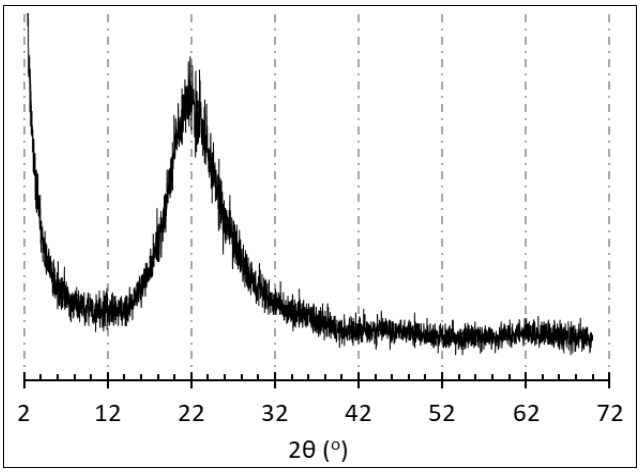


Figure 1. XRD spectrum of diatomite.

BET surface area, pore volume, and pore size of diatomite samples were given in Table 1. BET surface area of raw diatomite was measured as 21.7 m^2/g and BET surface area of calcined diatomite was measured as 75.1 m^2/g. As expected, the surface area of the diatomite increased by the calcination process. Pore size and pore volume also varied significantly.

Table 1. BET analysis results of the samples.

Sample	BET surface area (m^2/g)	Pore size (nm)	Pore volume (cm^3/g)
Raw diatomite	21,7	75,23	0,4079
Calcined diatomite	75,1	91,64	1,7210

3.1. Drug Release

The r^2 value was calculated as 0.9998 in the HPLC method developed for the determination of diphenhydramine HCl. It was determined that the method developed by applying validation parameters such as linearity, reproducibility, recovery, accuracy was appropriate in the determined concentration range. LOQ and LOD values were determined as 0.241 and 0.072 µg/mL, respectively. The developed method was found to be highly reproducible and suitable for the quantification of diphenhydramine hydrochloride.

In order to make the prepared product easier to use by the patient, the drug-loaded mixture was filled into a hard gelatin capsule. Orally used capsule formulations are formulations with high patient compliance, easy use

and low cost [7]. Basket method (USP Apparatus I) was used in the release studies of formulations filled into capsules. This method is a frequently used dissolution method for capsule formulations [8-10]. As seen in Figure 2, it was observed that the active ingredient passed into the release medium after the 5th minute, with the capsule wall breaking down due to temperature and medium. This indicates that the capsule wall begins to break down within 5 minutes. At the same time, this situation was observed observationally during the study. The rapid transition of the active ingredient from the carrier system to the release medium is related to the fact that DPH is an active substance with high solubility in water [11].

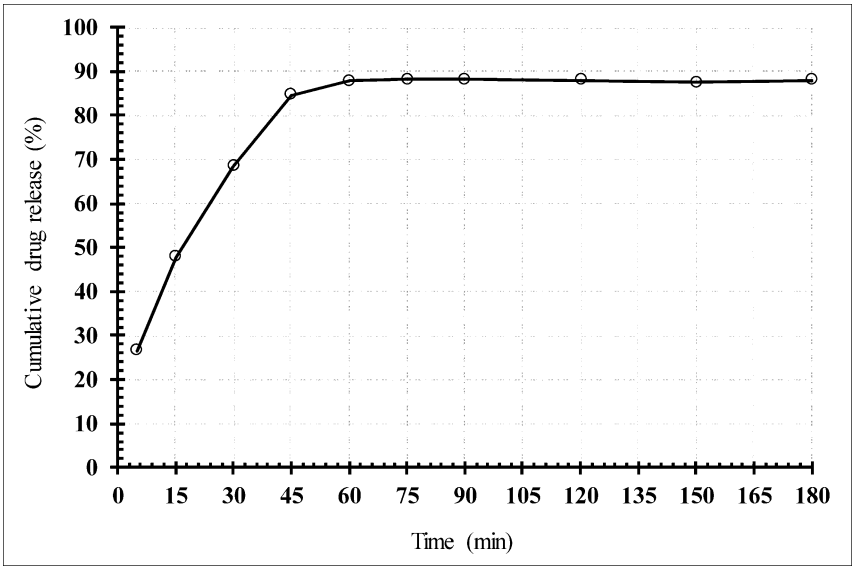


Figure 2. DPH release profile of calcined diatomite as a function of time.

When the drug release profile is examined, a rapid release occurred in the first 5 minutes. In the following period, the release rate slowed down a bit. It can be seen from Figure 2 that the drug release occurred during 60 min. At the point where the release was completely over, it was determined that the release rate was 80% in total.

4. Conclusions

BET analyzes were revealed that raw diatomite sample was successfully calcined and advanced properties such as high surface area and high pore volume were obtained. The calcination process is known to increase the drug loading capacity as it increases the surface area and porosity. It also causes the carrier system to show a slower release profile. It was determined that the loading of DPH on calcined diatomite was realized by physical adsorption, that is, mostly by the effect of electrostatic forces. As a result, it was determined that calcined diatomite enriched with organic pollutants released DPH for 60 minutes.

References

[1] S. M. Ibrahim, M. N. Bin Jumah, S. I. Othman, R. S. Alruhaimi, N. Al-Khalawi, Y. F. Salama, A. A. Allam, M. R. Abukhadra, "Synthesis of chitosan/diatomite composite as an advanced delivery system for ibuprofen drug; equilibrium studies and the release profile," *ACS Omega*, *vol.* 6, no. 20, pp. 13406-13416, 2021.

[2] M. Goldberg, R. Langer, X. Jia, "Nanostructured materials for applications in drug delivery and tissue engineering," *Journal of Biomaterials Science, Polymer Edition* vol. 18, no. 3, pp. 241-268, 2017.

[3] H. Zhang, M. A. Shahbazi, E. M. Mäkilä, T. H. da Silva, R. L. Reis, J. J. Salonen, J. T. Hirvonen, H. A. Santos, "Diatom silica microparticles for sustained release and permeation enhancement following oral delivery of prednisone and mesalamine," *Biomaterials*, vol. 34 no. 36, pp. 9210-9219, 2013.

[4] I. Rea, N. M. Martucci, L. De Stefano, I. Ruggiero, M. Terracciano, P. Dardano, N. Migliaccio, P. Arcari, R. Taté, I. Rendina, A. Lamberti, "Diatomite biosilica nanocarriers for siRNA transport inside cancer cells," *Biochimica et Biophysica Acta (BBA)-General Subjects*, vol. 1840, no.12, pp. 3393-3403, 2014.

[5] J. Janićijević, D. Krajišnik, B. Čalija, B. N. Vasiljević, V. Dobričić, A. Daković, M. D. Antonijević, J. Milić, "Modified local diatomite as potential functional drug carrier - A model study for diclofenac sodium," *International Journal of Pharmaceutics*, vol. 496, no. 2, pp. 466-474, 2015.

[6] I. Ruggiero, M. Terracciano, N. M. Martucci, L. De Stefano, N. Migliaccio, R. Tatè, I. Rendina, P. Arcari, A. Lamberti, I. Rea, "Diatomite silica nanoparticles for drug delivery," *Nanoscale Research Letters*, vol. 9, no. 1, pp. 1-7, 2014.

[7] M. A. Hadi, N. G. Raghavendra Rao, A. S. Rao, G. Shiva1, J. W. Akram, "Impact of capsules as a carrier for multiple unit drug delivery and the importance of HPMC capsules," *Research J. Pharm. and Tech*., vol. 6, no. 1, pp. 34-43, 2013.

[8] L. Lo, X. Lu, D. Lloyd, "Dissolution testing of a controlled-release capsule formulation: challenges and solutions using a semi-automated dissolution system," *Dissolution Technologies*, pp. 1-12, 2013.

[9] N. Kumara, D. Sangeethab, P. S. Reddya, A. M. Reddy, "Development and validation of a dissolution test for delayed release capsule formulation of duloxetine hydrochloride," *Current Pharmaceutical Analysis*, vol. 8, pp. 236-246, 2012.

[10] F. Damian, M. Harati, J. Schwartzenhauer, O. V. Cauwenberghe, S. D. Wettig, "Challenges of dissolution methods development for soft gelatin capsules," *Pharmaceutics*, vol. 13, no. 214, pp. 1-30.

[11] Chenguang Wang, Shenye Hu, and Changquan Calvin Sun, "Expedited development of diphenhydramine orally disintegrating tablet through integrated crystal and particle engineering," *Molecular Pharmaceutics*, vol. 14, pp. 3399-3408, 2017.

Influence of zinc borate and borax decahydrate on the flame retardancy of polymer composite

Nada ALLOUSH[1] Atilla Evcin[2] and Mustafa Uçar[3]

[1] Idlib, Suriye

[2] Afyon Kocatepe University, Materials Science and Engineering Department, Afyonkarahisar, Turkiye

[3] Afyon Kocatepe University, Chemistry Department, Afyonkarahisar, Turkiye

Abstract

The use of fire retardants in order to prevent the occurrence of fire is an application that is becoming more common day by day. The most effective application area of fire retardants is polymers. fire retardants; Bromine added fire retardants, melamine-based fire retardants, metal hydroxides, antimony oxide and zinc borate are grouped into five groups. Zinc borate has gained a large share in the fire retardant market in recent years and this share is increasing day by day.

In this study, zinc borate and borax decahydrate was mixed into the polymer at different rates and homogenized. It was then left to dry at room temperature for one day. Then, the UL-94 test was made ready by carefully cutting our samples to be 3 cm - 9 cm. The samples were characterized by XRD, SEM, EDX, Elemental mapping.

Keywords : Polymer, flame retardancy, zinc borate

Corrsponding Author e-mail : nada.alloush97@gmail.com

1. Introduction

The use of fire retardants in order to prevent fire formation is becoming more common day by day. The area where fire retardants are most effective and applied is polymer composites. fire retardants; Bromine added fire retardants, melamine-based fire retardants, metal hydroxides, antimony oxide and zinc borate are grouped into five groups. Zinc borate has gained a large share in the fire retardant market in recent years and this share is increasing day by day. Studies on alternative fire extinguishers are also ongoing. One of these alternatives is borax decahydrate [1-4].

2. Materials and Method

Commercial zinc borate (Melos Co.) and borax decahydrate (Eti Mine Co., BDH) were used as fire retardant materials in the study. The matrix part of the composite is silicon rubber (RTV2). The composition of the prepared mixtures is given in Table 1.

Table 1. Composite compositions.

Sample Code	Polymer	Zincborate	BDH	Total Composite
P0	20 g	-	-	20 g
PZ	18 g	2 g	-	20 g
PB	18 g	-	2 g	20 g
PZB	18 g	1 g	1 g	20 g

Fire retardants in powder form were added to RTV 2 silicone and mixed until homogeneous. It was then molded as 3x9 cm as specified in the UL-94 test. While XRD analysis was performed on the powders used, UL-94 test and SEM analysis were performed on the composite.

UL-94 Test

The test stick is connected vertically and flame is applied several times for 10 seconds. Between flame applications, the time until the stick goes out is measured. Afterwards, the burn time characteristic after the flame is removed is evaluated.

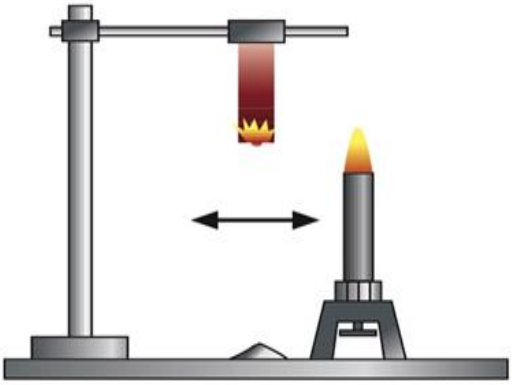


Figure 1. UL 94 test setup

Table 2 Flammability Ratings to Classify Plastics

Class	**Orientation of Test Sample**	**Definition**	**Time of Burn Allowed**	**Particle Drop Allowed**		**plaque Holes**
				Flaming	**Non-Flaming**	
UL 94 HB	Horizontal	Slow Burning	Burning rate of less than 76mm/min for a specimen less than 3mm thick and burning stops before 100mm			
UL 94 V-2	Vertical	Burning Stops	30 seconds	Yes	Yes	
UL 94 V-1	Vertical	Burning Stops	30 seconds	No	Yes	
UL 94 V-0	Vertical	Burning Stops	10 seconds	No	Yes	
UL 94 5VB	Vertical	Burning Stops	60 seconds	No	No	Yes
UL 94 5VA	Vertical	Burning Stops	60 seconds	No	No	No

3. Results and Discussion

UL 94 results

Table 3. 2. UL-94 test results

Sample code	P0	PZ	PZ	PZB
Burning image				
Thype of rating	NR	UL 94 V2	UL 94 V2	UL 94 V2

UL 94 test results are given in Table 3. According to these results, pure silicone polymer could not be evaluated because it burned. However, composites containing zinc borate, borax deca hydrate and both are in the UL 94 V2 class. Accordingly, when the added amounts are taken into consideration, it is seen that it improves the incombustibility.

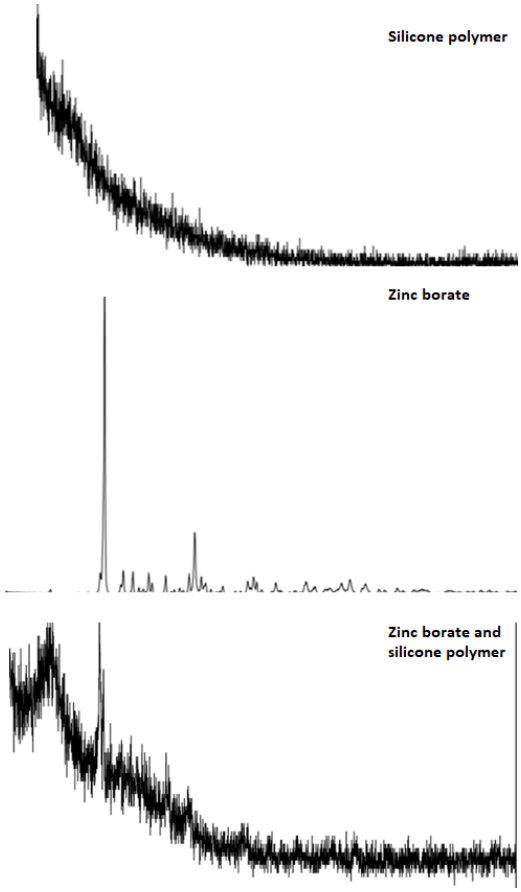


Figure 2. XRD analysis of samples.

XRD analyzes of the samples are given in Figure 2. Accordingly, the amorphous structure of the samples containing polymers is clearly visible. Zinc borate crystals exist in crystalline form.

SEM analyzes of the cross-section of the sample (PZB) with the best results are given in figure 3. Accordingly, it is seen that the solid phase is homogeneously dispersed in the polymer. Since boron element cannot be seen in this model of the device, zinc, silicon, calcium and carbon elements were observed in the edx analysis.

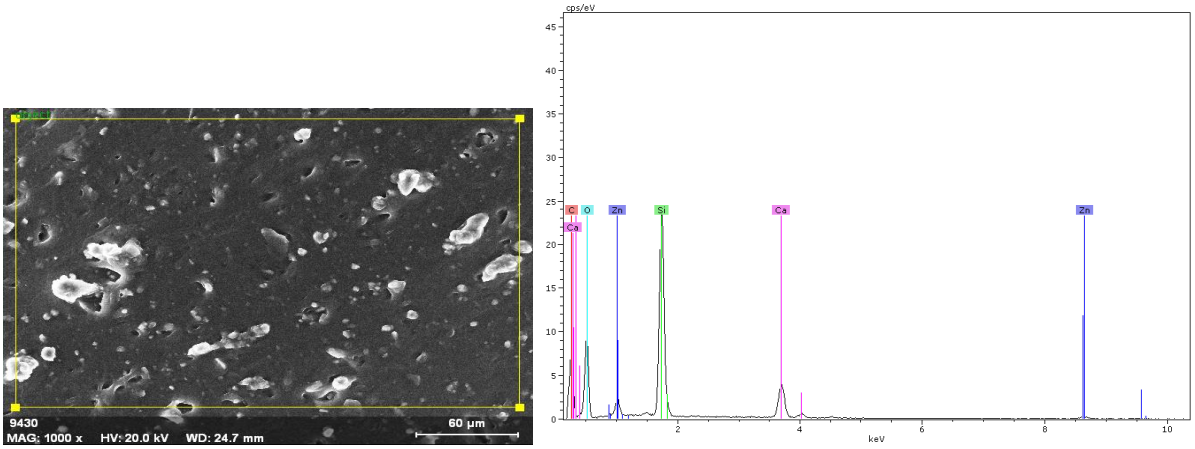


Figure 3 Cross section of polymer PZB composite

References

[1] Grover, Taruna & Khandual, Asimananda & Chatterjee, kalesh nath & Jamdagni, R.. (2014). Flame retardants: An overview. 61. 29-36.

[2] Schartel, B. & Rabe, Sebastian & Pérez-Chávez, Ricardo & Carosio, Federico & Alongi, Jenny & Jaramillo, Mario & Manero, Octavio & Solis, Antonio & Sanchez-Olivares, Guadalupe. (2020). Advanced Flame Retardant Materials Book 2020.

[3] Al-Mosawi, Ali and Shaymaa Abbas Abdulsada. (2015). Inorganic flame retardants. International Journal of Advanced Research , Volume 3, Issue 6, 1473-1477

[4] Weil, Edward & Levchik, Sergei. (2008). Flame Retardants in Commercial Use or Development for Textiles. Journal of Fire Sciences - J FIRE SCI. 26. 243-281. 10.1177/0734904108089485.

Improvements in Characterization of Pozzolanic Cement Mortars After Different Grinding Methods

Abdul Vahap KORKMAZ

avkorkmaz@aku.edu.tr

Afyon Kocatepe University, İscehisar Vocational School, Department of Construction, İscehisar/Afyonkarahisar/Turkey.

Abstract

In the cement sector, a large amount of energy is consumed in the grinding of clinker. In order to reduce energy consumption, materials with pozzolanic properties are widely used together with Portland cement. In this study, the pozzolanic and grindability properties of a natural volcanic diabase rock were investigated for the first time as a potential clinker replacement material. In order to increase the reactivity of the diabase, mechanical activation processes were comparatively tested in two different grinding media containing ball and silpeps. The aim here is to find the best grinding medium at lower costs and to make the diabase more reactive in a shorter time. It has been observed that the best mechanical activation for the diabase material is done in the medium with silpeps due to the high particle contact angle. In addition, the microstructures of the diabase particles obtained as a result of mechanical activation in different grinding media were examined by means of SEM images and the mechanical activation particle interaction relationship was investigated. Then, the pozzolanic properties of diabase were determined and cement samples were produced at 10%, 30% and 50% diabase admixtures. It has been observed that diabase-added cements meet the Turkish standard values (TS EN) in all the replacement ratios tried. An innovative approach has been presented for the successful use of diabase as a cement additive material in an environmentally friendly way with an additive ratio of up to 50% as a pozzolanic additive material.

Keywords:

Diabase, volcanic tuff, Mechanical activation, Cement, Pozzolanic activity

Introduction

Energy consumption increases day by day as a result of the increasing trend in technological development in the World. More attention should be paid on this issue in order to save the energy resources. Cement industry consumes 2% of the global primary energy and/or approximately 5% of the total global industrial energy. Clinker production is responsible for 70-80% of the consumed energy while material preparation/blending and size reduction/grinding are the following intensive energy requiring steps [1]. Therefore, composite cement production has attracted increasing attention owing to its economical, ecological and energy saving sides [2]. Besides, a very small gain in grinding efficiency is of great importance in terms of energy reduction [1].

Cement industry has focused on natural pozzolan materials such as volcanic tuff, zeolite, perlite, pumice and diatomite [4, 5, 6, 7, 8] besides industrial by products such as fly ash, silica fume, slag etc. [9, 10, 11, 12]. As artificial pozzolanic materials, composite bonding rice ash [13], bamboo leaf ash [14], ground brick waste [15], sugarcane pulp ash [16], palm oil ash [17], soda sludge [18], activated charcoal washing waste [19], bottle glass [20], different biomass ashes have become the most popular pozzolans [21]. The common feature of all these pozzolanic additives is the possible effective partial replacement of clinker. It is widely seen that the grindability of the belended cements is easier than the sole grinding of the clinker. For example, grinding clinker and trass blends for cement production may require less energy, especially than separate grinding processes [22, 23].

Although volcanic pumice is easy to grind in coarse sizes, it is more difficult to grind in fine sizes as in all other pozzolans. The reason underneath of this phenomena is that the existing pores of the pumice disappear when grinding size comes closer to the crystal size. In addition, SiO_2 causes the abrasion problem during grinding. In dry grinding, the moisture content of the ore is required to be less than 1%. Otherwise, the moist ore is smeared on both the balls and the liners. It has been seen that the optimal feed size for fine grinding is 1 mm. Sometimes it cen be fed in greater sizes more 1.0 mm. The grain size of the ore fed in a mill containing 3 cm diameter balls is approximately 1 mm.

Use of perlite and travertine seems to be suitable in order both to produce composite cements and reduce the energy costs. When the composite cements produced using Perlite and travertine wastes are evaluated in terms of grinding time, it is obvious that it will provide savings in terms of grinding time and energy consumption since grinding of such materials are easier than that of ordinary Portland Cement clinker. Fly ash, on the other hand, increases its specific gravity and fineness as the grinding time increases [9]. Moreover, the morphology of fly ash was changed by grinding and the number of spherical particles decreased with increasing grinding. Fly ash only reached the optimum fineness after about 4 hours of grinding time [24].

Compared to Portland cement clinker, zeolite, which is a softer material, makes the grinding process easier [26]. The energy costs required to grind the clinker containing 20% zeolitic tuff saves 11.19 kWh / ton of energy compared to to the sole grinding of the clinker to the same grain size. However, this is an expected result when compared to the Cem I 42.5R Portland cement production. Because it is known that energy consumption duıring cement production will decrease with the increase in the amount of additives added in cement production. When the amount of zeolite is increased up to 30%, the grinding time decreases by 30% resulting in lower energy costs [25].

Turkey is rich in volcanic tuff reserves. It has been observed that the quality of volcanic tuffs varies according to the region as a result of geological formation characteristics. Therefore, volcanic tuffs have different properties i.e. pozzolanic characteristics, grindability etc. related to the use of substitution in cement production. For this reason, volcanic tuffs containing local differences can affect the cost of cement production due to different energy consumption rates in composite cement production [27].

More than 60% of Portland cement has been produced recently in Turkey using supplemanetary pozzolans [28]. Most of the studies are on the usability of volcanic tuffs as pozzolanic material in cement production. On the other hand, although there have been many studies on volcanic rocks in Turkey, pozzolanic properties of these rocks has not been investigated sufficiently, yet [29]. Among these volcanic rocks, diabase is a solid and durable volcanic rock. However, the pozzolanic properties of diabase have not been discovered and no research has been carried out to up to date as a cement replacement material. There are few studies on the use of diabase as aggregates only in concrete production [28]. Since diabase mineral deposits and reserves are high in Turkey in different geographic regions, the current study is focus on its potential use as a cement substitution pozzolana [28].

In this study, better grindability techniques of diabase and volcanic tuff were investigated as a comparison with under different grinding media. The product grain size analysis results were compared by using balls and cylpebs separately as grinding elements in the laboratory type cylindrical mill. With the products obtained, pozzolanic cements with 10, 30 and 50% admixtures were obtained. Hydraulic and mechanical tests were performed with blended cement samples. SEM images of cement mortar samples produced with different additive ratios were examined.

2. Experimental Studies

In the experimental studies, diabase mine residues, Portland cement clinker and gypsum samples belonging to the quarries of the Çamlıbel region of Tokat province were used. The samples brought to the Istanbul University Mining Engineering Mineral Processing Department were first weighed. Coarse sized materials were passed through a two-stage jaw crusher and then sample reduction. The amount of 15 kg each was used in the Bond work index test and the remaining amounts were used in the physical, chemical, mineralogical and grinding tests.

2.1. Chemical and Mineralogical Characterization of the materials

Chemical analyzes of natural diabase, volcanic tuff, Portland cement clinker and natural gypsum were made according to the TS EN197-1 and TS EN 196-2, and the results are given in Table 1 [31, 32].

X-ray diffraction method was used under a Riguku Ultima IV X-Ray Diffractometer in order to determine the mineralogical compositions of the materials. Natural volcanic tuff consists of plagioclast (andesine), biotite, hornblende, quartz and magnetite minerals. It has been observed that the rock is composed of plagioclasts dominated by more than 40% andesine, 10-15% hornblende and consists of abundant glassy material. [33].

Diabase consists of basic plagioclase, generally consisting of labradorite, and basaltic with a distinctive ophitic texture, consisting of basic monoclinic pyroxene generally consisting of augite, and containing secondary apatite, quartz, oligoclase, andean, magnetite, ilmenite, orthoclase, hornblende, biotite and olivine minerals. is a stone. When Çamlıbel diabases are examined; diabase, andesine, pyroxene, opaque mineral, less than 2% olivine and about 1% secondary minerals are found to be composed of plagioclasts.

Table 1. Chemical compositions of the materials

Chemical compounds	Diabase	Volcanic Tuff	Clinker	TS 25 Pozzolana Standarts
	%	%	%	%
SiO_2	53.85	54,62	20.58	>70
Al_2O_3	14.11	19.32	5.34	
Fe_2O_3	11.13	8.13	3.29	
CaO	6.72	7.33	65.88	
MgO	3.48	2.61	1.93	5<
Na_2O	5.25	0.42	0.29	
K_2O	0.44	1.57	0.95	
Cl	0.02	0.01	0	
TiO_2	1.15	0.36	0	
P_2O_5	0.66	0.87	0	
Cr_2O_3	0.05	0.01	0	
MnO	0.10	0.05	0	
SO_3	0.02	0.35	1.26	<3
Loss on ignition	2.22	3.95	0.15	<5
Total	99.20	99.60	99.67	
Moisture	3.1	6.7	0.2	

2.2. Pozzolanic activity tests

In the current study, volcanic tuff was used as control/comparison material which is a commonly used pozzolan. Since one of the influential factor affecting the pozzolanic activity of the pozzolans is the fineness of the materials, the fineness of diabase and volcanic tuff was set to of about 5500 g/cm^2 for pozzolanic activity test. Pozzolanic activity of a potential pozzolan should be more than 4 MPa. In this study, blaine test was performed in accordance with TS EN 196-6 standard while pozzolanic activity test is conducted according to TS 25 standard. In addition, reactive SiO_2 test were performed based on TS 369 standard.

2.3. Specimen preparation and Grinding Procedures

Natural diabase, volcanic tuff, Portland cement clinker and natural gypsum samples were firstly grinded in a standard Bond mill, and then in a 22 lt cylindrical laboratory type ball mill (305 * 305 mm (Q * L); 36 mm, 30 mm 25 mm, 19.05 mm and 12.70 mm in diameter with balls rotating at 70 rpm). The pozzolans were ground in 4 min, 8 min, 12 min, 15 min and 30 min duration. Then, sieving analyses were done.

The work index (Wi) is determined by simulating the closed-loop dry grinding process in the Bond ball mill until a 250% cycle load is reached. For this purpose, a sample with a volume of 700 cm^3 reduced below 3.327 mm (6 mesh) was used. This sample was placed in a Bond ball mill which has a standard ball distribution size and speed, and is ground at a randomly selected number of turns in the first grinding phase. At the end of each grinding phase, the whole product is emptied and sieved through the test sieve. For the second grinding phase, the number of turns is calculated so that the load from 250% cycle is gradually reached. After the second phase, the same sieving and grinding process continues until the amount of test sieve produced at each number of revolutions becomes constant in the last three grinding phases. In this case, it will be reached at 250% circuit load. The standard Bond test can be completed after approximately 7-15 grinding cycles. The product obtained from the final grinding stage is subjected to sieve analysis and the work index is calculated according to the formula below.

$$Wi = \frac{44,5}{(P1)^{0,23}\ x\ (G)^{0,82}\ x\ \left|\left(\frac{10}{\sqrt{P}}\right)-\left(\frac{10}{\sqrt{F}}\right)\right|}\ x\ 1,1 \qquad [35]$$

Wi: Bond work index (kwh/t), P_1: selected test sieve size (µm), G: standard Bond grindability value (g/rev), P: It shows the sieve size (µm) through which 80% passes.

The same laboratory type ball mill was also used to produce composite cement samples. After the diabase and volcanic tuff samples were grinded in the laboratory mill for an equal time (45 minutes) by balls, the grinding balls were replaced by cylpebs in the same mill. Then, the grain size distribution of ground diabase and volcanic tuff samples for an equal time (45 min) was determined using a sympatec helos model particle size tester. Ball size distribution is an important parameter in ball mill applications. Depending on the type of grinding elements in the mill, the grinding performance can be affected significantly. Both balls and cylpebs are widely used in grinding plants in cement plants in Turkey. In this way, it was aimed to compare the grindability of diabase and volcanic tuff using two different grinding media (balls and cylpebs) in the same laboratory type cylindrical mill.

2.4. Study on the grindability and energy cost estimation

Using a laboratory-sized horizontal ball mill (in the range of 30-22 mm ball diameter), composite cements were produced with diabase and volcanic tuff at 30% of replacement ratio.The energy consumptions of each composite cement sample were calculated and unit energy consumption costs were compared.

The main purpose in determining the Hardgrove grindability index is to obtain an approximate value about the capacity and energy consumption of the grinding systems of the raw materials. The energy consumed in grinding is directly proportional to the work index, and the relation between the work index (Wi) and the Hardgrove index (HGI) is given as follows:

Wi = 88/HGI 0,5

According to the formula, the higher the Hardgrove grindability index, the lower the work index; that is, energy consumption per ton is reduced.

2.5. Microscopic Examination under Scanning Electorn Microscope (SEM)

SEM image analyses of composite cements including 30% diabase (Fig. 8a) and 30% volcanic tuff were performed to under a JEOL JSM 5600 brand SEM device in Adaçal Industrial Minerals laboratory.

3. Results and Discussion

3.1. Evaluation of the Pozzolanic Properties of Diabase and Volcanic Tuff

Diabase and volcanic tuff provides sufficient amount of reactive SiO2 which are 26.42 and 28.35, respectively. Pozzolanic activities of the natural diabase and volcanic tuff were found as 6.4MPa and 6.9 MPa, respectively. Sum of SiO2 + Al2O3 + Fe2O3 are 79.09 and 82.07 for diabase and volcanic tuff, respectively. It can be seen from pozzolanic activity tests that natural diabase provides the required standard values as volcanic tuff.

3.2. Bond Work Indexes of the Materials

The Bond method is the most widely used approach in the design of the grinding circuits of the ore preparation plants. Using this method, the mill size and power requirement for an ore to be grinded are determined [34]. In the cement grinding stage, bond work indexes of clinker, diabase, volcanic tuff and gypsum are firstly found, separately (Table. 2) The main purpose of calculating bond work indexes is to get an idea about the grinding energy consumption of materials for composite cement production based on the work index of clinker.

As can be seen from Table 2, clinker reveals the highest work index while while gypsum has the least. However, when comparing volcanic tuff and diabase, the work index of diabase is lower than that of volcanic tuff. These results provide that composite cements can be produced with diabase replacement with lower energy costs.

Table 2. Bond work indexes of clinker and additives

Clinker kWh/t	Volcanic Tuff kWh/t	Diabase kWh/t	Gypsum kWh/t
13,71	12,37	11,65	12,18

3.3. Test Results of Grindability of materials and cement samples

Diabase and volcanic tuff samples to be used as additives in pozzolanic cement production were subjected to grinding times of 4, 8, 12, 15 and 30 minutes using a laboratory scale ball mill, and then the cumulative under-sieve curves of the products were drawn (Fig. 1 and 2). The d80 size of the cement raw materials, diabase and volcanic tuff, is required to be thinner than 75 microns. The purpose of grinding is to reduce at least 80% of the grain size of the raw materials under 75 microns in order to produce pozzolanic cement.

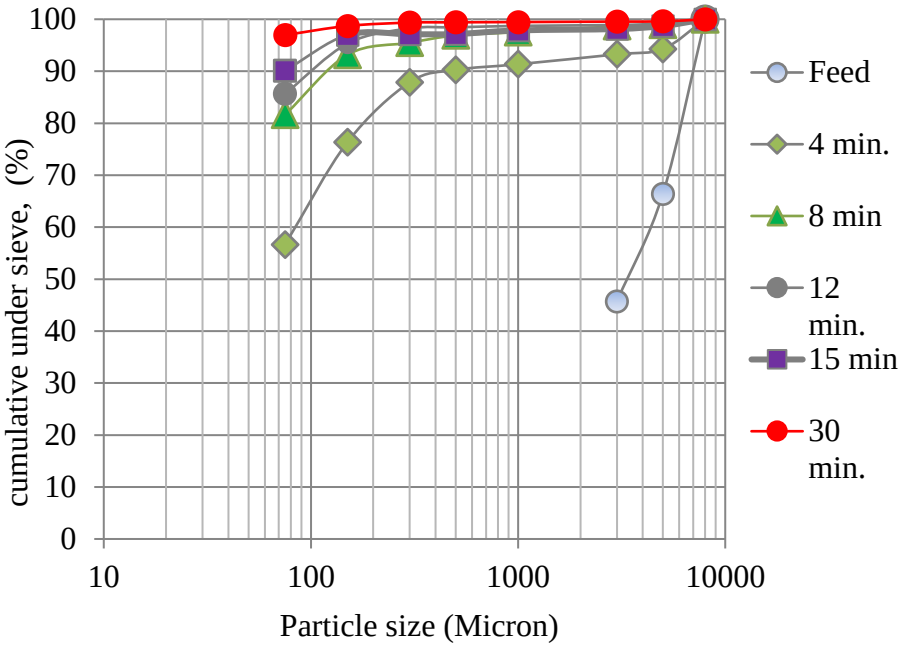


Fig. 1. Under-sieve curves of products obtained by grinding sole diabase at different times

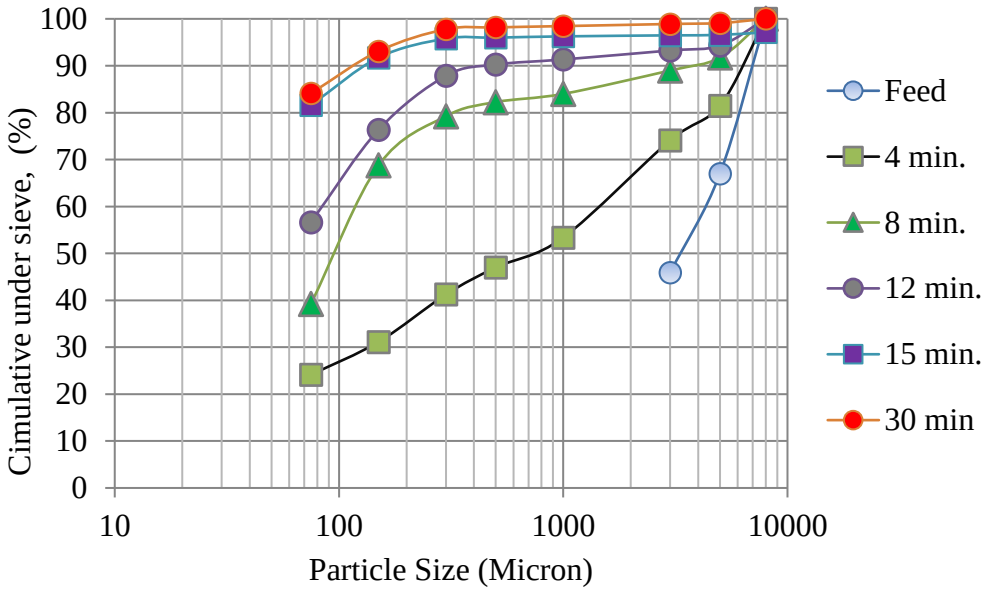


Fig. 2. Under-sieve curves of products obtained by grinding sole volcanic tuff at different times

As can be seen from Fig. 1 and 2, size reduction of diabase under 75 microns was reached after a grinding period of approximately 8 minutes while the duration is at about 15 minutes for volcanic tuff. It simply shows that diabase raw material is grind ~53% faster than the volcanic tuff in terms of grinding time for cement production. Therefore, it is concluded that diabase reaches the desired grain fineness in a shorter time than volcanic tuff.

3.4. Hardgrove Grindability Test and Energy Cost Calculation

In the hardgrove grindability tests, a ball mill was used and the HGI values of the raw materials were determined separately. Then, using the HGI-Wi conversion formulas, Wi (work index) values were calculated and the obtained Wi value was compared with the literature data. Considering the faster grinding result (~53%) of the diabase, the HGI value of diabase is expected to be greater and the work index value to be less in this respect. When modeling the obtained grinding data according to the formula below;

HGI=13,60+6,93. M

HGI: Hardgrove grindability index

M (g):

The following comments can be made according to the obtained HGI values:

HGI> 70, material can be grinded easily,

HGI = 50-70 is a sample of material with medium grindability,

HGI = 30-50, it is an example of hard-ground material.

As a result of the original Hardgrove test applied to cement raw materials, the results in Table 3 were obtained. In addition, HGI values were converted into Work index (Wi) values with an equation proposed by Bond in 1954. The formula for the conversion of the HGI value to the work index is given below [35].

$Wi = 88/HGI^{0.5}$

Table 3. HGI and Wi values of Volcanic tuff and diabase raw materials

Material	M (gr)	HGI (-)	W_i (kwh/t)
Diabase	16.50	127.95	7.78
Volcanic Tuff	11	89.83	9.29

HGI value of diabase was found to be ~42% higher than volcanic tuff and as a result ~16% less Wi. According to these results, diabase and volcanic tuff have HGI values above 70 indicating easier grinding process. On the other hand, if the Bond job indexes are interpreted according to the Table 4, diabase is seen to be easily grinded than volcanic tuff which is clearly expected to result in lower energy costs during grinding/size reduction processes.

Table 4. Grindability results according to the work index value [35].

Work index (Wi)	6-9	10-14	15-20	>20
Grindability	Easy	Middle	Hard	So hard

3.5. Comparison of the efficiency of the different grinding methods

Determination of the fineness values of cements or pozzolans is evaluated by different methods such as calculating the amount remaining on the 32 μm, 45 μm and 90 μm sieve or determining the particle size distribution by laser diffraction. All these methods have some advantages or disadvantages in determining the

fineness of materials. It is stated that the use of laser diffraction method is a more informative method for the particle size distribution of the materials [35]. The particle size distributions of diabase and volcanic tuff subjected to ball and cylpebs grinding environment for 45 minutes in a laboratory type cylindrical mill are given in Figs. 3 and 4. Considering Table 5 and Fig. 3-4, diabase can be seen to be finer than volcanic tuff for both grinding media for a given particle size (D_{1O}, D_{50}, D_{97}) as a result of easier grinding fetures of diabase. Besides, cylpebs grinding environment seems to be more effective than that of ball grindind media.

Table 5. Particle size analysis results

Grinding element type	Material	D_{1O}(µm)	D_{50}(µm)	D_{97}(µm)
Balls	Diabase	0,89	6,93	70,17
Balls	Volcanic Tuff	1,25	12,12	86,65
cylpebs	Diabase	0,89	6,79	66,57
cylpebs	Volcanic Tuff	1,07	9,55	76,61

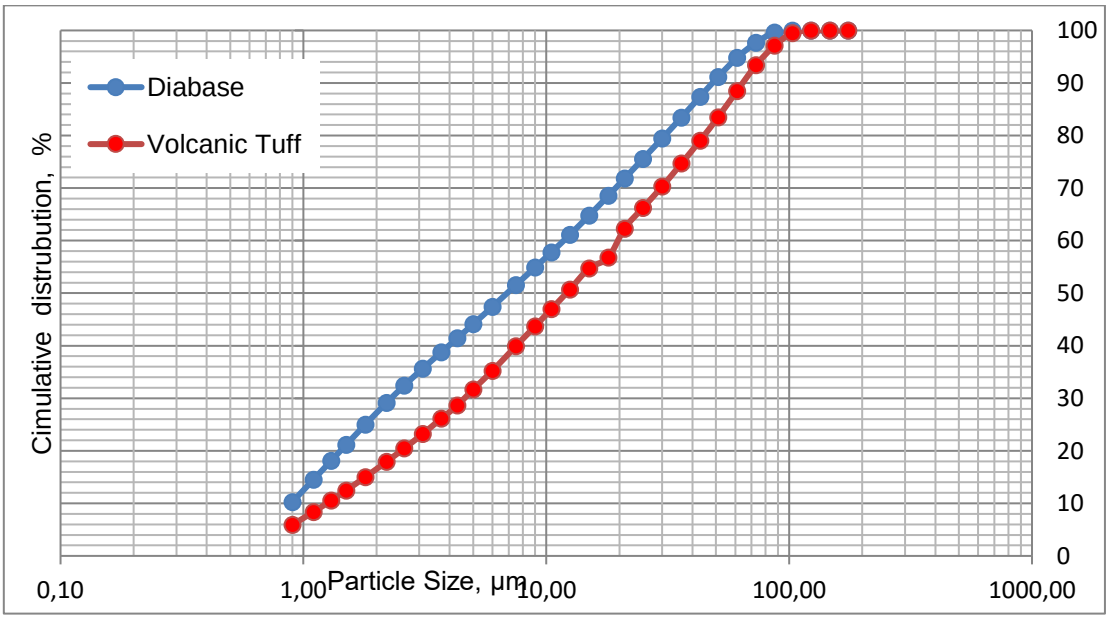


Fig. 3. Particle size distribution of the pozzolanic materials by ball grinder

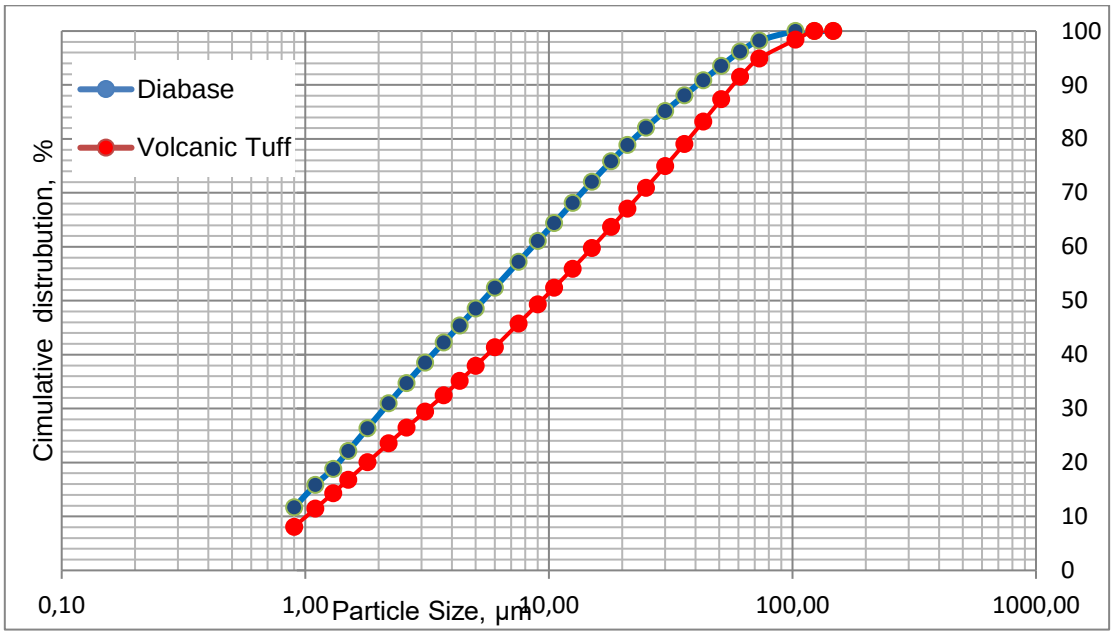


Fig. 4. Particle size distribution of the pozzolanic materials by cylpebs grinder

For many years, balls in different sizes and different chemical compositions have been used as grinding media in ball mills. Later, cylindrical grinding media called cylpebs started to be used. cylpebs are cylindrical, slightly conical for easy removal from the mold or slightly spherical cylindrical on both sides. An important advantage of cylpebs over balls is that while the balls provide a single point contact with each other, cylpebs provide superficial, linear and point contact. Therefore, the final product has a narrower/finer granulometric size distribution [36].

Comparisons of ball and cylpebs in terms of shape, density and bulk also show additional advantages for cylpebs. In a loosely-stacked charge, the bulk density of hardened cast iron cylpebs is 4.9 t/m^3, while this value is 4.4 t/m^3 for cast iron balls and 4.5t/m^3 for steel balls. If a mill is loaded with an equal volume of cast iron cylpebs or balls as grinding media, the cylpebs charge is 12% more by weight than the ball charge.

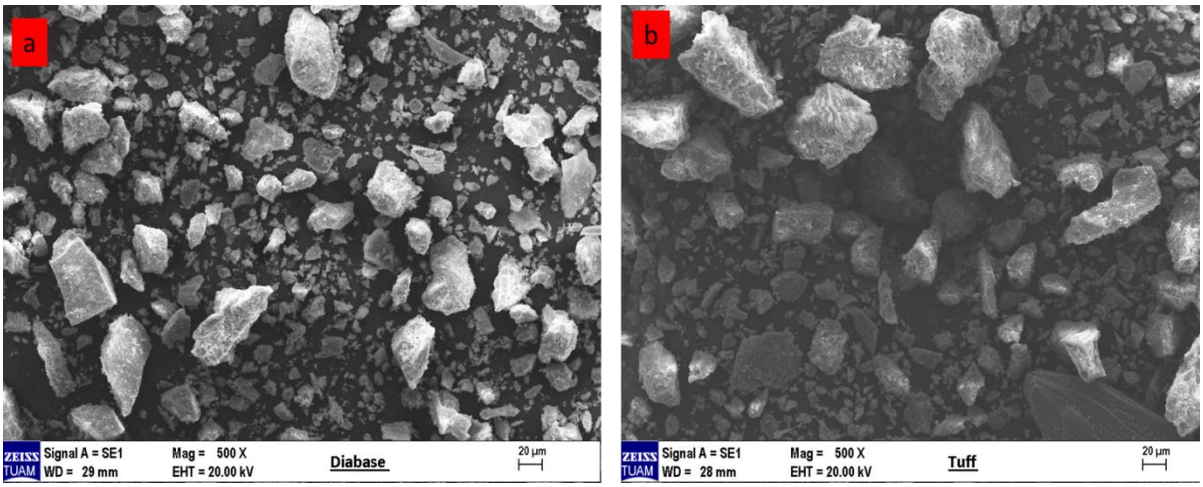


Fig. 5. SEM images of the particle size (ball grinding media)

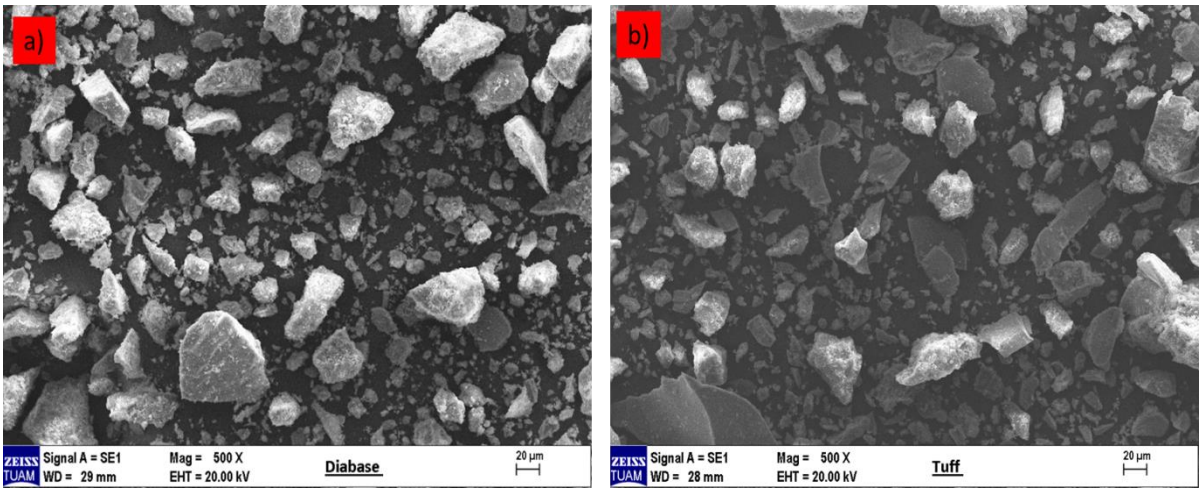


Fig. 6. SEM images of the particle size (cylpebs grinding media)

3.6. Microscobic Evaluation of the Diabase and Volcanic Tuff Replaced Composite Cements

SEM image analyses of pozzolanic cements including 10%, 30% and 50% diabase (Fig. 9a) and 30% volcanic tuff additive (Fig. 9b) were performed to better understand the effect of grinding on the cements composite. The morphology of the volcanic tuff blended cement grains are angular, quite rough and longer while diabase blended cement grains are round and smooth. In the diabase sample, amount of finer grains seems to be higher than those of volcanic tuff.

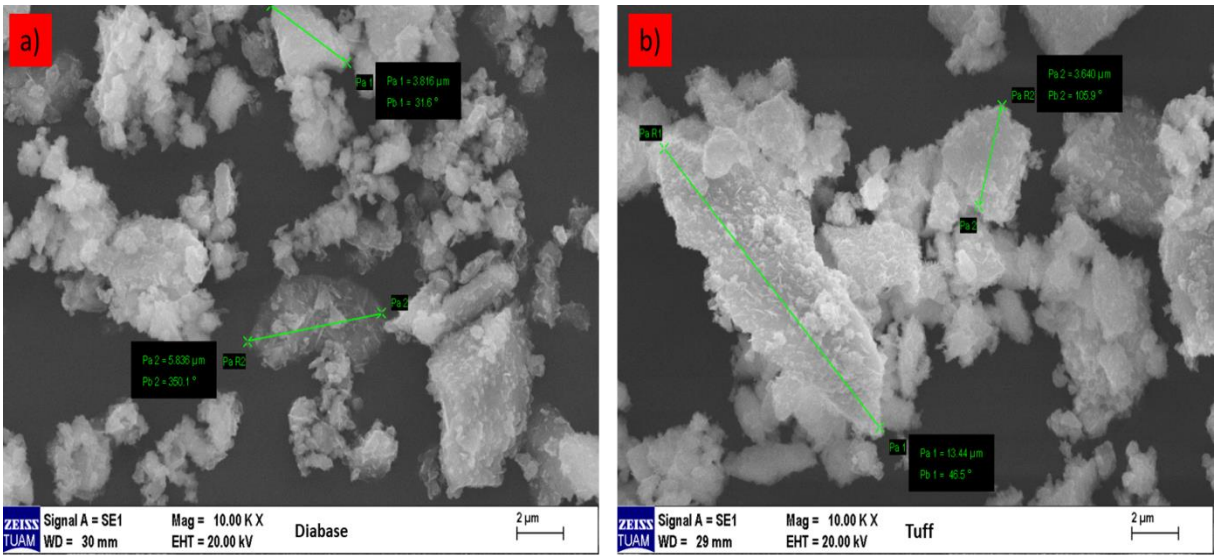


Fig.7. SEM images of cement samples with 10% diabase (a) and 10% volcanic tuff (b)

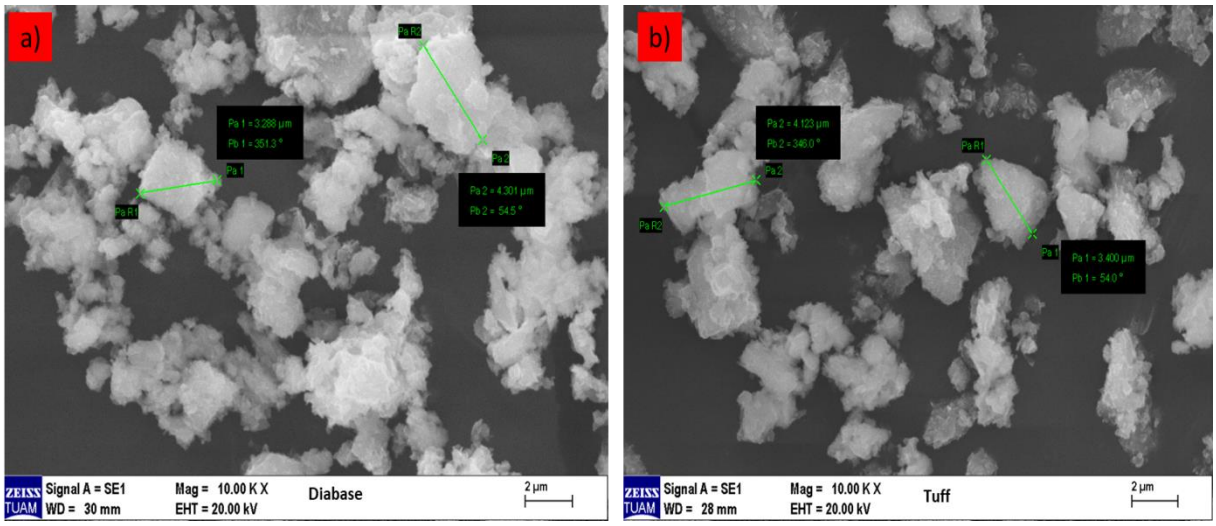


Fig.8. SEM images of cement samples with 30% diabase (a) and 30% volcanic tuff (b)

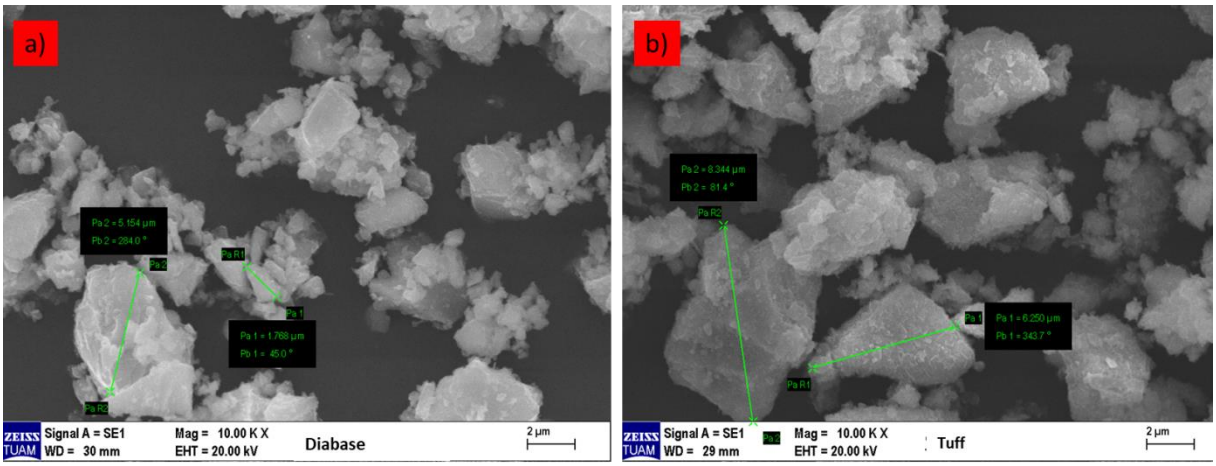


Fig.9. SEM images of cement samples with 50% diabase (a) and 50% volcanic tuff (b)

3.7 Hydraulic and mechanical properties of blended cements

In mortars produced with natural diabase-added cement, there was a significant delay in setting time in parallel with the increase of diabase material. Setting times in Tras-doped Cements have extended as tras-doped rates increase, which is also expected in this literature. However, final setting times were longer compared to volcanic tuff blended cements (Fig. 7).

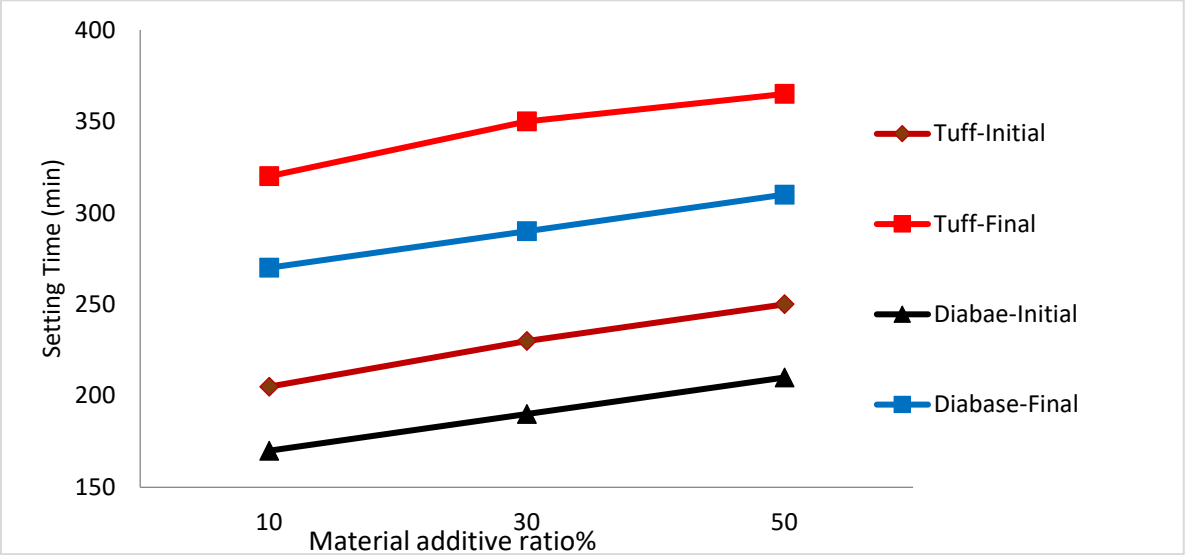


Fig. 10. The heat of the hydration of the blended cement

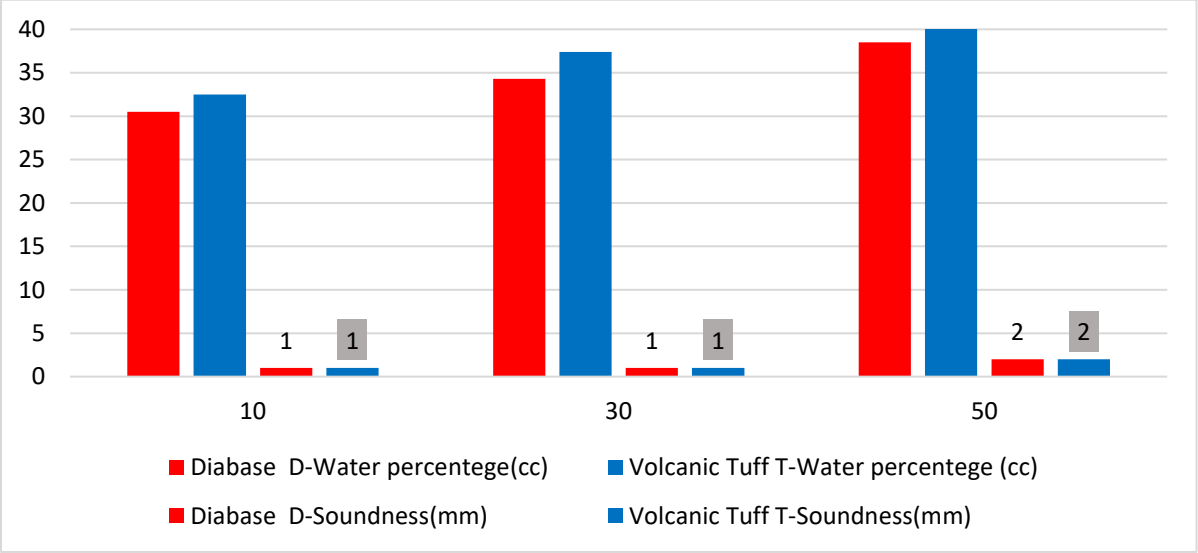


Fig. 11. Water absorption and volume expansion graphics of prepared mortars

Since the hardening speed increases shrinkage, it decreases in shrinkage and cracks that occur due to the concretes made with doped cement. This situation resulting from the shrinkage of the volume that occurs during drying, is almost completely eliminated by using cement with additives. The workability of mortars and concretes made with admixed cements is less compared to the mortars and concretes made with portland cement. To increase the workability, the water.cement ratio is slightly required, which lowers the strength.

The need for water varies depending on values such as chemical structure, specific surface and porosity in cements [14]. As the amount of diabase added to the cement increases, there is a relative increase in the amount of water required for workability, and hence to achieve the same consistency (Figure 7). The volume expansion did not exceed 2 mm for both trass and diabase-added cements and remained within the standards.

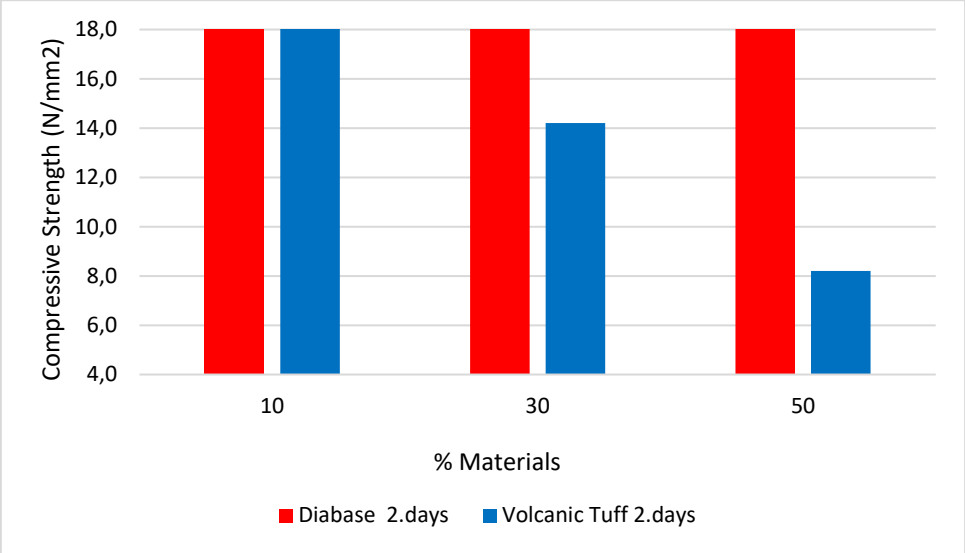


Fig. 12 Compressive strength of the studied diabase cement compositions.

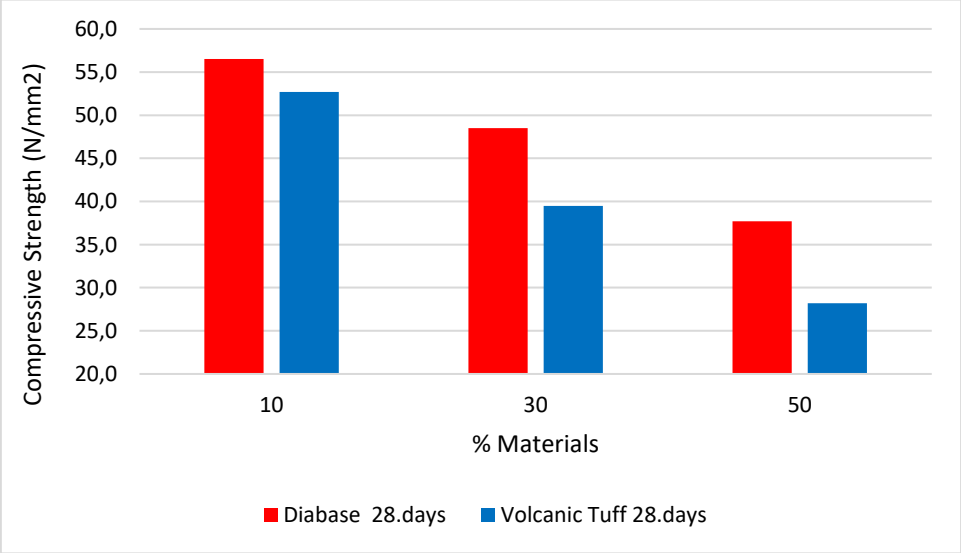


Fig. 13 Compressive strength of the studied trass cement compositions.

All diabase-added cements meet the standard strength value requirement specified in TS EN 196-1 standard. If the main purpose in our use of pozzolanic additives is to meet the compressive strength values given in TS EN 196-1 standard, it can be said that diabase-added cements that meet both early strength and standard strength conditions can be used instead of CEM IV 32.5R.

At the same time, it is observed that 20%, 25, and 30% cement mortars are provided above the lowest strength of 32.5 MPa in TS EN 197-1 [17]. In this case, it indicates that a lower strength standard cement can be obtained in the first stage by adding relatively high amounts of diabase to especially high strength cements. However, with this method, it is thought that the durability condition will be provided without compromising the strength due to the properties of the pozzolanes.

It is expected that the first strength in pozzolanic cements is expected to be low. As can be seen in the figure, as the contribution rates increase, the initial strengths of both diabase cements and shaded cements decreased. The main difference here is that the first strengths of diabase cements are higher than the strengths of shaded cements. Unlike Portland cements, pozzolanic cements increase their durability as their curing time increases. Although the contribution rates increase at the end of the day, the strength of both trass and diabase cement increases. When the contribution rate of Em increases, the strength of diabase cements provides higher and standard values compared to shaded cements. This shows that diabase cements can have the same strength as shaded cements by using more additives.

SEM pictures were taken to determine the microstructures of Trass and Diabase-added mortars and are given in Figure 5. When the SEM images of the trab doped and diabase doped pulp on the 28th hydration day were examined; It is observed that the presence of CSH layered on top of CHs or needle-like crystallized in Tras doped pulp, and the top of CHs in diabase pulp is covered with cloudy CSH. According to the SEM drawing, it is observed that CSH layers are formed on the hydrated particles in both cement paste. In addition, since the pozzolanic property of the diabase-added cement is good as well as the grain size is smaller than that of trass-added cement,It has been observed that the voids in the diabase cement paste are filled with hydration products and a relatively more void-free structure is formed and they have a homogeneous size distribution. Also, morphology of microcapsules in diabase cement paste is global. SEM images of microcapsules also show the presence of large polymer particles without microcapsules. It is seen that the aggregate grain and the cement bond are surrounded by hydration products very well around the aggregate. The CSH structure attached to the aggregate surface with hydrated diabase grains has a significant density. It is seen that the microstructure of diabase-added concrete is more gapless and tight compared to trass-added cement concrete.

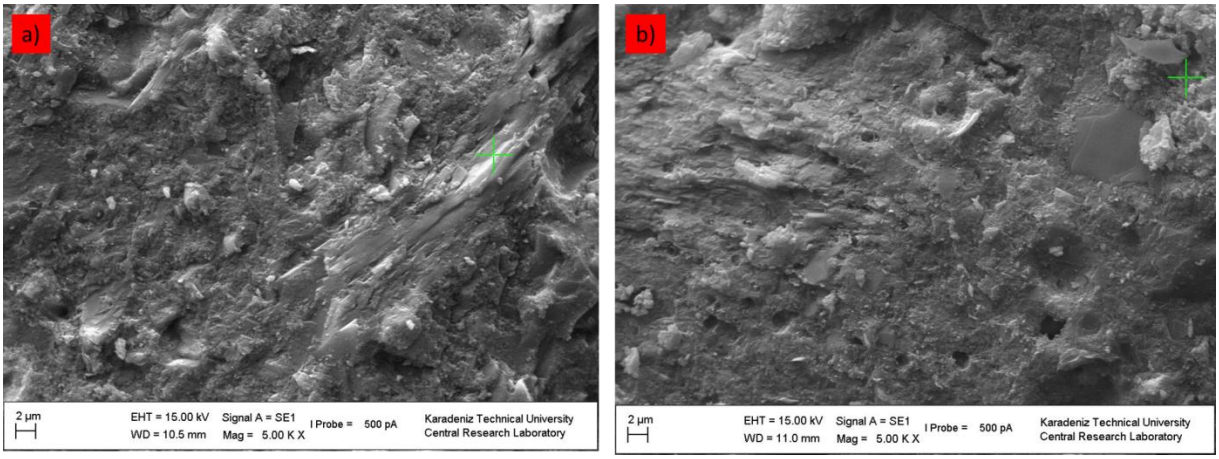


Fig. 14. Sem images of diabase 10%(a) and volcanic tuff 10% (b)blended cement mortar

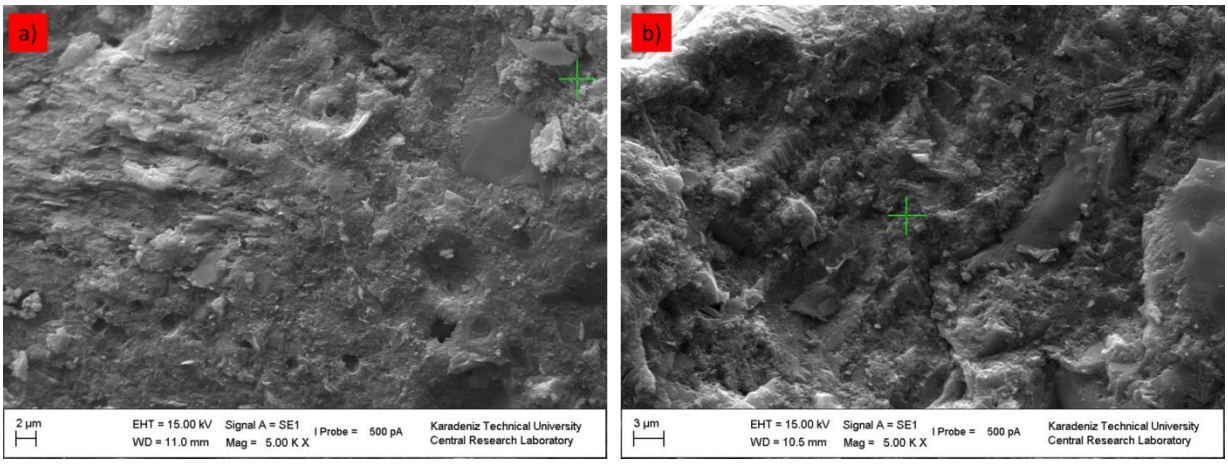


Fig. 15. Sem images of diabase 30%(a) and volcanic tuff 30% (b)blended cement mortar

4. Conclusions

Chemical composition and pozzolanic properties of diabase provided sufficient features for use as a substitution material for composite cement production.

It is seen from the decrease of the relative crystallinity in the microstructures of the diabase particles that the amorphous structures increase, that the Silpeps grinding medium performs the mechanical activation process more efficiently than the ball milling medium.

Increasing the mechanical activation time led to a gradual decrease in the relative crystallinity and an increase in the pozzolanic activity index of the diabase particles.

As a result of the grinding studies, it was revealed that diabase is a more easily grindable material than volcanic tuff, therefore it can reduce the cost of grinding and cement production.

The low pozzolanic activity of diabase was improved by mechanical activation in medium with silpepsia and increased its pozzolanic activity index met the standard usage requirements as an active additive in cementitious materials up to 50%.

Acknowledgements

This paper was supported by Tübitak 2224-B Domestic Scientific Activities Participation Support Program.

References

[1]. World Energy Counc. (**1995).** Efficient Use of Energy Utilizing High Technology: An Assessment of Energy Use in Industry and Buildings. London: World Energy Counc.
[2]. Deniz, V. (2004). Relationships between Bond's grindability (Gbg) and breakage parameters of grinding kinetic on limestone. Powder Technology, 139(3), 208-213.
[3]. Worrell, E., Martin, N., and Price, L. (2000). Potentials for energy efficiency improvement in the US cement industry. Energy, 25(12), 1189-1214.
[4]. Al-Zboon, K. K., and Al-Zou'by, J. (2016). Effect of volcanic tuff on the characteristics of cement mortar. European Journal of Environmental and Civil Engineering, 20(5), 520-531.

[5]. Perraki, T., Kontori, E., Tsivilis, S., and Kakali, G. (2010). The effect of zeolite on the properties and hydration of blended cements. Cement and Concrete Composites, 32(2), 128-133.
[6]. Sun, D., and Wang, L. (2015). Utilization of paraffin/expanded perlite materials to improve mechanical and thermal properties of cement mortar. Construction and Building Materials, 101, 791-796.
[7]. Hossain, K. M. A. (2005). Volcanic ash and pumice as cement additives: pozzolanic, alkali-silica reaction and autoclave expansion characteristics. Cement and Concrete Research, 35(6), 1141-1144.
[8]. Degirmenci, N., and Yilmaz, A. (2009). Use of diatomite as partial replacement for Portland cement in cement mortars. Construction and Building Materials, 23(1), 284-288.
[9]. Canpolat, F., Yılmaz, K., Köse. M.M., Sümer, M., Yurdusev, M.A., Use of zeolite, coal bottom ash and fly ash as replacement materials in cement production, Cement and Concrete Rsilicaesearch, 34, 731-735, 2004.
[10]. Song, H. W., Pack, S. W., Nam, S. H., Jang, J. C., and Saraswathy, V. (2010). Estimation of the permeability of silica fume cement concrete. Construction and Building Materials, 24(3), 315-321.
[11]. Vegas, I., Cano, M., Arribas, I., Frias, M., and Rodríguez, O. (2015). Physical–mechanical behavior of binary cements blended with thermally activated coal mining waste. Construction and Building Materials, 99, 169-174.
[12]. Aziz, A., Stocker, O., El Hassani, I. E. E. A., Laborier, A. P., Jacotot, E., El Khadiri, A., and El Bouari, A. (2021). Effect of blast-furnace slag on physicochemical properties of pozzolan-based geopolymers. Materials Chemistry and Physics, 258, 123880. A
[13]. Tulashie, S. K. K., Ebo, P., Ansah, J. K., and Mensah, D. Production of Portland Pozzolana Cement from Rice Husk Ash. Available at SSRN 3739628.
[14]. Kolawole, J.T., Olusola K.O., Babafemi A.J., Olalusi O. B., and Fanijo E.,(2021), Blended cement binders containing bamboo leaf ash and ground clay brick waste towards the use for sustainable concrete, Cement and Concrete Composites, 103975.
[15]. Kolawole, J.T., Olusola K.O., Babafemi A.J., Olalusi O. B., and Fanijo E.,(2021), Blended cement binders containing bamboo leaf ash and ground clay brick waste towards the use for sustainable concrete, Cement and Concrete Composites, 103975.
[16]. Kolawole, J. T., Babafemi, A. J., Fanijo, E., Paul, S. C., and Combrinck, R. (2021). State-of-the-art review on the use of sugarcane bagasse ash in cementitious materials. Cement and Concrete Composites, 103975.
[17]. Alabi, S.T., Mahachi, j., (2021)i Compressive strength of concrete containing palm oil fuel ash under different curing techniques, Materialstoday:Proceedings, https://doi.org/10.1016/j.matpr.2020.11.426
[18]. Wang, Q., Li, J., Zhang, J., Wu, P., Lyu, X., Hu, S., and Yu, H. (2021). Reuse of the soda sludge dealt with water washing as a supplementary material for the synthesis of clinker binders. Journal of Cleaner Production, 126433.
[19]. Frías, M., De Rojas, M. S., García, R., Valdés, A. J., and Medina, C. (2012). Effect of activated coal mining wastes on the properties of blended cement. Cement and Concrete Composites, 34(5), 678-683.
[20]. Ali-Boucetta, T., Behim, M., Cassagnabere, F., Mouret, M., Ayat, A., and Laifa, W. (2021). Durability of self-compacting concrete containing waste bottle glass and granulated slag. Construction and Building Materials, 270, 121133.
[21]. Bonfim, W. B., and de Paula, H. M. (2021). Characterization of different biomass ashes as supplementary cementitious material to produce coating mortar. Journal of Cleaner Production, 291, 125869.
[22]. Tokyay, M., (1999). Effect of chemical composition of clinker on grinding energy requirement. Cement and Concrete Research, 29(4), 531-535.
[23]. Genç, Ö., and Benzer, A. H. (2009). Single particle impact breakage characteristics of clinkers related to mineral composition and grindability. Minerals Engineering, 22(13), 1160-1165.
[24]. Deniz, V. (2013). Effects of mill speed on kinetic breakage parameters of four different particulate pumices. Particulate Science and Technology, 31(2), 101-108.
[25]. Ozkan, A., Yekeler, M., and Calkaya, M., (2009). Kinetics of fine wet grinding of zeolite in a steel ball mill in comparison to dry grinding. International Journal of Mineral Processing, 90(1-4), 67-73.

[26]. Kunecki, P., Panek, R., Wdowin, M., Bień, T., and Franus, W. (2020). Influence of the fly ash fraction after grinding process on the hydrothermal synthesis efficiency of Na-A, Na-P1, Na-X and sodalite zeolite types. International Journal of Coal Science and Technology, 1-21.

[27]. Allahverdi, A., and Ghorbani, J. (2006). Chemical activation and set acceleration of lime-natural pozzolan cement. Ceramics Silikaty, 50(4), 193

[28]. Colak, A. (2003). Characteristics of pastes from a Portland cement containing different amounts of natural pozzolan. Cement and Concrete Research, 33(4), 585-593.

[29]. Escalante-Garcia, J. I., Martínez-Aguilar, O. A., and Gomez-Zamorano, L. Y. (2017). Calcium sulphate anhydrite based composite binders; effect of Portland cement and four pozzolans on the hydration and strength. Cement and Concrete Composites, 82, 227-233.

[30]. Záleská, M., Pavlíková, M., Pavlík, Z., Jankovský, O., Pokorný, J., Tydlitát, V., and Černý, R. (2018). Karışımlı çimentolarda uygulanacak teknojenik puzolanların fiziksel ve kimyasal karakterizasyonu. İnşaat ve Yapı Malzemeleri (in Turkish), 160 , 106-116.

[31]. TS EN 196-1. (2016). Cement test methods - part 1: determination of strength.

[32]. TS EN 197-1. (2012). Cement - Part 1: Compositions and suitability criteria for general cements. At the Turkish Standards Institution.

[33]. Alp, I., Deveci, H., Süngün, Y. H., Yilmaz, A. O., Kesimal, A., and Yilmaz, E., (2009). Pozzolanic characteristics of a natural raw material for use in blended cements. Iranian Journal of Science and Technology, 33(B4), 291.

[34]. TS EN 196-6. Cement test methods - Part 6: determination of fineness.

[35]. BOND, F.C., 1960, Three Principles of Comminution, Mining Congress Journal, August, 53-56.

[36]. Yılmaz, A., 2004, An Environment To Increasing Milling Productivity: cylpebs, Mining Technology.

[37]. Ardoğa, M. Kemal, Sinan T. Erdoğan, and Mustafa Tokyay. "Effect of particle size on early heat evolution of interground natural pozzolan blended cements." Construction and Building Materials 206 (2019): 210-218.

[38]. Bumanis, G., Vitola, L., Stipniece, L., Locs, J., Korjakins, A., and Bajare, D. (2020). Evaluation of Industrial by-products as pozzolans: A road map for use in concrete production. Case Studies in Construction Materials, 13, e00424.

Preliminary Investigation of the Use of Magnesium Slag as a New Cement Replacement Pozzolan.

Abdul Vahap Korkmaz[1]

[1]Afyon Kocatepe University, İscehisar Vocational School, Department of Construction, İscehisar, Afyonkarahisar, avkorkmaz@aku.edu.tr

Highlights

- The compressive strength of concrete did not decrease with up to 20% magnesium slag content.
- Use of magnesium slag may improve concrete's long-term properties.

ABSTRACT

Since 2016, Turkey has started to produce domestic magnesium metal from the dolomite mine in its integrated facility, including in Europe, for the first time. Magnesium metal ingots with a purity of 99.80% and a weight of 8-12 kg are produced at the facility. 60,000 tons of magnesium slag is stored in the open air area of the facility as waste without being recycled to production. The problem of disposal of magnesium slag, which occurs in the production of metallic magnesium, awaits an academic solution by the metal industry. Since magnesium slag has mineral compositions similar to Portland cement, it was first aimed to be used as an additive in the cement industry. Thus, magnesium will not be a waste material in the metal sector and will be recycled to the economy by being a by-product. In addition, if magnesium slags are evaluated in the cement sector, it will enable to reduce cement production costs, to use cement raw material resources more economically and with a long life, and to make an environmentally friendly production as a result of decreasing CO_2 emissions.

In this study, the content of magnesium slag, its mineral structure, hydraulic, mechanical properties as cement additives were investigated. First, pure magnesium slag cement was produced using pure 96% magnesium slag and cement properties were compared with Cem I 42.5 R cement. Afterwards, 5%, 10%, 15% and 20% magnesium slag was added to Cem I 42.5 R Portland cement and magnesium slag added cements were produced. Cement performance properties were examined within the scope of TSE standard values on cement samples. Cement samples showed superior performance properties close to Cem I 42.5R cement in all additive ratios, including 20%. In this context, it has also provided all cement standard values. The superior performance properties of the cement samples with magnesium slag were attributed to the presence of allite and belite minerals, which are found in their structures and play a major role in cement strength. Thus, it provided a perfect chemical compatibility with clinker and increased cement performances.

1.Introduction

About 85% of the world's metallic magnesium demand is met by China. In 2016, the first magnesium facility in Turkey and the only one in Europe was opened and magnesium ingot metal production started. Magnesium metal ingots with 99.80-99.95% purity and 8-12 kg weight are produced in the integrated facility [1]. The magnesium facility operating in Turkey has approximately 90 million tons of dolomite reserves and the reserves of Turkey's dolomite deposits are many times higher than this value. The magnesium plant in Turkey uses the Pidgeon Process (silicothermic reduction) production method, which is widely used in China [2]. After the reduction of the raw materials in the magnesium metal production facility in Turkey, 165 tons of waste material per day is stored in the factory waste site without recycling as magnesium slag. Annually, this amount is over 60,000 tons. Worldwide, more than 1,000,000 tons/year of magnesium slag waste is generated during magnesium metal production[3].

As in all industrial activities, waste is generated as a result of the operation of mines. These mine wastes pose a threat to the environment and human health when they are released into the environment in an inappropriate way

[4]. There is a large amount of mining waste generation in our country and in Europe. For example, the amount of waste generated as a result of mining activities in the European Union (EU) constitutes 29% of the annual waste generated in Europe. In other words, mine wastes exceed 400 million tons annually [5]. The fact that the accidents that occurred in the pools/dams where mining wastes were stored in Europe, especially towards the 2000s, caused serious environmental problems, intensified academic studies on this subject [6]. In order to prevent waste generation and the harmfulness of waste, it is necessary to develop and use clean technologies where natural resources are used as little as possible [7]. For the final disposal of hazardous materials that remain after production, use or recovery, it is necessary to prevent and reduce them by developing and applying appropriate techniques. In cases where waste generation is unavoidable, it is essential to recover the waste or use it as an energy source with other processes for recycling, reuse and obtaining secondary raw materials [8].

There are many studies on the use, disposal and waste management of wastes in the world and our country. Ke Yin et al. (2018) used different types of ash in cement production and worked on recycling them in the industry [9]. Gui-Rok Kwon et al. (2015) identified industrial ecology-based strategies for reducing CO2 emissions of magnesium metal [10]. Zuhau Zhang et al. (2017) examined the example of high magnesium nickel slag with Geopolymer technology on the conversion of local industrial wastes into environmentally friendly cement [11]. G. Young and Mei Yang (2019) studied the use of iron ore waste as a raw material for the production of Portland cement clinker and the characterization of the produced clinker [12]. Pavez et al., (2019) The use of copper slag as a partial substitute for cement in mortar preparation were investigated [13]. Alp et al. (2008) studied the recovery of metals from the waste of copper slag due to flotation processes. In this study, they aimed to use copper slag, flotation waste, as an iron source in Portland cement clinker production and as a substitute for iron ore in cement production [14]. Cai et al. (2011) investigated that magnesium slag, which is produced during the production of magnesium metal from dolomite, can be used as a cement raw material. It has been investigated that slaked magnesium slag (SMS) can play a raw material role in the cement industry and the raw material properties of portland cement are investigated by clinker firing experiments [15].

Cement is the most important component that affects the strength and cost of the structure. However, the CO_2 released during cement production constitutes 8% of the world production. In addition, waste materials and new components are used instead of cement to improve the properties of cement and reduce its cost [16]. Although Turkey has large amounts of industrial waste reserves, their industrial reuse is very low [17,18]. However, it is an important issue that industrial wastes are brought into the economy by supporting the sustainability of the cement and concrete industry. In this study, magnesium slag has been evaluated as an alternative raw material source to the existing additives in Portland cement production to reduce production costs in the cement industry, to evaluate wastes, to make the use of natural resources more economical and controlled and to protect the natural environment.

2. Material and Method

In this study, magnesium slag, which is formed as a result of reduction of magnesium metal in reduction furnaces of integrated magnesium metal production facility in Turkey, was used as an additive material in cement production. The image of obtaining the magnesium slag is given in figure 1.



Figure 1. Recovery of magnesium slag from reduction furnaces

As can be seen in Figure 2, the production process of magnesium slag and Portland cement production process show similarities.

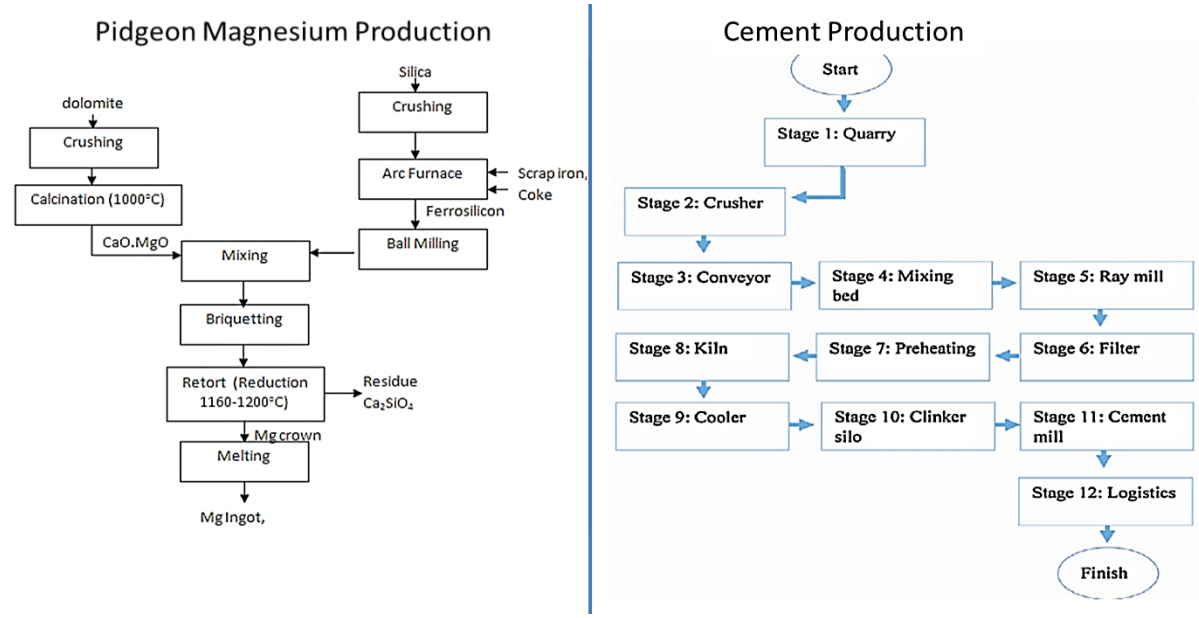


Figure 2. Flow chart of magnesium and cement production processes

The raw material used for the production of magnesium metal is carbonate-containing dolomite, which is calcined in a rotary kiln at a temperature close to the firing temperature of Portland cement clinker. In addition, ferrosilicon and fluorite minerals are added to the calcined material, and the raw material mixture is ground up to 100 microns, and then the materials that become pellets are kept for 12 hours at a temperature close to the firing temperature of the cement clinker (1160-1300 degrees). During this period, almost all of the magnesium minerals in the material are reduced. The remaining material, defined as magnesium slag, is stored as waste in the open field (Fig. 3).



Figure 3. Magnesium slag stockpile

2.2. Metot

In this study, Cem I 42.5 R Portland cement (PC) was used in the preparation of the reference samples. Magnesium slag was added to Portland cement at the rates of 0%, 5%, 10%, 15% and 20%. Thus, a total of five different cement samples were produced and these were named as RPC, 5MS, 10MS, 15MS and 20MS. In addition, 96% magnesium slag and 4% gypsum added pure magnesium slag (PMS) cement were produced. Chemical analyzes of magnesium slag, clinker and cement samples were made using RIGAKU / ZSX PRIMUS 2 brand XRF device. The conformity criteria of cement samples were determined according to TS EN 197-1. Each of the mortar samples used in the compressive strength tests were produced by mixing them in a mortar mixing machine in accordance with TS EN 196-1, using 450 gr cement, 1350 gr standard sand and 225 ml water. In line with these criteria, standard mortar mixes of 40x40x160 mm were obtained. Compressive strength tests of cement mortar samples were carried out according to TS EN 196-1 standard by using "Compressive Strength Determination Method". TS EN 196-3 standard was used for the consistency test and setting times of cement mortar samples. Bruker Brand D 8 Advance model X-ray diffraction (XRD) device was used to define the mineralogical properties of magnesium slag and clinker.

3. Experimental Results and Discussion

3.1. Chemical And Mineralogical Analysis

Portland cement clinker is mainly obtained by mixing limestone and clay in appropriate proportions and heating it in a rotary kiln at high temperatures until sintering. Therefore, according to the results of chemical analysis, cement consists of higher ratios of CaO and lower ratios of Al_2O_3, Fe_2O_3 and SO_3 compounds. The ideal composition of a clinker to be produced is % CaO: 60-67; %SiO_2: 17-25; %Al_2O_3: 3-8; %Fe2O3: 0.5-6; %MgO:0.5-6. It is expected to be between %Na_2O + K_2O 0.2-1.3 and %SO_3 0-3[19]. The chemical analysis results of the clinker and magnesium slag used in this study are given in Table 1.

Table 1. Chemical analysis results of cement samples

Sample Name	Content	SiO_2	Al_2O_3	Fe_2O_3	CaO	MgO	SO_3	Na_2O	K_2O	F	MnO	Loi
MS	%	26,47	0,50	3,25	62,98	5,82	0,09	0,07	0,05	0,69	0,04	0,00
Clinker	%	20,84	5,14	3,82	66,75	1,32	0,62	0,38	0,76	0	0	0,28

According to Table 1, the clinker sample meets the TSE EN 197-1 compliance criteria, while magnesium slag provides CaO content, Fe content, MgO content, SO_3 contents, although it is a metallic facility waste. Considering that the magnesium slag is fired in kilns at 1200-1300 ºC, the results of the clinker phase and quality modules calculated according to the Bogue formulas of the same sample as Portland cement clinker are shown in Table 2.

Table 2. Bogue formula results of magnesium slag and clinker samples

Sample	LSF	S.M.	A.M.	C_3S	C_2S	C_3A	C_4AF
MS	81,90	7,06	0,15	38,92	46,52	-4,17	9,89
Clinker	99,75	2,33	1,35	63,23	11,15	7,17	11,63

The fact that the production processes of Portland cement clinker and magnesium slag have great similarities and the use of common raw materials for production suggests that the mineral structures may be similar. It is very likely that the minerals Alite (C3S), Belite (C2S), Celite (C3A) and C4AF are present in the magnesium slag, just as in the Portland cement clinker. Moreover, the results of the chemical analysis of Magnesium slag and Portland cement clinker and the results of Bogue calculations also prove this. While mineral formation in magnesium slag takes place at temperatures of 1200-1300 degrees; Most of the minerals in Portland cement clinker occur at firing temperatures below 1400-1450 °C. In the clinker production process with magnesium slag, the main difference, apart from the firing temperature, is the rapid cooling of Portland cement clinker after sintering. Thus, the Alite (C_3S) crystals formed in the clinker are protected and prevent them from turning back into Belite (C_2S) mineral. Magnesium slag, on the other hand, is left on its own in the open air to cool after heating in reduction furnaces. XRD images of magnesium slag and Portland cement clinker sample are given in Figure 4 and Figure 5.

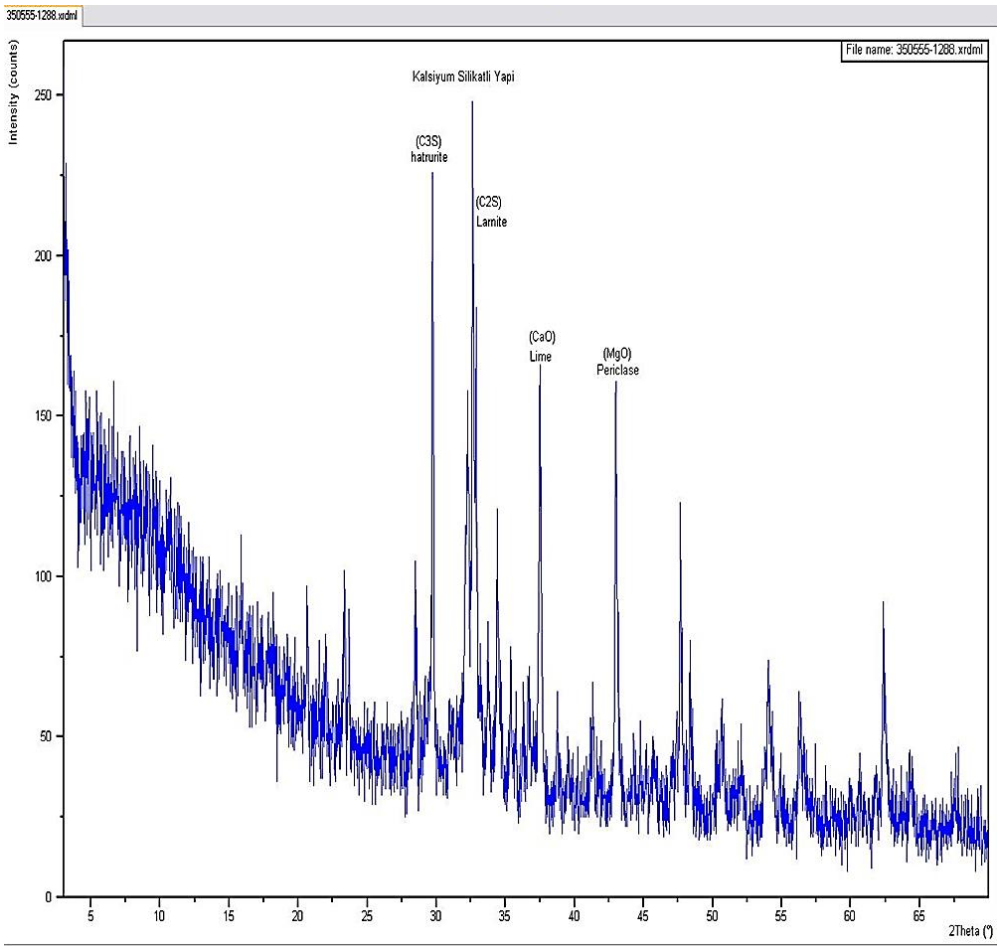


Figure 4. XRD graphic image of magnesium slag

According to the XRD analysis results in Figure 4, there is Periclase (MgO), Lime (CaO) and calcium silicate structure in the magnesium slag sample. This calcium silicate structure also originates from slag, minerals that peak in the same place are generally given as calcium silicate structure. When examined in detail, this calcium silicate structure.

Alite=(Ca_3SiO_5)=Hatrurite and Belite=(Ca_2SiO_4)= Larnite sourced minerals. In the XRD graph of the magnesium slag sample, it is seen that the peaks correspond to the peaks of Alite and Belite minerals in the literature (Fig.5).

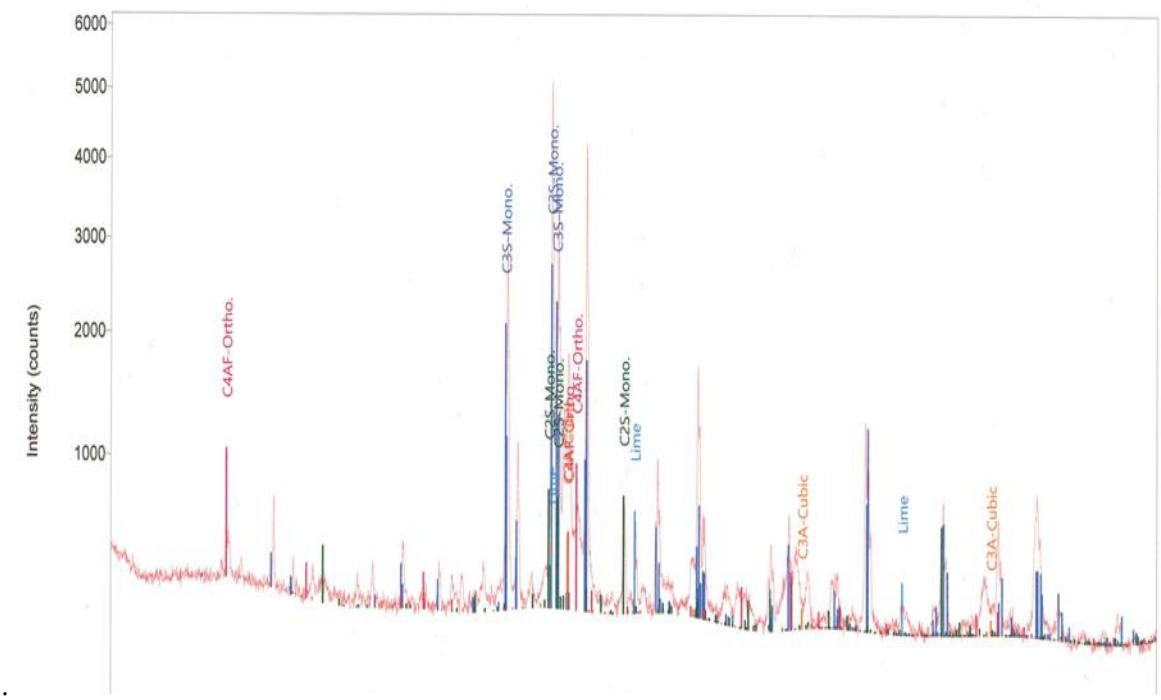
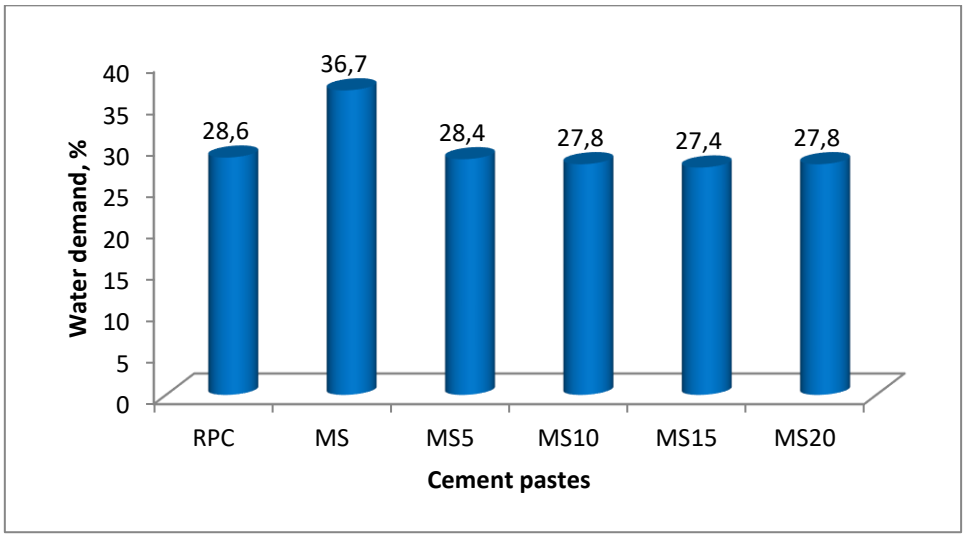


Figure 5. Clinker XRD graphic image

When the XRD graphs of the magnesium slag mineral phase structure of Portland cement clinker were compared, it was seen that the C_2S phase gave higher peaks, while the C_3S phase gave lower peaks in magnesium slag. It is thought that this difference is due to the fact that the magnesium slag is not cooled rapidly, but left to cool on its own, and thus the C_3S formed by sinter turns back into the C_2S phase with late cooling.

3.2. Hydraulic Features

It has been tried to use 100% pure magnesium slag and it is expected to behave like a Portland cement clinker due to the clinker minerals it contains. Then, the hydraulic properties of magnesium slag were compared with Cem I 42, R Reference Portland Cement (RPC). The water demand of cement mortar samples can vary according to the chemical composition of cements, fineness, blaine and porosity values. In this study, the blaine values of cements with PRC and magnesium slag were determined as 4000 g/cm^2. In addition, the results of the tests performed according to TS EN 196-3 for the water requirement of the cement samples obtained by adding 0%, 5%, 10%, 15% and 20% magnesium slag to the Cem I 42, R reference Portland cement are given in Figure 6. The water requirement of Cem I 42.5 R cement samples varies between 26-30% according to the literature. The required water requirement for the consistency of PMC was 28.32% higher than that of RPC. However, with the addition of magnesium slag in the blended cement samples, the water requirement decreased by 0.69%, 2.79%, 4.19% and 2.79%, respectively, even if it was very little. However, except for PMS, all cement samples met the Cem I 42.5 R cement standard.



Şekil 6. Water demand of cement pastes.

The volume expansion values obtained for the cement paste samples were found in the range of 0-1 mm as a result of the tests performed according to TS EN 196-3. Volume expansion of cements with additives is within standard limits. The initial setting time is an important indicator of hydration at an early age. Setting inital time and final time of pure magnesium slag (PMS) cement are 94% and 175% longer than reference Portland cement, respectively. With the addition of 5%, 10%, 15% and 20% magnesium slag to the reference Portland cement, the setting on set time was prolonged by 16.66%, 16.66%, 19.44% and 22.22%, respectively. The setting time was longer than the reference Portland cement by 16.66%, 18.75%, 16.66% and 12.50%, respectively. The decrease in C3A as a result of the dilution of clinker can increase the setting times of cements with additives. In addition, the increase in the water requirement of the cements with additives also increases the setting times.

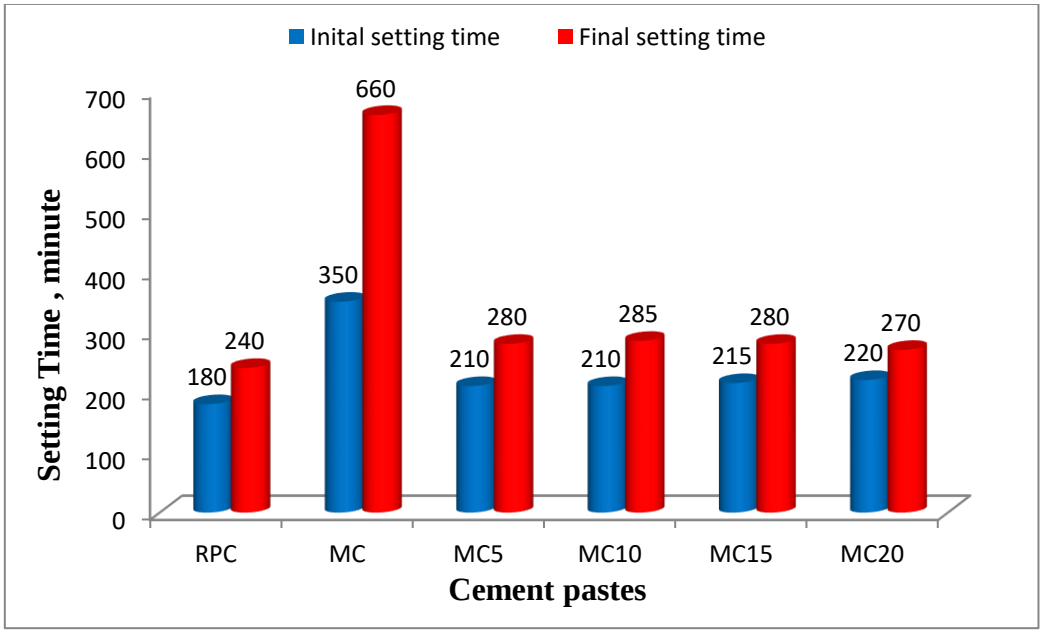


Figure 7. Setting time of cement pastes.

It is well known that, similar to magnesium slag, the hydraulic activity of steel slag is much lower than that of Portland cement because the cementitious mineral phases (mainly C_2S and C_3S) in steel slag are significantly less. Relative to Portland cement clinker, the cementitious mineral phases in steel slag have higher crystallinity than in

cement, as the steel slag is naturally cooled as the cement is quenched. Replacing Portland cement with steel slag additive due to the dilution effect significantly extends the setting time. However, it was observed that the addition of Magnesium slag minimally extended the initial and final setting time of the magnesium slag.

3.3. Mechanical Properties

Reference Portland cement has higher compressive strength than cement mortar produced with pure magnesium slag. Although this is an expected situation, it is thought that the amount of alite in the clinker mineral structure of Portland cement is higher than that of magnesium slag. For a Cem I 42.5 R cement, the two-day compressive strength result should meet the 20 MPa limit. Even though the PMS is below this limit, 5%, 10%, 15% and 20% MS blended cements are 84%, 70%, 47.5% and 52% of the two-day standard value (Two-day strength ≥ 20 MPa), respectively. It gave very good results. For a Cem I 42.5 R cement, the twenty-eight-day compressive strength result should meet the limit of 42.5 MPa. The compressive strength results of 5%, 10%, 15% and 20% MS blended cement mortars were 37.45%, 24.94%, respectively (twenty-eight-day strength ≥ 42.5 MPa), while the PMS twenty-eight-day compressive strength result remained below the standards. 20.47%, 22.35% gave a result well above the standard value. they have provided more. According to the data obtained as a result of the tests, the compressive strength obtained for all magnesium slag replacement ratios gave similar results to the values obtained for pure cement (RPC). According to the findings obtained in the study, the compressive strength of all cement mortar samples at the end of 28 days is above the minimum 42.5 N/mm^2 compressive strength.

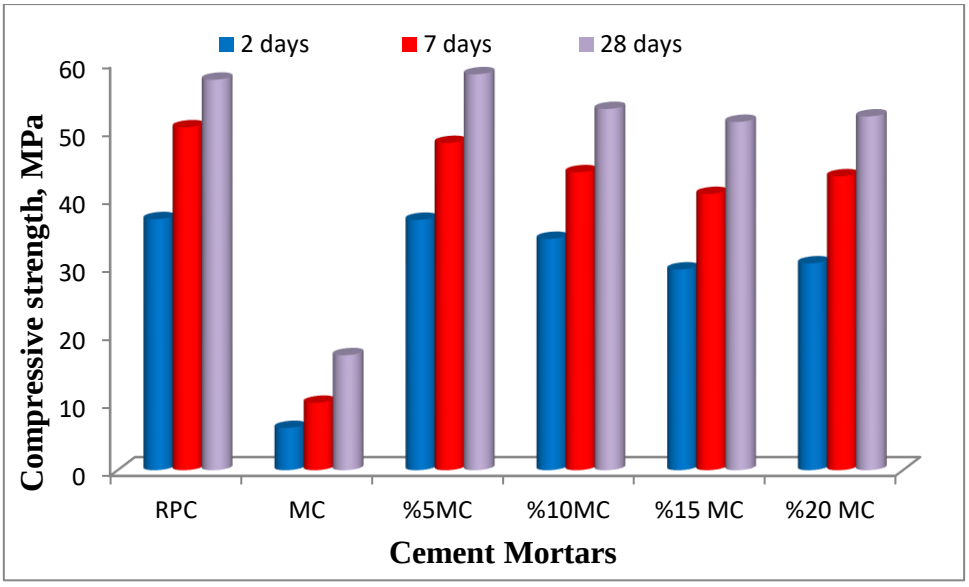


Fig. 8. Compressive strength of cement mortars.

According to the literature, the main factors affecting the strength development in cements with additives are the filling effect, the dilution effect and the pozzolanic reaction of the added materials with CH. The most basic reasons affecting the strength development of magnesium slag added cement are the allite and belite minerals it contains [20].

Results

Alite, belite, celite and alumino ferrite were found in the mineral structure of magnesium slag. This has made magnesium slag advantageous to be used in cement production.

Although magnesium slag contains clinker minerals at high rates, the products obtained by using pure magnesium slag instead of Cem I 42.5 R could not meet TSE standards hydraulically and mechanically.

The hydraulic properties of the mortars obtained as a result of the use of 5%, 10%, 15% and 20% magnesium slag provided the results of Cem I 42.5R Portland cement and a perfect clinker slag compatibility was achieved.

The compressive strength results of the mortars obtained as a result of using 5%, 10%, 15% and 20% magnesium slag were far above the Cem I 42.5 R TSE standards. This means that by adding up to 20% magnesium slag additive, high performance quality concretes are produced at lower costs.

It has been clearly demonstrated that the use of magnesium slag in cement production will not only ensure the recycling of waste, but also be beneficial in reducing environmental pollution. For this reason, the use of magnesium slag in high volumes of cement and concretes with high mineral volumes should be investigated in the following stages.

Acknowledgements

In the research and preparation of this paper, support was received within the scope of Afyon Kocatepe University Scientific Research Career Project (Project No: 21.KARİYER.04).

Resources

[1]- KORKMAZ, A. V. Occupational Accidents in the Metal Industry and Their Effects on Workers: Case Study of Magnesium Metal Production Plant. Düzce University Journal of Science and Technology, 9(4), 1570-1591.

[2]- KORKMAZ, A. V. (2020). Industrial Accident Investigations and Regulatory Interventions; Magnesium Metal Production. Work and Society, 67(4).

[3]- HAN, Feng Lan, et al. Treatments of magnesium slag to recycle waste from Pidgeon process. In: *Advanced Materials Research*. Trans Tech Publications Ltd, 2012. p. 1657-1667.

[4]- Lottermoser, B. (2007). Mine wastes (pp. 43-118). Springer-Verlag Berlin Heidelberg.

[5]- Deng, T., Ling, Y.2004. ‘’Processing of copper converter slag formetals reclamation. Part II: Mineralogical study’’ ,Waste Management, 22, 376–382.

[6]- Gorai, B., Jana, R., K. Premchand K. 2003.’’ Characteristics and utilisation of copper slag—a review’’, Resources, Conservation and Recycling ,39, 299–313.

[7]- Shen, H., Forssberg, E. 2003. ‘’An overview of recovery of metals from slags’’, Waste Management, 23, 933–949.

[8]- Franks, D. M., Boger, D. V., Côte, C. M., & Mulligan, D. R. (2011). Sustainable development principles for the disposal of mining and mineral processing wastes. Resources policy, 36(2), 114-122.

[9]- Yin, K., Ahamed, A., and Lisak, G. 2018. ‘Environmental perspectives of recycling various combustion ashes in cement production–A review’. Waste Management, 78, 401-416.

[10]- Kwon, G., woo, S., Lim, S. 2015. ‘Industrial ecology-based strategies to reduce the embodied CO2 of magnesium metal’. Resource, Conservation and Recycling, v. 104, p. 206-212.

[11]- Zhang, Z., Zhu, Y., Yang, T., Li, L., Zhu, H., and Wang, H. 2017. ‘Conversion of local industrial wastes into greener cement through geopolymer technology: a case study of high-magnesium nickel slag’. Journal of Cleaner Production, 141, 463-471.

[12]- Young, G., and Yang. M. 2019. "Preparation and characterization of Portland cement clinker from iron ore tailings". Construction and Building Materials 197, 152-156.

[13]- Pavez, O., Nazer, A., Rivera, O., Salinas, M., and Araya, B. 2019. 'Copper slag from different dumps in the Atacama Region used in mortars as partial replacement of cement''. Matéria (Rio de Janeiro), 24(2).

[14]- Alp, I., Deveci, H., and Süngün, H. 2008. ''Utilization of flotation wastes of copper slag as raw material in cement production''. Journal Of Hazardous Materials, 159(2-3), 390-395.

[15]- Cai, Ji Wei, et al. 2011. "Research on slaked magnesium slag as a raw material and blend for portland cement." Advanced Materials Research. Vol. 335. Trans Tech Publications.

[16]- Zhang, Z., Liu, S., Yang, F., Weng, Y., & Qian, S. (2021). Sustainable high strength, high ductility engineered cementitious composites (ECC) with substitution of cement by rice husk ash. Journal of Cleaner Production, 317, 128379.

[17]- Korkmaz, A. V. (2019). Evaluation of chemical, mineralogical and clinker burnability properties of mudstones as cement raw materials. *Case Studies in Construction Materials*, *11*, e00254.

[18]- Kaçar, A., & Altuğ, D. T. (2019). Attenuation Gamma Rays Properties of Cement Paste–Waste Paper Composites. Acta Physica Polonica, A., 135(4).

[19]- Her, S., Park, T., Zalnezhad, E., & Bae, S. (2021). Synthesis and characterization of cement clinker using recycled pulverized oyster and scallop shell as limestone substitutes. *Journal of Cleaner Production*, *278*, 123987.

[20]- Deng, J. P., Wang, X. L., and Guo, Y. P. 2014. 'Research on the Hydration Mechanism of Portland Cement with Magnesium Slag'. In Applied Mechanics and Materials (Vol. 576, pp. 57-62). Trans Tech Publications.

[21]- Berodier, E., Scrivener, K., (2014). Understanding the Filler Effect on the Nucleation and Growth of C-S-H. Journal of the American Ceramic Society, 97(12), 3764-3773.

Coating of Glass Substrate with Luminescent Powder Added Silicone Polymer

Atilla Evcin[1]

[1] Afyon Kocatepe University, Materials Science and Engineering Department, Afyonkarahisar, Türkiye

Abstract

Luminescent materials have attracted the attention of scientists for a long time. Studies on the luminescence of these powders in different colors and durations have intensified. The aim of this study is to reduce the contact of glass surfaces with water and to make the glass surfaces glow at night with the additive of luminescence material. In the study, firstly, strontium aluminate powders were produced and mixed into silicon rubber in different proportions and a thin film was drawn on the glass surface with a film applicator. As a result, a self-luminous and hydrophobic surface was obtained.

Keywords: Luminescence, polymer, silicone, powder.

Corresponding Author e-mail : evcin@aku.edu.tr

1. Introduction

Sol-gel process is a quite practial method in obtaining both inorganic and organic-inorganic hybrid polymers. The basic advantage of this technique is the conduct of the whole process provides controllabillty on molecular level on the way to reaction during transformation of the pre-initiator types to end product. By this way sol-gel process enables synthesis of the very high purity and homogeneity level, uniform crystal morphology and well-defined nanoparticles [1-8].

Studies on long-term luminescent luminescent materials have generally focused on ZnS-based traditional phosphors and today's phosphors, alkaline earth aluminate, and silicate-based luminescent materials. The first example of luminescent materials that provide long-term luminescence are Cu and Co-doped ZnS-based phosphors with luminescence times of approximately 40 minutes. These materials were replaced by alkaline earth sulfide-based phosphors such as CaS and SrS phosphors, which were later developed by Lenard et al. In the 1970s, Lehman et al. obtained solar-excitable, Bi+3, Eu+2, Ce+3 bulk, alkaline earth sulfide-based phosphors. In 1995, Matsuzawa et al. produced Eu+2, Dy+3 bulk SrAl2O4-based phosphorus, which provides a new generation of long-term radiation. These new generation phosphors; They have replaced traditional ZnS-based and alkaline earth sulfide-based phosphors with features such as long-term irradiance, high luminous intensity, pure color, high chemical and thermal resistance, chemically inertness [9-13].

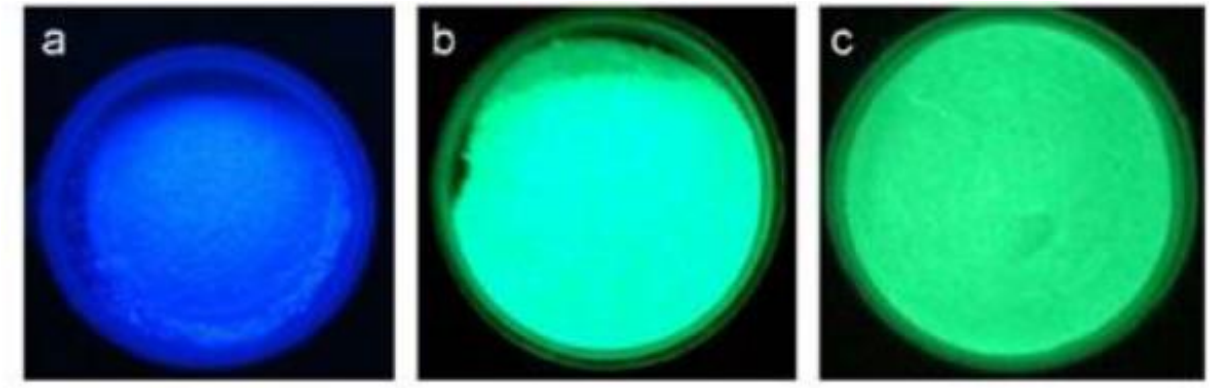


Figure 1: Glow colors: (a)CaAl2O4:Eu2+, Nd3+, (b) BaAl2O4:Eu2+ Dy+3 (c)SrAl2O4:Eu2+,Dy3+ [1]

The principal objective of this study is to determine the material synthesis of the varying additive elements added SrAl2O4 based long-term radiating phosphorescence and characteristics of the synthesized material. The synthesis method selected to obtain phosphorescence material is the modified sol-gel process.

2. Materials and Method

In experimental studies, high purity strontium nitrate [$Sr(NO_3)_2$] and aluminum nitrate [$Al(NO_3)_3$] powders were used as precursors. The modified sol-gel process was chosen for the samples prepared for use in experimental studies. First, the chemical powder amounts required for the production of the final product phosphorescent material were calculated. Nitrate-based compounds were mixed in pure water in a separate beaker on magnetic stirrers set at 100ºC for 1 hour until they became homogeneous. Then they mixed for 1 hour and calcined at 1200°C. Sintered powders is shown in Fig 2.



Figure 2. Sintered photoluminescence powder

3. Results and Discussion

XRD analyzes were performed using Cu-Kα irradiation in Bruker D8 Advance brand device (Fig 3.). Microstructures of the samples were examined under scanning electron microscope (SEM Leo 1430 VP) (Fig 4-5).

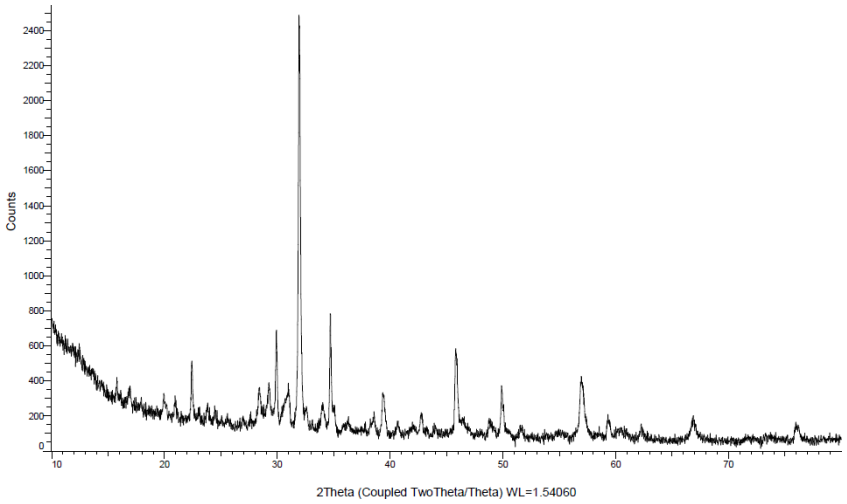


Figure 3. XRD analysis of sintered photoluminescence powder

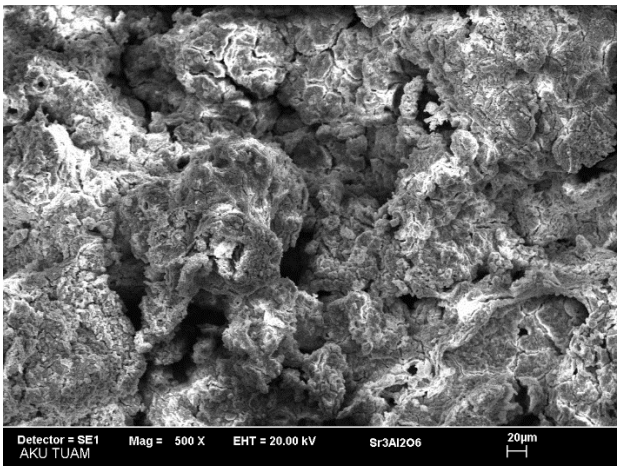


Figure 4. SEM images of sintered photoluminescence powder (500X)

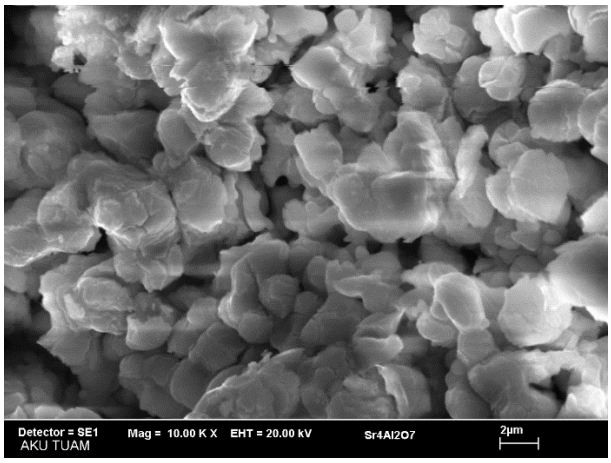


Figure 5. SEM images of sintered photoluminescence powder (10KX)

It is seen from the SEM images that the grains are homogeneous and 1 µm in size.

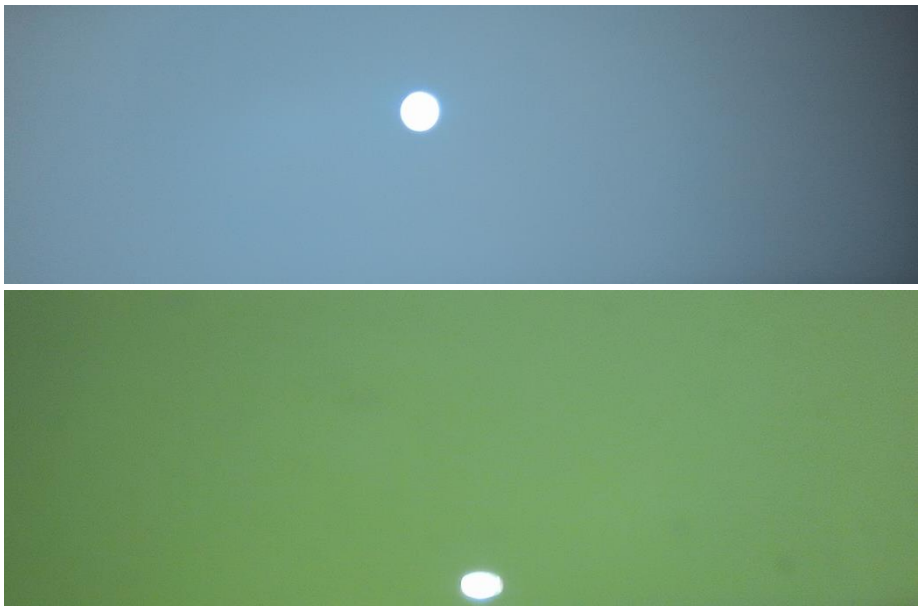


Figure 6. Images of photoluminescence powder in dark and light.

Figure 6 shows the luminescence of the composite coating in dark and light.

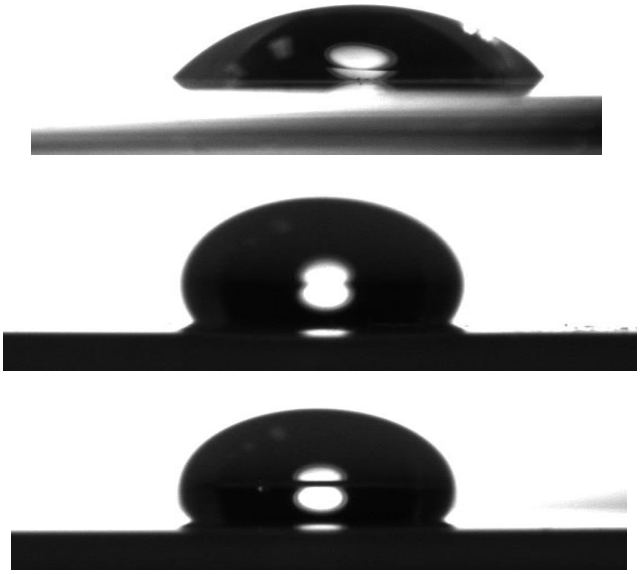


Figure 7. Contact angles of composite film with photoluminescence powder.

The contact angle measurements of the composite film with water were made with the Attention Theta Lite device. As can be seen from the figure, the hydrophilic surface became hydrophobic after coating (Fig 7.)

As a result of the study, both hydrophobic and photoluminescent surfaces were obtained.

References

[1] Pfuch, Andreas & Tölke, T. & Keil, Doreen & Marschner, Carmen & Homuth, Marion & Matthes, Georg & Hering, Wolfgang & Grünler, Bernd. (2015). Sol-Gel-coatings - Versatile possibilities for surface functionalization. Galvanotechnik. 1849-1854.

[2] W. Beier: "Sol-Gel Coating Processes", in Thin Films on Glass, ed.by H. Bach, D. Krause (Springer, Berlin 2003 2nd Ed.), Chap. 3.3, pp.66–82

[3] Wu, B.Y. & Chiang, Anthony. (1996). Sol-gel coating and its applications. Ch.J.Mater.Sci.. 28. 169-181.

[4] A. EVCIN, H. GÜNEY & N. ÇIÇEK BEZIR, Sol-gel Preparation of Silan based Titania Hybrid Composite Thin Film, International Journal of Computational and Experimental Science and Engineering, 2021, 2149-9144, 7, 1, 25-28.

[5] A. EVCIN, H. GÜNEY & N. ÇIÇEK BEZIR, Sol-gel Preparation of Silan based Zirconia Hybrid Thin Film, International Journal of Computational and Experimental Science and Engineering, 2021, 2149-9144, 7, 1, 9-12.

[6] A. EVCIN, E. ARLI, Z. BAZ, R. ESEN & E. G. SEVER, Characterization of Ag-TiO2 Powders Prepared by Sol-Gel Process, ACTA PHYSICA POLONICA A, 2017, 0587-4246, 132, 3, 608-611

[7] N. C. BEZIR, A. EVCIN, R. KAYALI, M. K. OZEN & K. ESEN, Comparison of Five-Layered ZrO2 and Single-Layered Ce, Eu, and Dy-Doped ZrO2 Thin Films Prepared by Sol-Gel Spin Coating Method, ACTA PHYSICA POLONICA A, 2017, 0587-4246, 132, 3, 612-616.

[8] N. C. BEZIR, A. EVCIN, R. KAYALI, M. K. OZEN & G. BALYACI, Comparison of Pure and Doped TiO2 Thin Films Prepared by Sol-Gel Spin-Coating Method, ACTA PHYSICA POLONICA A, 2017, 0587-4246, 132, 3, 620-624.

[9] Roa, Ricardo & Roa Bohórquez, Karol & Castro, H & Rodriguez, G. (2019). Characterization of commercial luminescent powders. Journal of Physics: Conference Series. 1386. 012106. 10.1088/1742-6596/1386/1/012106.

[10] Gnidakouong J and Yun G 2019 Dislocation density level induced divergence between stress-free afterglowand mechanoluminescence in SrAl2O4:Eu2+, Dy3+ Ceram. Int. 45(2) 1794

[11] Matsuzawa T, Aoki Y, Takeuchi N, and Murayama 1996 A new long phosphorescent phosphor with highbrightness, SrAl2 O 4: Eu2+, Dy3+.Journ. Electro. Soci. 143(8) 2670

[12] Abumelha, Hanna. (2021). Simple production of photoluminescent polyester coating using lanthanide-doped pigment. Luminescence. 36. 10.1002/bio.4030.

[13] Khoroshko, Liudmila & Gaponenko, N. & Tumilovich, M. & Kravtsov, A.. (2020). Sol-gel derived nanostructured powders and combined luminescent coatings based on them.

Sol-jel Yöntemiyle Kumaşların Antibakteriyel Kaplanması

Mustafa Uçar

Afyon Kocatepe Üniversitesi, Fen Edebiyat Fakültesi, Kimya Bölümü Afyonkarahisar, Turkiye, ucarm@aku.edu.tr

Abstract

In this study, Titanium dioxide coating was made on cotton fabric with sol-gel technique at low temperatures below 150 °C. A study was carried out on the photocatalytic activity of the titanium coated fabric on its antibacterial properties. In the SEM analysis examination, it was observed that titanium dioxide was throughout the layer. The spherical Titanium microstructure could be observed throughout the diameter of 20 nm. The study was carried out on titanium coated material with UV effect. As a result of XRD analysis, small phases were found throughout the Titanium coated layer.

Keywords: Photocatalytic, TiO_2, Cotton, Sol-gel

1. Giriş

Yüzey işleme teknikleri, hem kimyasal hem de fiziksel yöntemlerle uygulanan kaplamaları içerir. Endüstride yüzeylerin modifikasyonunu ve fonksiyonelleştirilmesine yönelik yeni teknikler büyük önem kazanmıştır. Yüzey kaplama, bir malzemenin en dış yüzeyine uygulanan bir kaplama olarak tanımlanabilirken, yüzey modifikasyonu en iyi özelliklere sahip olacak şekilde dış yüzeyin doğasını değiştirmek olarak tanımlanır. Literatürde malzemelerin yüzeylerini korumak için çok çeşitli kaplama yöntemlerivardır. Bu koruyucu tabaka farklı amaçlar için uygulanabilir. Bunlar arasında estetik, korozyon, aşınma, sürtünme, hidrofilik veya hidrofobik, optik, elektriksel işlevin geliştirilmesi gibi amaçlarla uygulanır. Bugüne kadar, fiziksel/kimyasal buhar biriktirme, mikro ark oksidasyonu, sol-jel, termal püskürtme ve elektrobiriktirme gibi çok sayıda proses araştırılmıştır. Bu işlemlerin her biri avantaj ve dezavantajlara sahiptir. Uygulanacak malzeme ve yerine göre bu kaplama yöntemlerinden birisi seçilir [1-2].

Sol-jel prosesi, organik ve inorganik malzeme hazırlamak için kolloidal ortamda yaş bir kimyasal metoddur. Bu proseste başlangıç maddeleri (alkoksit ve metal tuzları) alkollerde çözündükten sonra jel haline getirilir. Jelin kurutulması sonucu katı forma dönüştürülür. Sol-jel prosesi, kaplama, ince film, nanolif, mikronaltı tozlar ve monolitler oluşturmak amacıyla tercih edilir [3-5].

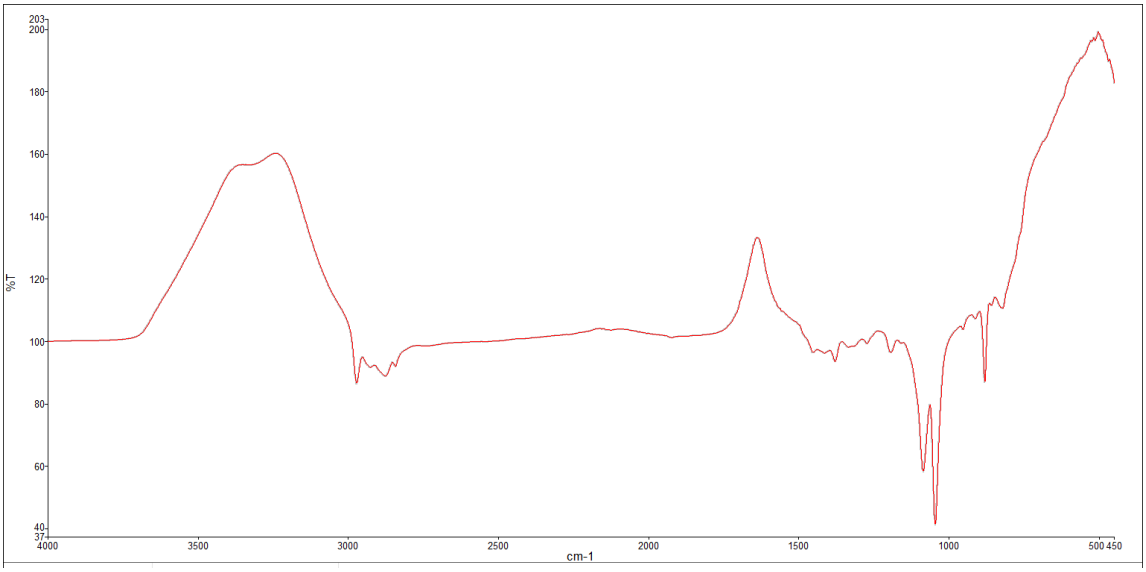
Tekstil sektöründe kumaş, halı, döşeme, iş kıyafetlerinde su, yağ ve kir iticiliği sağlayan kaplamalarda sol-jel tekniği en yaygın kullanılan metodlardandır. Halılarda esneklik ve leke tutmazlık için poli(metakrilik asit) (PMMA), hidrofobiklik için tetraetilortosilikat (TEOS) ve su/kir tutmazlık için floroalkilsilan (FAS) bileşiklerinin kaplamaları incelenmiştir [5]. 3-(glisidoksipropil)trimetoksisilan (GLYMO) kaplama, yünlü kumaşın sıcak

yıkanması sırasında keçeleşmesini önlemiştir. Titanyumdioksit içerikli kaplamalar fotokatalitik uygulamalar ve antibakteriyel özellik kazandırmak için uygulanmıştır [5].

2. Materials and Method

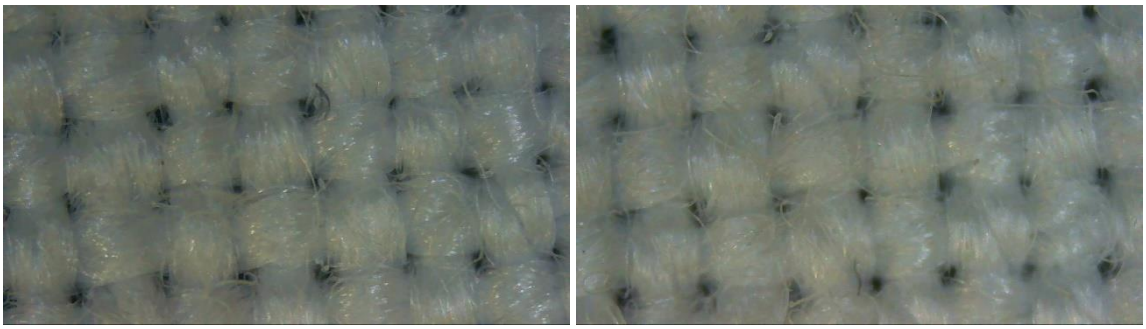
3-(glisidoksipropil)trimetoksisilan (GLYMO), Titanium tetraizopropoksit (TTIP), mutlak etanol, gliserin analitik saflıkta olup, herhangi bir işlem uygulanmadan direk kullanılmıştır. Kaplama çözeltisi GLYMO, TTIP, etanol ve gliserin karışımından oluşturulmuştur. Ultrasonik karıştırıcıda 15 dakika karıştırılan çözelti kumaş yüzeyine 0,8 mm nozul çapına sahip sprey tabancasıyla püskürtme yöntemiyle uygulanmıştır. Oda sıcaklığında kurutulan kumaşlar etüvde 120°C'de 1 saat bekletilmiştir. Daha sonra FTIR ve kaplama tabakasının kumaş liflerine bağlanma yapısını görmek için dijital mikroskop ile karakterizasyonu yapılmıştır.

3. Results and Discussion

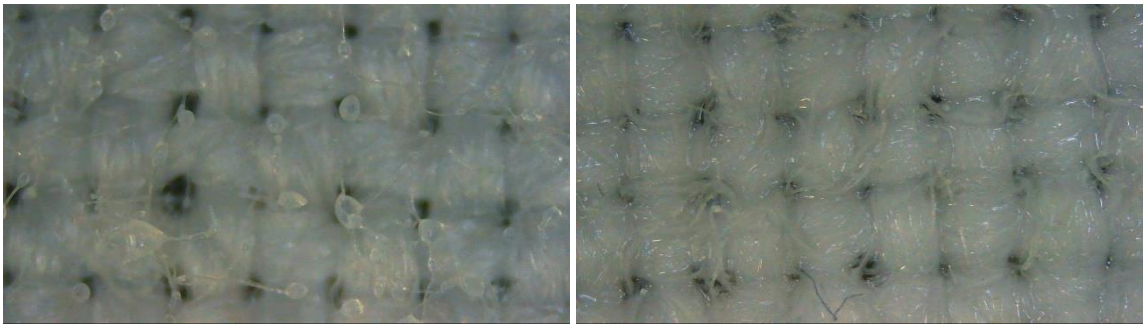


Şekil 1. Kaplama çözeltisinin FTIR analizi

Şekil 1'den de görülebileceği gibi GLYMO, hem hidrolize hem de yoğuşmaya neden olabilen epoksi- ve metoksi-silil olmak üzere iki fonksiyonel grup içerir. FTIR spektrumundaki epoksi bandı korunurken Si–O–Me bandının yoğunluğu azaltılır. Si–O–Me gruplarının hidrolizi nedeniyle OH grubu bandı 3000 cm^{-1}'de görünür. Ayrıca, 1050 cm^{-1}'de Si–O–Si bağlarının oluşumuna atanabilecek bir tepe noktası belirir [6]. Si-O-Si'nin karakteristik pikleri 1100 cm^{-1} ve 800 cm^{-1} dalga sayılarında mevcuttur. Si-O-R ve Si-O piki 1045 cm^{-1} 'de gözlendi. Ayrıca, bu durumda 950 cm^{-1}'lik bir dalga sayısında yeni bir karakteristik zirve meydana gelir ve bu, yeni Ti-O-Si bağlarının oluşumunu gösterir [7].



Şekil 2. Kaplanmamış kumaşın görüntüsü



Şekil 3. Kaplanmış kumaşın görüntüsü

Şekil 2 ve 3 'ün kıyaslanmasından kumaş lifleri üzerindeki kaplama çözeltisinin varlığı görülmektedir. Şekil 3 de soldaki resimde tek kat kaplama, sağdaki resimde ise 3 kat kaplama görülmektedir. Buna göre 3 kat kaplama daha homojen ve tüm liflere nüfuz etmiş durumdadır.

Antibakteriyel analiz için zon çapları ölçülmüştür. Bu amaçla gram negatif ve gram pozitif bakteriler kullanılmıştır. Analiz sonucu Tablo 1 'de verilmiştir.

Tablo 1. Numunelerin zon çapı değerleri.

Numune Adı	*E.coli* (zon çapı) (gram-negatif)	*S.aureus* (zon çapı) (gram-pozitif)
Saf kumaş	-	-
GLYMO-TiO_2 Çözeltisiyle kaplı kumaş	13 mm	15 mm

Tablo 1'den de görüldüğü gibi antibakteriyel özelliğe sahip olmayan kumaş, kaplama GLYMO ve TiO2 içeren kaplama çözeltisiyle kaplandığında hem E.coli ve hem de S. Aureus'a karşı etkili olduğunu göstermiştir.

References

[1] John H. Dumbleton, Paul Higham, Coating and Surface Modification, CRC Press, 1984

[2] Fotovvati, Behzad & Namdari, Navid & Dehghanghadikolaei, Amir. (2019). On Coating Techniques for Surface Protection: A Review. 3. 10.3390/jmmp3010028.

[3] Wang, D.; Bierwagen, G.P. Sol–gel coatings on metals for corrosion protection. Prog. Org. Coat. 2009, 64,327–338.

[4] Zheludkevich, M.; Salvado, I.M.; Ferreira, M. Sol–gel coatings for corrosion protection of metals.J. Mater. Chem. 2005, 15, 5099–5111

[5] McNeil, Steve & Standard, Owen & Pailthorpe, Mike. (2005). Hybrid Organic-Inorganic Coatings For Wool Textiles.

[6] Halbus, Ahmed & Horozov, Tommy & Paunov, Vesselin N. (2019). Self-grafting copper oxide nanoparticles show a strong enhancement of their anti-algal and anti-yeast action. Nanoscale Advances. 1. 10.1039/C9NA00099B.

[7] Kaygusuz, Meruyert. (2019). Sol-Gel Synthesis of TiO2-SiO2-GlYMO Nanocomposite. Revista Romana de materiale = Romanian journal of materials = RRM. 49. 179 - 184.

Symposium Pictures






SPA HOTEL




ÖZGE TOPLANTI SALONU




ISC'22
22-25
September
2022
AFYONKARAHISAR
TURKEY
TÜBİTAK
MAM
NED
UNIVERSITY OF
ENGINEERING & TECHNOLOGY
GİRESUN ÜNİVERSİTESİ
2006
Evcin ArGe
2022/09/24 15:47




2022/09/25 14:45




DATE
22-25
September


2nd International Symposium on Characterization ISC'22
CERTIFICATE
of Appreciation
Fayaz Hussain
INVITED SPEAKER


2nd International Symposium on Characterization ISC'22
CERTIFICATE
of Appreciation
Award for the best (third) poster presentation to
Hammad Siddiqui


2nd International Symposium on Characterization ISC'22
CERTIFICATE
of Appreciation
Award for the best (third) oral presentation to
Beyza Kasal


2nd International Symposium on Characterization ISC'22
CERTIFICATE
of Appreciation
Cenk Aktaş
INVITED SPEAKER
DATE
22-25


2nd International Symposium on Characterization ISC'22
CERTIFICATE
of Appreciation
Hakan Ünsal
DATE
22-25


CERTIFICATE
of Appreciation
Salih Vezircioğlu
INVITED SPEAKER


2nd International Symposium on Characterization ISC'22
CERTIFICATE
of Appreciation
Award for the best (second) poster presentation
Yusuf Karaca

==========

SPONSORS

AnkaAnalitik
Mekatronik Sanayi ve Ticaret LTD.ŞTİ.

Tales Analitik
Limited Şirketi

1968'den Günümüze
ORUÇOĞLU®

Evcin ArGe
Mühendislik Danışmanlık Organizasyon Sanayi Tic. Ltd. Şti.

AFYONKARAHİSAR BELEDİYESİ
www.afyon.bel.tr

A

Abdul Vahap Korkmaz, 371
Abdul Vahap KORKMAZ, 354
Abdulkadir Sirit, 187
Abdullah Alawadhi, 339
Ahmet B. BATIBAY, 332
Andaç Akdemir, 81
Andaç AKDEMİR, 295
Arham Iqbal khan, 216
Arslan Can MARTOĞLU, 295
Atila Gürhan Celik, 152, 166, 253, 313
Atilla Evcin, 317, 323, 339, 350, 382
Ayşegül BODUR YILMAZ, 270

B

Ben Ammar Ben Khadda, 111
Büşra Alomar, 317

C

Cem TANYERİ, 35
Cenk TÜRKÜZ, 196

D

Darob M. Berdiev, 326
Doğuş ÖZKAN, 196

E

Ediz Ercenk, 93
Erdoğan KANCA, 115
Esra Tavukçuoğlu, 93

F

Fatih Acer, 261
Furkan Günday, 70, 280
Furkan Şen, 225, 241

G

Gökhan Akarca, 339
Gözde ZÜBARİOĞLU, 115
Gürol Yıldırım, 22, 44, 137, 170

H

Hakan Burak Karadağ, 101
Hakan Çiftçi, 345
Hasan KOTAN, 332
Hayri Metin Numanoğlu, 225, 241

İ

İbrahim Günes, 152, 166, 253, 313
İsmail Hakki KARAHAN, 115

M

Mahmudova Rasmiyya Sharif, 257
Mehmet DEMİR, 115
Muhammed İhsan Özgün, 101, 326
Musa Demir, 241
Mustafa Uçar, 355, 387
Mürsel Ekrem, 63
Müşerref Rana Kavuncu, 63

N

Nada ALLOUSH, 350

O

Orçun YÖNTEM, 270
Ozan DEVLEN, 35

R

Ravshan K. Toshmatov, 326
Recep KURTULUŞ, 234
Resul Kazanbaş, 81

S

S. Bahar Baştürk, 261
Salim Erol, 88
Seçil Çelik Erbaş, 261
Seda ATAŞ BAKDEMİR, 196
Sedef Arslan, 88
Serdar SALMAN, 196
Sertaç Tuhta, 156, 304
Shafagat MAHMUDOVA, 267
Syed Sajjad Ali, 216

Ş

Şenol ŞAHİN, 270
Şenol Yılmaz, 93

T

Taner KAVAS, 234
Tuba BAHTLI, 204
Turakhodjayev Nodir, 290
Tursunbaev Sarvar, 290

U

Ummu Ozgun, 187

V

Veysel Murat BOSTANCI, 204

Y

Yasin Ramazan Eker, 101
Yoncagül ÇELİK EREZ, 35

Z

Zeynep Özkan, 345